

NPS ARCHIVE
1998.06
SPECKHAHN, M.

DUDLEY KNOX LIBRARY
NAVAL POSTGRADUATE SCHOOL
MONTEREY CA 93943-5101

NAVAL POSTGRADUATE SCHOOL MONTEREY, CALIFORNIA



THESIS

**IDENTIFICATION OF ACOUSTICALLY ACTIVE ARCTIC
PRESSURE RIDGES THROUGH THE USE OF RADARSAT
GEOPHYSICAL PROCESSOR SYSTEM (RGPS) SEA ICE
PRODUCTS**

by

Marcus M. Speckhahn

June, 1998

Thesis Co-Advisors:

Robert H. Bourke
James H. Wilson

Second Reader:

Peter S. Guest

Approved for public release; distribution is unlimited

REPORT DOCUMENTATION PAGE

Form Approved
OMB No. 0704-0188

Public reporting burden for this collection of information is estimated to average 1 hour per response, including the time for reviewing instruction, searching existing data sources, gathering and maintaining the data needed, and completing and reviewing the collection of information. Send comments regarding this burden estimate or any other aspect of this collection of information, including suggestions for reducing this burden, to Washington headquarters Services, Directorate for Information Operations and Reports, 1215 Jefferson Davis Highway, Suite 1204, Arlington, VA 22202-4302, and to the Office of Management and Budget, Paperwork Reduction Project (0704-0188) Washington DC 20503.

1. AGENCY USE ONLY (Leave blank)		2. REPORT DATE June 1998	3. REPORT TYPE AND DATES COVERED Master's Thesis	
4. TITLE AND SUBTITLE Identification of Acoustically Active Arctic Pressure Ridges through the Use of RADARSAT Geophysical Processor System (RGPS) Sea Ice Products			5. FUNDING NUMBERS	
6. AUTHOR(S) Marcus M. Speckhahn				
7. PERFORMING ORGANIZATION NAME(S) AND ADDRESS(ES) Naval Postgraduate School Monterey, CA 93943-5000			8. PERFORMING ORGANIZATION REPORT NUMBER	
9. SPONSORING / MONITORING AGENCY NAME(S) AND ADDRESS(ES)			10. SPONSORING / MONITORING AGENCY REPORT NUMBER	
11. SUPPLEMENTARY NOTES The views expressed in this thesis are those of the author and do not reflect the official policy or position of the Department of Defense or the U.S. Government.				
12a. DISTRIBUTION / AVAILABILITY STATEMENT Approved for public release; distribution is unlimited.			12b. DISTRIBUTION CODE	
13. ABSTRACT (maximum 200 words) The identification of acoustically active pressure ridges in the Arctic Ocean represents an important step in the development of a physics-based, operational Polar ambient noise model. One method to accomplish this goal is through the use of satellite-based remote sensors, specifically synthetic aperture radar (SAR). A proof-of concept study was conducted that determined that the RADARSAT Geophysical Processor System (RGPS), currently being developed at NASA JPL, Pasadena, CA, produces SAR-derived sea ice products capable of quantifying large-scale ice deformation that may produce significant levels of low frequency ambient noise. This research also identifies the meteorological forcing that causes the sequence of divergent and convergent events in the ice cover, which results in the creation of open water leads and subsequent generation of noisy pressure ridges. Offshore followed by onshore winds near coasts and land-fast ice and atmospheric lows/troughs followed by atmospheric highs/ridges or velocity shear in straight isobaric flow result in significant pressure ridge formation. The RGPS ridging algorithm shows that more ridges exist in RGPS cells exhibiting large cell area changes than in those with small area changes, assuming relatively constant sail heights in all cells. The feasibility of using ice divergence fields generated by Fleet Numerical Meteorology and Oceanography Center's (FNMOC's) Polar Ice Prediction System (PIPS) was evaluated. PIPS modeled ice divergence patterns reasonably well, although divergence values in the high Arctic ice cover were underestimated.				
14. SUBJECT TERMS Polar Oceanography, Pressure Ridges, Open Water Leads, Ice Deformation, Synthetic Aperture Radar, RADARSAT Geophysical Processor System, Polar Ice Prediction System, Low Frequency Ambient Noise, Arctic Submarine Operations, Remote Sensing.			15. NUMBER OF PAGES 333	
			16. PRICE CODE	
17. SECURITY CLASSIFICATION OF REPORT Unclassified	18. SECURITY CLASSIFICATION OF THIS PAGE Unclassified	19. SECURITY CLASSIFICATION OF ABSTRACT Unclassified	20. LIMITATION OF ABSTRACT UL	

NSN 7540-01-280-5500

Standard Form 298 (Rev. 2-89)
Prescribed by ANSI Std. Z39-18 298-102

Approved for public release; distribution is unlimited

**IDENTIFICATION OF ACOUSTICALLY ACTIVE ARCTIC PRESSURE RIDGES
THROUGH THE USE OF RADARSAT GEOPHYSICAL PROCESSOR SYSTEM
(RGPS) SEA ICE PRODUCTS**

Marcus M. Speckhahn
Lieutenant Commander, United States Navy
B.S., State University of New York Maritime College, 1988

Submitted in partial fulfillment of the
requirements for the degree of

**MASTER OF SCIENCE IN METEOROLOGY AND PHYSICAL
OCEANOGRAPHY**

from the

**NAVAL POSTGRADUATE SCHOOL
June 1998**

ABSTRACT

The identification of acoustically active pressure ridges in the Arctic Ocean represents an important step in the development of a physics-based, operational Polar ambient noise model. One method to accomplish this goal is through the use of satellite-based remote sensors, specifically synthetic aperture radar (SAR).

A proof-of concept study was conducted that determined that the RADARSAT Geophysical Processor System (RGPS), currently being developed at NASA JPL, Pasadena, CA, produces SAR-derived sea ice products capable of quantifying large-scale ice deformation that may produce significant levels of low frequency ambient noise.

This research also identifies the meteorological forcing that causes the sequence of divergent and convergent events in the ice cover, which results in the creation of open water leads and subsequent generation of noisy pressure ridges. Offshore followed by onshore winds near coasts and land-fast ice and atmospheric lows/troughs followed by atmospheric highs/ridges or velocity shear in straight isobaric flow result in significant pressure ridge formation.

The ridging algorithm shows that more ridges exist in RGPS cells exhibiting large cell area changes than in those with small area changes, assuming relatively constant sail heights in all cells.

The feasibility of using ice divergence fields generated by Fleet Numerical Meteorology and Oceanography Center's (FNMOC's) Polar Ice Prediction System (PIPS) was evaluated. PIPS modeled ice divergence patterns reasonably well, although divergence values in the high Arctic ice cover were underestimated.

TABLE OF CONTENTS

I. INTRODUCTION	1
A. POLITICAL/NAVAL CONTEXT.....	1
B. RESEARCH OBJECTIVES	1
1. Background.....	1
2. Ambient Noise Modeling Efforts.....	2
3. Long Term Research Goals	2
4. Thesis Objectives.....	3
C. SOURCES OF ARCTIC AMBIENT NOISE	4
II. THE POLAR ICE PREDICTION SYSTEM (PIPS)	7
A. BACKGROUND.....	7
B. MODEL DESCRIPTION	7
1. Momentum Balance Equation.....	7
2. Ice Rheology.....	8
3. Ice Thickness Distribution	9
4. Ice Strength	9
5. Heat Budget.....	9
C. MODEL GRID.....	10
D. MODEL FORCING.....	10
E. PIPS INITIALIZATION	10
F. MODEL WEAKNESSES.....	11
III. THE SYNTHETIC APERTURE RADAR (SAR).....	13
A. SAR SENSOR THEORY	13
B. BRIEF HISTORY OF THE SAR SENSOR	15
1. SAR Technology	15
2. Spaceborne SAR Sensors	16
C. SAR SENSORS	16
1. ERS-1.....	17

	a. General.....	17
	b. SAR Sensor	17
2.	RADARSAT-1.....	17
	a. General.....	17
	b. SAR Sensor	18
3.	JERS-1	18
	a. General.....	18
	b. SAR Sensor	18
4.	ERS-2	18
D.	SAR DATA COLLECTION EFFORT	19
	1. Raw SAR Imagery Versus Derived Geophysical Products.....	19
	2. ERS-1 Versus RADARSAT-1 Data.....	20
IV.	THE RADARSAT GEOPHYSICAL PROCESSOR SYSTEM (RGPS)	21
	A. ACKNOWLEDGEMENTS.....	21
	B. INTRODUCTION.....	21
	C. MISSION PLANNING AND DATA ACQUISITION	21
	D. RGPS PRODUCT BACKGROUND.....	22
	1. Product Format.....	22
	2. RGPS Sea Ice Products	22
	3. Station Masks	23
	4. Spatial Resolution	23
	5. Temporal Resolution	24
	6. The RGPS Working Group.....	24
	E. THE RGPS SEA ICE ALGORITHMS	24
	1. Introduction.....	24
	2. Lagrangian Ice Motion	25
	3. Ice Age/Thickness Distribution.....	25
	a. Ice Age Calculations.....	25
	b. Ice Thickness Calculations.....	26
	c. Ridge Thickness Calculations.....	27
	4. Ice Deformation Products	27
	5. Other RGPS Products.....	28
	6. Measurement Errors.....	28
V.	DATA ANALYSIS.....	29

A.	BACKGROUND.....	29
B.	DATA SETS.....	30
	1. RGPS Deformation Data.....	30
	2. NOGAPS Meteorological Data	32
	3. PIPS Data.....	35
	4. RGPS Ridging Algorithm Data	35
	5. Ambient Noise Data	35
C.	GENERAL OBSERVATIONS.....	35
D.	COMPARISON OF RGPS DEFORMATION TO NOGAPS METEOROLOGICAL DATA.....	37
	1. Analysis Technique	37
	a. General.....	37
	b. Meteorological Variables Investigated.....	38
	(1) On/offshore Flow of the Surface (10 m) Wind	38
	(2) Wind Divergence.....	38
	(3) Advection of the 10 m Wind Divergence	39
	(4) NOGAPS Model Ice Divergence.....	39
	2. Analysis Results	40
	a. Area A Analysis Observations.....	40
	b. Area B Analysis Observations.....	43
	c. General Observations and Conclusions.....	50
E.	ANALYSIS USING THE RGPS RIDGING ALGORITHM.....	52
	1. Ridging Algorithm Plotting Features	52
	2. General Observations	56
	3. Ridging Characteristics for Area A.....	56
	4. Ridging Characteristics for Area B	61
	5. Conclusions.....	65
F.	COMPARISON OF PIPS AND NOGAPS MODEL ICE DIVERGENCE FIELDS	65
	1. Background.....	65
	2. Analysis Technique	66
	3. Analysis of Specific Locations.....	71
	4. Analysis Discussion.....	75
	a. Ice Divergence Comparison at Point 1 (74°N/155°E)	75
	b. Ice Divergence Comparison at Point 2 (71°N/150°W).....	79
	c. Ice Divergence Comparison at Point 3 (78°N/155°W).....	81
	d. Ice Divergence Comparison at Point 4 (76°N/175°W).....	87

5.	Analysis Conclusions	88
VI.	CONCLUSIONS AND RECOMMENDATIONS	91
A.	CONCLUSIONS.....	91
B.	RECOMMENDATIONS.....	92
APPENDIX A.	RGPS DEFORMATION PRODUCT ANALYSIS OF AREA A AND COMPARISON TO NOGAPS METEOROLOGICAL DATA.....	95
APPENDIX B.	RGPS DEFORMATION PRODUCT ANALYSIS OF AREA B AND COMPARISON TO NOGAPS METEOROLOGICAL DATA.....	103
APPENDIX C.	CYCLE 15 RGPS SEA ICE DEFORMATION PRODUCTS: PERCENT CELL AREA CHANGE	113
APPENDIX D.	CYCLE 15 RGPS SEA ICE DEFORMATION PRODUCTS: ICE SHEAR.....	121
APPENDIX E.	NOGAPS METEOROLOGICAL DATA FOR RGPS ANALYSIS PERIOD: 07-24 NOVEMBER 1996	129
APPENDIX F.	NOGAPS MODEL ICE DIVERGENCE DATA FOR RGPS ANALYSIS PERIOD: 07-24 NOVEMBER 1996	167
APPENDIX G.	PIPS ICE DIVERGENCE DATA: 13 FEBRUARY-31 MARCH 1998.....	205
APPENDIX H.	NOGAPS MODEL ICE DIVERGENCE DATA: 13 FEBRUARY-31 MARCH 1998..	253
	LIST OF REFERENCES.....	301
	INITIAL DISTRIBUTION LIST	305

LIST OF FIGURES

1. Basic schematic of SWATH SAR imaging geometry from an airborne platform (from Sandia National Laboratories, 1997).....13
2. ERS-1 SAR image showing the complexity of this type of imagery. Dark patches represent young ice in open water leads, while lighter areas represent older ice types (from Alaska SAR Facility, 1998).....19
3. “Ideal” thesis process flow diagram possible if all data sets had been coincident in time. Numbers represent the sequence of research steps.29
4. Actual thesis process flow diagram. The isolation of an “intermediate” meteorological variable was necessary because the RGPS and PIPS data sets were not coincident in time. Numbers represent the sequence of research steps.....30
5. Sample graphic showing output of the RGPS percent cell area change sea ice product. Red, orange and yellow cells are undergoing ice divergence (opening), while green and blue cells are experiencing ice convergence (closing). Light green cells are experiencing little deformation. Numbers in legend represent percentages of cell area change over the snapshot temporal resolution, approximated to be three days. The two investigated areas, A and B, are also depicted.31
6. Sample chart of NOGAPS meteorological data. Blue wind barbs are $2.5^{\circ} \times 2.5^{\circ}$ 10 m winds (knots), red lines are mean sea level pressure (MSLP) isobars (mb), yellow lines are air temperature ($^{\circ}\text{C}$) isotherms, green solid lines are isolines of 10 m wind divergence ($\times 10^{-5} \text{ s}^{-1}$), green dashed lines are isolines of 10 m wind convergence ($\times 10^{-5} \text{ s}^{-1}$).....33
7. Sample chart showing NOGAPS model ice divergence. Solid contours show ice divergence ($\times 10^{-7} \text{ s}^{-1}$) and dashed contours show ice convergence ($\times 10^{-7} \text{ s}^{-1}$). Grid point wind barbs are rotated 28° to the right from the 10 m wind direction. The wind barbs show the direction of ice drift, but the velocity feathers on this product are meaningless.34
8. View of two rapidly opening strain-hardened intersecting leads with preferred values of θ36
9. Wind and ice con/divergence associated with low (L) and high (H) pressure systems. The circles represent an idealized closed isobar around the system center. Big arrowheads on circles represent the geostrophic wind direction. Dashed arrows show surface wind convergence into a low pressure system and out of a high pressure system due to friction and continuity. Solid arrows depict the ice divergence associated with

the wind divergence patterns. The ice drifts 28° to the right of the surface wind vector. Ice convergence is associated with atmospheric highs and ice divergence with atmospheric lows.....	40
10. RGPS percent cell area change product for 10-12 Nov 96, showing the creation of open water leads (arrow) during the first (divergent) phase of active acoustic ridge formation.	44
11. RGPS percent cell area change product for 13-15 Nov 96, showing the creation of an acoustically active pressure ridge (arrow) during the second (convergent) phase of active acoustic ridge formation.	45
12. RGPS shear product for 10-12 Nov 96, showing that little shear deformation is associated with the divergent phase of the pressure ridge formation (arrow).	46
13. RGPS shear product for 13-15 Nov 96, showing that little shear deformation is associated with the convergent phase of the pressure ridge formation (arrow).....	47
14. RGPS percent cell area change product for 19-21 Nov 96. The deformation depicted here is explained very well by the NOGAPS model ice divergence product.	49
15. RGPS percent cell area change product for 07-09 Nov 96. This chart shows net closing in one three-day snapshot period that was not preceded by opening in a previous image. The deformation data may still represent a short ridging event.	51
16. RGPS ridging algorithm output for area B. The ice in cell #1 undergoes two distinct ridging events, while only one occurs in cell #2.....	53
17. RGPS ridging algorithm output for area A. The ice cover in cell #3 undergoes only convergence during the observation period. No new ice or pressure ridges are created.	55
18. Four data streams containing RGPS ridging algorithm output for the cycle 15 analysis period. Areas “A” and “B,” discussed in previous sections are depicted.	57
19. RGPS ridging algorithm output for area A. Ridges of two different thicknesses are created in the second ridging event inside cell #4, as depicted by the two yellow horizontal bars in the bottom graph.....	58
20. RGPS ridging algorithm output for area A. Only one major ridging event takes place in cells #5 and #6.....	60

21. RGPS ridging algorithm output for highly deformed cells in area B. Cell #7 undergoes short deformation events, while cell #8 is subjected to longer ones. Cell #12 represents another highly active cell.	62
22. RGPS ridging algorithm output for “benign” cells in area B. Cells #9 through #11 display little area change over the observation period.	63
23. PIPS vs. NOGAPS Model Ice Divergence - Point 1 (74N/155E in Area A).	67
24. PIPS vs. NOGAPS Model Ice Divergence - Point 2 (71N/150W).	68
25. PIPS vs. NOGAPS Model Ice Divergence - Point 3 (78N/150W in Area B).	69
26. PIPS vs. NOGAPS Model Ice Divergence - Point 4 (76N/175W).	70
27. Geographic locations of the two RGPS data areas and the four points investigated for the PIPS-NOGAPS model ice divergence correlation.	72
28. NIC weekly ice analysis for 16-20 Feb 98, showing the location of point 1 in the flaw lead of the East Siberian Sea. It is classified as land-fast ice at this time as indicated by the “8” in the bottom section of the corresponding “egg code”.	73
29. NIC weekly ice analysis for 23-27 Feb 98, showing the location of point 2 off the coast of Alaska in the Beaufort Sea. It is also classified as land-fast ice at this time.	74
30. 10 m NOGAPS Wind Speed, 07-18 Nov 96 at point 1 (74N/155E).	77
31. 10 m NOGAPS Wind Speed, 13 Feb-31 Mar 98 at point 1 (74N/155E).	78
32. PIPS model ice drift analysis for 19 Feb 98, showing the normal anti-cyclonic rotation of the Beaufort Gyre. Ice speeds are 3.7 km/day at point 1 and 29.6 km/day at point 2. Points located at ends of arrow heads.	82
33. PIPS model ice drift analysis for 10 Mar 98, showing the reversed flow of the Beaufort Gyre. Ice speeds are 3.7 km/day at point 1 and 1.9 km/day at point 2. Points located at ends of arrow heads.	83
34. 10 m NOGAPS Wind Speed, 07-24 Nov 96 at point 3 (78N/150W).	85
35. 10 m NOGAPS Wind Speed, 13 Feb-31 Mar 98 at point 3 (78N/150W).	86
36. RGPS cycle 15 percent cell area change product for 07 to 09 Nov 96.	114
37. RGPS cycle 15 percent cell area change product for 10 to 12 Nov 96.	115

38. RGPS cycle 15 percent cell area change product for 13 to 15 Nov 96.....	116
39. RGPS cycle 15 percent cell area change product for 16 to 18 Nov 96.....	117
40. RGPS cycle 15 percent cell area change product for 19 to 21 Nov 96.....	118
41. RGPS cycle 15 percent cell area change product for 22 to 24 Nov 96.....	119
42. RGPS cycle 15 ice shear product for 07 to 09 Nov 96.....	122
43. RGPS cycle 15 ice shear product for 10 to 12 Nov 96.....	123
44. RGPS cycle 15 ice shear product for 13 to 15 Nov 96.....	124
45. RGPS cycle 15 ice shear product for 16 to 18 Nov 96.....	125
46. RGPS cycle 15 ice shear product for 19 to 21 Nov 96.....	126
47. RGPS cycle 15 ice shear product for 22 to 24 Nov 96.....	127
48. NOGAPS meteorological data for 0000Z 07 Nov 96.....	130
49. NOGAPS meteorological data for 1200Z 07 Nov 96.....	131
50. NOGAPS meteorological data for 0000Z 08 Nov 96.....	132
51. NOGAPS meteorological data for 1200Z 08 Nov 96.....	133
52. NOGAPS meteorological data for 0000Z 09 Nov 96.....	134
53. NOGAPS meteorological data for 1200Z 09 Nov 96.....	135
54. NOGAPS meteorological data for 0000Z 10 Nov 96.....	136
55. NOGAPS meteorological data for 1200Z 10 Nov 96.....	137
56. NOGAPS meteorological data for 0000Z 11 Nov 96.....	138
57. NOGAPS meteorological data for 1200Z 11 Nov 96.....	139
58. NOGAPS meteorological data for 0000Z 12 Nov 96.....	140
59. NOGAPS meteorological data for 1200Z 12 Nov 96.....	141

60. NOGAPS meteorological data for 0000Z 13 Nov 96.....	142
61. NOGAPS meteorological data for 1200Z 13 Nov 96.....	143
62. NOGAPS meteorological data for 0000Z 14 Nov 96.....	144
63. NOGAPS meteorological data for 1200Z 14 Nov 96.....	145
64. NOGAPS meteorological data for 0000Z 15 Nov 96.....	146
65. NOGAPS meteorological data for 1200Z 15 Nov 96.....	147
66. NOGAPS meteorological data for 0000Z 16 Nov 96.....	148
67. NOGAPS meteorological data for 1200Z 16 Nov 96.....	149
68. NOGAPS meteorological data for 0000Z 17 Nov 96.....	150
69. NOGAPS meteorological data for 1200Z 17 Nov 96.....	151
70. NOGAPS meteorological data for 0000Z 18 Nov 96.....	152
71. NOGAPS meteorological data for 1200Z 18 Nov 96.....	153
72. NOGAPS meteorological data for 0000Z 19 Nov 96.....	154
73. NOGAPS meteorological data for 1200Z 19 Nov 96.....	155
74. NOGAPS meteorological data for 0000Z 20 Nov 96 (data missing).....	156
75. NOGAPS meteorological data for 1200Z 20 Nov 96.....	157
76. NOGAPS meteorological data for 0000Z 21 Nov 96.....	158
77. NOGAPS meteorological data for 1200Z 21 Nov 96.....	159
78. NOGAPS meteorological data for 0000Z 22 Nov 96.....	160
79. NOGAPS meteorological data for 1200Z 22 Nov 96.....	161
80. NOGAPS meteorological data for 0000Z 23 Nov 96.....	162
81. NOGAPS meteorological data for 1200Z 23 Nov 96.....	163

82. NOGAPS meteorological data for 0000Z 24 Nov 96.....	164
83. NOGAPS meteorological data for 1200Z 24 Nov 96.....	165
84. NOGAPS model ice divergence chart for 0000Z 07 Nov 96.	168
85. NOGAPS model ice divergence chart for 1200Z 07 Nov 96.	169
86. NOGAPS model ice divergence chart for 0000Z 08 Nov 96.	170
87. NOGAPS model ice divergence chart for 1200Z 08 Nov 96.	171
88. NOGAPS model ice divergence chart for 0000Z 09 Nov 96.	172
89. NOGAPS model ice divergence chart for 1200Z 09 Nov 96.	173
90. NOGAPS model ice divergence chart for 0000Z 10 Nov 96.	174
91. NOGAPS model ice divergence chart for 1200Z 10 Nov 96.	175
92. NOGAPS model ice divergence chart for 0000Z 11 Nov 96.	176
93. NOGAPS model ice divergence chart for 1200Z 11 Nov 96.	177
94. NOGAPS model ice divergence chart for 0000Z 12 Nov 96.	178
95. NOGAPS model ice divergence chart for 1200Z 12 Nov 96.	179
96. NOGAPS model ice divergence chart for 0000Z 13 Nov 96.	180
97. NOGAPS model ice divergence chart for 1200Z 13 Nov 96.	181
98. NOGAPS model ice divergence chart for 0000Z 14 Nov 96.	182
99. NOGAPS model ice divergence chart for 1200Z 14 Nov 96.	183
100. NOGAPS model ice divergence chart for 0000Z 15 Nov 96.	184
101. NOGAPS model ice divergence chart for 1200Z 15 Nov 96.	185
102. NOGAPS model ice divergence chart for 0000Z 16 Nov 96.	186
103. NOGAPS model ice divergence chart for 1200Z 16 Nov 96.	187

104. NOGAPS model ice divergence chart for 0000Z 17 Nov 96.	188
105. NOGAPS model ice divergence chart for 1200Z 17 Nov 96.	189
106. NOGAPS model ice divergence chart for 0000Z 18 Nov 96.	190
107. NOGAPS model ice divergence chart for 1200Z 18 Nov 96.	191
108. NOGAPS model ice divergence chart for 0000Z 19 Nov 96.	192
109. NOGAPS model ice divergence chart for 1200Z 19 Nov 96.	193
110. NOGAPS model ice divergence chart for 0000Z 20 Nov 96 (data missing).	194
111. NOGAPS model ice divergence chart for 1200Z 20 Nov 96.	195
112. NOGAPS model ice divergence chart for 0000Z 21 Nov 96.	196
113. NOGAPS model ice divergence chart for 1200Z 21 Nov 96.	197
114. NOGAPS model ice divergence chart for 0000Z 22 Nov 96.	198
115. NOGAPS model ice divergence chart for 1200Z 22 Nov 96.	199
116. NOGAPS model ice divergence chart for 0000Z 23 Nov 96.	200
117. NOGAPS model ice divergence chart for 1200Z 23 Nov 96.	201
118. NOGAPS model ice divergence chart for 0000Z 24 Nov 96.	202
119. NOGAPS model ice divergence chart for 1200Z 24 Nov 96.	203
120. PIPS model ice divergence chart for 0000Z 13 Feb 98.	206
121. PIPS model ice divergence chart for 0000Z 14 Feb 98.	207
122. PIPS model ice divergence chart for 0000Z 15 Feb 98 (data missing).	208
123. PIPS model ice divergence chart for 0000Z 16 Feb 98.	209
124. PIPS model ice divergence chart for 0000Z 17 Feb 98.	210
125. PIPS model ice divergence chart for 0000Z 18 Feb 98.	211

126. PIPS model ice divergence chart for 0000Z 19 Feb 98.....	212
127. PIPS model ice divergence chart for 0000Z 20 Feb 98.....	213
128. PIPS model ice divergence chart for 0000Z 21 Feb 98.....	214
129. PIPS model ice divergence chart for 0000Z 22 Feb 98.....	215
130. PIPS model ice divergence chart for 0000Z 23 Feb 98.....	216
131. PIPS model ice divergence chart for 0000Z 24 Feb 98.....	217
132. PIPS model ice divergence chart for 0000Z 25 Feb 98.....	218
133. PIPS model ice divergence chart for 0000Z 26 Feb 98.....	219
134. PIPS model ice divergence chart for 0000Z 27 Feb 98.....	220
135. PIPS model ice divergence chart for 0000Z 28 Feb 98.....	221
136. PIPS model ice divergence chart for 0000Z 01 Mar 98.....	222
137. PIPS model ice divergence chart for 0000Z 02 Mar 98.....	223
138. PIPS model ice divergence chart for 0000Z 03 Mar 98.....	224
139. PIPS model ice divergence chart for 0000Z 04 Mar 98.....	225
140. PIPS model ice divergence chart for 0000Z 05 Mar 98.....	226
141. PIPS model ice divergence chart for 0000Z 06 Mar 98.....	227
142. PIPS model ice divergence chart for 0000Z 07 Mar 98.....	228
143. PIPS model ice divergence chart for 0000Z 08 Mar 98.....	229
144. PIPS model ice divergence chart for 0000Z 09 Mar 98.....	230
145. PIPS model ice divergence chart for 0000Z 10 Mar 98.....	231
146. PIPS model ice divergence chart for 0000Z 11 Mar 98.....	232
147. PIPS model ice divergence chart for 0000Z 12 Mar 98.....	233

148. PIPS model ice divergence chart for 0000Z 13 Mar 98.	234
149. PIPS model ice divergence chart for 0000Z 14 Mar 98 (data missing).....	235
150. PIPS model ice divergence chart for 0000Z 15 Mar 98.	236
151. PIPS model ice divergence chart for 0000Z 16 Mar 98.	237
152. PIPS model ice divergence chart for 0000Z 17 Mar 98.	238
153. PIPS model ice divergence chart for 0000Z 18 Mar 98.	239
154. PIPS model ice divergence chart for 0000Z 19 Mar 98.	240
155. PIPS model ice divergence chart for 0000Z 20 Mar 98.	241
156. PIPS model ice divergence chart for 0000Z 21 Mar 98.	242
157. PIPS model ice divergence chart for 0000Z 22 Mar 98.	243
158. PIPS model ice divergence chart for 0000Z 23 Mar 98.	244
159. PIPS model ice divergence chart for 0000Z 24 Mar 98.	245
160. PIPS model ice divergence chart for 0000Z 25 Mar 98.	246
161. PIPS model ice divergence chart for 0000Z 26 Mar 98.	247
162. PIPS model ice divergence chart for 0000Z 27 Mar 98.	248
163. PIPS model ice divergence chart for 0000Z 28 Mar 98.	249
164. PIPS model ice divergence chart for 0000Z 29 Mar 98.	250
165. PIPS model ice divergence chart for 0000Z 30 Mar 98.	251
166. PIPS model ice divergence chart for 0000Z 31 Mar 98.	252
167. NOGAPS model ice divergence chart for 0000Z 13 Feb 98.	254
168. NOGAPS model ice divergence chart for 0000Z 14 Feb 98.	255
169. NOGAPS model ice divergence chart for 0000Z 15 Feb 98 (data missing).....	256

170. NOGAPS model ice divergence chart for 0000Z 16 Feb 98.	257
171. NOGAPS model ice divergence chart for 0000Z 17 Feb 98.	258
172. NOGAPS model ice divergence chart for 0000Z 18 Feb 98.	259
173. NOGAPS model ice divergence chart for 0000Z 19 Feb 98.	260
174. NOGAPS model ice divergence chart for 0000Z 20 Feb 98.	261
175. NOGAPS model ice divergence chart for 0000Z 21 Feb 98.	262
176. NOGAPS model ice divergence chart for 0000Z 22 Feb 98.	263
177. NOGAPS model ice divergence chart for 0000Z 23 Feb 98.	264
178. NOGAPS model ice divergence chart for 0000Z 24 Feb 98.	265
179. NOGAPS model ice divergence chart for 0000Z 25 Feb 98.	266
180. NOGAPS model ice divergence chart for 0000Z 26 Feb 98.	267
181. NOGAPS model ice divergence chart for 0000Z 27 Feb 98.	268
182. NOGAPS model ice divergence chart for 0000Z 28 Feb 98.	269
183. NOGAPS model ice divergence chart for 0000Z 01 Mar 98.....	270
184. NOGAPS model ice divergence chart for 0000Z 02 Mar 98.....	271
185. NOGAPS model ice divergence chart for 0000Z 03 Mar 98.....	272
186. NOGAPS model ice divergence chart for 0000Z 04 Mar 98.....	273
187. NOGAPS model ice divergence chart for 0000Z 05 Mar 98.....	274
188. NOGAPS model ice divergence chart for 0000Z 06 Mar 98.....	275
189. NOGAPS model ice divergence chart for 0000Z 07 Mar 98.....	276
190. NOGAPS model ice divergence chart for 0000Z 08 Mar 98.....	277
191. NOGAPS model ice divergence chart for 0000Z 09 Mar 98.....	278

192. NOGAPS model ice divergence chart for 0000Z 10 Mar 98.....	279
193. NOGAPS model ice divergence chart for 0000Z 11 Mar 98.....	280
194. NOGAPS model ice divergence chart for 0000Z 12 Mar 98.....	281
195. NOGAPS model ice divergence chart for 0000Z 13 Mar 98.....	282
196. NOGAPS model ice divergence chart for 0000Z 14 Mar 98 (data missing).	283
197. NOGAPS model ice divergence chart for 0000Z 15 Mar 98.....	284
198. NOGAPS model ice divergence chart for 0000Z 16 Mar 98.....	285
199. NOGAPS model ice divergence chart for 0000Z 17 Mar 98.....	286
200. NOGAPS model ice divergence chart for 0000Z 18 Mar 98.....	287
201. NOGAPS model ice divergence chart for 0000Z 19 Mar 98.....	288
202. NOGAPS model ice divergence chart for 0000Z 20 Mar 98.....	289
203. NOGAPS model ice divergence chart for 0000Z 21 Mar 98.....	290
204. NOGAPS model ice divergence chart for 0000Z 22 Mar 98.....	291
205. NOGAPS model ice divergence chart for 0000Z 23 Mar 98.....	292
206. NOGAPS model ice divergence chart for 0000Z 24 Mar 98.....	293
207. NOGAPS model ice divergence chart for 0000Z 25 Mar 98.....	294
208. NOGAPS model ice divergence chart for 0000Z 26 Mar 98.....	295
209. NOGAPS model ice divergence chart for 0000Z 27 Mar 98.....	296
210. NOGAPS model ice divergence chart for 0000Z 28 Mar 98.....	297
211. NOGAPS model ice divergence chart for 0000Z 29 Mar 98.....	298
212. NOGAPS model ice divergence chart for 0000Z 30 Mar 98.....	299
213. NOGAPS model ice divergence chart for 0000Z 31 Mar 98.....	300

LIST OF TABLES

1. Summary of the qualitative analysis in area A comparing the RGPS ice deformation to various meteorological variables generated by the NOGAPS model. It must be emphasized that the characterizations of “strong,” “moderate,” “weak” and “negative” in the subjective correlation columns do not refer to a particular meteorological variable, but to its subjective correlation with the deformation observed in the RGPS sea ice data.....41
2. Summary of the qualitative analysis in area B comparing the RGPS ice deformation to various meteorological variables generated by the NOGAPS model. It must be emphasized that the characterizations of “strong,” “moderate,” “weak” and “negative” in the subjective correlation columns do not refer to a particular meteorological variable, but to its subjective correlation with the deformation observed in the RGPS sea ice data.....42
3. Statistical comparison of PIPS and NOGAPS model ice divergence fields from 13FEB98 to 31MAR98 for point 1 (74°N/155°E) located in area A.76
4. Statistical comparison of PIPS and NOGAPS model ice divergence fields from 13FEB98 to 31MAR98 for point 2 (71°N/150°W).79
5. Comparison of the surface wind speed and ice drift to the calculated PIPS divergence values for the six most deformative events during the investigative period at point 2...
.....81
6. Statistical comparison of PIPS and NOGAPS model ice divergence fields from 13FEB98 to 31MAR98 for point 3 (78°N/150°W) located in area B.84
7. Statistical comparison of PIPS and NOGAPS model ice divergence fields from 13FEB98 to 31MAR98 for point 4 (76°N/175°W).88

ACKNOWLEDGEMENTS

The author would like to thank a variety of people without whom this research would not have come to fruition. First and foremost, my deepest gratitude extends to Professors Robert H. Bourke and James H. Wilson for their support during this thesis effort. They were never too busy to provide guidance and encouragement when it was most needed and had faith in my abilities when I clearly did not. A special “thank you” is also due to Dr. Peter S. Guest, my second reader, who provided timely advice to ensure that the effects of atmospheric forcing in the polar regions were correctly represented in this research. In addition, the following individuals provided essential data, expertise and assistance during my research: Mr. Robert Creasey of the Meteorology Department, Naval Postgraduate School for his unselfish assistance in manipulating NOGAPS meteorological data; Dr. Ronald Kwok of the Jet Propulsion Laboratory for providing the RGPS data set which provided the basis for this research; Mr. Glenn F. Cunningham of the Jet Propulsion Laboratory for his technical expertise in all matters pertaining to the SAR sensor and RGPS sea ice products; Mr. Kenneth Pollak of the Fleet Numerical METOC Center for furnishing the PIPS data evaluated in this thesis; LCDR Donald Taube, USN of the Naval Ice Center for his operational expertise and data collection efforts; Dr. Harry L. Stern of the University of Washington, Polar Science Center for sharing various computer codes with me; Dr. Christopher Olsen of the Physics Department, Naval Postgraduate School for giving me access to his IDL software package; Drs. Jeffrey D. Paduan and Pierre Marie Poulain of the Oceanography Department, Naval Postgraduate School for the use of their computer resources and Mr. Michael Cook and Mrs. Arlene Guest for general computing assistance. Finally, I would like to thank my wife, Kimberly, for her patience, understanding and support during those times when I was busy with this research and could not give my full attention to her and our little daughter Annie.

I. INTRODUCTION

A. POLITICAL/NAVAL CONTEXT

The most recent issue (June, 1998) of the Naval Institute's *Proceedings* magazine contained a thought-provoking article by Boyle and Lyon entitled "Arctic ASW: Have We Lost?" which focuses attention on a new potential Russian submarine threat from the vastness of the Arctic Ocean. The current economic difficulties in Russia and the general dissatisfaction of its populace could easily precipitate an overthrow of the ruling Russian government and lead to the installation of a more anti-Western one. If the potential deterioration in diplomatic relations between Russia and the United States should lead to war, the nature of the hostilities would have a vastly different character than it would have had just 15 years ago. Instead of an all-out war, possibly escalating to the use of tactical or even strategic nuclear weapons, tomorrow's conflict would likely be on a smaller and conventional scale. In a Naval war, the Russian Northern Fleet would most certainly rely on their still impressive nuclear and diesel submarine force to threaten U.S. and Allied merchant and fishing traffic and land-based targets of economic value in the Marginal Ice Zone surrounding the Arctic Ocean. Specific scenarios could include a littoral winter-time campaign, where small coastal submarines play havoc with shipping in the ice-covered approaches to the Gulf of St. Lawrence, as was successfully done by German U-boats from 1942 to 1944, or an attack by submarine-launched cruise missiles on the oil production facilities at Prudhoe Bay, Alaska (Boyle and Lyon, 1998).

The scenarios described above are quite frightening in view of the fact that Anti-Submarine Warfare (ASW), or Undersea Warfare (USW) as it is referred to now, has rapidly dropped down the priority list of a rapidly-shrinking post-Cold War U.S. Navy. This is particularly true for Arctic USW initiatives and Polar research in general. Additionally, with the decommissioning of the last Sturgeon-class attack submarine, the U.S. Navy has also lost its premier submerged platform for operations under the ice. Its reinforced sail and superior depth-keeping ability made it ideal for operations on the shallow, extensive continental shelves of the Arctic Ocean. Although Los Angeles-class attack submarines can operate under the ice cover, they were not designed for this purpose and would be at a severe disadvantage to their Russian counterparts.

B. RESEARCH OBJECTIVES

1. Background

It should be readily apparent that Polar USW has become more challenging since the end of the Cold War. It is therefore important to provide technical and scientific innovations that can favorably tilt the odds in the event of future Arctic submarine engagements. Such advances should ideally be relatively cheap, since funding for new programs is scarce. One such innovation is the development of an operational Arctic ambient noise (AN) prediction system. Tactically important low frequency ambient noise (<500 Hz) in the Arctic is dominated by ice-ice interactions, which differs from the mid-latitude open ocean

environment, where most noise is caused by distant shipping (Urlick, 1983). Ambient noise also represents the most variable term in the passive (and active noise-limited) sonar equation, with variations of 20 to 30 dB over several hours common, due to the passage of an atmospheric storm as it moves across the ice surface (Feller, 1994; Fritsch, 1995).

The effect of ambient noise on submarine sonar ranges compromises both offensive and defensive submarine operations under the ice. For an attack submarine conducting offensive ASW, passive search and detection ranges will be reduced when ambient noise levels are high, increasing the likelihood that the targets will only be detected at very close range, if at all. This may necessitate drastic action, such as a maneuver to avoid collision or a low percentage bearings-only torpedo launch, resulting in a possible loss of the tactical advantage (or worse). In defensive submarine operations, periods of high AN levels may mask the execution of necessary housekeeping and preventive maintenance chores, such as blowing down steam generators, dumping trash or cycling torpedo tube doors. Low AN levels, on the other hand, serve to increase sonar detection ranges and may prevent a submarine from conducting noisy evolutions.

2. Ambient Noise Modeling Efforts

A prediction system that can provide the submarine commander a 12 to 24-hour alert to periods of very low or high background noise could provide a tactically significant advantage to the U.S. submariner. At least one AN forecasting system has been run operationally in the past (Pollak, personal communication, 1998). The Arctic Ambient Noise Prediction System (AANPS), developed by Science Applications International Corporation (SAIC), predicted under-ice noise through empirical algorithms. It was active at the Fleet Numerical Oceanography Center (FNOC) from 1988 until the early 1990s. AANPS used the Polar Ice Prediction System (PIPS) model ice drift output to predict noise levels at various frequencies for up to six days (AANPS Users and Operations Manual).

More recently, Collins (1996) developed a dynamic model, the Arctic Storm Noise Model (ASNM), to predict the occurrence of extreme noise events in ice-covered Arctic waters. ASNM was adapted from the Ambient Noise Directional Estimation System (ANDES) for use in an Arctic environment. ANDES models the noise contributions from shipping densities and wave action. Since these noise sources do not exist in the Arctic, they were replaced by empirically-derived source level density lookup tables for noise caused by pressure ridges. The source level density values were derived from a correlation of noise measurements from ice-mounted drifting buoys and concurrent wind observations.

3. Long Term Research Goals

Both the AANPS and ASNM have two drawbacks. First, they use empirical calculations instead of physically based algorithms that predict the mechanical failure of the ice sheet and its resultant noise generation. Second, both models use indirect environmental variables (ice drift for AANPS and wind speed/wind stress for ASNM) to model the noise field instead of the direct measurements of ice divergence,

ice shear and internal ice stress. The next step in the further development of the ASNM is to replace the current NOGAPS wind forcing by fields of PIPS ice divergence, available now, and ultimately by the energy dissipation rate, determined from the product of the ice stress and the strain rate. Energy dissipation fields are currently not a product of the PIPS model, although it is calculated implicitly to solve the ice momentum balance equation (discussed in Chapter II). Code modifications by Hibler in 1998 will generate the energy dissipation level due to buildup of ice stress during convergence as a discrete output field (Bourke and Hibler, personal communication, 1998).

One of the challenges of using PIPS as a forcing mechanism for ASNM is its model initialization procedure. Until very recently, the daily PIPS model run was initialized from the previous day's 24-hour forecast, while the Naval Ice Center provided a weekly hand-drawn ice analysis, which served as an "ice observation" to the model. Over time, PIPS model errors, which were not corrected by the low density of ice observations, would increase in magnitude and result in a poor representation of the Arctic ice cover. Remotely sensed ice data would appear to be an ideal avenue for providing periodic updates to the PIPS model. In the past year, observed ice conditions from the Special Sensor Microwave/Imager (SSM/I), microwave radiometers flown aboard the three Defense Meteorological Satellite Program (DMSP) platforms, have provided such observations to PIPS (Bertoia, 1998). Although the SSM/I observations should improve all the PIPS output fields, the relatively coarse spatial resolution of 12.5 km will not image small-scale ice deformation events, the detection of which would improve the energy dissipation fields of the improved PIPS model. Synthetic Aperture Radar (SAR) imagery, with pixel resolutions as good as 30 m, would be needed to provide this fine-scale data. Future versions of PIPS are then envisioned to use SAR-derived ice deformation products to provide input data for the PIPS model instead of wind or ice stress fields. Perhaps the PIPS model could be circumvented completely and SAR data used to calculate ambient noise values directly. However, this would require deformation products to be routinely available at any geographic location in the Arctic and to be output in hours instead of weeks. Neither requirement can currently be met, as will be discussed later, since the ice deformation algorithms that produce SAR data sets do so "after the fact", not in an operational time frame.

To summarize, the long-term goals of this research effort are to:

- Continue the development of a high fidelity, operational Arctic ambient noise model to support Polar submarine operations.
- To formulate a method to routinely use PIPS model output to initialize the ASNM.
- To explore the possibility of using SAR or SAR-derived data to directly initialize the ASNM.

4. Thesis Objectives

In view of the research goals stated above, this thesis attempts to do accomplish two main objectives to further the development of the Arctic Storm Noise Model. It sets out to perform a proof-of-concept study to determine the utility of SAR imagery or SAR-derived products in identifying large-scale deformation of the Arctic ice cover. As is discussed in the next section, the dominant sources of ambient

noise from the Arctic ice cover are recently formed pressure ridges created by convergent activity in the ice cover. The ability to geo-locate these features constitutes an important step towards the creation of a more sophisticated ASNM for two reasons. First, their location can be fed to the PIPS model to update its data fields of ice divergence and shear and, in the future, those of energy dissipation level. Second, the ridge locations may be used to forecast median ambient noise events. Currently, ASNM is able to forecast only very loud (>95th percentile) and extremely quiet (<5th percentile) periods, because there currently exists no method to detect the location of individual acoustically active ridges. The model forecasts a homogeneous, wide-field source level density for each 1°×1° grid square. This forecast is only valid if no near-field sources, in the form of pressure ridges in close proximity, are present to “contaminate” the homogeneous noise field. In other words, the contribution from distant pressure ridges can be modeled well, while one loud active ridge in the near-field dominates the far-field sources and invalidates the AN predictions. During high wind speed events, the pressure ridge density is high and nearly isotropic, so that no one ridge’s input dominates. During low wind speed events, the ridge density is anisotropic, but the chances of any one ridge dominating the noise field is small, because of the low ridge density. During median wind speed events, however, the likelihood of a ridge dominating the noise field is quite high and ASNM predictions are not valid (Collins, 1996). If SAR data could provide the geographic positions of all acoustically active ridges in the forecast area, the ASNM could be adapted to make AN predictions based on this data instead of a median area-wide source-level density.

The second goal of this thesis project is to establish the ability of the PIPS divergence output to reproduce the deformation of the Arctic ice cover well enough to make them valid as ASNM forcing fields. A direct comparison between SAR and PIPS data would accomplish this goal, but as will be seen later, the lack of temporally coherent data sets prevented such a straightforward approach.

C. SOURCES OF ARCTIC AMBIENT NOISE

A variety of sources contribute to the ambient noise frequency spectrum below 1000 Hz in the Arctic. Some of these include seismic vibrations (1-10 Hz), ice ridging (10-300 Hz), lead formation, rafting (50-100 Hz), ice/ice interactions, wind (100-600 Hz), ice/ice interactions, pressure ridging, wind thermal cracking, wind, lead formation (600-800 Hz) and ice/crystal interactions, wind (900-1000Hz) (Oard, 1987; Parsons, 1992). Two schools of thoughts exist as to the dominant source of ambient noise generated by the Arctic ice cover. Makris and Dyer (1986) and Langley (1988) argue that cracking of the ice sheet resulting from the flexure of the ice cover and energy release from natural inhomogeneities in the structure of the ice due to the actions of wind and ice and thermal stresses are the dominant contributors to the ambient noise field. On the other hand, Pritchard (1983, 1990), Buck and Wilson (1986) and Bourke and Parsons (1993) believe that pressure ridging of the ice cover represent the highest intensity Arctic noise events. In this phenomena, an open water lead opens in the ice cover under the influence of an external force such as a divergent surface wind field above the ice. If the ambient air temperature at the lead is below freezing, young ice immediately forms on the surface of the water inside the open lead. This thin ice

is easily deformed and crushed into a new pressure ridge under convergent atmospheric forcing. High levels of low frequency noise (in the vicinity of 90 dB) accompany the ridging process (Buck and Wilson, 1986). Pressure ridge formation has been found to be associated with high ambient noise levels in the previous research of Parsons (1992), Feller (1994), Fritsch (1995) and Collins (1996). These studies found that the high wind speeds and wind stress associated with the passage of deep Arctic low- pressure systems correlated directly to increased levels of background noise and associate them with spatially discrete point sources of low frequency ambient noise, i.e., pressure ridges. These studies are supported by Greening et al. (1997) who used matched-field processing to isolate a discrete number of active acoustic sources, later classified as pressure ridges, in the ice cover of the Lincoln Sea. Matched-field processing uses beam-forming techniques to detect and localize a finite number of acoustic targets in both range and depth (Wilson and Veenhuis, 1997). The processor models the acoustic field produced by simulated sources on a set of receiver arrays and “matches” these to the actual sound field received at that array. The highest statistical agreement occurs when the number, range and depth of both simulated and real sources are matched (Greening et al., 1997). Additionally, Pritchard (1990) showed that ridging activity accounted for more energy dissipation in the ice cover than mixed layer shearing (where ice velocity is significantly different from the underlying current velocity) and micro-cracking through small-scale stresses. These findings appear to refute the theories that plate flexure or ice cracking represents the dominant Arctic ambient noise formation mechanism. These latter phenomena, although undoubtedly contributors to the background noise field, are not intense enough acoustically to cause statistically (and operationally) significant ambient noise levels. Additionally, flexure and cracking events would more likely cause a homogeneous noise field, which would preclude the isolation of spatially discrete point sources.

Data analysis during this research concentrates on the divergent/convergent phases of pressure ridging events, i.e., the opening and closing of the ice cover, while mostly neglecting shear ridging. Pritchard (1990) successfully modeled the source levels associated with the energy dissipation of four different sea-ice noise-making mechanisms, using 1988 CEAREX Drift Experiment acoustic data. He found that convergent pressure ridging activity accounted for the highest energy dissipation values of the processes and correlated well with quantitative increases in ambient noise. In contrast, shear ridges accounted for less energy dissipation over the investigation period, although their levels were more constant than those of convergent ridges. Since the ASNM currently models only extremely high or low intensity noise events, shear ridging is neglected in this study.

II. THE POLAR ICE PREDICTION SYSTEM (PIPS)

A. BACKGROUND

Accurate sea ice predictions have always been important to support military, commercial and scientific research operations in Arctic waters. Early sea ice prediction models hosted at the Fleet Numerical Oceanography Center (now FNMOC) used empirical algorithms to simulate the interaction between the sea, ice and the atmosphere. Initial models were only able to predict ice drift and used geostrophic winds and mean ocean currents as their only input parameters. More sophisticated models have been developed over the last twenty years. The first of these models emphasized thermodynamics in calculating the ice motion (Maykut and Untersteiner, 1971; Bryan et al., 1975; Semtner, 1976; Washington et al., 1976; Parkinson and Washington, 1979 and Manabe et al. 1979). Dynamic/thermodynamic models followed, in which thin ice is redistributed into thicker ice categories through pressure ridging. These models were based on the works of Thorndike et al. (1975), Rothrock (1975) and Coon et al. (1974). Correct representations of ice rheology were added and combined with the thermodynamic sea ice model of Semtner (1976) to form a dynamic/thermodynamic sea ice model (Hibler, 1979; 1980). Unlike previous efforts, this model predicts not only ice movement, but also the ice thickness and concentration. In 1984, the Naval Ocean Research and Development Activity (NORDA) began to test the Hibler model for use as an operational ice forecast model at FNOC for short-range forecasting. Full implementation of the model occurred in the summer of 1985 and the model was designated as the Polar Ice Prediction System (PIPS) (Preller and Posey, 1989). The premier customer of PIPS output is the Naval Ice Center (NIC), formerly the Naval Polar Oceanography Center, which uses it for guidance in producing its own ice forecast products. In return, NIC ice analyses are used to correct and initialize new PIPS runs on a weekly basis.

B. MODEL DESCRIPTION

The PIPS model development and description are discussed in the papers of Preller and Posey (1989) and Riedlinger and Preller (1991). Much of the material in the following section is derived from these reports.

The PIPS model has five major components: Momentum balance, ice rheology, ice thickness distribution, ice strength and air/ice/ocean heat balance.

1. Momentum Balance Equation

The momentum balance equation provides information on ice motion, ice deformation (convergence, divergence, shear) and horizontal transports (mass, heat and salt.) In PIPS it is used to determine the ice drift and is given by (in simplified form):

$$m \frac{d\vec{V}_{ice}}{dt} = \vec{\tau}_a + \vec{\tau}_w + \vec{C} + \vec{T} + \vec{F}$$

where (on the right hand side):

$\vec{\tau}_a$ is the air/wind stress,

$\vec{\tau}_w$ is the water stress,

\vec{C} is the Coriolis force,

\vec{T} is the tilt of the ocean surface,

\vec{F} is the internal ice stress.

The left side of the equation represents the ice momentum (mass times acceleration), while the right side represents the summation of forces responsible for the ice motion. The air and water stresses are listed below. They are defined using constant turning angles between air and ocean geostrophic velocities and their stresses on ice:

$$\begin{aligned}\tau_a &= \rho_a C_a |\vec{U}_g| \left(\vec{U}_g \cos \phi + \hat{k} \times \vec{U}_g \sin \phi \right) \\ \tau_w &= \rho_w C_w |\vec{U}_w - \vec{u}| \left[(\vec{U}_w - \vec{u}) \cos \theta + \hat{k} \times (\vec{U}_w - \vec{u}) \sin \theta \right]\end{aligned}$$

where:

\vec{U}_g is the geostrophic wind,

\vec{U}_w is the geostrophic ocean current,

C_a and C_w are the geostrophic air-ice and water-ice drag coefficients,

ρ_a and ρ_w are the air and water densities,

ϕ and θ are the air and water turning angles.

In the future, RGPS data may be assimilated directly into the PIPS model by inserting dv/dt observed from SAR at the PIPS grid points overlapping the RGPS observations.

2. Ice Rheology

The PIPS model is based upon a viscous-plastic constitutive law relates the ice stress to ice deformation and ice strength in the following manner:

$$\sigma_{ij} = 2\eta(\epsilon_{ij}, P)\epsilon_{ij} + [\xi(\epsilon_{ij}, P) - \eta(\epsilon_{ij}, P)]\epsilon_{kk}\delta_{ij} - P\delta_{ij}/2$$

where:

σ_{ij} is the two-dimensional stress tensor,

ϵ_{ij} is the strain tensor,

$P/2$ is a pressure term,

ξ and η are nonlinear bulk and shear viscosities.

Ice flows plastically for normal strain rates and deforms in a linear viscous manner for small strain rates. Linear viscosity is analogous to linear elasticity. The velocity of viscous deformation corresponds to elastic displacement and viscous strain rates correspond to elastic strain rates. The equilibrium equations

remain unchanged, provided that there is slow flow with zero acceleration. If the ice is assumed to be homogeneous and isotropic, the viscous properties can be described by the two constants ξ and η .

3. Ice Thickness Distribution

The ice thickness distribution model in PIPS uses both dynamic and thermodynamic effects in its calculations. Originally, the Hibler model (Hibler, 1979) used two levels of ice thickness: thick ($\geq 0.5\text{m}$) and thin ice ($< 0.5\text{m}$). The compactness, A , is defined as the area of a model grid cell covered by thick ice, while $(1-A)$ is the area covered by thin ice. A specific ice thickness distribution function is not used in the model. Furthermore, ridging of ice was not allowed to take place in the modeled ice cover. This approach resulted in an Arctic ice cover that was thinner than in-situ observations showed. To correct for this, a seven-level ice thickness formulation was added to PIPS in 1988. This method divides thick ice into seven categories which are allowed to grow and decay independently in each grid cell. During ice growth periods, when snow can collect on top of the ice, snow cover is also divided into a seven-level distribution of snow depth, spaced between zero and twice the cell mean thickness. When melting occurs, snow is assumed to be uniformly distributed over the ice-covered portion of the grid cell. Snowfall rates are based on mean monthly climatology. This improved treatment of sea ice corrected the initial faults of the model.

4. Ice Strength

The ice strength (P) is treated as a function of the ice thickness and its compactness as shown in the following equation:

$$P = P^* h \exp[-C(1 - A)]$$

where:

the maximum strength (P^*) and C are fixed empirical constants,
 h is ice thickness,
 A is the compactness.

The equation shows that the ice strength is inversely dependent on the amount of thin ice present ($1-A$) and that ice gains strength as it grows thicker.

5. Heat Budget

The growth and decay rates of ice are based on the heat budget balance between the ice, ocean and atmosphere. Heat transferred to the ocean via open leads is first used to reduce the vertical growth rate of the ice layer in the cell. Any remaining heat is then used by the model to produce lateral melting or to raise the temperature of the mixed layer. However, when ice is present, the mixed layer temperature is always set to freezing (the lowest temperature that can be reached for a given salinity) and all excess heat is used to reduce the ice cover laterally until it disappears. Conversely, during growth periods, ice is not allowed to form until the mixed layer temperature reaches freezing.

C. MODEL GRID

The original PIPS model (PIPS 1.0, September 87) grid of PIPS covered the central Arctic, Barents Sea and the northern half of the Greenland and Norwegian Seas using a polar stereographic 127 km grid. Additionally, higher-resolution regional basin models, RPIPS-B (25 km grid, June 89) and RPIPS-G (20 km grid, October 91), extended over the Barents, Kara and White Seas as well as the western Greenland Sea, respectively. The current version of PIPS (PIPS 2.0), implemented in 1995, encompasses all ice-covered regions of the Northern Hemisphere in a grid size of 20 km. The operational PIPS model time step is six hours. All model boundaries are impermeable except for the southern boundary in the Greenland-Norwegian Seas. Ice is transferred out of the model domain at this location via advection and cannot be recovered.

D. MODEL FORCING

Both atmospheric and oceanic forcing are needed to drive PIPS. Atmospheric forcing is obtained from the Navy Operational Global Atmospheric Prediction System (NOGAPS). This model provides surface pressure fields, which are used to derive geostrophic winds. Additionally, NOGAPS provides surface vapor pressure, air temperature, incoming short wave radiation, sensible and total heat flux. PIPS 2.0 is coupled to the Cox primitive equation ocean model (Cox, 1984) to predict ocean currents, changes in horizontal and vertical velocity, water temperature, salinity and monthly mean deep oceanic heat fluxes. The inclusion of a coupled ocean model in PIPS 2.0 has resulted in a much-improved ability to detect the ice edge in the model domain.

E. PIPS INITIALIZATION

PIPS creates a 120-hour ice forecast every day. A file that contains the model's 24-hour forecast of ice thickness, concentration, drift, as well as surface ice temperature and open water heat absorption is saved. Values for ice divergence are also calculated, but not routinely saved. PIPS can be initialized by using the previous day's PIPS 24-hour forecast field, a forecast field from the previous week, or model climatology. Once a week, the model receives ice concentration updates from observations through the Naval Ice Center. These concentrations are based on in-situ observed (from ships, submarines and aircraft) and remotely-sensed (AVHRR, OLS, SSM/I) data. The model performs corrections to its initialization based on these data.

F. MODEL WEAKNESSES

There are two noticeable weaknesses in the PIPS model: (1) constant turning angles (θ , ϕ) between air and ocean geostrophic velocities are assumed and (2) empirical values are assumed for P^* and C during ice strength calculations. Shortcoming (1) would be resolved through the introduction of more

sophisticated boundary layer dynamics and (2) through an improved ice rheology model. These weaknesses will be resolved in PIPS Version 3.0, currently undergoing development.

III. THE SYNTHETIC APERTURE RADAR (SAR)

A. SAR SENSOR THEORY

Much of the material for this section was adapted from two texts: Curlander and McDonough (1991), and Kingsley and Quegan (1992). Two worldwide web sites were also used to obtain background material: the Sandia National Laboratories website (www.sandia.gov/RADAR/sar_sub/sar_intro1.htm), as well as NASA/JPL's Imaging Radar web site (southport.jpl.nasa.gov/desc/imagingradarv3.html).

One of the major advantages of SAR over other radar systems is its all-weather capability. It achieves this through the use of cm-length wavelengths, which are not adversely affected by precipitation and cloud features. Popular wavelengths include X-band (3 cm), C-band (6 cm) and L-band (24 cm). Despite this advantage, one must remember that intense tropical rainfall events (in the troposphere) and ionospheric anomalies in the post-sunset equatorial regions and the auroral zones can destroy the phase coherence on which the SAR processor depends.

SAR can operate in three basic modes. SWATH SAR used by ERS-1, RADARSAT, etc; spotlight SAR; and SWATH patch SAR. Figure 1 presents a basic schematic of how an airborne SWATH SAR sensor images the earth's surface. The SAR is imaging perpendicular to the aircraft's course, and the footprint (or area illuminated by the radar) is moved along the surface in a swath. SARs typically produce a two-dimensional image, although interferometric SAR can produce 3-D images of (relatively) stationary objects by viewing them from different directions. This is accomplished by using different SAR sensors on the same craft or data from SARs on different platforms. In a 2-D SAR sweep, one direction is called the

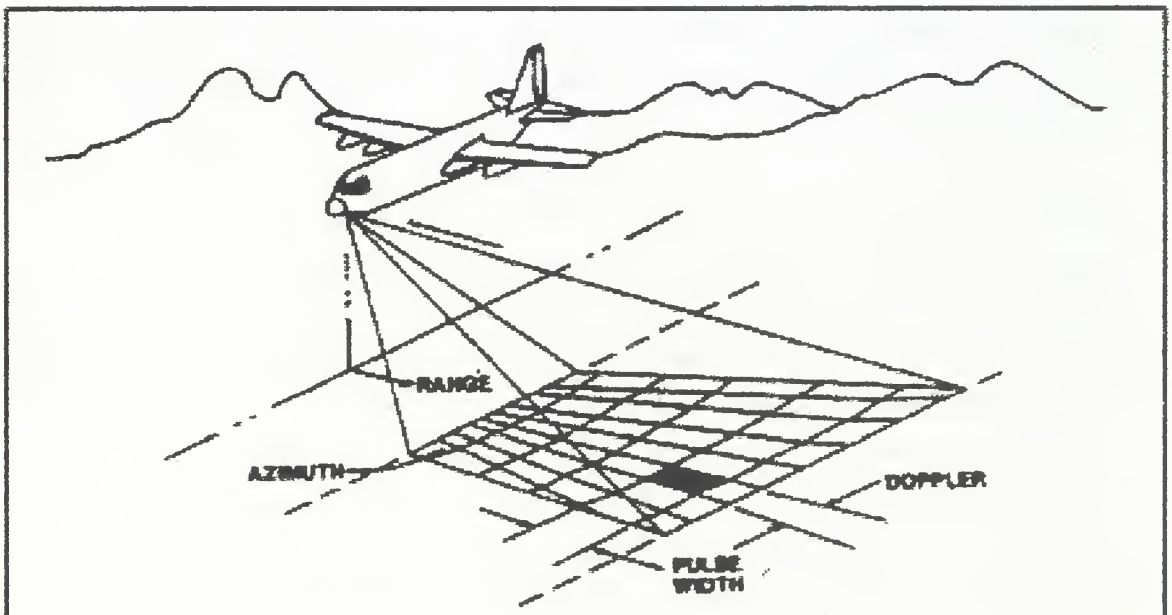


Figure 1. Basic schematic of SWATH SAR imaging geometry from an airborne platform (from Sandia National Laboratories, 1997).

range (or along-track) and is the “line-of-sight” distance from the radar to the target. Range measurement and resolution are obtained by measuring the time from transmission of the pulse to the reception of the target echo (as in ordinary radars). Range resolution is determined by the pulse width. A high frequency, or narrow pulse will yield finer resolution.

The other dimension is called the azimuth (cross-track) and is perpendicular to the range. Ordinarily, a physically large antenna is needed (in both radar and other wavelength imaging systems) to focus the transmitted and received radar energy into an image of acceptable resolution. With the relatively long wavelength of the SAR and the long distance above ground of the satellite (or aircraft) orbit, an antenna of impractical length would have to be flown to achieve acceptable resolution. Airborne SAR is able to achieve good resolution in the azimuthal direction by moving a short antenna a set distance down-range and collecting data (returned echoes) during this interval. This gives the radar a “synthetic aperture” much larger than the physical length of the actual antenna and results in a fine “synthetic” beamwidth.

The ground resolution of a SAR in the along track direction is independent of the range and the wavelength and one must actually shorten the antenna to get better resolution. This completely contrasts what is known about “real” antennas, but occurs because shorter physical antennas give rise to longer synthetic arrays. For example, the C-band (6-cm wavelength) antenna on ERS-1 has a length of 10 m and obtains a practical resolution of 6m.

Another way of defining the resolution of the SAR is to state that it is the minimum range separation of two points on the ground that can be distinguished as separate by the system. As the radar moves down-range, a pulse is transmitted at each position, and the return echoes are collected by the receiver and stored. Wiley (1965, citing his 1951 work) observed that two point scatterers on the earth surface, at slightly different angles with respect to the radar track, have different speeds relative to the platform. The radar pulse reflected from the two points will have two Doppler frequency shifts (negative as the radar approaches the target, positive as it moves away) that are recorded. The method of separating radar returns into distinct groups based on their Doppler shift improved the azimuth resolution of the radar significantly. Wiley (1965) referred to this technique as Doppler beam sharpening. His original SAR design is known today as squint mode SAR. Curlander and McDonough (1991) state that if the arrival time of the leading edge of the pulse echo from the more distant point is later than the arrival time of the trailing edge of the echo from the nearer point, each point can be distinguished in the time history of the radar echo. This time, or phase, history is resident in the sequence of returns from one particular scatterer on the earth’s surface. It is unique to a scatterer in a certain geographic position. The SAR processor stores the sequence of returns and corrects for its phase history, bringing all returns from the scatterer into phase. In other words, the processor compares them to a reference frequency. This focusing operation is known as SAR processing and is the most computationally demanding phase of the SAR imaging process. The returns add up constructively by summing all the corrected pulses together. The process is destructive for scatterers with different phase histories, which contribute less to the summation of the scatterers. Scatterers close together in the along track direction will have similar phase histories and will have comparable weightings

in the summation. Kingsley and Quegan (1992) explain that the separation that causes one of them to suffer significant destructive interference when the processing is tuned to the position of the other is a measure of the system resolution.

To achieve the small minimum separation between two points that yield high resolution, a short pulse duration is necessary. The required pulse duration would normally be too short to deliver adequate energy to the surface scatterer to return an observable echo from it (Curlander and McDonough, 1991). A pulse compression technique is employed to achieve both high resolution (with a longer pulse) and high signal-to-noise ratio (SNR).

B. BRIEF HISTORY OF THE SAR SENSOR

Curlander and McDonough (1991) provide an interesting history of SAR sensor development. This section is based on their work.

1. SAR Technology

In the early 1950s, radar design engineers realized the advantages of a non-rotating antenna. A fixed antenna could be easily attached to the fuselage of an aircraft and provide an increase of the radar's aperture and improved along-track resolution. The early high frequency versions of these side-looking aperture radars (SLAR) were used by the military for reconnaissance missions and collected data were highly classified. Declassified SLAR data became available to the scientific community in the mid-1960s and SLAR was immediately recognized as an important new data-gathering device for a variety of scientific fields.

The earliest theoretical description of imaging an object through the use of Doppler frequency analysis is attributed to Carl Wiley of Goodyear Aircraft Corporation in June 1951. He referred to his technique as Doppler beam sharpening. The first operational airborne SAR flew onboard a Goodyear Aircraft DC-3 in 1953.

A group of scientists at the University of Illinois under the direction of C.W. Sherwin undertook a similar project in 1962. John Kovaly, a research team member, had studied the possibility of detecting moving objects through their Doppler characteristics in 1952. He realized that variations in terrain height produced distinctive peaks visible in the azimuth frequency spectrum. Sherwin had recognized in 1952 that a fully focused Doppler radar could be built by providing signal phase corrections at each range bin. The motion of the platform was corrected for by applying aircraft accelerometer readings to the radar signal before storage. This research effort produced a fully functional coherent X-band radar system.

A large-scale follow-on study, Project Wolverine, coordinated by the University of Michigan, was based on the work of the University of Illinois group. This group improved platform motion compensation and developed optical recorder equipment to aid in sensor data collection. Their development of a ground optical correlator was a breakthrough achievement, since it provided a workable solution to SAR processing's biggest challenge (in the pre-digital computing era): How to store SAR information during the

synthesis period and how to apply range-dependent quadratic phase correction to achieve a fully-focussed synthetic array.

Advances in radar component technology were necessary in making SAR an operational reality. The development of linear beam power amplifiers, in the form of the klystron and later the traveling wave tube (TWT) provided the high peak power and phase stability required for SAR systems. The TWT has generally been replaced by monolithic microwave integrated circuit (MMIC) technology in the 1990s.

2. Spaceborne SAR Sensors

The earliest SAR systems, as well as a number of current regional sensors, were flown on aircraft for only a limited mission duration. To obtain a continuous time series of global observations, SARs would have to be mounted on orbiting spacecraft. The first spaceborne SAR sensor was an experimental L-band sounding radar mounted on a rocket launched at the White Sands, New Mexico missile test range. The sensor success (it was later flown on conventional aircraft) led to the approval of the SEASAT SAR system. In the interim period, NASA deployed the Apollo Lunar Sounder Experiment (ALSE) used for mapping the subsurface geological features of the moon and to map the heights of the lunar surface.

Data received by spaceborne sensors in the 1970s and 1980s gave an indication of the sensitivity and all-weather capability of the SAR. In particular, imagery obtained by the U.S. SEASAT satellite, which briefly flew during 1978, confirmed the vast potential of SAR in imaging the earth. Specifically, the SEASAT SAR observed a number of unique ocean features that contributed to the understanding of the global scales of oceanographic phenomena. SEASAT was a single-frequency L-band single polarization, fixed look angle radar.

A number of the features on the SEASAT SAR were transferred to the Shuttle Imaging Radar-A (SIR-A), which flew in 1981, SIR-B, which was launched in 1984, and SIR-C /X-SAR, which was deployed in 1994. SIR-A was a L-band radar with a fixed look angle and was intended to provide data for geologic disciplines, while SIR-B data had broader applications adding multi-look angle capability. SIR-C provided improved imaging capability by transmitting in the L-, C- and X-bands.

In recent years, a number of non-U.S. civilian government agencies have embarked on several air- and space-borne SAR development programs. The platforms and sensors deployed through these efforts are listed in the next section.

C. SAR SENSORS

The following section describes the characteristics of the various satellites that are (or were recently) capable of collecting microwave SAR data (none of which are U.S. systems). Much of the material for this section was collected from the Alaska SAR Facility worldwide web site (www.asf.alaska.edu) and Alaska SAR Facility Prelaunch Science Working Team (1989).

1. ERS-1

a. General

The European Space Agency (ESA) First European Remote Sensing Satellite (ERS-1) was launched into orbit on 17 July 1990 by an Ariane 4 launch vehicle from Kourou, French Guiana and commenced archiving data on 7 September 1991. ERS-1 had a sun-synchronous, near-polar, near-circular orbit at a mean altitude of 785 km and an inclination of 98.5°. The majority of the satellite's missions were conducted with a 35-day repeat cycle, meaning that the satellite duplicated its exact orbit every 35 days or 501 orbits. ERS-1 is no longer an active platform.

b. SAR Sensor

ERS-1 carried a variety of sensors and instruments. Of primary interest to sea ice research was the Active Microwave Instrumentation (AMI), which combines the functions of a Synthetic Aperture Radar (SAR) and a Wind Scatterometer (WNS). The AMI operated in one of three modes: image, wind or wave. It was designed to measure wind fields and wave spectra over the open ocean and recorded all-weather, fine resolution images over the ocean, polar ice, coastal zones and land. The AMI had an image mode (swath) SAR, operating at 5.3 GHz and a wavelength of 5.66 cm (C-Band). The sensor had VV (vertical transmitting and vertical receiving) polarization, a swath width of 100 km and maximum resolution of 30 m. The SAR and Wind/Wave modes were mutually exclusive during operation. The AMI data rate was 105 Mbit/sec. ERS-1 had no onboard data storage capability. The operational design lifetime of the satellite was 2-3 years.

2. RADARSAT-1

a. General

The RADARSAT-1 is an advanced earth observation satellite developed by the Canadian Space Agency (CSA) to monitor environmental change and to support resource sustainability. A NASA Delta II launch vehicle, sited at Vandenberg Air Force Base, California, transported RADARSAT into a polar, sun-synchronous 24-day exact repeat orbit at a height of 798 km and an inclination of 98.6° on 4 November 1995. In exchange for this service, NASA became a "junior partner" to the CSA in the RADARSAT program, and gained access to the satellite on a pro rata basis through its Alaska SAR Facility (ASF), located in Fairbanks, Alaska. The CSA is responsible for the satellite control and operation in orbit and for the operation of some of the data reception and processing stations. The ASF is also tasked with data reception and processing. The RADARSAT SAR is considered the most capable such sensor for Arctic mapping missions, due to its large swath width.

b. SAR Sensor

RADARSAT only carries one instrument, a SAR, which is capable of an extensive range of operating modes. These modes include the steerable basic mode with incidence angles from 20° to 49°,

and experimental modes at higher angles. Swath widths vary between 35 to 500 km and resolution between 10 and 100 m. Similar to the ERS-1 sensor, the RADARSAT SAR operates at 5.3 GHz and has a wavelength of 5.66 cm (C-Band). Polarization is HH (horizontal transmitting and horizontal receiving). The ScanSAR Wide B mode, with a maximum swath width of 500 km and a resolution of 100 m, is used to provide the data for the RGPS “Arctic snapshot” sea ice products, discussed in a later section. The RADARSAT-1 SAR image swath can cover much of the Arctic daily and most of Canada every 72 hours, depending on beam selection. The entire earth can be covered every 24 days using the standard 100 km swath mode. In order to map the Antarctic continent at fine resolution, the satellite is capable of rotating itself to orient the SAR antenna left for a few days and then returning to its normal configuration. This has already happened from August to October 1997 to satisfy the requirements of the Antarctic Mapping Mission. RADARSAT carries two ODETICS high data-rate tape recorders that can store imagery for up to 10 minutes each. The SAR’s data rate is 105 Mbit/sec to the ground stations, and 85 Mbit/sec to the onboard recorders. RADARSAT has a design lifetime of 5.25 years.

3. JERS-1

a. General

The Japanese Earth Resources Satellite-1 (JERS-1) was launched by the H-1 launch vehicle on 11 February 1992 from the Tanegashima Space Center into a sun-synchronous orbit at an altitude of 568 km with a recurrent period of 44 days. Its orbit has a height of 570 km and an inclination of 98°. Its mission is to establish the technologies of active microwave and optical sensors, specifically those of the SAR and Optical Scanner (OPS).

b. SAR Sensor

JERS-1’s main sensor is a SAR operating at 1.275 GHz and a wavelength of 23.5 cm (L-Band) with HH polarization. Its swath width is only 75 km and it has a resolution of 30m. The JERS-1 orbit is designed to view 100% of the earth surface in about five repeat-cycle periods, or about 220 days. With a design lifetime of two years, the JERS-1 has carried out three of these mapping missions. The SAR carries one onboard recorder that can store 20 minutes of imagery. The sensor’s data rate is 60 Mbit/sec.

4. ERS-2

The Second European Remote Sensing Satellite (ERS-2) is essentially the same as the ERS-1 spacecraft, except that it has an additional sensor in its payload to measure the chemical composition of the atmosphere, in support of the Global Ozone Monitoring Experiment (GOME). Some existing sensor performance characteristics were also improved. The AMI characteristics remain essentially unchanged. ERS-2 was built by a consortium led by Deutsche Aerospace and was launched into orbit on 20 April 1995 by a French Ariane rocket. Platform characteristics are identical to those of the ERS-1 craft.

D. SAR DATA COLLECTION EFFORT

1. Raw SAR Imagery versus Derived Geophysical Products

One of the basic decisions that had to be made while searching for a suitable data set to support this research effort was whether to use raw SAR imagery or SAR-derived geophysical products. Raw RADARSAT-1 imagery, as well as image interpretation training, was available from the Operations Department, Naval Ice Center (NIC), Suitland, MD. Initial trial analysis of raw SAR imagery revealed several shortcomings to this approach. Although the 100 m resolution of the RADARSAT SAR sensor is sensitive enough to image wide open water leads, most pressure ridges are too narrow to be directly discernable in raw imagery. This shortcoming leaves an indirect approach for identifying pressure ridges, i.e., ridge formation is inferred by the absence of pre-existing leads. If the first in a sequence of SAR images shows an open lead and the next image does not, ice convergence must have compressed the thin ice in the lead (assuming below-freezing air temperatures) into a pressure ridge. This type of analysis represents a very labor-intensive and arbitrary process. Despite this drawback, SAR imagery, as seen in Figure 2, presents an overwhelming amount of detail that make it difficult and laborious to interpret on the

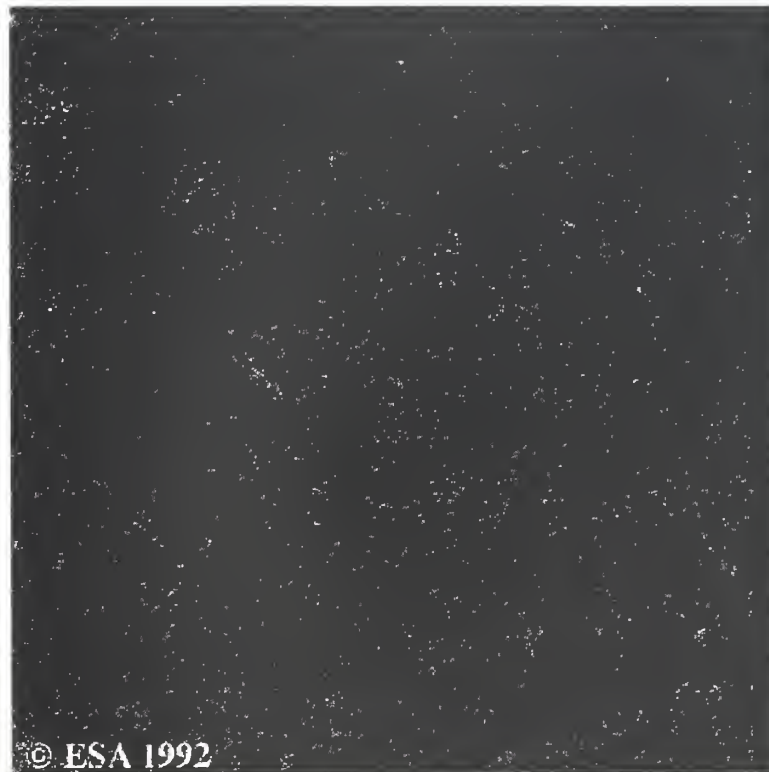


Figure 2. ERS-1 SAR image showing the complexity of this type of imagery. Dark patches represent young ice in open water leads, while lighter areas represent older ice types (from Alaska SAR Facility, 1998).

large scales required for this research. Of additional concern are the large file sizes containing the raw imagery which tax the storage capacities of resident computer systems.

Further investigative effort revealed that algorithms have been developed by Kwok et al. (1990; 1992) and McConnell et al. (1991) that process raw SAR imagery into Arctic-wide derived sea ice products. The Geophysical Processor System (GPS) (Kwok, 1995) has been active at the Alaska SAR Facility (ASF), Fairbanks, AK since 1992 and derived products from ERS-1 and ERS-2 imagery, while its successor, the RADARSAT Geophysical Processor System (RGPS) (Kwok, 1994;1997), is currently undergoing development at the Jet Propulsion Laboratory (JPL), Pasadena, CA. The GPS/RGPS products have several advantages over raw SAR imagery. They relieve the investigator of initial analysis chores, which avoids misinterpretation of unprocessed SAR data. GPS/RGPS presents a variety of ice data in sets of easily interpreted products, which can be manipulated at will by the polar researcher. Lastly, the data files which contain the GPS/RGPS products are approximately one tenth of the size of those containing equivalent raw imagery. RGPS data also has several weaknesses. It takes a long time to derive the sea ice products from raw imagery, ice deformation on time scales shorter than the GPS/RGPS temporal resolution may be lost and initial data may have geo-location and radiometric calibration errors. (The RGPS and its products are discussed in detail in the next chapter.) Despite these shortcomings, derived GPS/RGPS sea ice products were judged to be superior to raw imagery for this research effort.

2. ERS-1 Versus RADARSAT-1 Data

Once the decision was made to use algorithm-derived sea ice products, the choice of whether to analyze ERS-1/2 or RADARSAT products had to be made. A sample of ERS-1 GPS-derived ice motion and deformation data provided by Stern of the University of Washington, Polar Science Center showed that the spatial scales of the GPS product were relatively short, making it difficult to detect large-scale ice deformation changes. RGPS-derived products, obtained from Kwok during a November, 1997 visit to JPL, had larger spatial scales, attributable to the larger swath width of the RADARSAT SAR sensor, and were easier to interpret. Kwok provided a complete set of RGPS ice deformation products to support this research.

IV. THE RADARSAT GEOPHYSICAL PROCESSOR SYSTEM (RGPS)

A. ACKNOWLEDGEMENTS

Material for this section was gleaned from four main references. The primary source was a chapter, titled “The RADARSAT Geophysical Processor System”, of a yet unpublished book on remote sensing by Kwok. Much of the information on the Geophysical Processor System was taken from Kwok et al. (1990). Details on the determination of ice age and ice thickness using sea ice algorithms were taken from Kwok et al. (1992; 1995). Additional resources include the worldwide web (home) pages of the Alaska SAR Facility (<http://www.asf.alaska.edu>), the NASA JPL Radar Division (web address restricted) and the Polar Science Center at the University of Washington’s Applied Physics Laboratory (<http://psc.apl.washington.edu/RGPS/rgps.html>), as well as the proceedings of the most recent meeting of the RGPS Working Group (18-19 February, 1998).

B. INTRODUCTION

The RADARSAT Geophysical Processor System (RGPS) was designed for the analysis of raw SAR imagery of sea ice acquired by the RADARSAT satellite (Raney, 1991). It is planned that RGPS will provide Arctic-wide sea ice products using ScanSAR wide B (SWB) data from RADARSAT, with products updated at least every six days.

The RGPS algorithms were developed by Kwok et al. (1995) at JPL between 1995 and 1996. Raw data received from RADARSAT constitute a huge amount of imagery, an order of magnitude more than that produced by previous-generation SAR sensors. At a resolution/pixel spacing of 100m, approximately a gigabyte of SAR data is received from the sensor everyday (Kwok, 1997). These data are cumbersome to store and manipulate by a majority of investigators in the geophysical research community. RGPS can relieve investigators of the initial, time-consuming, repetitive step of geophysical analysis, since few of them have a need for raw SAR imagery. The RGPS is being developed in order to process the image data into processed fields of geophysical variables useful to a wide scientific audience. This methodology also avoids the possible misinterpretation of raw SAR imagery by an untrained observer.

C. MISSION PLANNING AND DATA ACQUISITION

Mission planning for RGPS is currently performed by Kwok’s RGPS group at JPL. It creates the RGPS acquisition plan according to spacecraft and planning constraints. This plan is passed to the ASF acquisition planners, who merge the RGPS plan with requests by the National/Naval Ice Center, Suitland, MD to create the “Arctic Snapshot”. The request is submitted to CSA for approval. CSA plans acquisitions and provides ASF with a planning status report for the next two weeks. It then tasks the ground stations at Fairbanks, Alaska (ASF Operations Center), Tromso, Norway, Prince Albert, Saskatchewan and Gatineau, Quebec through definitive reception schedules. Ground stations ingest these schedules into their tracking systems and acquire the desired data. Data received at ASF is available

immediately for scanning and processing, while images from other ground stations must be ordered by the ASF acquisition planners. The foreign station data tapes are dubbed to the appropriate media needed for processing. Both types of data are then put in a queue, awaiting scanning as scheduled by the ASF Production Planner. The prioritization of the pending scan requests is driven by ASF User Services and Production Planning along guidelines provided by the ASF Chief Scientist (LaBelle-Hamer, 1998).

D. RGPS PRODUCT BACKGROUND

1. Product Format

The RGPS geophysical data products take the form of "snapshots". Since the exact repeat orbit, or cycle, of the RADARSAT satellite is 24 days, the number of snapshots received per cycle is dependent on the selected repeat coverage. The RGPS sea ice algorithms detect differences between subsequent SAR images (called the "source" and the "target" image) to generate the geophysical products. The algorithms try to select a target image that is separated by the exact selected repeat coverage, three days for example. If no spatial match is found, the algorithm searches its database for a target image located \pm one day from the repeat coverage period. If still no suitable match is found, an image \pm two days from repeat coverage is selected (Cunningham, personal communication, 1998). Because the RADARSAT scans do not overlay perfectly from one snapshot to the next due to the satellite's retrograding orbit, the sea ice products in each snapshot are calculated only for overlapping regions. These regions are called data streams or simply streams.

Areal coverage of the snapshot can be improved at the expense of temporal resolution and vice versa. Early difficulties in acquiring the snapshot data have been resolved and routine collection for the RGPS commenced on 11 October 1996 with a partial acquisition of cycle 14. The first complete data set collected was cycle 15 (07-30 November 1996.) Successful acquisition is defined as data takes that have been scheduled with $> 90\%$ success (Kwok, 1998).

2. RGPS Sea Ice Products

The RGPS offers a wide range of sea ice products whose value will be augmented by the good spatial coverage made possible by RADARSAT ScanSAR wide B data. The RGPS sea ice algorithms produce 15 geophysical products synthesized from the basic observations of ice motion and backscatter (Kwok, 1997).

Eight products are produced directly from the Lagrangian ice motion records and contain information about individual cells and their properties. Of particular interest to this research effort is the ice deformation product, discussed in a later section.

Six gridded products (50 km grid), plotted on a SSM/I polar stereographic projection, are summary products derived from the cell data sets. In addition to the sea ice products, daily fields of NCEP 2-m air temperature, surface pressure gradients and derived surface winds complete the data suite.

3. Station Masks

The RGPS will process raw RADARSAT imagery received within the ASF station mask directly. A station mask is a circular region, centered at the SAR receiving station, which represents the farthest geographic coverage limit of real-time data reception. The ASF mask encompasses the Western Arctic region, including the Beaufort, Chukchi, East Siberian and part of the Laptev Seas, as well as the Bering Strait and the Bering Sea (ASF home page, 1998).

To gain complete Arctic SAR coverage, the RGPS will also process SAR imagery via out-of-mask data acquisitions. This is accomplished by two means. First, the RADARSAT satellite has an onboard recorder (OBR) which can store limited out-of-mask imagery for time-late transfer to the Gatineau ground station. Second, data can be obtained from the Tromso receiving station mask, which collects data from the Kara and Barents Seas and the northern portions of the Greenland and Norwegian Seas. Data is transferred between Tromso and Fairbanks on magnetic data tapes at an annual cost to ASF of \$400,000. This transfer commenced in November 1997 after negotiations regarding transcription and shipping costs were concluded. All data acquired from Tromso after February 1998 will be delivered to ASF via digital tapes called DLTs. The ASF system currently is unable to ingest this data form. The ASF is investigating the feasibility of obtaining Eastern Arctic SAR data from the Svalbard ground station at the time of this writing. This avenue of obtaining data would lower the data cost and may alleviate the data transfer problems inherent with Tromso data (Kwok, 1998).

4. Spatial Resolution

The nominal resolution for Lagrangian ice motion and deformation products in the ASF mask is a 5 km grid covering the Arctic basin. Even though a 5 km grid spacing is adequate for most purposes, smaller-scale motion details are not resolved. The resolution can be decreased to 10 km, which speeds up the product processing time for two reasons. First, only 25% as many cells need to be tracked by the RGPS sea ice algorithms for the same given geographic area, and second, 10 km cells are not as easily "lost" through deformation in areas of high ice motion. Checking and correcting tracked tie points and accounting for "lost" cells require manual operator intervention, which slows the processing speed. The time saved by accepting a lower resolution is not insignificant when one considers that the RGPS is slated to operate on a "cycle for cycle" processing rate using basin-wide 5 km resolution (Kwok, 1998). This means that it would take roughly 24 days to process a cycle of SAR imagery. (The processing speed may also be increased by upgrading the ASF RGPS processor or obtaining a new computer to which some processing tasks may be shifted). Variable grid spacings for the same series of snapshots can be constructed by the operator on a case-by-case basis, depending on the product customers' needs. For example, a grid of 10 km may be selected near coastlines where high deformation values are expected, while the central pack ice at higher latitudes could be covered by the finer resolution grid to detect the smaller motion values characteristic of the region. The selectable grid resolution could also be valuable in the transition seasons, when ice deformation increases (Kwok, 1998):

Tromso mask data resolution is fixed at 10 km. Some summary data products have a coarser resolution of 50 km.

5. Temporal Resolution

The temporal resolution of RGPS is dependent on the resolution repeat rate selected and RADARSAT's orbit mechanics. The resolution repeat coverage of data in the ASF mask is approximately three days, giving eight snapshots during one cycle. As stated above, the repeat coverage can be decreased to six days, improving both geographic coverage of the streams and decreasing processing time at the expense of the number of snapshots per cycle (four vice eight). The Tromso mask temporal resolution is fixed at six days. Some geophysical parameters, open leads among them, will be underestimated at this temporal resolution as was pointed out by Fowler et al. (1996). This occurs because the opening and closing of leads happen at a time scale which is shorter than the sampling record possible with current SAR observations. The use of correction factors has been studied by Coon et al. (1996) to compensate for this deficiency.

6. The RGPS Working Group

Decisions regarding the definition of RGPS data product processing, the scheduled incorporation of new products and recommendations of future RADARSAT coverage are made by the members of the RGPS Working Group (RGPSWG). The RGPSWG consists of JPL and ASF scientists involved with RGPS development, as well as about a dozen scientists from various research and learning institutions interested in the use of SAR-derived products. The Group is chaired by Rothrock of the Applied Polar Laboratory at the University of Washington. The general responsibility of the RGPSWG is to advise the RGPS implementation team, led by Kwok at JPL, assist in conducting RGPS data validation and interface with the modeling and global change communities (ASF home page, 1998).

E. THE RGPS SEA ICE ALGORITHMS

1. Introduction

The RGPS algorithms derive five sea ice parameters: ice motion, ice age/thickness, date of melt onset/freezup, open water fraction and backscatter histograms. These basic data fields are used to produce a total of 15 sea ice products. The calculations of the five basic parameters are based directly on the actual measurements of ice motion and backscatter history from a time sequence of SAR imagery. The algorithms described below are strongly dependent on the availability of a complete time series of ice motion. Computations of some of the geophysical variables would not be possible without continuous observations of the ice cover by the RADARSAT sensor (Kwok, 1997).

2. Lagrangian Ice Motion

A fundamental RGPS measurement is ice motion, obtained by tracking common features in successive SAR images. The algorithm was developed by Kwok et al. (1990) for the RGPS' predecessor, the Geophysical Processor System, active at ASF from 1992 to 1994. The ice tracking algorithm selects image pairs separated by a predetermined amount of days (the RGPS temporal resolution), usually three or six (Kwok, 1997). An initial grid of evenly spaced points is defined on the first image of a series covering the region investigated. These "tie-points" constitute the corners of an array of square cells measuring five or ten km on each side. The ice features at these points are tracked in each of the subsequent images in the repeat SAR observations using the ice tracking algorithm. This algorithm uses a combination of area- and feature-matching techniques to track an array of "tie-points" from a "source" to a "target" image (Kwok, 1997). After a set of usable image pairs is selected, the algorithm chooses between these two procedures to perform the ice motion analysis. If the image pairs are located within the central ice pack, where ice motions are largely translational, with only moderate rotations, area-based matching techniques can be used for direct extraction of ice-motion data. Area-based matching techniques involve the calculation of two-dimensional cross-correlation peaks between images (Kwok et al., 1990). Area-based matching becomes unreliable if large rotation of ice features is present as occurs near shore and in the MIZ. In these areas feature tracking is used to match features in a series of image pairs that have translated and rotated. The reader is referred to Kwok et al. (1990) for a more detailed description of area and feature matching techniques.

The RGPS tracking approach produces a Lagrangian motion field possible because of the improved spatial resolution of RADARSAT over earlier SAR sensors. In other words, the RGPS ice tracker can usually follow an individual cell from freezing onset in the fall throughout the whole ice season.

3. Ice Age/Thickness Distribution

a. Ice Age Calculations

This product gives an estimate of the age of the sea ice cover in the RGPS data swaths. The algorithm calculates the age of the newly formed young ice in a cell between subsequent RADARSAT passes, or put another way, between the "source" and "target" images. Young ice is judged to have formed (in a newly opened lead) if a cell area increases beyond an initial value of 1.00. The youngest ice in a lead is assumed to have ridged if a decrease below the initial cell area is detected. The above young ice formation process only occurs if the air temperature above the cell is below freezing (Kwok, 1997).

The procedure described above only classifies young ice not older than a few days or perhaps weeks. A different strategy is used to classify multiyear ice. The cell percentage of multiyear ice is computed by comparing actual data cell radar backscatter values to those expected of this ice type through an ice classification algorithm developed by Kwok et al. (1992). The ice type algorithm assigns each image pixel to one of four classes: multiyear ice, deformed first year ice, undeformed first year ice and smooth younger ice types or calm open water. Since the percentage of young and multiyear ice is known, the

remaining ice is simply classified as first year ice. The algorithm is not accurate enough to categorize this first year ice into different types. Multiyear ice classification errors due to wind-roughened open water and frost flower formation on new ice are easily corrected, since the amount of multiyear ice should not vary in a SAR image series, since none is created in winter. Any inconsistency in the percentage of multiyear ice in an image series can thus be filtered out. Radiometric calibration errors will also adversely affect the performance of the MYI algorithm (Kwok et al., 1992).

b. Ice Thickness Calculations

RGPS uses its database of 2 m air temperature to convert the young ice of the age distribution in each cell into a thickness distribution using an empirical relation between accumulated freezing-degree days and ice thickness derived by Lebedev (1938):

$$H = 1.33\theta^{.58}$$

where:

H is the ice thickness of young ice (in meters),

θ is the cumulative number of freezing degree days ($^{\circ}\text{C}$ days), expressed as:

$$\theta \equiv \int_0^t (T_f - T_a) dt$$

where T_f is the freezing point of water ($^{\circ}\text{C}$)

T_a is the air temperature ($^{\circ}\text{C}$) at 2 m above the surface.

Lebedev's relation is considered superior to others for this algorithm because it is based on 24 station-years of observations throughout the Russian (or former Soviet) Arctic and because it describes ice growth under "average" snow conditions. This contrasts Anderson's (1961) formula, which describe ice growth under varying amounts of snow cover and Zubov's (1943), which is based on observations at one physical locale near Cape Schmidt. The snow thickness is an important parameter controlling ice growth, but since there are no routine measurements of snow depth available, errors will be minimized if an average snow thickness is used (Maykut, 1986 and Kwok, 1997).

In the RGPS output fields there is an upper and lower bound (error bar) on the age of the ice for each area of young ice because one cannot resolve the start of the ice growth beyond the sensor repeat coverage interval. For example, if one uses a repeat time step of three days, one does not know if the ice growth started a short time after the satellite took its first measurement or just before its next pass. Theoretically, ice could have been growing for a few minutes or for three days. The high rate of ice growth when the ice is very young results in larger error bars for newer young ice classes.

Three facts must be emphasized regarding the ice thickness algorithm. First, this scheme does not provide estimates of the thickness of first year or multiyear ice. It does give a basin-wide two-dimensional estimation of the thickness of young ice at a fine spatial and temporal resolution and the areal

fraction (cell area percentage) of first year and multiyear ice at regular time intervals. Second, it must be re-emphasized that the young ice thickness calculated above is the thickness of the ice that is formed in a lead during a divergent event, not the thickness of the ridged ice that forms when the young ice is compacted during ice convergence. Ridge thickness calculations are discussed below. Third, it must be understood that the thicknesses calculated are that of the whole ice depth, i.e., the draft and freeboard of a young ice sheet (Kwok et al., 1992).

c. Ridge Thickness Calculations

The ice thickness calculations for ridged ice are determined by compressing the previously calculated young ice in the newly formed lead and conserving its volume in the resultant ridge. The dimensional calculations are centered around the k parameter, which is based on a ridging study conducted by Parmerter and Coon (1972). This study assigned a value of five to the k parameter and concluded that a typical ridge will occupy a (horizontal) width of approximately $1/(k-1)$, or one fourth, units of the open lead and will have a sail height k , or five, times that of the thin ice that undergoes ridging. This is a simplification that does not take into account the fact that ice on the order of a fraction of a meter may ridge to five or six times its original thickness, while thicker ice ($>1\text{m}$) will not, due to its inherent strength. The algorithm also does not take into account that even ice of the same thickness may have different strengths, depending on the salinity of the ice as well as other factors. It also ignores the fact that a pressure ridge has some air pockets between the rubble pieces, which has been estimated to make up as much as 30% of the ridge volume. As has been stated before, the relatively coarse temporal resolution of RADARSAT imagery results in an underestimate of lead and ridging events in RGPS output.

4. Ice Deformation Products

The sea ice algorithm calculates the area changes and individual ice motion spatial derivatives of all the grid cells. Deformation values for divergence, shear and vorticity are calculated from the manipulation of the individual spatial derivatives as listed below:

$$\text{divergence} = \frac{\partial u}{\partial x} + \frac{\partial v}{\partial y}$$

$$\text{shear} = \left[\left(\frac{\partial u}{\partial x} - \frac{\partial v}{\partial y} \right)^2 + \left(\frac{\partial u}{\partial y} + \frac{\partial v}{\partial x} \right)^2 \right]^{1/2}$$

$$\text{vorticity} = \frac{\partial v}{\partial x} - \frac{\partial u}{\partial y}$$

Areas of divergence imply open water leads that fill with young ice if the air temperature is below the freezing point. Convergence implies the formation of pressure ridges. Ice deformation motion is rarely purely divergent and some aspects of shear and vorticity are associated with it. The algorithm calculates the ice thickness of young and ridged ice using data from both the RGPS thickness and deformation files.

It is noteworthy that the units for these deformation products are not the usual inverse seconds (s^{-1}), but inverse days, as the interval between subsequent SAR operations is measured in days (Kwok, personal communication, 1997).

5. Other RGPS Products

Other RGPS sea ice algorithm products are the summer time open water fraction, melt onset/freeze-up dates and backscatter histograms. These products are not discussed in detail, since they have no direct bearing on this research.

6. Measurement Errors

Three types of errors are associated with the RADARSAT sensor. Radiometric errors can contaminate the raw imagery. These errors are correctable through sensor calibration. A calibration routine in the RADARSAT processor converts digital numbers in raw data to normalized backscatter values. Geolocation errors of the individual image pixels may contaminate some of the RGPS products, especially those of ice deformation. These errors are due to frame-to-frame misregistration difficulties. For ERS-1 data, these errors caused an uncertainty in ice displacement of 0.3 km. The tracking error is the uncertainty in identifying common features in an image pair (Kwok, 1997).

Not all of these errors have been assessed for RADARSAT. Preliminary processing of cycle 15 data showed that up to 50% of cells may have along-track geolocation errors of 0.4 km due to PRF ambiguity. This creates artificial “openings” and “closings” perpendicular to the satellite track, when the error is present in one image but not the other of a repeat pair. These errors may necessitate a total reprocessing of the cycle (Stern, 1998).

V. DATA ANALYSIS

A. BACKGROUND

Once the cycle 15 RGPS data set was obtained from Kwok, SAR data analysis could commence. Figure 3 shows that the investigative actions that would have to be taken to satisfy the research goals

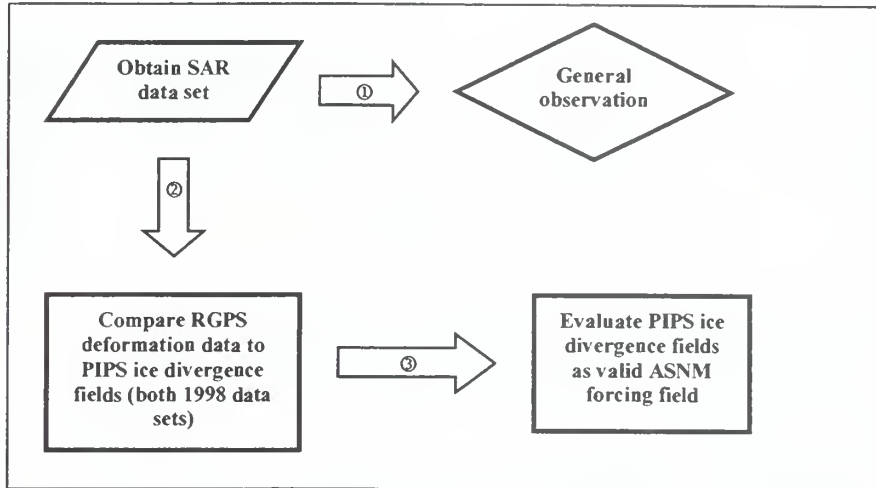


Figure 3. “Ideal” thesis process flow diagram possible if all data sets had been coincident in time. Numbers represent the sequence of research steps.

should be relatively straightforward. First a qualitative, large-scale investigation of the sea ice data presented in the RGPS data streams would describe the nature of the ice cover’s deformation on a basin scale. Next, PIPS ice divergence fields would be compared to the RGPS ice divergence and percent area change charts to ascertain if PIPS does a creditable job of quantifying the actual ice deformation. An evaluation of the PIPS model’s performance could then be made.

Unfortunately, the actual data investigation progression of this research effort was not as simple as described above as depicted in Figure 4. The reason for this is that the only RGPS data set that had been processed at the time of this research (Oct 1997 to May 1998) was cycle 15, collected in Nov 1996. A matching set of PIPS ice divergence fields could not be located, since FNMOC does not archive PIPS data for extended periods. This lack of temporal coincidence in the two data sets necessitated the search for an “intermediate” meteorological variable in Navy Operational Global Atmospheric Prediction System (NOGAPS) data, which was available for both the 1996 RGPS and 1998 PIPS data periods. If such a variable could be shown to relate the nature of atmospheric forcing to the deformation of the ice cover evident in the RGPS products, that same variable could then be compared to current PIPS data to ascertain how well the ice model is able to reproduce the ice divergence patterns resulting in leads and pressure ridges. In addition to the RGPS deformation data, which consists of percent cell area change, ice divergence, shear and vorticity, the RGPS ridging algorithm output is used to calculate ridging statistics that help characterize the deformation of the ice cover during the cycle 15 period. This analysis is related

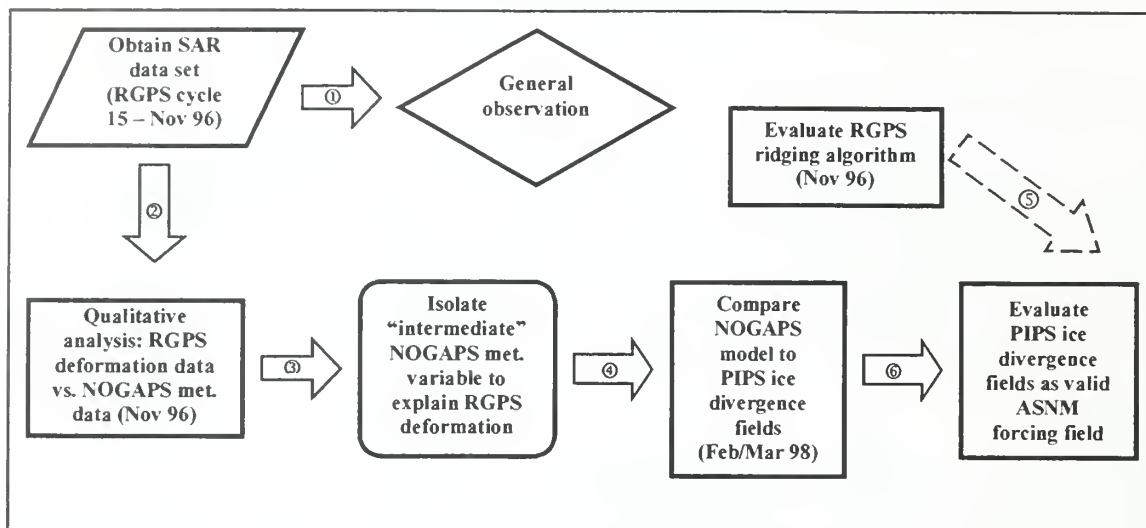


Figure 4. Actual thesis process flow diagram. The isolation of an “intermediate” meteorological variable was necessary because the RGPS and PIPS data sets were not coincident in time. Numbers represent the sequence of research steps.

to the evaluation of the PIPS model by a dashed arrow in Figure 4, since it is accomplished indirectly. This means that conclusions drawn from 1996 ridging statistics are loosely compared to pressure ridges implied by 1998 PIPS ice divergence data. One does not expect good quantitative correlation during these periods due to differing environmental forcing, but this comparison is still useful.

B. DATA SETS

1. RGPS Deformation Data

As described previously, Kwok of JPL provided a complete set of hardcopy cycle 15 RGPS deformation data products for this research. The set consists of percentage cell area change (analogous to ice divergence), ice divergence, shear and vorticity products. Two data streams exist for cycle 15 in this data set. The first one extends from the Beaufort Sea at approximately 85°N southwest into the East Siberian Sea. It contains one of the investigated areas, A, at its extreme shoreward end (see Figure 5). The other data stream is located in the Beaufort Sea and extends from approximately 87°N in a southwesterly direction towards Point Barrow, Alaska. This data stream contains the other investigated area, B, at its southern end (see Figure 5). The data set spans the period from 07 to 27 Nov, however data is not present for the whole cycle at all geographic locations in the two data streams. The spatial resolution of the initial data cell grid is 5 km initially, but changes size as a result of the ice cover’s deformation. The temporal resolution (time between subsequent snapshots) of the RGPS data products is normally three days. This data set represents the ground truth that the NOGAPS meteorological data is directly and the PIPS data is indirectly compared to. Complete sets of the hardcopy cycle 15 RGPS cell area change and shear products are contained in Appendix C and D. Hardcopy of the ice divergence is not included in an appendix since it

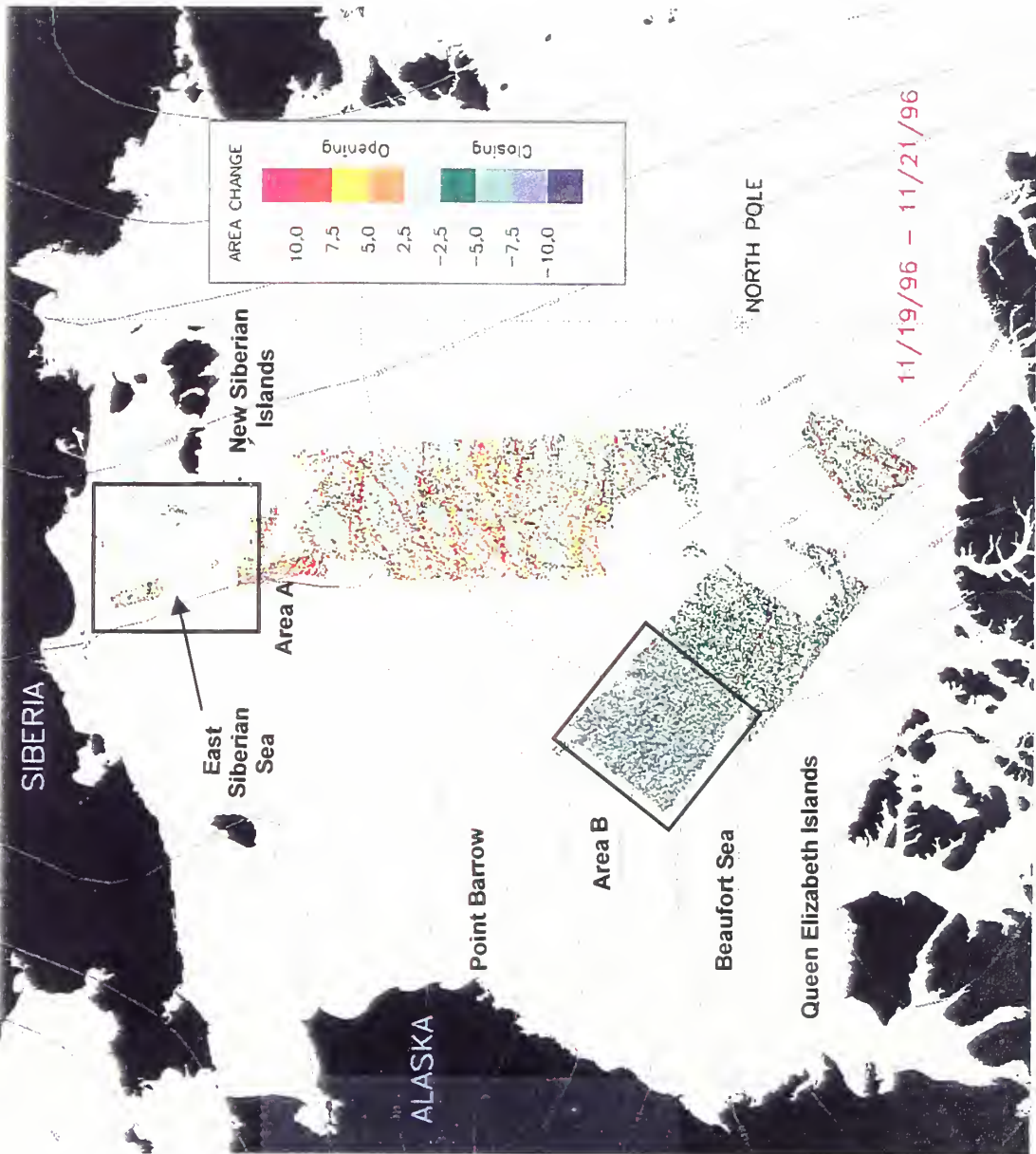


Figure 5. Sample graphic showing output of the RGPS percent cell area change sea ice product. Red, orange and yellow cells are undergoing ice divergence (opening), while green and blue cells are experiencing ice convergence (closing). Light green cells are experiencing little deformation. Numbers in legend represent percentages of cell area change over the snapshot temporal resolution, approximated to be three days. The two investigated areas, A and B, are also depicted.

is nearly identical to the percent cell area change product. Hardcopy of the vorticity product is not included since vorticity has little bearing on this research effort.

2. NOGAPS Meteorological Data

NOGAPS meteorological data for this research was obtained from the NPS Meteorology Department. 1996 meteorological data were recovered from 8 mm archive tapes. Only 2.5°×2.5° grid spacing NOGAPS data was available for this period. NOGAPS data for the 1998 PIPS evaluation period was of finer 1°×1° resolution, resident in the GEMPAK database.

Meteorological data was displayed and printed using GEMPAK version 5.2.1 meteorological data display software. Color plots of 0000Z and 1200Z analyses were generated for the two investigation periods. Plotted data included the mean sea level pressure, 10 m wind, the divergence of the 10 m wind and the surface air temperature. Figure 6 represents a sample plot of this data. To simulate the free ice drift, the 10 m wind vectors at each NOGAPS gridpoint were rotated 28° to the right and their speed decreased by 98% using a GEMPAK script file. New ice divergence fields were then calculated and plotted (see Figure 7). These new divergence plots represent the ice drift in response to the forcing imposed by the 10m (surface) wind and are called the NOGAPS model ice divergence fields in this research.

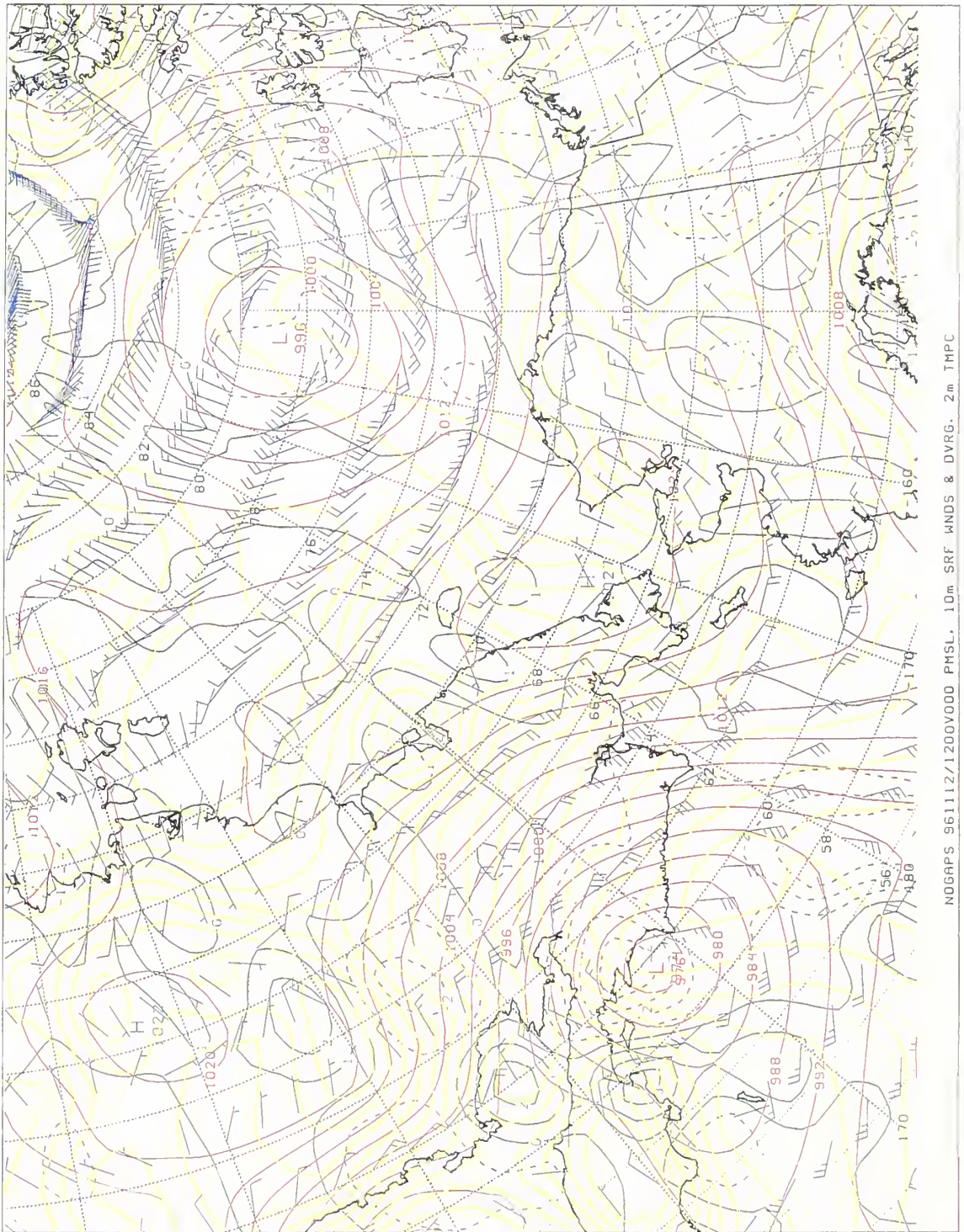
European Centre for Meteorology and Weather Forecasting (ECMWF) wind data have generally been judged superior to NOGAPS wind fields (Maslowski, personal communication, 1998). ECMWF wind data was available for this research, but was not chosen, because the PIPS model is forced by NOGAPS, not ECMWF, wind fields. The goal of this study was to evaluate the PIPS model's performance, not the validity of NOGAPS winds. The comparison of ECMWF meteorological data to PIPS sea ice fields would have introduced an unknown error into the analysis process which needed to be avoided.

Model analyses of weather data have proven to be inaccurate at times because of the sparsity of meteorological observations in the polar regions. Comparison of the NOGAPS model fields to actual observations from the International Arctic Buoy Program (IABP) sensors would have been beneficial to validate meteorological data, but were beyond the scope of this study.

The GARP meteorological software program was initially used to display weather data for the cycle 15 RGPS data period. Although GARP is more user-friendly and has a better graphical user interface than does the GEMPAK software, it has several shortcomings that made it unsuitable for this research effort.

1. GARP did not allow the manipulation of NOGAPS variables as does GEMPAK. No method, such as a scrip file, exists for rotating the 10 m wind at model gridpoints to calculate the NOGAPS model ice divergence.

2. GARP did not allow the display of the 10 m or surface wind field. An atmospheric pressure level had to be chosen for which weather elements were calculated and displayed, i.e., 1000 mb or 925 mb.



NOGAPS 961112/1200000 PMSL. 10m SRF MNDS & DVRG. 2m TMPC

Figure 6. Sample chart of NOGAPS meteorological data. Blue wind barbs are $2.5^{\circ} \times 2.5^{\circ}$ 10 m winds (knots), red lines are mean sea level pressure (MSLP) isobars (mb), yellow lines are air temperature ($^{\circ}\text{C}$) isotherms, green solid lines are isolines of 10 m wind divergence ($\times 10^{-5} \text{ s}^{-1}$), green dashed lines are isolines of 10 m wind convergence ($\times 10^{-5} \text{ s}^{-1}$)

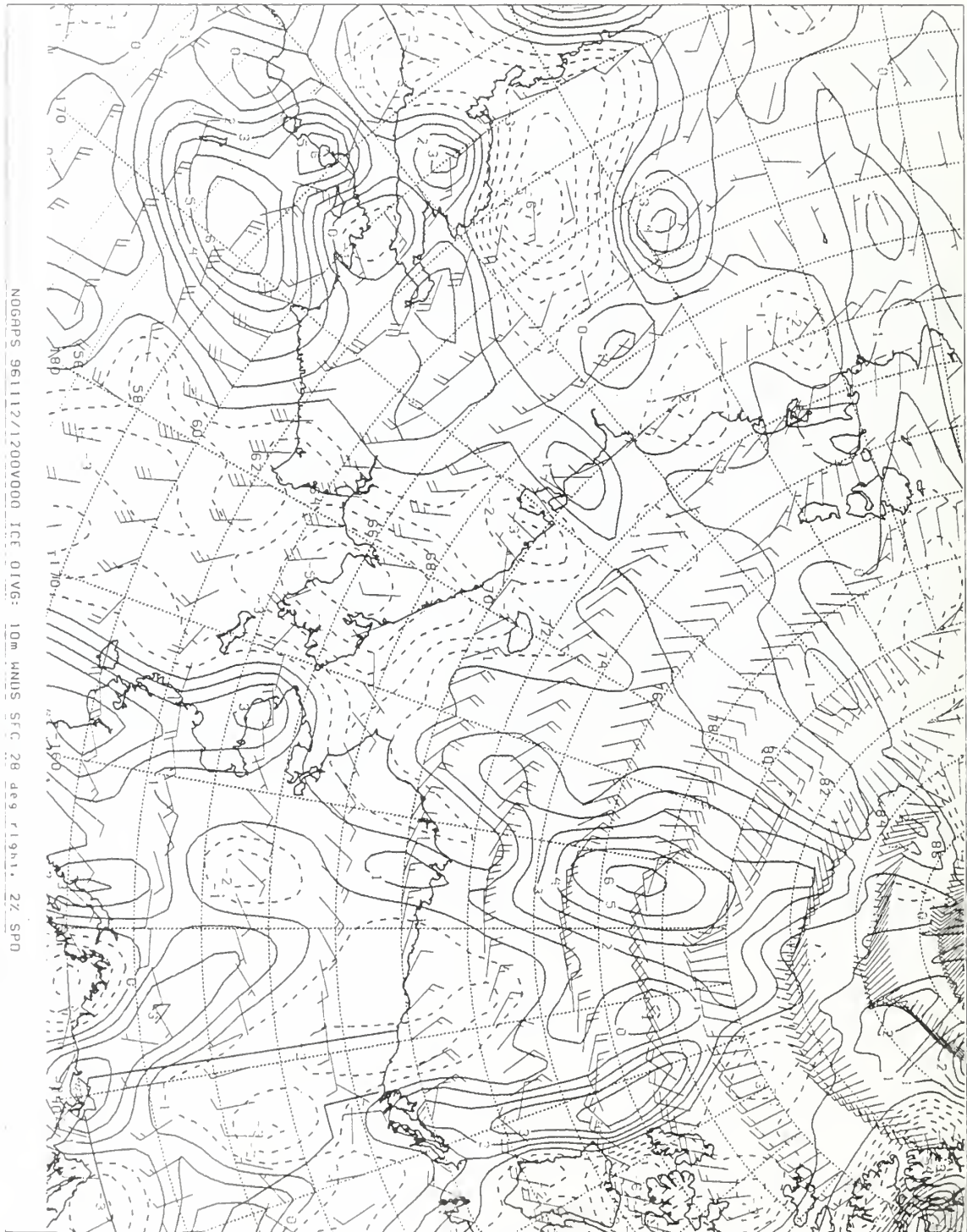


Figure 7. Sample chart showing NOGAPS model ice divergence. Solid contours show ice divergence ($\times 10^{-7} \text{ s}^{-1}$) and dashed contours show ice convergence ($\times 10^{-7} \text{ s}^{-1}$). Grid point wind barbs are rotated 28° to the right from the 10 m wind direction. The wind barbs show the direction of ice drift, but the velocity feathers on this product are meaningless.

This is an unsuitable plotting method, since large fluctuations of atmospheric pressure in Arctic latitudes would produce data at various heights above the ice surface instead of at a constant one.

3. Wind divergence values calculated by GARP were of suspect accuracy because they did not appear to match expected positions in relation to surface pressure features. In other words, one expects wind convergence into a surface low pressure system and wind divergence out of a surface high. Additionally, the whole wind divergence field took on an unrealistic, jagged appearance if the GARP map boundaries extended too close to the North Pole, i.e., when the map latitude approached 90°N.

3. PIPS Data

PIPS 2.0 model data was collected in hardcopy form directly from FNMOC. Products collected include ice coverage, thickness, drift and divergence and wind stress data for an area roughly matching the RGPS data products, i.e., the Canadian Basin of the Arctic Ocean.

4. RGPS Ridging Algorithm Data

The JPL RGPS Development Team has written a program using the Interactive Development Language (IDL) that calculates ice ridging statistics from the thickness and deformation products of the RGPS sea ice algorithms (Cunningham, personal communication, 1998). This program is currently being incorporated as a permanent addition to the suite of RGPS sea ice algorithms. Cunningham of JPL was kind enough to provide a copy of the IDL code to the author, which was adapted to run on a NPS Oceanography Department SUN Sparc 4 workstation. The output of this program provides useful data, complementing the conclusions reached by analysis of the SAR data cycle 15 deformation products in areas A and B. Two ridging algorithm data streams match those of the RGPS deformation data. Two additional streams can be displayed by the ridging program, but were not investigated in this study.

5. Ambient Noise Data

No submarine or buoy ambient noise data was available for either the 1996 RGPS deformation or the 1998 PIPS data period in the analysis area. Unfortunately, this denies the investigator the opportunity to make direct comparisons between RGPS deformation observations, PIPS model output and observed AN data. Although no quantitative correlations between environmental forcing and extreme AN events can be made, the intensity of AN can be implied from the degree of ice deformation observed.

C. GENERAL OBSERVATIONS

The following observations were made by performing a subjective, large-scale investigation of the two data streams presented in the RGPS ice deformation products.

1. Well-defined areas of lead formation (ice divergence) and ridged ice (ice convergence) dominate all the snapshots.

2. Leads appear stronger and more pronounced than ridges in the deformation data, as evidenced by more adjacent cells in leads showing opening area change percentages or increasing divergence values (depending on which product one investigates). Leads generally extend for greater distances than ridges do. Ridges are fewer in number and lack continuity. This was first thought to be a function of the ScanSAR Wide B sensor's 100 m resolution. In other words, pressure ridges generally have a smaller width than leads and some may therefore not be picked up by RADARSAT. However, one must remember that RGPS deformation maps are based on area change calculations between subsequent sensor passes and not the physical identification of ridge and lead pixels in raw SAR imagery. In other words, ridges and leads are derived by the RGPS algorithm, not sensed in the raw image. It seems logical that there are more leads than ridges, since not all open water leads necessarily compress into pressure ridges, but every ridge is preceded by a lead.

3. Areas of lead formation align themselves perfectly with the three-day average of the four millibar (mb) surface pressure gradient in the western data stream during the 07 to 09 Nov 96 snapshot (see Figure 5). This pattern does not repeat itself in subsequent snapshots and no explanation can be given for its singular appearance.

4. Hibler and Schulson (1997) state that leads and ridges in sea ice appear to have preferred orientations when examined on a large scale. The Arctic ice cover can be thought of as a thick ice sheet interspersed with leads covered by thin ice. The thick and lead ice obey an isotropic constitutive law with a yield curve approximating a truncated ellipse. When an outside force is applied to the system, in the form of wind forcing for example, the thick/thin ice sheet system, or aggregate, tries to achieve plastic equilibrium (large strain rates) or a viscous-plastic approximation (small strain rates). Laboratory measurements of aggregates show that some leads in a system appear to open rapidly, while others open slowly or not at all during biaxial failure. Leads that form rapidly in such a manner are called “strain-hardened”. The orientation of the strain hardened leads depends on the orientation of the stress in the stress-strain system. In other words, a certain preferred angular separation between two leads or ridges, θ , will form depending on the stress-confinement ratio of the system (see Figure 8). This response is isotropic in a sense, since it behaves identically regardless of the direction from which the wind forcing, i.e., stress,

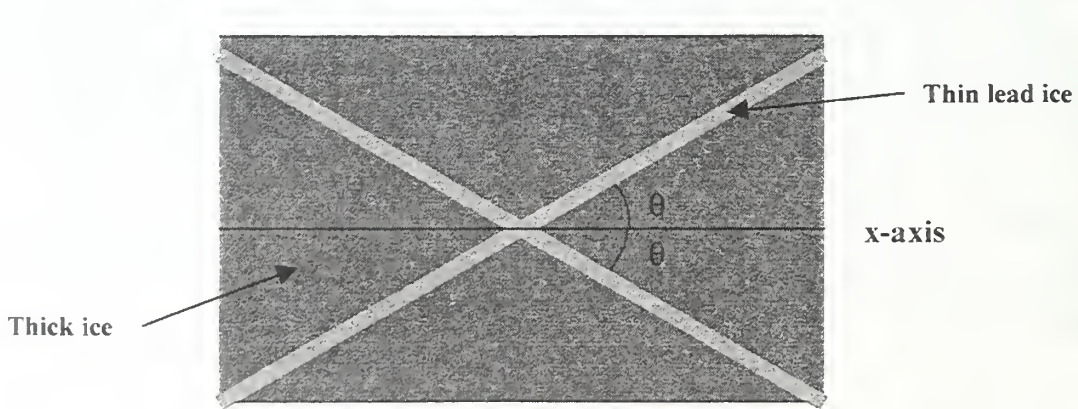


Figure 8. View of two rapidly opening strain-hardened intersecting leads with preferred values of θ .

is applied. For systems of two intersecting leads, frequently observed values for θ are $\pm 18^\circ$ and $\pm 36^\circ$ relative to the x-axis as shown in Figure 8.

The orientation of leads around preferred angles is easily observed in the cycle 15 RGPS deformation data. Leads exhibit these preferred orientations particularly well because they appear more pronounced in the data streams. In addition to parallel lead-ridge systems, specific angles between intersecting lead-ridge systems appear to fall into two broad categories in the deformation data, one less acute, perhaps close to 18° , the other more acute, approximately 36° (actual angles were not measured).

D. COMPARISON OF RGPS DEFORMATION TO NOGAPS METEOROLOGICAL DATA

1. Analysis Technique

a. General

The NOGAPS model fields of the atmospheric variables, described in Section V. B. 2. of this chapter, were compared to the RGPS ice deformation hardcopy graphics, described in Section V. B. 1. of this chapter, in two different geographic areas covered by RGPS data streams referred to as area A and area B. Correlations are qualitative and referred to as “strong”, “moderate”, “weak” or “negative”. These descriptors attempt to quantify how well the meteorological variables explain the ice deformation observed in the RGPS data. For example, if a moderately strong wind of 25 knots provided constant onshore flow over three days, and resulted in massive ice convergence in the RGPS data, the correlation is called “strong”. Alternately, if the same onshore flow showed nothing but ice divergence, the correlation would be classified as “negative”. Likewise, if constant and steady wind divergence or NOGAPS model ice divergence results in RGPS ice divergence, correlation is “strong”, while wind convergence or NOGAPS model ice convergence in the presence of pure RGPS ice divergence is classified as “negative”. The “moderate” and “weak” classifications are assigned to less extreme cases than those described above.

Area A is approximately square in shape and is located in the East Siberian Sea at the extreme shoreward end of the western cycle 15 RGPS datastream (see Figure 5). The East Siberian shore is located approximately 130km to the south of area A, while the five major islands of the New Siberian Archipelago form a barrier 130 to 220 km to the west. Area A’s ice cover is coastal in origin, relatively thin and highly deformed.

Area B lies in the thick, permanent and uniform ice sheet of the high Arctic in the Beaufort Sea. It is also roughly square in shape and is located at the southern end of the more easterly cycle 15 RGPS data stream (see Figure 5). Although this area is not considered coastal in origin, with the closest land, Banks and Prince Patrick Island located approximately 460 km to the east, some of its ice cover may have been advected into it from coastal regions. These investigation areas were selected for three reasons. First, they are geographically distant from each other, which causes them to undergo different environmental forcing. Second, area A is located in a coastal environment, while area B lies in the open ice of the high Arctic. The differing nature of each area’s ice cover makes for an interesting comparison between the two locales. Third, since each area is located at the extremity of a RGPS data

stream, they are easy to locate in successive images.

NOGAPS ice divergence values were calculated as described in Section V. B. 2. A complete discussion of ice drift due to atmospheric forcing is provided in Section V. D. 2.

Each RGPS snapshot of approximately three-day duration was compared to the six 12-hour weather analysis charts corresponding to the same period. Each of the meteorological variables is evaluated to ascertain if the quantitative changes seen in the analysis charts can qualitatively explain the ice deformation that is taking place in the Arctic snapshot data stream. It would have been easy to average the meteorological values over the three-day RGPS time step. This was not done however, because the RGPS ice deformation could not have been explained by the averaged surface winds, wind divergence or ice divergence fields. The 12-hour change of these variables over the three-day observation period, not the mean values, provided the answers to the ice deformation observed. Averaging the 12-hourly meteorological parameters in the NOGAPS charts to match the temporal resolution of the RGPS deformation output would result in the loss of available detail to understand what is happening in the RGPS products. Although a quantitative correlation analysis between three day-averaged NOGAPS model ice divergence and RGPS divergence may be a valid follow-on to the work done here, one must not discount the value of a subjective analysis.

b. Meteorological Variables Investigated

Each meteorological variable analyzed and compared to RGPS deformation data is briefly described below.

(1) On/offshore Flow of the Surface (10 m) Wind. The direction of flow of the 10 m wind is expected to correlate well with RGPS ice divergence in the coastal locale of area A (see Figure 5). For investigation purposes, any wind veering from the NNW to the SSE is considered an onshore wind in area A. Winds from NNW to NE are onshore to the coast of the East Siberian Sea, while NE to SSE winds push ice into the virtually closed sound between the Siberian coast and the New Siberian Islands. Winds in a sector from NW to NE are considered onshore in area B, however the nearest land is located 445 km to the east, which should diminish its influence on area B ice deformation.

One would expect divergent activity and lead formation in the ice cover with an offshore wind, while an onshore wind should result in ice convergence and ridge building in pre-existing open water leads in coastal ice regions.

(2) Wind Divergence. Wind divergence (convergence) can be visualized as the net air outflow (inflow) from (into) a specific geographic location. Divergence (convergence) is associated with an atmospheric high (low) pressure system or ridge (trough) at the surface, where a vertical downdraft (updraft) of air is forced outwards (inwards) to satisfy the law of continuity. Divergence and convergence pattern changes may also result as the velocity of the wind changes in a horizontal direction, resulting in velocity shear. The mathematical expression for divergence is:

$$\frac{\partial u}{\partial x} + \frac{\partial v}{\partial y}$$

and its units are seconds⁻¹. If sea ice moved directly downwind of the surface wind, one would expect ice convergence under the influence of a surface low and ice divergence in the presence of a surface high. However, since the ice moves to the right of the surface wind or roughly parallel to the geostrophic wind (see Section V. D. 2.), a good correlation between wind divergence and the RGPS ice deformation is not expected.

(3) Advection of the 10 m Wind Divergence. Since the deformation of the ice cover may not be a function of the local atmospheric forcing through wind divergence, the advection of the 10 m wind divergence is also investigated. Regions of divergence and convergence that are located upstream in the surface wind flow pattern outside of the investigated areas' boundaries are moved with the flow into the investigated area. The distance that advected wind divergence values are moved is arbitrary, with higher wind speeds bringing wind divergence values from farther distances than low speeds. Advection distances average approximately 280 km and do not exceed a maximum of 465 km. Only weak to moderate correlation between wind divergence advection and ice deformation is expected, for the same reasons described in the preceding paragraph.

(4) NOGAPS Model Ice Divergence. 10 m wind divergence fields were rotated 28° to the right of the surface wind direction and the ice drift speed was assumed to be 2% of the surface wind speed, to simulate free ice drift in response to surface wind as described by Zubov (1943). Subsequent research has provided slightly different surface wind-ice drift angles and wind-ice drift speeds, depending on differing Arctic geographic locations and seasons, but Zubov's Law (1943) is generally still valid today and sufficiently accurate for purposes of this research.

This approach to modeling ice drift is relatively simplistic, since Zubov's Law is valid for free ice drift only, not for ice motion in the thick, locked ice cover of the high Arctic in the winter season. The local wind direction is also important to the calculation of the angle between the surface wind and ice drift and the ratio between wind and ice drift speeds, since the advection of warm air from the south and cold air from the north changes the stability of the local atmospheric boundary layer (ABL) (Overland and Davidson, 1992). This, in turn, affects the direction of the thermal wind. The forcing provided by Arctic oceanic currents is also assumed to be constant, which is not a valid assumption. One must remember that the goal of creating the ice divergence plots from the NOGAPS surface winds field is not to develop a sophisticated ice drift model, but to define an environmental variable, easily isolated from NOGAPS data files, that links atmospheric forcing to ice deformation. One must also not forget that this step would be unnecessary if data sets of RGPS ice deformation and PIPS ice divergence existed concurrently in time.

The deflection of the ice motion to the right of the surface wind reverses the association between wind divergence and atmospheric lows and highs discussed in Section V. D. 1. b. (2)., i.e., ice movement is divergent in association with a surface low and convergent with a surface high (as shown in Figure 9). NOGAPS model ice divergence is expected to provide better correlation to ice deformation than wind

divergence, but since the Arctic ice sheet is not in free drift and oceanic forcing is ignored, only moderate correlations are expected.

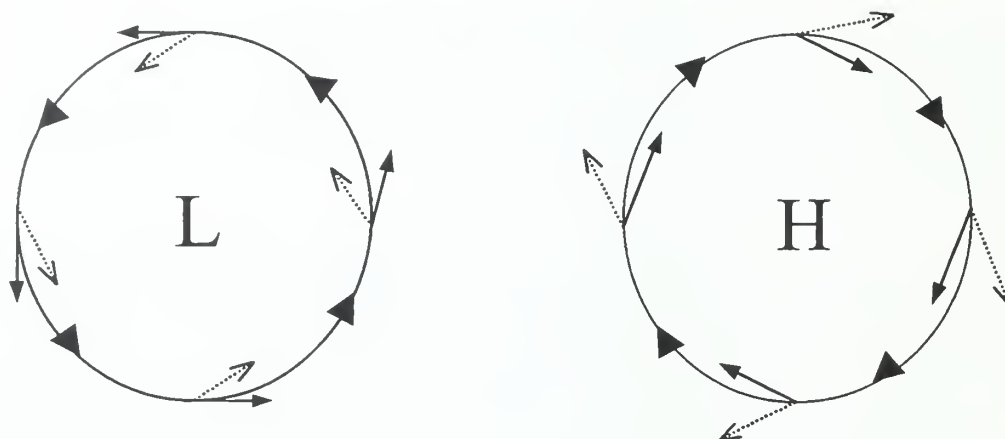


Figure 9. Wind and ice con/divergence associated with low (L) and high (H) pressure systems. The circles represent an idealized closed isobar around the system center. Big arrowheads on circles represent the geostrophic wind direction. Dashed arrows show surface wind convergence into a low pressure system and out of a high pressure system due to friction and continuity. Solid arrows depict the ice divergence associated with the wind divergence patterns. The ice drifts 28° to the right of the surface wind vector. Ice convergence is associated with atmospheric highs and ice divergence with atmospheric lows.

2. Analysis Results

Analysis results and observations regarding the qualitative correlation between the NOGAPS meteorological variables and RGPS ice deformation are presented in the paragraphs below and in Tables 1 and 2. More detailed period-by-period analyses for areas A and B, which describe the weather patterns, specific meteorological forcing present and RGPS ice deformation and their correlation, are presented in Appendices A and B, respectively.

a. Area A Analysis Observations

- The meteorological situation that causes the ice divergence followed by ice convergence sequence in this region is the alternation of atmospheric lows/troughs and highs/ridges in the East Siberian Sea coastal zone. The passage of these weather systems changes the direction of the 10 m wind from offshore to onshore in the first three snapshot periods and back to offshore in the last snapshot period.
- Open water lead events correlate more with the offshore flow of the wind than with any other correlation parameter in this area. The ice ridging events correlate most with onshore winds than with any other parameter.
- The next best qualitative correlator for area A during the cycle 15 period is the NOGAPS model ice divergence field. It does not explain all ice deformation events, but it performs better than the physical location or advection of the wind divergence field.

		Meteorological situation	Wind speed (knots)	RGPS deformation analysis (divergence values expressed as % of cell area change over the temporal resolution, assumed as 3 days)	Subjective correlation, comparing RGPS ice deformation with the:		
					On/offshore flow of the 10 m wind	Divergence of the 10 m wind	Advection of 10 m wind divergence
Period 1	11/07	High pressure ridge	5-10	Mostly divergent (>+10.0), 3 "super-leads" present in vicinity of East Siberian Sea flow lead, some ridges (-2.5 to -5.0).	Strong	Weak	Weak
	11/08	Trough, then low	10-30				
	11/09	Low	5-15				
Period 2	11/10	Low, then high pressure ridge	10-15	Exclusively divergent (+2.5 to >+10.0), continued "super-lead" formation.	Strong	Strong	Moderate
	11/11	High pressure ridge	10-15				
	11/12	High pressure ridge	5-10				
Period 3	11/13	High pressure ridge, then trough	5-10, then 15-35	Almost exclusively convergent (-2.5 to >-10.0), strong ridging activity.	Strong	Moderate	Weak
	11/14	Trough	15-30				
	11/15	Trough	15-25				
Period 4	11/16	Deep low	10-30	Very sparse, scattered data Widespread divergence (+2.5 to >+10.0), few scattered areas of strong convergence (>-10.0).	Strong	Weak	Moderate
	11/17	Deep low to NNW, low approaching from SE	15-45				
	11/18	Low to SE, then E	5-15				

Table 1. Summary of the qualitative analysis in area A comparing the RGPS ice deformation to various meteorological variables generated by the NOGAPS model. It must be emphasized that the characterizations of "strong", "moderate", "weak" and "negative" in the subjective correlation columns do not refer to a particular meteorological variable, but to its subjective correlation with the deformation observed in the RGPS sea ice data.

	Metereological situation	Wind speed (knots)	RGPS deformation analysis (divergence values expressed as % of cell area change over the temporal resolution, assumed as 3 days)	Subjective correlation, comparing RGPS ice deformation with the:				
				On/offshore flow of the 10 m wind	Divergence of the 10 m wind	Advection of 10 m wind divergence	NOGAPS model ice divergence	
Period 1	11/07	Low to N, high to SW	Broad area of convergence to the north (-2.5 to >-10.0), divergence to the south (+2.5 to +7.5).	Moderate (north), weak (south)	Weak	Weak	Moderate (north), weak (south)	
	11/08	Low to N, high to S then SE						10-25
	11/09	Low to N, high to SE						20-25
Weak	11/10	Ridge	Broad area of convergence (-2.5 to -5.0), intermittent opening areas (+2.5 to +10.0) in SW.	Moderate	Strong (except negative in western area)	Weak	Strong	
	11/11	Between ridge & approaching low						10-20
	11/12	Trough then low						10-20
Period 3	11/13	Low	Mostly divergent, some convergent activity in SE and SW. Ridge-building may actually be occurring in divergent areas.	Weak	Weak	Weak	Strong	
	11/14	Low to NE, high to S						15-20
	11/15	Ridge, deep low approaching from SE						10-30
Period 4	11/16	Under influence of deep low	No RGPS data	N/A	N/A	N/A	N/A	
	11/17	Ridge						10-25
	11/18	Under influence of low						20-30
Period 5	11/19	Low to N, ridge to S	Major convergence (-2.5 to >+10.0), especially in the southern sector. Very few divergent cells in SW	Negative	Negative	Negative	Strong	
	11/20	High to E						30-35
	11/21	Low to SW, high to E						25-35
Period 6	11/22	Low to W, high to E	Central portion of RGPS deformation product missing. Mostly non-divergent, except convergence (-2.5 to >+10.0) in SE.	Negative	Moderate	Weak	Strong	
	11/23	High to E, trough to SW						10-20
	11/24	Weak trough						5-10

Table 2. Summary of the qualitative analysis in area B comparing the RGPS ice deformation to various meteorological variables generated by the NOGAPS model. It must be emphasized that the characterizations of “strong”, “moderate”, “weak” and “negative” in the subjective correlation columns do not refer to a particular meteorological variable, but to its subjective correlation with the deformation observed in the RGPS sea ice data.

- Neither the local wind divergence fields or the advection of wind divergence provide strong correlation to the RGPS ice deformation observed in area A. Only one snapshot period, 10 to 12 Nov 96, shows strong correlation between the two quantities, the remaining snapshots show only moderate or weak correlation.

- Maximum surface winds of 25 to 35 knots are sufficient to cause significant ice deformation. Although winds of this strength are high, but not considered extreme by Arctic winter-time standards, their action results in percent cell area changes in excess of 10% over the three-day snapshot period.

- The ice deformation in area A occurs in isolated and discrete locations except for the 16 to 18 Nov 96 period. The major deformative region in area A is a parallel series of three large “super leads”, so named because of their prominence in the RGPS snapshots, which coincides with the climatological position of the semi-permanent (in winter) East Siberian flaw lead described in Reimnitz et al. (1993). These leads are the largest and most persistent deformative features seen anywhere during this analysis. They represent a semi-permanent shear zone that separates the slowly rotating anti-cyclonic Beaufort gyre from the basin to the south. The “purest” example of what is deemed to be an acoustically active lead exists to the southwest (shoreward side) of the “super lead” area (see Figure 10). The feature shows divergent cell area changes of 5.0 to 7.5% for most of its length with one section showing divergent area change of > 10% during the 10 to 12 Nov 96 snapshot. In the next snapshot, 13 to 15 Nov 96 (Figure 11), the previously divergent feature is now moderately to strongly convergent (2.5% to > 10% convergence). This sequence of RGPS snapshots shows the creation of an open water lead followed by the convergence associated with pressure ridge formation. This is an almost purely divergent event, since the RGPS shear products associated with this time period (Figures 12 and 13) show only low to moderate shear associated with this event. Since this feature extends for hundreds of kilometers and persists for a period of approximately six days, it would most likely represent a significant source of low frequency ambient noise in this region. This feature is also discussed in Section V.E.3.

Although much of the RGPS algorithm data is missing for 16 to 18 Nov 96 (Appendix C, Figure 39) in area A, it is noteworthy that massive homogeneous ice divergence appears to occur during that period. This divergence occurs under the strongest atmospheric forcing observed in the area, with peak winds reaching 45 knots. It is possible that ice deformation in area A is discrete and localized when the atmospheric forcing intensity is below a threshold value and becomes widespread and homogeneous (as in area A) when the forcing exceeds this value. Although very little RGPS deformation data exists in area A to make a confident estimate of this threshold value, it appears to occur above 30 and below 45 knots.

b. Area B Analysis Observations

- The on/offshore flow of the 10 m wind is a weak qualitative correlator to the RGPS ice deformation seen in the snapshots. This fact is not surprising, since area B is located no closer than approximately 445 km to land.

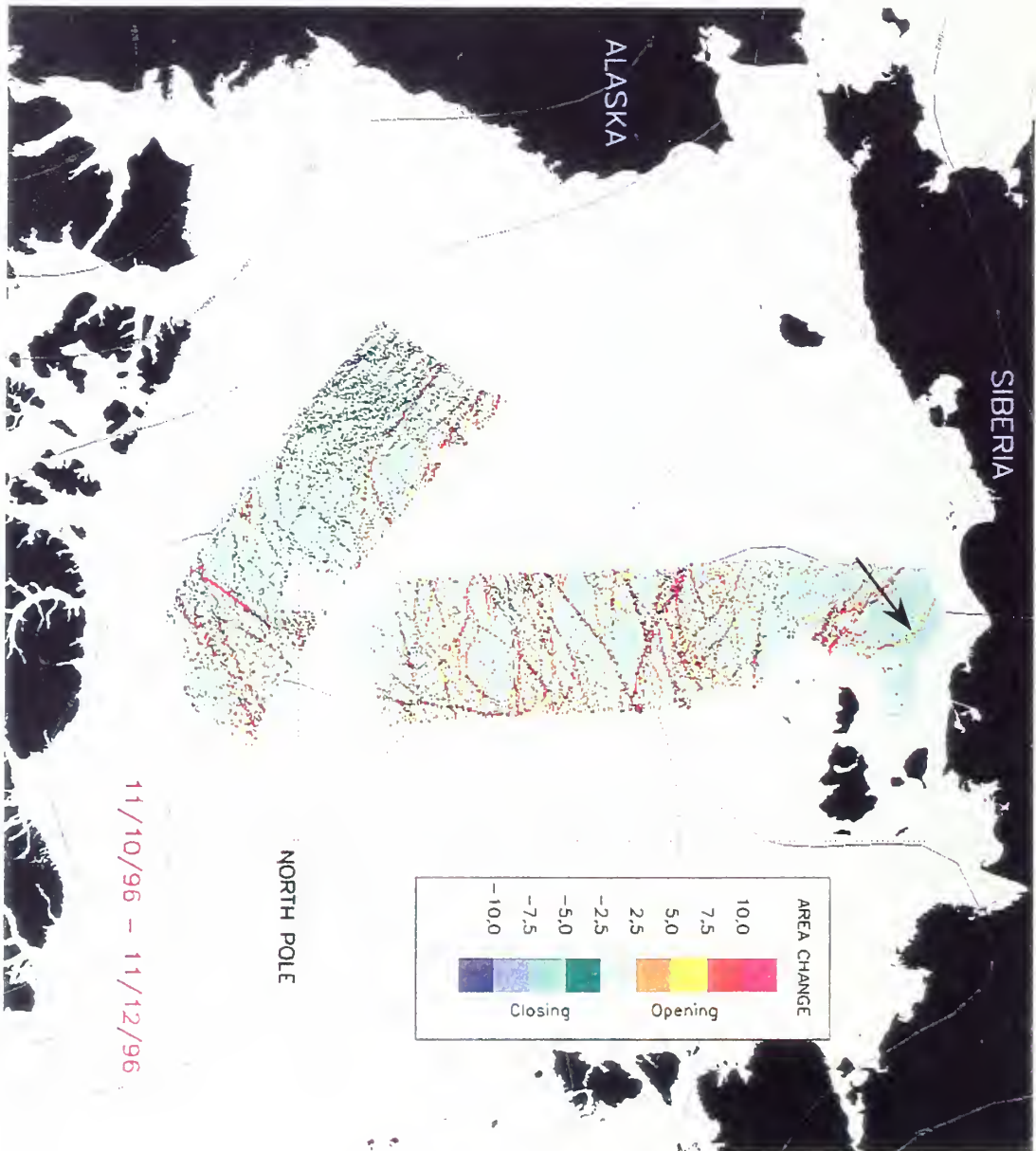


Figure 10. RGPS percent cell area change product for 10-12 Nov 96, showing the creation of open water leads (arrow) during the first (divergent) phase of active acoustic ridge formation.

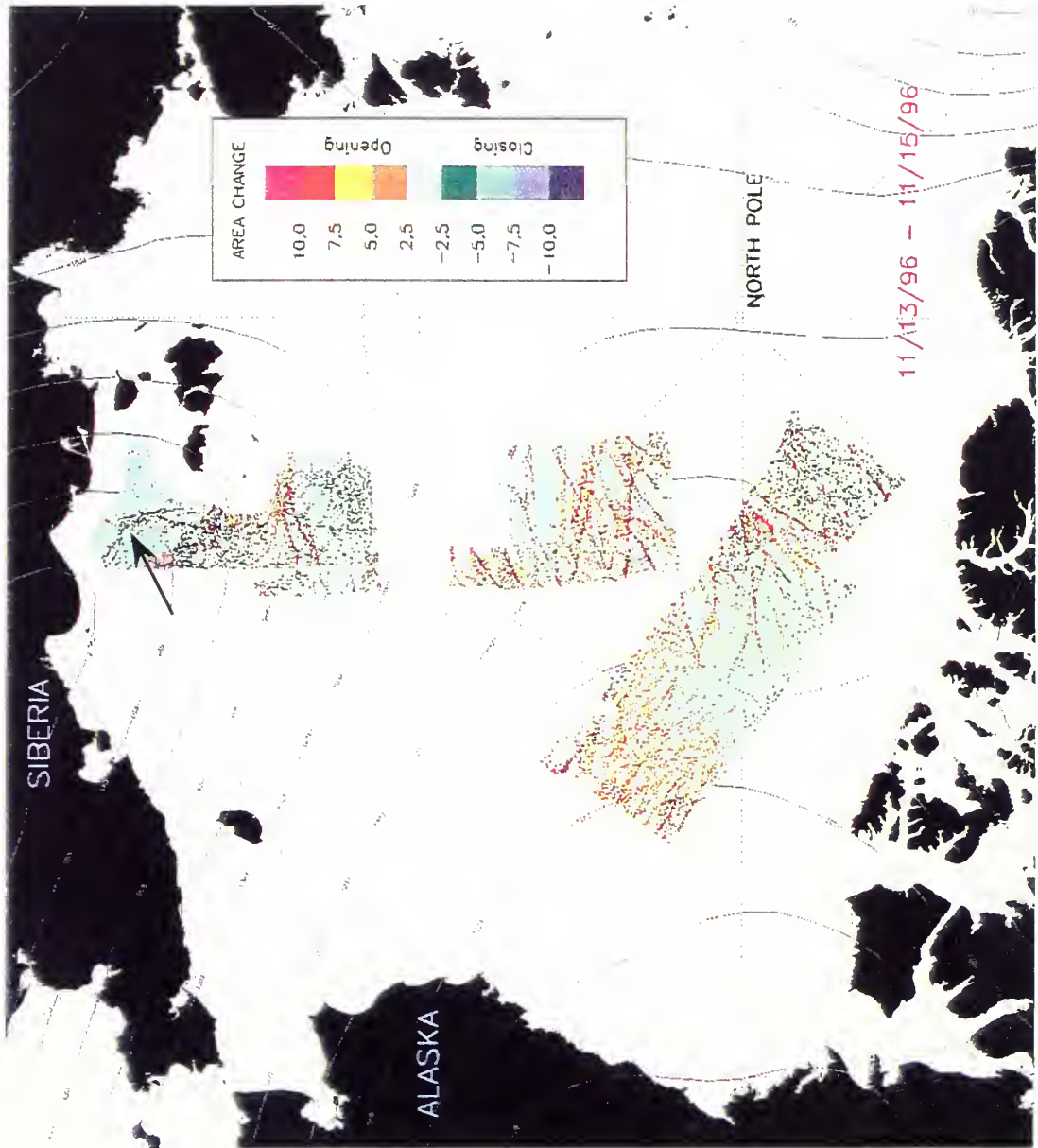


Figure 11. RGPS percent cell area change product for 13-15 Nov 96, showing the creation of an acoustically active pressure ridge (arrow) during the second (convergent) phase of active acoustic ridge formation.

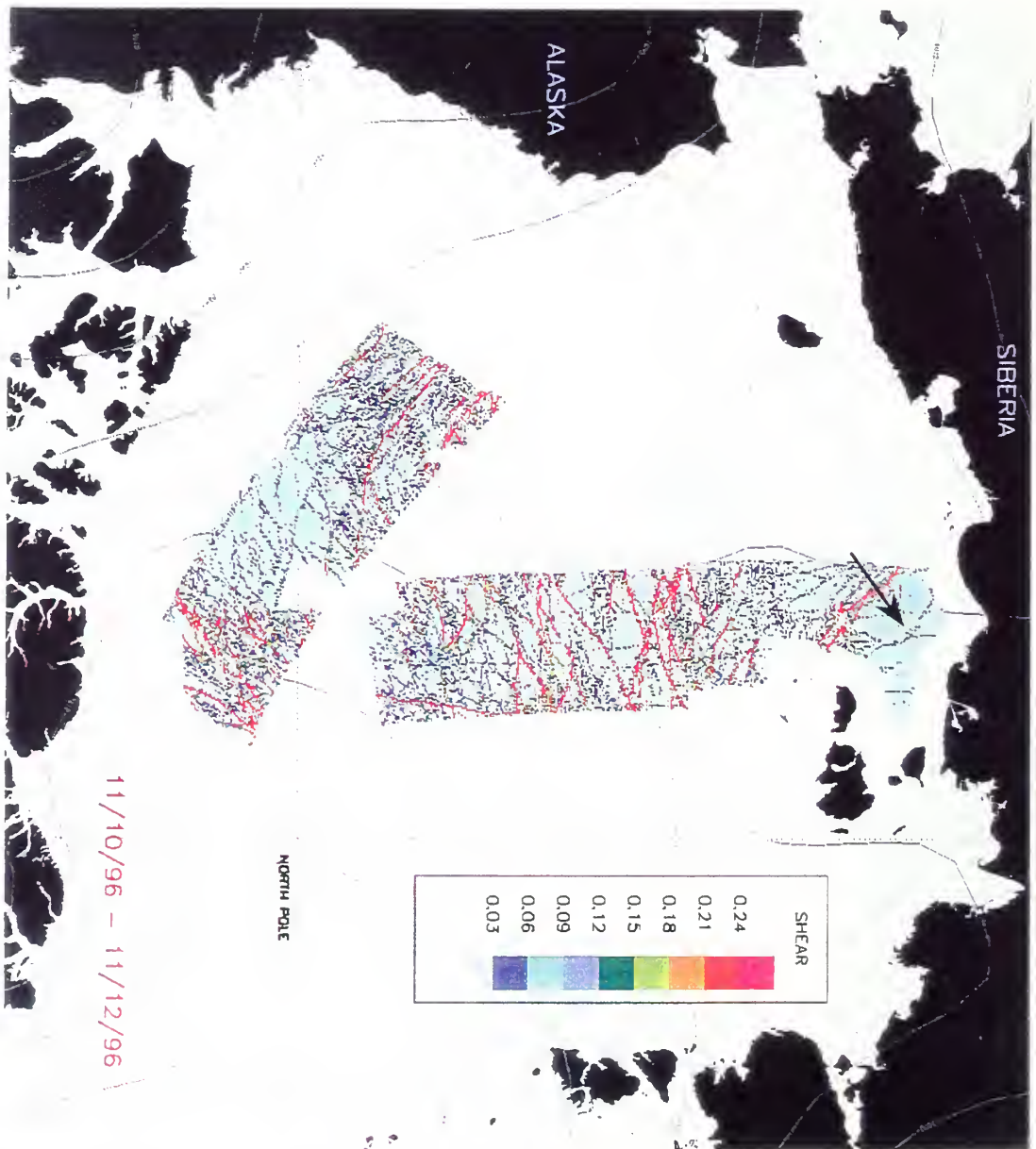


Figure 12. RGPS shear product for 10-12 Nov 96, showing that little shear deformation is associated with the divergent phase of the pressure ridge formation (arrow).

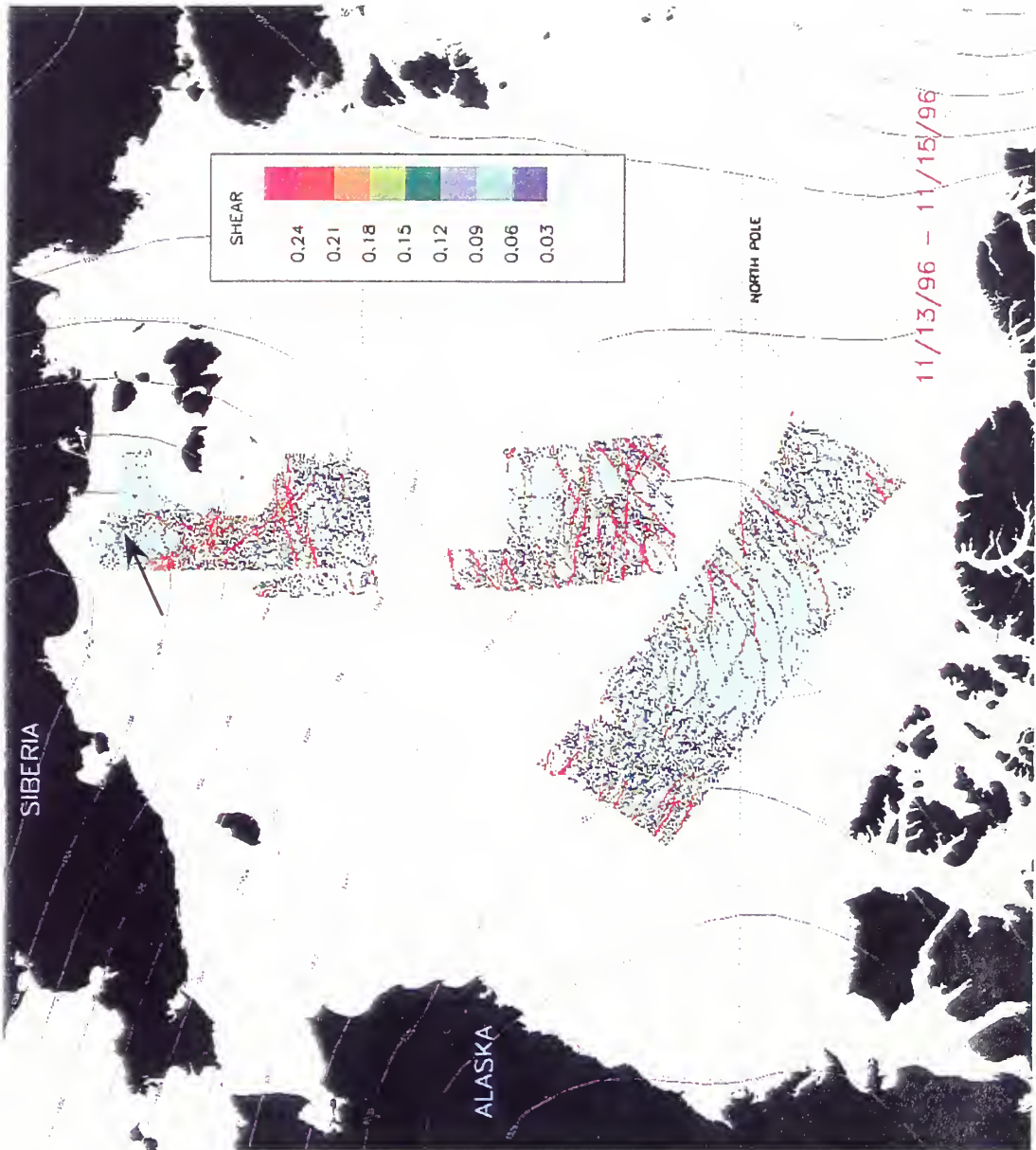


Figure 13. RGPS shear product for 13-15 Nov 96, showing that little shear deformation is associated with the convergent phase of the pressure ridge formation (arrow).

- The NOGAPS model ice divergence variable explains the ice deformation observed in the RGPS products very well. With the exception of the 07 to 09 Nov 96 period, strong correlation existed between NOGAPS model ice divergence fields and ice divergence in the RGPS plots. NOGAPS model ice convergence correlated equally well with RGPS ice convergence.

- As in area A, the 10 m wind divergence fields and the advection of wind divergence do not correlate well with the observed RGPS ice deformation.

- Area A ice deformation tended to be concentrated in specific locales. Leads and ridges in area B cover the whole region and appear to represent a more homogeneous deformation field. The degree of the deformation, however, as represented by the percent cell area change, is less in area B. These characteristic differences in the ice cover's response to environmental forcing are most likely a function of its geographic location. While area A is located in a coastal ice zone, with a relatively thin, young ice cover, area B is located in the permanent, thick and "locked" ice cover of the high Arctic latitudes. Area B also lacks features such as the East Siberian flaw lead, which can act as a preferred location for large deformative activity.

- The period of 19 to 21 Nov 96 records the highest wind speeds in area B during cycle 15. The RGPS divergence plot (Figure 14) shows widespread, isotropic convergent activity throughout the region, most likely resulting in many relatively closely spaced acoustically active pressure ridges. This particular deformation is significant for three reasons. First, it occurs in thick multiyear ice, which was not thought to deform in the winter season to as a high degree it does in this snapshot. Second, peak winds never exceed 35 knots during this period, high but not extreme by Arctic winter standards. These winds, however, cause extensive failure of the Arctic ice sheet. These winds maintained their peak wind speeds for roughly 72 hours. It appears that in addition to the peak wind speeds achieved, the duration of a high wind speed event is also important. Third, the massive ice deformation observed is not associated with the passage of a meteorological low, but results from generally straight isobaric flow with a tight pressure gradient.

- The period of 19 to 21 Nov 96 (Figure 14) also represents the best example of NOGAPS model ice divergence correctly predicting the resulting ice deformation. The ice is strongly divergent for the first twelve hours of the period causing lead openings to form, then becomes generally non-divergent and is then strongly convergent for the last 36 hours of the period resulting in pressure ridges. This sequence of divergence patterns explains the resulting ice deformation very well. It is also interesting to note that the resulting ice convergence is not attributable to the passage of a low pressure system and associated curving wind vectors, but the result of velocity shear, since the winds in the central region of area B are approximately five knots stronger than in the eastern section, inducing an anti-cyclonic shear and ice convergence.

- The RGPS percent cell area change image for 10 to 12 Nov 96 (Figure 10) shows mostly ice convergence, while its successor from 13 to 15 Nov 96 (Figure 11) displays ice divergence. If

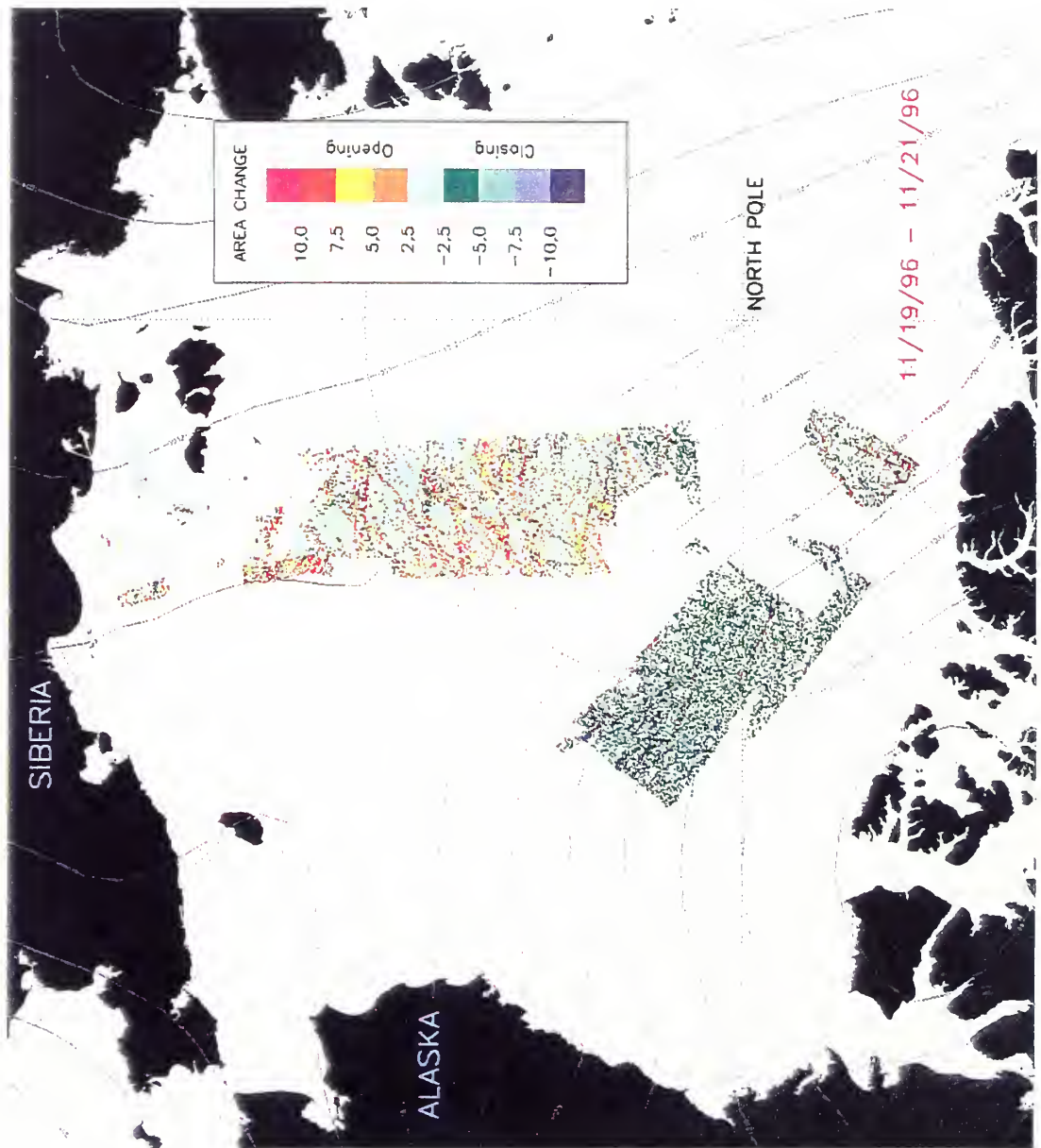


Figure 14. RGPS percent cell area change product for 19-21 Nov 96. The deformation depicted here is explained very well by the NOGAPS model ice divergence product.

the two images are overlaid, one sees very little intersection of the deformed areas in each time period. This picture is consistent with the conceptual model of pressure ridge formation, since one would not expect new leads opening where ridges have recently formed. The new leads are forming between the recently created ridges instead.

c. General Observations and Conclusions

- The best overall subjective correlation between an atmospheric forcing parameter and the ice deformation represented in the RGPS products is the NOGAPS model ice divergence. Even though the ice motion in the Arctic in November can hardly be classified as free drift, the NOGAPS model ice divergence works extremely well, especially in area B, to explain the observed ice deformation.

- Pressure ridge formation occurs under three meteorological conditions in cycle 15 data.
 1. A surface low or trough causing ice divergence followed by a high-pressure system or ridge resulting in ice convergence.

2. Changes in the ice divergence patterns resulting from wind velocity shear in strong straight isobaric flow.

3. Offshore winds followed by onshore winds in the vicinity of a shoreline or land-fast ice.

- One must be careful in interpreting RGPS deformation products. It is easy to forget that the RGPS deformation product does not indicate lead or ridging events, but just relative area change over a three-day period. The formation of leads and ridges is only implied.

- Interpretation of the RGPS products is relatively easy if deformation events last longer than the temporal resolution of the RGPS algorithm. For example, the NOGAPS model may show ice divergence in one period, matched by divergence in the RGPS deformation product. This may then be followed by convergence in both the NOGAPS model and RGPS product in the next period. The interpretation of this sequence is easy, as it represents a long period of lead formation, followed by a pressure ridging phase. It is more difficult to interpret a short-lived ridging event. The RGPS product may show net closing in one three-day snapshot period that was not preceded by opening in a previous image. This may still represent a ridging event, albeit a short one. The NOGAPS model ice divergence charts provide the key, since they may show one day of ice divergence followed by two days of ice convergence. The 07 to 09 Nov 96 area B data stream provides an example of this sequence (Figure 15). An RGPS deformation chart may show net positive area change (divergence) and still represent ridge building as seen in the 13 to 15 Nov 96 area B data stream (Figure 11). The key, once again, are the NOGAPS model divergence charts. Even though divergence activity exceeded convergence during the period (showing yellow or red area change in the RGPS percentage cell area change product), if the divergent phase preceded the convergent event and the air temperature is below freezing, pressure ridge building can take place. A large percentage of thin, unridged ice remains present in the leads though, i.e., the leads are not completely closed.

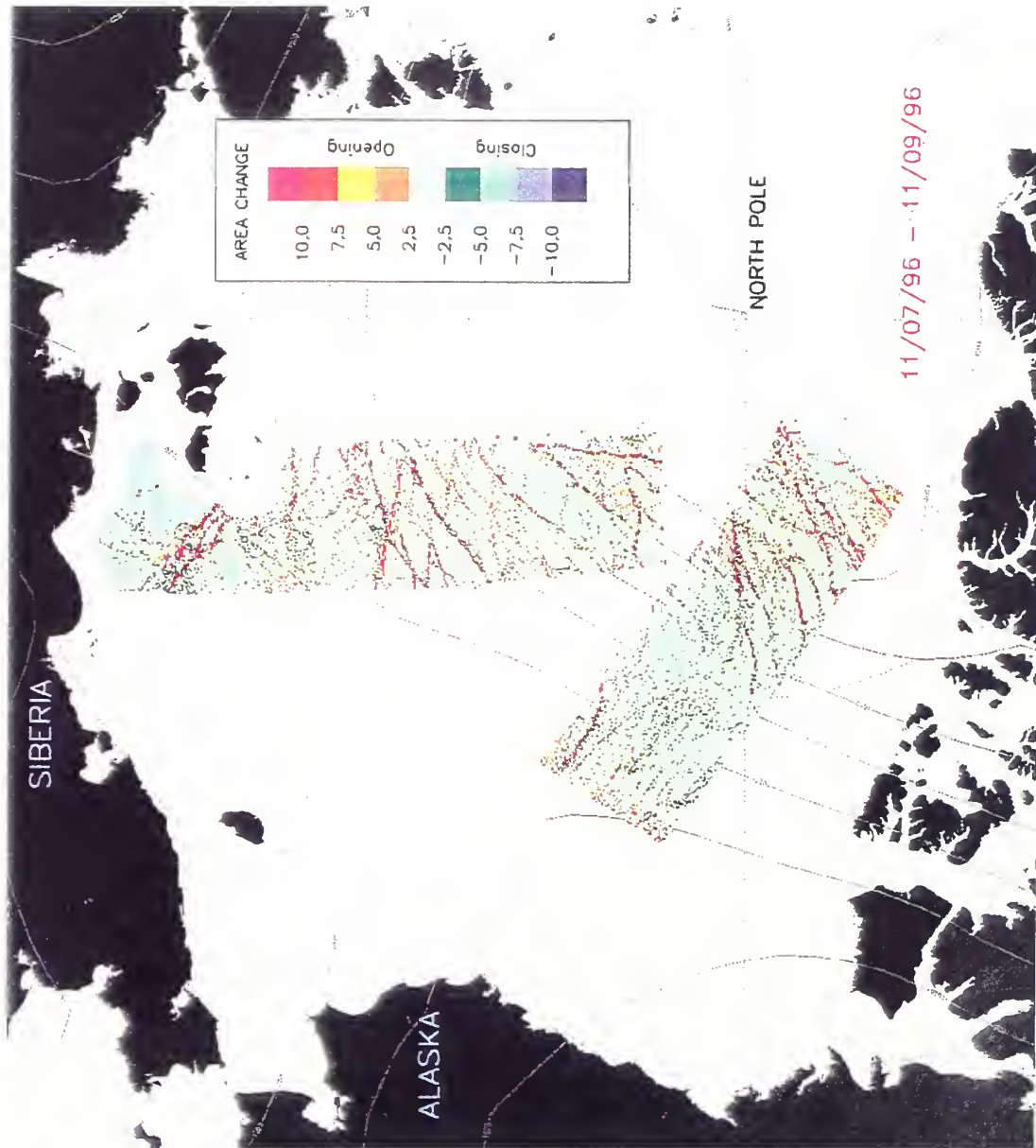


Figure 15. RGPS percent cell area change product for 07-09 Nov 96. This chart shows net closing in one three-day snapshot period that was not preceded by opening in a previous image. The deformation data may still represent a short ridging event.

E. ANALYSIS USING THE RGPS RIDGING ALGORITHM

1. Ridging Algorithm Plotting Features

Personal communication with Cunningham (1998) provided the technical details of the RGPS ridging algorithm discussed in this section.

The ridging algorithm presents ridging statistics in two ways. The first relates to the color-coded RGPS swath segments (data streams), which plot the percentage of each cell area that contains newly ridged ice (see Figure 16). The scale ranges from 0% (gray), no newly ridged ice, to >10% newly ridged ice (red). It is important to note that the data streams plotted represent data for the whole duration of the cycle; in the case of Cycle 15 the period covered is 18 days. This differs from the presentation of the sea ice deformation products, which show color-coded data streams at the interval of the RGPS temporal resolution, three days for Cycle 15. Although a maximum of 18 days worth of statistical data is theoretically available for this cycle, the data period available for each individual cell may be shorter. This data availability is a function of the RADARSAT orbital mechanics, sensor data coverage and possible loss of individual cells in the RGPS algorithm due to extreme deformation events.

The second presentation method in the ridging algorithm displays ridging statistics via a series of graphs. Three graphs are displayed for each selected cell. The desired cell is chosen by the user through a simple point and click routine. The algorithm places a black “target” box around a group of cells, with the target cell at the center. It is important to note that the ridging statistics are not calculated for all the cells contained within the black “target” box, just the center cell. Statistical data for a maximum of four cells can be displayed simultaneously on the plot.

The description of the data presented in these graphs is given in the next six sub-paragraphs. One cell, marked “cell #1” in Figure 16, displays most of the data attributes described below and is referenced frequently. Other cells are referenced as necessary.

The top graph for a given cell shows the change in cell area over the available data period. Cell #1 shows that statistics for it were computed from 05 to 22 Nov 96, a total of 17 days. Additionally, the five-digit cell identification number is displayed in the upper right-hand corner of the top graph, “16919” for cell #1. The cell area change graph always starts at a unit value of 1.00 at the beginning of the cycle for each cell. Cell area increases due to ice divergence and lead formation will result in an increase of cell area above 1.00 on subsequent days. For example, divergence between 05 and 09 Nov 96 increases cell #1’s area from 1.00 to 1.04, an increase of 4% over the cell’s initial area. Cell area can decrease due to convergence and ridging. This occurs in cell 1 from 09 to 12 Nov 96, when cell area decreases from 104% to 81%. Another divergent period occurs from 12 to 15 Nov 96, followed by convergence from 15 to 22 Nov 96. Net convergence characterizes cell #1 over the entire observation period; the cell decreases a total of 14% from 05 to 22 Nov 96.

The middle graph plots the thickness of new ice (in cm) formed in open leads if divergence has occurred. It does this as a function of the net percentage of the cell area covered by this form of ice on the last day of the observation period. In other words, all new ice that was formed during the observation

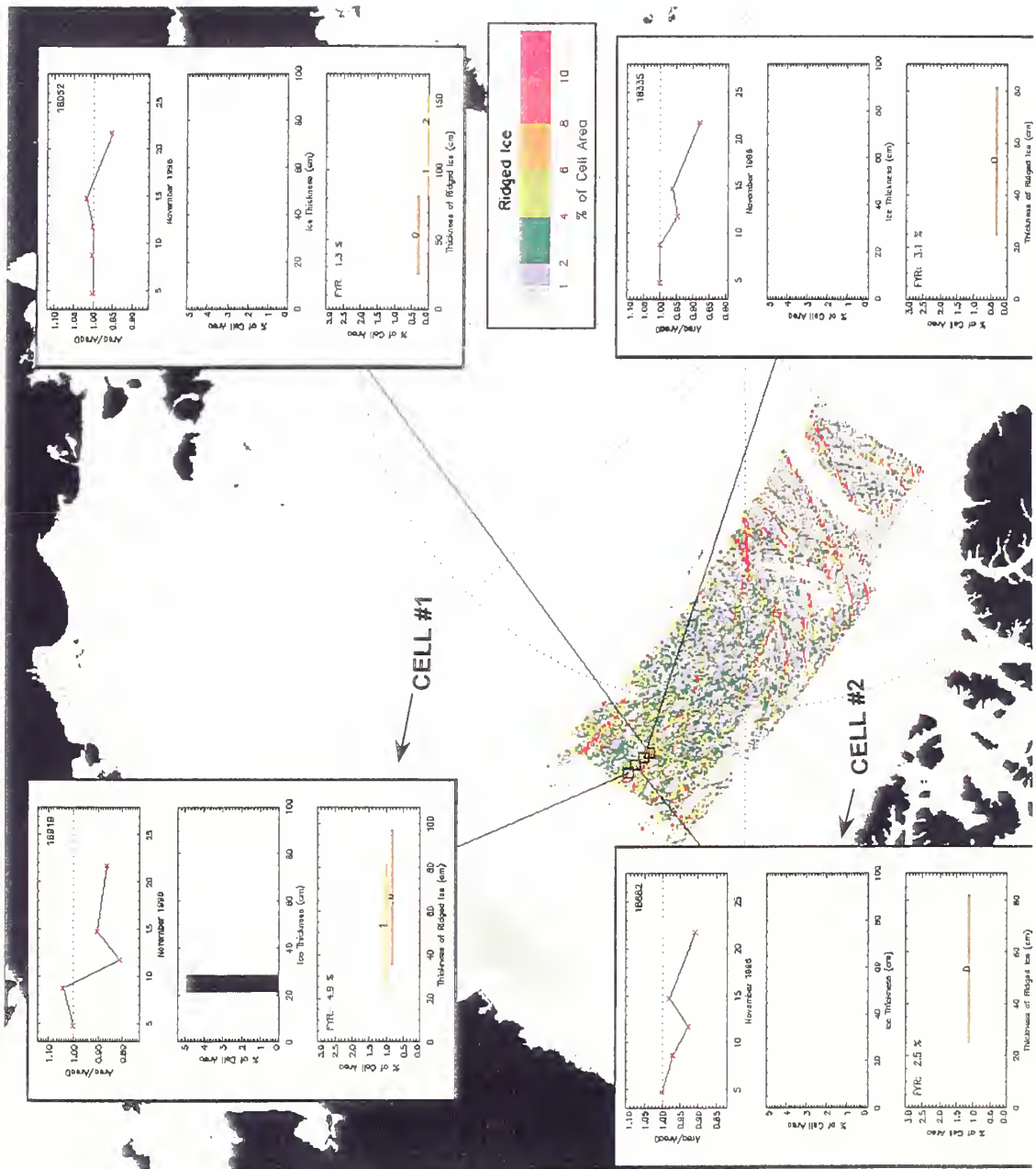


Figure 16. RGPS ridging algorithm output for area B. The ice in cell #1 undergoes two distinct ridging events, while only one occurs in cell #2.

period, but was not ridged, falls into this category. Ice thickness of new ice is plotted in 10 cm bins. Referring once again to cell #1 (Figure 16), one sees that approximately 4.9% of the cell area is covered by new ice on 22 Nov 98. This ice could have formed during any divergent phase of the period, i.e., from 09 Nov to 12 Nov or 15 to 22 Nov 98.

This middle graph may be left blank under three differing circumstances. First, if the cell underwent only convergent activity or was entirely non-divergent for the period, the graph will not be plotted, since new thin ice only forms in open leads. In cell #3 (Figure 17), an extended period of convergence takes place from 05 to 15 Nov 98. No divergence events occur and consequently no new ice is formed; the middle graph is blank. It may also be left blank if all the thin ice in the cell was used in the subsequent formation of pressure ridges. Finally, if the air temperature field at the location of the lead is above 0°C, no ice is formed in the lead; only open water remains.

The bottom graph plots the sail height of ridged ice (in cm) as a function of cell area percentage. Each different color bar represents the sail height associated with a ridging event depicted in the top graph. It must be noted that the algorithm only forms pressure ridges due to ice convergence after a preceding divergent period. In other words, ridges can only form from crushing of new ice inside a previously open lead. The number and magnitude of ridging events in each cell can be easily quantified by investigating the top graph. For example, cell #1 shows two ridges in the bottom graph, the first one represented by a brown bar labeled “0”, the second one yellow, labeled “1”. Ridge “0” is associated with the first ridging event observed in the top graph. This event consists of a divergent phase from 05 to 09 Nov 96 followed by convergence from 09 to 12 Nov 96. Ridge “1” forms from the divergent event of 12 to 15 Nov 96 and the convergence observed from 15 to 22 Nov 96. In contrast, cell #2 shows only one ridge forming due to the deformation activity between 12 and 22 Nov 96. Since one does not know if the convergence from 05 to 12 Nov 96 is preceded by divergence, or lead formation, no ridge building is implied or indicated in the bottom graph. If there are two bars of the same color in the bottom graph, ridges of differing thickness were formed by the same ridging event. Cell #4 in Figure 3 shows three ridges in the bottom graph. The first, ridge “0” was formed during the ridge building event from 05 to 09 Nov 96. The next divergent-convergent phase from 09 to 15 Nov 96 formed ridges “1” and “2”.

The varying sail heights of the ridges are represented by (error) bars, vice points, in the bottom graph, since the estimated ridge height is partially a function of the temporal resolution of the RGPS algorithm. In other words, the ridging algorithm does not know when the convergent phase of the pressure ridging event commenced between RADARSAT passes. The sail height would be near the left extreme of the bar (relatively thin) if it occurred late in the time interval between subsequent sensor passes and near the right extreme (relatively thick) if it occurred early in the time interval between passes. Referring to cell #1, one sees that the sail height in ridge “0” is estimated to range from 35 to 98 cm and occupies approximately 0.8% of the total cell area. Furthermore, the sail height of ridge “1” could be as thin as 25 cm or as thick as 82 cm. Ridge “1” constitutes 1.0% of the entire cell area.

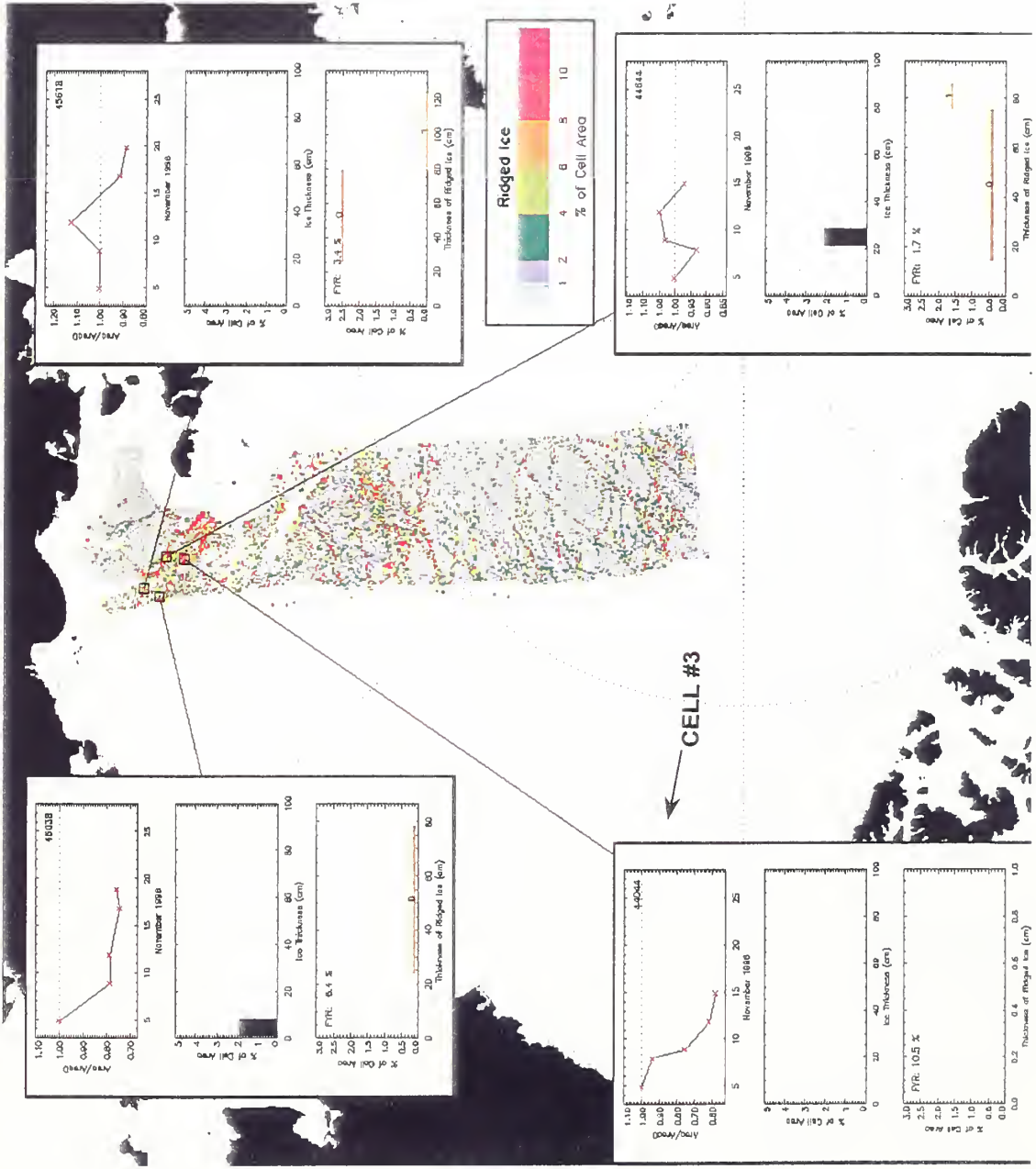


Figure 17. RGPS ridging algorithm output for area A. The ice cover in cell #3 undergoes only convergence during the observation period. No new ice or pressure ridges are created.

The bottom ridge thickness graph will be blank if the cell underwent only convergent activity or was non-divergent for the period, since the algorithm assumes that pressure ridges are only formed from thin ice in previously open leads under suitable atmospheric temperature conditions. Again, cell #3, Figure 2, illustrates this point. The first year ridged (FYR) ice percentage displayed in the upper left corner of the bottom graph shows the percentage of ridged ice in the cell that is either not associated with deformation in the current cycle (i.e., “old” ridged ice) or ice that has been ridged more than once by the algorithm. We must add this FYR percentage to that shown in the graph in order to ascertain the total amount of ridged ice in the cell. In cell #1, FYR constitutes 4.9% of the cell area. If this number is added to the 0.8% ridged ice from ridge “0” and the 1.0% ridged ice from ridge “1”, a total percentage of 6.7% ridged ice is calculated. This percentage represents newly ridged ice, as well as older ridged ice compressed before the cycle 15 observation period.

2. General Observations

Figure 18 presents the ridging algorithm output for four Cycle 15 data streams. One must be careful to avoid interpreting cells where ridged ice is present as individual ridge structures. There appears to be some linear continuity to these cells, but they represent *systems of ridges*, not ridges themselves.

There appear to be preferred directions to the ridge systems. In any geographic location, two ridge systems appear to intersect at a relatively constant angle of approximately 30°. This compares favorably to the findings of Hibler and Schulson (1997) discussed in Section C. of this chapter.

Concentrated areas of heavy ridging activity, where more than 10% of the cell area is covered by ridged ice, are found close to shore in the East Siberian Sea (flaw lead in area A), the Beaufort Sea and off the coast of the Queen Elizabeth Islands.

3. Ridging Characteristics for Area A

As is expected, the strongest ridging events in area A are associated with the three “super-leads” identified previously. The ridging algorithm computed statistical data for a general mean period of ten days in area A. During this period, the more active northwestern or poleward “end” of the lead complex underwent two distinct ridging events, one commencing around 07 Nov 96, the other between 10 Nov and 12 Nov 96. Cell #4 in Figure 19 shows the first ridging event commencing (cell area decreasing) on 08 Nov 96, while the second ridge starts to form on 12 Nov 96. We must be careful when we use the term “ends” (of the leads), since they are not the limits of the leads per se. The leads/ridges most likely continue past the limits of the RGPS deformation data swath, since they represent a portion of the semi-permanent flaw lead described in Reimnitz et al. (1993). These deformation events result in a large percentage of the cell areas in these “super-leads” containing ridged ice, exceeding 50% in some cases. It is interesting to note that individual divergence and convergence events in area A appear to be rather severe, as evidenced by a large change in cell area, but are relatively short-lived. Leads open for no more than two days before

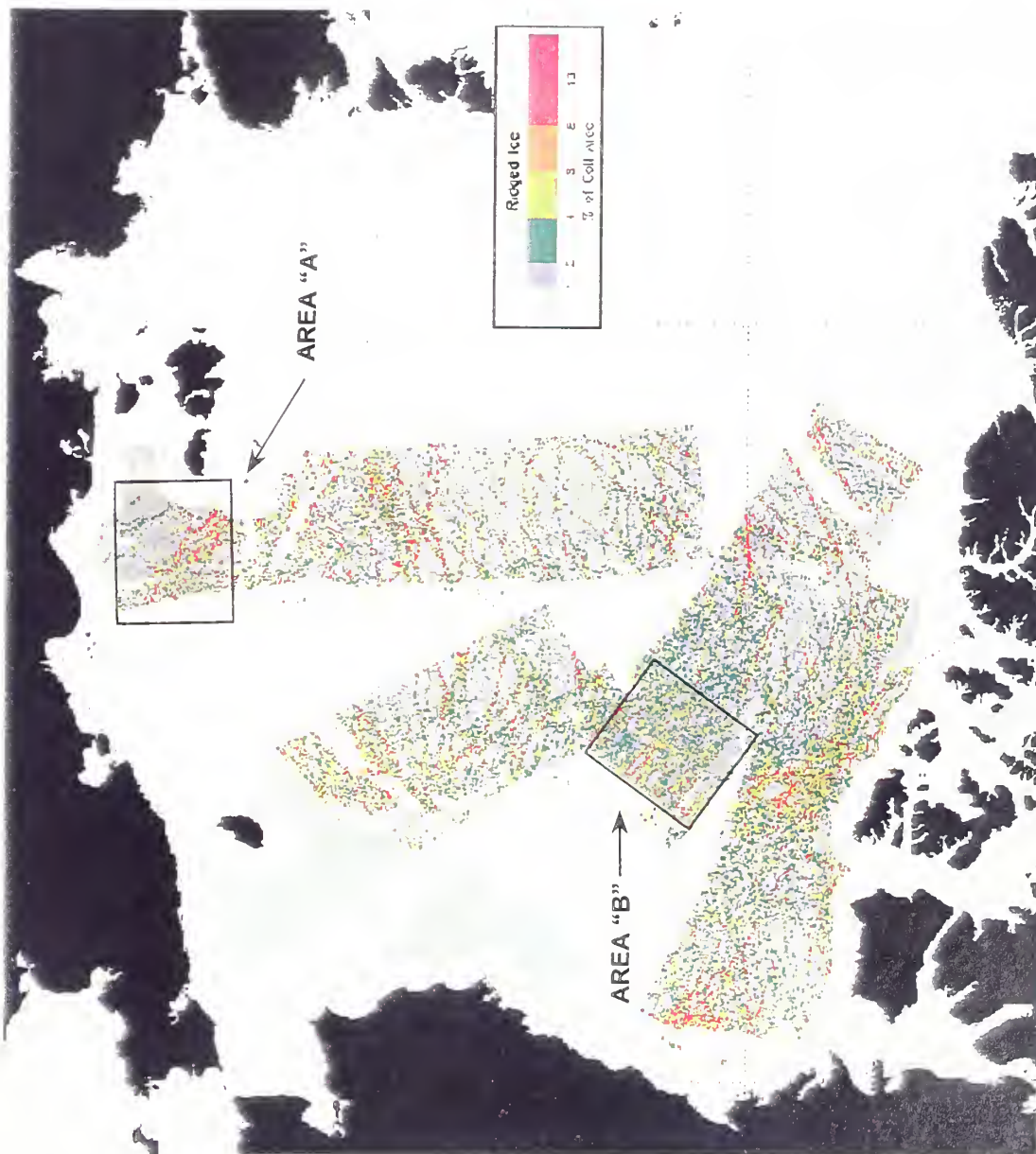


Figure 18. Four data streams containing RGPS ridging algorithm output for the cycle 15 analysis period. Areas "A" and "B", discussed in previous sections are depicted.

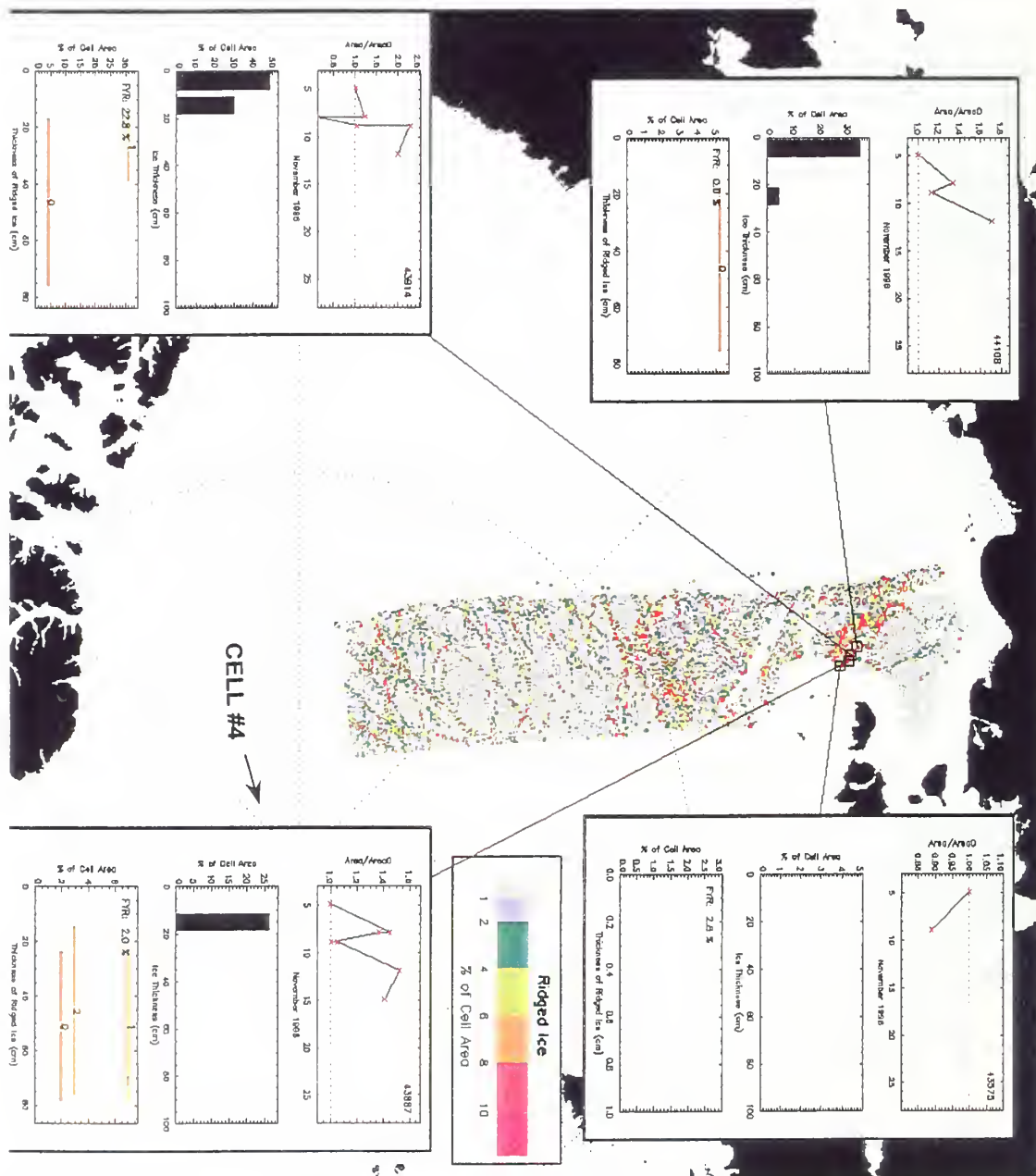


Figure 19. RGPS ridging algorithm output for area A. Ridges of two different thicknesses are created in the second ridging event inside cell #4, as depicted by the two yellow horizontal bars in the bottom graph.

the convergent phase begins. This phase, in turn, lasts for no more than three days, most times much less. The degree of deformation can be partially explained by the stronger atmospheric forcing present in this area, as compared to area B and the presence of the flaw lead to seaward of the New Siberian Islands discussed above.

Sail heights in area A do not exceed 1.20 m. This value compares to *mean* ridge heights of 1.26 m calculated by Tucker et al. (1979) for the Chukchi Sea. If one assumes a keel draft to sail height ratio of 4:1 for recently formed ridges (Hnatiuk et al., 1979), the largest ridges in the flaw lead would have a draft of 4.8 m and an approximate total thickness of 6.0 m. Wadhams and Davy (1986) only consider pressure ridges with a draft of at least 5 m in their statistical study on the spacing and draft distribution of pressure ridge keels to avoid confusion with irregularities in the unridged ice cover. McLaren (1988) evaluated submarine data to gain statistics on under-ice thickness distributions in the Arctic. He found the mean thickness of ice keels at 85°N, 155°W to range from 5.17 m (1958 data) to 4.77 m (1970 data). Ridges with a keel draft of > 9m comprised 10.2% of the 1958 data set, with a mean draft of 10.18 m, while the 1970 data showed that 7.8% of the ridges exceeded this criteria (mean draft 11.84 m). In view of the high deformation present in the flaw lead, the ridge thickness values calculated for area A appear to be slightly conservative. One possible explanation for this anomaly is the fact that the *k* factor (Thorndike et al., 1975) used to calculate ridge sail heights only uses the rubble thin ice to form a ridge's sail and does not account for the extra volume contributed by the multiyear ice that is fractured during the ridge-building process.

The less active southeastern or shoreward end of the “super-leads” in general undergoes only one ridging event, which results in lower ridges and less ridged ice per cell area. The remaining thin ice in open leads here is also generally thinner than at the northwestern end. This may occur because the leads here only underwent an average of four days of divergence, while their counterparts on the other “end” underwent divergence for a total of four to eight days during cycle 15. The longer period of divergent activity at the western “end” dominates the offsetting air temperature parameter, which is generally 1.0° to 1.5°C warmer here than in the southeastern sector of area A during the period and therefore accounts for a smaller number of freezing degree-days. This, in turn, should result in the formation of thinner new ice in the open leads, all other factors being equal.

The lead in the southwestern sector of area A, shoreward of the flaw lead, is depicted as having only one major ridge building event from 09 to 15 Nov 96. Cells #5 and #6 in Figure 20 show this clearly. The major event is preceded by a relatively small event, only seen in cell #5 from 05 to 09 Nov 96. This agrees well with what is depicted in the divergence plots of the RGPS sea ice deformation product, which shows medium to strong opening of a lead from 10 to 12 Nov 96 and definite closing/ridging from 13 to 15 Nov 96. This deformation zone provides the best example of an active acoustic ridge in all of the cycle 15 data. The lead formation and subsequent ridging phase is purely a divergence/convergence event for two reasons. First, no thin ice remains in cells #5 and #6 at the end of the period; it has all been ridged. Second, the RGPS deformation products show medium to strong divergence in the feature, but little shear

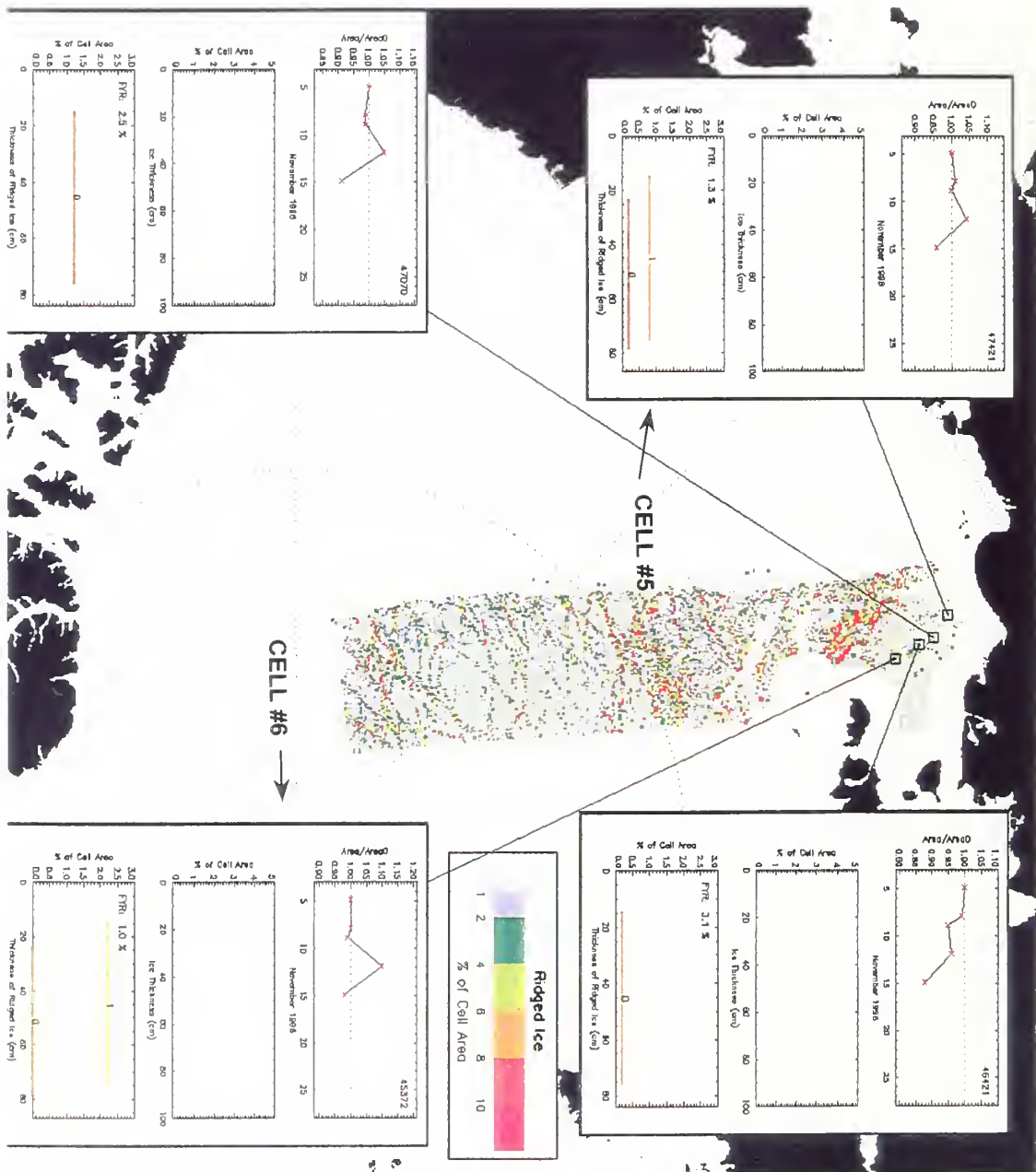


Figure 20. RGPS ridging algorithm output for area A. Only one major ridging event takes place in cells #5 and #6.

(see Figures 37 and 38 in Appendix C and Figures 43 and 44 in Appendix D). Another clue that the ridge is a very distinct entity is the fact that the ridged ice occupies no more than 2.5% of the cell area. This is in stark contrast to the “super-leads” where ridged ice can occupy over 50%. The southwestern sail height is not the tallest (an approximate mean of 55 cm) encountered in the data set, implying only moderate ambient noise levels. However, since it extends for hundreds of kilometers, it still represents a major ysource of operationally significant ambient noise, active for over 36 hours, which may be exploited (or need to be avoided) by a patrolling submarine.

4. Ridging Characteristics for Area B

The ridge characteristics in area B differ in several ways from those in area A. The deformation activity is not confined to a few distinct locations as in area A, but generally extends over the whole region. Strong ice deformation areas are located in distinct “rows” extending roughly from the NNE to the SSW (see Figures 16, 21 and 22). The areas of the heaviest ice deformation, where >10% of the cell area contains ridged ice, appear to be located in regions experiencing the greatest magnitude extremes in NOGAPS model ice divergence and convergence.

If one uses the 4% to 6% (yellow) ridged ice per cell area values as an arbitrary threshold between light and heavy ridging activity and measures the spacing of these features cross-swath in area B, one sees interesting results. The lines of heavy ridging appear roughly every 37-46 km, except in the southeastern corner of the area (lower left corner of area B in Figure 18), where the heavy ridging activity is spaced 93-111 km apart. This finding is significant because Buck and Wilson (1986) concluded that a uniform active pressure ridge spacing of 37 km yields model noise spectra equal to 50 percentile-omnidirectional noise level spectra measured during April in the Beaufort Sea. However this median density was calculated before the authors had an appreciation of the considerable length (hundreds of kilometers) that acoustically active ridges can attain (Wilson, personal communication, 1998). Buck and Wilson (1986) estimated that the active length in a typical ridge may be as short as 1 km. The RGPS ridge plots appear to contradict this finding, showing that a forming ridge may be active for a large percentage of its length. However, one must also remember that the temporal resolution of the RGPS ridging data is only three days. If pressure ridges are viewed on a time scale of minutes, individual ridge segments will most likely exhibit alternating periods of noisy activity and relative quiet, as described in Buck and Wilson (1986). Concurrent ambient noise and RGPS deformation data from the SHEBA experiment (1997-98) should provide updated ridge density/ambient noise correlations in a future study.

The ridge spacing data of this study presented above compares somewhat favorably with Newton and Coles’ (1991) thin ice feature distribution study conducted north of Svalbard, between Geenland and Franz Josef Land. One must take into account several differences between the two data sets. Data were collected in differing geographic locations. Newton and Coles’ study evaluated March, vice November, data collected over four years (1988 to 1991). Newton and Coles evaluated raw Defense Meteorological

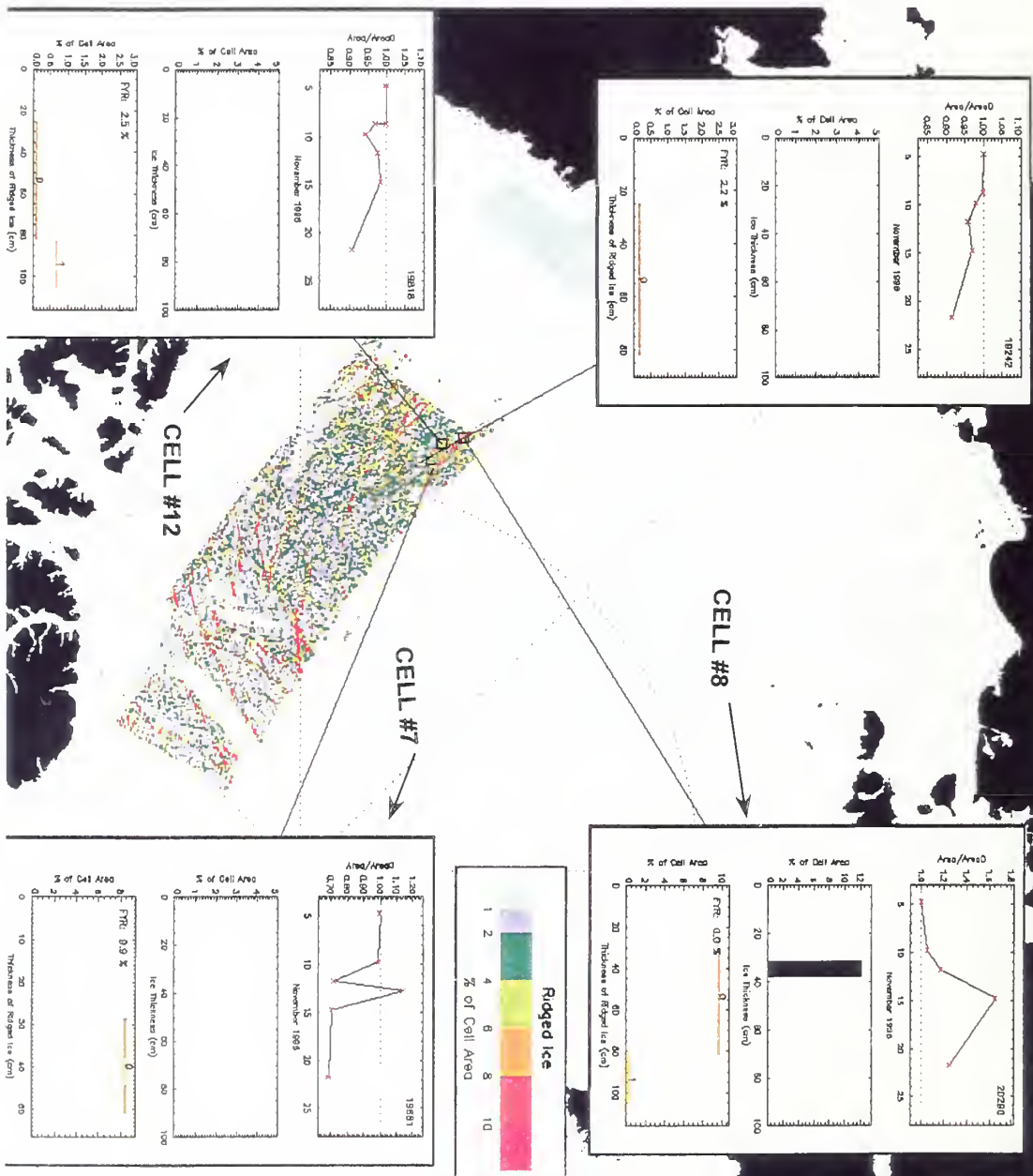


Figure 21. RGPS ridging algorithm output for highly deformed cells in area B. Cell #7 undergoes short deformation events, while cell #8 is subjected to longer ones. Cell #12 represents another highly active cell.

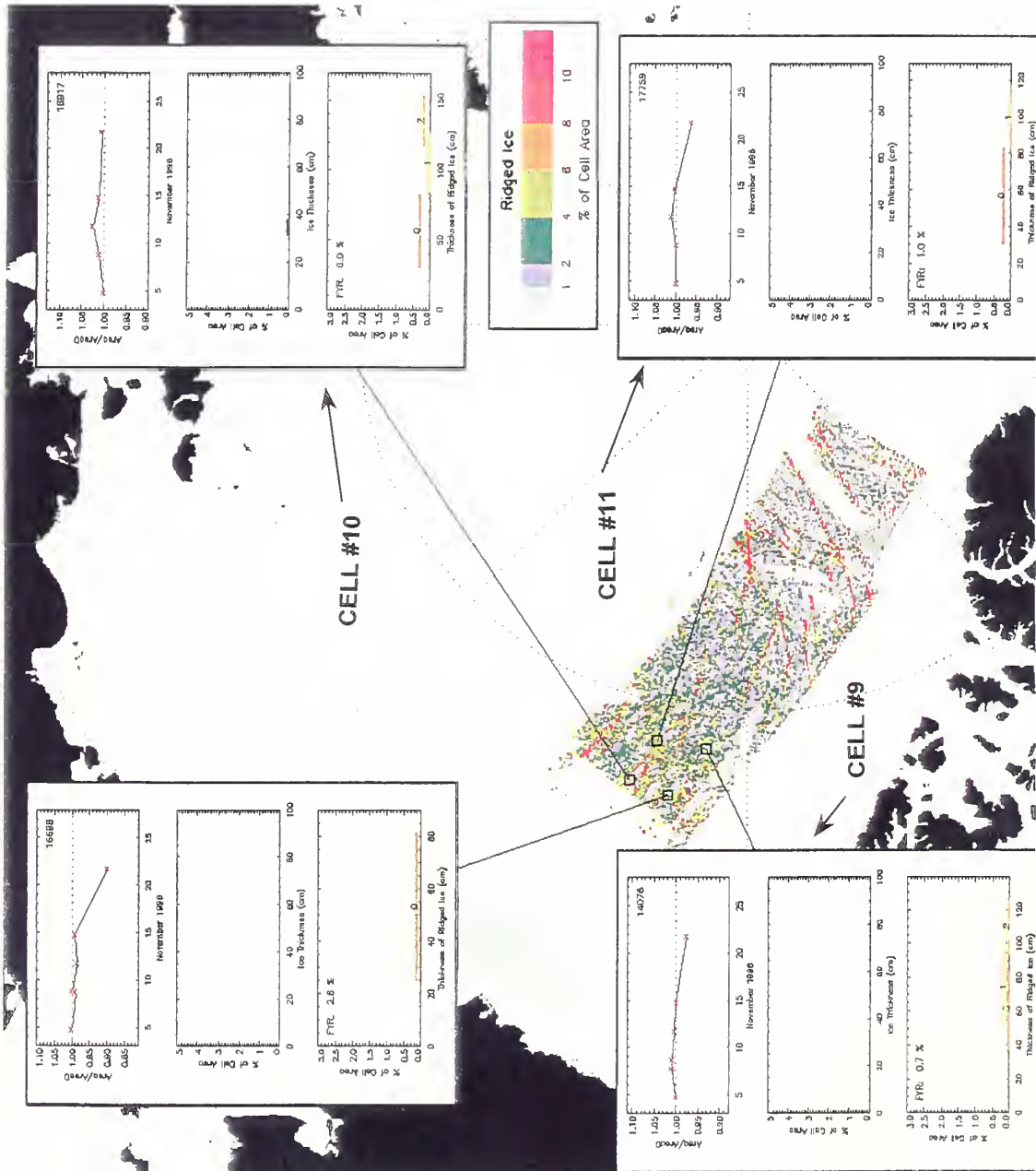


Figure 22. RGPS ridging algorithm output for “benign” cells in area B. Cells #9 through #11 display little area change over the observation period.

Satellite Program (DMSP) Operational Line Scan (OLS) data with 600 m resolution, as compared to RADARSAT-derived RGPS algorithm data, with a 5 km (initial) cell width, used in this study. Newton and Coles' study identify individual leads, while RGPS data only picks up general areas of high deformation. Taking these differences into account, Newton and Coles calculated a mean lead separation of 14.35 km with a standard deviation of ± 2.24 km. The smallest average distance between leads for all four years was 11.95 km, while the largest was 61.12 km. This compares to a mean of 42.60 km for this study in area B.

A variety of ice deformation patterns are evident in area B. The ones in regions where $>10\%$ of the cell area contains ridged ice are similar to those observed in area A, i.e., the observed cell area changes are large, but the divergent/convergent phases last a relatively short time and produce ridges of moderate height. Cell #7 in Figure 21 shows a divergent phase lasting only one day, from 12 to 13 Nov 96, which results in a net area change of 44%. It is followed by a major period of convergence lasting from 13 to 15 Nov 96, which causes a 46% net compression of the cell's area. A subsequent, minor convergence event compresses the cell an additional 3%. In contrast, cell #8, Figure 21 shows a long divergent period of 10 days, resulting in a significant increase in cell size (65%), followed by a relatively long period of ridge formation (seven days), decreasing the cell size by 40%. Resultant ridge heights are medium in size and a significant amount of thin ice remains unridged (12% in cell #8). The thickness and amounts of ridged ice recorded in these areas are commensurate with what one would expect in regions of strong deformation, such as those in the flaw lead of area A. Ambient noise in this region would be expected to be highly anisotropic, with discrete, localized sources dominating the noise field.

However, ice cover that contains less than 6% ridged ice characterizes most of area B. It is not surprising to observe very small divergent and convergent events here, since area B is located in the thick, permanent ice pack of the high Arctic. The relatively constant sail heights are unexpected, though. Ice convergence forms roughly similar sail heights independent of the cell area change observed. For example, if one examines cells #9 through #11 in Figure 22, one notes a maximum negative area change of 96% of the original cell area (convergence) and a maximum positive area change of 103% (divergence). The sail heights (range of the error bars) for these cells vary from 30 to 155 cm. These numbers differ markedly from the more "active" cells (cells #7, #8 and #12 in Figure 21), which exhibit maximum changes from 68% to 170% of the cells' original area. However, the variability of sail height is actually less than for the more "benign" cells, with values ranging from 25 to 105 cm. These data are hard to reconcile, since one expects cells with larger area changes to build larger ridges. The explanation for this disparity must lie with the number of ridges created. Even though the general size of the ridges in "benign" and "active" areas appears to be generally similar, there must be a far greater number of ridges created in the cells that exhibit large area changes. A rough comparison of cell area percentage covered by ridges in "benign" and "active" areas shows that as many as 20 times the number of new ridges should exist in areas of large cell area change than in less active cells. This estimate is based on assumptions of roughly equal sail heights in both areas and a fixed ridge geometry, i.e., vertical sail height is proportional to horizontal ridge width.

The assumption of a fixed ridge geometry is valid as long as one assumes that the ridge has not yet reached its limiting height. After reaching this height, a ridge ceases to expand vertically but grows only laterally, forming a rubble field (Parmerter and Coon, 1972).

5. Conclusions

The ridging algorithm represents a valuable addition to the suite of existing RGPS sea ice algorithms. It provides a useful tool in the study of Arctic ambient noise since it provides the first coherent, large-scale spatial and temporal characterization of potential acoustically active pressure ridges. The following general observations can be made:

1. Pressure ridge characteristics vary with geographic location and proximity to land in the Arctic Basin.
2. Acoustically active ridges can extend for hundreds of kilometers and may remain active for days.
3. The number of ridges created, not their individual physical size, correlates with the percentage of a cell area covered by ridged ice. It may well be that the cumulative summing of numerous smaller ridges leads to loud ambient noise events, not just the creation of a few “super-ridges”.
4. The length of divergent/convergent activity, as well as the intensity of these events determine the amount of ridge-building encountered in a cell.
5. The current algorithm underestimates the ridge sail height because it includes only the new ice refrozen in the leads and excludes the portion of the pack ice near the lead’s edge fractured during the ridging process.

F. COMPARISON OF PIPS AND NOGAPS MODEL ICE DIVERGENCE FIELDS

1. Background

Recall from Section V. D. 3. that the best subjective correlator between RGPS ice deformation data and a meteorological forcing variable differed as a function of distance from land. In area A the on/offshore component of the 10 m (surface) wind matched the deformation activity observed in the RGPS output quite well. An onshore wind resulted in ice convergence and ridge-building in open leads. Conversely, an offshore wind caused ice divergence and created open leads. The next best correlator was the wind divergence field turned 28° to the right, in accordance with free ice drift approximations, termed the NOGAPS model ice divergence in this research. In area B, a location well removed from an influencing shoreline, the NOGAPS model ice divergence proved to be the parameter that best explained the RGPS ice deformation. Values of NOGAPS model ice divergence matched divergent activity in RGPS output; NOGAPS model ice convergence related positively to convergent activity in RGPS deformation data. One of the stated goals of this thesis effort was to determine if deformation fields (not necessarily limited to those of ice divergence) generated by the PIPS model could be used to initialize the ASNM. In this section, the author compares the on/offshore component of the 10 m wind and the NOGAPS model ice

divergence values with PIPS ice divergence fields in different geographic locations in the Canadian Basin to investigate this goal.

2. Analysis Technique

Hardcopy of PIPS ice area coverage, ice divergence, ice thickness, ice drift and wind stress analysis fields were collected for the period 13 Feb 98 to 31 Mar 98 from FNMOC for a geographic area roughly matching that of the RGPS output (Canadian Basin). Companion charts of NOGAPS model ice divergence were created, as before, by writing a script file for the GEMPAK meteorological software suite that calculated the 10 m wind divergence field and then rotated it 28° to the right while decreasing its speed by 98% in accordance with free ice drift approximations. 1°×1° resolution NOGAPS wind data were available and used for this analysis period as opposed to the 2.5°×2.5° resolution winds used previously. NOGAPS model data is missing for 15 Feb 98 and 14 Mar 98. PIPS and NOGAPS model ice divergence values were compared and plotted at four locations in the Canadian Basin. Because divergence fields are calculated by PIPS only every 24 hours, the 0000Z PIPS and 0000Z NOGAPS model fields are compared. (PIPS divergence fields are in reality a 24-hour forecast product based on the ice drift vectors, which are calculated from the previous day's model forcing fields.)

Numerical correlation calculations were conducted between PIPS and NOGAPS model ice divergence time series and plotted using Microsoft Excel software (see Figures 23 through 26). Additional data included on all four graphs is the 10 m wind speed (in knots), listed in black just above the abscissa.

For points influenced by the proximity of a shoreline (points 1 and 2), the on/offshore component of the 10 m wind for each day of the investigated period is listed in black at the top of the graph. At point 1, any wind veering from the NNW to the SSE is considered an onshore wind for analysis purposes. Winds from NNW to NE are onshore to the coast of the East Siberian Sea, while NE to SSE winds push ice into the virtually closed sound between the Siberian coast and the New Siberian Islands. At point 2, winds in a sector from NW to NE are considered onshore.

Below the on/offshore wind values, a letter designating the ice divergence observed in the PIPS field is printed in gray. These designations are selected from the graphed values of PIPS divergence and are intended to make the comparison between the on/offshore wind component and PIPS ice divergence easier for the reader.

One must note that none of the surface wind speeds encountered over the 47-day investigative period at all four locations can be classified as "high". The maximum wind speed recorded at any point and time was 30 knots at point 3 on 22 Mar 98. These moderate winds do not represent extreme forcing events and would therefore are not likely to result in 95th percentile ambient noise levels.

Another comment must be made regarding the nature of the analysis winds. The surface wind fields are model, not measured buoy winds. One does not know how much model interpolation and smoothing took place during the model's data ingestion phase or on what observational data density these winds are based. Numerical correlations between wind forcing and ice deformation may therefore be better

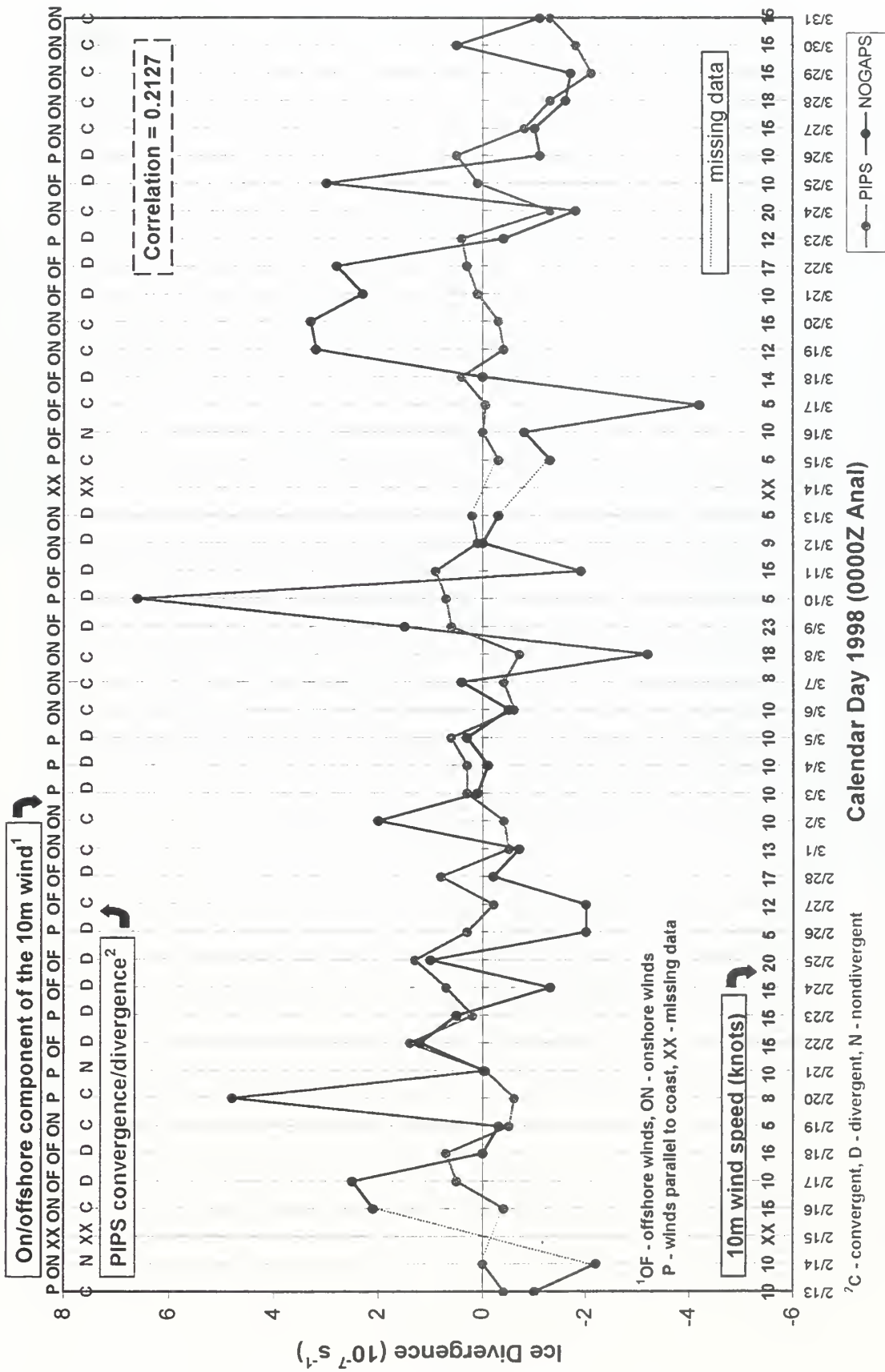


Figure 23. PIPS vs. NOGAPS Model Ice Divergence - Point 1 (74N/155E in Area A)

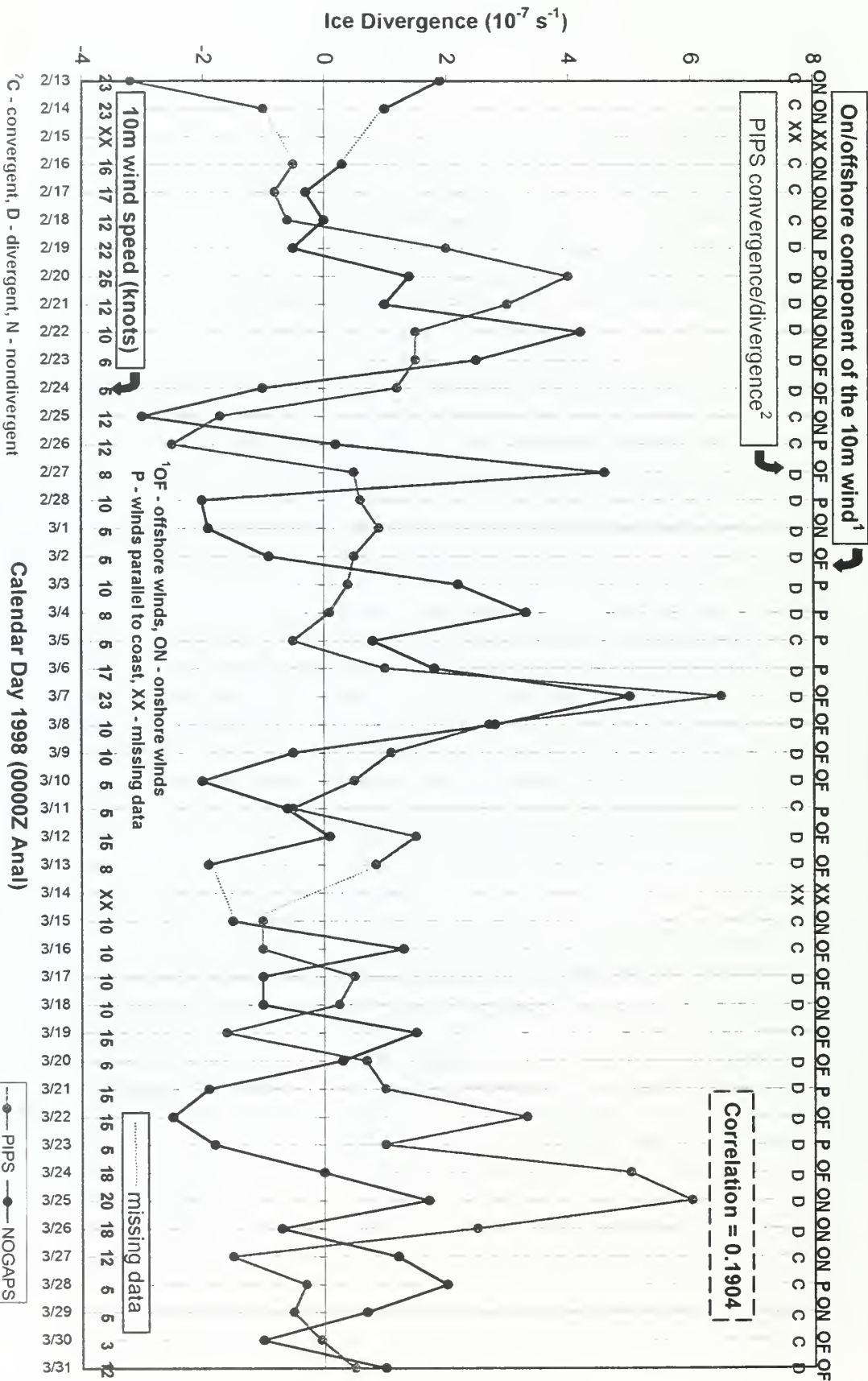


Figure 24. PIPS vs. NOGAPS Model Ice Divergence - Point 2 (71N/150W)

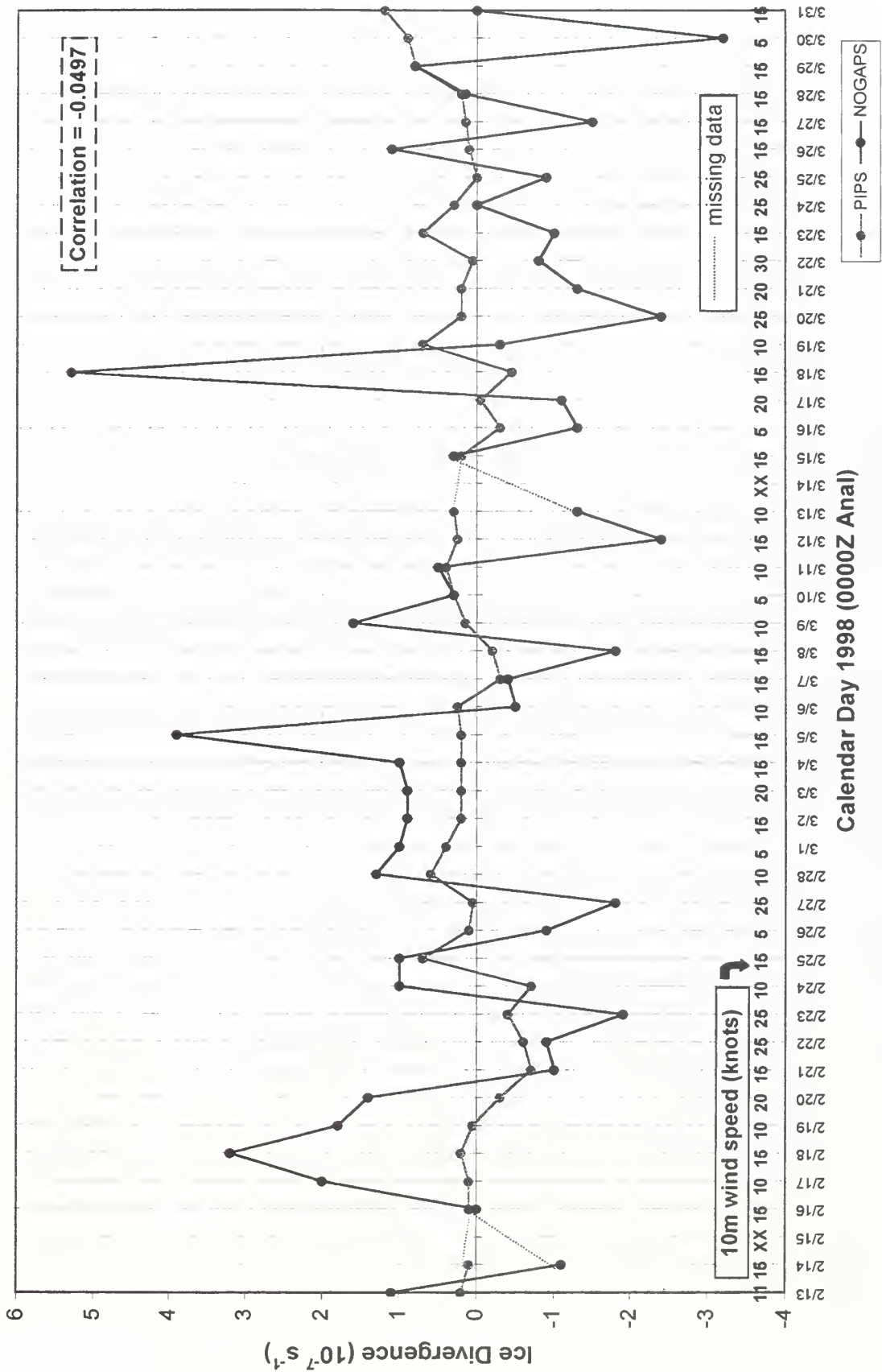


Figure 25. PIPS vs. NOGAPS Model Ice Divergence - Point 3 (78N/150W in Area B)

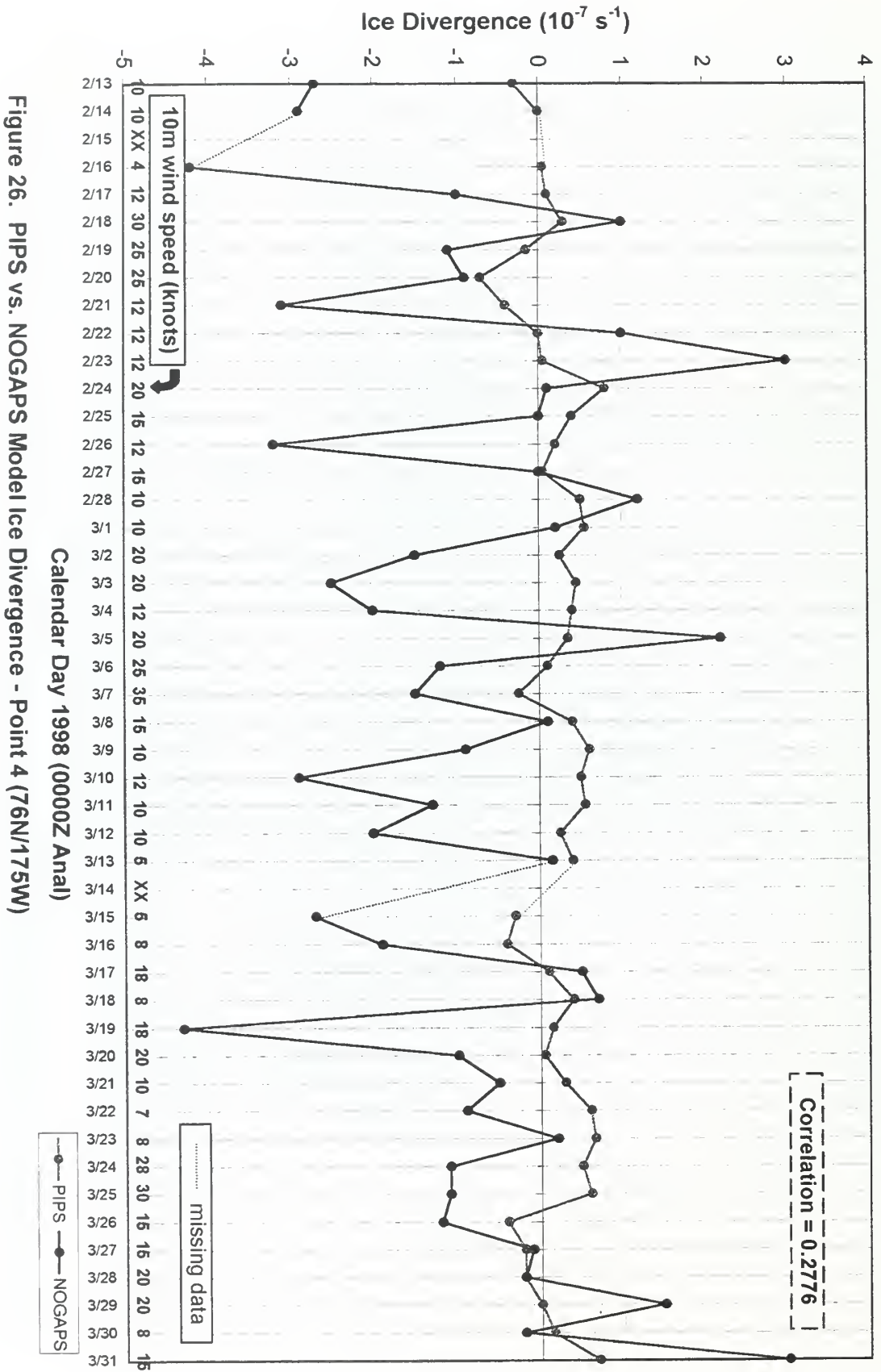


Figure 26. PIPS vs. NOGAPS Model Ice Divergence - Point 4 (76N/175W)

or worse than those arrived at if actual meteorological observations were available at the four investigated locations.

3. Analysis of Specific Locations

Points 1 and 3 were selected due to their location in previously analyzed areas. Point 2 is located near shore approximately 222 km east of Point Barrow, Alaska. Point 4 represents another open ice location, comparable to point 2. Figure 27 shows the geographic locations of all four points.

Point 1 is located at 74°N, 155°E in the East Siberian Sea and was selected for investigation because it is located in area A, a region that prominently demonstrated the semi-permanent New Siberian Island flaw lead, as documented by Reimnitz et al. (1993), in the RGPS Nov 96 deformation products. National Ice Center (NIC) weekly ice analysis charts, using the World Meteorology Organization (WMO) system for ice symbology (“egg code”), were consulted to determine the location of point 1 in relation to the flaw lead during the investigated period. The charts show that point 1 is resident in land-fast ice from 16 Feb to 06 Mar 98 and from 23 Mar to 03 Apr 98. (NIC analysis weeks are only five days long). From 09 Mar to 20 Mar 98, point 1 was located in the new and first year ice of the flaw lead. Figure 28, the NIC analysis from 16-20 Feb 98, is representative of point 1 during its land-fast stage. It shows 10/10^{ths} total ice coverage, of which 5/10th is first year thin ice (30-70cm thick), 4/10th gray ice (10-15cm thick) and 1/10th new ice (0-10 cm), most likely frazil and grease ice. The “8” indicates its land-fast origin. Point 1 is therefore located in a generally active ice deformation region (The reader can gain a complete understanding of the WMO “egg code” by consulting “<http://www.natice.noaa.gov/egg.htm>”).

Point 2, at 71°N, 150°W, is located close to the Alaskan coast in an area that showed consistently high contours of PIPS ice divergence. This makes it an interesting locale to investigate and compare to the NOGAPS model ice divergence. The ice deformation at point 2 can also be compared to that of point 1, similarly influenced by its proximity to the shore. Again, analysis of the NIC period ice analysis is conducted. The WMO “egg code” shows that point 2 alternately lies in land fast ice and in the open ice of the flaw lead off the Alaskan coast (Figure 29 gives a sense of the point’s location). Ice types at point 2 mainly consist of gray ice (10-15cm) and medium first year ice (70-120cm). Point 2, like point 1, appears to be located in a region in which the possibility of extensive deformation characterizes the nature of the ice cover.

Point 3 (78°N, 150°W) is located in the solid ice pack of the high Arctic in Area B. The NIC ice analysis shows a generally homogeneous ice cover, of which 8/10th is old ice (survived at least one season’s melt) with a thickness of >2m, 1/10th is first year ice of 30-120cm thickness, while the last 10th is divided between young ice (10-30cm) and new ice. This analysis leads one to believe that the generally thick ice cover is transected by a fair number of old and new leads, as evidenced by the amount of first year, young and new ice.

Point 4, located at 76°N, 175°W, was picked to corroborate any conclusions drawn from the analysis of point 3, since it is located in another region covered by permanent pack ice in the high Arctic.

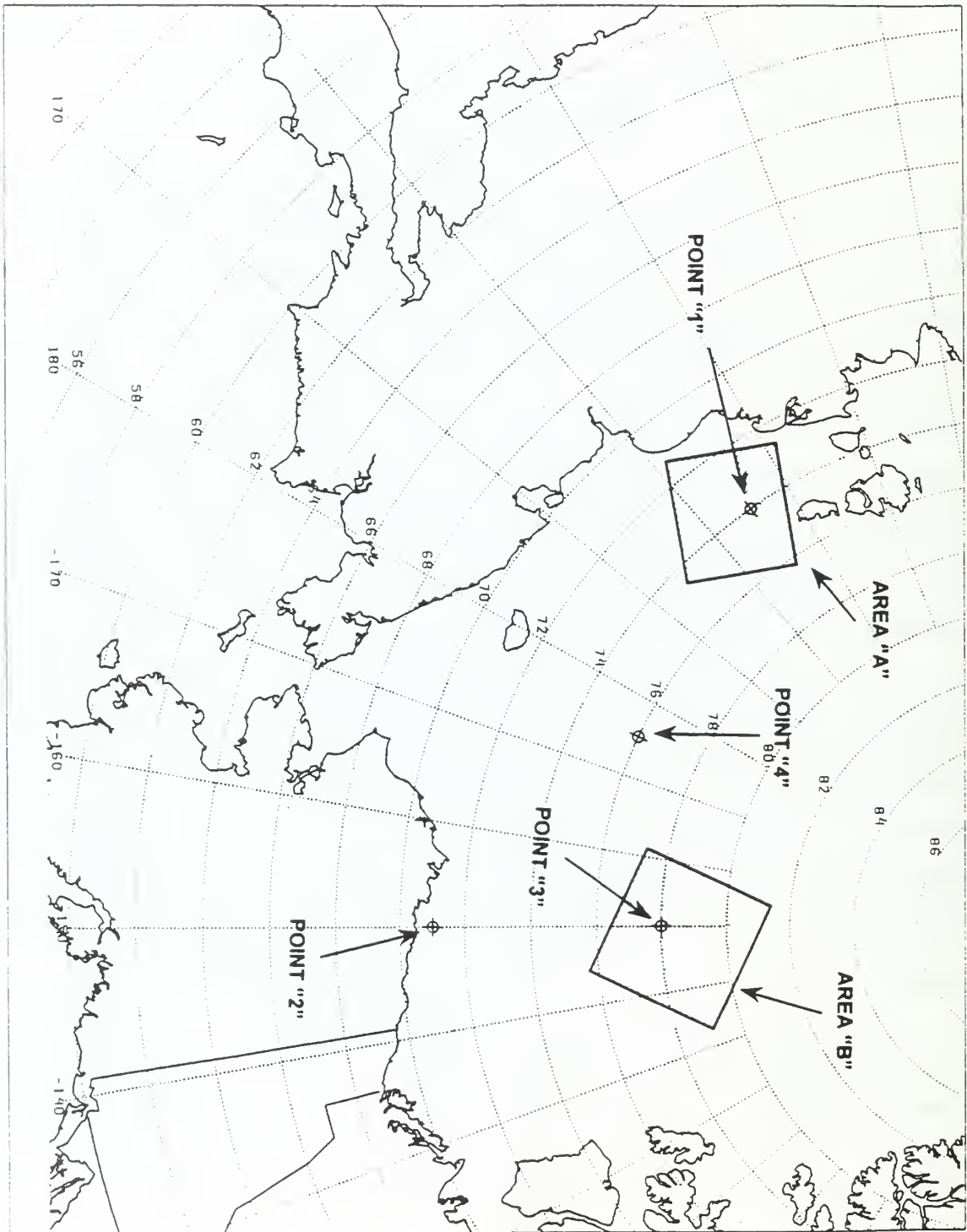


Figure 27. Geographic locations of the two RGPS data areas and the four points investigated for the PIPS-NOGAPS model ice divergence correlation.

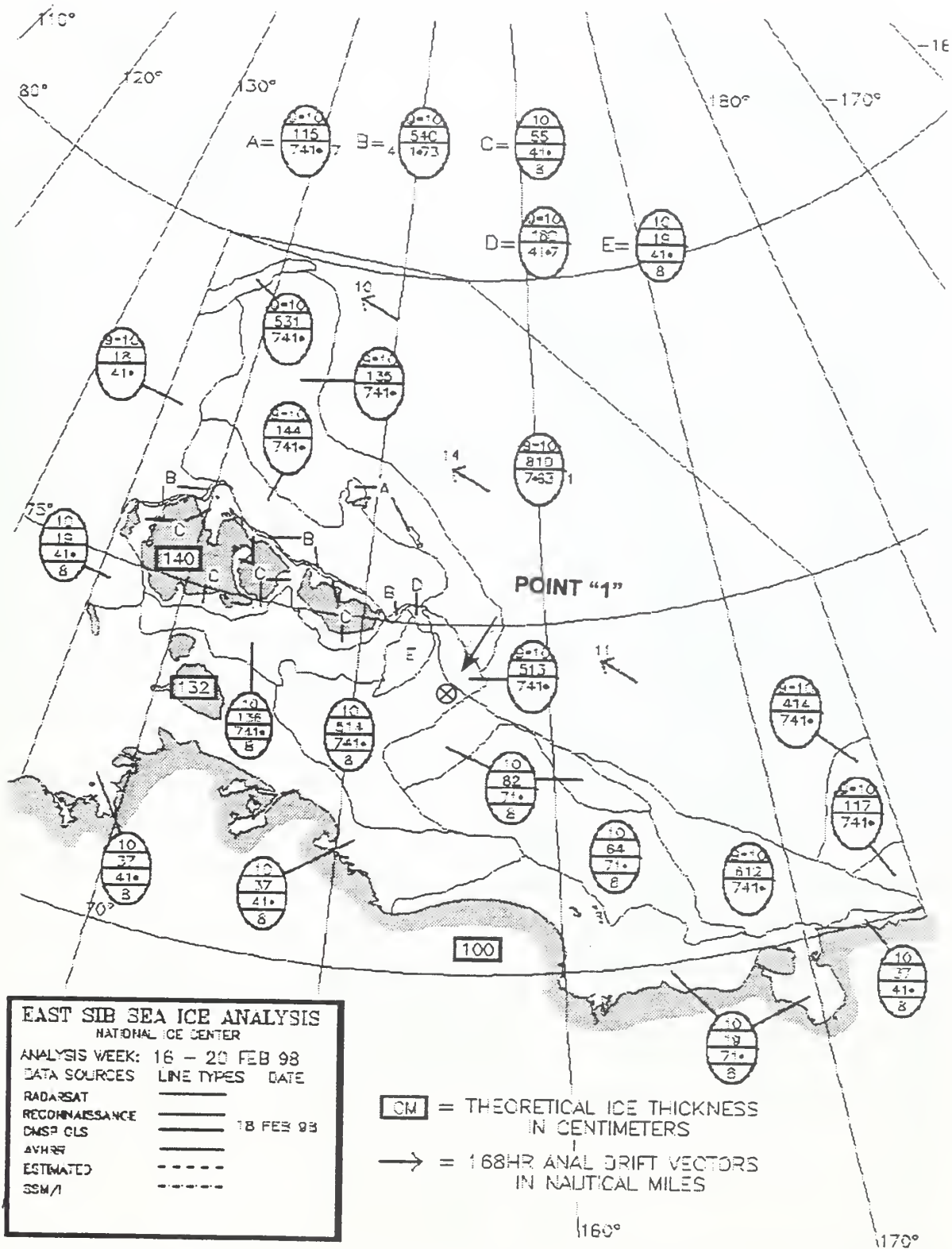


Figure 28. NIC weekly ice analysis for 16-20 Feb 98, showing the location of point 1 in the flaw lead of the East Siberian Sea. It is classified as land-fast ice at this time as indicated by the "8" in the bottom section of the corresponding "egg code".

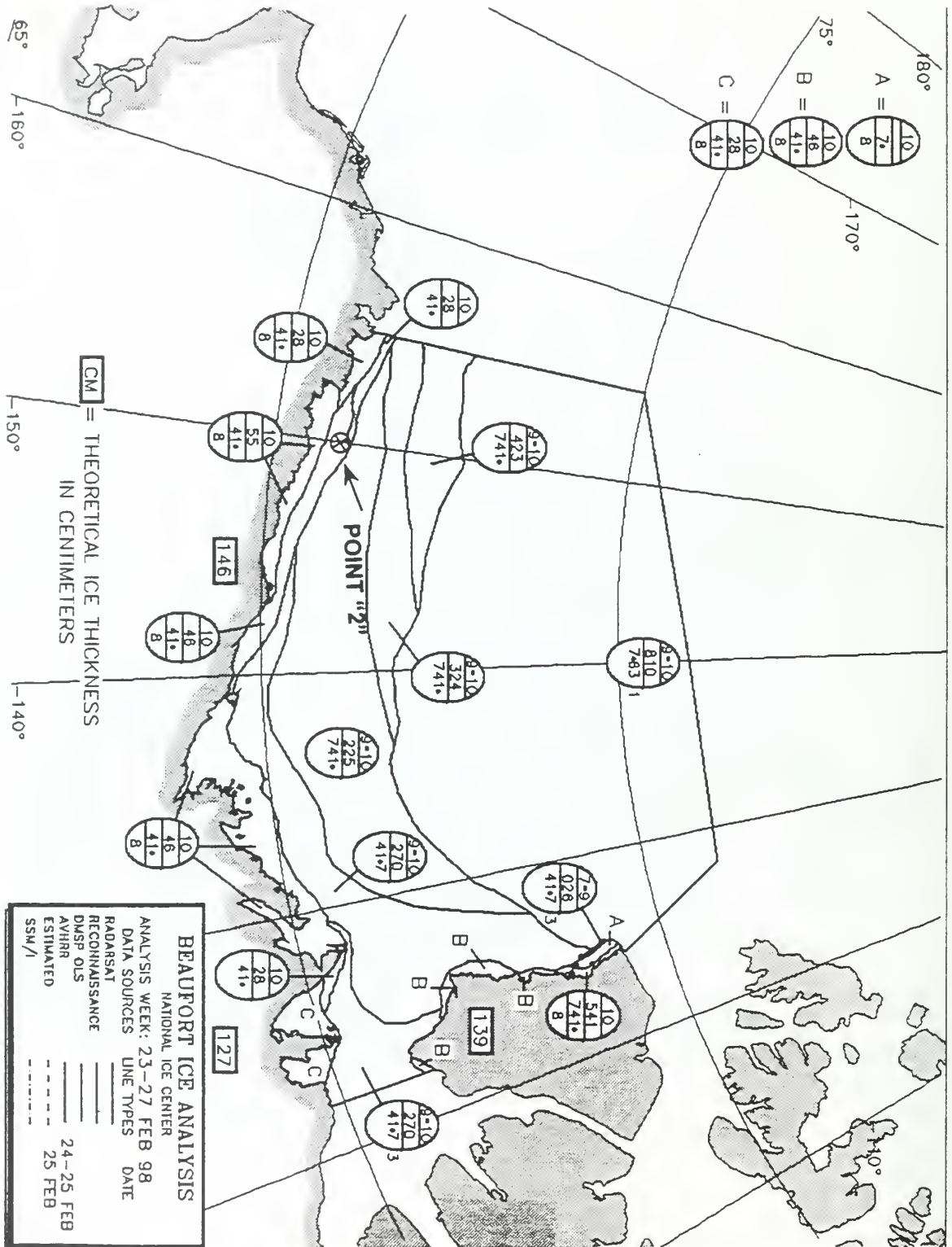


Figure 29. NIC weekly ice analysis for 23-27 Feb 98, showing the location of point 2 off the coast of Alaska in the Beaufort Sea. It is also classified as land-fast ice at this time.

Point 4, however, is undergoing slightly different environmental forcing than point 3. The ice cover is identical to that at point 3, as analyzed by NIC.

4. Analysis Discussion

a. Ice Divergence Comparison at Point 1 (74°N/155°E)

Investigation of cycle 15 RGPS deformation data has demonstrated that at point 1 the ice cover deforms predominantly as a function of the on/offshore component of the surface wind as summarized in Section D.3.a. of this chapter. A strong correlation between on/offshore flow and PIPS con/divergence is therefore expected. Ignoring days when the wind is parallel or nearly parallel to the coast or when PIPS shows non-divergence in the ice field, the wind field and PIPS ice divergence align correctly for 27 days but are not in alignment four times for an in-phase (both show convergence or divergence on the same day) percentage of 87%. It should be noted that the ice divergence values are very small on the four days when no correlation exists: -0.2, 0.1, -0.2 and $-0.05 \times 10^{-7} \text{ s}^{-1}$. These observations are encouraging and indicate that the PIPS model does a creditable job in reproducing the subjective correlation between the wind's directionality and the ice divergence patterns observed in the RGPS data.

High numerical correlation between PIPS and NOGAPS model ice divergence is not expected, since the subjective correlation between them was not strong during the RGPS data analysis phase. The PIPS and NOGAPS model ice divergence correlation is only weakly positive (correlation of 0.21). Surprisingly, this value represents the second highest correlation between these two quantities at any of the four points investigated. The two divergence fields are in-phase only 23 out of 45 times. Investigation shows that agreement in the sign of the divergence values in the two fields is weakly related to wind speed, i.e., high wind speeds equate to marginally better correlation in the two divergence fields. The average wind speed for days of divergence value agreement is 12.30 knots and 7.75 knots during out of phase days, while the overall average wind speed for point 1 is 12.16 knots.

If we assume that a divergent phase (of any magnitude) followed by a convergent period results in pressure ridge formation, then the PIPS ice divergence data shows that eight separate ridge-building episodes occurred during the 45 day observation period, as compared to 10 for the NOGAPS model data. Since RGPS deformation data is not available for this period, it is difficult to establish if the number of ridges implied by PIPS and the NOGAPS model is accurate. A comparison of Cycle 15 RGPS ridging data to the ridging implied by the 1998 ice divergence data sets would obviously not be very conclusive, nor is it expected to be. However, a comparison would nevertheless prove useful, if only to establish if similar ice deformation characteristics are observed.

The analysis of the Nov 96 RGPS data showed that from one to two ridging events occurred in the flaw leads of area A over a period of roughly 10 days. If we extrapolate this data for 45 days, one would expect to see from five to 10 ridges at point 1 (located in proximity of the flaw lead) during the 1998 observation period. Between eight to 10 were implied by the PIPS and NOGAPS model ice divergence as stated previously. One must also remember that the temporal resolution of the RGPS deformation products

is, on average, limited to three days. The RGPS sea ice algorithms may therefore not detect ridging events of limited duration.

Comparison of 1996 to 1998 deformation data is not desirable, but necessary, due to the lack of data sets coincident in time. One can, however, compare the nature of atmospheric forcing during both time periods to obtain an estimate of the differences that exist in the respective surface wind fields. Although this research shows that pressure ridge formation is not solely a function of the magnitude of the surface wind speed, this variable is easily quantifiable and is used here to obtain a feeling for the atmospheric forcing present during both analysis periods. Figures 30 and 31 quantify the surface wind speeds for the RGPS cycle 15 period (07-18 Nov 96) and the PIPS analysis period (13 Feb – 31 Mar 98), respectively. These figures show that the average wind speed was 4.6 knots higher during the 1996 RGPS analysis period. Greater atmospheric forcing is also implied by the peak 10 m wind speeds observed during both periods: 32 knots in 1996 as compared to only 23 knots in 1998.

Variation in the magnitude of the NOGAPS model ice divergence is much greater than that of the PIPS divergence as shown in Table 3 and Figure 23. However the mean value of both divergence fields is

	PIPS ice divergence	NOGAPS model ice divergence
Maximum value	$1.4 \times 10^{-7} \text{ s}^{-1}$	$6.6 \times 10^{-7} \text{ s}^{-1}$
Minimum value	$-0.7 \times 10^{-7} \text{ s}^{-1}$	$-4.2 \times 10^{-7} \text{ s}^{-1}$
Standard deviation	$0.7458 \times 10^{-7} \text{ s}^{-1}$	$2.0854 \times 10^{-7} \text{ s}^{-1}$
Mean value	$-0.0667 \times 10^{-7} \text{ s}^{-1}$	$0.2081 \times 10^{-7} \text{ s}^{-1}$
Correlation	0.2127	

Table 3. Statistical comparison of PIPS and NOGAPS model ice divergence fields from 13FEB98 to 31MAR98 for point 1 (74°N/155°E) located in area A.

close to zero, an expected value since we expect the intensity of divergence and convergence to be in balance over a long period of time. Furthermore, the days of onshore winds resulting in PIPS ice convergence almost equal those during which offshore winds cause ice divergence: 15 versus 12. RGPS deformation plots provide an indication of the degree of ice divergence observed at point 1, albeit during a different season and at a different time. RGPS charts show divergence as a function of percent area change. The highest values of divergence in the flaw lead regime show an area change of greater than 10% over the RGPS time differential, approximately three days. Since three days are equivalent to 2.6×10^5 seconds, a 10% area change translates to a divergence value of $> 3.85 \times 10^{-7} \text{ s}^{-1}$ or roughly $> 4.0 \times 10^{-7} \text{ s}^{-1}$. Maximum convergence values likewise measure $> -4.0 \times 10^{-7} \text{ s}^{-1}$. In light of these values, it would seem that the NOGAPS model ice divergence matches the RGPS divergence values better and that the PIPS model (Table 3) underestimates the degree of deformation actually occurring in the flaw lead. This observation is highly speculative though, since the exact location of point 1 in relation to the flaw lead is not known. The

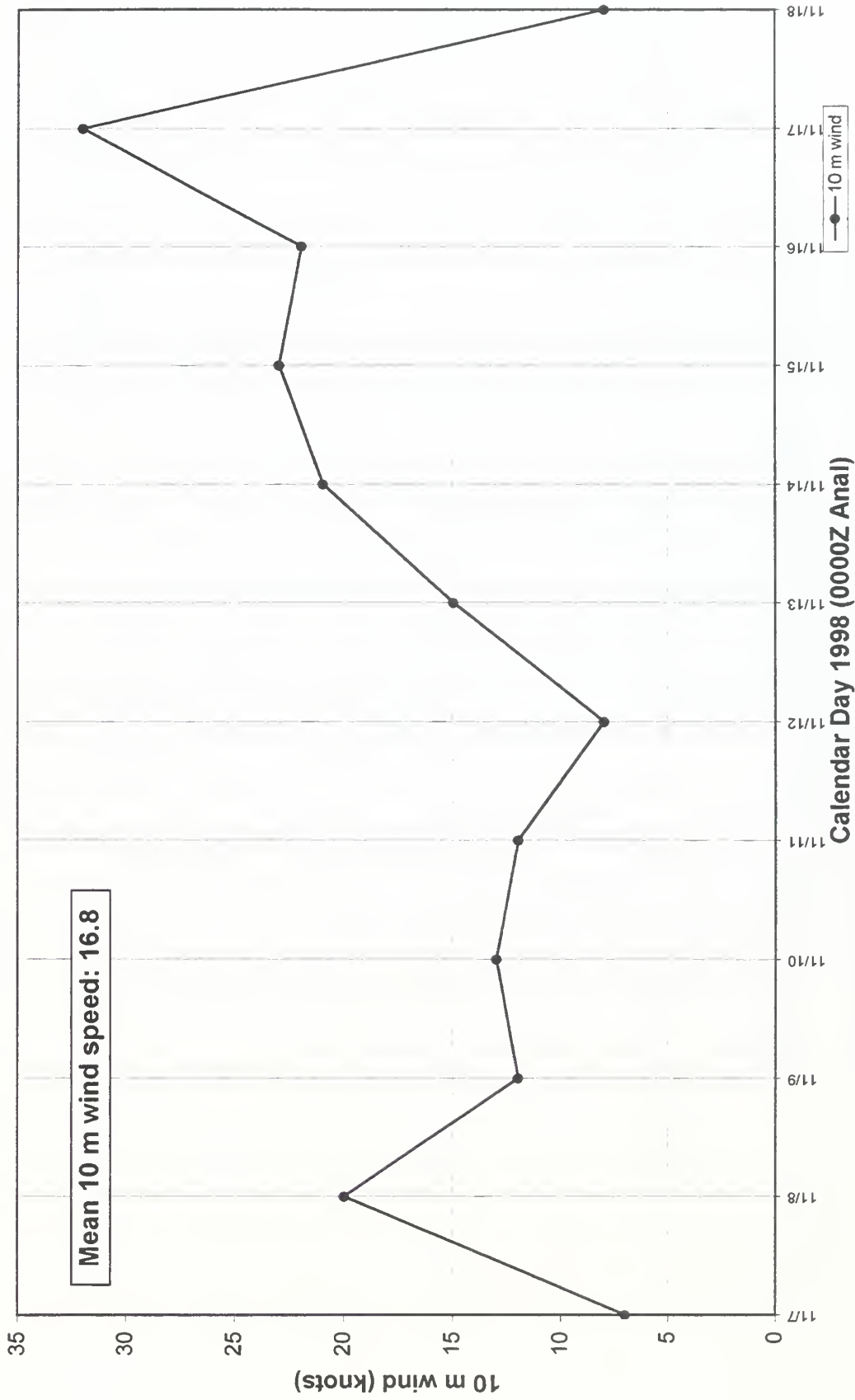


Figure 30. 10 m NOGAPS wind speed, 07-18 Nov 96 at point 1 (74N/155E)

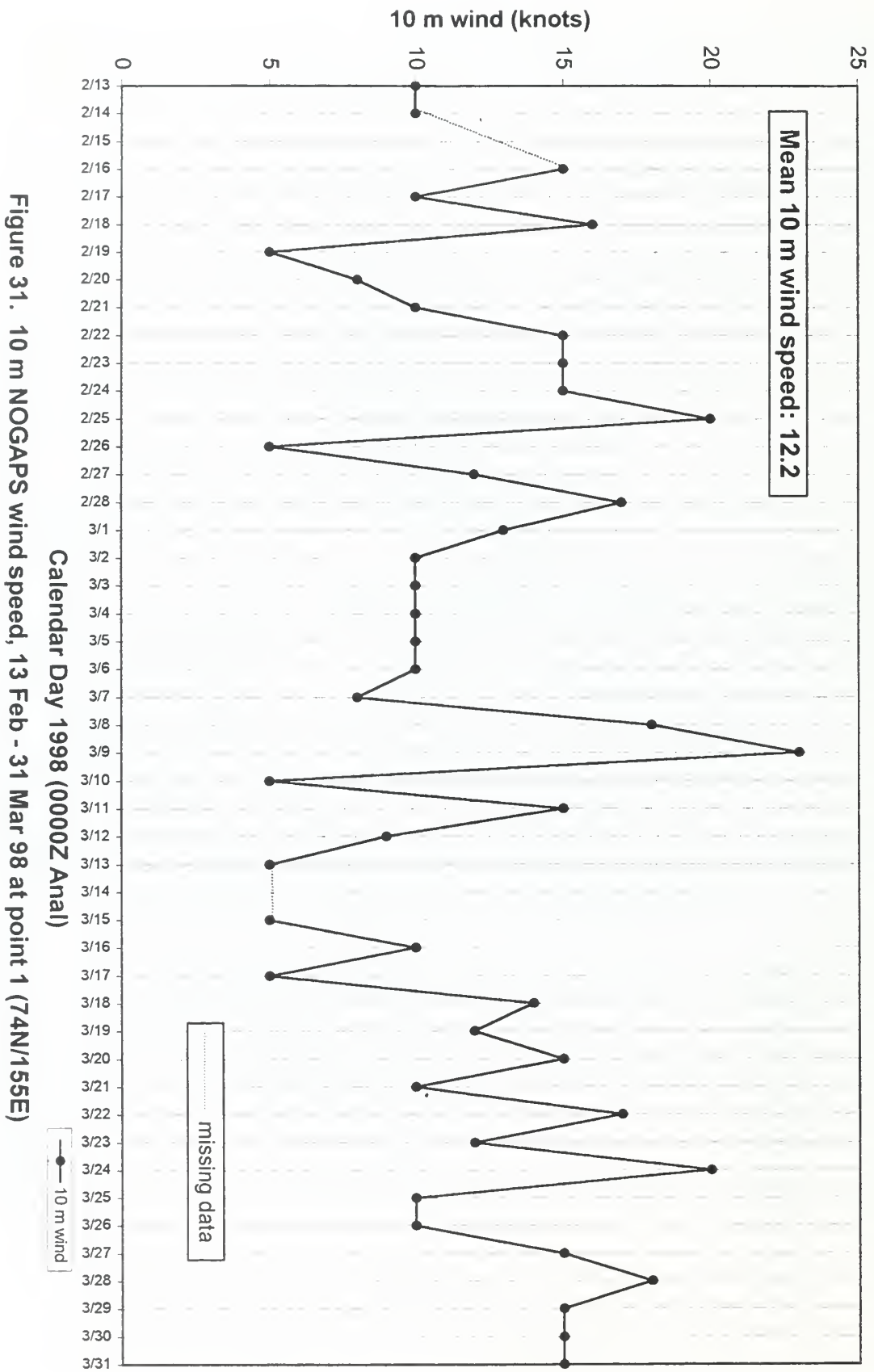


Figure 31. 10 m NOGAPS wind speed, 13 Feb - 31 Mar 98 at point 1 (74N/155E)

RGPS data show that the actual zones of high deformation are very isolated and narrow and point 1 may lie in an area of lesser deformative activity.

One of the conclusions drawn by the investigation of NOGAPS meteorological data is that the magnitude of wind and ice divergence is not necessarily related to the magnitude of the wind speed. For example, horizontal shear in the wind field is also an important factor in altering the wind and, consequently, the ice divergence patterns. These observations are borne out by the data in Figure 23. Three of eight maxima (38%) during NOGAPS model ice convergence events actually appear when wind speeds are below the period wind speed average. (Extreme (loud) ambient noise events only occur during ice convergence events, not during the divergent, or lead-forming, phase). The majority of maxima during PIPS ice convergence events, likewise, occur when the wind is below the period average (three of eight). Feller (1994), however, found a lag of seven to ten hours between peak winds and corresponding ambient noise peaks in his study of environmental forcing of ambient noise in the Arctic. This agrees with Collins (1996) who calculated a 12-hour time lag between moderate wind speeds (15-30 knots) and increases in ambient noise caused by active pressure ridging. The correlation between peak winds and the maximum PIPS ice convergence values for the period investigated in this study shows that three of six (50%) local convergence maxima are preceded by stronger winds in the previous 24 hours than those on the day of the maximum convergence. Missing wind data preceded two events, so only six of eight convergent points could be examined. Additionally, 12-hour winds would be more useful for comparison, but were not available. In contrast, five of eight (63%) NOGAPS model local convergence maxima were preceded by stronger winds in the previous 24 hours. These percentages are only reflective of general trends, and therefore both PIPS and NOGAPS model data are judged to represent the correlation between wind speed and ice convergence equally well.

b. Ice Divergence Comparison at Point 2 (71°N/150°W)

If the ice deformation patterns near any shoreline are controlled by the on/offshore component of the surface wind, then the ice divergence fields for point 2 should resemble those of point 1. A casual examination of Figure 24 and Table 4 shows that this is not the case. The greatest disparities can

	PIPS ice divergence	NOGAPS model ice divergence
Maximum value	$6.5 \times 10^{-7} \text{ s}^{-1}$	$5.0 \times 10^{-7} \text{ s}^{-1}$
Minimum value	$-3.2 \times 10^{-7} \text{ s}^{-1}$	$-3.0 \times 10^{-7} \text{ s}^{-1}$
Standard deviation	$2.0043 \times 10^{-7} \text{ s}^{-1}$	$1.8986 \times 10^{-7} \text{ s}^{-1}$
Mean value	$0.7522 \times 10^{-7} \text{ s}^{-1}$	$0.3733 \times 10^{-7} \text{ s}^{-1}$
Correlation	0.1904	

Table 4. Statistical comparison of PIPS and NOGAPS model ice divergence fields from 13FEB98 to 31MAR98 for point 2 (71°N/150°W)

be observed by studying Table 4. Point 2 is the only one of the four points investigated that shows maximum and minimum PIPS divergence values and a standard deviation higher than that of the NOGAPS model divergence. Before addressing these disparities, the other statistical data will be evaluated.

Numerical correlation between PIPS and NOGAPS model ice divergence is comparable to that at point 1: weakly positive at 0.19. As discussed before, this correlation is not expected to be high near the influence of a shoreline.

The correlation between the on/offshore component of the 10 m wind and PIPS con/divergence is not as good as at point 1: the two properties are in phase 24 days and out of phase 10 days, again ignoring days of parallel wind flow (There were no days of total non-divergence in the ice cover). This converts into an in-phase percentage of 71% (as compared to 87% at point 1). Divergence values on the out of phase days were large, the largest was $6.0 \times 10^{-7} \text{ s}^{-1}$ (as compared to a maximum of $-0.2 \times 10^{-7} \text{ s}^{-1}$ at point 1). The agreement of the phase of divergence is not related to wind speed: The average wind speed during days of phase agreement was 11.92 knots and 12.80 knots during phase disagreement, as compared to an average wind speed of 11.73 knots for the period. It is interesting to note that the maximum divergent event in both the PIPS and NOGAPS data sets, which occurred on 07 Mar 98, was in phase and correlated to the second-highest wind speed recorded during the observation period: 23 knots. The mean value of divergence for the PIPS model ($0.75 \times 10^{-7} \text{ s}^{-1}$) implies a greater number of days with offshore than onshore flow. This observation is borne out by the data: 15 days show offshore flow and ice divergence, while only nine show the opposite.

RGPS deformation data in this geographic area is not available for this period or during Nov 96. However comparison of PIPS and NOGAPS model (implied) ridging frequency to that observed in area A may prove interesting. As at point 1, PIPS shows two fewer ridging events than NOGAPS model data: six as compared to eight. These numbers are comparable to those at point 1 and most likely represent a good estimation of ridging events in this highly deformative area. One can speculate that the number of shear ridges, which probably produce lower values of ambient noise than convergent ridges, predominate at point 2. The reason for this is the greater influence of the anti-cyclonic Beaufort Gyre, which consistently shows higher current speeds here than at point 1 and area A.

Investigation of local convergence maxima to wind speed shows that the magnitude of the wind speed was related even less to maxima in convergent activity at point 2 as compared to point 1. Five of eight (63%) NOGAPS model convergence events appear when the 10 m wind speeds were below the period average. This compares to three of seven (43%) PIPS events. When taking the lag between wind forcing and convergence maxima into account (as discussed in Section F. 4. a. of this chapter), four events out of eight (50%) show higher wind speeds on the day previous to the event for the NOGAPS model, two of six (33%) for the PIPS model (one PIPS event was preceded by missing wind data). Again, these numbers do not reveal any strong correlation between potential ridging activity and the strength of the wind speed before or during the events.

The answer to the obvious differences between the deformation activity at points 1 and 2 has already been alluded to. While the ice deformation at point 1 appears to be directly linked to the nature of

	PIPS Ice Divergence ($\times 10^{-7} \text{ s}^{-1}$)	10m Wind Speed (knots)	PIPS Ice Drift (km/day)
2/13/98	-3.2	23	22.2
2/20/98	4.0	25	29.6
2/26/98	-2.5	12	9.3
3/7/98	6.5	23	20.4
3/24/98	5.0	18	7.4
3/25/98	6.0	20	27.8

Table 5. Comparison of the surface wind speed and ice drift to the calculated PIPS divergence values for the six most deformative events during the investigative period at point 2.

the atmospheric forcing present, i.e., the on/offshore flow of the wind, another force, aside from the surface wind, is influencing the ice cover at point 2. This force is the rotating Beaufort Gyre. Over the 47-day 1998 observation period, the PIPS model showed that ice drift speeds, resulting from both atmospheric and oceanic forcing, averaged 2.20 km/day at point 1, while the average drift computed at point 2 was 9.06 km/day. Ice motion is generally highest at point 2 when the gyre is in its usual anti-cyclonic cycle. Figure 32 shows the ice drift during this phase. When the gyre reverses, depicted in Figure 33, as it did twice during the observation period, point 2 drift speeds generally decrease. Ice drift speeds at point 1 stay low during both events. High wind and ice drift speeds combined in four out of six cases to cause extreme PIPS divergence events, defined as those during which divergence values equal to or are greater than $4.0 \times 10^{-7} \text{ s}^{-1}$ and convergence values exceed $-2.0 \times 10^{-7} \text{ s}^{-1}$ (see Table 5). It is surprising, in view of the significant effect of the Beaufort Gyre on the deformation of the ice cover, that the correlation between the PIPS and NOGAPS wind divergence is as high as it is. This occurs because all six highly deformative events are accompanied by relatively high wind speeds (12 to 25 knots). There are no examples of significant deformation occurring solely due to the effect of the gyre, i.e., low wind speeds and high ice drift speeds in this data set. It must be noted (again) that reference to “high” wind speeds at point 2 are intended to be relative to the highest wind speed observed: 25 knots. These are by no means high wind speeds in an absolute sense.

c. Ice Divergence Comparison at Point 3 (78°N/150°W)

It was not unexpected to see that the NOGAPS model ice divergence did not match that of PIPS at points 1 and 2, since the predominant correlator of ice deformation near the shore was found to be the on/offshore component of the 10 m wind. At point 3, however, a better numerical correlation is

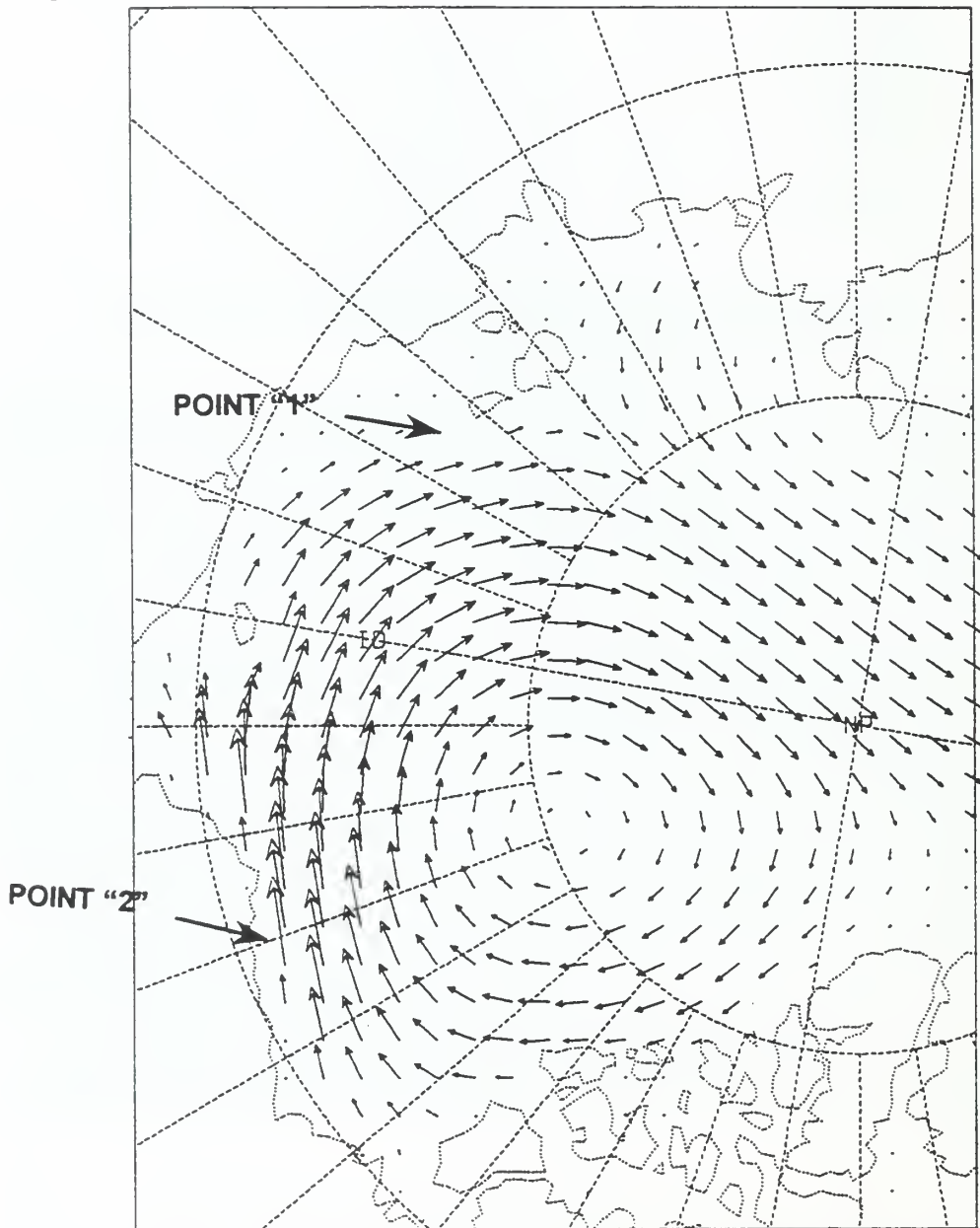


Figure 32. PIPS model ice drift analysis for 19 Feb 98, showing the normal anti-cyclonic rotation of the Beaufort Gyre. Ice speeds are 3.7 km/day at point 1 and 29.6 km/day at point 2. Points located at ends of arrow heads.

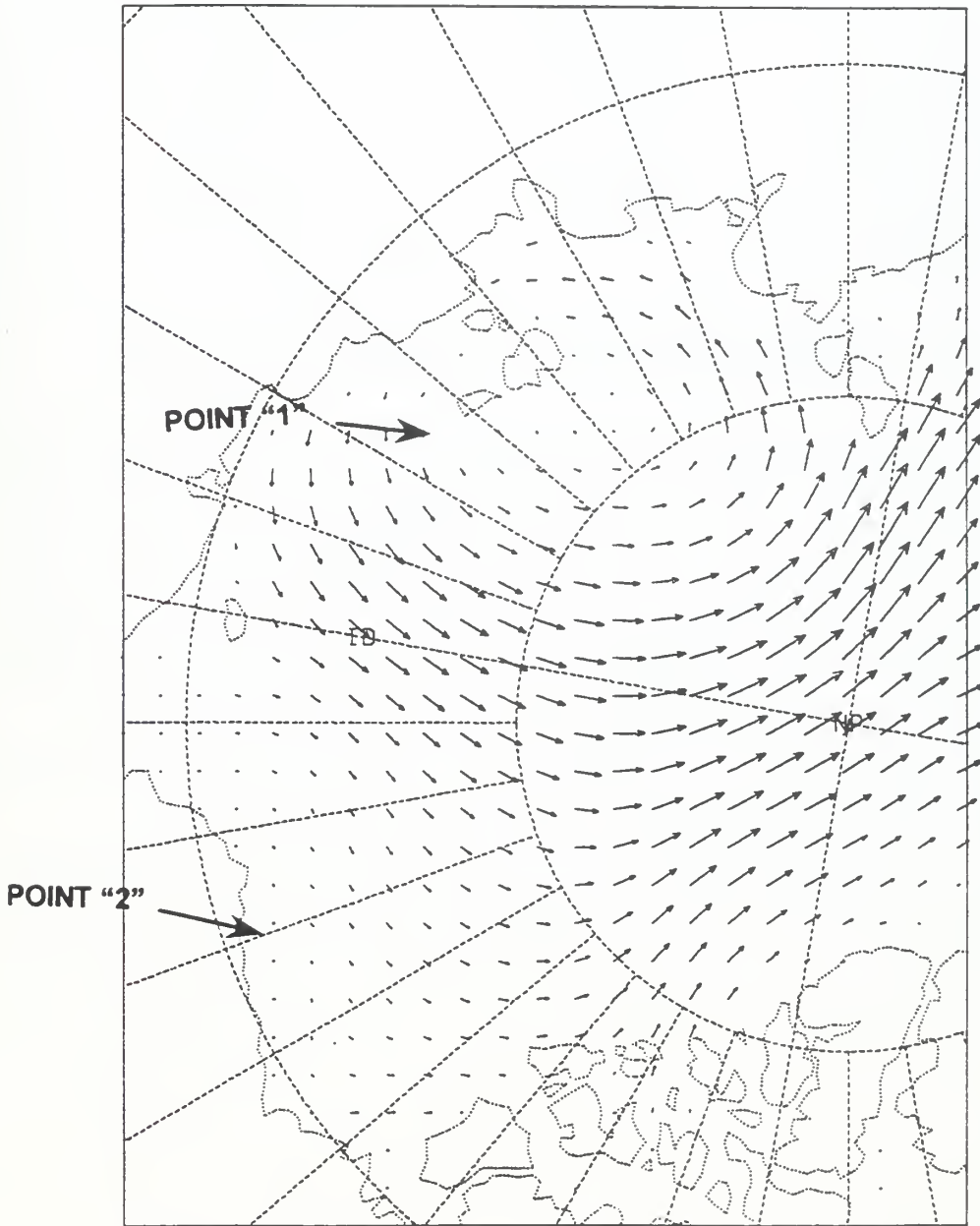


Figure 33. PIPS model ice drift analysis for 10 Mar 98, showing the reversed flow of the Beaufort Gyre. Ice speeds are 3.7 km/day at point 1 and 1.9 km/day at point 2. Points located at ends of arrow heads.

directly derived from the surface wind field. The PIPS ice divergence field is not very energetic when compared to that of the NOGAPS model. Likewise, the 1996 Cycle 15 RGPS data show less individual expected. Surprisingly, the correlation at point 3 is the lowest of all the four points (see Table 6). Comparison of the maximum and minimum values and the standard deviation in Table 6 shows that PIPS

	PIPS ice divergence	NOGAPS model ice divergence
Maximum value	$1.2 \times 10^{-7} \text{ s}^{-1}$	$5.3 \times 10^{-7} \text{ s}^{-1}$
Minimum value	$-0.7 \times 10^{-7} \text{ s}^{-1}$	$-3.2 \times 10^{-7} \text{ s}^{-1}$
Standard deviation	$0.3972 \times 10^{-7} \text{ s}^{-1}$	$1.6727 \times 10^{-7} \text{ s}^{-1}$
Mean value	$0.1500 \times 10^{-7} \text{ s}^{-1}$	$0.0611 \times 10^{-7} \text{ s}^{-1}$
Correlation	-0.0497	

Table 6. Statistical comparison of PIPS and NOGAPS model ice divergence fields from 13FEB98 to 31MAR98 for point 3 (78°N/150°W) located in area B.

ice divergence responds less to external forcing than that implied by the NOGAPS ice divergence, which is extreme deformation events, such as the flaw leads observed at points 1 and 2. Instead, divergence and convergence values of lesser magnitude are spread over a greater spatial extent. If one estimates that the mean ice divergence and convergence encountered in area B is represented by a $\pm 4.0\%$ area change (less than $4/10^{\text{ths}}$ that observed in the flaw leads) over the three-day RGPS temporal resolution, an average ice divergence value of $\pm 1.54 \times 10^{-7} \text{ s}^{-1}$ is calculated. This reduced activity makes sense in the latitudes of the high Arctic where in winter the ice thickness is greater than near the coasts and can respond less to environmental forcing, i.e. the ice cover is essentially locked. Therefore, the strong changes of divergence implied by the NOGAPS model ice divergence in Figure 25 cannot physically be justified.

The average RGPS ice divergence value computed above represents an approximate condition, estimated from data observed during a different season and year and under different environmental forcing than the 1998 PIPS data. The comparison between RGPS and PIPS data is therefore interesting, but must be treated with extreme caution. The mean divergence value observed in the PIPS divergence field at point 2 is $0.32 \times 10^{-7} \text{ s}^{-1}$ and the mean convergence value $-0.40 \times 10^{-7} \text{ s}^{-1}$. These values are less than those estimated from the RGPS data. One can glean an estimate of the different degrees of environmental forcing by comparing average surface wind speeds encountered during each period, 21.2 knots for the 1996 RGPS observation period (Figure 34) and 14.9 knots over the 1998 PIPS period (Figure 35). Likewise, maximum wind speeds are higher during the 1996 RGPS period: 35 knots as compared to 30 knots in the 1998 PIPS period. One must remember that wind speed alone is not a definitive indicator of wind divergence and wind-derived ice divergence, but it does give a sense of the environmental forcing present. Since the average wind speed is approximately 6 knots less in 1998, we would expect less ice divergence. It does appear though that PIPS underestimates the magnitude of the ice divergence present.

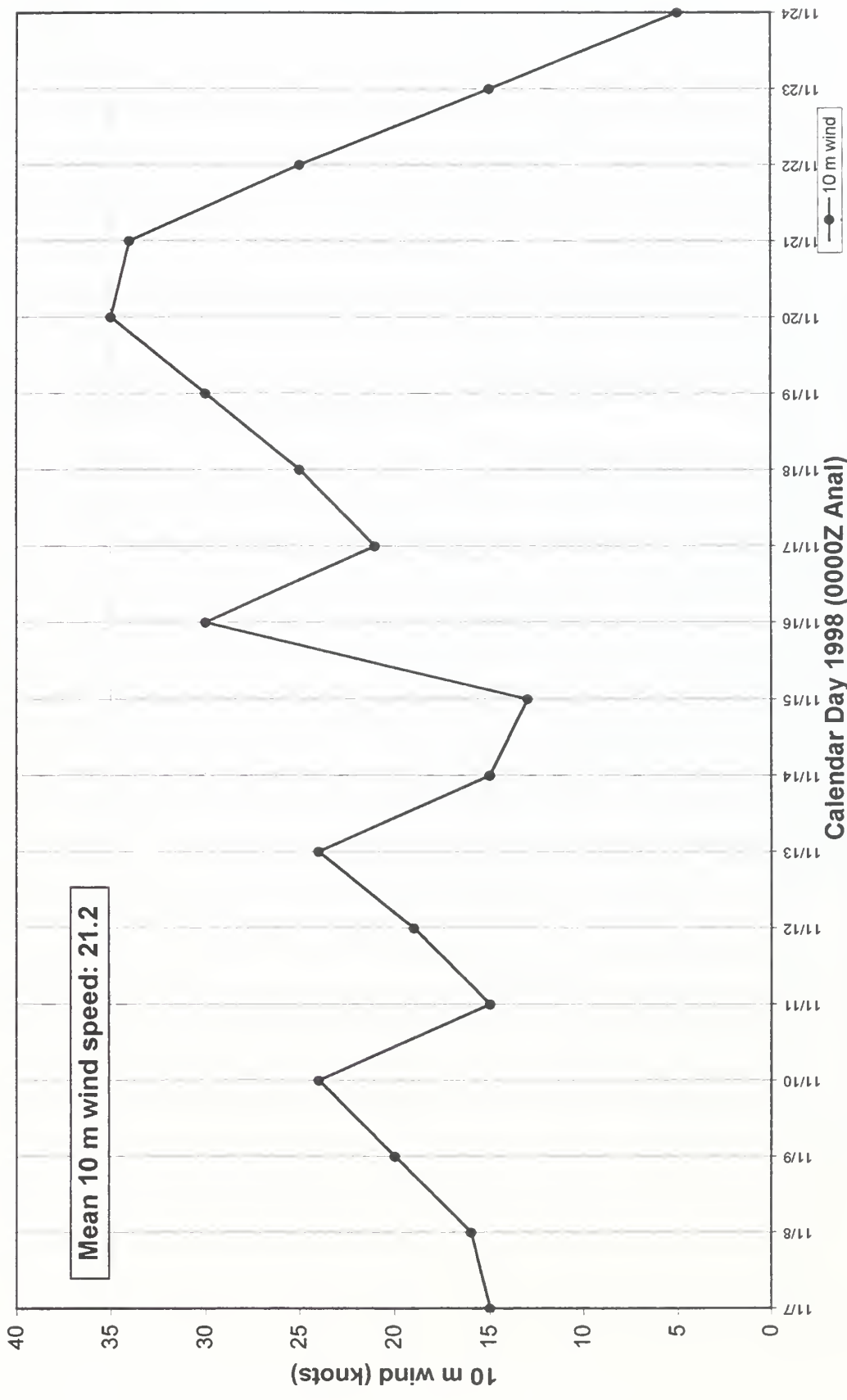


Figure 34. 10 m NOGAPS wind speed, 07-24 Nov 96 at point 3 (78N/150W)

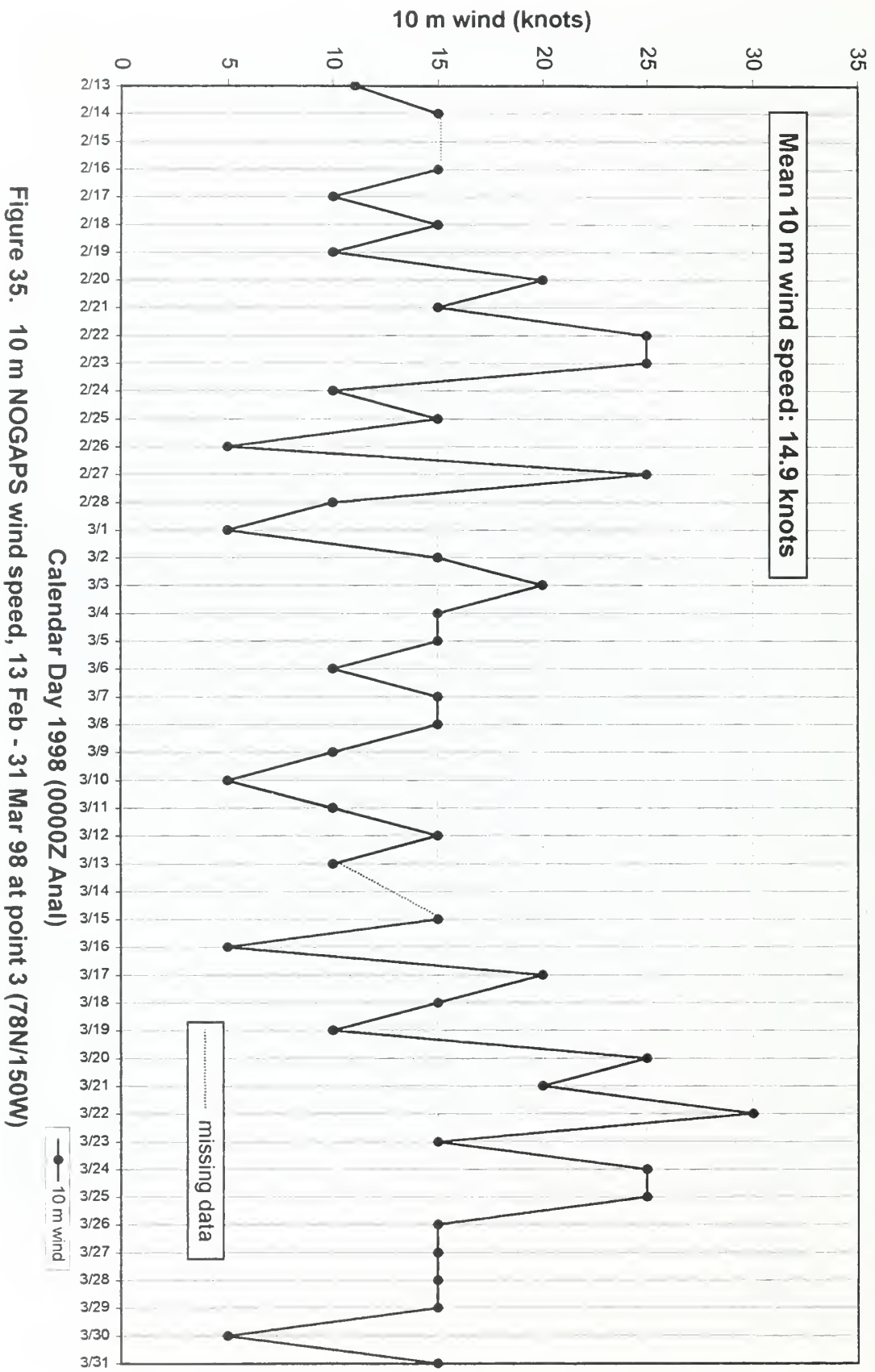


Figure 35. 10 m NOGAPS wind speed, 13 Feb - 31 Mar 98 at point 3 (78N/150W)

Analysis documented in Appendix B and summarized in Section D. 3. B. of this chapter shows a strong subjective correlation between the NOGAPS model ice divergence and the deformation observed in RGPS data. In light of the large differences in ice divergence magnitude shown in Figure 25, one can question whether PIPS appears to estimate the sign of divergence (divergence versus convergence) correctly. If we ignore the four days when either PIPS or NOGAPS show non-divergence, the two models agree on the sign of divergence on only 25 out of 41 days (61%). This percentage in itself is not encouraging, but there are modifying circumstances. First, the subjective correlation between NOGAPS model ice divergence and the observed area change (divergence) in the RGPS data was not determined through a day-by-day comparison. Instead, the changes in the sign and magnitude of 12-hour ice divergence plots were compared to the changes observed in the RGPS ice cover over a three-day period. Second, the average velocity of ice drift through the actions of wind and the Beaufort Gyre was almost as high at point 3 as it was at point 2 for the 1998 period, 7.78 km/day. The impact of the current is not considered in the NOGAPS model calculations.

The RGPS data shows that one to two ridging events occurred over 18 days in area B during the cycle 15 observation period or from three to five ridging events over 47 days. This number compares to nine ridges (implicitly) predicted by the NOGAPS model and three by PIPS over 47 days during the 1998 observation period. It is difficult to say if the PIPS predictions are correct, considering that the data were taken over different seasons and years, but they are not totally unbelievable. NOGAPS certainly seems to over-predict the number of implied ridges for the 1998 data; in other words the NOGAPS model's temporal stationarity is quite short. However, it must be stated that only the number, not the magnitude, of potential ridging events was considered to arrive at the numbers cited above. Some of the ridging events implied by the NOGAPS model would most likely result in very small ridges producing low levels of ambient noise (the ridging event implied for 15 to 17 Mar 98 in Figure 25, for example). Likewise, there are a number of changes in the PIPS divergence pattern that "almost" result in ridges (as seen in the PIPS divergence pattern from 23 to 25 Mar 98 in Figure 25). Perhaps an increase in the PIPS model resolution would improve its ability to predict high Arctic open ice deformation events.

In light of the above discussion, it may be necessary to take a step back and take a qualitative look at the data presented in Figure 25. Of particular interest are the divergence values for the period 16 Feb 98 to 21 Feb 98 and 27 Feb 98 to 04 Mar 98. The trends of the increase and decrease of divergent activity match exactly in both fields, even though their magnitudes differ. This is encouraging and leads the investigator to believe that PIPS divergence fields would be useful in predicting pressure ridge formation at an open ice location, even though their magnitude may be underestimated.

d. Ice Divergence Comparison at Point 4 (76°N/175°W)

Examination of point 4, also located in the high Arctic, corroborates the findings from point 3. Statistical data presented in Tables 6 and 7 are very similar, except for the correlation, which is weakly positive at point 4. Correlation between PIPS and NOGAPS model ice divergence is actually the

highest at this location of all the points investigated. Other parameters examined in the previous section are also comparable to those observed at this location. For example, 22 of 40 days (55%) show agreement in the sign of divergence. The mean PIPS divergence was $0.36 \times 10^{-7} \text{ s}^{-1}$, the mean PIPS convergence - $0.33 \times 10^{-7} \text{ s}^{-1}$. The PIPS divergence data implies 4 ridges for the period, the RGPS data implies 9 ridges.

	PIPS ice divergence	NOGAPS model ice divergence
Maximum value	$0.8 \times 10^{-7} \text{ s}^{-1}$	$3.0 \times 10^{-7} \text{ s}^{-1}$
Minimum value	$-0.7 \times 10^{-7} \text{ s}^{-1}$	$-4.3 \times 10^{-7} \text{ s}^{-1}$
Standard deviation	$0.3497 \times 10^{-7} \text{ s}^{-1}$	$1.6821 \times 10^{-7} \text{ s}^{-1}$
Mean value	$0.1811 \times 10^{-7} \text{ s}^{-1}$	$-0.7833 \times 10^{-7} \text{ s}^{-1}$
Correlation	0.2776	

Table 7. Statistical comparison of PIPS and NOGAPS model ice divergence fields from 13FEB98 to 31MAR98 for point 4 (76°N/175°W)

The ice drift was 8.76 km/day. Qualitative analysis of Figure 26, again shows very “noisy” NOGAPS model data, but no extended time periods where the two divergence fields appear to be synchronized (as compared to point 3).

5. Analysis Conclusions

A comparison of the PIPS and NOGAPS model ice divergence fields conducted in this section leads to the following conclusions:

- The subjective correlation between RGPS deformation data and the onshore component of the 10 m wind in proximity of a coastline is borne out by strong numerical correlation between PIPS ice divergence and 10 m wind data at points 1 and 2.
- The strong qualitative correlation between the PIPS and NOGAPS model ice divergence at an open ice location is not numerically reinforced by statistical data in this section. Qualitative correlation between the divergence fields at point three, however, is encouraging. Perhaps wide area correlation measures should be established rather than single point correlations in future research efforts.
- PIPS appears to underestimate the magnitude of ice divergence present at open ice locations (points 3 and 4). This is likely a function of the relatively large grid spacing of the PIPS model (20 km) and the fact that ice divergence may not be the best indicator of ice deformation. Future upgrades to the PIPS model may remedy this shortcoming. The PIPS computer code is currently being modified by Hibler to output energy dissipation due to both normal and shear stresses. This full-physics approach incorporates the forcing described in the above analysis and other factors in a complex, balanced way. Additionally, the future spatial resolution will be increased to approximately 10 km or near the resolution of the RGPS sea ice products. Ice deformation values should therefore improve in accuracy, regardless of the geographic location (near shore or in the central basin), and be in good agreement with the RGPS data.

- Both the PIPS and NOGAPS model ice divergence fields appear to predict a reasonable number of pressure ridging events at near-shore locations.

- PIPS appears to slightly underestimate, while NOGAPS overestimates, the number of pressure ridging events at the high Arctic open ice locations.

- The magnitude of oceanic forcing, manifested by the varying strengths of the Beaufort Gyre, has a significant impact on the degree of ice deformation in coastal regions. PIPS divergence fields capture this forcing quite well. The influence of the anti-cyclonically rotating Beaufort Gyre plays an important part in the massive ice deformation at point 2 and most likely also does so at the high arctic observation points.

- Although ice divergence is related to the magnitude of the surface wind speed, other factors, such as horizontal shear in the wind field, are important in determining the amount of wind and ice divergence encountered.

- The NOGAPS ice divergence “model,” based solely on the surface wind-derived free drift of the ice field, is a much poorer indicator of ice deformation than the full-physics coupled PIPS model.

VI. CONCLUSIONS AND RECOMMENDATIONS

A. CONCLUSIONS

A proof-of-concept study was conducted to determine if SAR data can be used to identify large scale deformation of the sea ice cover in the Canadian Basin of the Arctic Ocean in the winter season, which may result in the creation of acoustically active pressure ridges. Additionally, PIPS model ice divergence fields were indirectly analyzed to decide if they could provide accurate indications of pressure ridging activity and would be suitable to replace surface wind speed fields as the environmental forcing mechanism in the ASNM developed by Collins (1996). Some conclusions from the results of this study follow.

- SAR-derived geophysical products, specifically those created by the RGPS sea ice algorithms, are superior to raw SAR imagery in identifying deformations of the ice cover which may result in low frequency acoustic disturbances. Individual unprocessed SAR images are too detailed to easily reveal the presence of acoustically active pressure ridges. Ironically, despite the wealth of data provided by SAR images, the spatial resolution of the RADARSAT-1 sensor (100m) may actually be too coarse to positively identify a newly formed pressure ridge in raw imagery (depending on the ridge's aspect to the sensor). The large size of the SAR image data files makes them cumbersome to manipulate. Furthermore, the deciphering of SAR imagery requires extensive training and experience in order to avoid interpretation errors. RGPS products, on the other hand, are easily interpreted, the files that contain them are of manageable size and changes in the character of the ice cover can be tracked easily both in time and space.
- RGPS sea ice products are well suited for identifying areas of tactically significant ambient noise. The temporal sequence of ice divergence and convergence evident in RGPS deformation products corresponds to the open water lead formation and subsequent pressure ridging associated with Arctic AN events. The spatial resolution of the RGPS grid can localize these regions within approximately five to ten kilometers (assuming an initial cell size of 5 km × 5 km), depending on the severity of cell deformation encountered.
- Despite all the advantages of RGPS products, they are currently only useful for the purposes of scientific research. Since the processing of one RGPS cycle takes approximately one month, the algorithm output products are not available to the operational forecasting center for the purposes of locating acoustically energetic portions of the ice cover. The lag between SAR image acquisition and RGPS product output may be reduced in the future by faster computer processors and an improved algorithm architecture which relies less on human interpreter intervention to guarantee accurate sea ice products.
- Pressure ridge formation occurs under three meteorological conditions in cycle 15 data, which corroborates the findings of previous efforts by Parsons (1992), Feller (1994) and Collins

(1996) regarding the creation of acoustically active pressure ridges. The presence of a synoptic-scale surface low pressure system initializes a pressure ridging event by opening leads in the ice, which form ridges through the crushing of their thin ice cover induced by the convergence associated with the atmospheric high pressure which follows the passage of the low. In addition to this mechanism, changes in the ice divergence pattern can result from velocity shear in straight isobaric flow associated with a tight pressure gradient. Lastly, the strongest correlation between atmospheric forcing and pressure ridge creation observed in this research existed when offshore winds were followed by onshore winds in the coastal regions of the Canadian Basin.

- The RGPS ridging algorithm provides a useful tool in the study of Arctic ambient noise. The algorithm's graphical and statistical output reveal that pressure ridge characteristics vary with geographic location in the Arctic Basin and proximity to land and that acoustically active ridges can extend for hundreds of kilometers and may remain sources of AN for temporal scales of days.
- The ridging algorithm shows that more ridges exist in RGPS cells exhibiting large cell area changes than in those with small area changes, assuming relatively constant sail heights in all cells.
- The PIPS model ice divergence fields give a fair indication of Arctic ice deformation, especially in the coastal regions of the Arctic Basin. PIPS, however, appears to underestimate the magnitude of ice deformation present in the heavy pack ice of the Polar ice cap, where the ice cover is thick and generally assumed to be more homogeneous than near the basin margins. This fact is most likely a function of the relatively large grid spacing of the PIPS model (20 km) and the fact that ice divergence by itself may not be the best indicator of ice deformation. Despite these shortcomings, the NOGAPS ice divergence "model", generated for the purposes of this research, based solely on the surface wind-derived free drift of the ice field, is a much poorer indicator of ice deformation than the full-physics coupled PIPS model.

B. RECOMMENDATIONS

Based on the conclusions reached in this thesis, the following recommendations are made to guide future research efforts dedicated to exploiting SAR data in conjunction with the creation of a physics-based operational Arctic ambient noise model.

- This research was complicated by a lack of temporally coincident RGPS and PIPS data sets and an absence of ambient noise data. This precluded the direct correlation between these three variables, which would have led to a definitive relationship between observed and predicted ice deformation and the acoustic signatures associated with it. However, the Naval Postgraduate School Meteorology Department is currently archiving fine-resolution NOGAPS meteorological data and PIPS ice divergence fields to support this research. Beaufort Sea

ambient noise data was collected in conjunction with the Surface Heat Budget of the Arctic Ocean (SHEBA) experiment from October 1997 to February of 1998. Additionally, a suite of SHEBA RGPS sea ice products should be processed and ready for analysis by July 1998 (Cunningham, personal communication, 1998). The completeness of this data set should be taken advantage of by future researchers to establish the validity of PIPS data and make a positive correlation between RGPS ice deformation products and ambient noise buoy data.

- The PIPS ice divergence fields were only partially successful in predicting the ice deformation present in the higher latitudes of the Arctic Ocean. Upgrades to the PIPS code will result in the generation of energy dissipation fields caused by both normal and shear stresses in the ice cover. These products will more correctly depict the failure of the ice sheet in response to environmental forcing. The modified PIPS model was unfortunately not available to generate products during the SHEBA experiment period discussed above. These new PIPS fields should be compared to future RGPS sea ice deformation products to gauge their ability to predict Arctic pressure ridging activity. The transition to a fully-coupled high resolution ice model such as the Semtner-Maslowski 9×9 km model should also be considered as a replacement for PIPS as a possible predictor of pressure ridge formation. Regardless of which model is chosen, the inclusion of full-physics-based internal ice stress input fields to replace the empirically-derived wind forcing would considerably improve the performance of Collins' (1996) ASNM and should therefore be actively pursued.
- One of the weaknesses of ASNM was its ability to only predict <10th and >90th percentile AN levels well. This shortcoming can be explained by the fact that pressure ridges behave in an isotropic manner during periods of low and extreme environmental forcing. Noise resulting from pressure ridging activity attributed to median forcing is highly anisotropic, because both the general background noise due to distant ridging events and the near-field noise from individual isolated pressure ridges contribute to the local noise field. In order to resolve this problem, both the geographic location and intensity of individual pressure ridges would need to be “fed” to an operational AN model in real or near-real time. Although this is not currently possible, due to the time-lateness of RGPS-derived ice deformation fields, long-term research should focus on the feasibility of using RGPS data as direct ASNM input, vice ice model-derived internal ice stress fields. RGPS data is preferred because they are not model output but represent observations of the changes occurring in the ice cover.

APPENDIX A

RGPS DEFORMATION PRODUCT ANALYSIS OF AREA A AND COMPARISON TO NOGAPS METEOROLOGICAL DATA

A. Background

This appendix contains detailed period-by-period analyses of the cycle 15 RGPS deformation products and their qualitative comparison to the NOGAPS meteorological variables in area A (see Figure 27). RGPS data streams were available from 07 to 18 Nov 96. Times are referenced to Greenwich Mean Time. Wind divergence values are abbreviated in the text and are assumed to be multiplied by 10^{-5} (s^{-1}). Ice divergence values are represented by the percent cell area change over the RGPS temporal resolution, assumed to be three days. RGPS deformation data is too sparse from 19 to 27 Nov 96 to conduct meaningful analysis.

B. Data Analysis for Period 1: 07-09 Nov 96

1. Meteorological Data

A strong ridge of high pressure (1039 mb) dominates area A on 11/07/96 (Figures 48 and 49). Winds shift from NW to NE during the day, but do not exceed 10 knots. Winds are slightly divergent in the area but do not exceed +1.0. The 0000Z 11/08/96 surface chart (Figure 50) shows that an area of low pressure troughing extends off a 980 mb low, located in the Sea of Okhotsk and extends into the Laptev Sea. This trough is spawning a new low, which deepens to 1004 mb and is located on the Siberian coast south of area A by 1200Z 11/08/96 (Figure 51). Interaction between this low and high pressure to the north are causing 25-30 knot easterly (onshore) winds over the area. Wind divergence values remain slightly divergent early on 11/08/96, except near the coast, where very slight wind convergence is observed. This area of convergence moves farther offshore, as the surface low moves towards the northeast and into the Laptev Sea. Wind convergence values reach a maximum of > -2.0 , with the higher values along the Siberian shore. By 0000Z 11/09/96 (Figure 52) the low has filled to 1008 mb and its elongated center has moved into the Laptev Sea. Wind speeds have decreased to 10-15 knots and are still onshore. By 1200Z 11/09/96 (Figure 53), the low's center has moved northeast and is exiting area A. The winds are offshore along the Siberian coast, but still onshore in the extreme northerly part of area A, as they rotate around the low's center. Maximum wind speeds do not exceed 15 knots. Wind convergence has spread over the whole of area A, with maximum values still not exceeding -2.0 . By 1200Z 11/09/96 (Figure 53), this convergence has given way to essentially zero divergence throughout the area of interest.

2. RGPS Deformation Analysis and Subjective Correlation with Wind Divergence

The most prominent feature in area A is a large area of divergent lead formation directly to the east of the New Siberian Islands. It is hard to imagine that large "super-leads" such as these would be directly related to the very slight wind divergence observed in area A from 0000Z 11/07/96 to 0000Z 11/08/96 (Figures 48 through 50). It is interesting to note that the relatively major convergence event associated with the approach of the surface low barely extends far enough offshore at 1200Z 11/08/96 (Figure 51) to reach the location of the "super-leads". At 0000Z 11/09/96 (Figure 52), the "super-leads" are definitely under the influence of major wind convergence and one would imagine that the leads would now

be in a ridging phase. The convergence event is relatively short-lived though (< 12 hours) and if we assume that wind positive divergence is directly related to lead formation, we must assume that the effects of the minor divergent forcing over a relatively long period is enough to offset the short-lived convergent activity. If we consider that ice moves to the right of the surface wind and that ice convergence occurs into a (perfect) high and ice divergence out of a (perfect) low, then the creation of the leads starts to make sense, since the low pressure system completely passes through area A during the period and should result in net ice divergence along its path.

Evidence of very slight ice convergence is evident shoreward of the three leads (Figure 36). It is oriented parallel to the leads (cross-isobaric) and occurs closer to shore. The orientation of its axis is roughly perpendicular to the strongest surface wind direction of the period and may be related to the convergent event of 0000Z 11/09/96 (Figure 52). However, if one remembers that ice drifts approximately 28° to the right of the surface wind, the orientation of the ridge no longer makes sense. It was most likely created in response to the shoreward movement of the ice in the “super-leads”, i.e., the leads to the north are forcing the ice against the Siberian coast.

Two additional deformation events exist south of the leads and are oriented at roughly right angles to them. The northerly one intersects the ridge described above in a "T" fashion. It shows neither strong convergence nor divergence, but exhibits strong shear characteristics, and the shearing motion probably accounts for the ridging. The southerly ridge actually crosses two of the three “super-leads” and can not be explained by the data presented in this section.

The area around the southeastern end of the “super-lead” also shows evidence of ridging. This ridging shows no strong directionality and may or may not be a result of the strong convergent winds in the area from 1200Z 11/08/96 through 0000Z 11/09/96 (Figures 51 and 52).

3. Subjective Correlation with NOGAPS Model Ice Divergence

Area A is dominated by ice convergence on 11/07/96 (Figures 84 and 85), with the maximum values near -1.0 in the western part of the area. Ice convergence increases on 11/08/96 (Figures 86 and 87) and values build to +3.0 close to shore, with the extreme eastern parts of the area being almost non-divergent. At 0000Z 11/09/96 (Figure 88), the center of area A is under extreme ice convergence, with a “bulls-eye” value of > -5.0. This changes dramatically at 1200Z 11/09/96 (Figure 89), when the entire area becomes strongly divergent, with two twin “bulls-eyes” located to the north and south of the previously discussed “super-leads”. Values in both “bulls-eyes” are > -5.0.

The NOGAPS model ice divergence charts (Figures 84 to 89) explain the RGPS deformation results better than the wind divergence fields (Figures 48 to 53) did. Since five out of the six charts in this period show convergence, the ridging around the area of the “super-leads” and to the south of (shoreward) them can be explained. One does not know if leads existed in this area previously (this is the first product of cycle 15) or if the convergence is strong enough to compress floes through rafting. The abrupt switch from strong convergence to divergence between 0000Z 11/09/96 (Figure 88) and 1200Z 11/09/96 (Figure

89) may well have resulted in the “super-leads” evident in the northern part of area A. It is counterintuitive to imagine the leads opening between the two maximums of divergence.

4. Subjective Correlation with Advection of Wind Divergence

No noteworthy correlation exists between these two variables for 11/07/96 (Figures 48 and 49) and 11/08/96 (Figures 50 and 51). If one assumes that the surface wind advects areas of divergence downstream, we see that the 0000Z 11/09/96 chart (Figure 52) explains the “super-lead” area marginally better than pure “stationary” wind divergence. Areas of convergence are advected to the shore, where the ridging event exists and there is some advection of wind divergence into the area of the “super-leads”. A fully satisfactory explanation for the “super-leads” is not gleaned from this analysis.

C. Data Analysis for Period 2: 10-12 Nov 96

1. Meteorological Data

The 1008 mb low continues to slowly fill and has become disorganized by 1200Z 11/10/96 (Figure 55). High pressure ridges in behind the low and dominates area A for the remainder of this period (Figures 56 to 59). Winds over the first two days maintain an offshore component near the coast but are parallel (to the coast) or even onshore to seaward. Wind speeds do not exceeding 15 knots. Winds are offshore throughout the area on 11/12/96 (Figures 58 and 59). Weak wind divergence dominates area A during the whole period, with values near zero existing predominantly, increasing to no more than +1.0. The weather pattern of period 2 is considerably less dynamic than that of period 1.

2. RGPS Deformation Analysis and Subjective Correlation with Wind Divergence

The “super-leads” that were the distinguishing feature of the last period still persist in the same geographic location. This fact implies that the leads are continuing to open during this period. It appears that the minor, but steady divergence and generally offshore winds over area A are enough to maintain the lead formation observed during period 1. They have also created a new lead shoreward of the existing “super-leads”. It is not opening as fast as the “super-leads” described previously but extends for roughly 333 km in the snapshot. It most likely extends further, but our length estimate is confined by the geographical limit of the RGPS data stream. Most of this lead is opening between +5.0% and +7.5%, with one small section, roughly oriented north-south, opening > 10.0%.

3. Subjective Correlation with NOGAPS Model Ice Divergence

The two “bulls-eyes” of ice divergence observed in period 1 are still present at 0000Z 11/10/96 (Figure 90), but are decreasing in strength. Ice divergence gradually subsides and by 0000Z 11/11/96 (Figure 92), the ice is essentially non-divergent, except the area between the New Siberian Islands and the shore, which shows a maximum of -2.0 convergence. This area of convergence moves offshore, over the

area of the “super-leads”, by 1200Z 11/11/96. Convergence decreases after this time, becoming, again, non-divergent by 1200Z 11/12/96.

One would expect more net divergence over the area to account for the almost complete lack of ridging in area A and continued lead formation during this period. One must remember that the leads may not need as much energy to open wider once the ice sheet fails. The lesser divergent activity of the southern shoreward lead can be explained by the fact that it is not located in the East Siberian flaw lead.

4. Subjective Correlation with Advection of Wind Divergence

Weak advection of divergence occurs from 11/10/96 to 11/12/96 (Figures 54 to 59), matching the deformation picture as well, but no better than the local wind divergence.

D. Data Analysis for Period 3: 13-15 Nov 96

1. Meteorological Data

The ridge of high pressure that dominated the weather in area A during period 2 is retreating to the north as two lows are moving towards the area of interest. The westerly one is filling, but the easterly one moves northerly and northwesterly until 11/14/00Z (Figures 60 to 62). It remains quasi-stationary for the next 24 hours and then continues to move to the northwestward and deepens again to 951 mb (Figures 63 to 65). After 1200 Z 11/13/96 (Figure 61), a trough associated with the low extends over area A. The trough causes an increase in surface winds, which remain onshore for the last 60 hours of the period. In the last 24 hours they are blowing directly onshore. Maximum winds reached 35 knots and minimum winds do not fall below 15 knots during the last 60 hours of the period. The wind is weakly divergent over most of area A on 11/13/96 (Figures 60 and 61), but convergence dominates from 0000Z 11/14/96 to 0000Z 11/15/96 (Figures 62 through 64) as the trough moves over the area. Wind convergence is generally weak, but does approach -3.0 in some parts of area A. Winds become weakly divergent on 1200Z 11/15/96 (Figure 65).

2. RGPS Deformation Analysis and Subjective Correlation with Wind Divergence

The period 3 percent cell area change snapshot (Figure 38) shows that the three “super-leads” have compressed into ridges, with the exception of the southernmost end of the southerly “major” lead, which continues to open. Of major interest to the investigator is the fact that these ridges are most certainly acoustically active. These active ridges extend for the width of the snapshot or more than 370 kilometers and are of major operational significance to the submariner operating in the region. It is interesting to note that the region which opened the most in the most recently formed lead is also depicted as closing the most and therefore represents the most active region of the ridge. The southernmost end of one of the original leads does not compress, but continues to open. It is difficult to correlate this fact with a particular feature in the wind divergence field. The overall ridge building does correlate somewhat with the three-day wind divergence fields (Figures 60 through 65), which is overall convergent, but more net wind convergence was expected over the period to result in the strong ice convergence building observed.

3. Subjective Correlation with NOGAPS Model Ice Divergence

The ice divergence correlates better to the observed ice deformation than the wind divergence fields did. While the wind was mostly divergent on 11/13/96 (Figures 60 and 61), the ice shows strong convergence on that date over the entire area A domain. Strong ice convergence is located over the Siberian coast, with a weaker area over the ice field of area A. Very weak ice convergence is seen at 0000Z 11/14/96 and 0000Z 11/15/96 (Figures 98 and 100), with weak divergence dominating at 1200Z 11/14/96 and 1200Z 11/15/96 (Figures 99 and 101). If one views the 11/13/96 convergent event as the dominant dynamic feature of the period, the ridging that occurs in area A makes sense. It is unlikely that the weak sporadic divergence during this period is strong enough to stop the ridge building that is occurring in the region.

4. Subjective Correlation with Advection of Wind Divergence

Advection of wind divergence does not explain ice deformation during this period. Since the strongest areas of wind convergence are already located near the coastline and the wind is generally onshore for the period, the areas of strongest wind convergence are advected inland and do not explain the strong ridging activity over area A.

E. Data Analysis for Period 4: 16-18 Nov 96

1. Meteorological Data

An extremely deep low, with a central pressure of 940 mb, is moving through the East Siberian Sea and is located over area A by 1200Z 11/16/96 (Figure 67). Winds steadily increase through 11/16/96 (Figures 66 and 67) and reach a maximum speed of 30 knots near the coast by the end of the day. At 0000Z 11/16/96 (Figure 66), a maximum wind convergence value of -7.0 is located near the coast, which moves offshore and weakens by 1200Z 11/16/96 (Figure 67). A small isolated area of divergence, with a maximum value of -2.0 , is located over the easternmost of the New Siberian Islands (Ostrov Novaya Sibir'). The low moves rapidly to the northwest through 11/17/96 (Figures 68 and 69) and fills to 946 mb. Winds behind the low turn southerly (offshore) and decrease to 20-25 knots by 1200Z 11/17/96 (Figure 69). Winds are convergent or non-divergent and become slightly divergent by the end of the day. A new 986 mb low is located over the Siberian peninsula at 0000Z 11/18/96 (Figure 70), but moves directly north, bypassing area A. The pressure gradient relaxes significantly throughout the day and winds decrease to 15, then to 5-10 knots. Winds remain offshore. The area becomes generally non-divergent on 11/18/96 (Figures 70 and 71).

2. RGPS Deformation Analysis and Subjective Correlation with Wind Divergence

RGPS deformation data is very sparse and scattered for this period. The largest coherent area of data exists on the extreme eastern side of the region. Even though it is difficult to conduct a complete

analysis of the area, the meteorological forcing was strong enough during this period to warrant a cursory investigation. The RGPS product (Figure 39) shows general ice divergence throughout the region, with a few strong ridging events interspersed throughout the area. This period shows widespread divergence in area A for the first time during cycle 15. This pattern contrasts the RGPS output for the first three periods, which showed strong, but discrete leads and ridges only.

The major wind convergence event for the period is that associated with the passage of the deep low on 11/16/96 (Figures 66 and 67). The value of -7.0 encountered near the coast represents the maximum value of wind convergence encountered at any location during this investigation. Although this event explains the isolated ridges in the RGPS product, it does not correlate well with the widespread RGPS ice divergence observed throughout the area in this period. This is especially noteworthy, since no major divergent events in the wind field could be identified during this period.

It is interesting to note that the 1200 Z 11/16/96 NOGAPS model chart (Figure 67) actually shows slight wind divergence to the north of the 943 mb low's center, then located southeast of the New Siberian Islands. This is unexpected, since one would expect only convergence into the low.

3. Subjective Correlation with NOGAPS Model Ice Divergence

The NOGAPS model ice divergence charts for 11/16/96 (Figures 102 and 103) shows the best example of the strong divergence of ice associated with a deep low pressure system encountered during this analysis. The maximum value of ice divergence is located just southeast of the pressure low at 11/16/96, a short distance northwest at 1200 Z 11/16/96 (Figure 103). The NOGAPS model ice divergence value of +11.0 is the strongest observed anywhere during this investigation. At 0000Z 11/17/96 (Figure 104), NOGAPS model ice divergence values are generally non-divergent, but they become strongly convergent again (-7.0) in the northeastern sector of area A twelve hours later. The ice is generally non-divergent in area A on 11/18/96 (Figures 106 and 107).

The NOGAPS model ice divergence charts explain the RGPS deformation quite well. The strong ice divergence of 11/16/96 (Figures 102 and 103) is reflected in the massive area of positive area change in the deformation product. The strong ridges interspersed in the predominantly divergent ice field may be a result of the ice sheet obeying the law of continuity. Since ice is diverging everywhere in the area, there must be regions where this ice concentrates and piles up. Although the RGPS image for this period is incomplete, one does see that the area of strongest ridging during this period coincides with the southerly end of the "super-ridge" observed in the last period. We recall that the southern end of this feature was still undergoing strong divergent lead-forming activity. This area would thus represent a major source of localized, high ambient noise on 11/16/96.

4. Subjective Correlation with Advection of Wind Divergence

The advection of wind divergence provides a marginally better explanation than local wind divergence of the ice deformation during this period, since divergence is advected into the area, replacing

the convergence observed in the pure wind divergence field. However this advected divergence is weak and does not explain the massive lead openings observed in the RGPS product.

APPENDIX B

RGPS DEFORMATION PRODUCT ANALYSIS OF AREA B AND COMPARISON TO NOGAPS METEOROLOGICAL DATA

A. Background

This appendix contains detailed period-by-period analyses of the cycle 15 RGPS deformation products and their qualitative comparison to the NOGAPS meteorological variables in area B (see Figure 27). RGPS data streams were available from 07 Nov 96 until 24 Nov 96. Times are referenced to Greenwich Mean Time. Wind divergence values are abbreviated in the text and are assumed to be multiplied by 10^{-5} (s^{-1}). Ice divergence values are represented by the percent cell area change over the RGPS temporal resolution, assumed to be three days. RGPS deformation data is missing from 25 to 27 Nov 96.

B. Data Analysis for Period 1: 07-09 Nov 96

1. Meteorological Data

Strong high pressure over the Bering Sea interacts with a low over the North Pole resulting in westerly or west-northwesterly winds at 10-20 knots on 11/07/96 (Figures 48 and 49). Winds are slightly divergent, but become totally non-divergent by 1200Z 11/07/96 (Figure 49). Winds remain constant in direction, but increase to 15-20 knots in the area through 11/08/96 (Figures 50 and 51) as the low fills slightly, but moves south and the area of strong high pressure moves eastward over the Alaskan Peninsula. Winds are slightly divergent throughout the area, not increasing above +1.0. The pressure gradient tightens further on 11/09/96 (Figure 52 and 53), increasing wind speeds to 25 knots. Winds back to the west, then west-southwest on 11/09/96 (Figures 52 and 53). Winds remain near non-divergent on this day. The 0000Z 11/09/96 NOGAPS model chart (Figure 52) shows very slight convergence (< -1), especially in the western part of the area.

2. RGPS Deformation Analysis and Subjective Correlation with Wind Divergence

The area is dominated by slight ridging activity in the northern part of area B (Figure 36). It is difficult to pick out any directionality to the ridges, but two appear to be oriented roughly northeast to southwest. One does not know if the ridging occurred in areas of previous lead activity, since this is the first image of the cycle 15 series. A prominent lead exists on the very western edge of the swath. The southern part of area B shows some slight divergent activity in the ice field. The wind divergence is either completely non-divergent or very slightly divergent in area B from 11/07/96 to 11/08/96 (Figure 48 through 51). The 0000Z 11/09/96 chart (Figure 52) shows slight wind convergence in the western part of area B, which is again replaced by non-divergence by 1200Z 11/09/96 (Figure 53). It is hard to explain the observed RGPS deformation based solely on the wind divergence patterns.

3. Subjective Correlation with NOGAPS Model Ice Divergence

On 11/07/96 (Figures 84 and 85), area B is dominated by divergent ice motion with values of +1.0 to +2.0. Southeast of the swath, a large bulls-eye of ice convergence exists with maximum values of -4. The picture of NOGAPS model ice divergence is exactly out of phase with the deformation seen in the RGPS deformation output. This general scene persists into 11/08/96 (Figures 86 and 87) but the divergent

activity in area B becomes weaker. At 1200Z 11/08/96 (Figure 87), however, an area of ice convergence of value -1.0 appears in the south central part of area B. By 0000Z 11/09/96 (Figure 88), the maximum convergence value has increased to -3.0 and weaker convergence extends to the north. By 1200Z 11/09/96 (Figure 89), ice convergence still dominates most of area B, but is getting weaker. This series of weak divergent activity followed by convergent forcing in the central and northern part of area B explains what we see in the RGPS deformation product quite well. The initial divergence, which lasted only a few days, created a series of small narrow leads, which were then compressed into ridges during the subsequent convergent period. The net ice convergence in the northern area is relatively weak in the RGPS deformation product, which correlates well with the time series of NOGAPS model ice divergence charts. It is however, hard to assign a subjective “strong” correlation between the NOGAPS model ice divergence and the RGPS product, because there is so much alternating divergent and convergent activity in the region. The divergent ice motion in the southern part of area B cannot be explained satisfactorily by looking at the NOGAPS model ice divergence fields, since weak ice divergence or non-divergence is replaced by moderate ice convergence. This series of events should result in a net decrease of cell area percentage for this period.

4. Subjective Correlation with Advection of NOGAPS Model Wind Divergence

This analysis is comparable to looking at the local wind divergence pattern. Slight wind divergence is advected into area B from 11/07/96 to 11/09/96 (Figures 48 through 53). This forcing does not explain the ridging activity in the central or northern part of area B.

C. Period 2: 11/10/96 - 11/12/96

1. Meteorological Data

The low over the North Pole is filling slowly as the building high continues moving east. At 1200Z 11/10/96 (Figure 55) the high has a central pressure of 1039 mb with a high pressure ridge extending into area B oriented from the southeast to the northwest. The low’s central pressure at this time is approximately 995 mb. The pressure gradient has relaxed sufficiently to decrease surface winds to 15-20 knots, southerly in the southern part of area B, southwesterly in the northern part. The wind throughout area B is divergent on 11/10/96 (Figures 54 and 55), with strongest values initially in the southeastern part of the area. By 0000Z 11/11/96 (Figure 56), a new low has started to form north of the Bering Strait, which deepens to 999 mb by 1200Z 11/11/96 (Figure 57). It continues to slightly deepen and move slowly to the northeast. By 1200Z 11/12/96 (Figure 59) the low has a central pressure of 996 mb and is located inside the western edge of area B. One must remember that this central pressure is not as significant in the relatively shallow atmosphere of the Arctic as it may be at mid-latitudes and this system is not an extremely deep. Winds remain generally southerly to southeasterly on 11/11/96 (Figures 56 and 57) with speeds of 15 to 20 knots. Winds are non-divergent for the whole day of 11/11/96 (Figures 56 and 57). On 0000Z 11/12/96 (Figure 58) winds are starting to be influenced by the approaching low and are southeasterly or

east-southeasterly in the northern part of area B, south-southeasterly in the southern area, at speeds not exceeding 20 knots. By 1200Z 11/12/96 (Figure 59) winds are rotating counter-clockwise around the surface low, varying in direction from west-southwest to northeast at speeds of 10 to 20 knots. Weak wind convergence, with values not exceeding -1.0, has replaced the non-divergence throughout most of area B.

2. RGPS Deformation Analysis and Subjective Correlation with Wind Divergence

Ridging activity is much more pronounced in area B during this time period. The area change percentage is between 2.5 and 5.0% closing in most of the area, with some ridges showing >10.0% closing (Figure 37). The extreme southwestern region of area B shows some new ice divergence and a prominent lead opening that was evident in the previous RGPS frame. It is interesting to note that the ridges are forming in areas where no leads were evident in the previous RGPS frame. Perhaps small leads formed in the beginning of this period, which then closed, resulting in net convergence over those three days. Unlike the “super-leads” in area 1, the shear associated with the scattered ridges in area B is much weaker (Figure 43). The pattern of wind divergence during this period does a satisfactory job of explaining the ice deformation picture. The slight divergence of 11/10 is replaced first by non-divergence, then by slight convergence. This implies the creation of small leads, which then compress into many relatively small pressure ridges. The leads formed on the western edge of area B are not explained by the pattern of wind divergence observed during this period.

3. Subjective Correlation with NOGAPS Model Ice Divergence

The analysis of NOGAPS model ice divergence for this period gives the best example seen so far of the divergence of the ice field under the influence of a low-pressure system. If we overlay the NOGAPS model ice divergence plot (Figure 95) over the atmospheric surface pressure analysis for 1200Z 11/12/96 (Figure 59), we see a strong maximum of divergence, with a central value of +6.0, located in the southwestern sector of the surface low.

The NOGAPS model ice divergence charts for this period (Figures 90 through 95) explain the RGPS deformation output quite well. The whole area is undergoing convergent activity on 11/10/96 (Figures 90 and 91) with maximum values of -3.0. This is most likely continuing to compress the leads that were starting to undergo convergence at the end of the last period. On 11/11/96, the NOGAPS model charts (Figure 92 and 93) shows ice divergence in the area split between strong convergence with maximums of -4.0, in the eastern half of the box and medium to strong divergence, with a maximum +3.0, in the western half. At 0000Z 11/12/96 (Figure 94), divergence still dominates the western area, while the eastern half is approaching non-divergence. By 1200Z 11/12/96 (Figure 95) the whole area is undergoing divergence, with maximum values of +6.0 recorded in the southwestern corner of the area. This sequence of events correlates well with the RGPS output, which shows ridge-building activity continuing in the eastern sector of area B, while the western sector shows new lead formation. The area-wide divergence of

1200Z 11/12/96 may not be strong enough to create new leads in the eastern sector or perhaps it occurs too late in the period to be part of the RGPS calculations.

4. Subjective Correlation with Advection of NOGAPS Model Wind Divergence

Analysis of the advection of wind divergence yields inconclusive results for this period.

D. Data Analysis for Period 3: 13 - 15 Nov 96

1. Meteorological Data

The low maintains a steady central pressure of 996 mb, but continues to move to the northeast out of area B. At 0000Z 11/13/96 (Figure 60), winds in the southern part of the area are west-northwesterly and reach speeds of 20-25 knots. The northern section of area B is closer to the low's center and correspondingly has weaker northerly winds of 15-20 knots. Although not in the area of interest, this analysis chart shows a good example of wind convergence across a surface trough extending from the low eastward. The pressure gradient tightens over the next twelve hours as an area of strong high pressure builds over Point Barrow, Alaska (Figure 61). Winds throughout area B strengthen to 20-25 knots. Wind divergence for 11/13/96 (Figures 60 and 61) is weakly convergent, becoming generally non-divergent. Wind speeds drop to 15 knots on 11/14/96 (Figures 62 and 63) as the low fills and moves over Greenland. Wind direction remains generally northwest throughout the day. Wind divergence remains non-divergent, becoming weakly divergent, with values $< +1.0$, by the end of the day. By 0000Z 11/15/96 (Figure 64), the dominant meteorological feature in area B is high pressure to the southeast with a central pressure of 1036 mb. Winds in area B are light at 10 knots with non-divergence dominating. By 1200Z 11/15/96 (Figure 65), a rapidly deepening low with a central pressure of 950 mb over the Siberian Peninsula tightens the pressure gradient in area 2, with resultant southerly winds of 20-30 knots. Wind divergence remains mostly non-divergent.

2. RGPS Deformation Analysis and Subjective Correlation with Wind Divergence

Investigation of the RGPS percent cell area change product (Figure 38) shows an opening area change of 2.5 to 7.5% throughout most of the area. Some isolated deformation lines show cell area opening of greater than 10%. Only the extreme southwestern and southeastern parts of the region show some evidence of ridging activity. It is tough to correlate the wind divergence fields with what we see in the RGPS product. There is very little divergence observed in the wind field over this three-day period and it is tough to imagine that the minor divergent activity of 11/14/12Z (Figures 62 and 63) would be sufficient to cause the lead openings evident in the RGPS product.

3. Subjective Correlation with NOGAPS Model Ice Divergence

After initial analysis, the NOGAPS model ice divergence calculations for this period in area B appear to be totally uncorrelated to the RGPS output. We would expect to see divergence for the whole period, since the RGPS image is dominated by "opening" area change. Investigation of the NOGAPS

model ice divergence fields shows that strong ice divergence, with maximum values of +5.0, indeed dominates at 0000Z 11/13/96, decreasing in strength until 1200Z 11/14/96 (Figures 96 through 99), when only the northeastern sector of area B is still undergoing slight divergence. The rest of the area is under convergent forcing, with maximum values of -3.0. At 0000Z 11/15/96 (Figure 100), the whole area is undergoing convergence with maximum values of -3. At 1200Z 11/15/96 (Figure 101), the eastern part of the area is still under the influence of ice convergence, while slight divergence appears in the southwestern quadrant.

In order to explain the RGPS deformation picture, we have to assume that the ice divergence over the three-day period exceeded the convergence giving net opening values in area B. We must remember that we are not looking at an ice ridging classification product in the deformation output, but just the net change in area over the three-day period in question. This means that both ridges and leads are present in the lines of deformation in area B during this period. This is, at first, counterintuitive, but since air temperature in the area varied between -5 C and -14 C from 11/13/96 to 11/15/96 (Figures 60 through 65), pressure ridges are being formed in the leads, as new ice is being compressed during the convergent period in the latter stages of this snapshot. However, the open water leads are not completely closed to their original position, hence the net divergent areas in the RGPS output.

4. Subjective Correlation with Advection of NOGAPS Model Wind Divergence

Analysis shows less correlation for advection of wind divergence than local wind divergence. On the first two days of the period, slight divergence is advected, but on 11/15/96 (Figures 64 and 65), it appears that convergence moves into area B.

E. Data Analysis for Period 4: 16-18 Nov 96

1. Meteorological Data

The low continues to deepen explosively to 940 mb and is tracking northwest through the East Siberian Sea bringing high winds to the basin. Winds throughout area B are southerly at 30 knots, increasing to 35 by 1200Z 11/16/96 (Figures 67). Even though the wind speeds are high, very little divergence is associated with the wind field in area B on 11/16/96. By 0000Z 11/17/96 (Figure 68), the low's center has filled to 948 mb and has moved northwest of the New Siberian Islands, relaxing the pressure gradient. Wind speeds in area B decrease to 20-25 knots as the wind veers to the south-southwest. Wind divergence is slightly convergent at a value not exceeding -1.0 . By 1200Z 11/17/96, slight divergence is located throughout area B, with wind speeds varying from 10 to 20 knots. At this time area B is under the influence of weak ridging from the southeast. A new, weaker 979 mb low is forming over the Bering Sea and following the path of the previous low. At 0000Z 11/18/96 (Figure 70), area B is at the intersection of the weak ridge and troughing from the low to the southwest. Winds are southerly at 20-25 knots. At 1200Z 11/18/96 (Figure 71), the 987 mb low is directly west of area B and winds are south-southwest at 25-30 knots. Divergence throughout the area is very slightly divergent.

2. RGPS Deformation Analysis and Subjective Correlation with Wind Divergence

RGPS deformation data is missing for period 4 in area B.

3. Subjective Correlation with NOGAPS Model Ice Divergence

RGPS deformation data is missing for period 4 in area B.

4. Subjective Correlation with Advection of NOGAPS Model Wind Divergence

RGPS deformation data is missing for period 4 in area B.

F. Data Analysis for Period 5: 19-21 Nov 96

1. Meteorological Data (0000Z 11/20/96 NOGAPS data missing)

By 0000Z 11/19/96 (Figure 72), the low has moved over the pole, but area B is experiencing a tight gradient because of interaction between the low and high pressure ridging in from the Northwest Territories of Canada. Winds are strong at 30-35 knots out of the southwest. Winds are slightly convergent in the northern half of area B, with values of -1.0, very slightly divergent in the southern half. Winds slightly decrease to 25-30 knots by 1200Z 11/19/96 (Figure 73). Meteorological data is missing for 0000Z 11/20/96. By 1200Z 11/20/96 (Figure 75) the pressure gradient over area B is tight again as the high's center moves north over Ellesmere Island and builds to 1053 mb. Winds are south-southeasterly, build back up to 30-35 knots and remain steady until 1200Z 11/21/96 (Figure 77) when speeds decrease slightly to 25-35 knots. Winds are either non-divergent or only very slightly divergent, with values not exceeding +1.0 for the last 60 hours of the period.

2. RGPS Deformation Analysis and Subjective Correlation with Wind Divergence

The RGPS deformation product shows the most significant and widespread convergent ice activity seen in this during this research. Several long, linear features show an area change of > 10.0% closing, especially in the southern part of area B (Figure 40). Between these major ridge-like features, convergent activity is only slightly less with values of 7.5 to 10.0% closing. The northern part of the area is only slightly less convergent. Only a few isolated divergent cells are observed, especially in the western part of area B. This major deformative activity cannot be explained by the wind divergence field. Although the winds have the strongest sustained force observed in area B during any period, wind divergence is noticeably absent. This is only partially explained by the strong surface pressure gradient encountered in area B during this period. Since the surface wind is approaching geostrophic flow it is therefore becoming non-divergent.

3. Subjective Correlation with NOGAPS Model Ice Divergence

NOGAPS model ice divergence analysis for this period correlates extremely well with the convergent ice activity in the RGPS deformation product. The ice is strongly divergent at 0000Z 11/19/96 (Figure 108), with a “bulls-eye” value of +3.0 in the center of the region. This activity is most likely opening leads in the ice, which will form active pressure ridges during the follow-on convergent phase. The area becomes overall non-divergent at 1200Z 11/19/96 (Figure 109) as transition to a large-scale convergent period commences. NOGAPS model ice divergence data for 0000Z 11/20/96 is not available, but by 1200Z 11/20/96 (Figure 111), 95% of the ice in area B is experiencing convergence varying from < -1.0 to -4.0. It is interesting to note that the ice divergence in this case is not due to directional shear, since the wind direction in all of area B does not vary at all at this time. The maximum value in the NOGAPS model ice convergence field on the extreme eastern boundary of area B is explained through velocity shear and the resultant convergence instead. Winds in the central region of area B are approximately five knots stronger than in the eastern section, inducing a cyclonic shear and ice convergence. Ice convergence reaches its maximum value for the 0000Z 11/21/96 period (Figure 112) in the eastern section of the area with a value of -5.0. After this time, convergence values decrease in area B, with western areas actually showing some signs of minor wind divergence. The strong ice convergence seen in the NOGAPS fields over the last 48 hours of the period correlate well with the convergent deformation seen in the RGPS product.

4. Subjective Correlation with Advection of NOGAPS Model Wind Divergence

Advection of wind divergence is as badly correlated to the RGPS ice deformation as is the wind divergence field itself. No significant convergence is advected into the area throughout the period.

F. Data Analysis for Period 6: 22-24 Nov 96

1. Meteorological Data

The pressure gradient remains tight in the beginning of the period, as area B is located between the slowly weakening high to the east and a 1012 mb low to the west (Figures 78 through 83). Winds are from the south at 20-30 knots and are slightly convergent in the southeastern quadrant, non-divergent elsewhere. By 0000Z 11/23/96 (Figure 80), winds have decreased to 15-20 knots as the whole area is under the influence of widespread high pressure. Winds are slightly divergent to non-divergent throughout the region. By 1200Z 11/23/96 (Figure 81), evidence of a weak trough of low pressure is evident to the SW of area B. Winds remain generally southerly and non-divergent at 10-15 knots. Throughout the day of 11/24/96 (Figures 82 and 83), the axis of the weak trough is located over area B. Winds vary from the southeast to the northeast, but do not exceed 10 knots. Winds are slightly convergent, especially in the eastern sector of the area, becoming, once again, non-divergent by 1200Z 11/24/96 (Figure 83).

2. RGPS Deformation Analysis and Subjective Correlation with Wind Divergence

Even though the central portion of the RGPS deformation product in area B (Figure 41) is missing for this period, one can still derive useful information from it. The western half of the area shows the least deformation activity of any period investigated. There are only a few cells of weak opening and closing present. The “sliver” of deformation data that is not missing in the eastern sector of the area shows quite strong convergent activity ranging from -2.5 to $> -10.0\%$ closing. The wind divergence patterns for this period do an adequate job in explaining the ice deformation. The western region shows general non-divergence for the period, which is reflected in the inactivity observed in the RGPS output. The small amount of wind convergence observed during the period occurs in the eastern half. This matches the ridging activity seen in the RGPS product, but one expects to see greater wind convergence values in an area where the ice deformation is so significant. Phrased another way, it is hard to believe that wind convergence values that never exceed -1.0 cause decreases in cell ice area of $> -10.0\%$.

3. Subjective Correlation with NOGAPS Model Ice Divergence

Ice convergence values for 11/22/96 (Figures 114 and 115) reflect the RGPS ice deformation data almost perfectly. The ice convergence gradient is very tight, with a maximum value of -5.0 between the eastern boundary of area B and the isoline of non-divergence located in the middle of the area oriented north-northeast to south-southwest. The western half is either non-divergent or very weakly convergent. The NOGAPS model ice divergence charts for 11/23/96 (Figures 116 and 117) show a similar pattern of convergence in the eastern half, albeit with lower maximum values (-3.0), but the western sector is either non-divergent or weakly divergent. This pattern holds through 11/24/00Z (Figure 118), but on 11/24/12Z (Figure 119), the eastern area is non-divergent, while the western sector shows ice divergence values of 0.0 to +2.0. This divergence may explain the isolated opening areas seen in the RGPS product.

4. Subjective Correlation with Advection of NOGAPS Model Wind Divergence

The advection of wind divergence characteristics for this period do a marginally worse job as local wind divergence in explaining the ice deformation observed. Weak wind convergence is advected into the western area, where little ice convergence is observed. The strong convergence in the southeastern corner of the RGPS product is hard to explain through advection.

APPENDIX C

**CYCLE 15 RGPS SEA ICE DEFORMATION PRODUCTS:
PERCENT CELL AREA CHANGE**

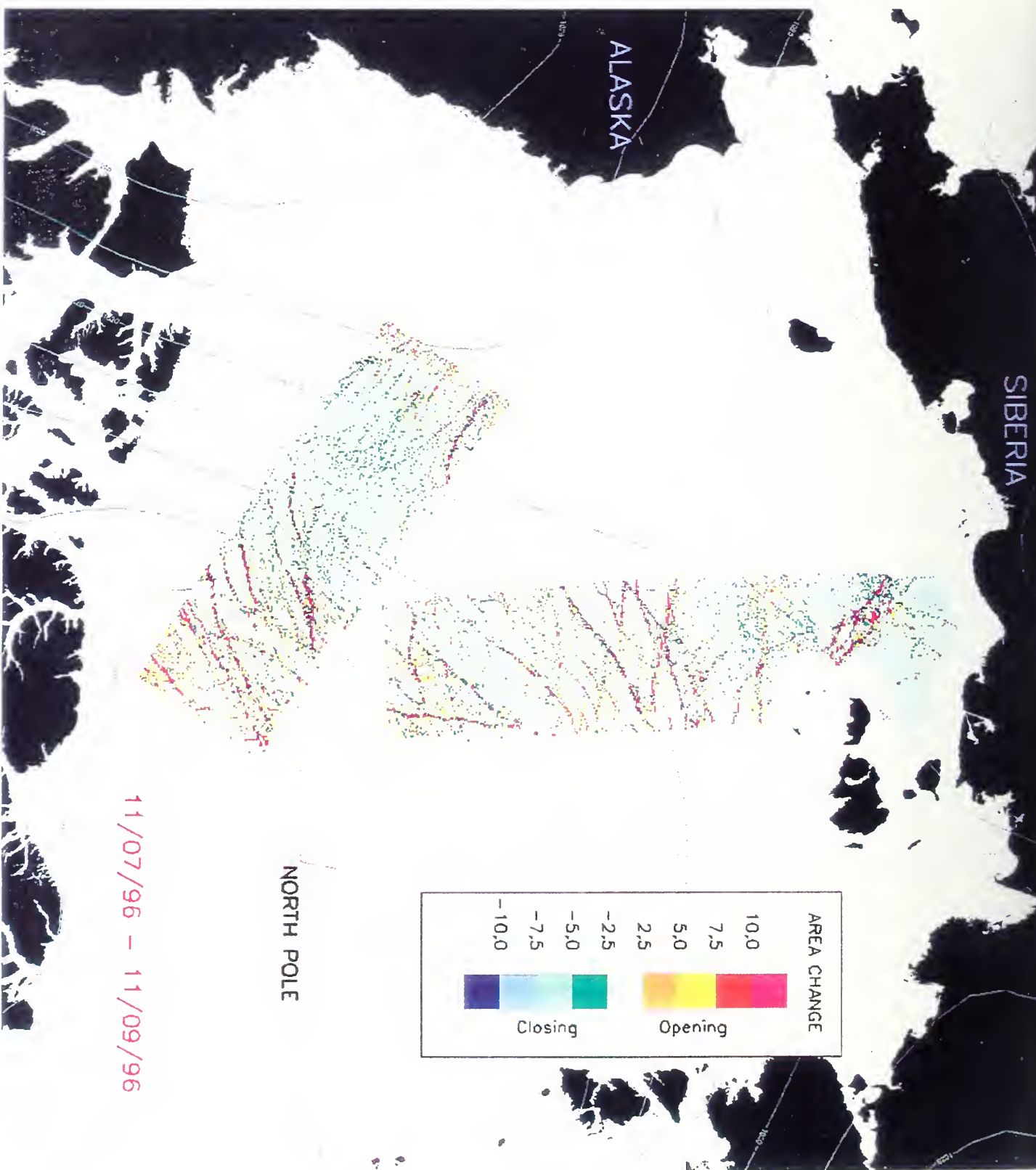


Figure 36. RGPS cycle 15 percent cell area change product for 07 to 09 Nov 96.

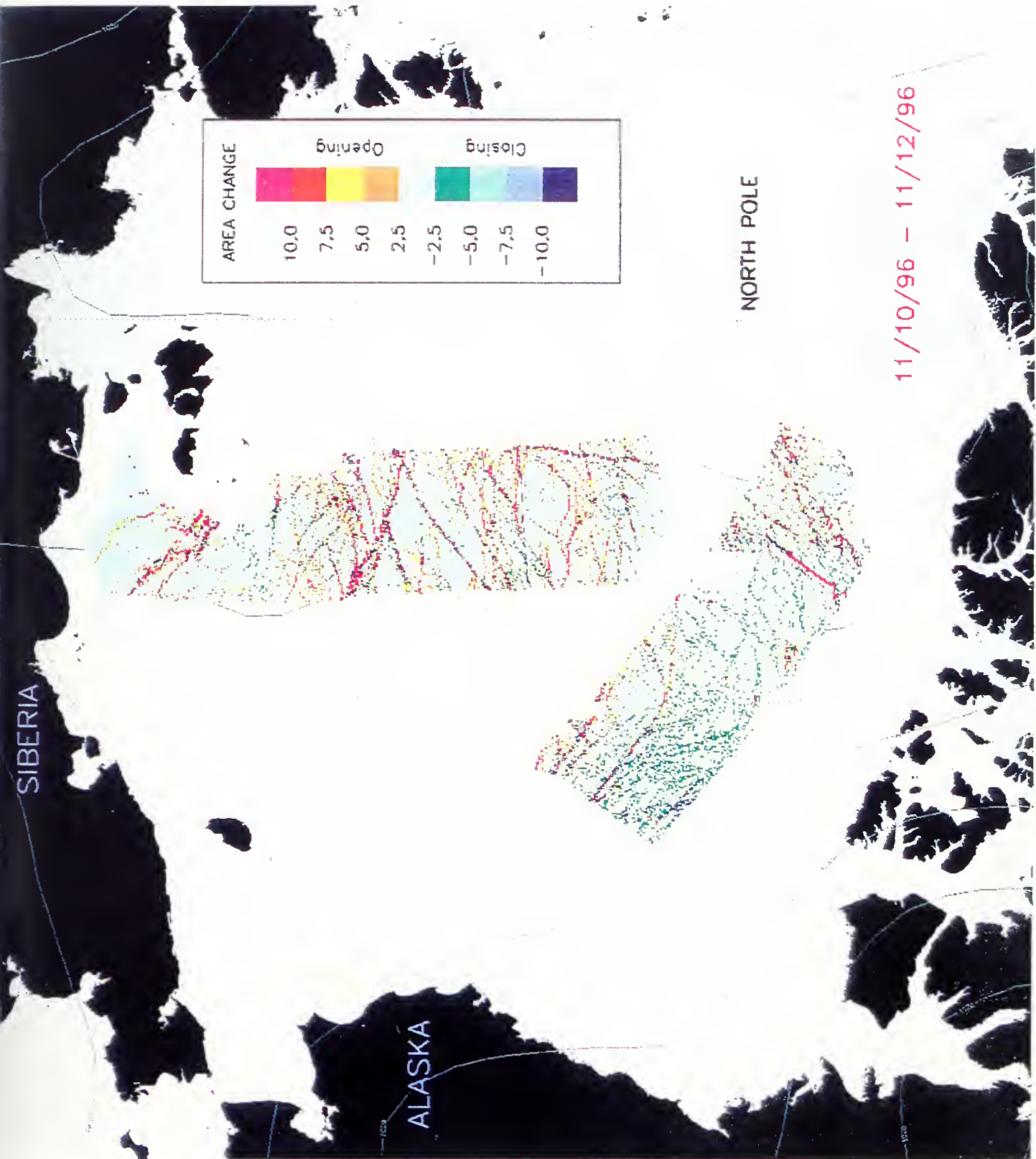


Figure 37. RGPS cycle 15 percent cell area change product for 10 to 12 Nov 96.

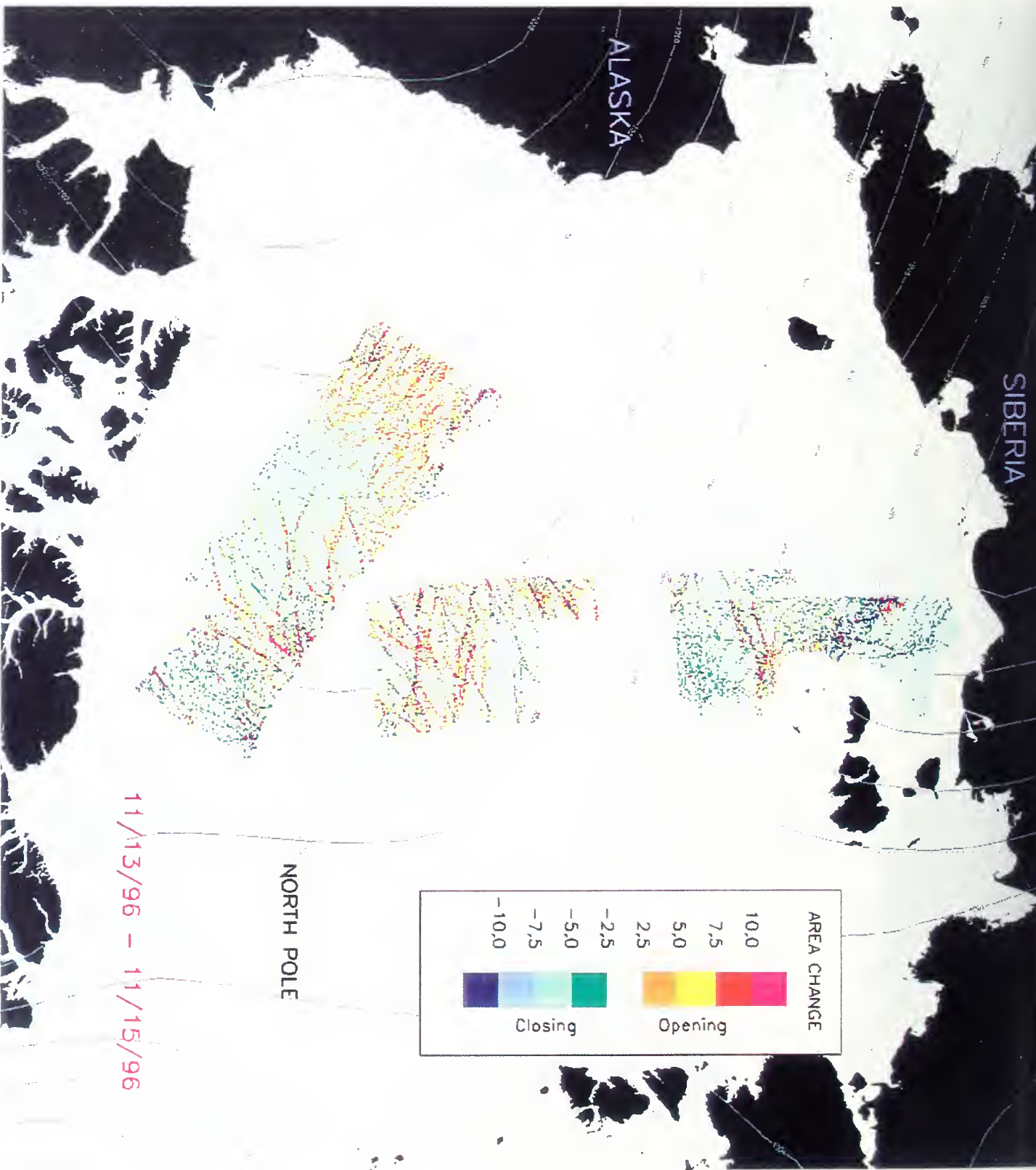


Figure 38. RGPS cycle 15 percent cell area change product for 13 to 15 Nov 96.

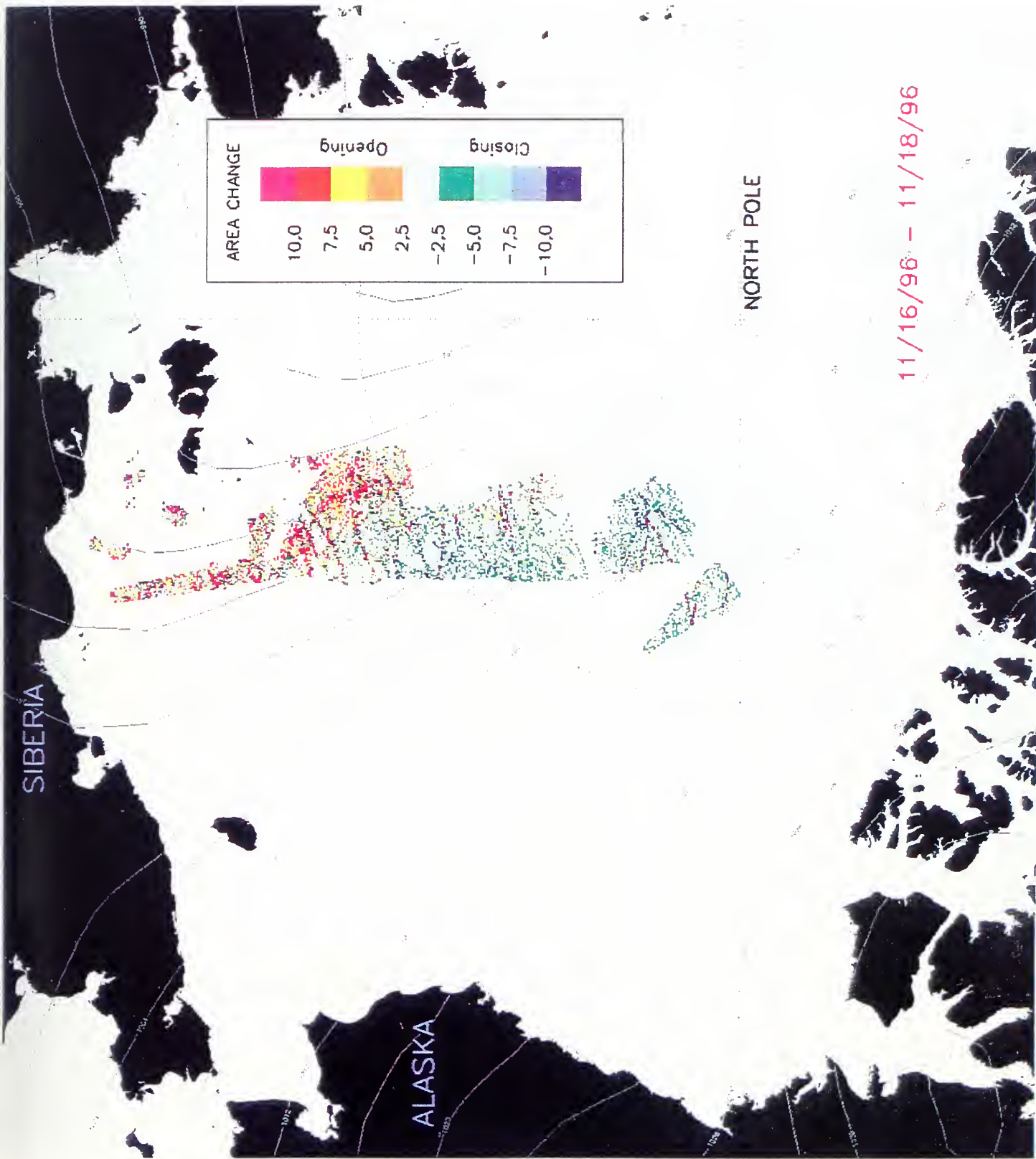


Figure 39. RGPS cycle 15 percent cell area change product for 16 to 18 Nov 96.

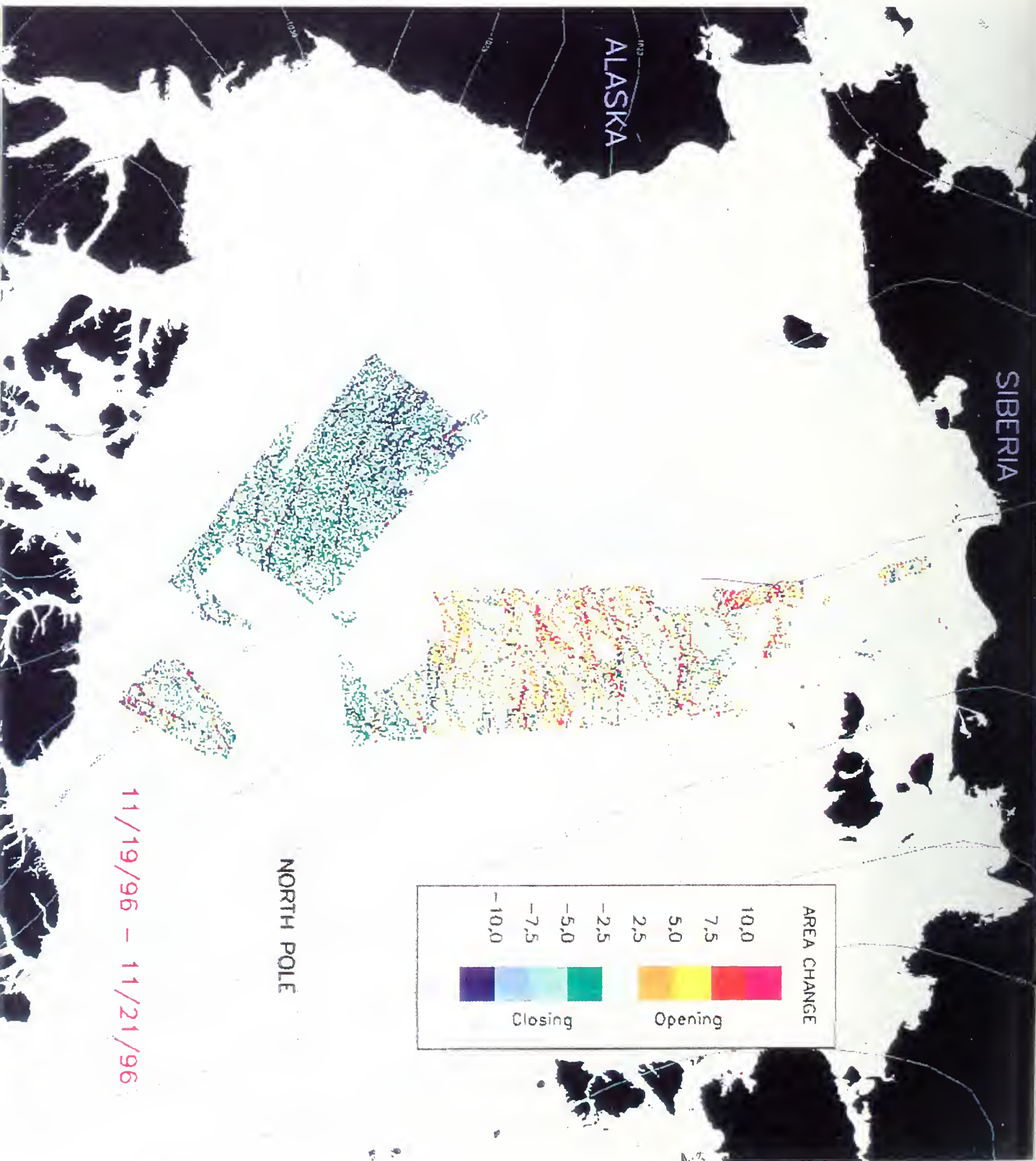


Figure 40. RGPS cycle 15 percent cell area change product for 19 to 21 Nov 96.

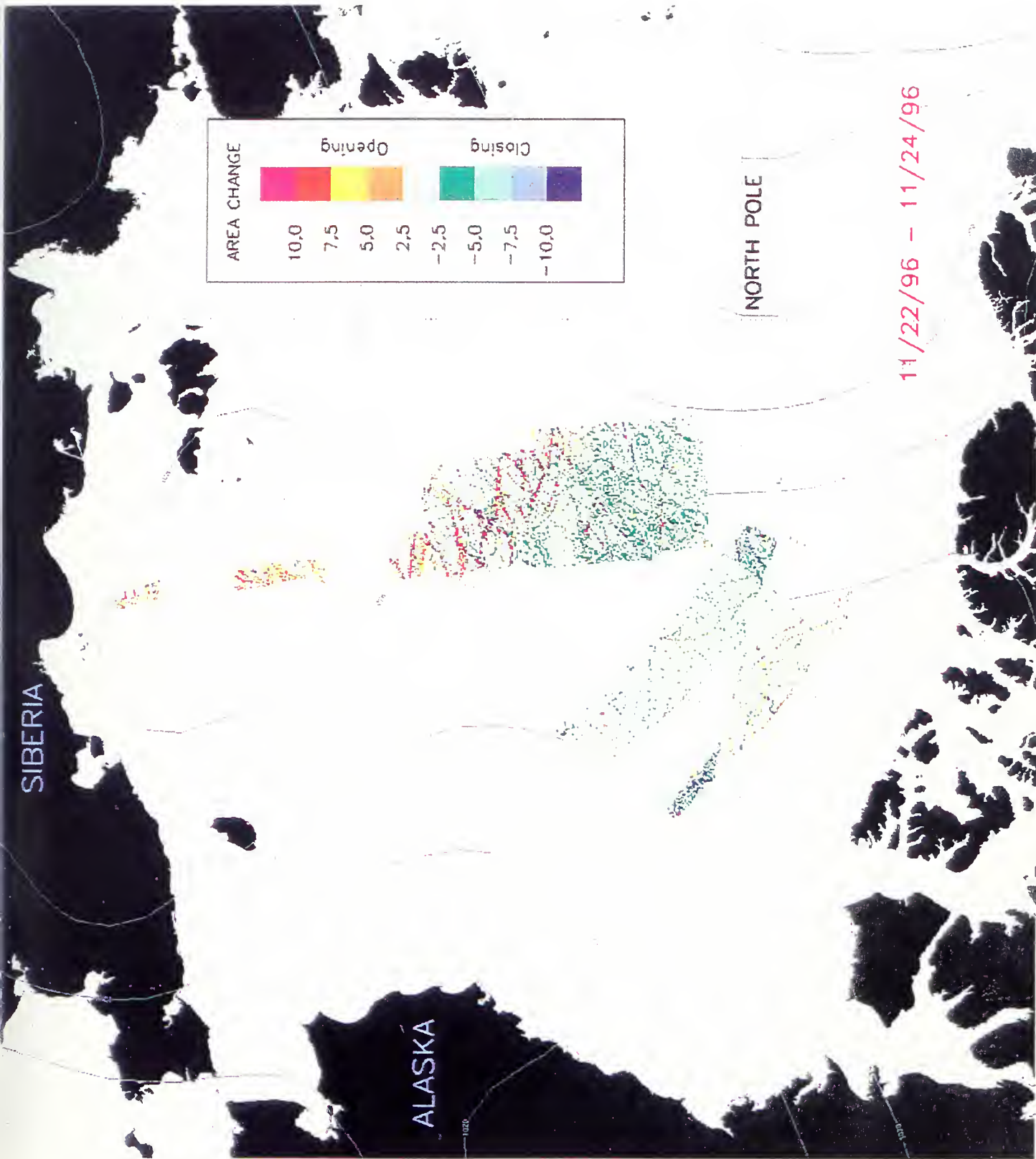


Figure 41. RGPS cycle 15 percent cell area change product for 22 to 24 Nov 96.

APPENDIX D

**CYCLE 15 RGPS SEA ICE DEFORMATION PRODUCTS:
ICE SHEAR**

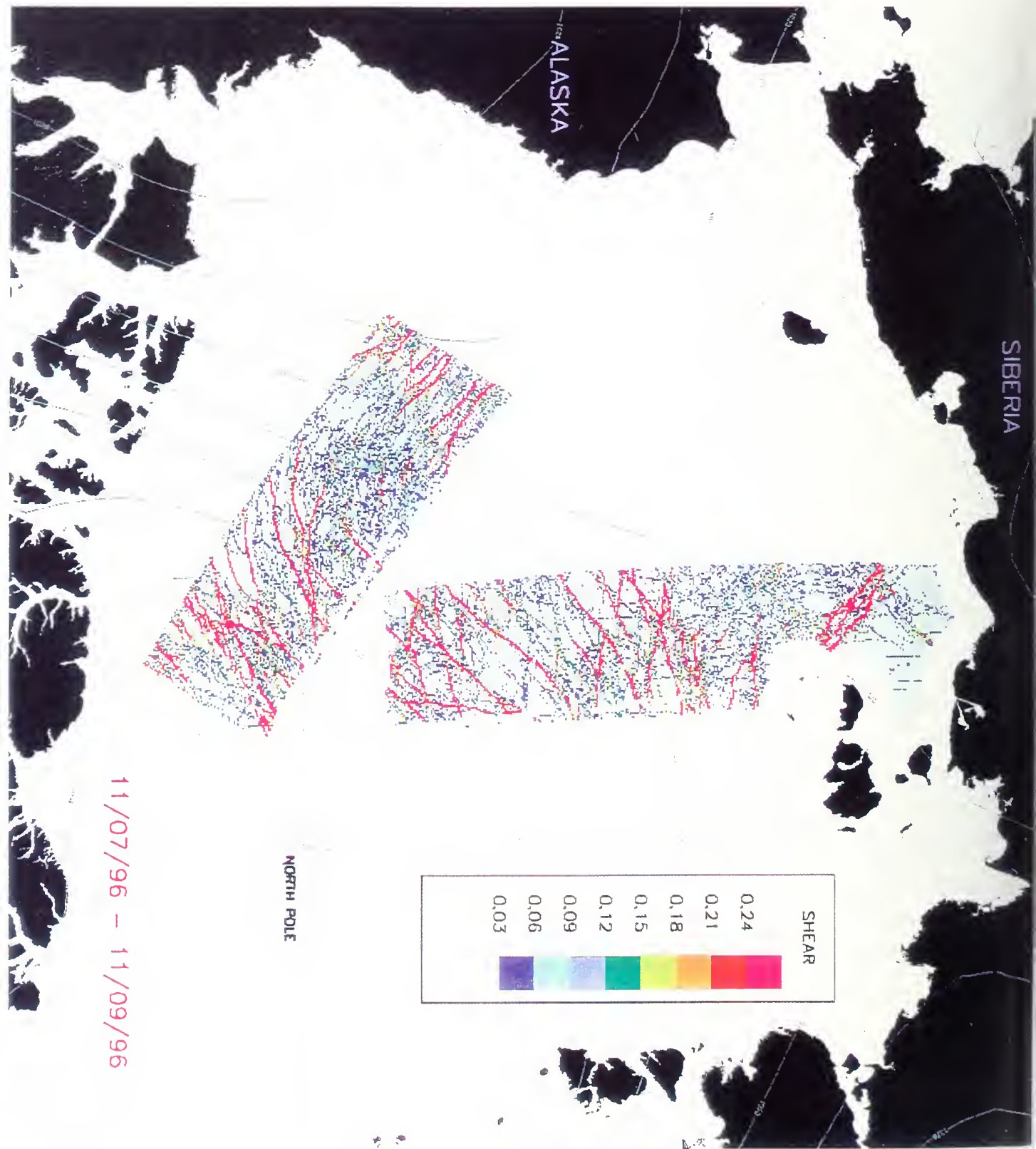


Figure 42. RGPS cycle 15 ice shear product for 07 to 09 Nov 96.

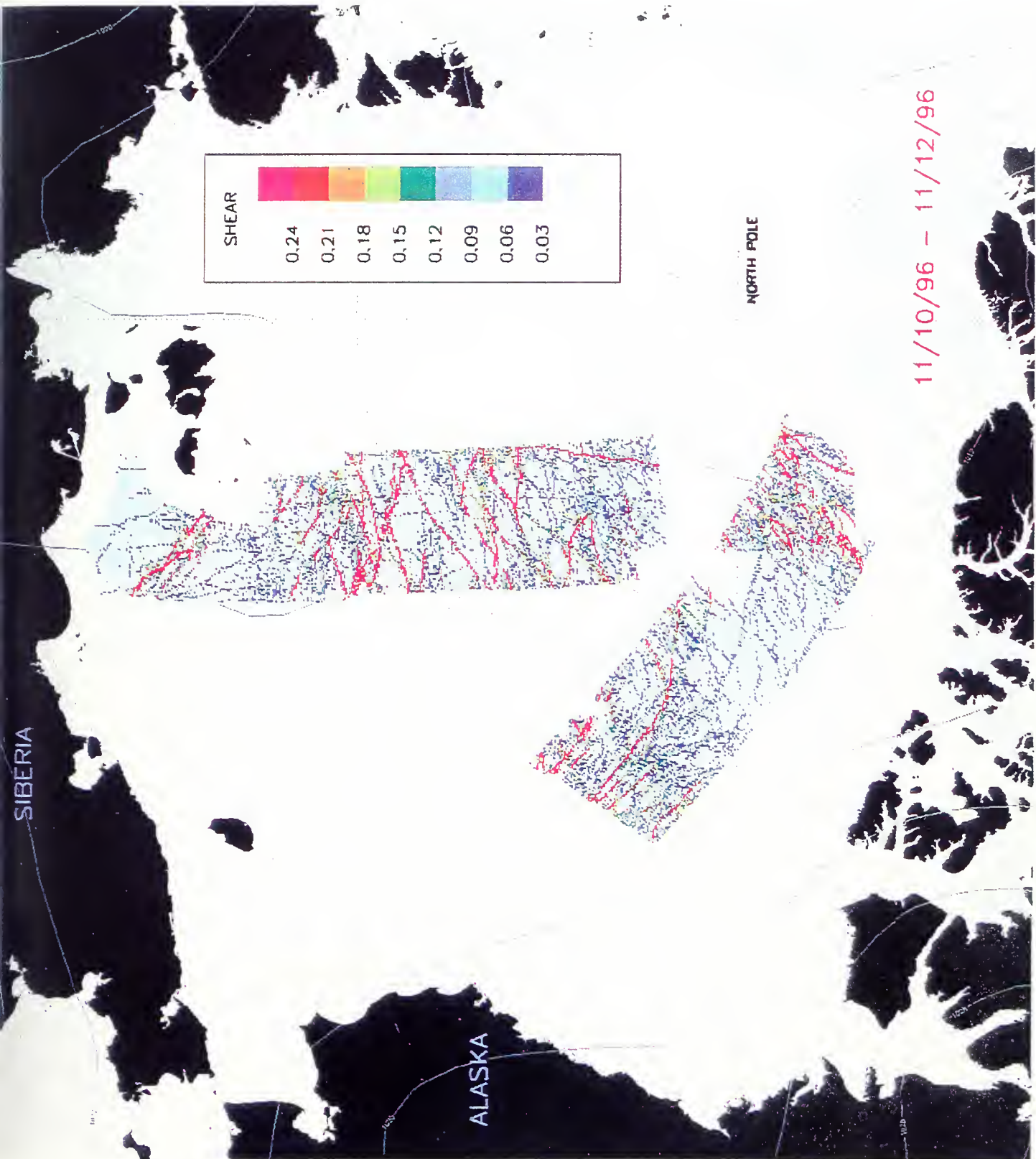


Figure 43. RGPS cycle 15 ice shear product for 10 to 12 Nov 96.

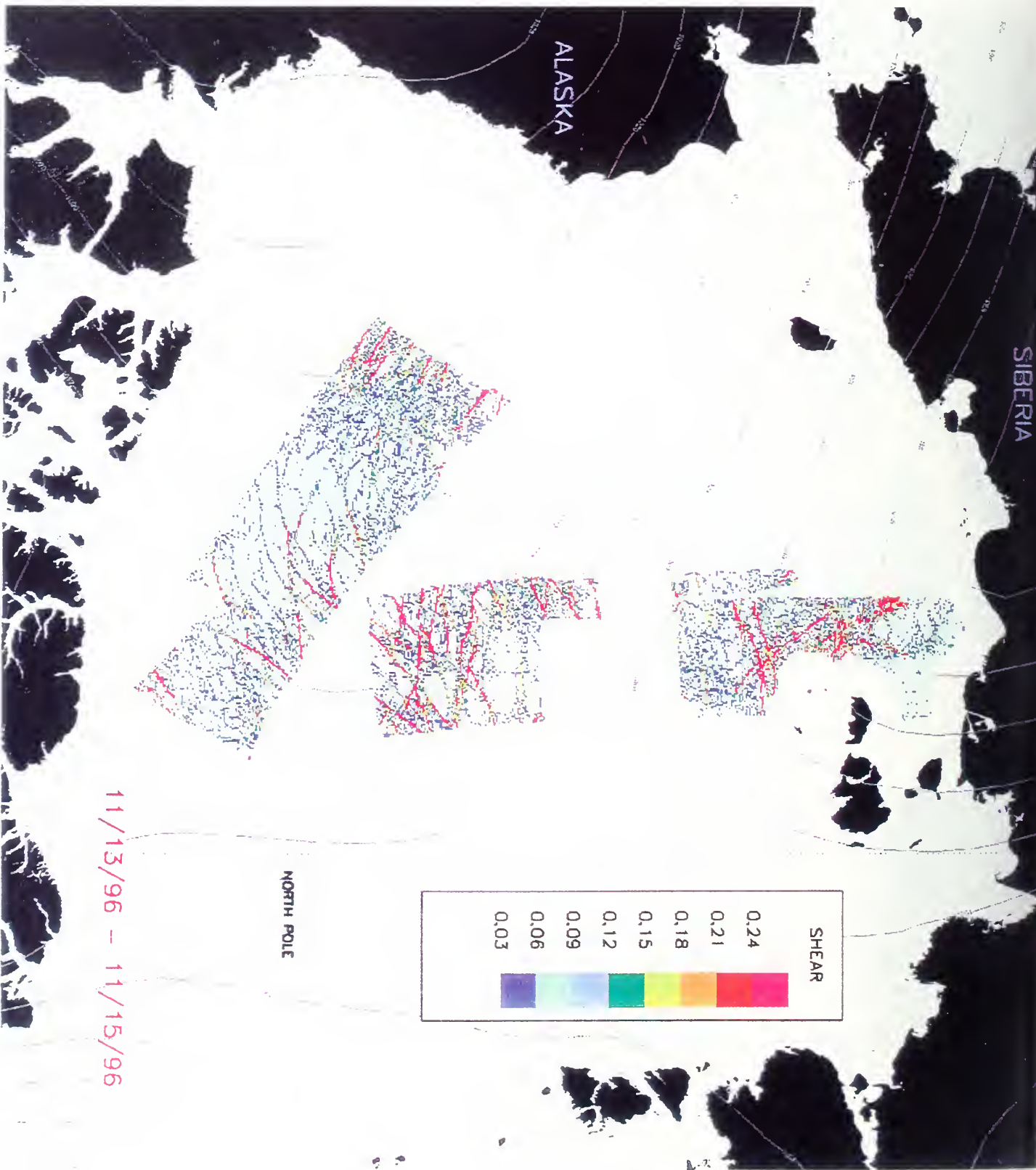


Figure 44. RGPS cycle 15 ice shear product for 13 to 15 Nov 96.

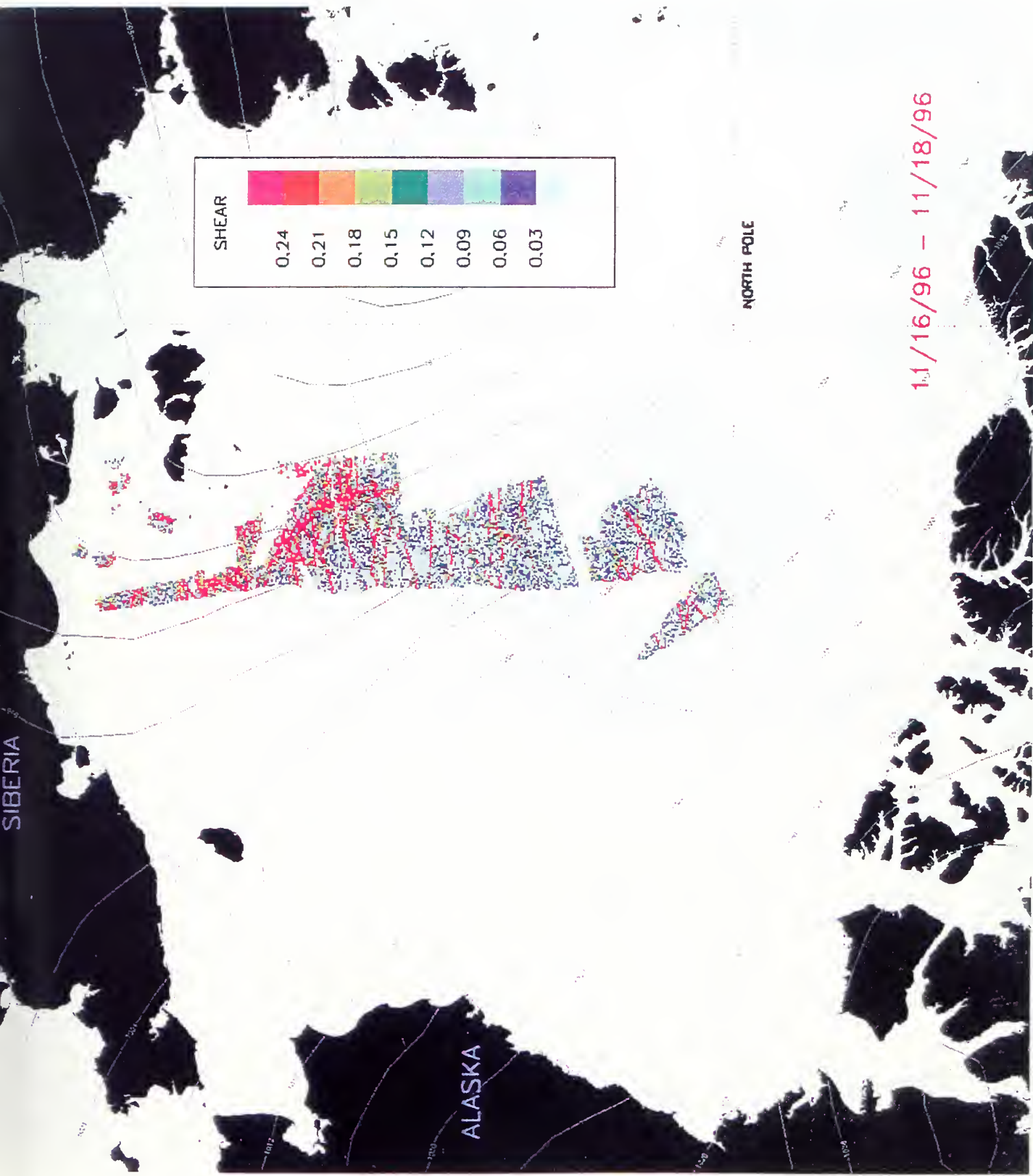


Figure 45. RGPS cycle 15 ice shear product for 16 to 18 Nov 96.

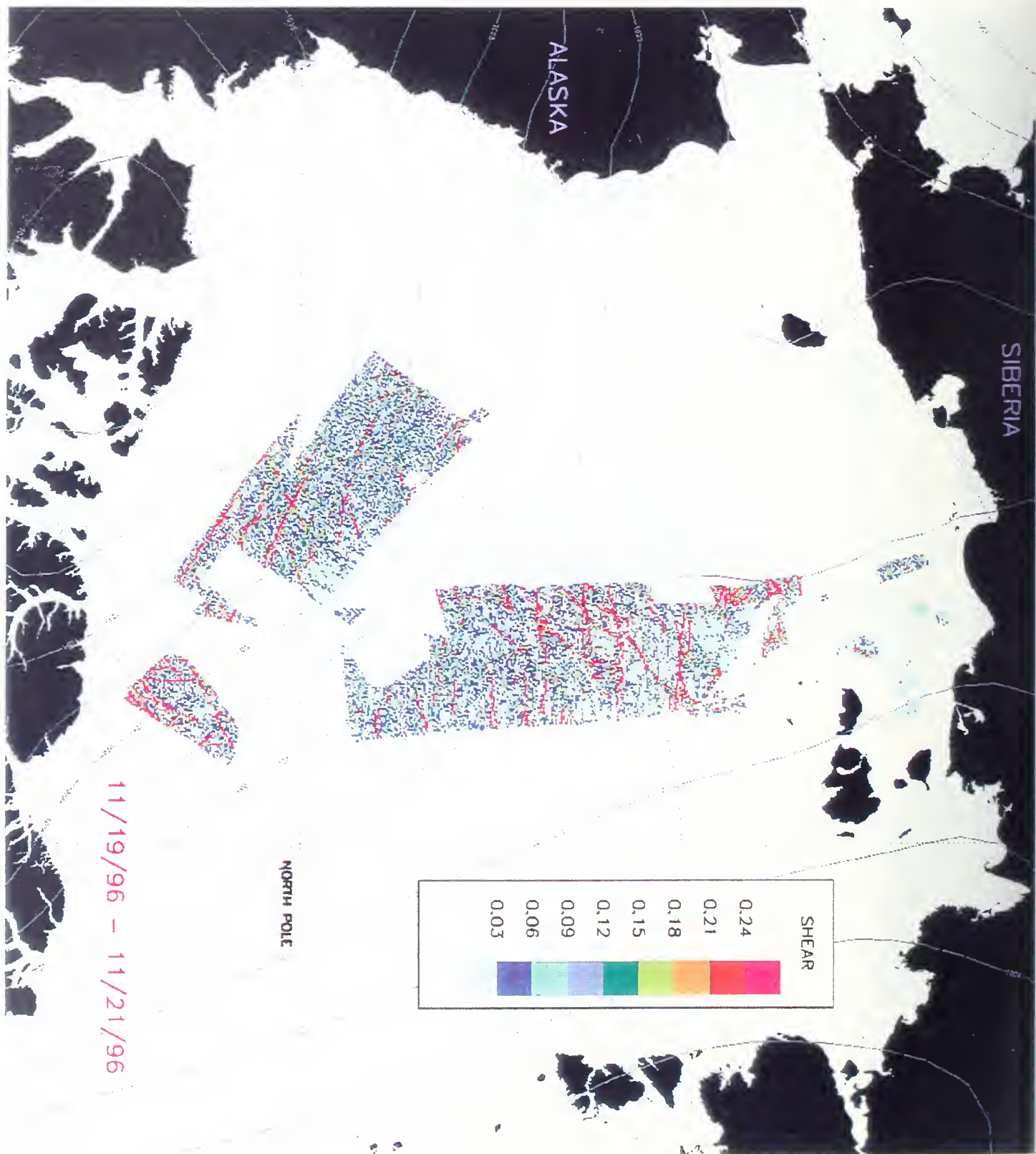


Figure 46. RGPS cycle 15 ice shear product for 19 to 21 Nov 96.

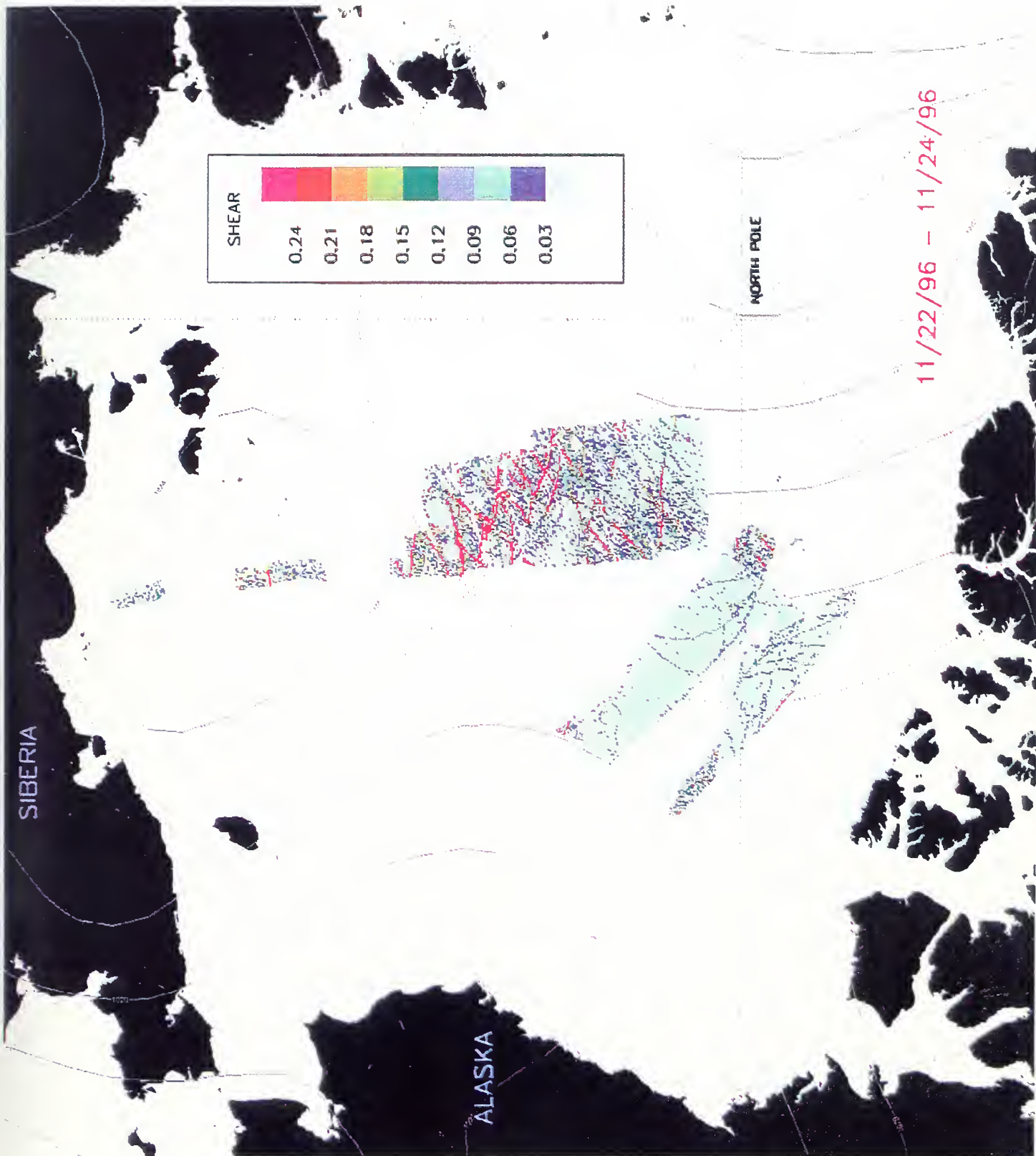


Figure 47. RGPS cycle 15 ice shear product for 22 to 24 Nov 96.

APPENDIX E

**NOGAPS METEOROLOGICAL DATA FOR RGPS ANALYSIS PERIOD:
07 TO 24 NOVEMBER 1996**

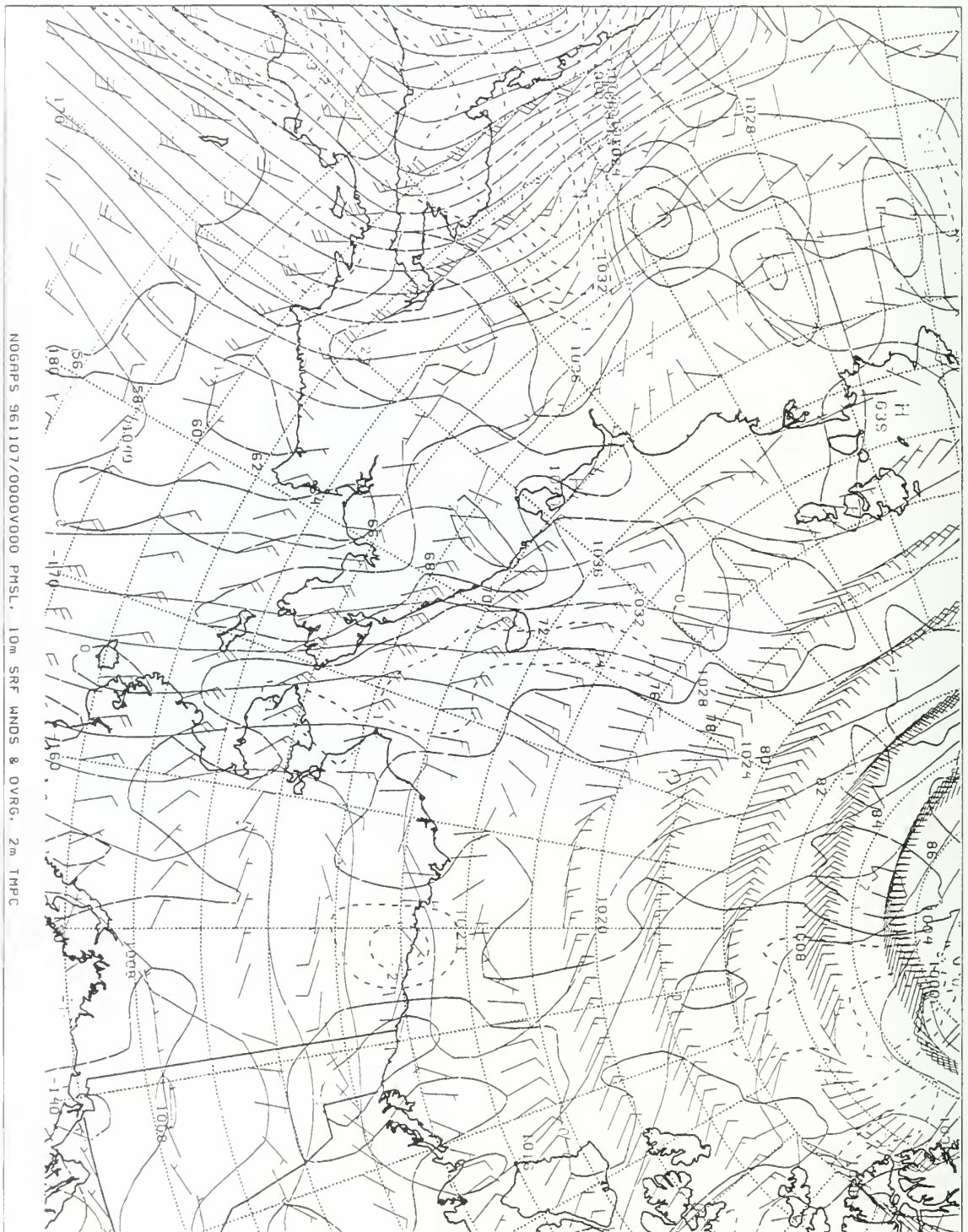


Figure 48. NOGAPS meteorological data for 0000Z 07 Nov 96.

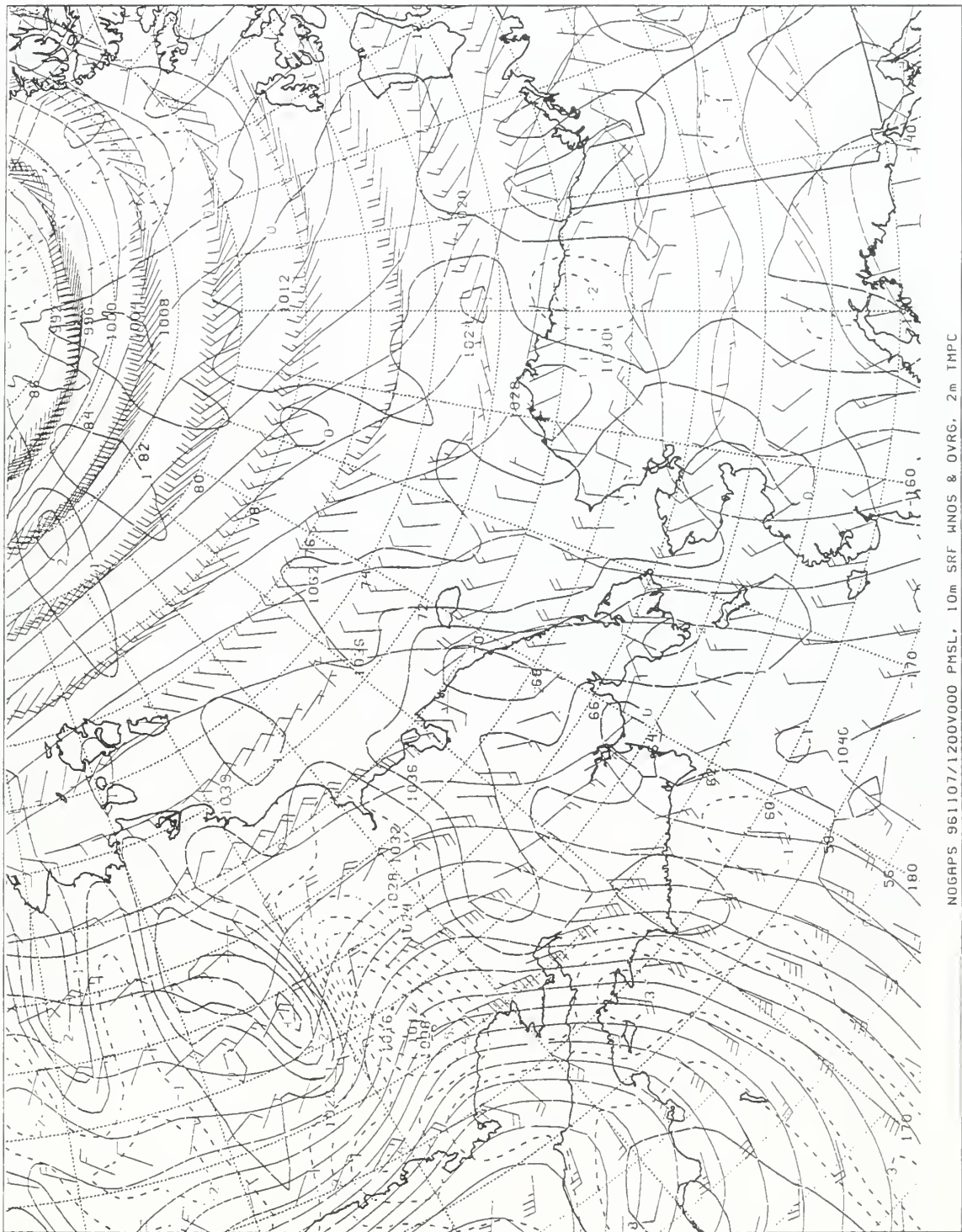


Figure 49. NOGAPS meteorological data for 1200Z 07 Nov 96.

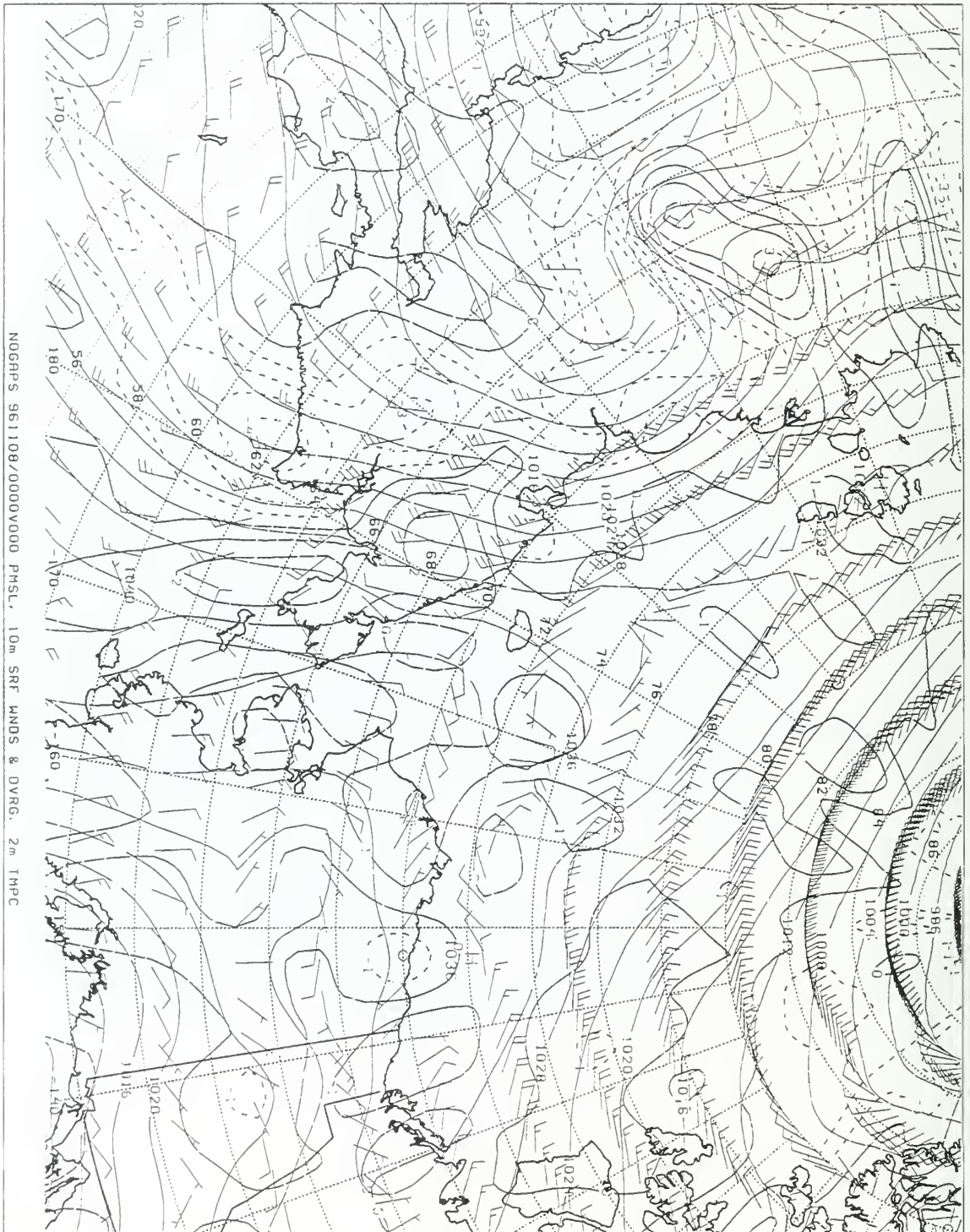


Figure 50. NOGAPS meteorological data for 0000Z 08 Nov 96.

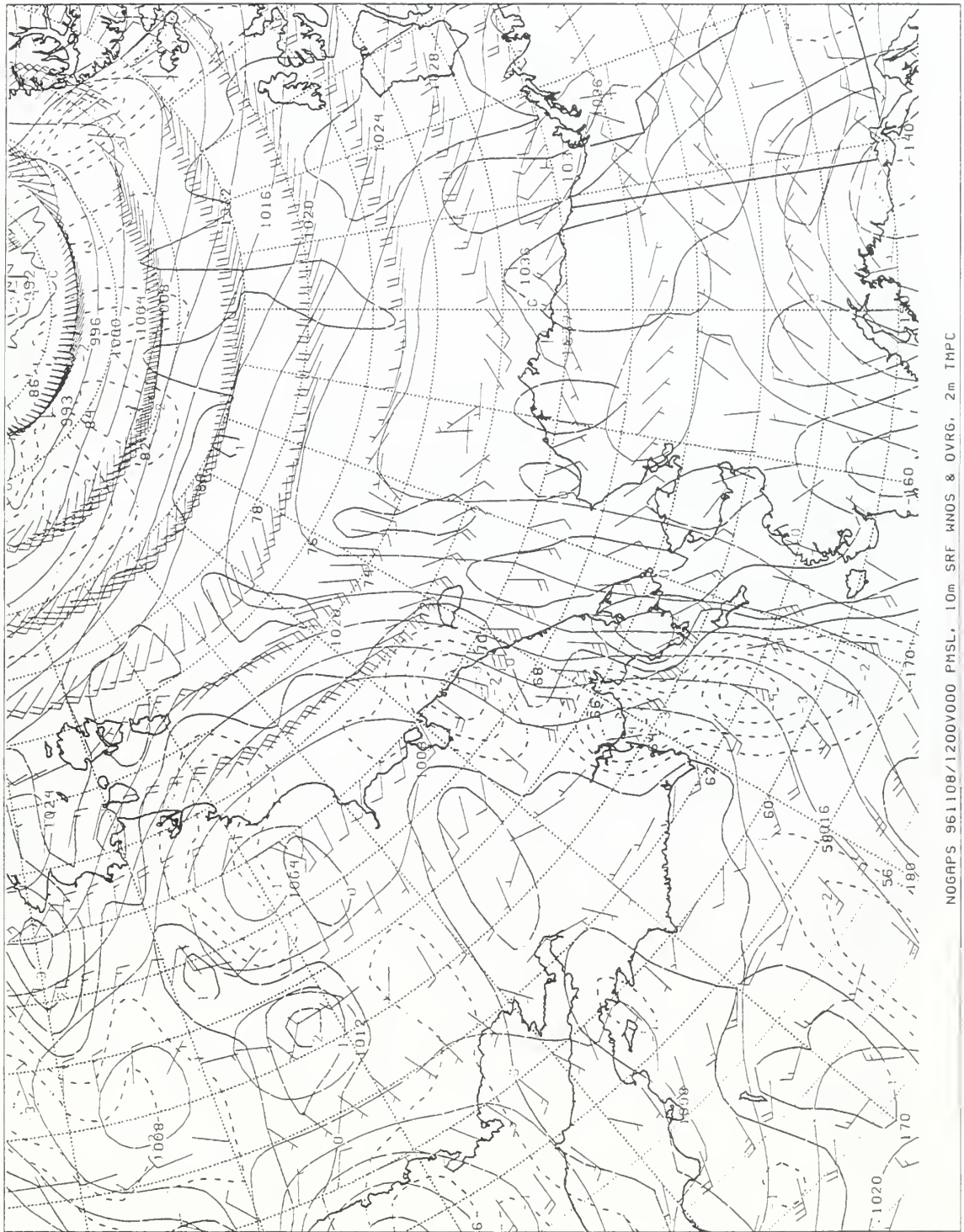


Figure 51. NOGAPS meteorological data for 1200Z 08 Nov 96.

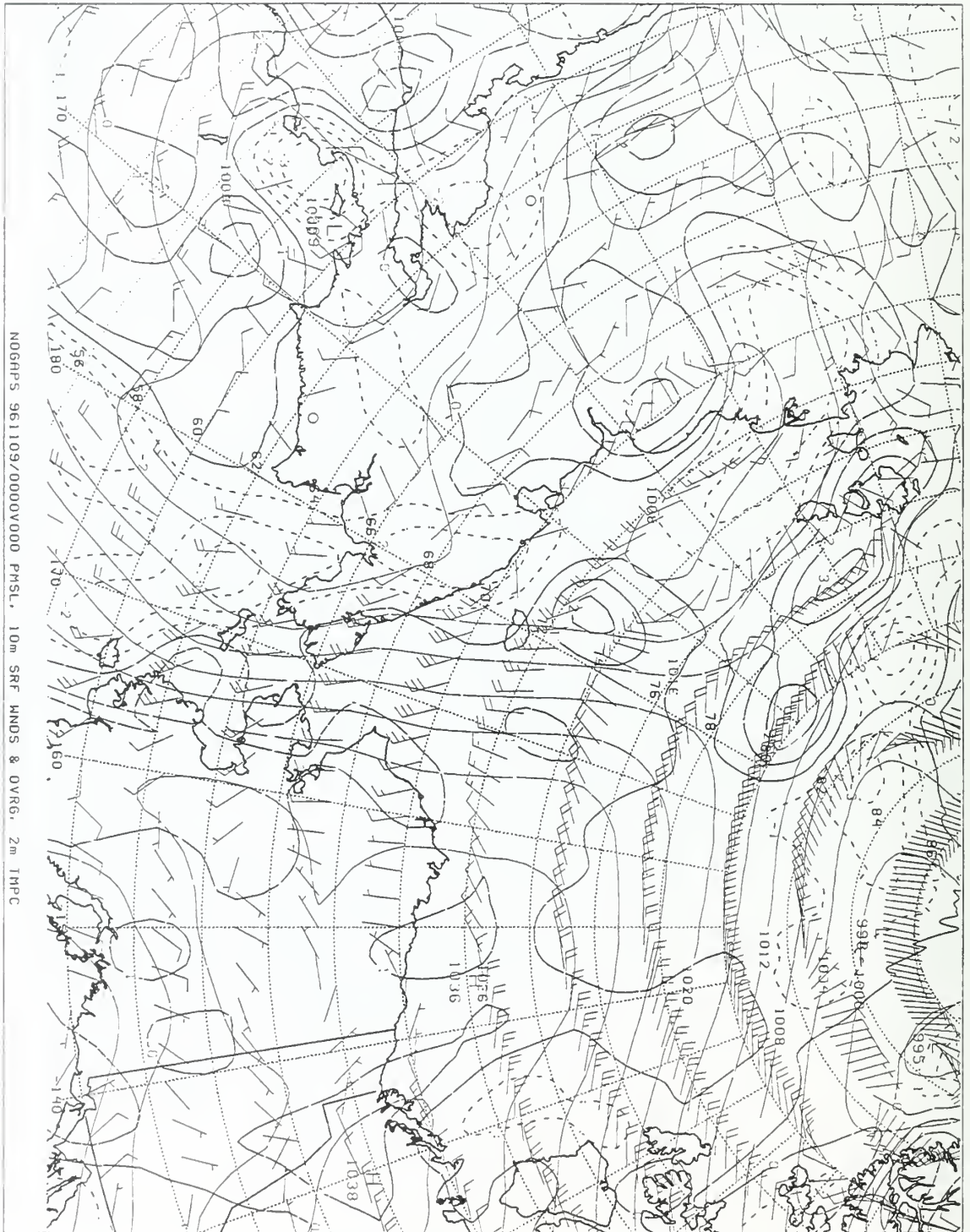
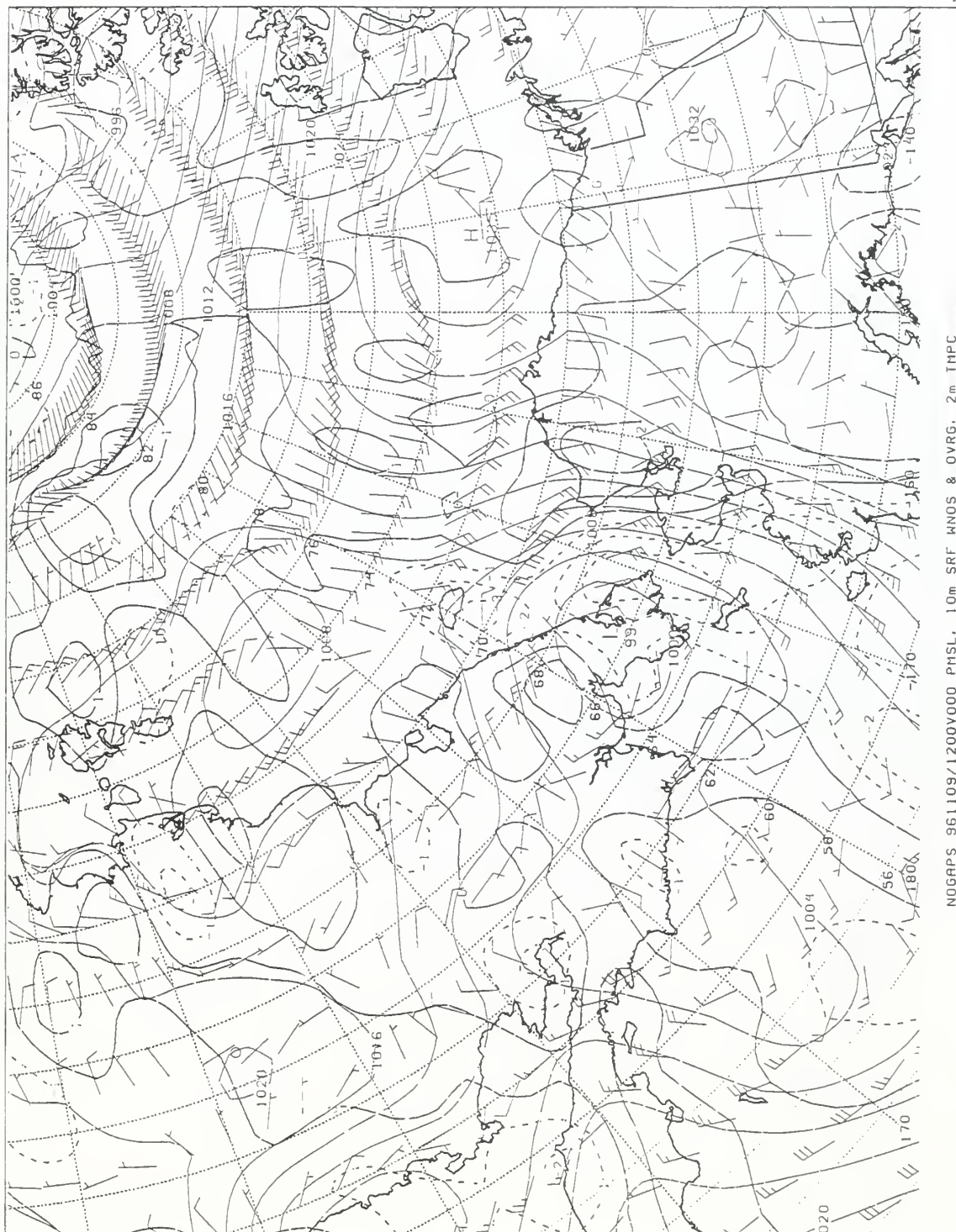


Figure 52. NOGAPS meteorological data for 0000Z 09 Nov 96.



NOGAPS 961109/1200V000 PMSL, 10m SRF MNOS & OVRG, 2m THPC

Figure 53. NOGAPS meteorological data for 1200Z 09 Nov 96.

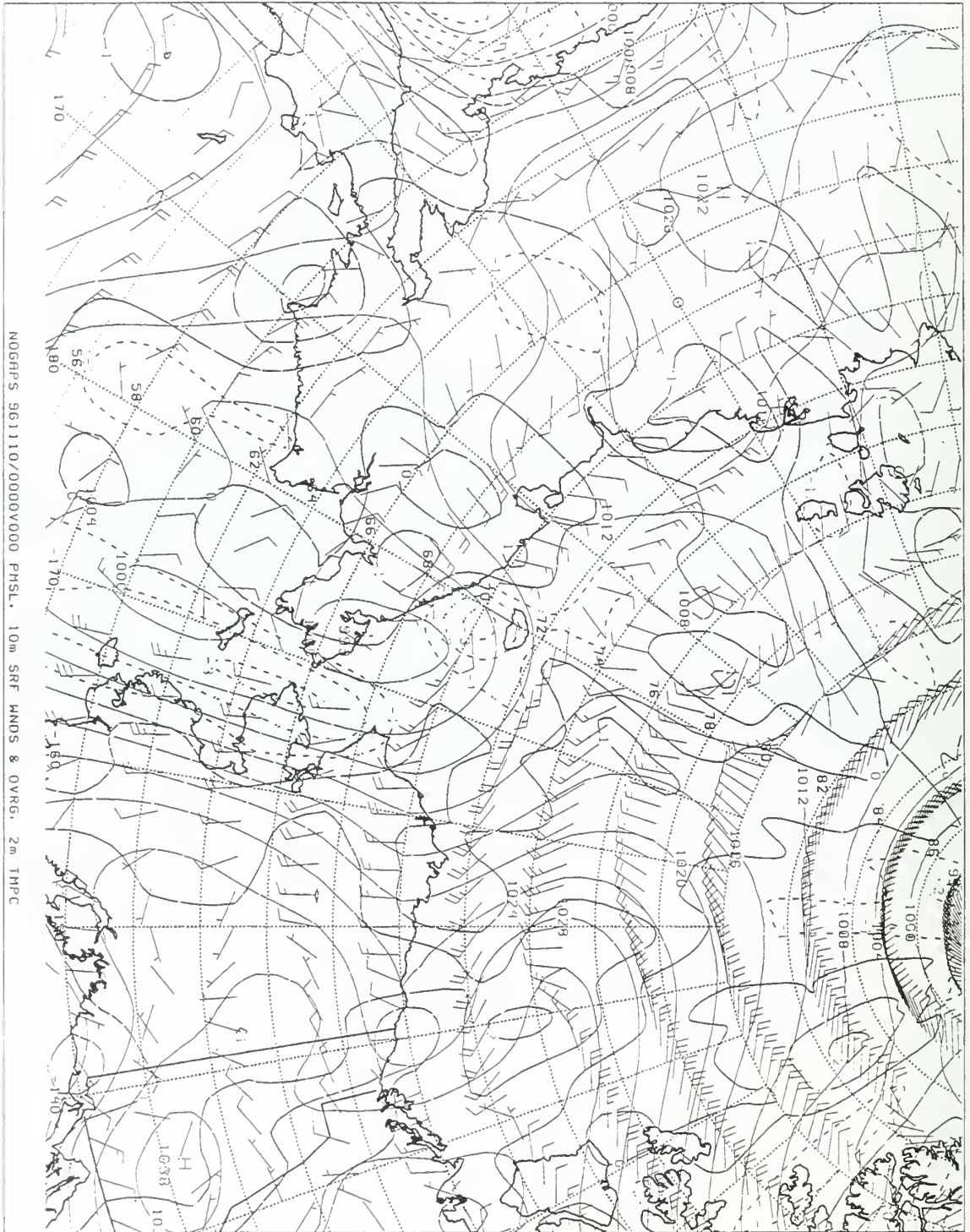
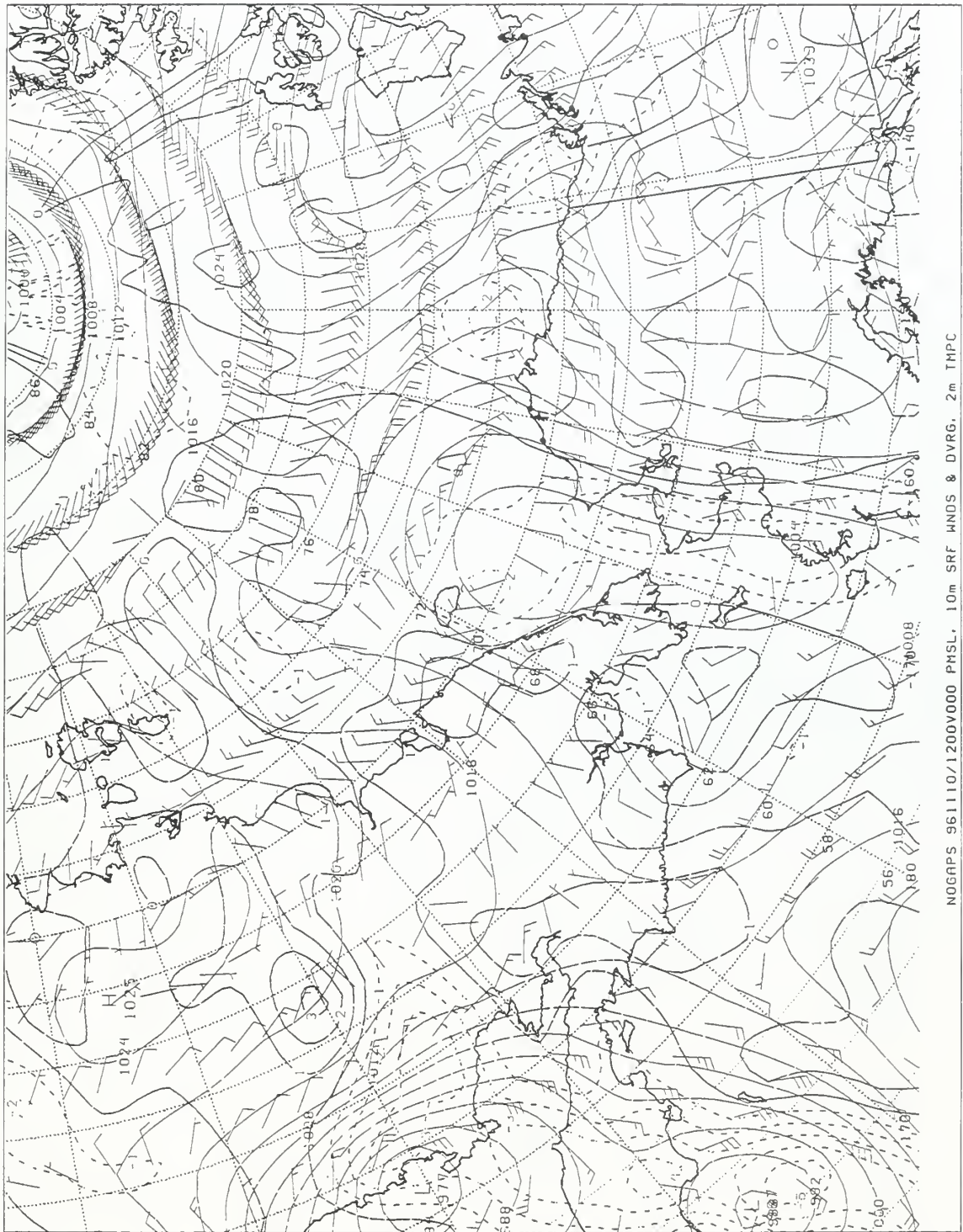


Figure 54. NOGAPS meteorological data for 0000Z 10 Nov 96.



NOGAPS 961110/1200V000 PMSL, 10m SRF HNDS & DVRG, 2m THPC

Figure 55. NOGAPS meteorological data for 1200Z 10 Nov 96.

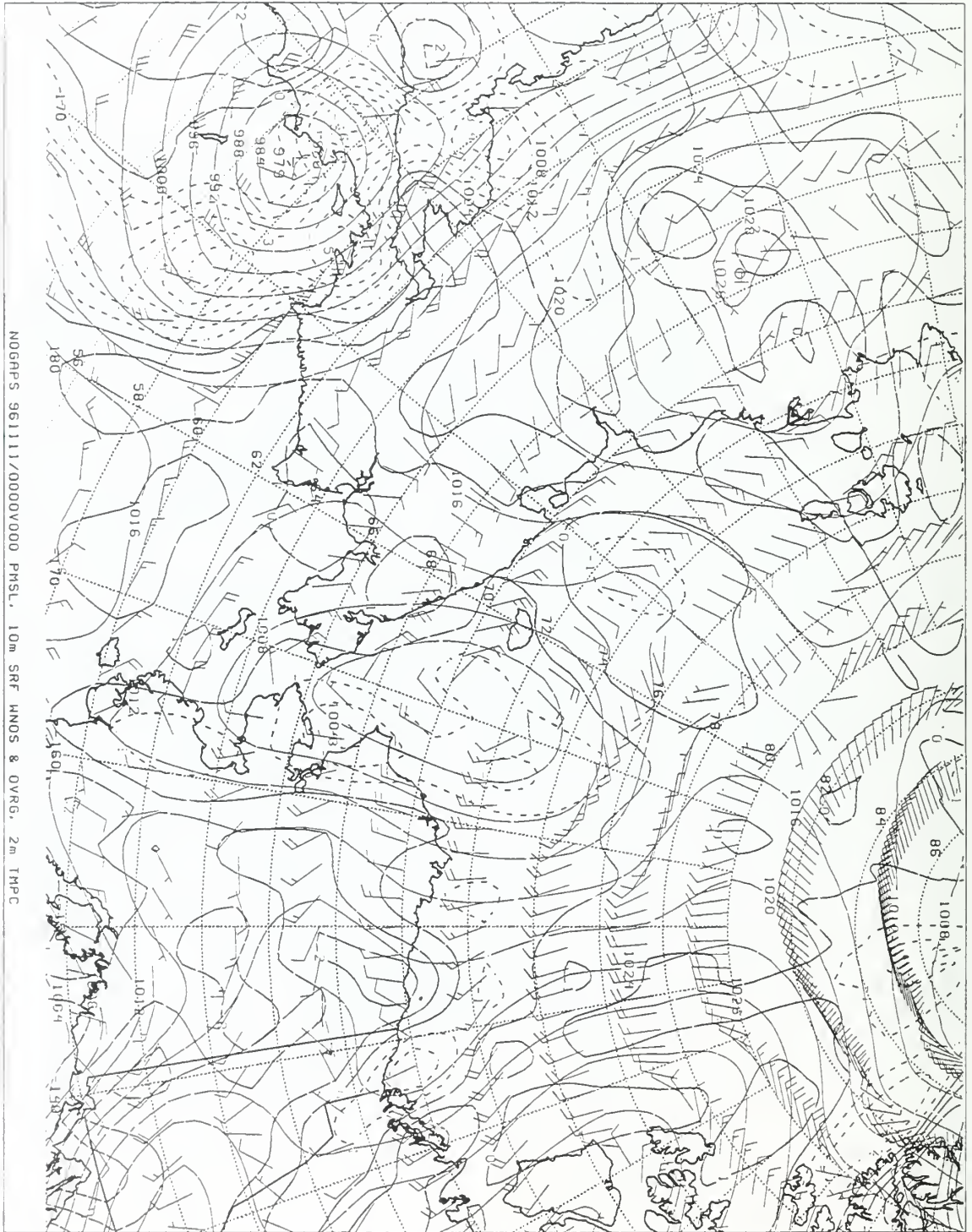
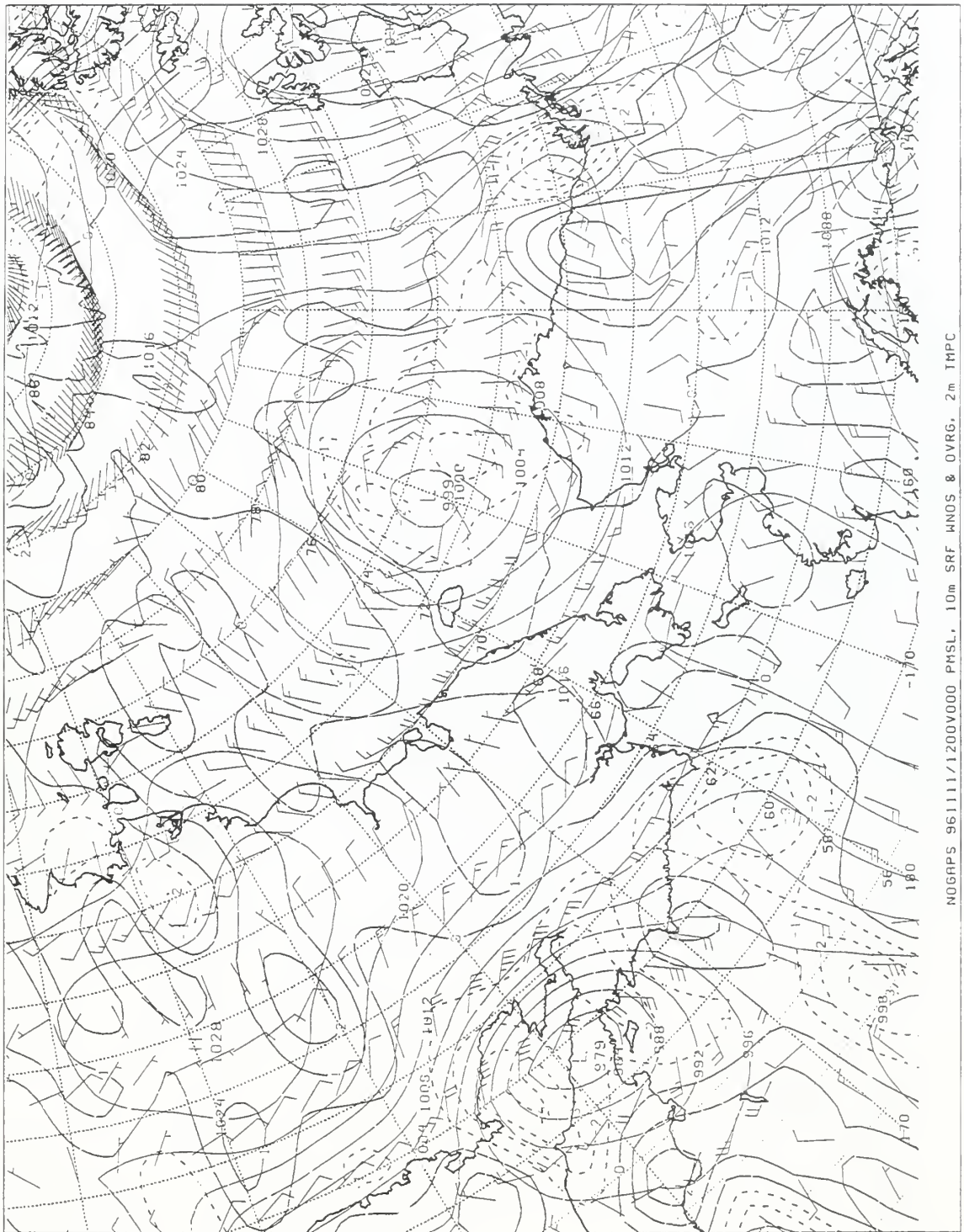


Figure 56. NOGAPS meteorological data for 0000Z 11 Nov 96.



NOGAPS 961111/1200000 PMSL. 10m SRF HNDS & OVRG. 2m IMPC

Figure 57. NOGAPS meteorological data for 1200Z 11 Nov 96.

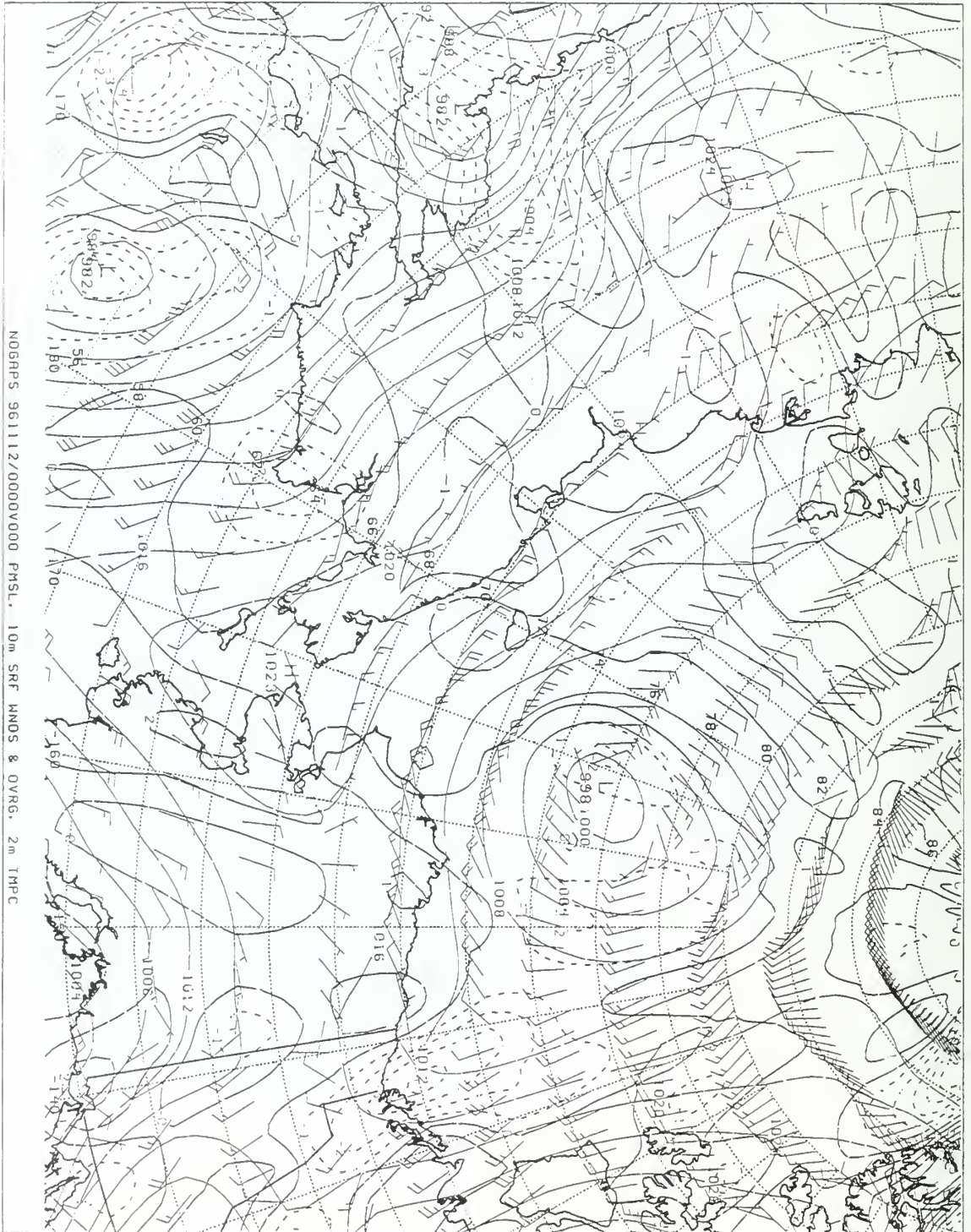


Figure 58. NOGAPS meteorological data for 0000Z 12 Nov 96.



NOGAPS 961112/1200V000 PMSL, 10m SRF HNDS & DVRG, 2m THPC

Figure 59. NOGAPS meteorological data for 1200Z 12 Nov 96.

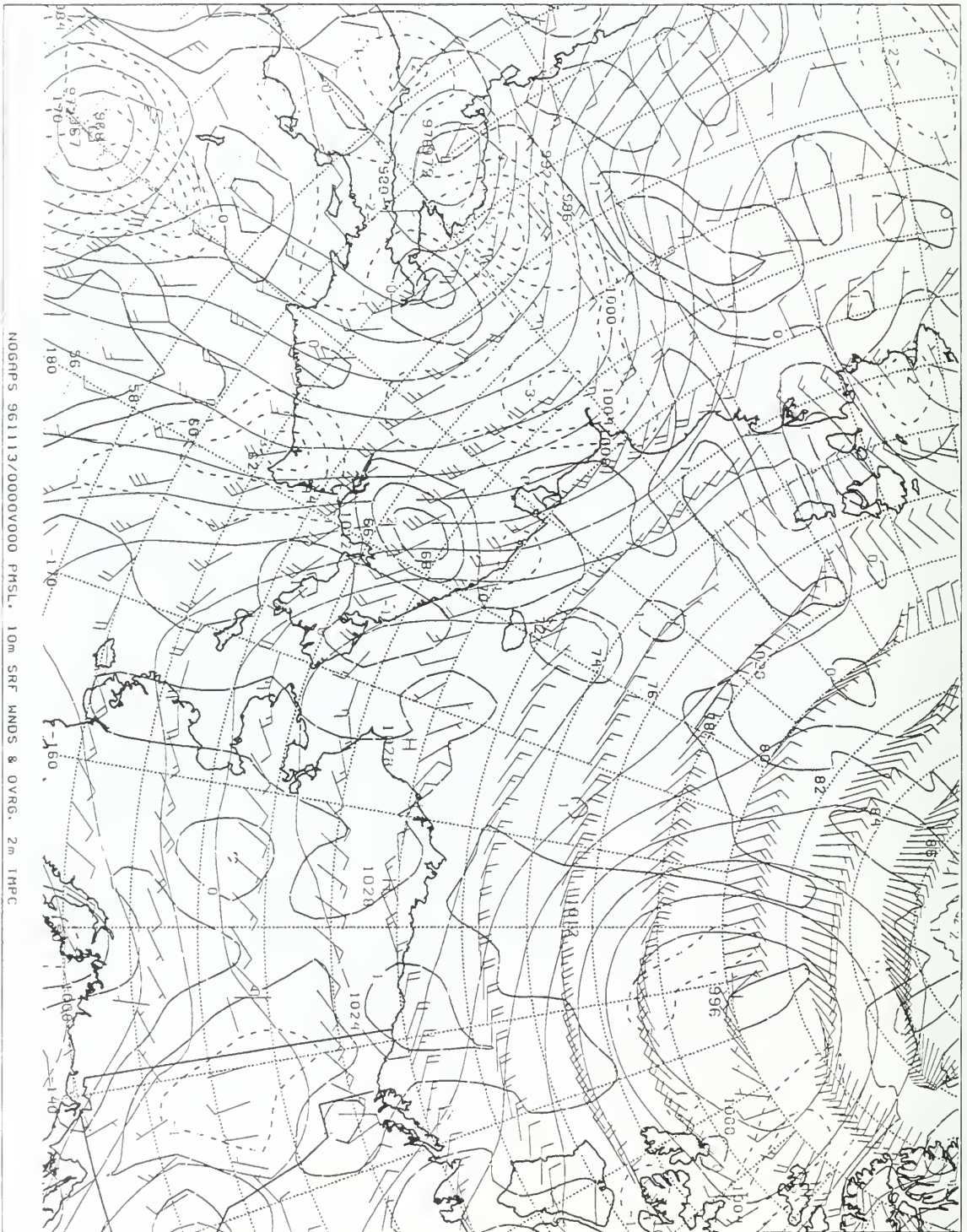
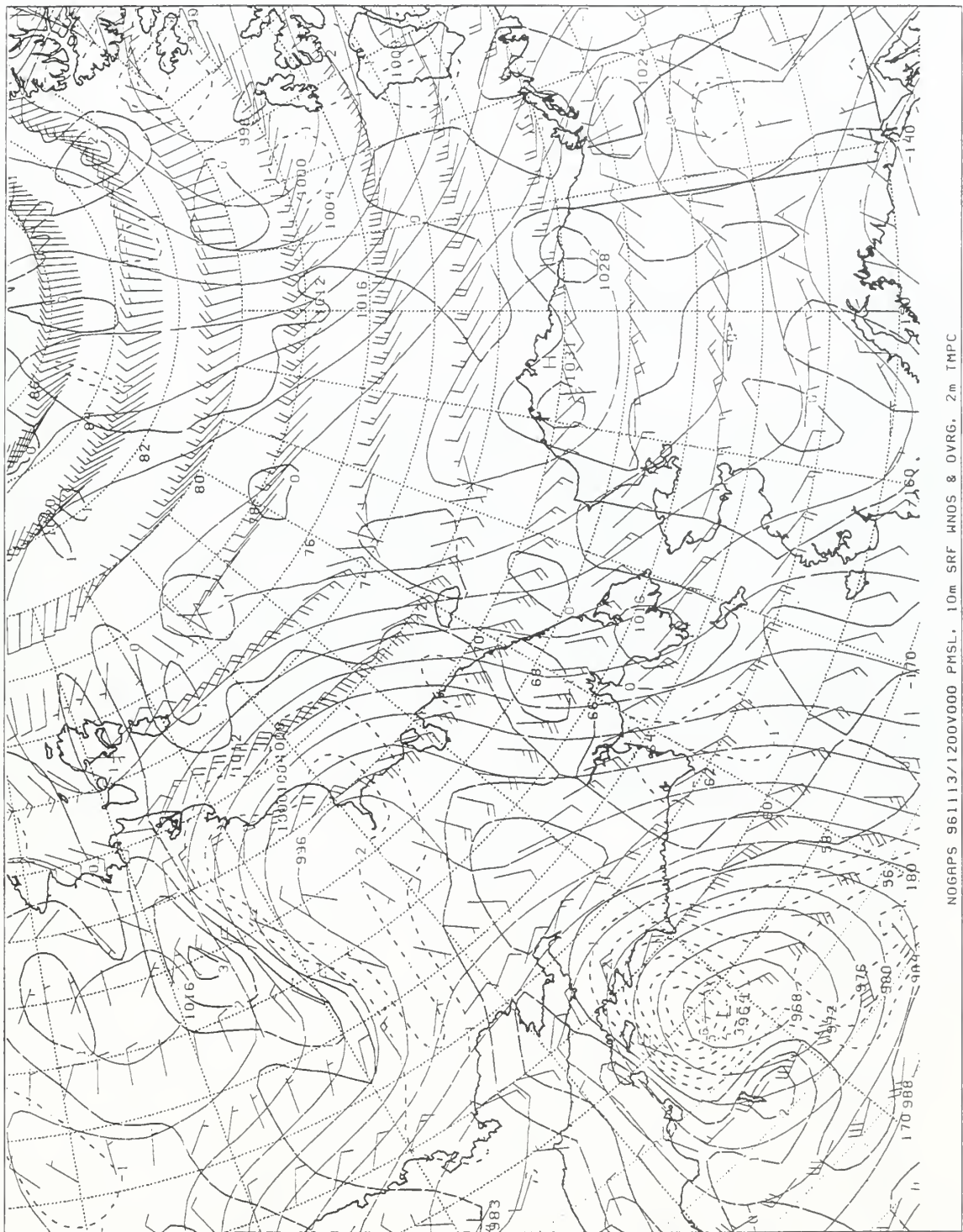


Figure 60. NOGAPS meteorological data for 0000Z 13 Nov 96.



NOGAPS 961113/1200V000 PMSL, 10m SRF WNDS & OVRG, 2m TMPC

Figure 61. NOGAPS meteorological data for 1200Z 13 Nov 96.

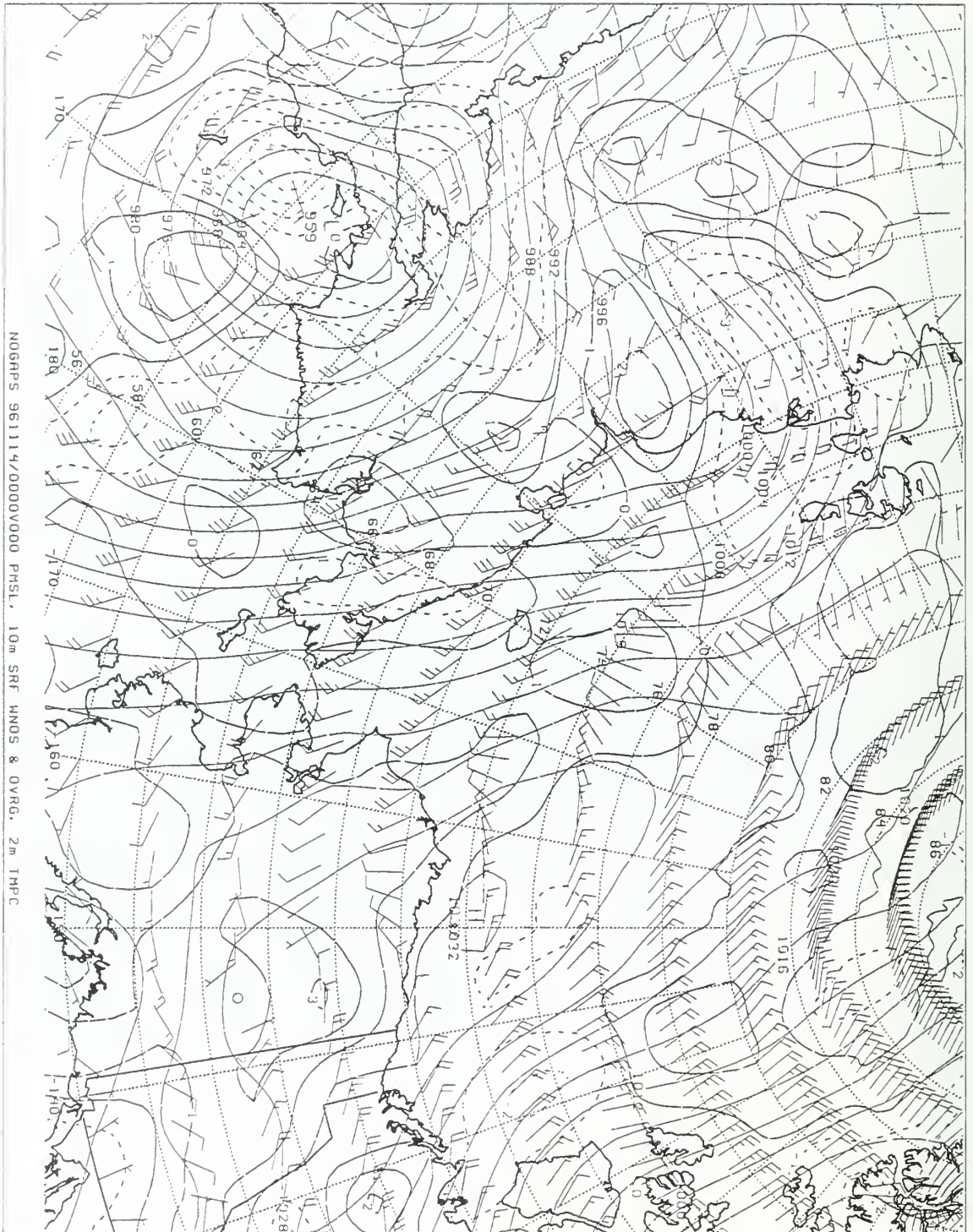


Figure 62. NOGAPS meteorological data for 0000Z 14 Nov 96.

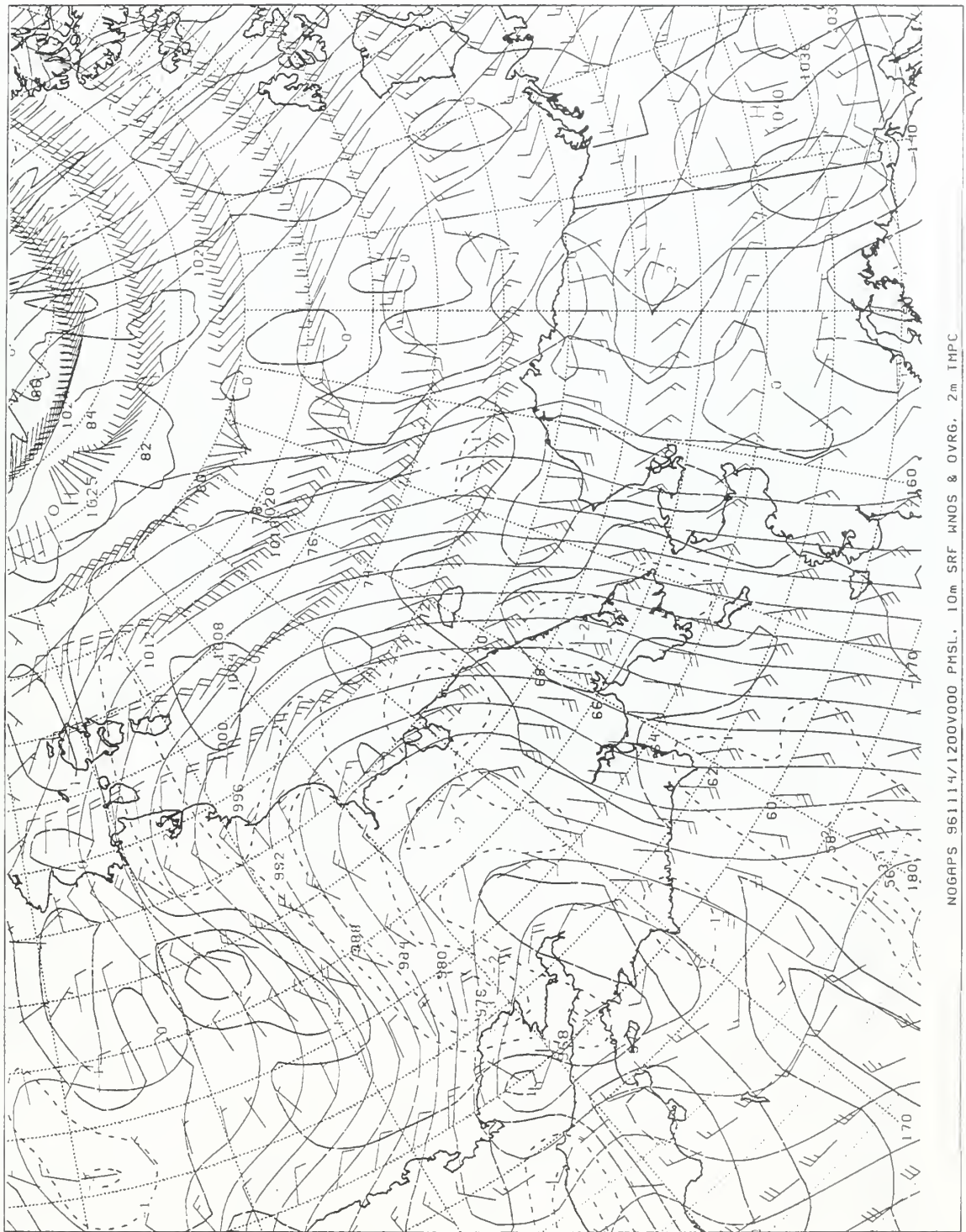


Figure 63. NOGAPS meteorological data for 1200Z 14 Nov 96.

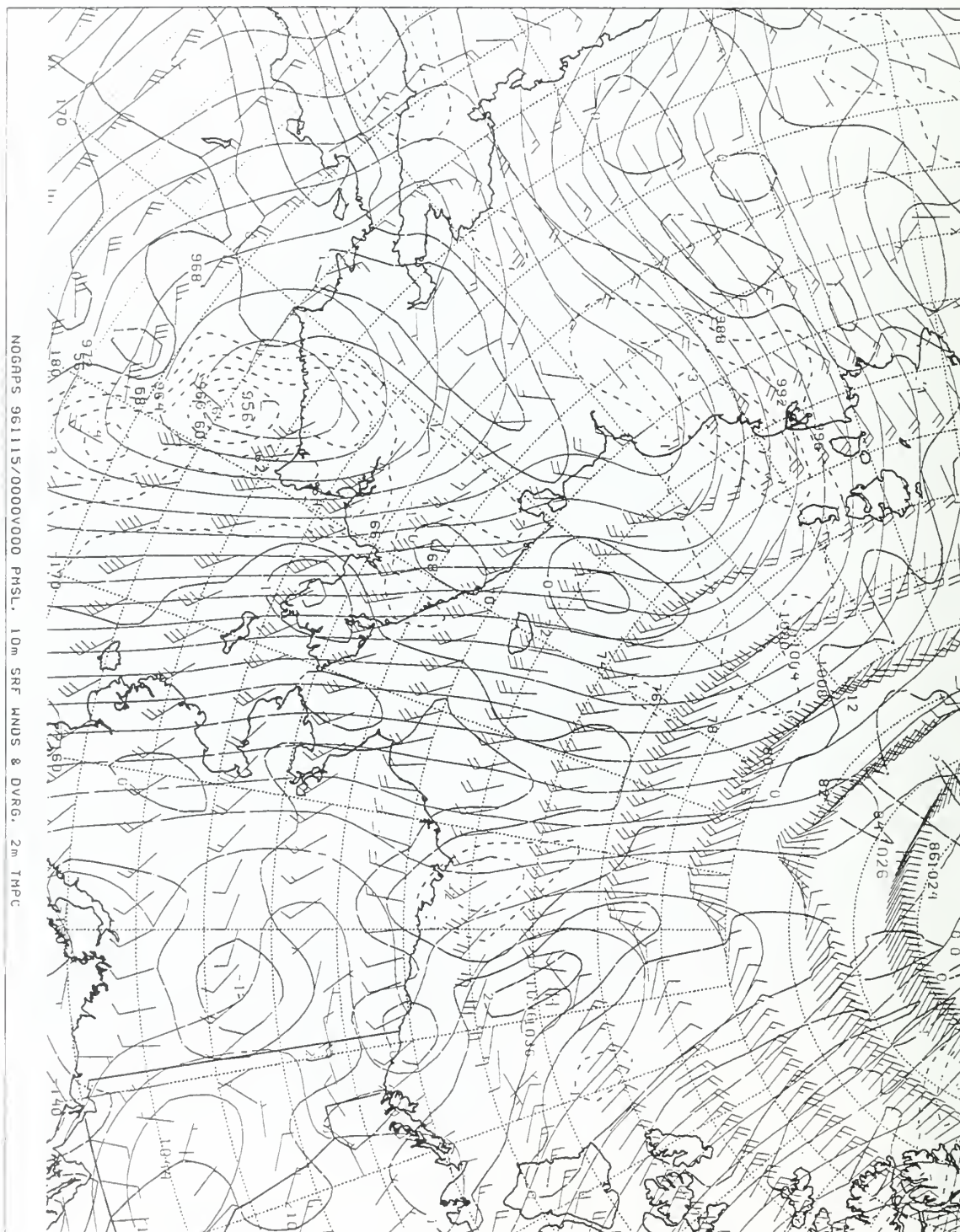


Figure 64. NOGAPS meteorological data for 0000Z 15 Nov 96.

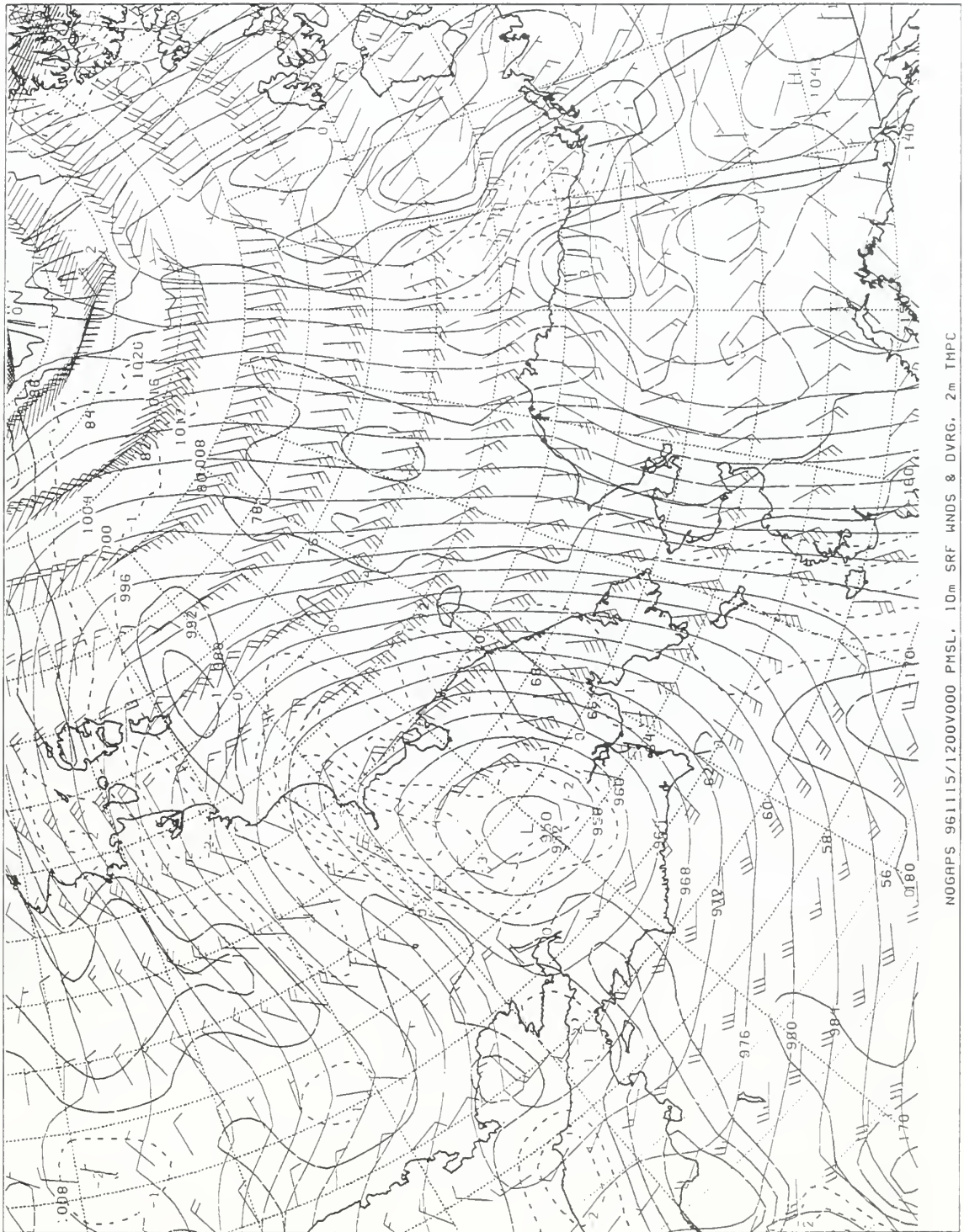


Figure 65. NOGAPS meteorological data for 1200Z 15 Nov 96.

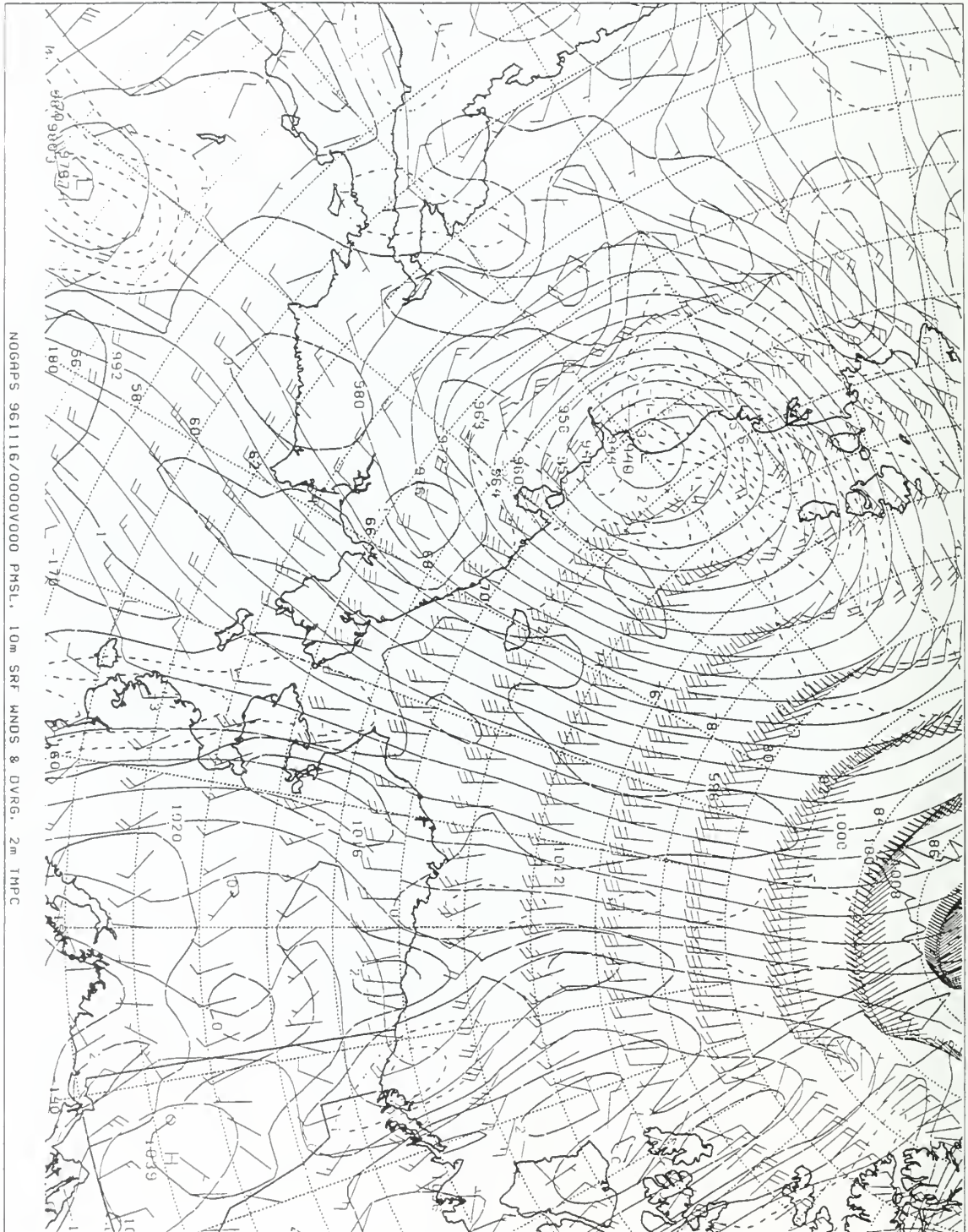
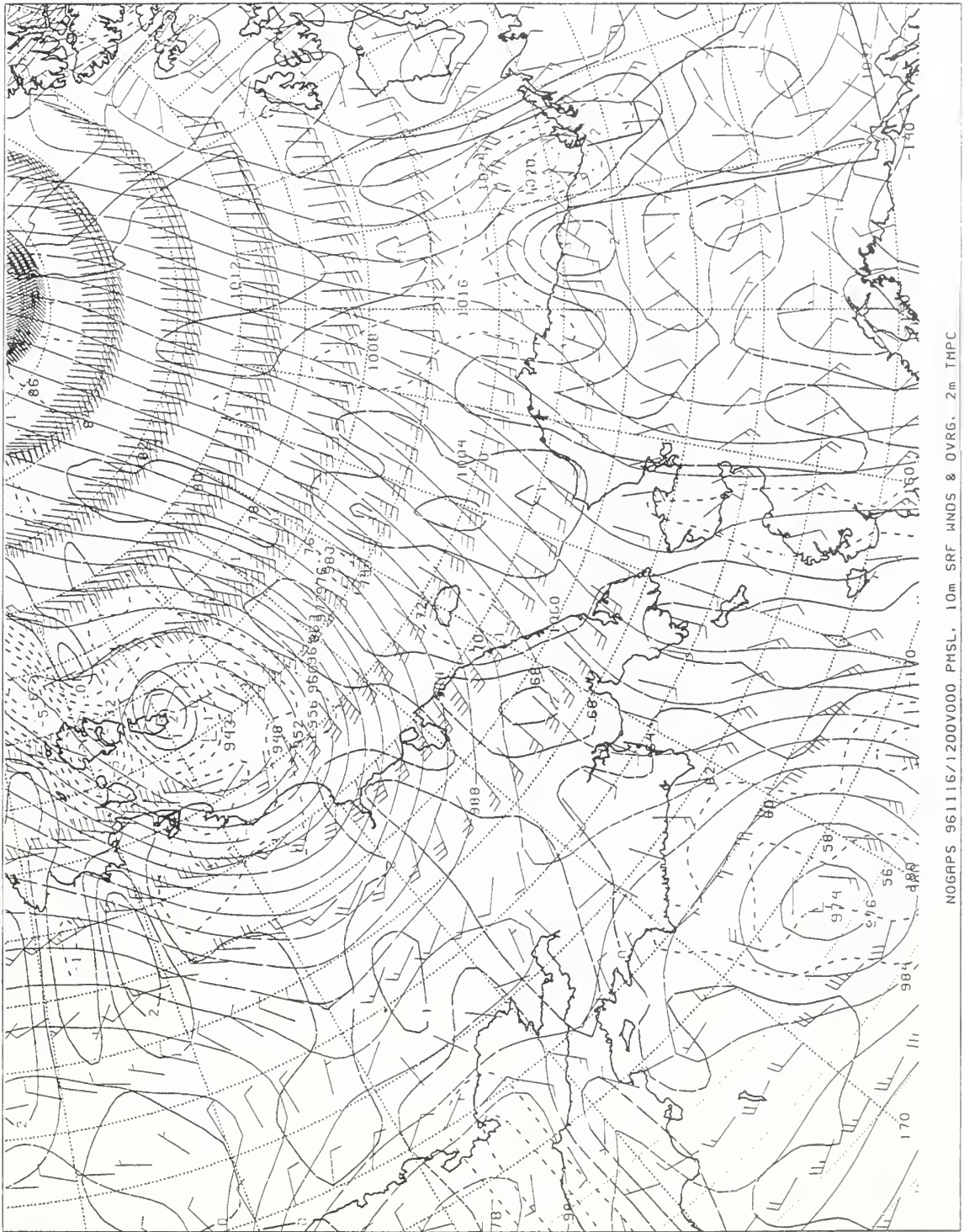


Figure 66. NOGAPS meteorological data for 0000Z 16 Nov 96.



NOGAPS 961116/1200V000 PMSL, 10m SRF HNDS & OVRG, 2m THPC

Figure 67. NOGAPS meteorological data for 1200Z 16 Nov 96.

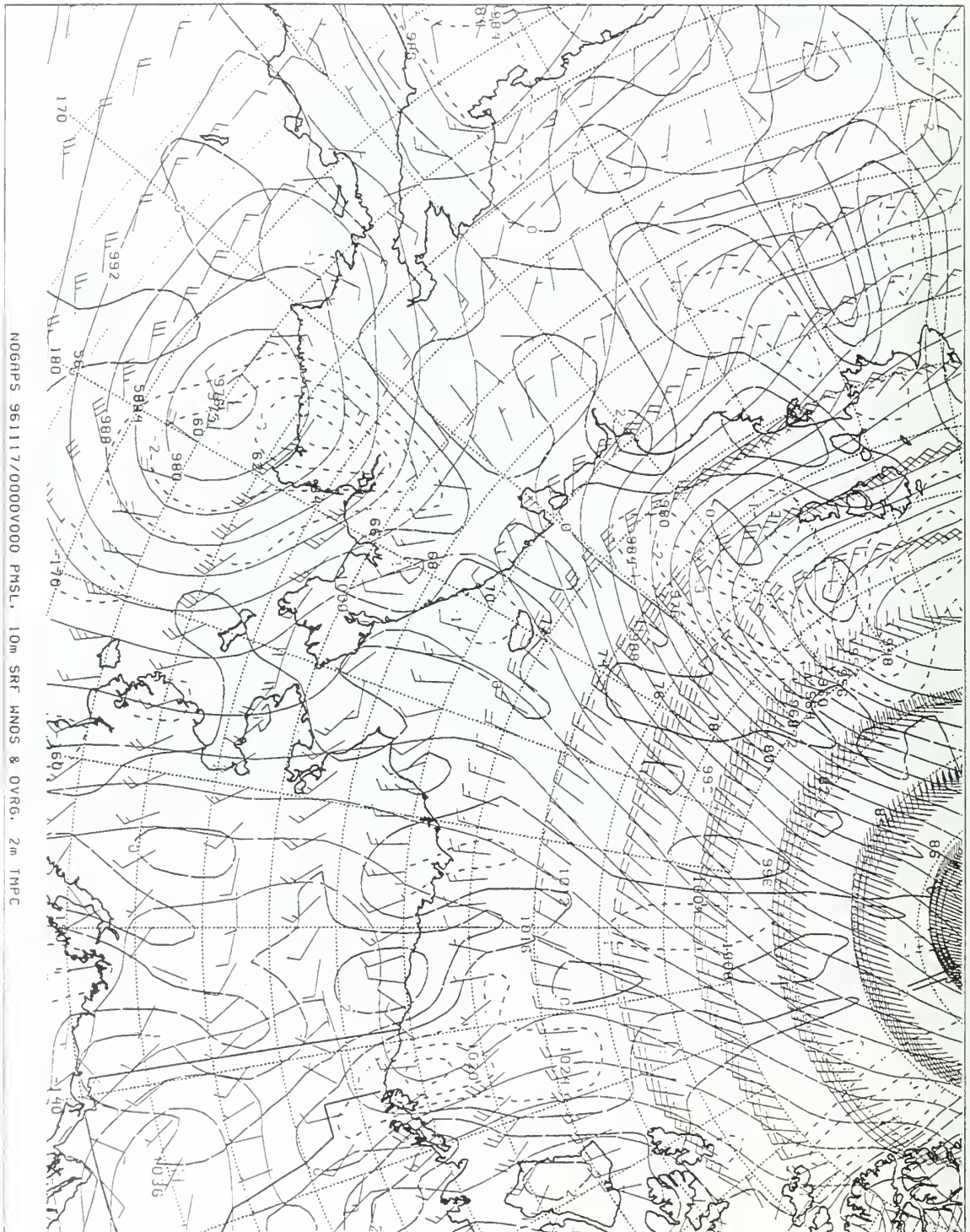
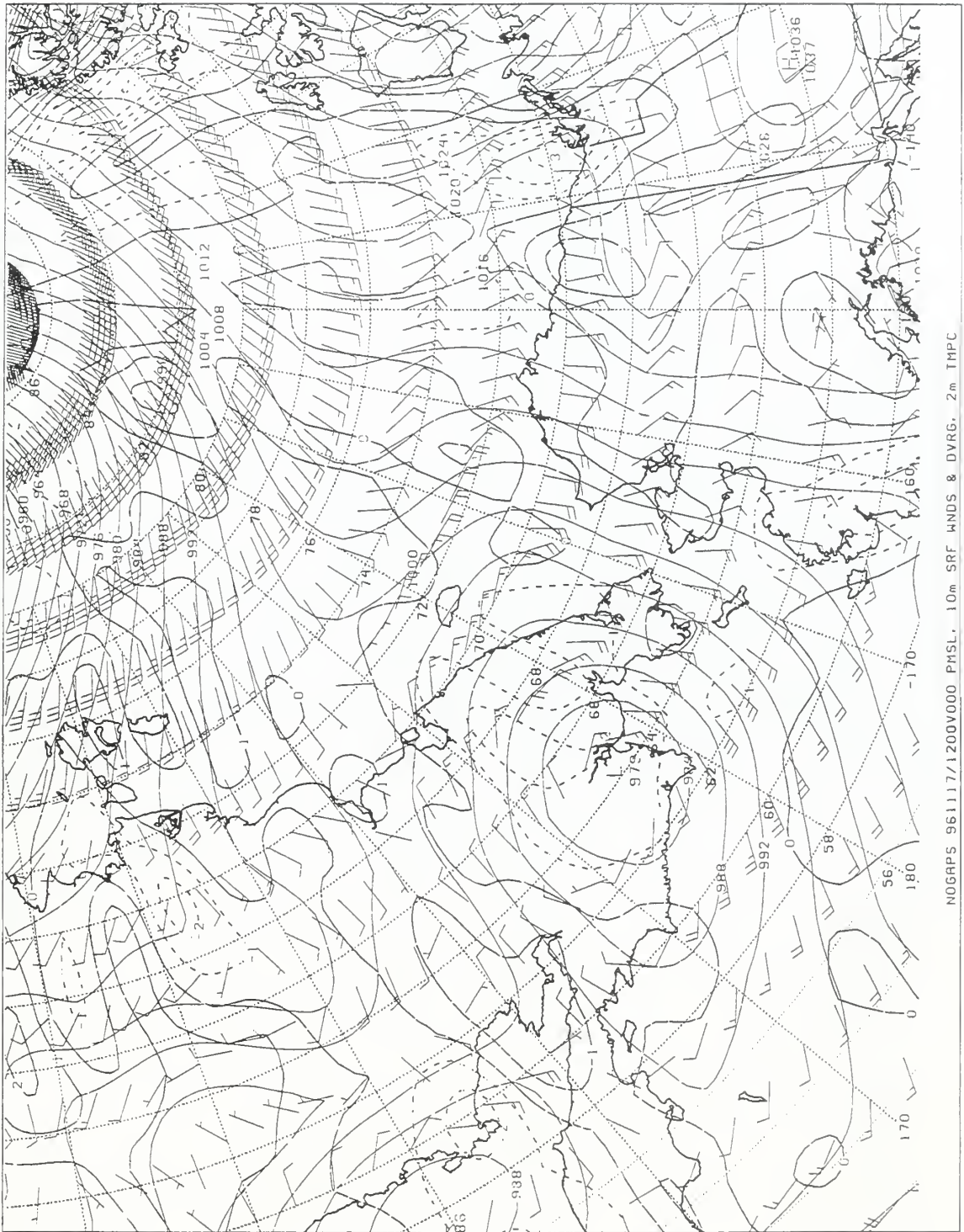


Figure 68. NOGAPS meteorological data for 0000Z 17 Nov 96.



NOGAPS 961117/1200V000 PMSL, 10m SRF WINDS & DVRG, 2m TMRG

Figure 69. NOGAPS meteorological data for 1200Z 17 Nov 96.

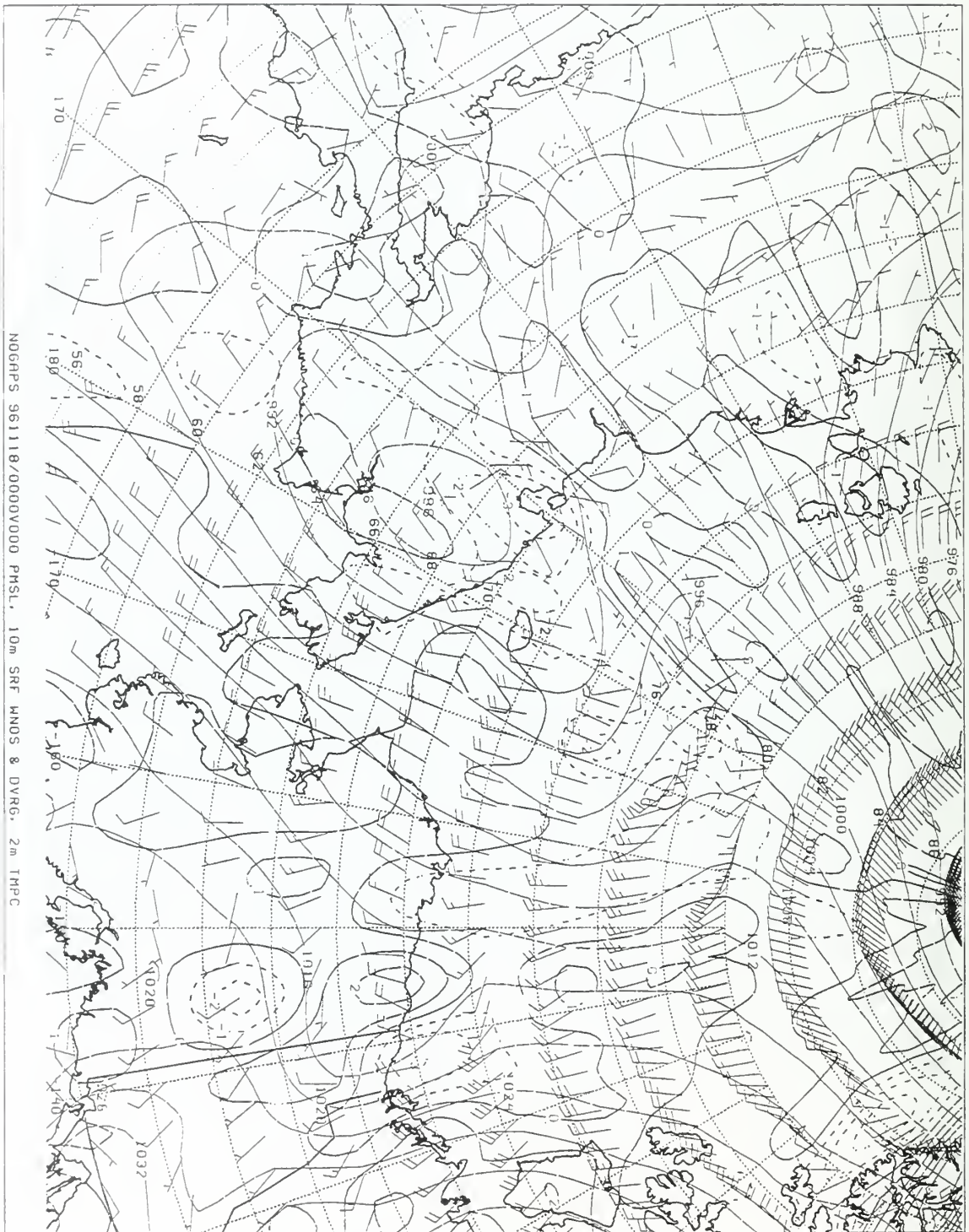
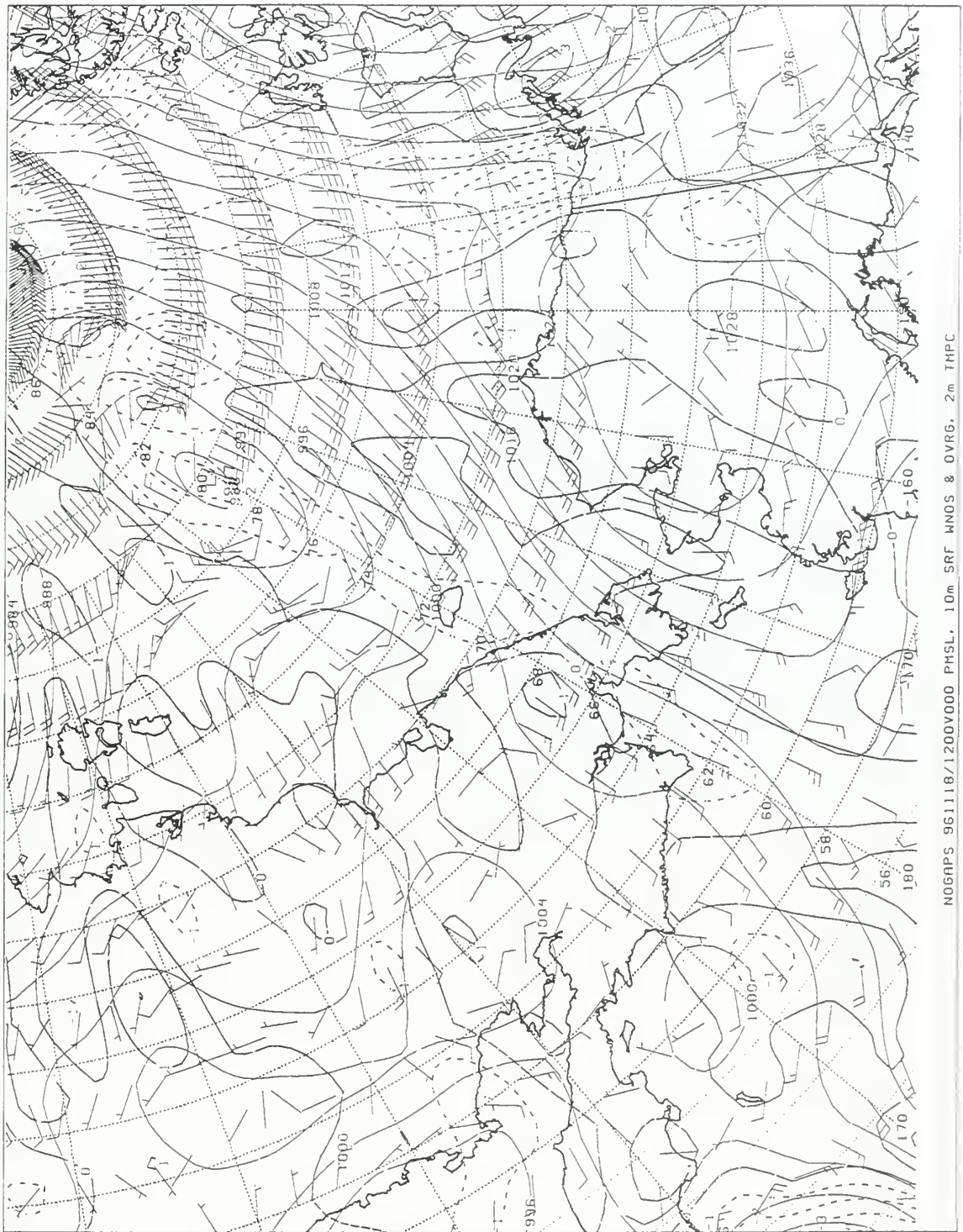


Figure 70. NOGAPS meteorological data for 0000Z 18 Nov 96.



NOGAPS 961118/1200000 MSL, 10m SRF WINDS & OVRG, 2m THPC

Figure 71. NOGAPS meteorological data for 1200Z 18 Nov 96.

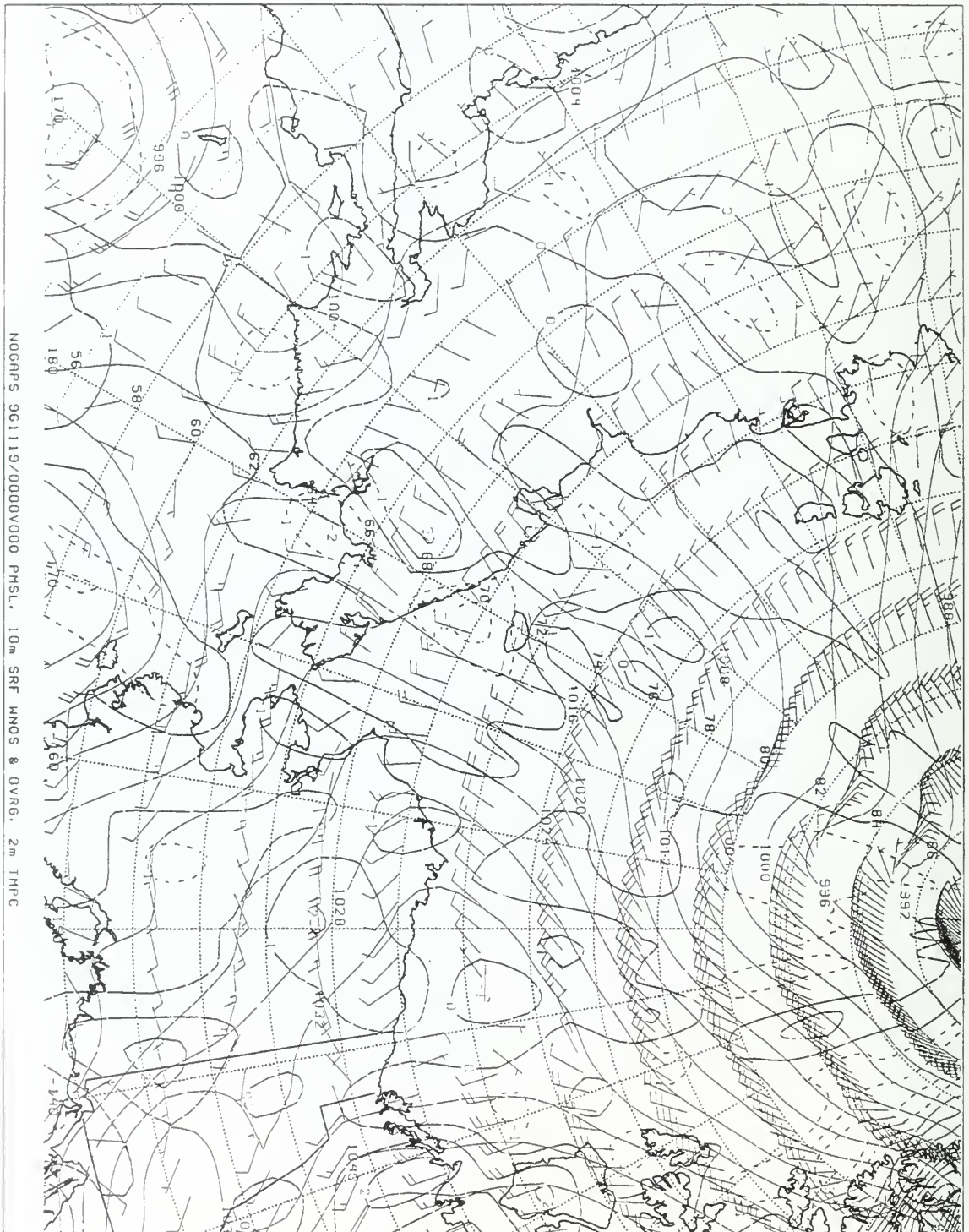
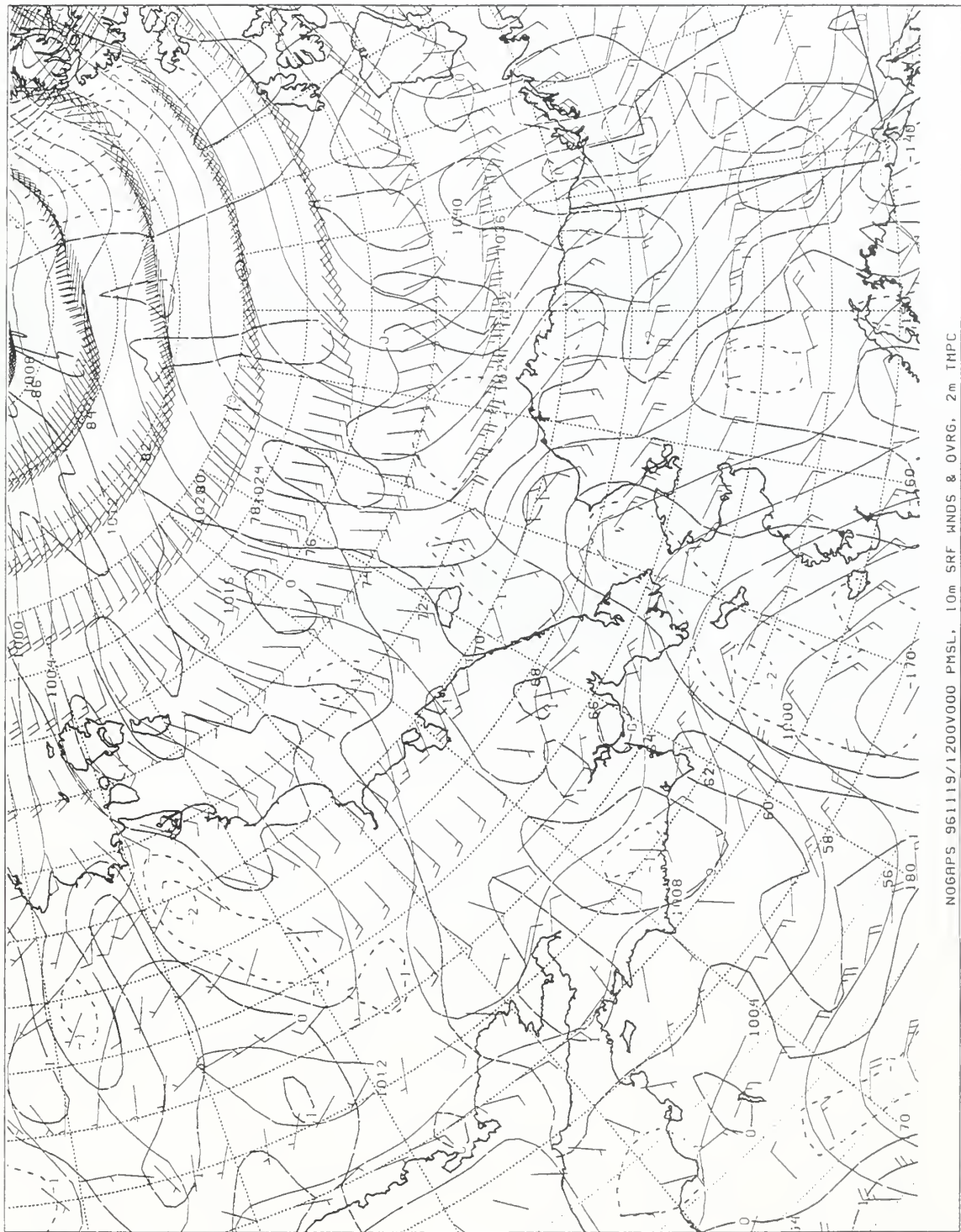


Figure 72. NOGAPS meteorological data for 0000Z 19 Nov 96.



NOGAPS 961119/1200V000 PMSL, 10m SRF MNDS & QVRG, 2m TMP C

Figure 73. NOGAPS meteorological data for 1200Z 19 Nov 96.

Figure 74.
0000Z 20 Nov 96
NOGAPS Meteorological Data Missing

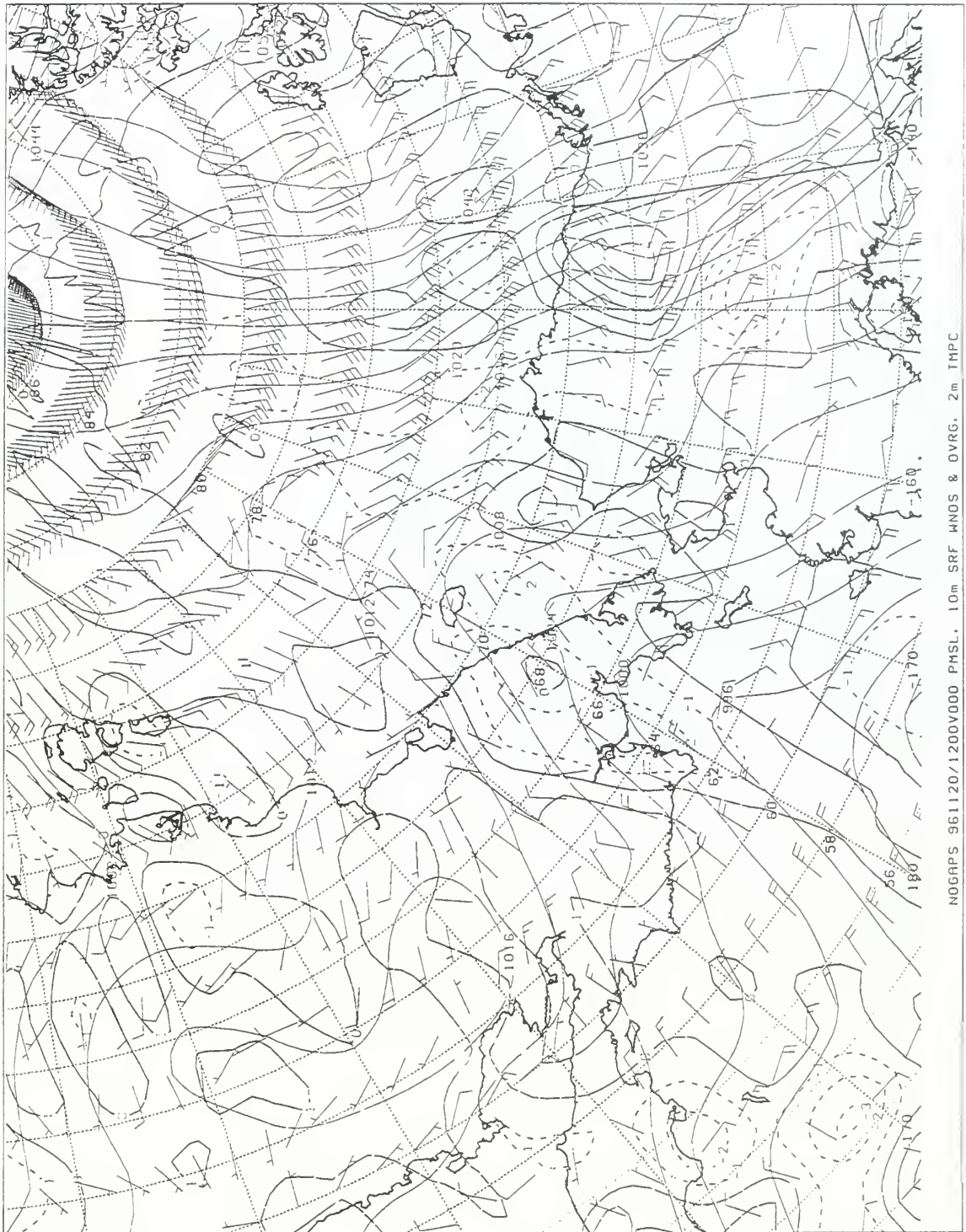


Figure 75. NOGAPS meteorological data for 1200Z 20 Nov 96.

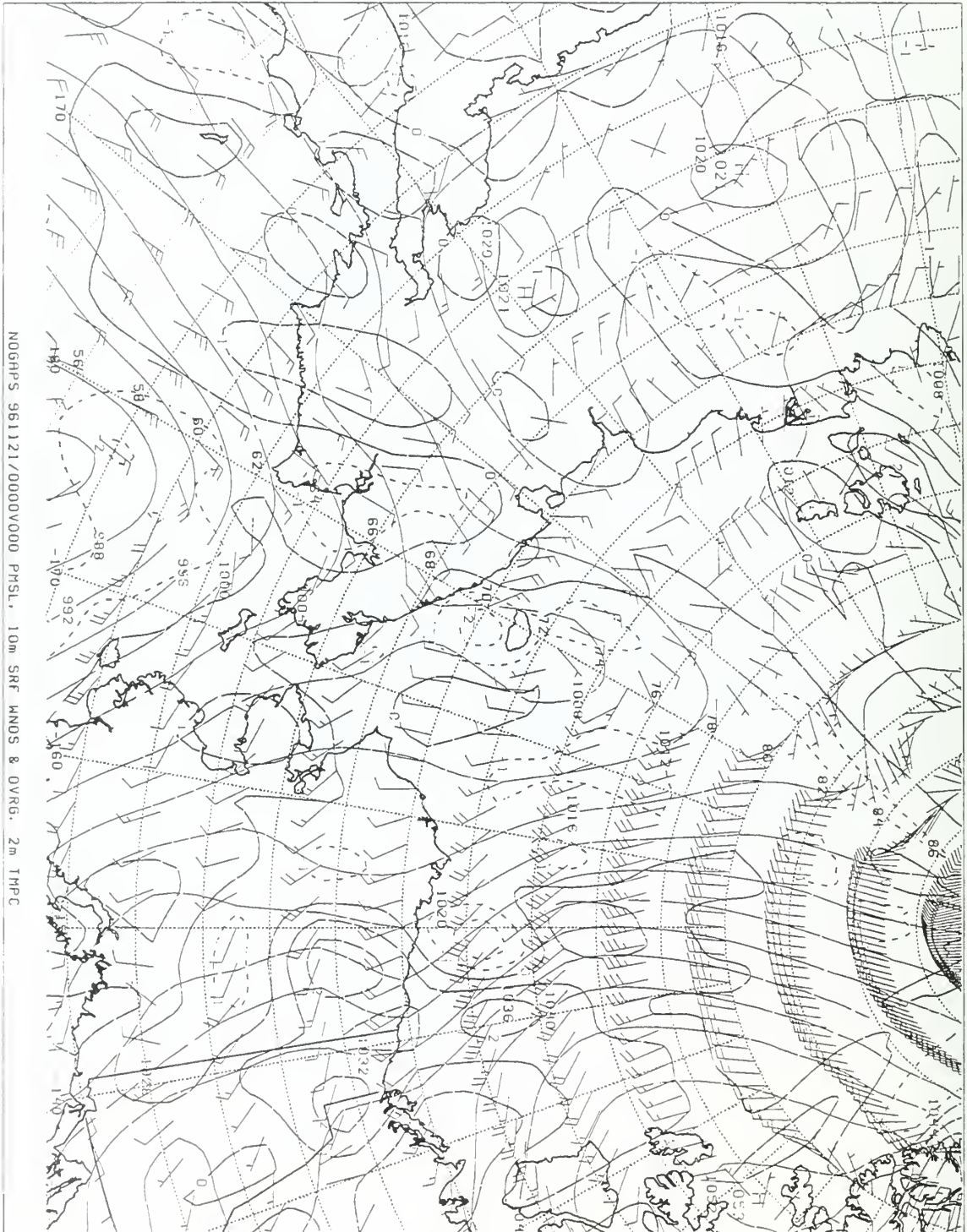
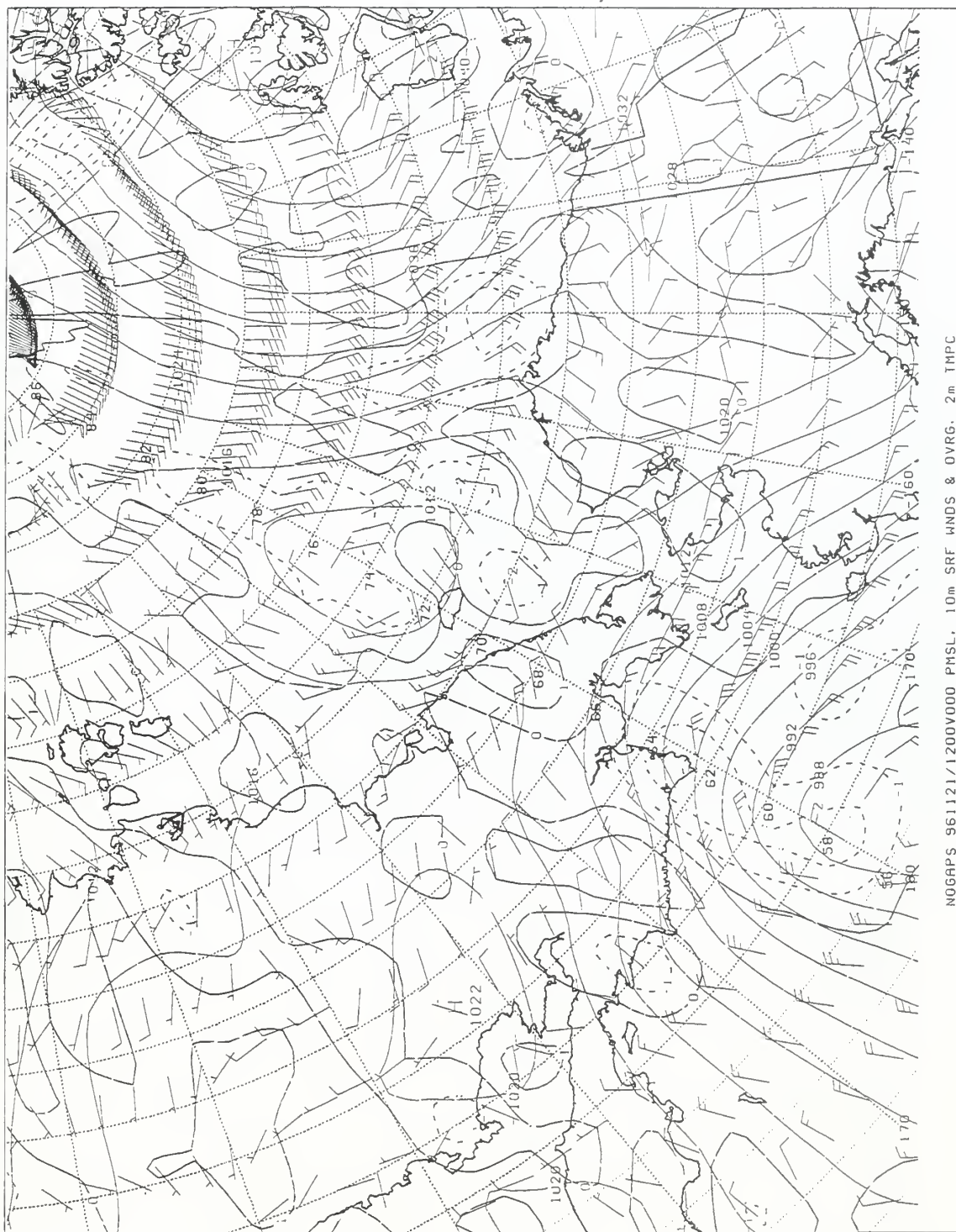


Figure 76. NOGAPS meteorological data for 0000Z 21 Nov 96.



NOGAPS 961121/1200V000 PMSL, 10m SRF WINDS & OVRG, 2m TMPC

Figure 77. NOGAPS meteorological data for 1200Z 21 Nov 96.

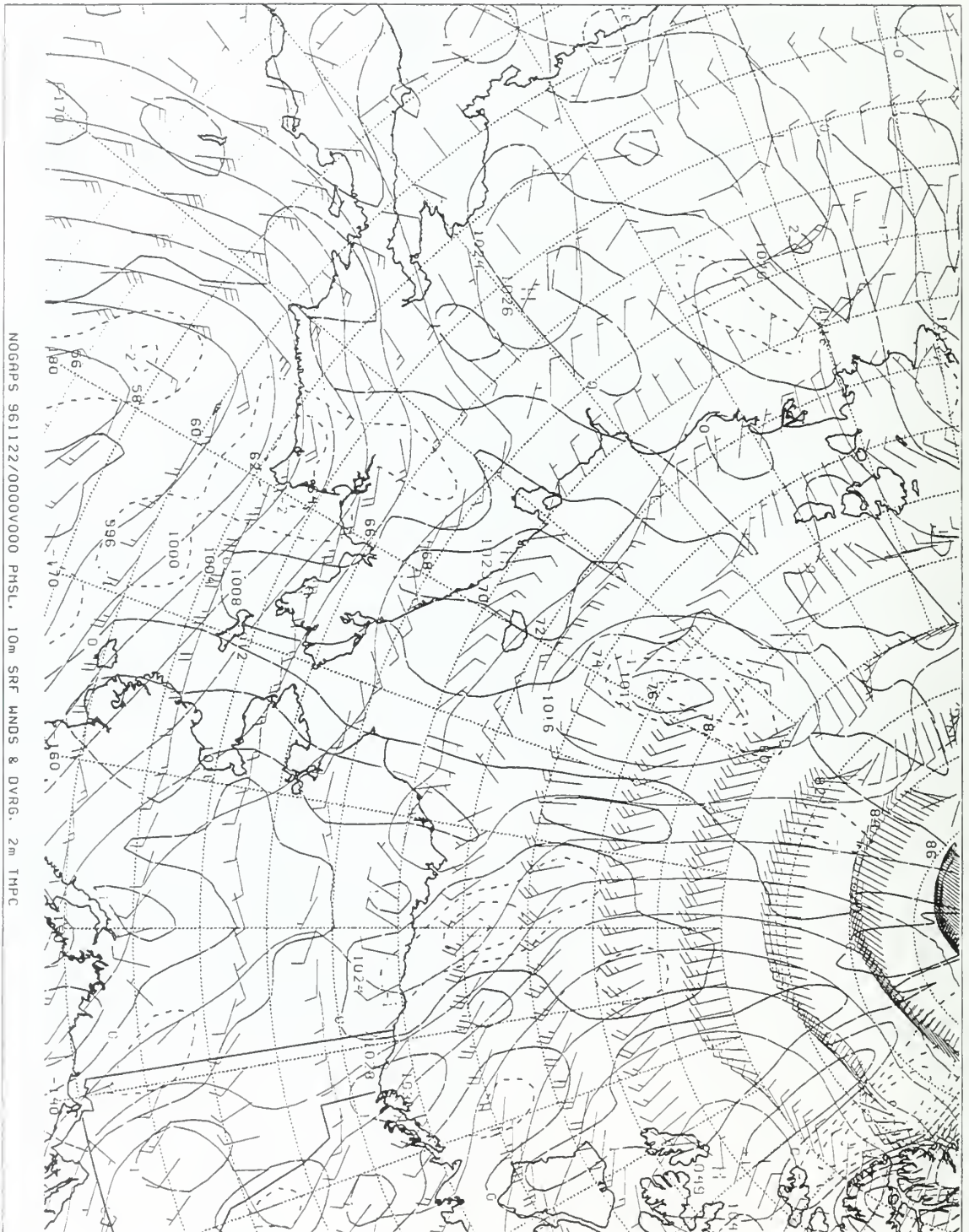
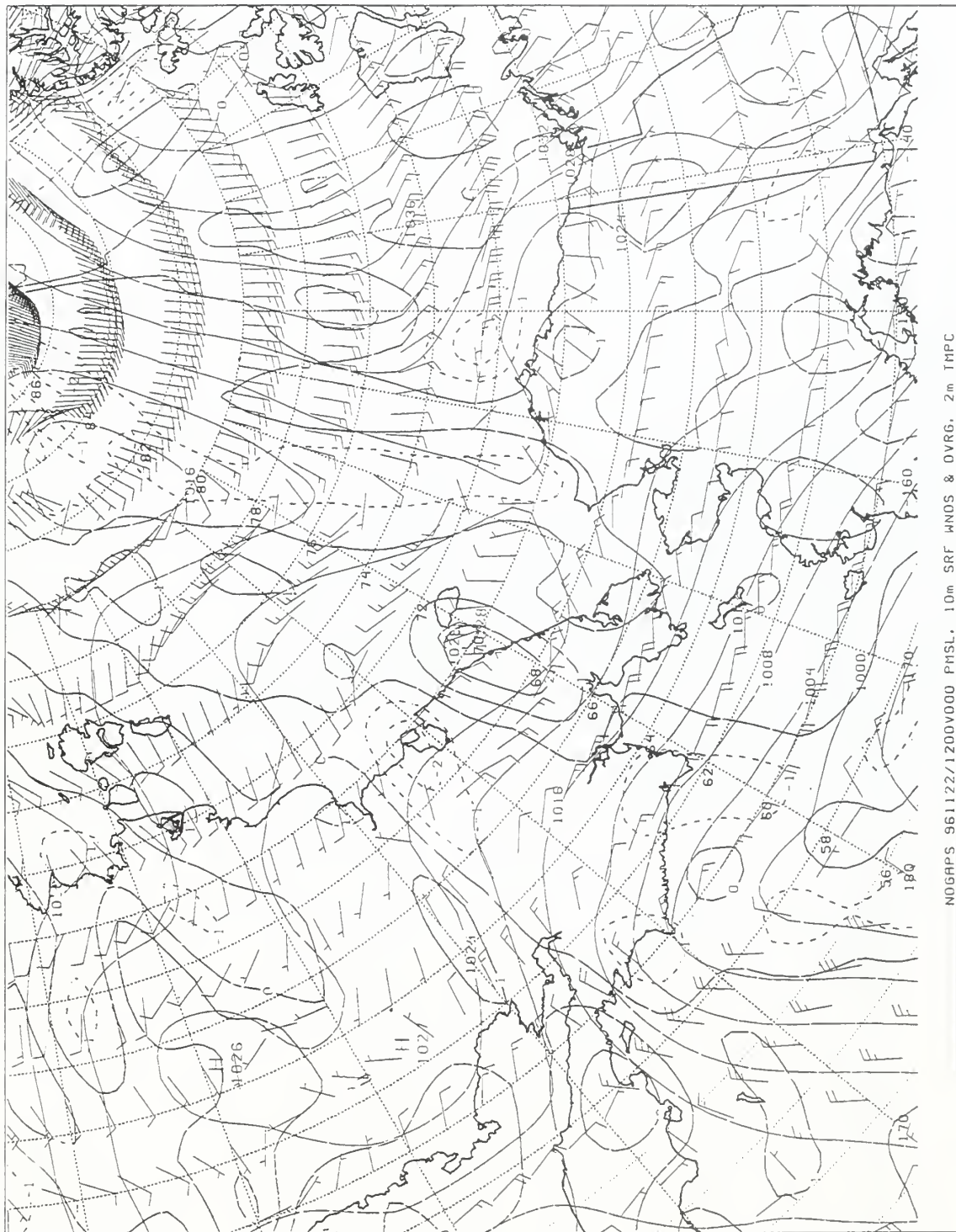


Figure 78. NOGAPS meteorological data for 0000Z 22 Nov 96.



NOGAPS 961122/1200V000 PMSL, 10m SRF ANOS & OVRG, 2m IMPC

Figure 79. NOGAPS meteorological data for 1200Z 22 Nov 96.

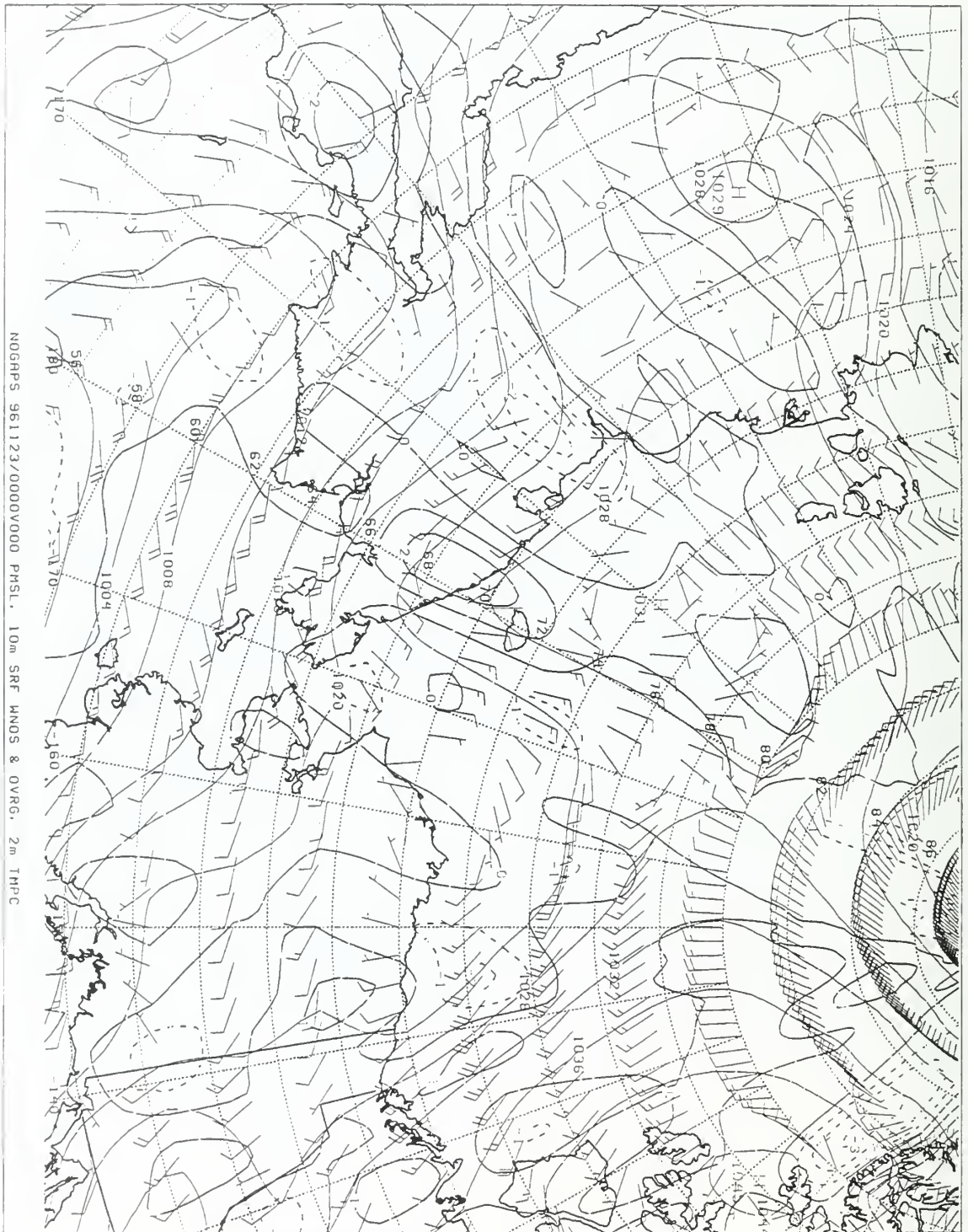
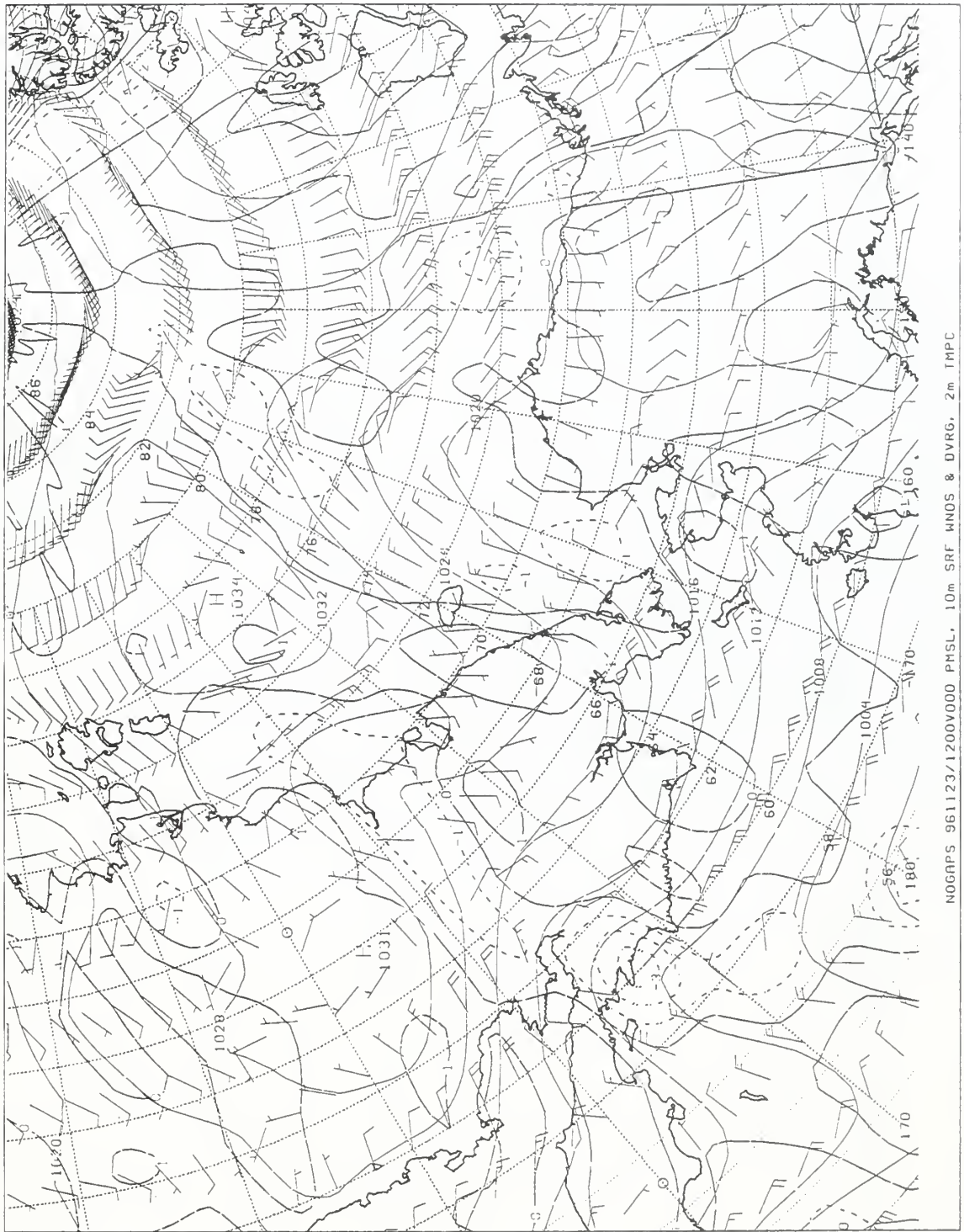


Figure 80. NOGAPS meteorological data for 0000Z 23 Nov 96.



NOGRPS 961123/1200V000 PMSL, 10m SRF WNOS & DVRG, 2m TMPC

Figure 81. NOGAPS meteorological data for 1200Z 23 Nov 96.

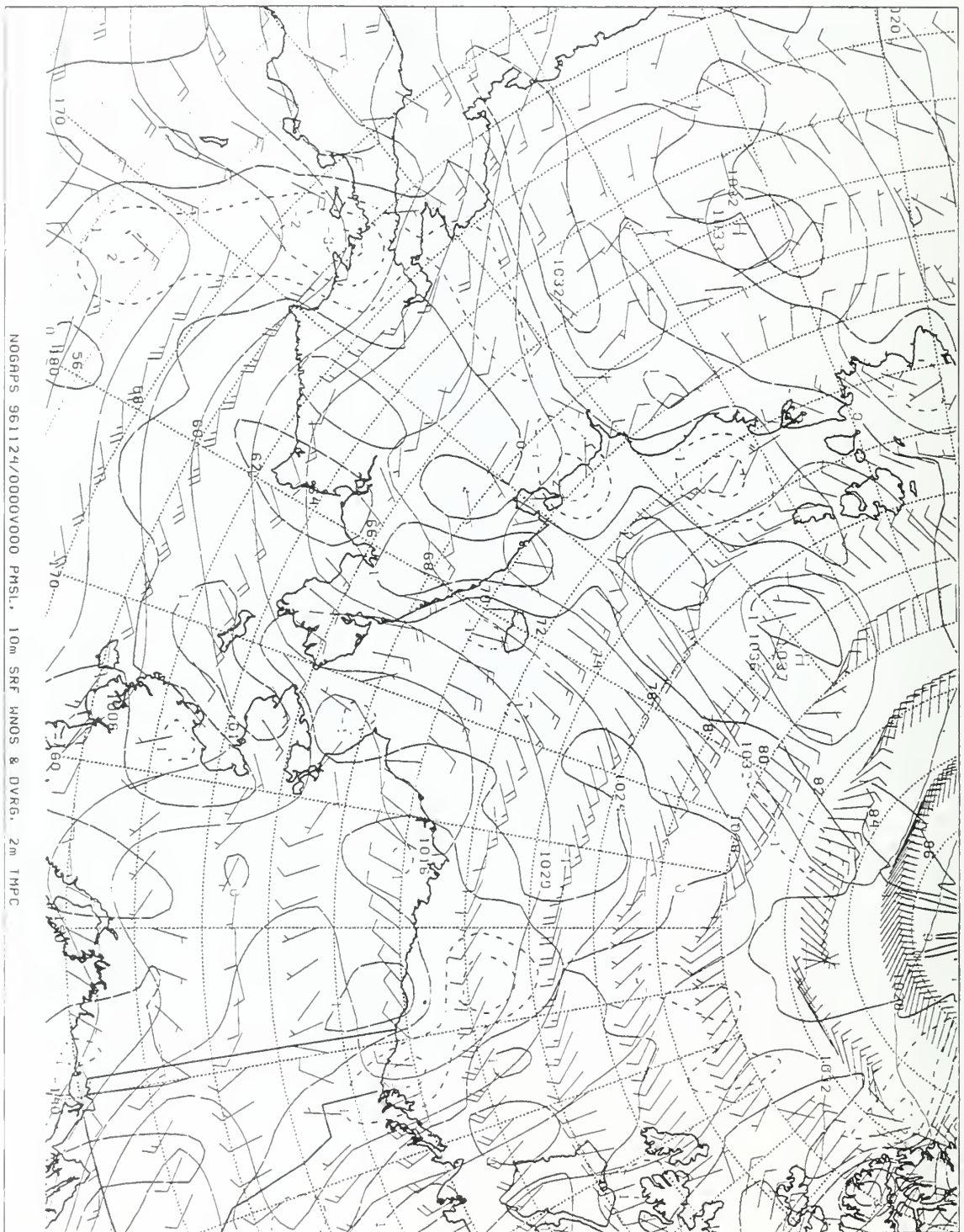


Figure 82. NOGAPS meteorological data for 0000Z 24 Nov 96.

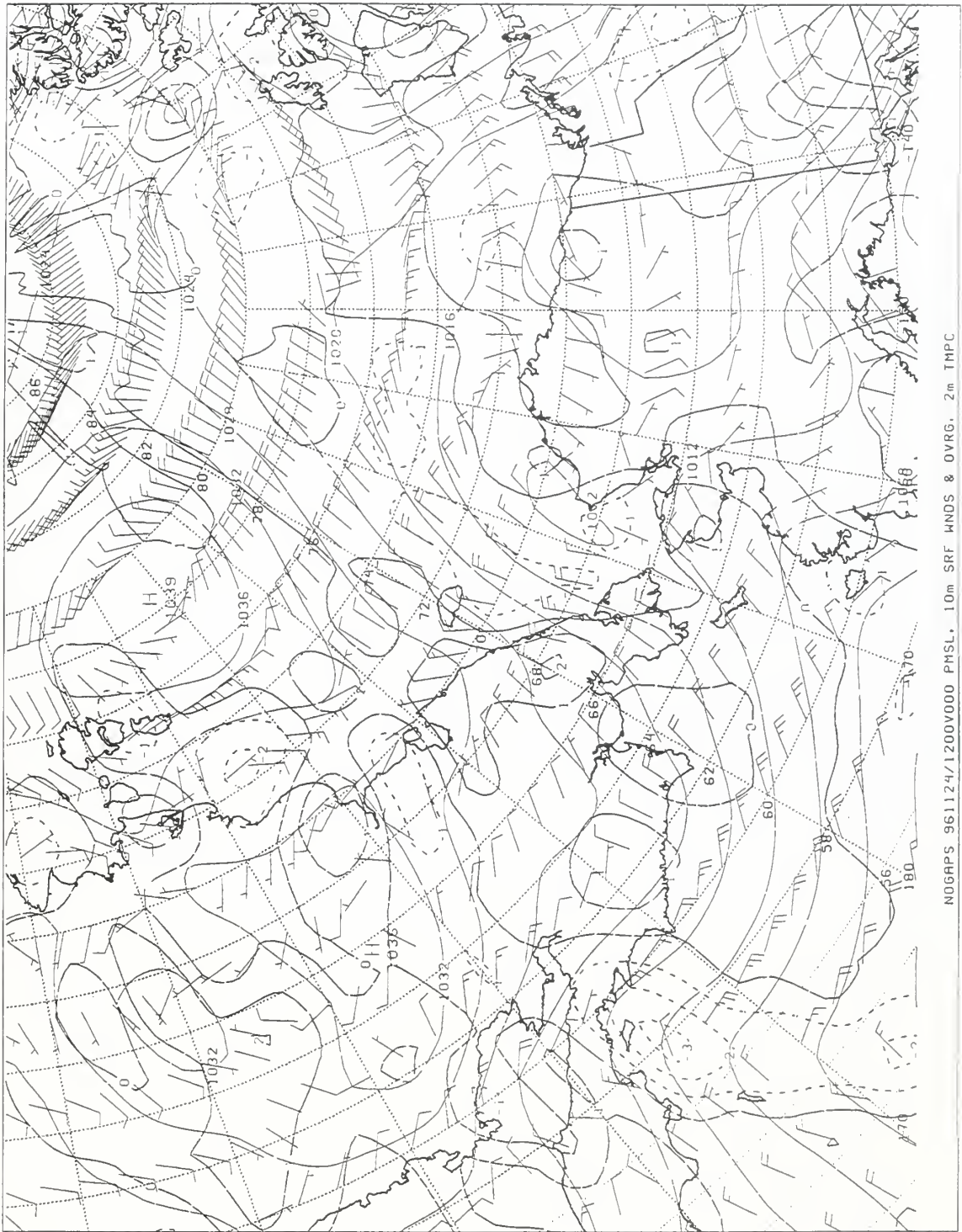


Figure 83. NOGAPS meteorological data for 1200Z 24 Nov 96.

APPENDIX F

**NOGAPS MODEL ICE DIVERGENCE DATA FOR RGPS ANALYSIS PERIOD:
07 TO 24 NOVEMBER 1996**

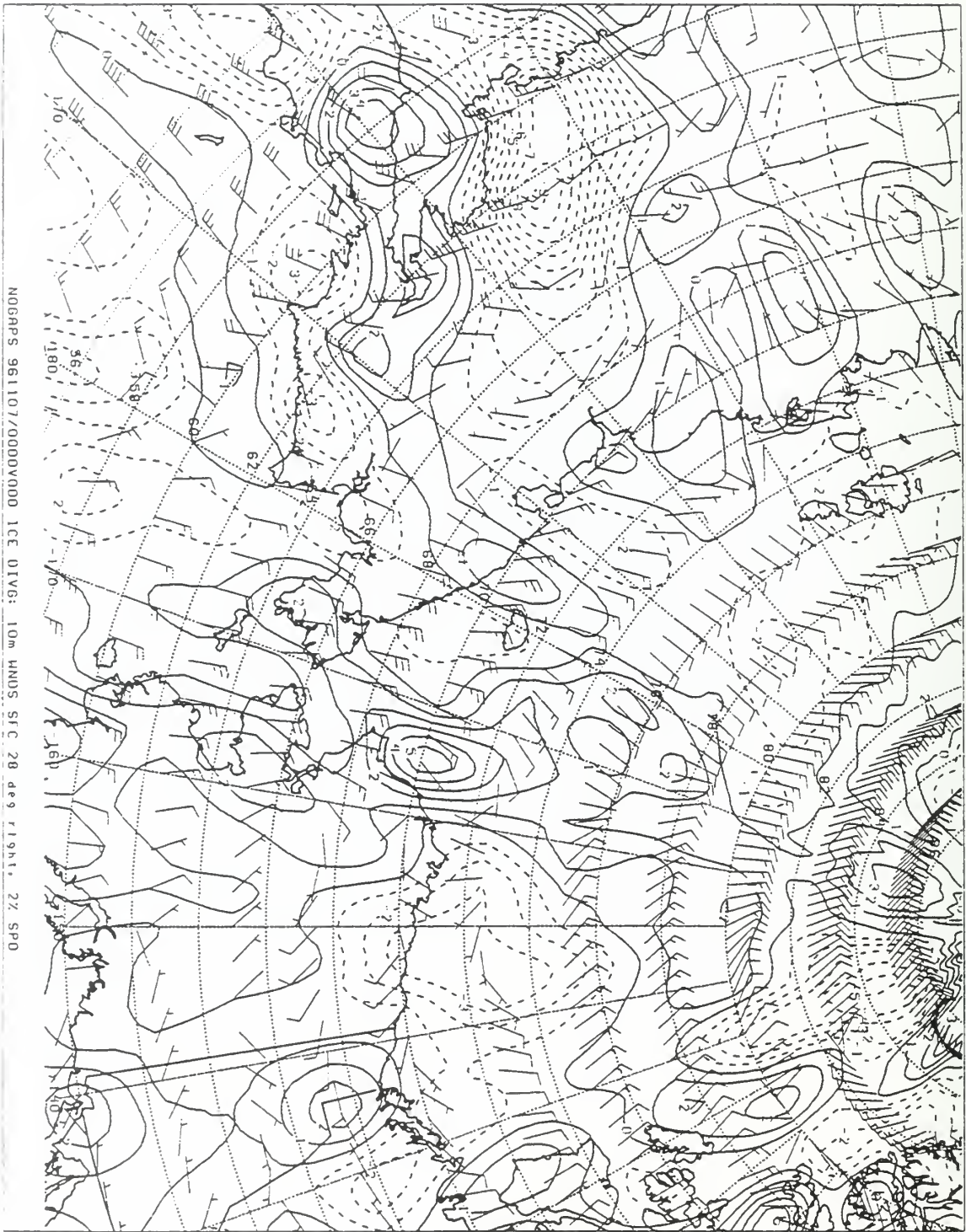


Figure 84. NOGAPS model ice divergence chart for 0000Z 07 Nov 96.



Figure 85. NOGAPS model ice divergence chart for 1200Z 07 Nov 96.

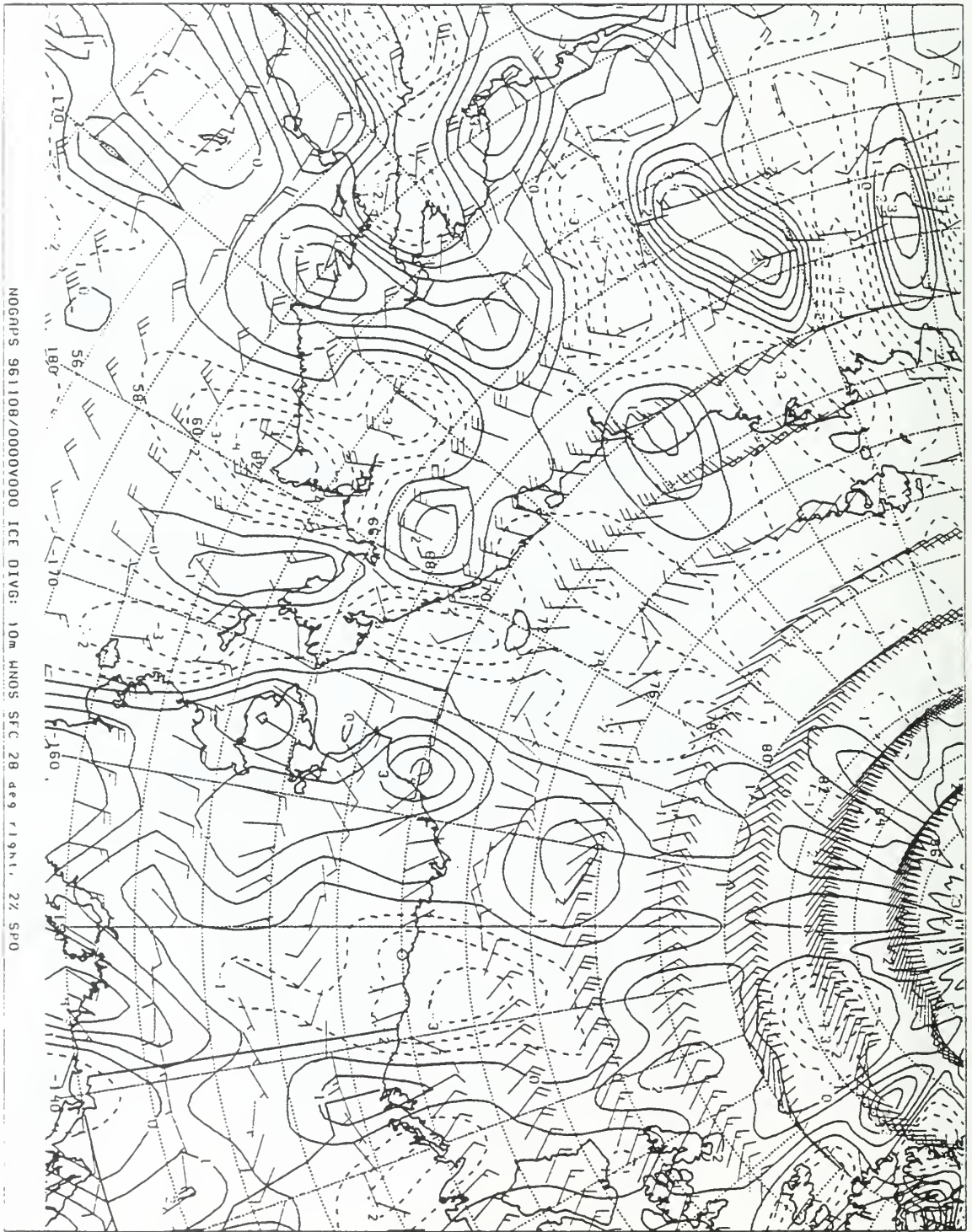


Figure 86. NOGAPS model ice divergence chart for 0000Z 08 Nov 96.

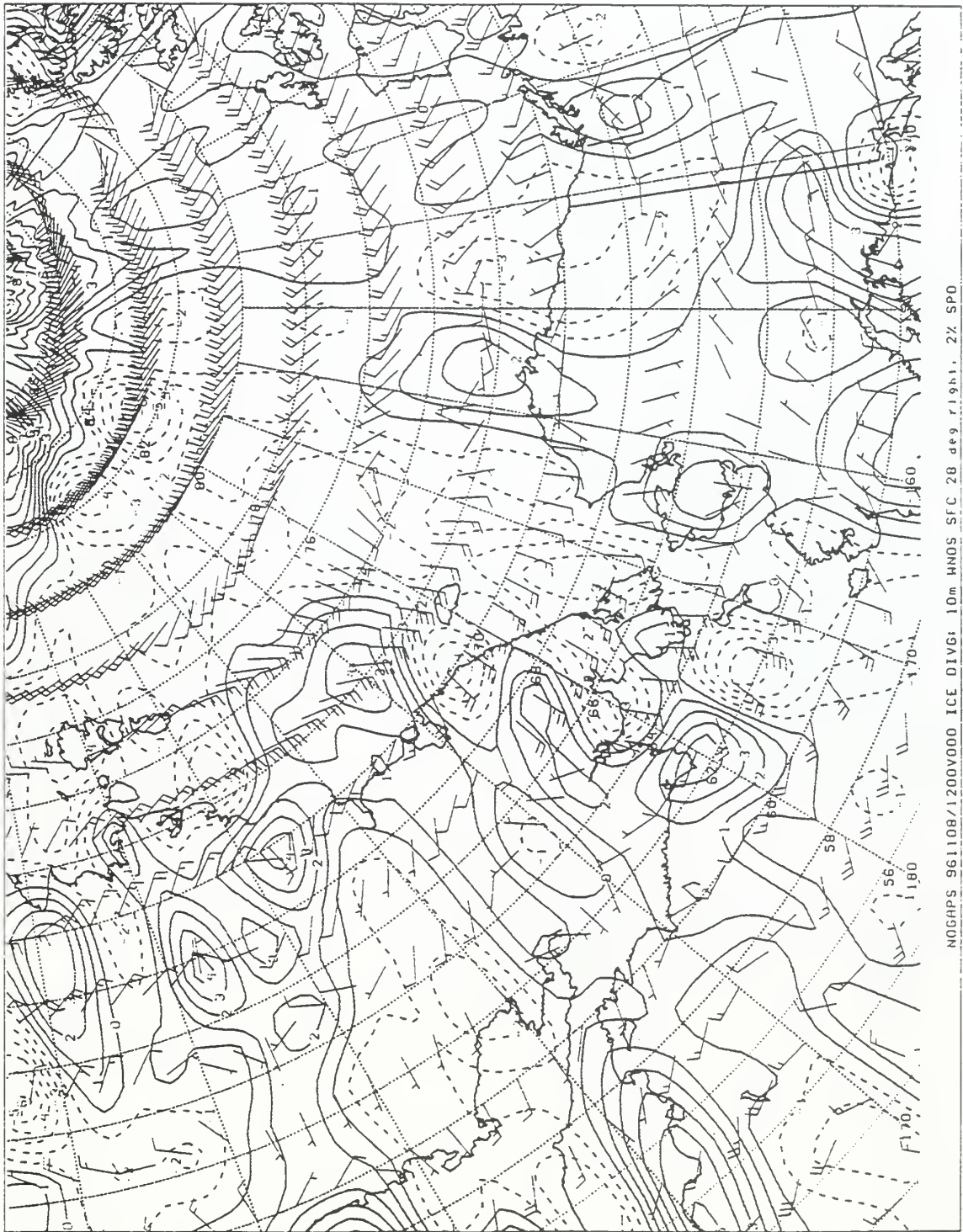


Figure 87. NOGAPS model ice divergence chart for 1200Z 08 Nov 96.

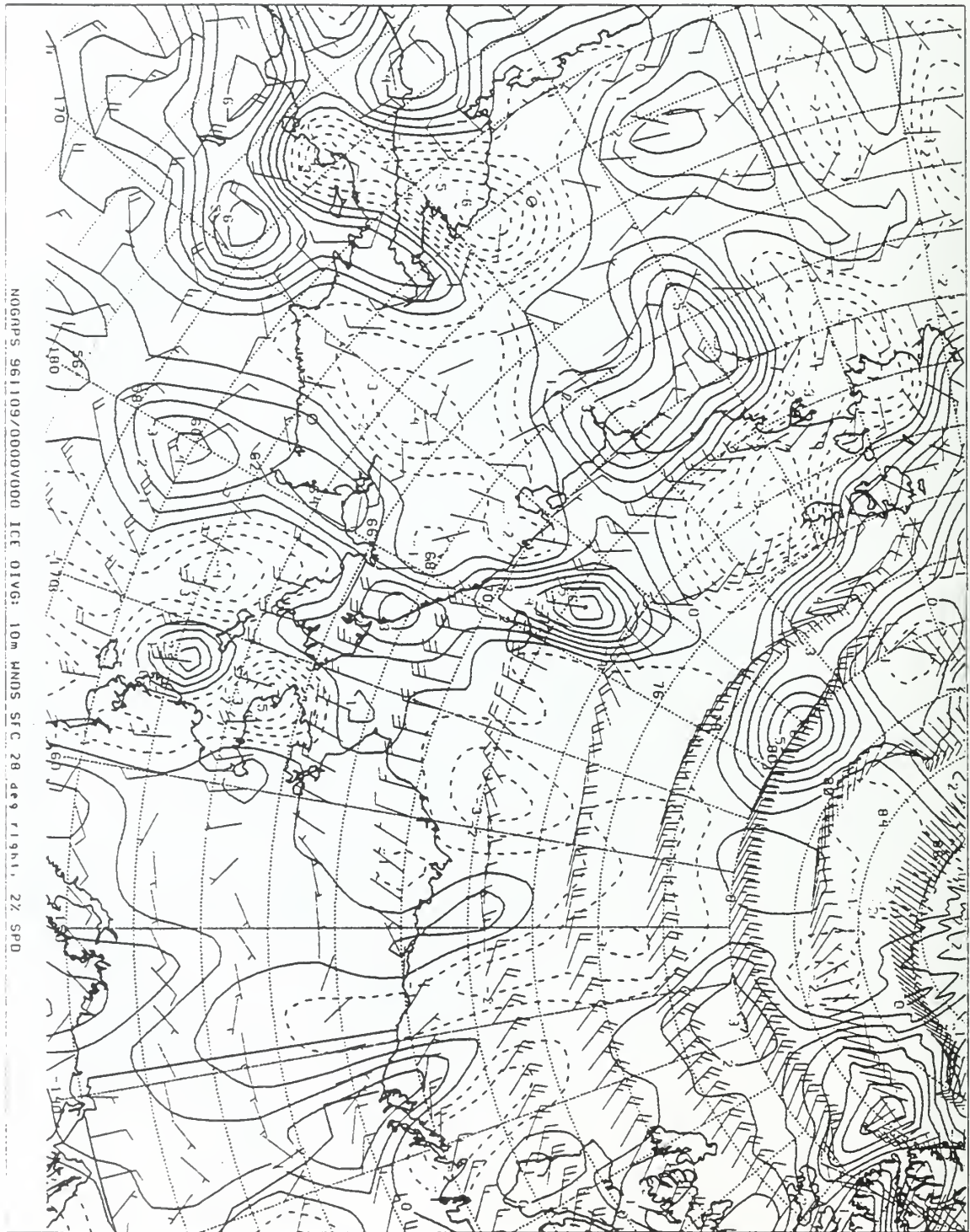


Figure 88. NOGAPS model ice divergence chart for 0000Z 09 Nov 96.

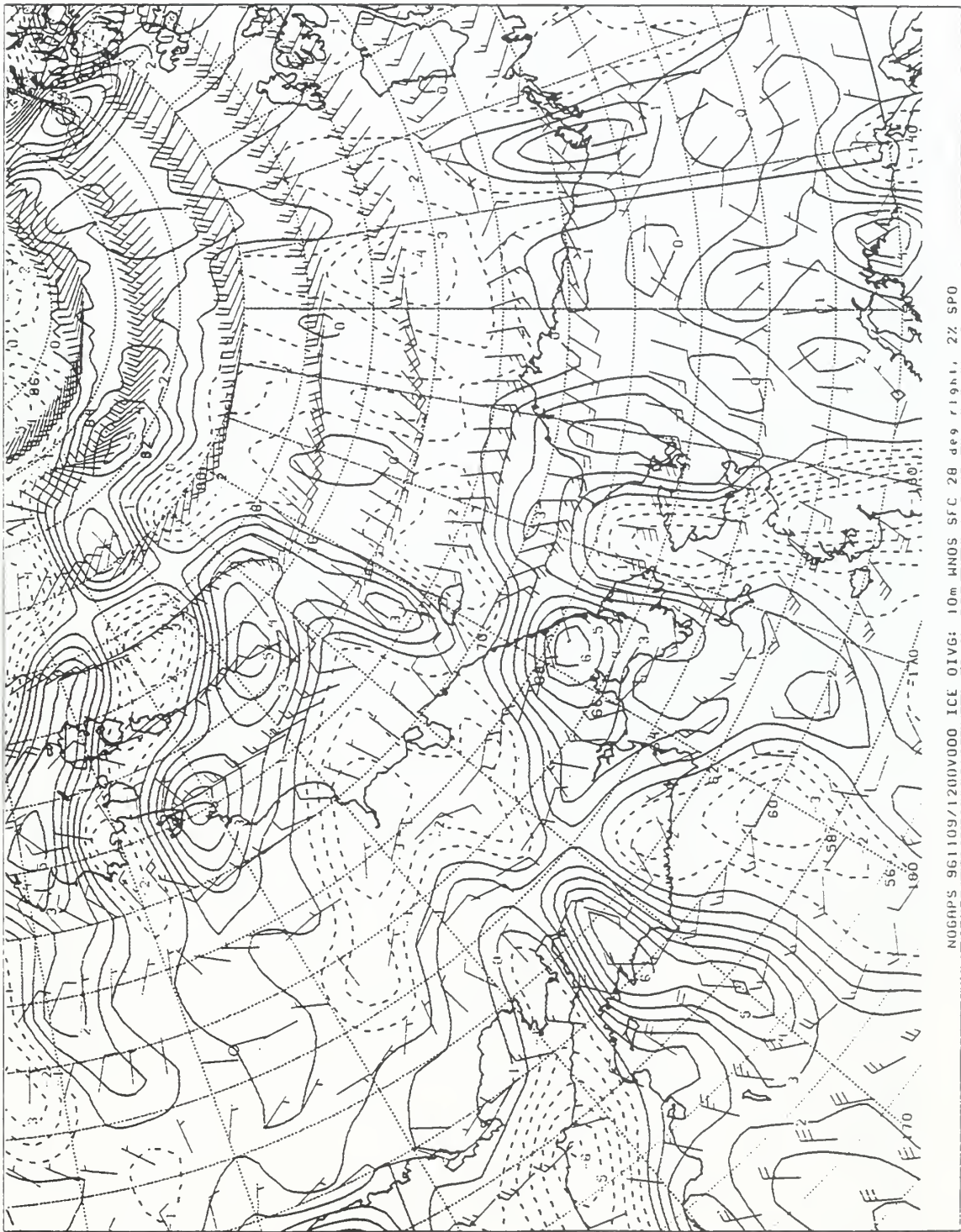


Figure 89. NOGAPS model ice divergence chart for 1200Z 09 Nov 96.

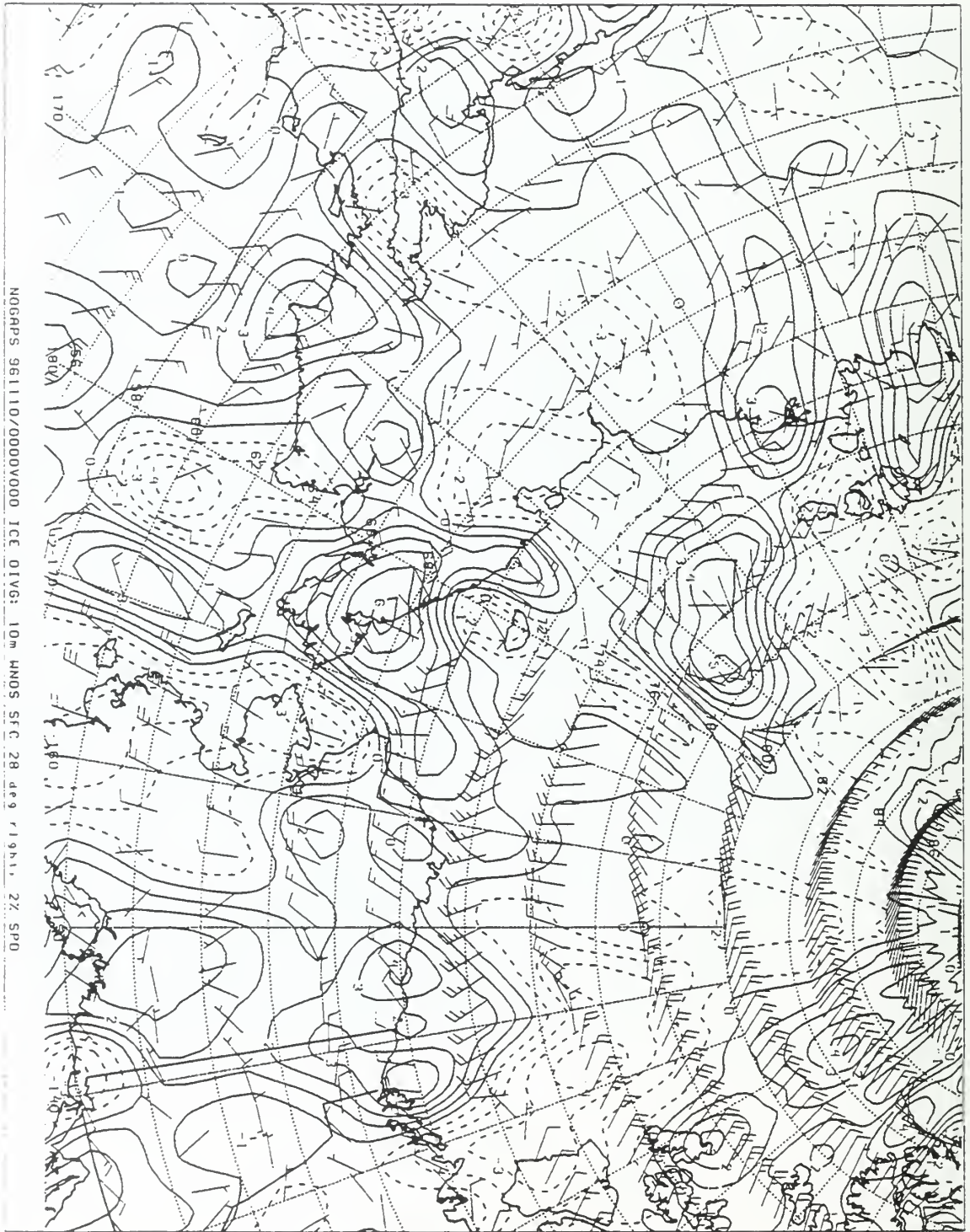


Figure 90. NOGAPS model ice divergence chart for 0000Z 10 Nov 96.



Figure 91. NOGAPS model ice divergence chart for 1200Z 10 Nov 96.

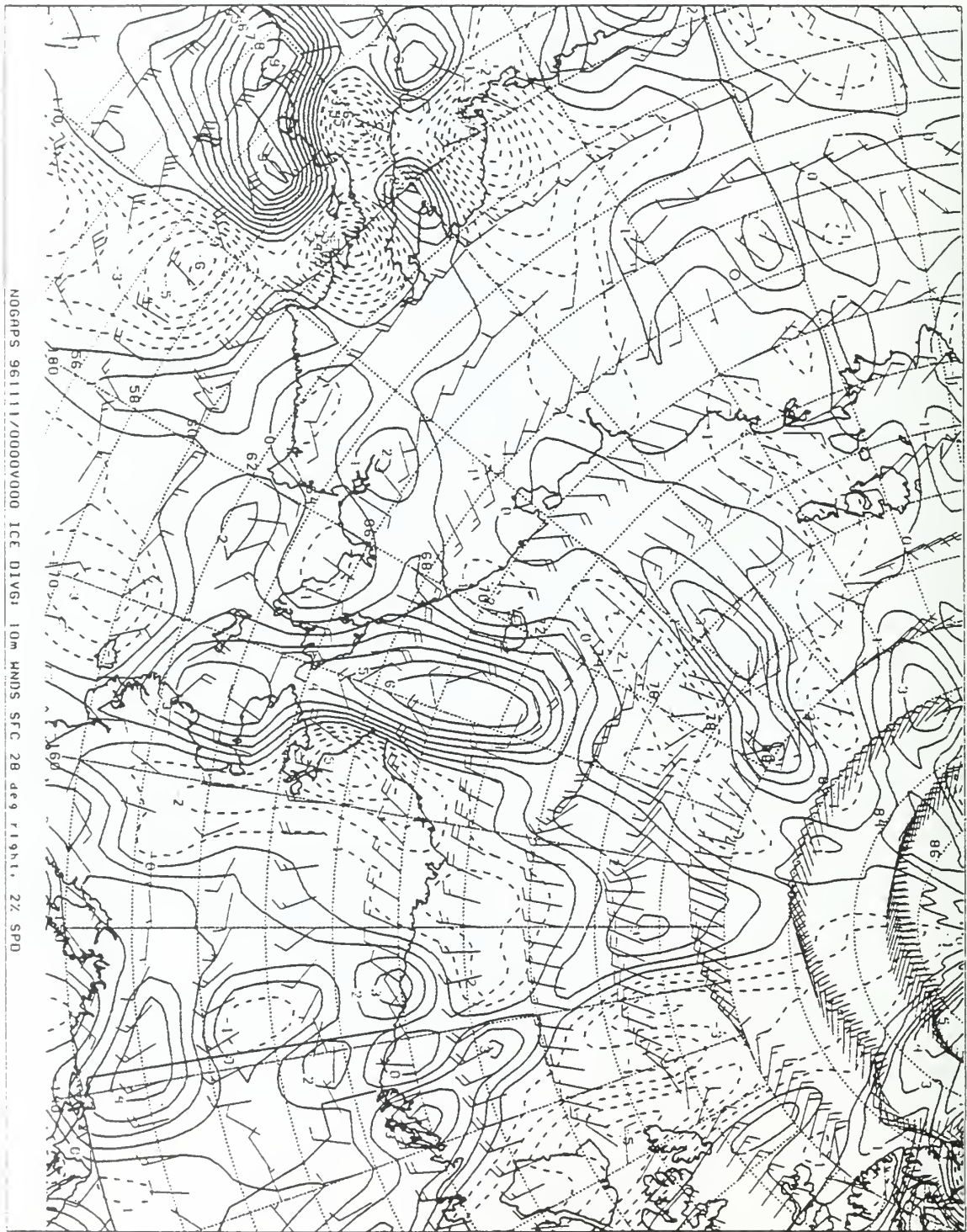


Figure 92. NOGAPS model ice divergence chart for 0000Z 11 Nov 96.



Figure 93. NOGAPS model ice divergence chart for 1200Z 11 Nov 96.

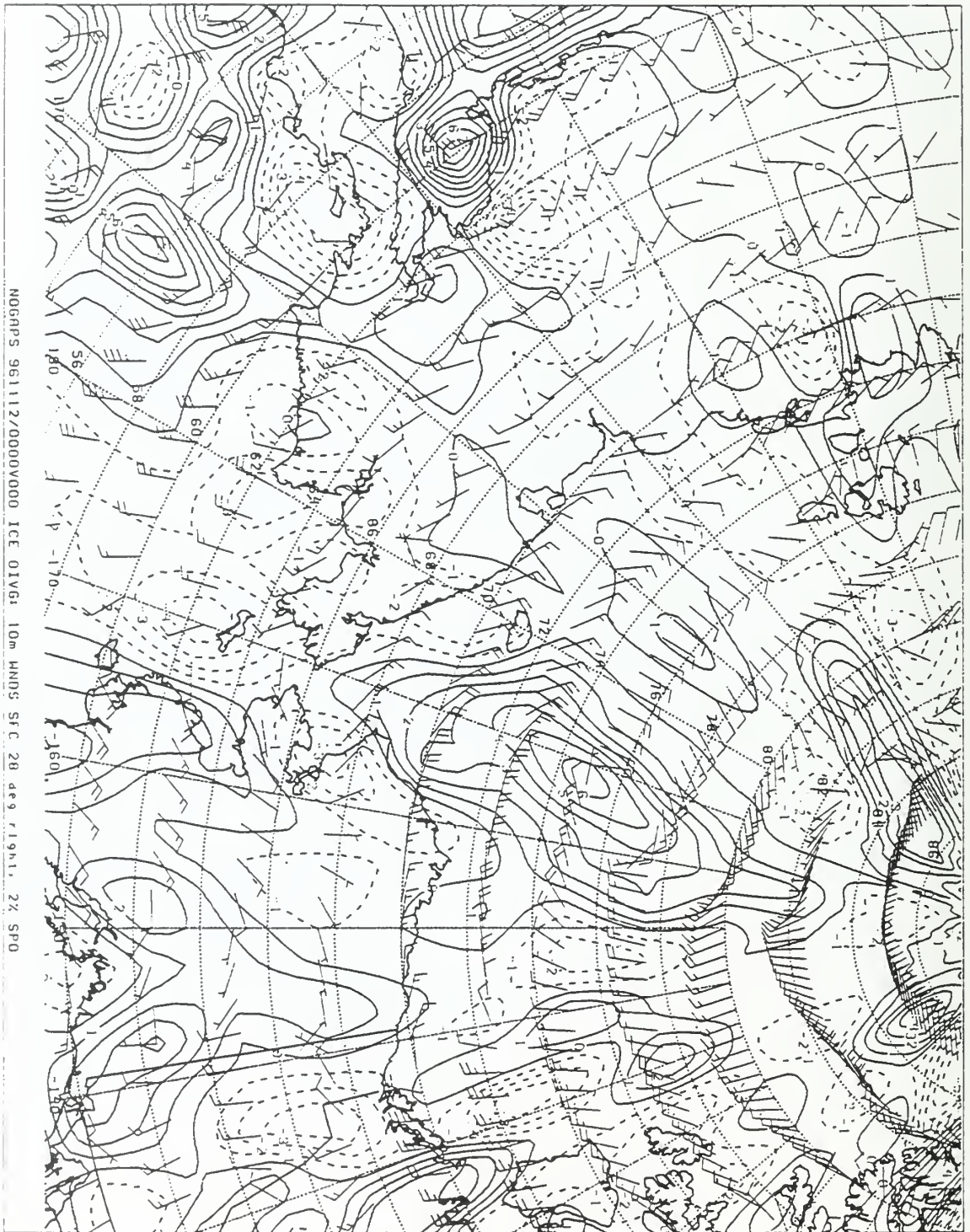


Figure 94. NOGAPS model ice divergence chart for 0000Z 12 Nov 96.

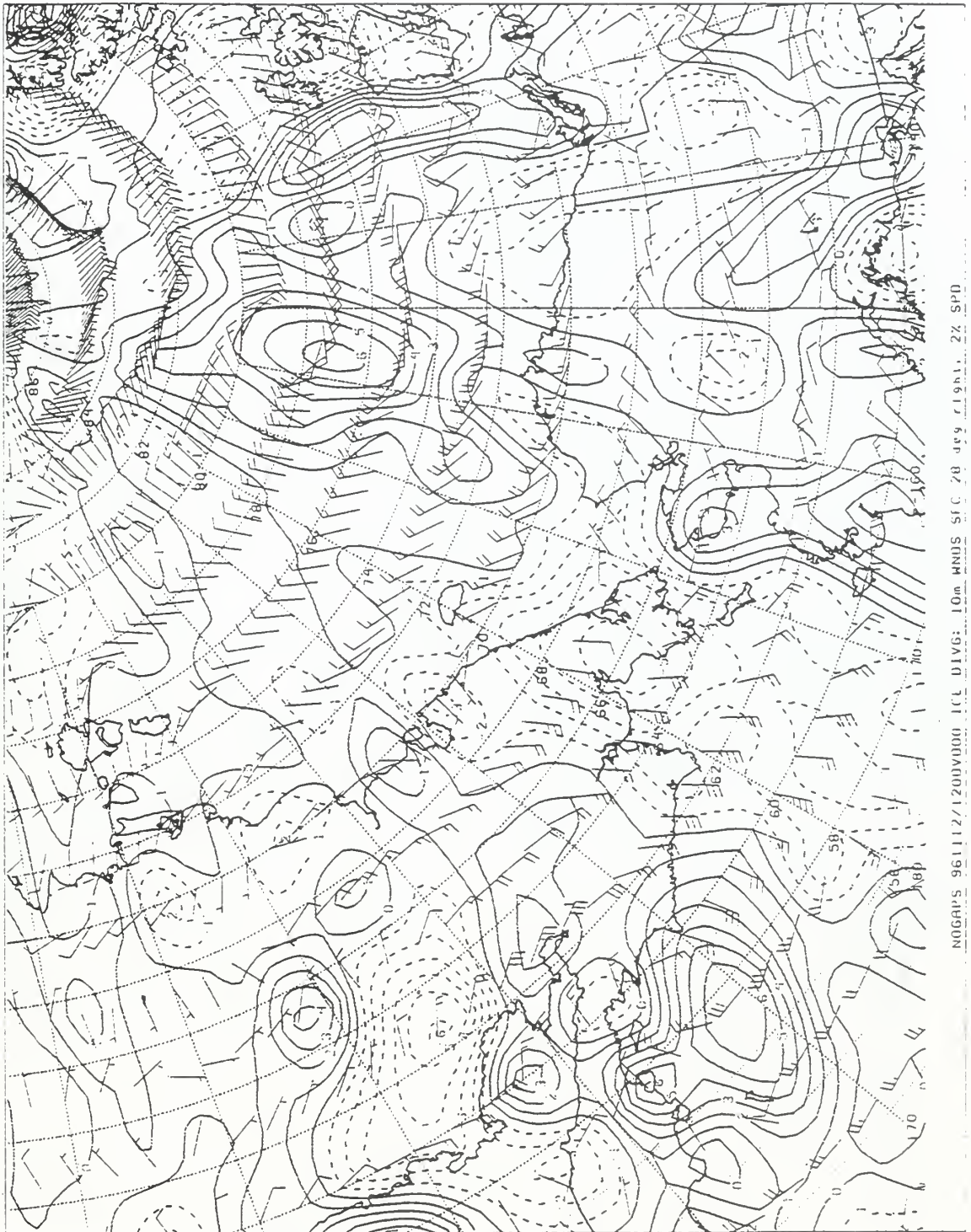


Figure 95. NOGAPS model ice divergence chart for 1200Z 12 Nov 96.

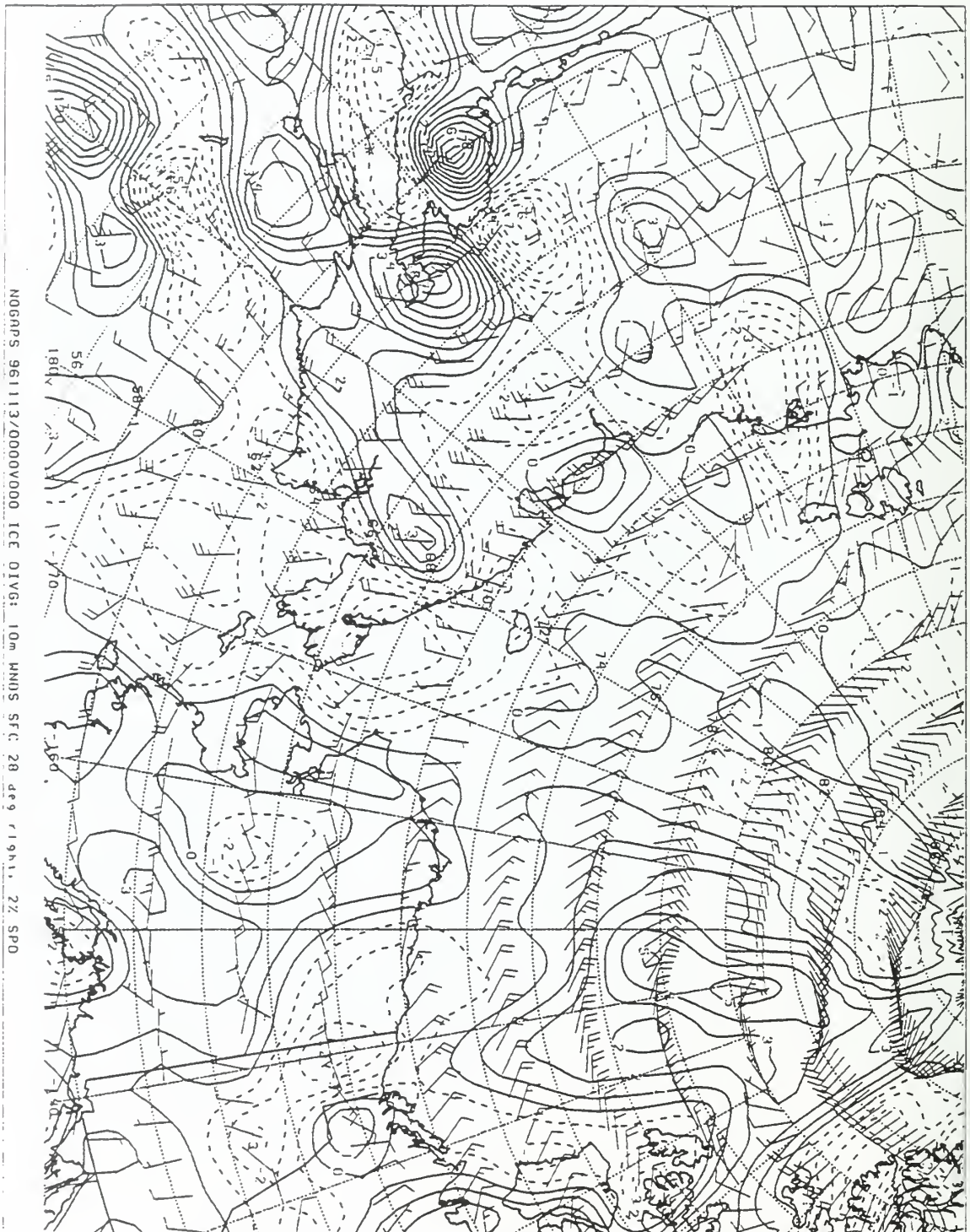


Figure 96. NOGAPS model ice divergence chart for 0000Z 13 Nov 96.

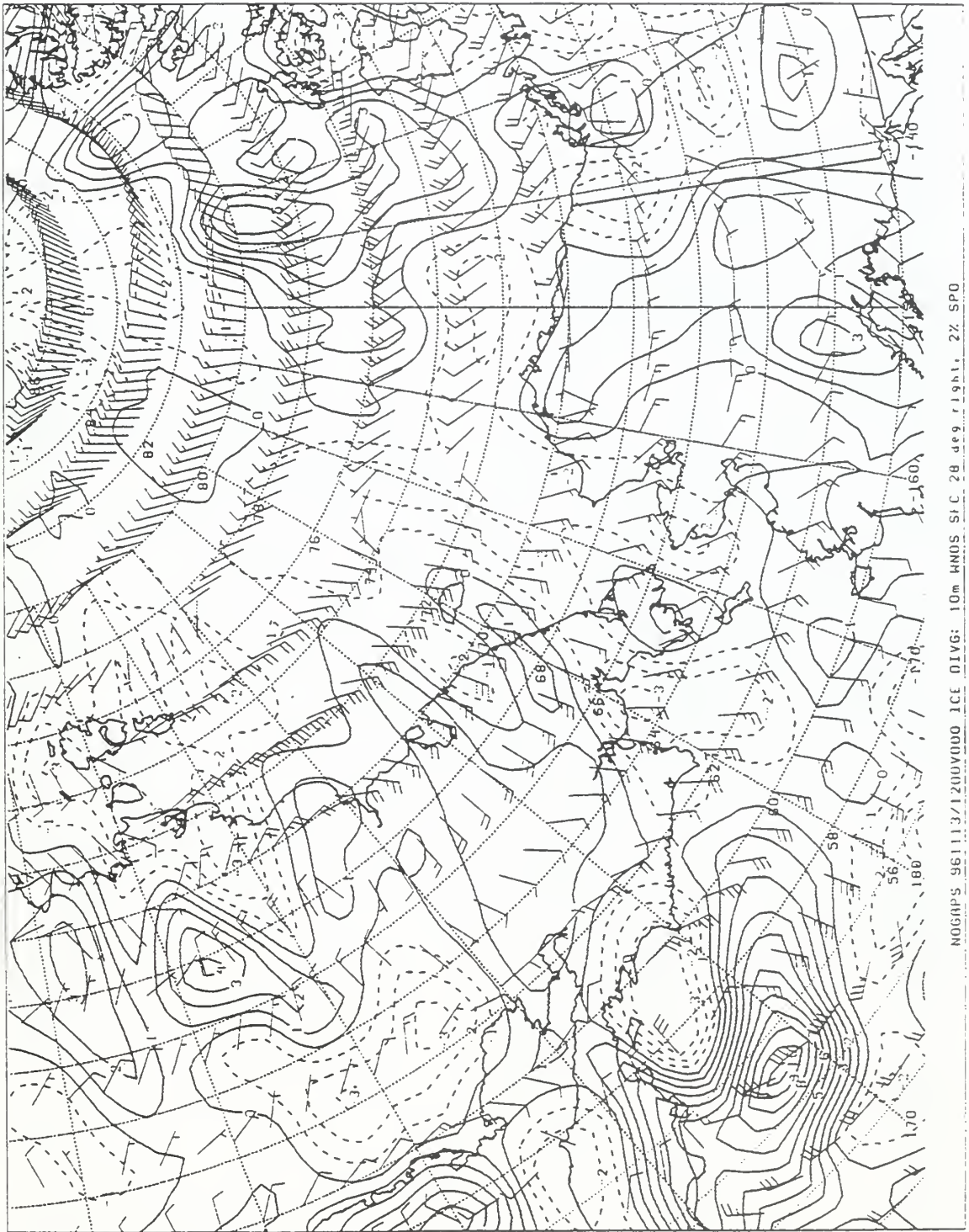


Figure 97. NOGAPS model ice divergence chart for 1200Z 13 Nov 96.

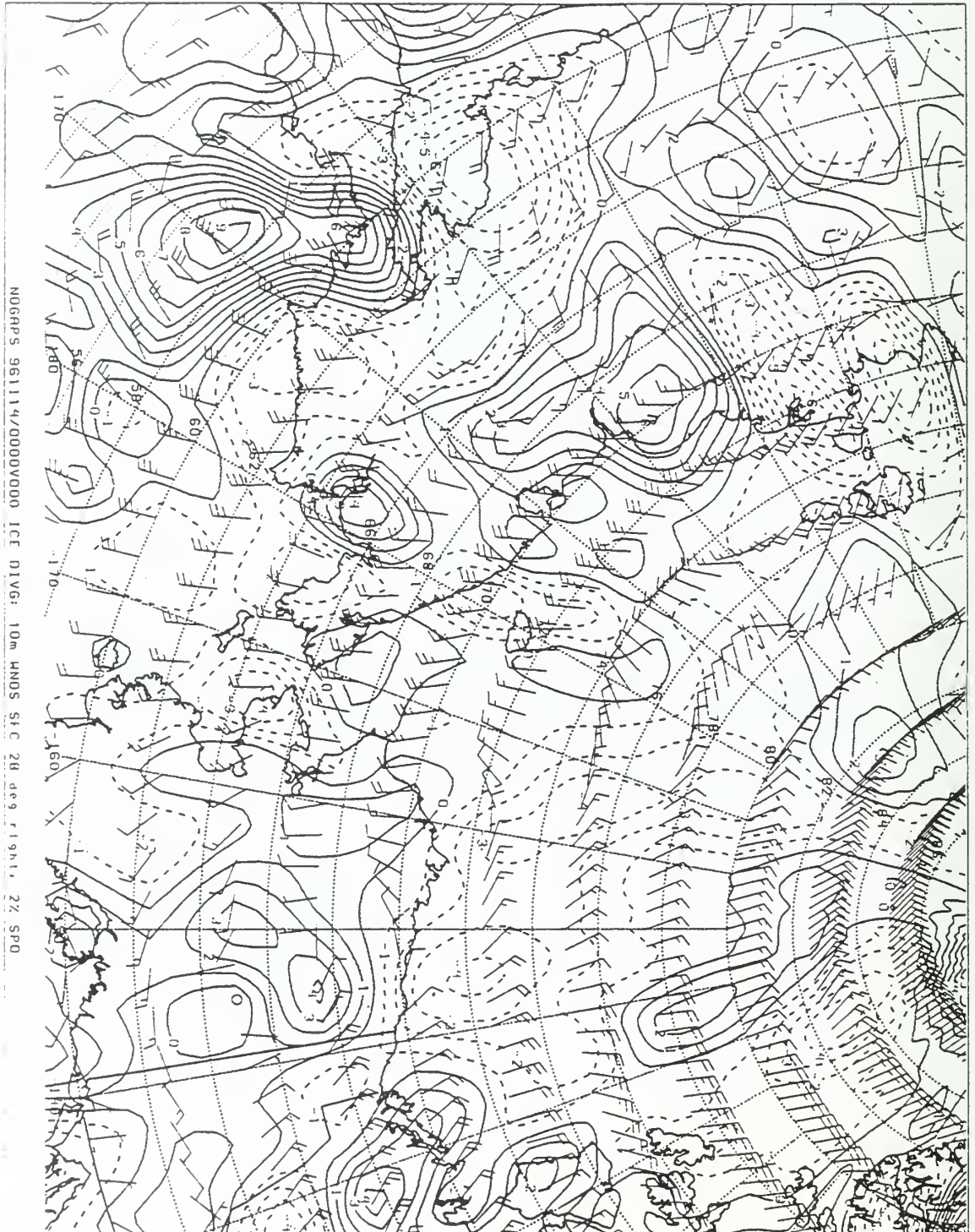


Figure 98. NOGAPS model ice divergence chart for 0000Z 14 Nov 96.



Figure 99. NOGAPS model ice divergence chart for 1200Z 14 Nov 96.

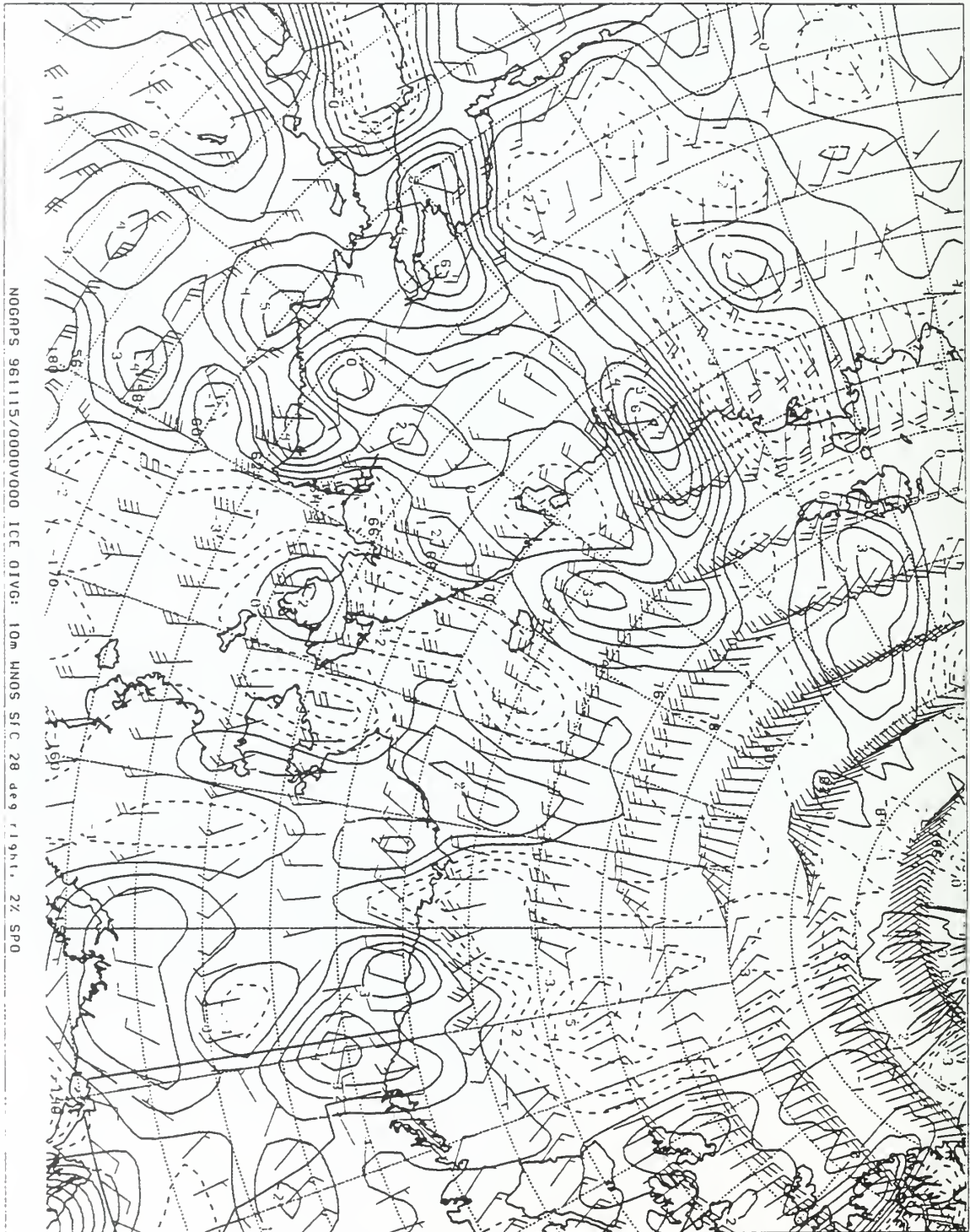


Figure 100. NOGAPS model ice divergence chart for 0000Z 15 Nov 96.

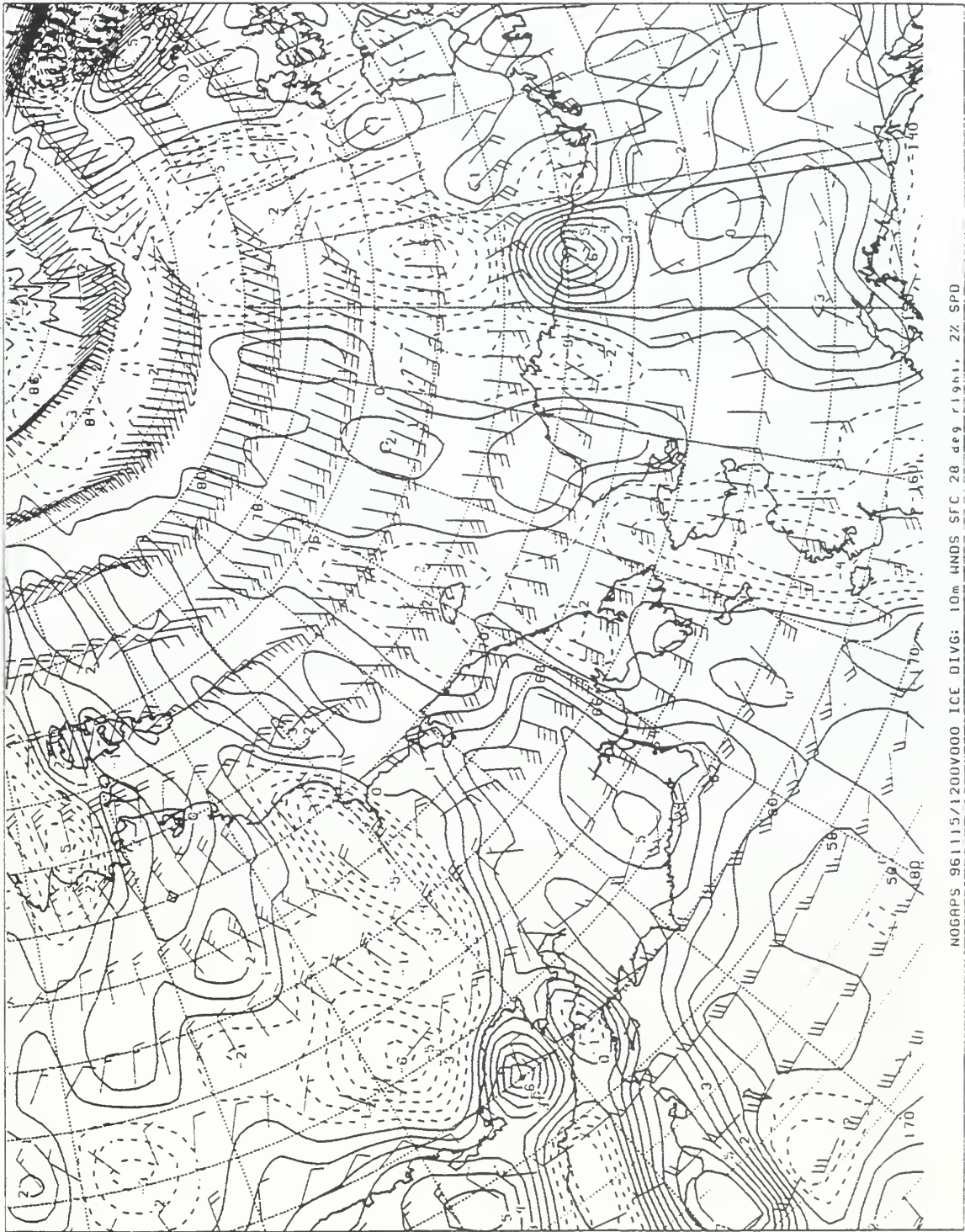


Figure 101. NOGAPS model ice divergence chart for 1200Z 15 Nov 96.

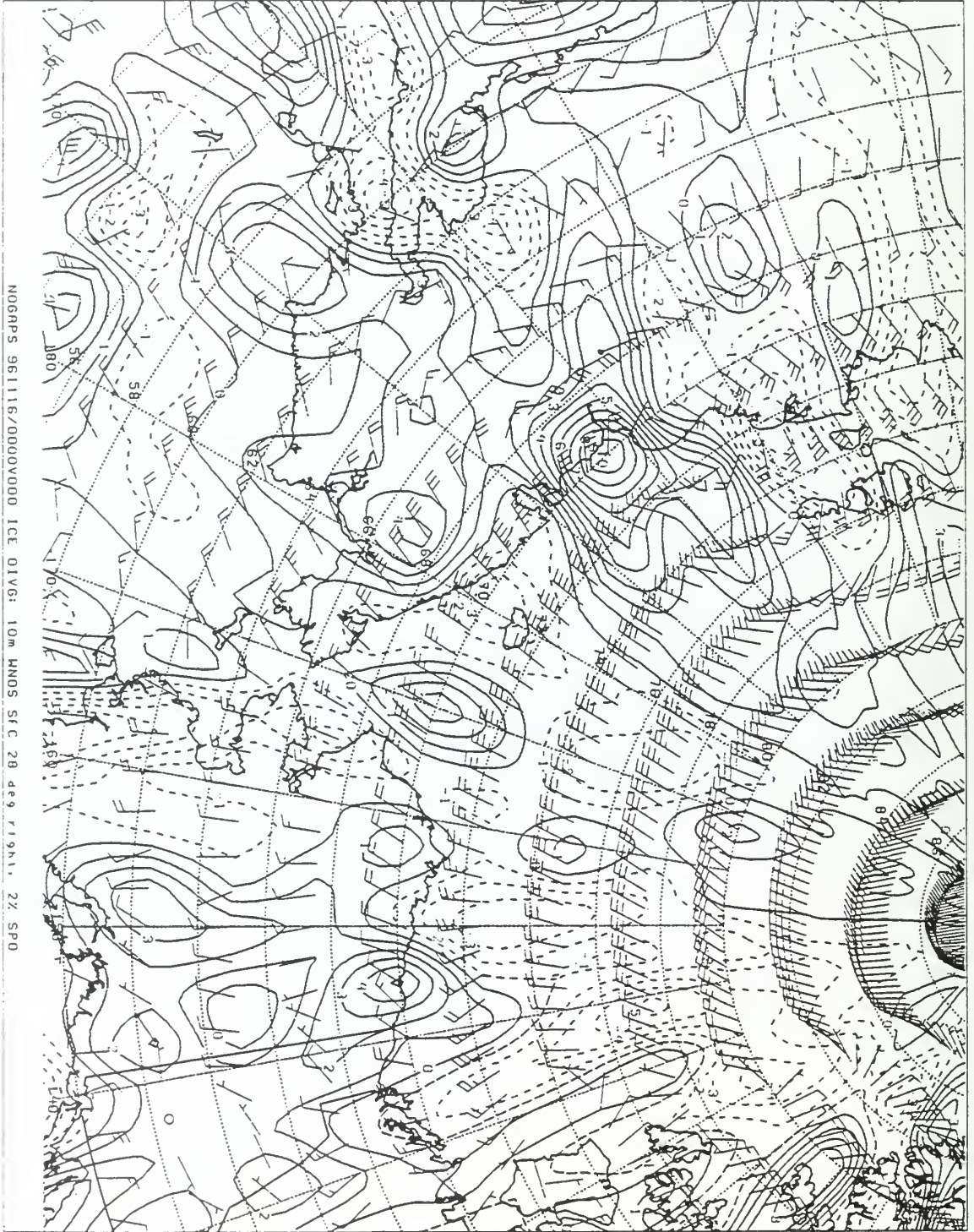


Figure 102. NOGAPS model ice divergence chart for 0000Z 16 Nov 96.

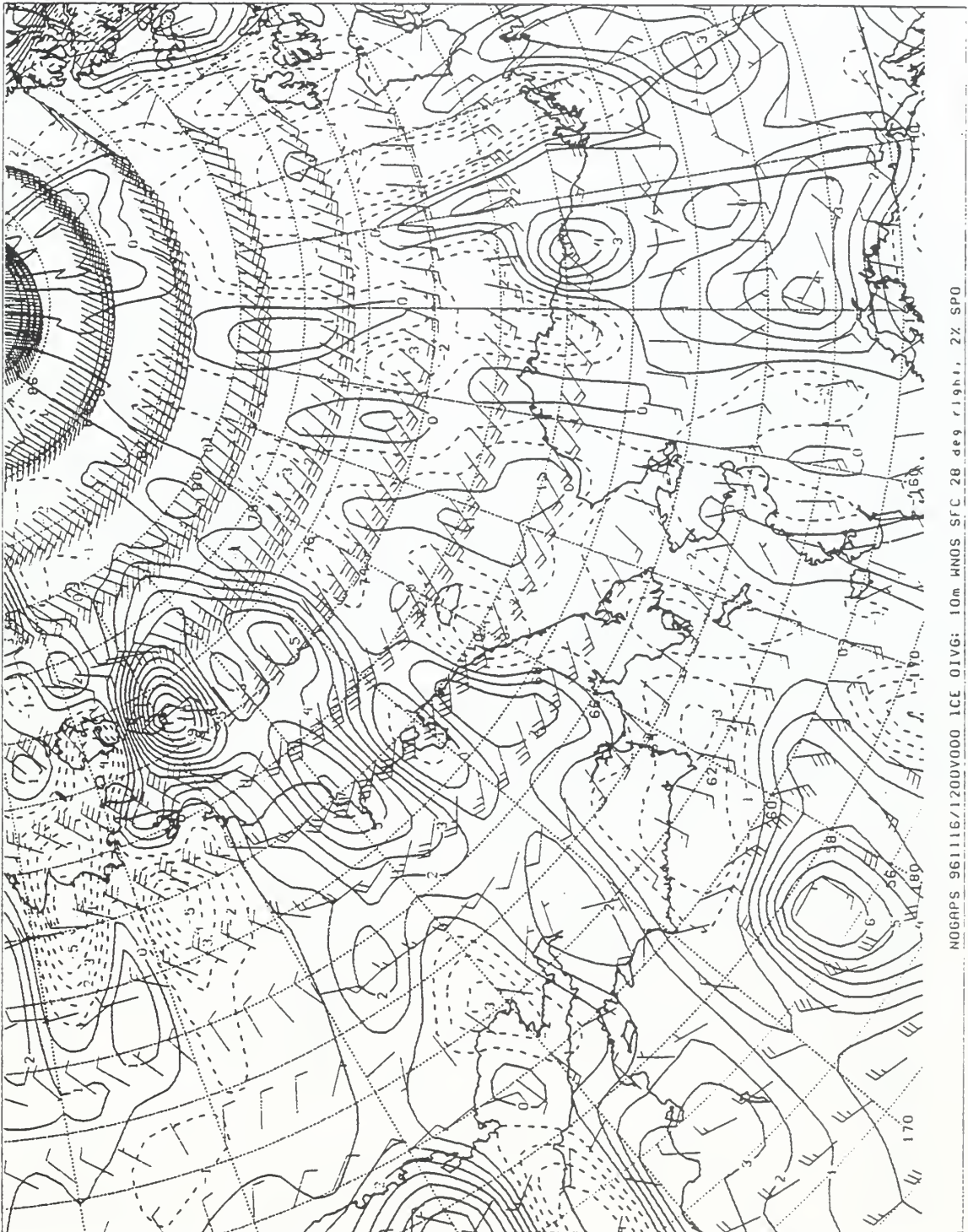


Figure 103. NOGAPS model ice divergence chart for 1200Z 16 Nov 96.

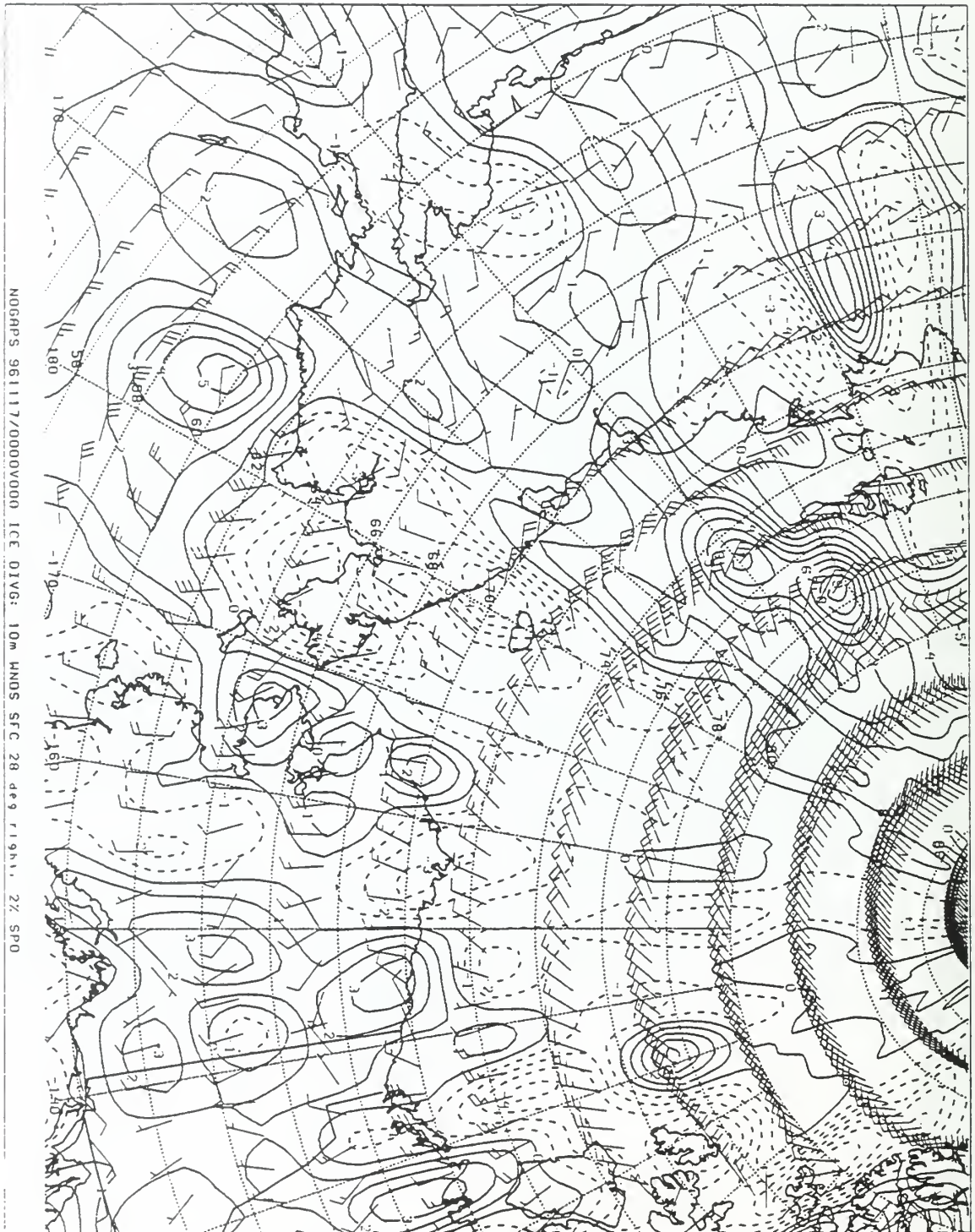


Figure 104. NOGAPS model ice divergence chart for 0000Z 17 Nov 96.

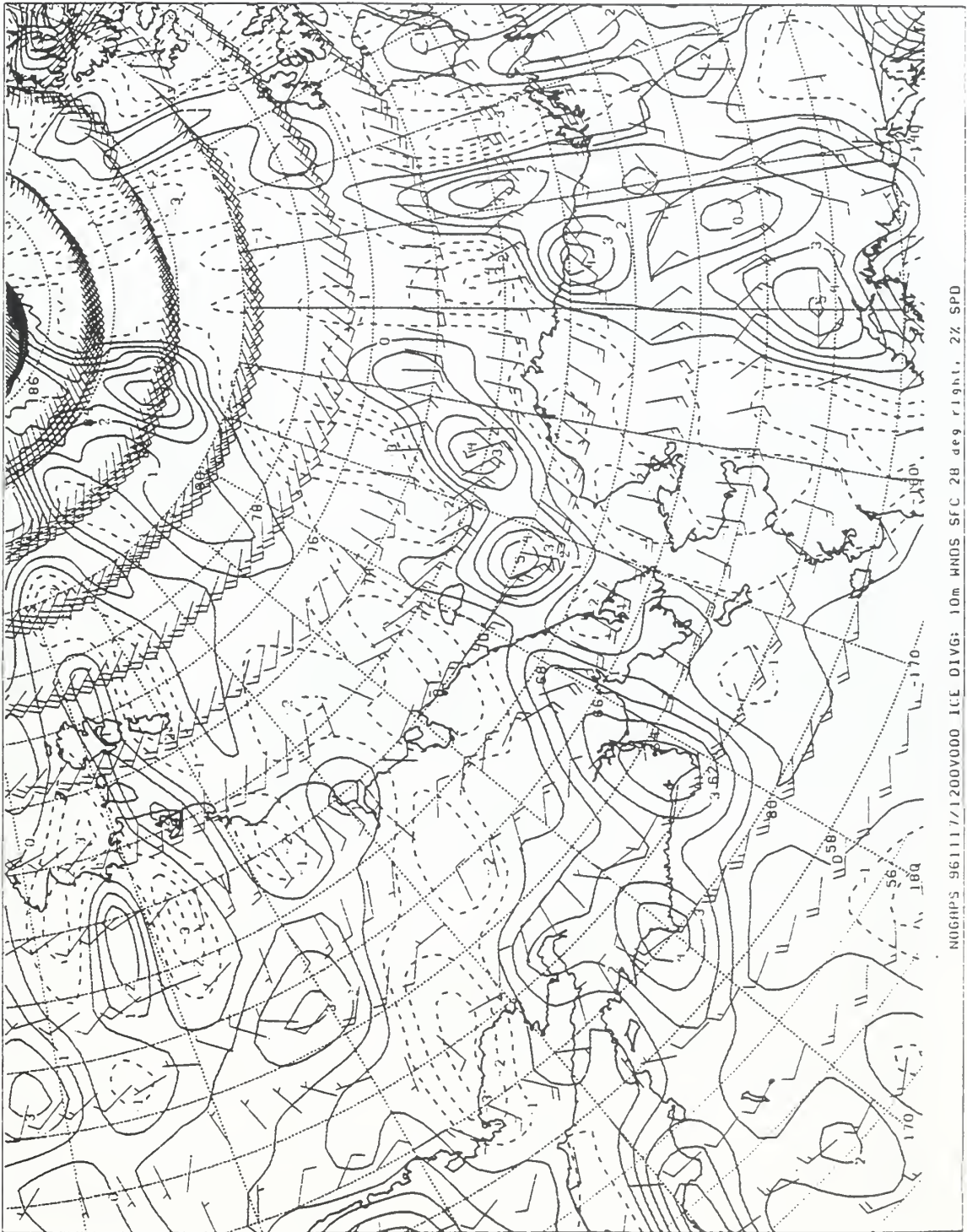


Figure 105. NOGAPS model ice divergence chart for 1200Z 17 Nov 96.

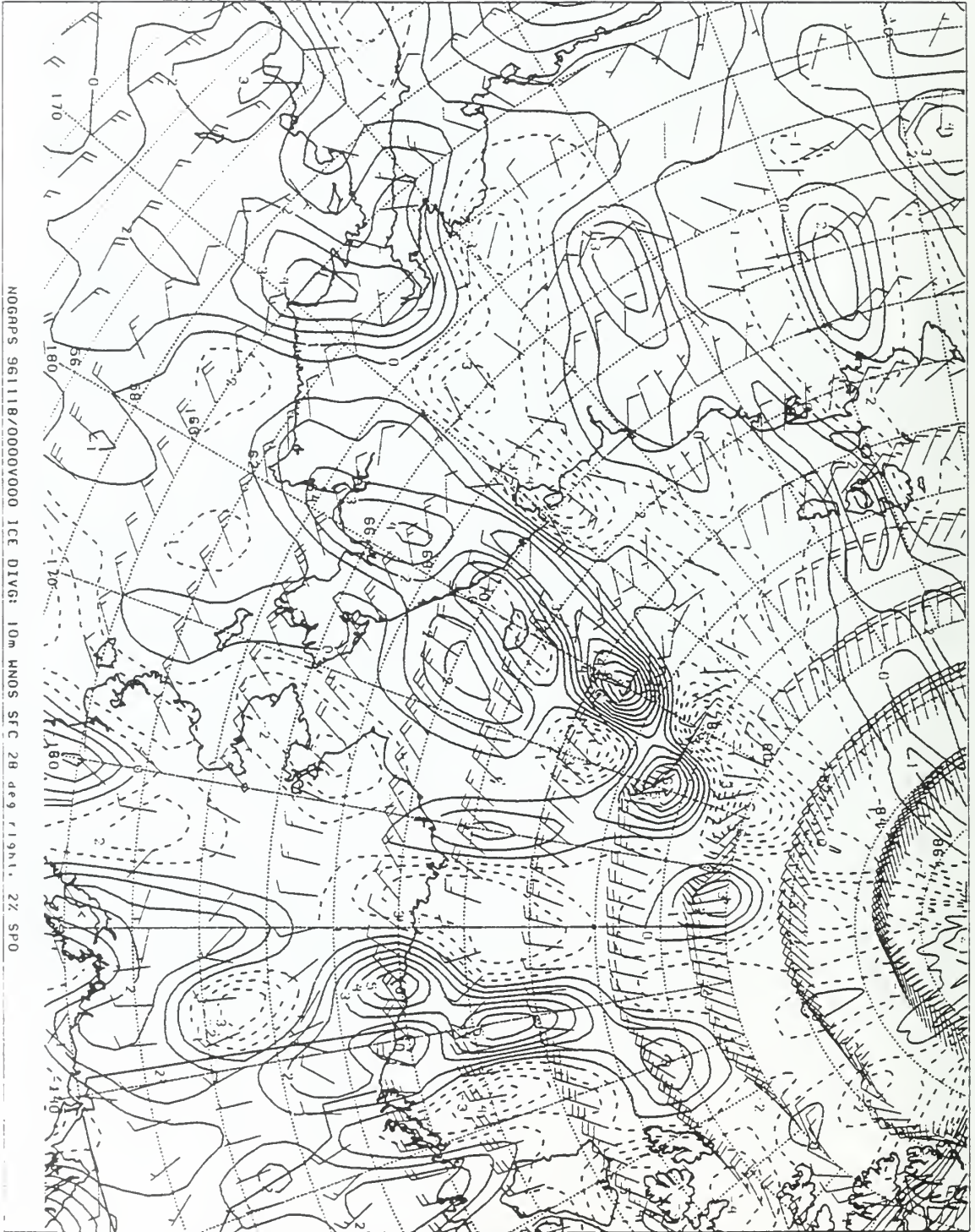


Figure 106. NOGAPS model ice divergence chart for 0000Z 18 Nov 96.

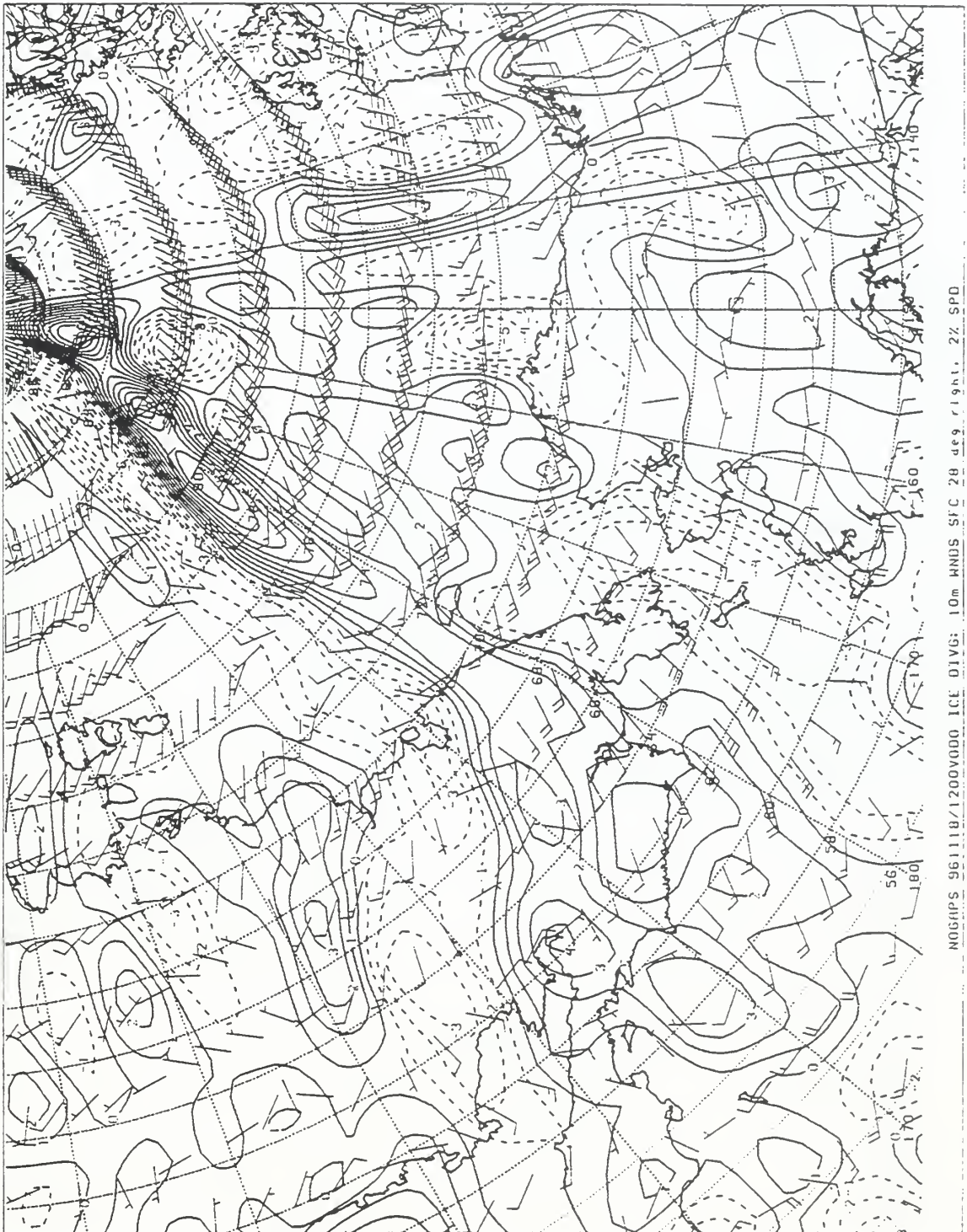


Figure 107. NOGAPS model ice divergence chart for 1200Z 18 Nov 96.

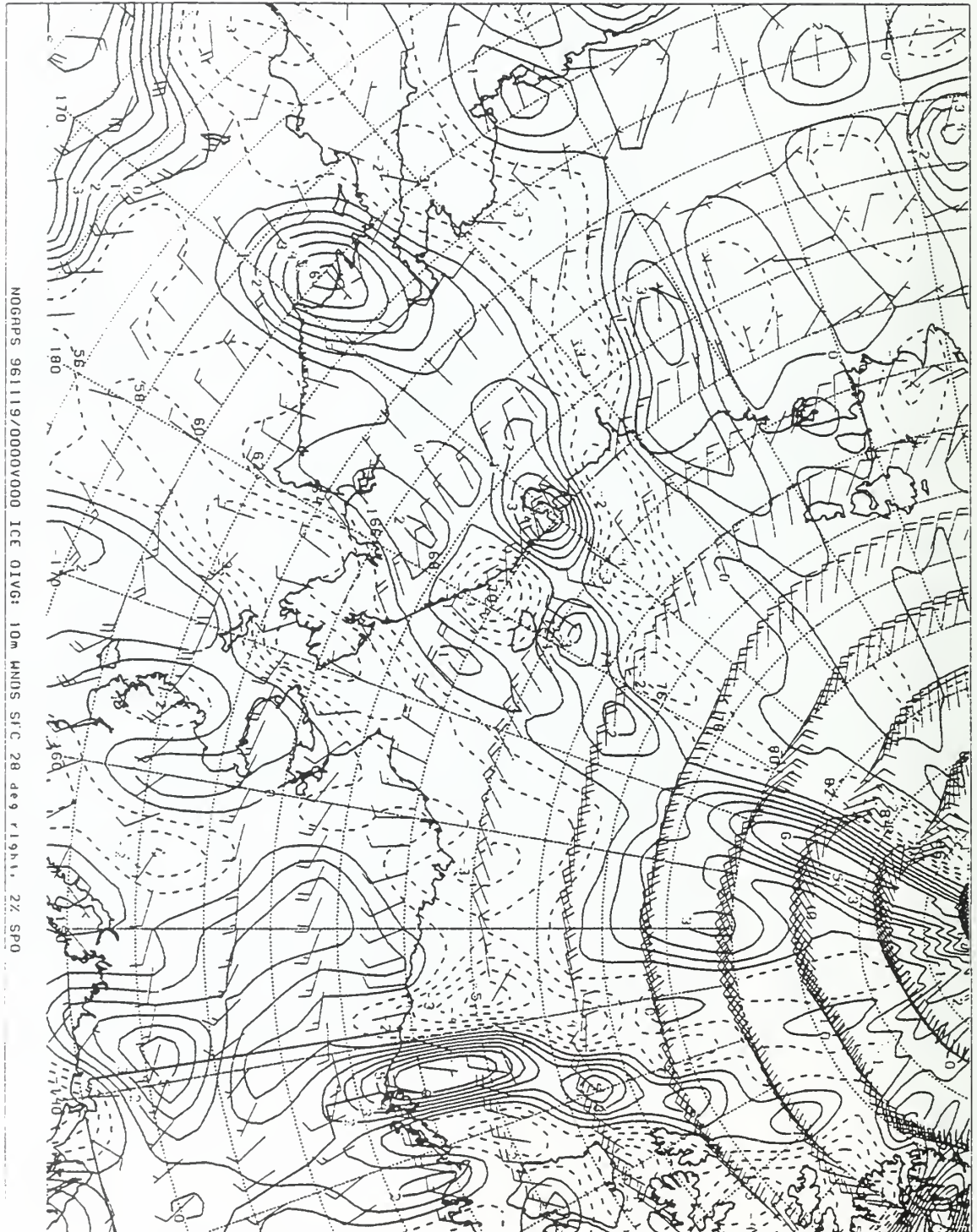


Figure 108. NOGAPS model ice divergence chart for 0000Z 19 Nov 96.

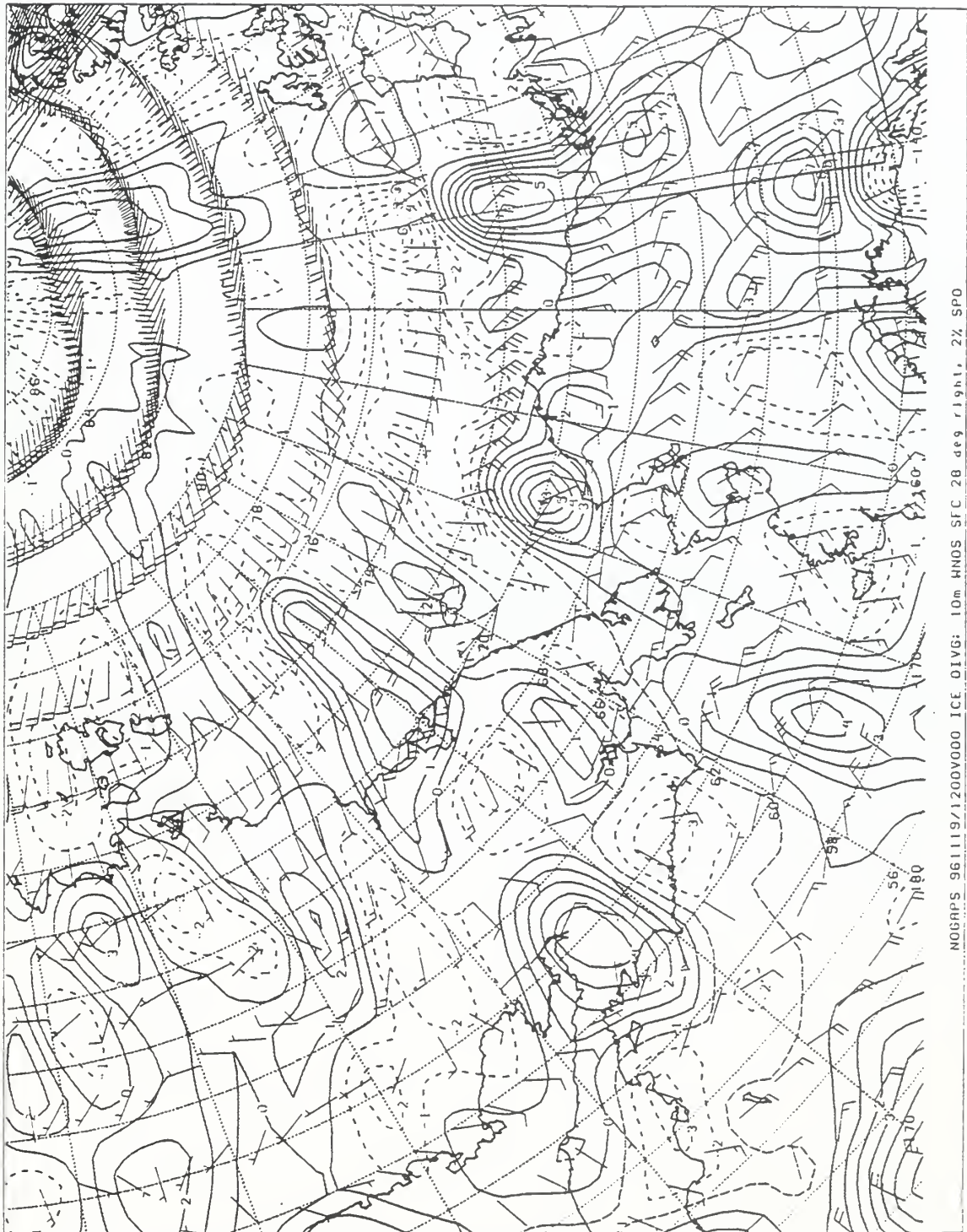


Figure 109. NOGAPS model ice divergence chart for 1200Z 19 Nov 96.

Figure 110.
0000Z 20 Nov 96
NOGAPS Ice Divergence Data Missing

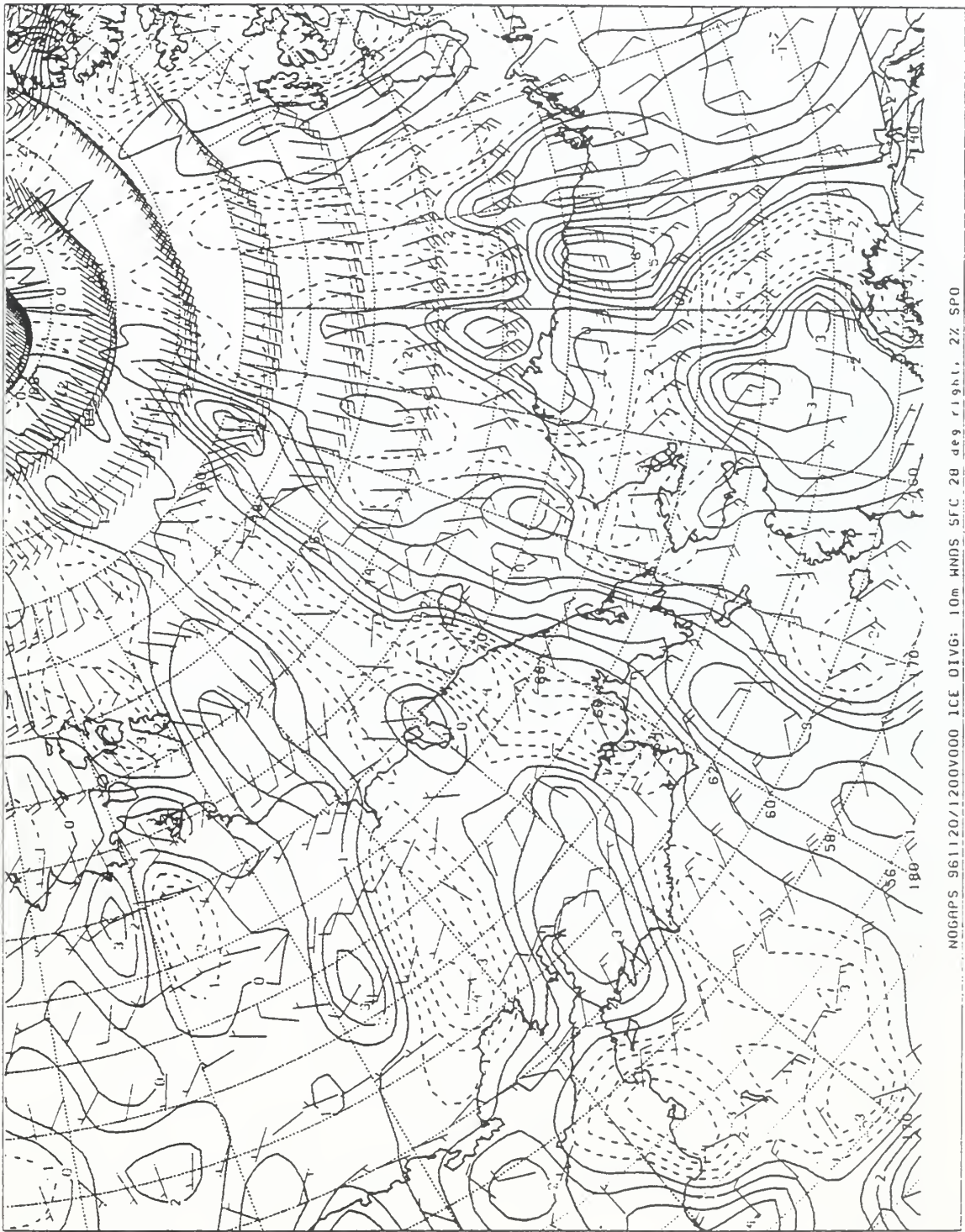


Figure 111. NOGAPS model ice divergence chart for 1200Z 20 Nov 96.



Figure 112. NOGAPS model ice divergence chart for 0000Z 21 Nov 96.

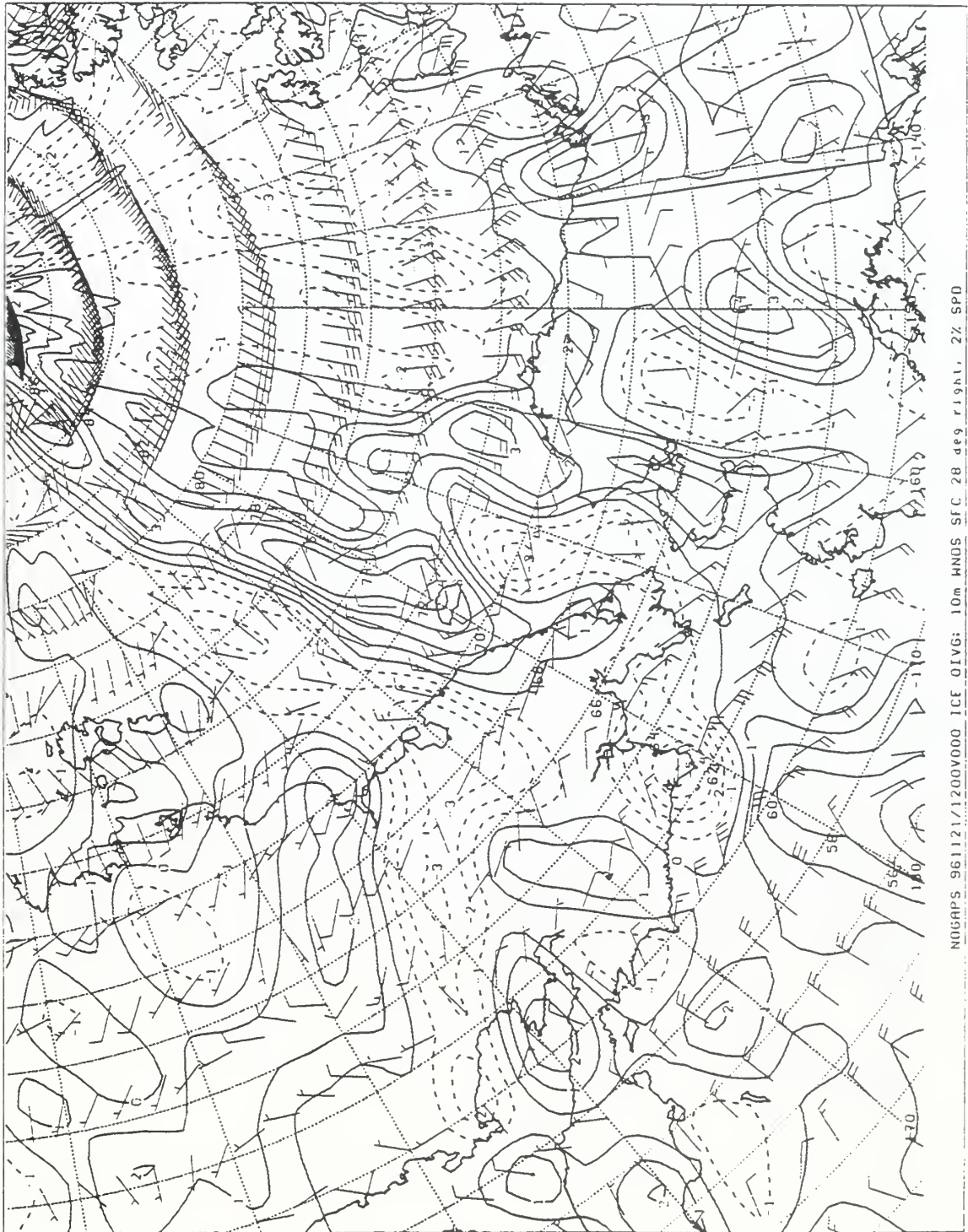


Figure 113. NOGAPS model ice divergence chart for 1200Z 21 Nov 96.

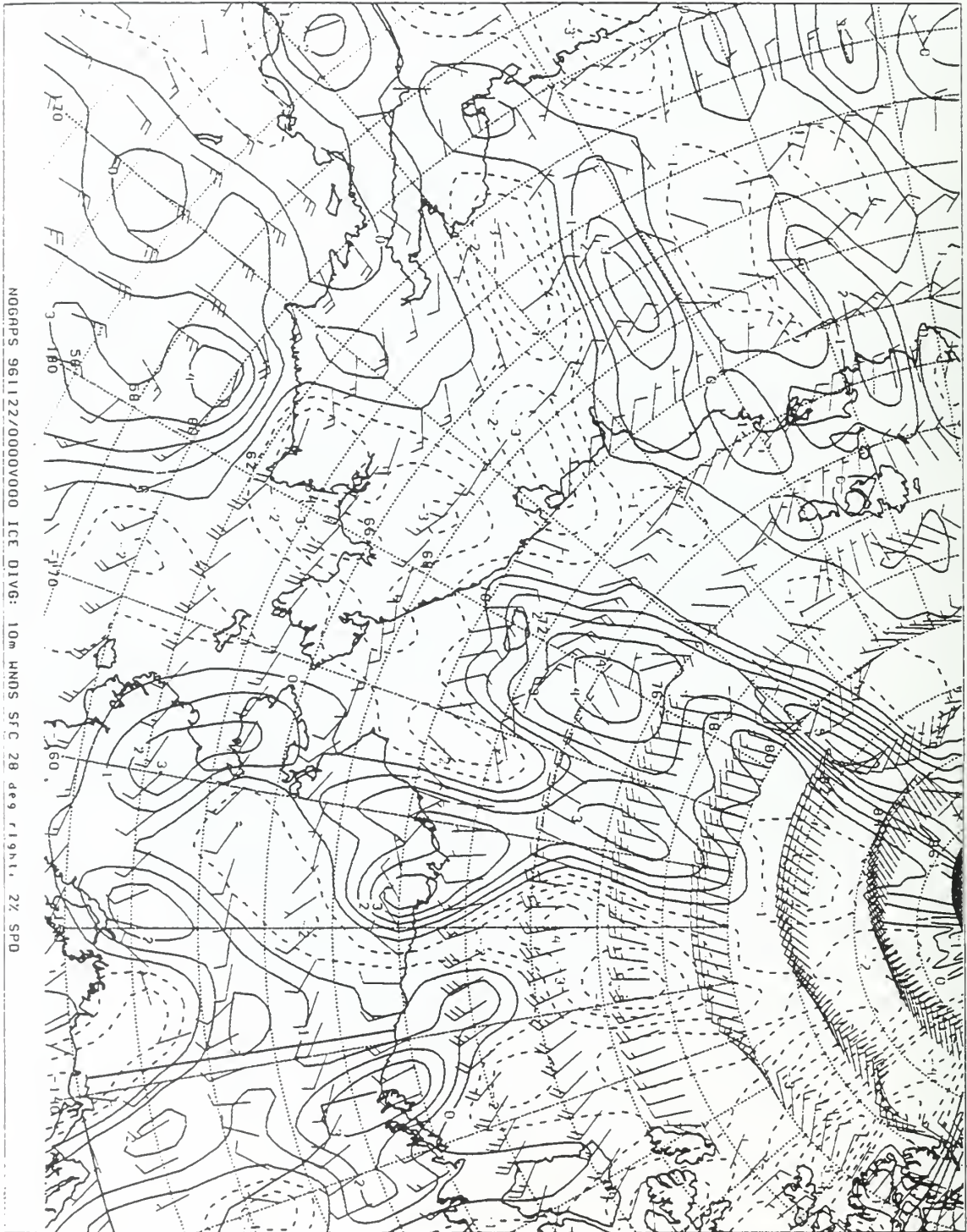


Figure 114. NOGAPS model ice divergence chart for 0000Z 22 Nov 96.

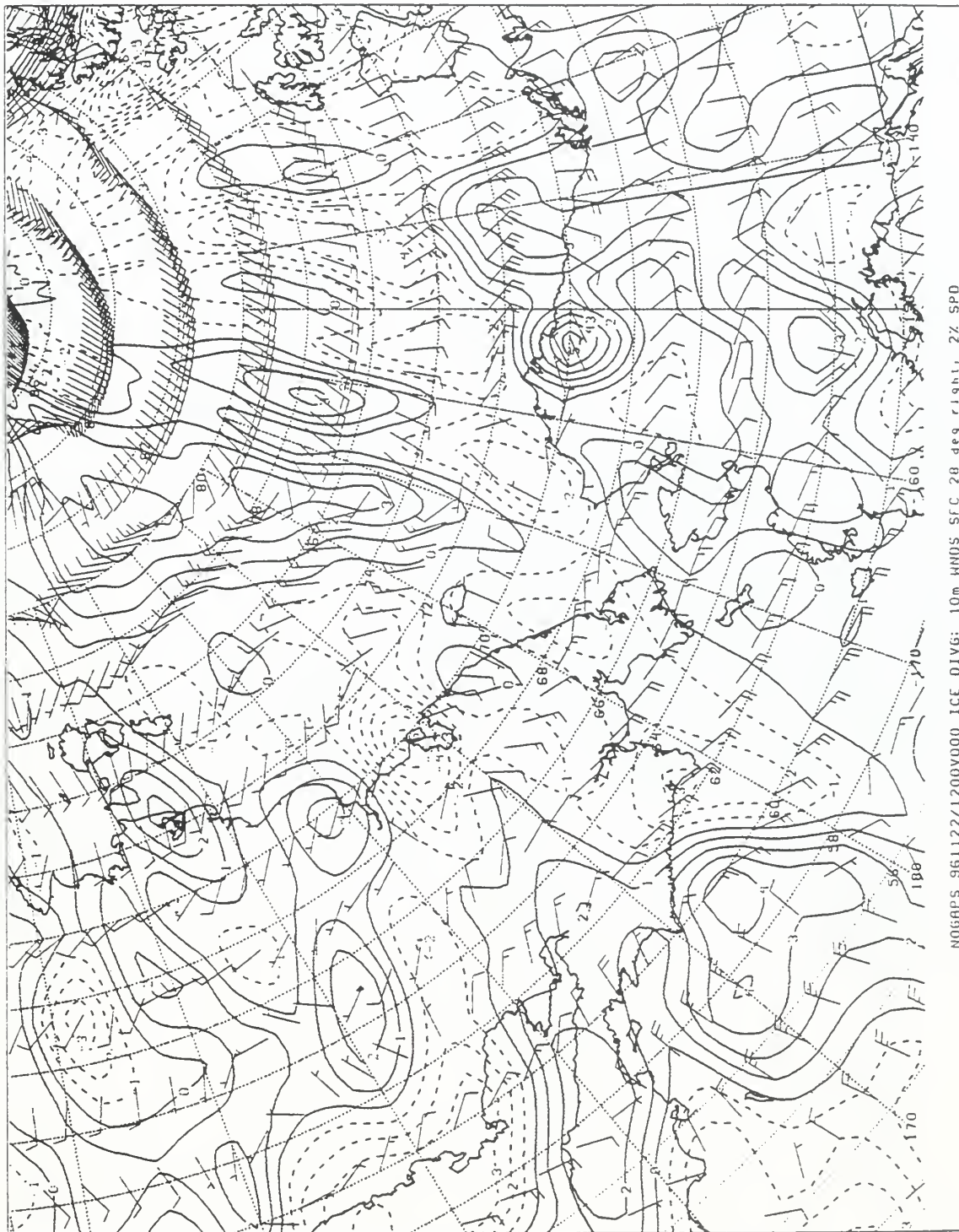


Figure 115. NOGAPS model ice divergence chart for 1200Z 22 Nov 96.

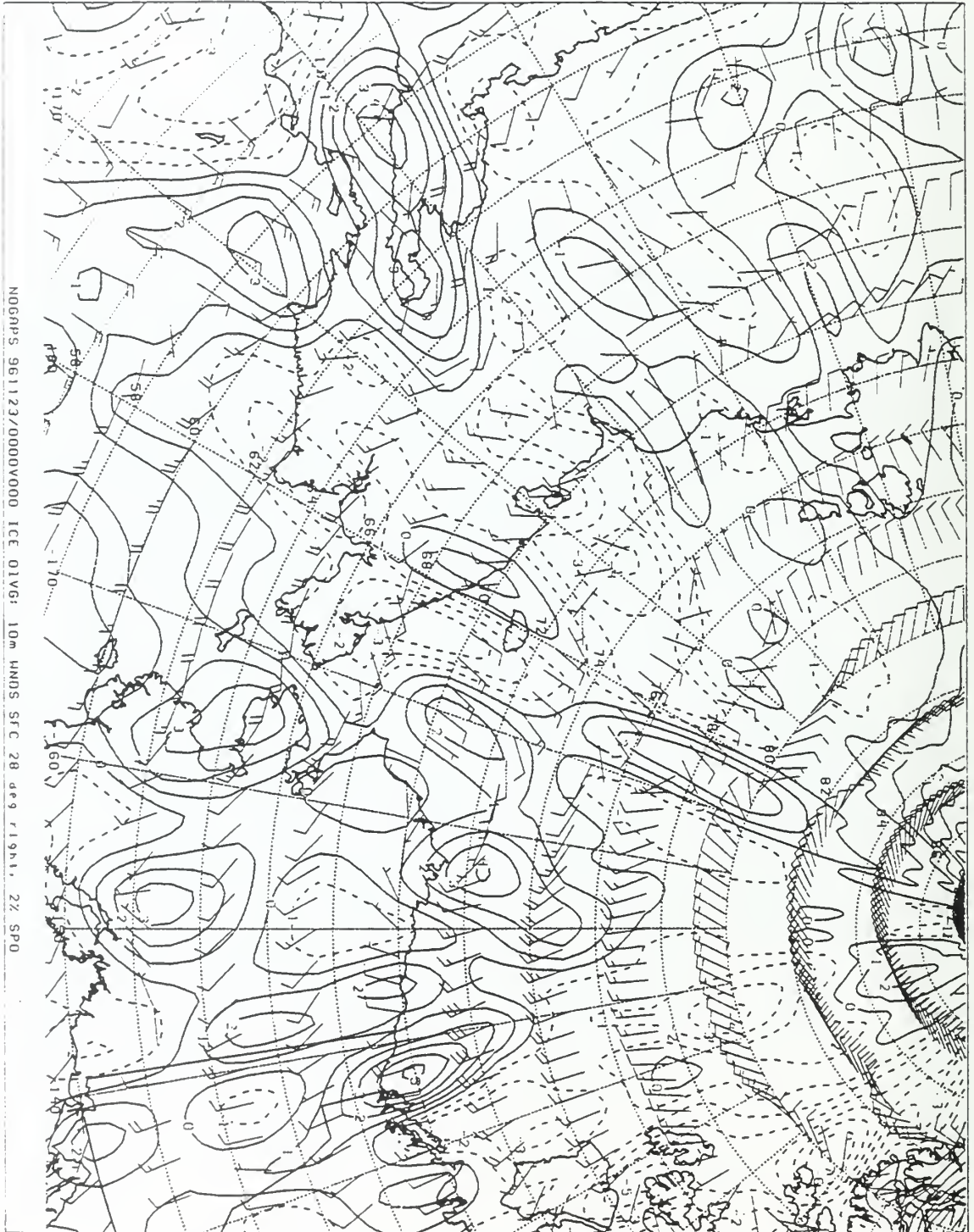


Figure 116. NOGAPS model ice divergence chart for 0000Z 23 Nov 96.

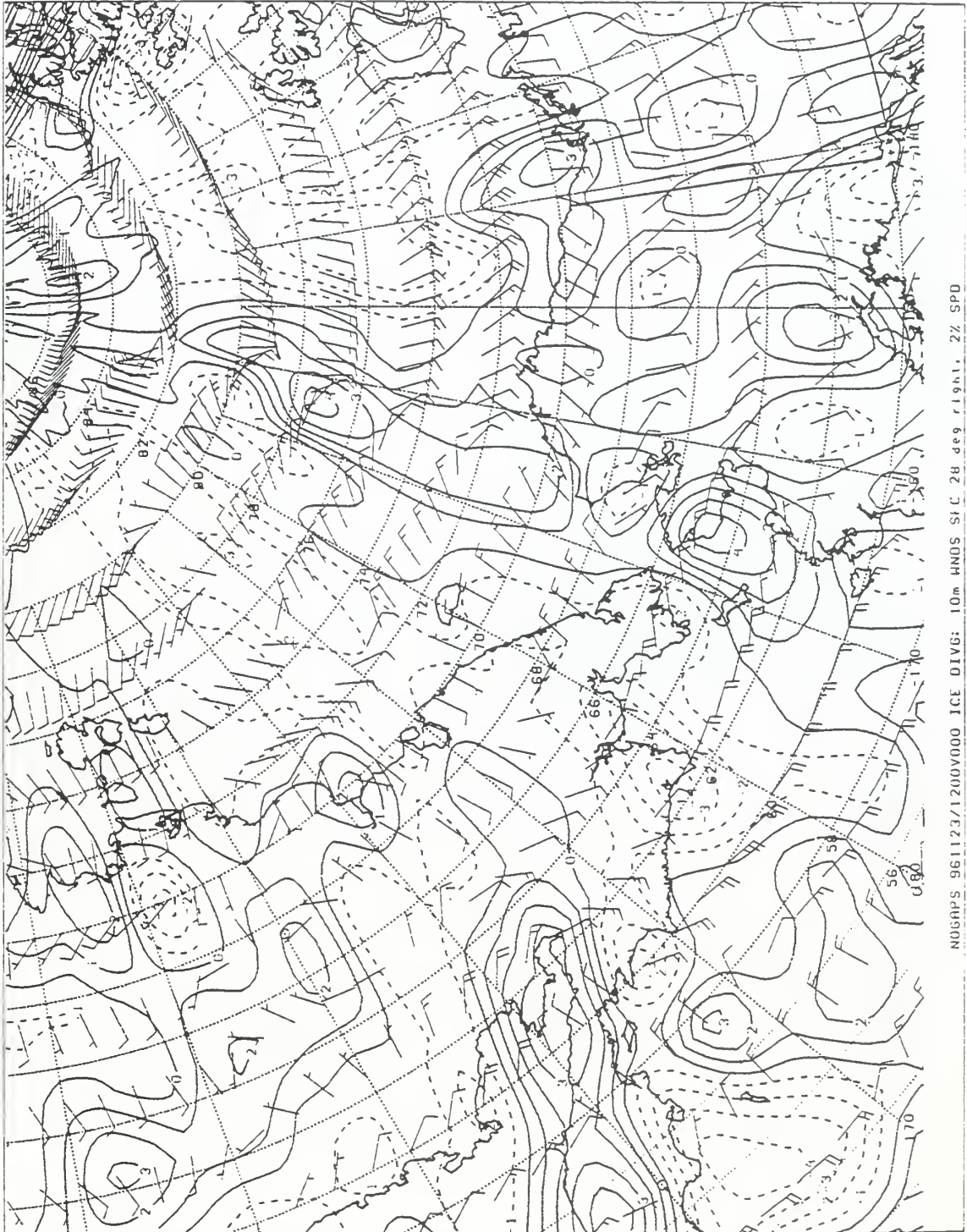


Figure 117. NOGAPS model ice divergence chart for 1200Z 23 Nov 96.

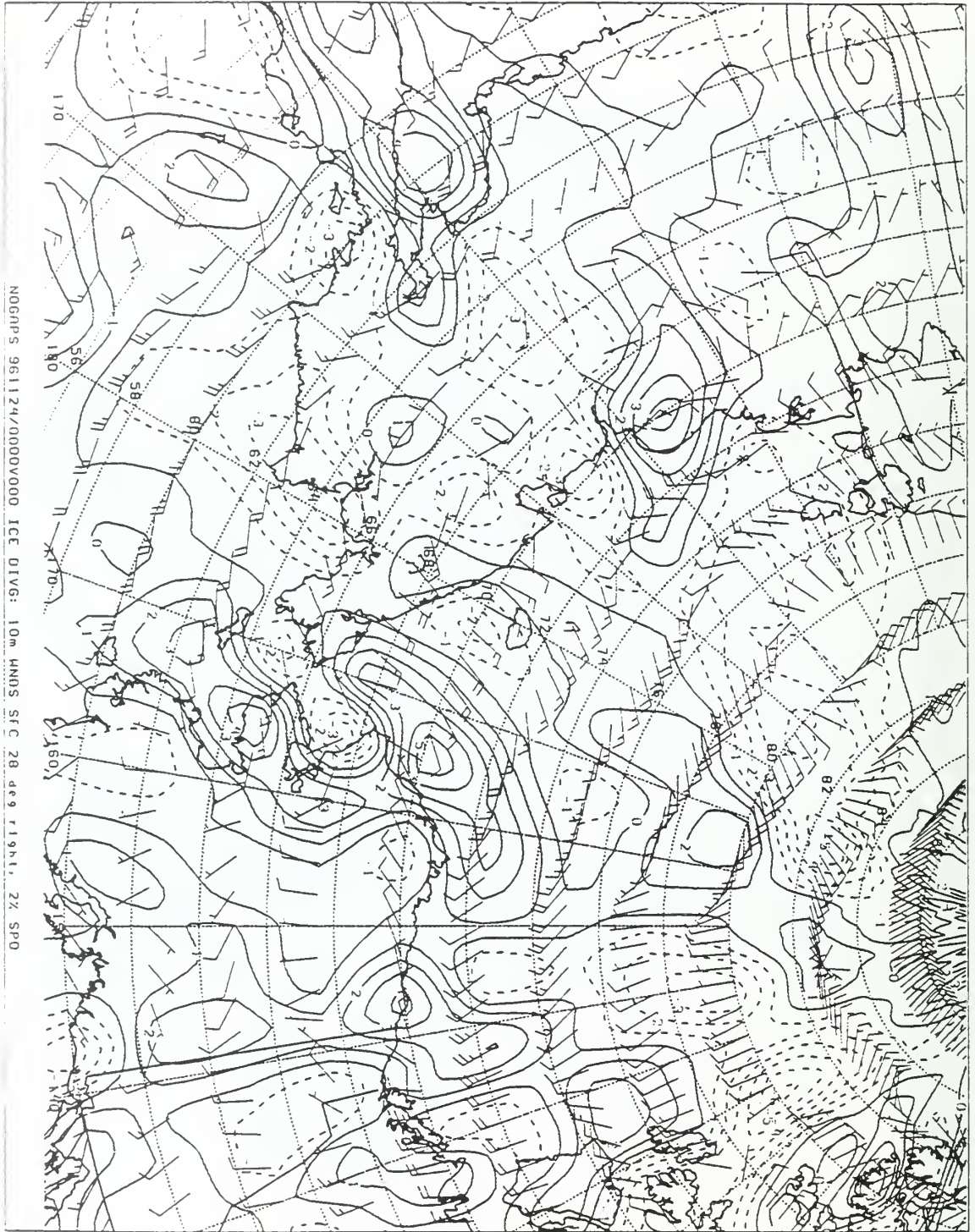


Figure 118. NOGAPS model ice divergence chart for 0000Z 24 Nov 96.

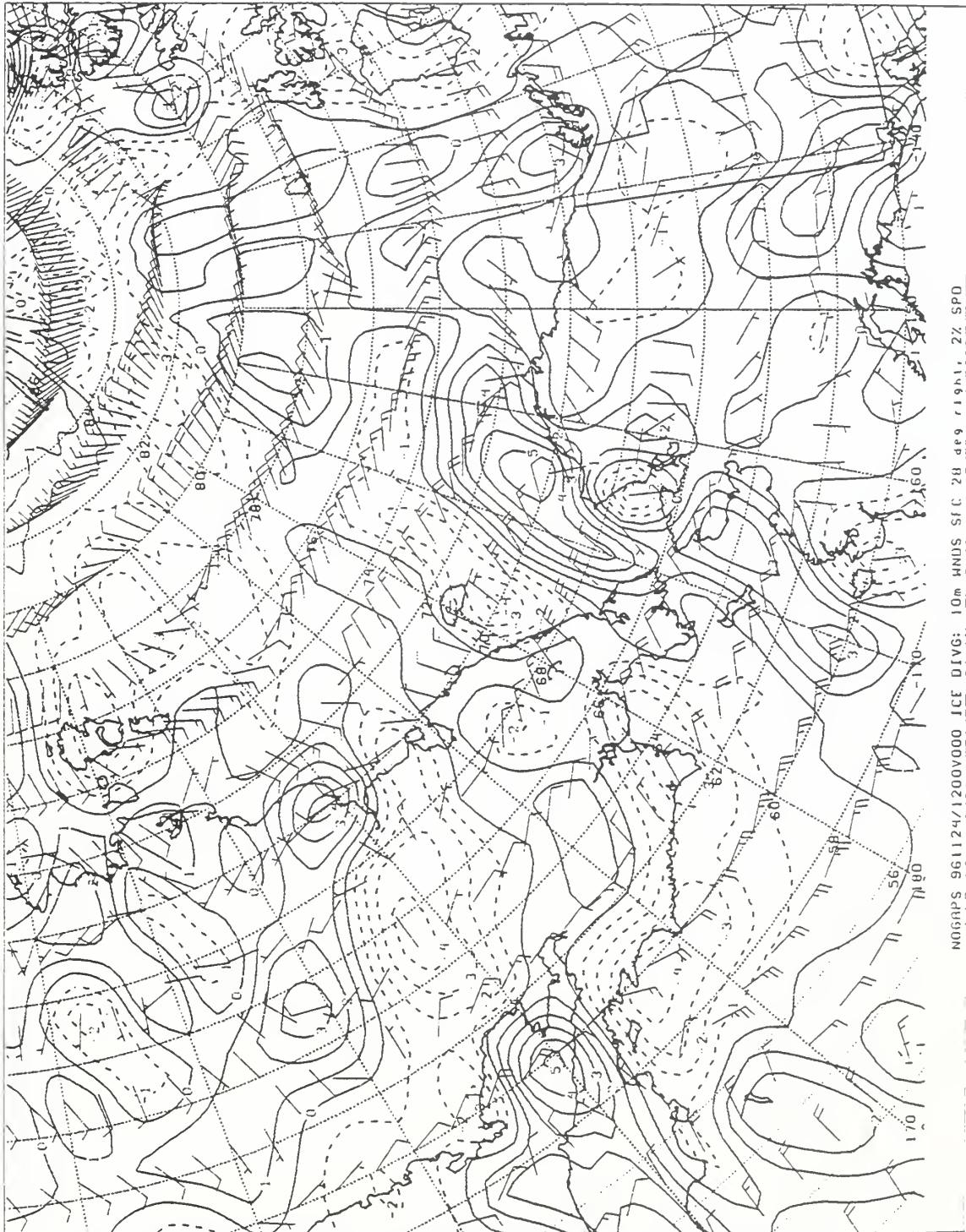


Figure 119. NOGAPS model ice divergence chart for 1200Z 24 Nov 96.

APPENDIX G

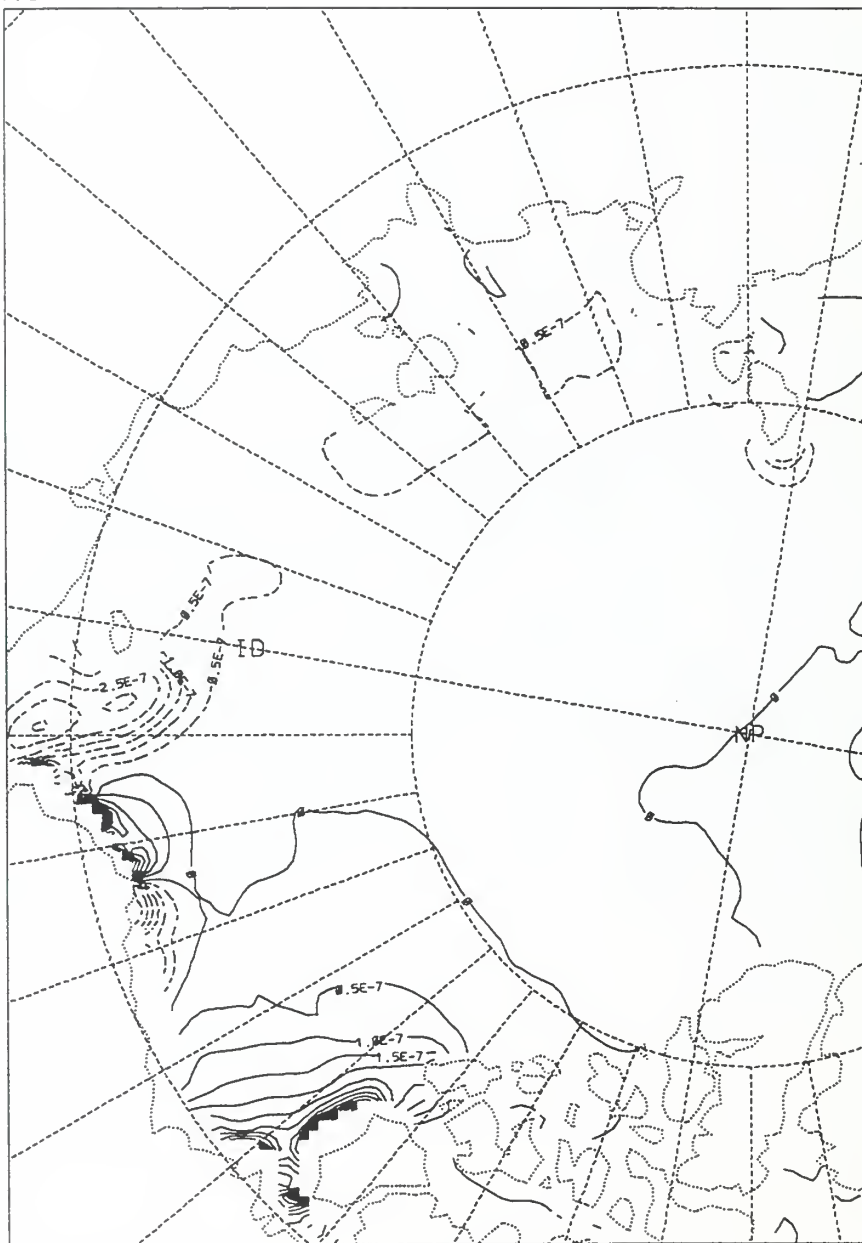
**PIPS ICE DIVERGENCE DATA:
13 FEBRUARY TO 31 MARCH 1998**

piPs_zoom
1998021200 TAU = 24

ice_div

1/s

LEVEL = 0.0



CONTOUR FROM -0.0000035 TO 9×10^{-7} BY .0000006

Figure 120. PIPS model ice divergence chart for 0000Z 13 Feb 98.

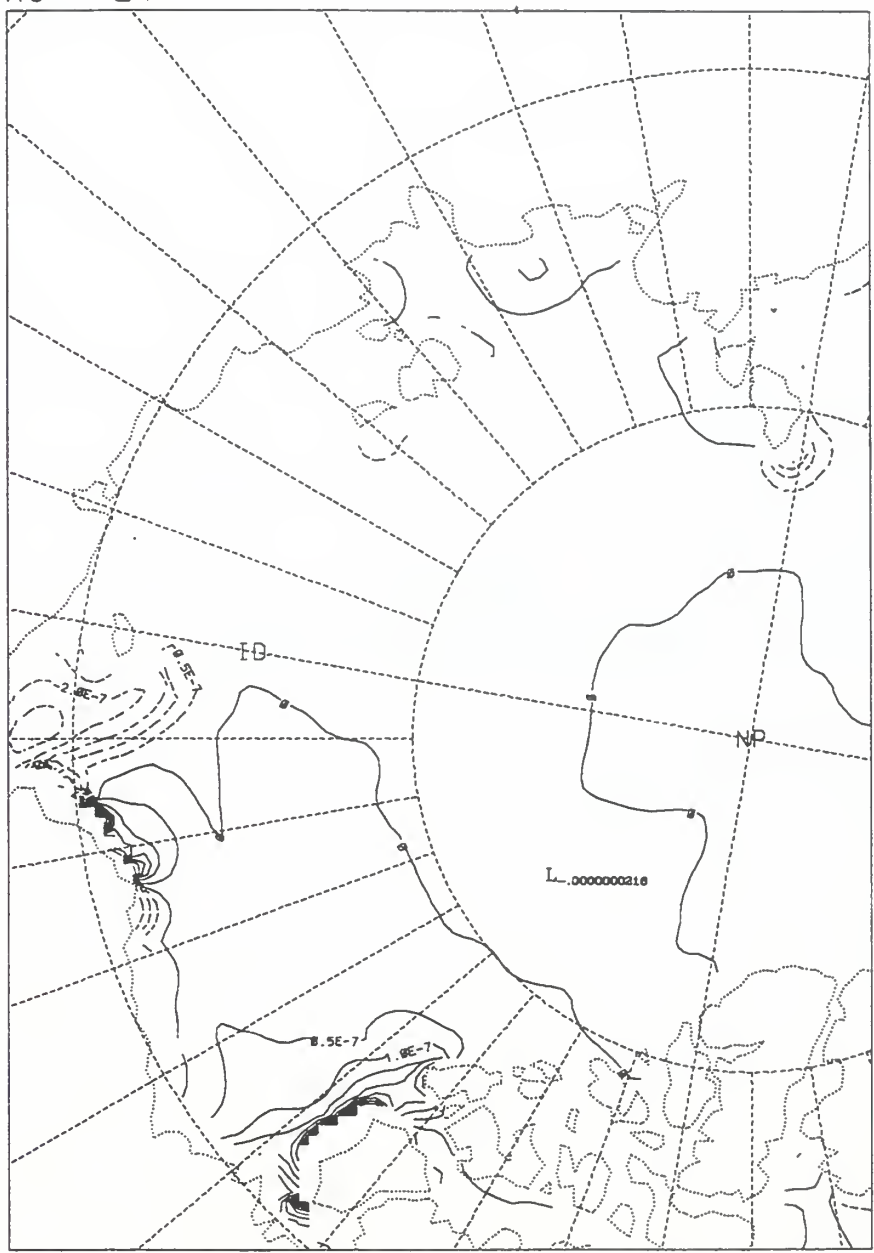
pips_zoom
1998021300

TAU = 24

ice_div

1/s

LEVEL= 0.0



CONTOUR FROM -.00000025 TO .00000085 BY .00000005

Figure 121. PIPS model ice divergence chart for 0000Z 14 Feb 98.

Figure 122.
15 Feb 98
PIPS Ice Divergence Data Missing

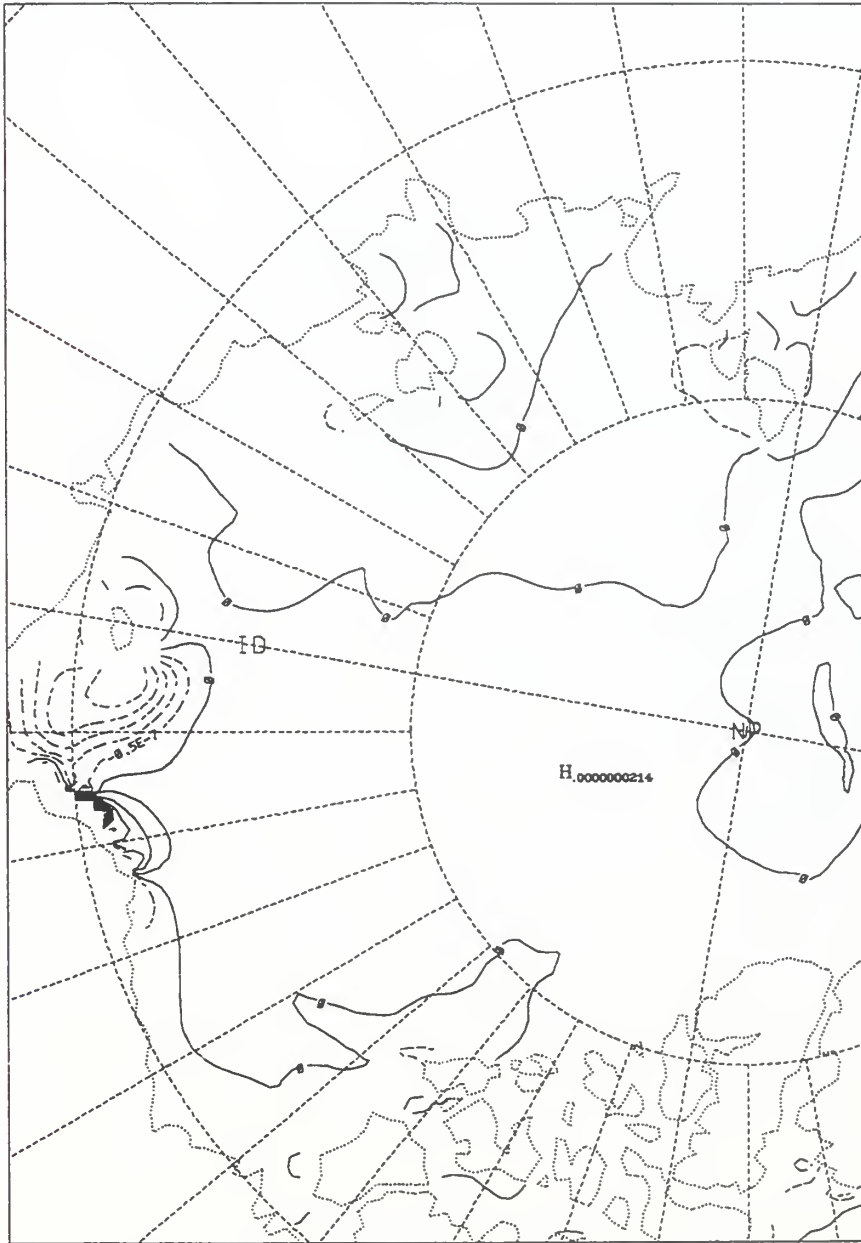
pips_zoom
1998021500

TAU = 24

ice_div

1/s

LEVEL= 0.0



CONTOUR FROM -0.00000025 TO 8×10^{-7} BY $.00000006$

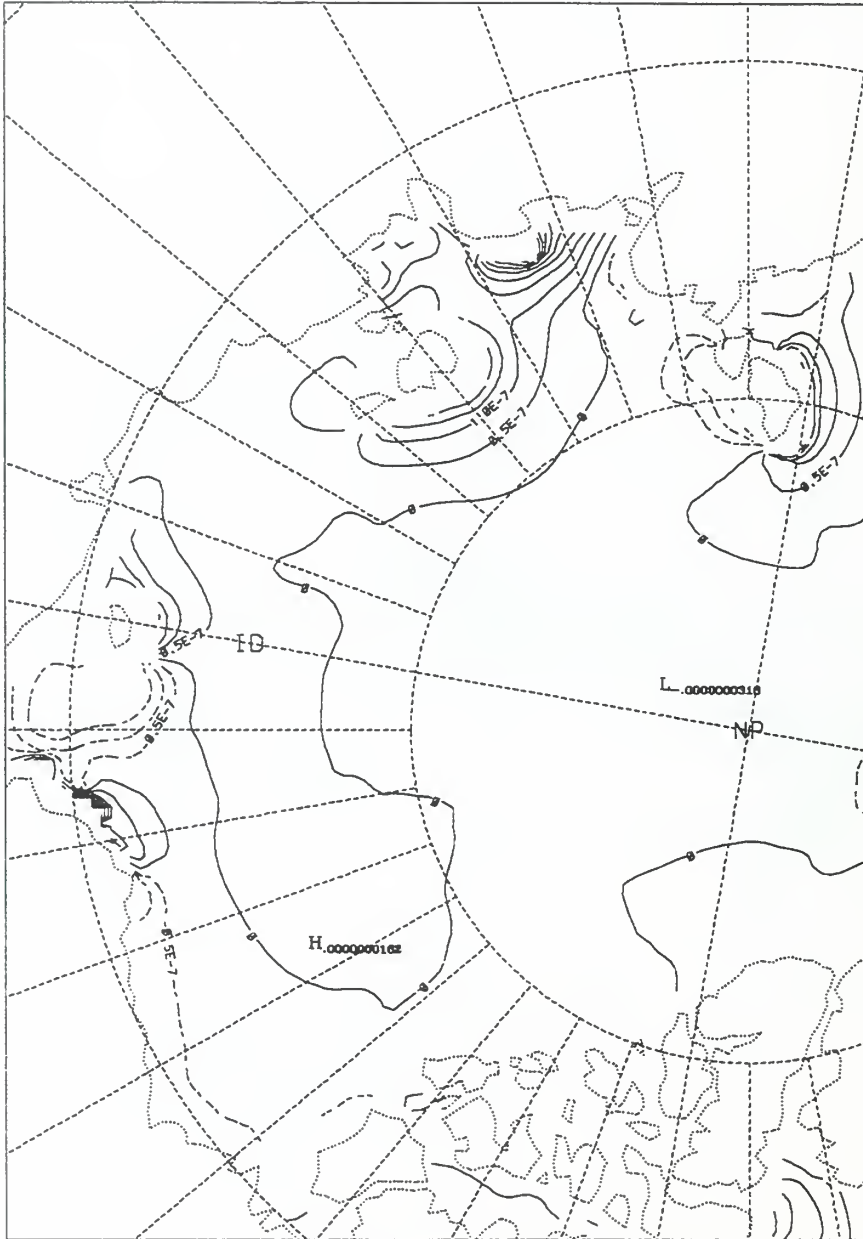
Figure 123. PIPS model ice divergence chart for 0000Z 16 Feb 98.

piPs_zoom
1998021600 TAU = 24

ice_div

1/s

LEVEL= 0.0



CONTOUR FROM -0.0000015 TO 0.0000045 BY 0.0000005

Figure 124. PIPS model ice divergence chart for 0000Z 17 Feb 98.

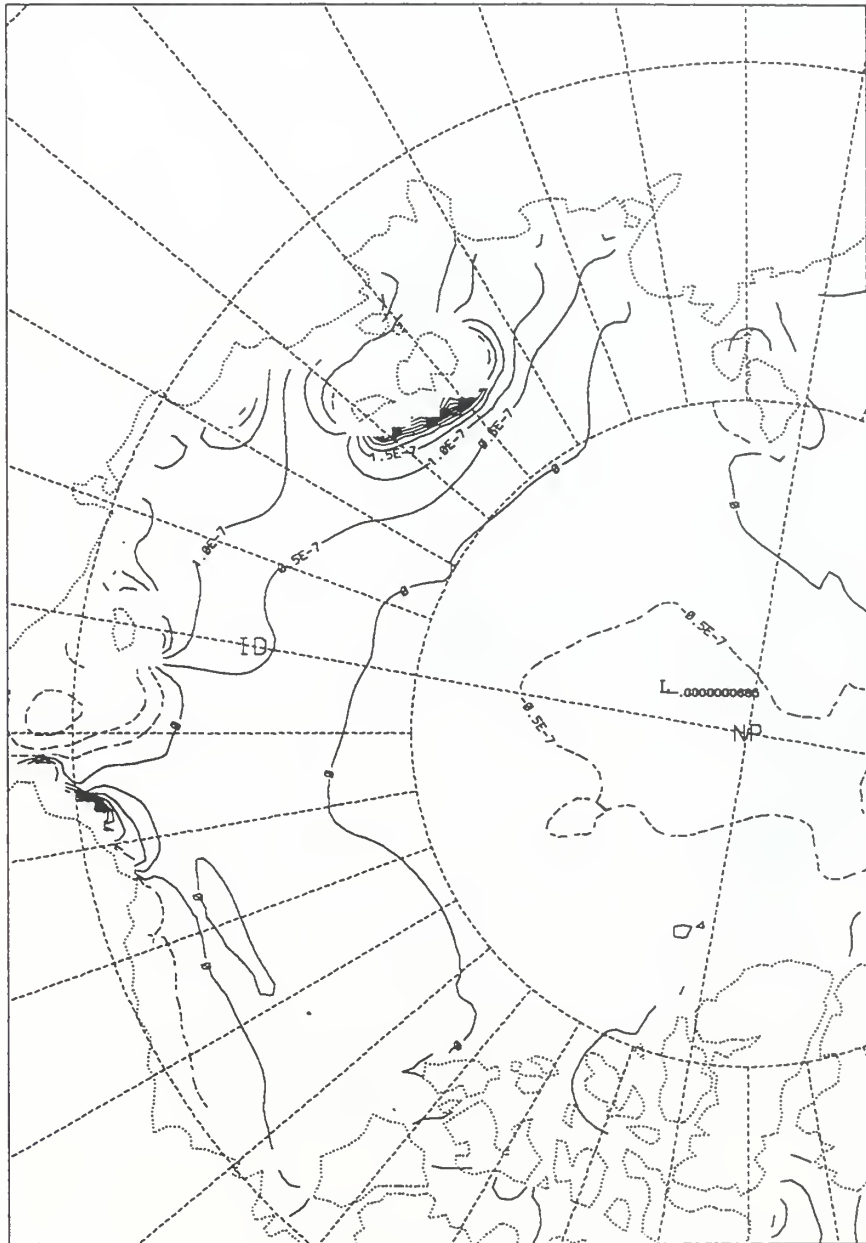
pips_zoom
1998021700

TAU = 24

ice_div

1/s

LEVEL = 0.0



CONTOUR FROM -.00000015 TO .00000055 BY .00000005

Figure 125. PIPs model ice divergence chart for 0000Z 18 Feb 98.

piPs_zoom
1998021800

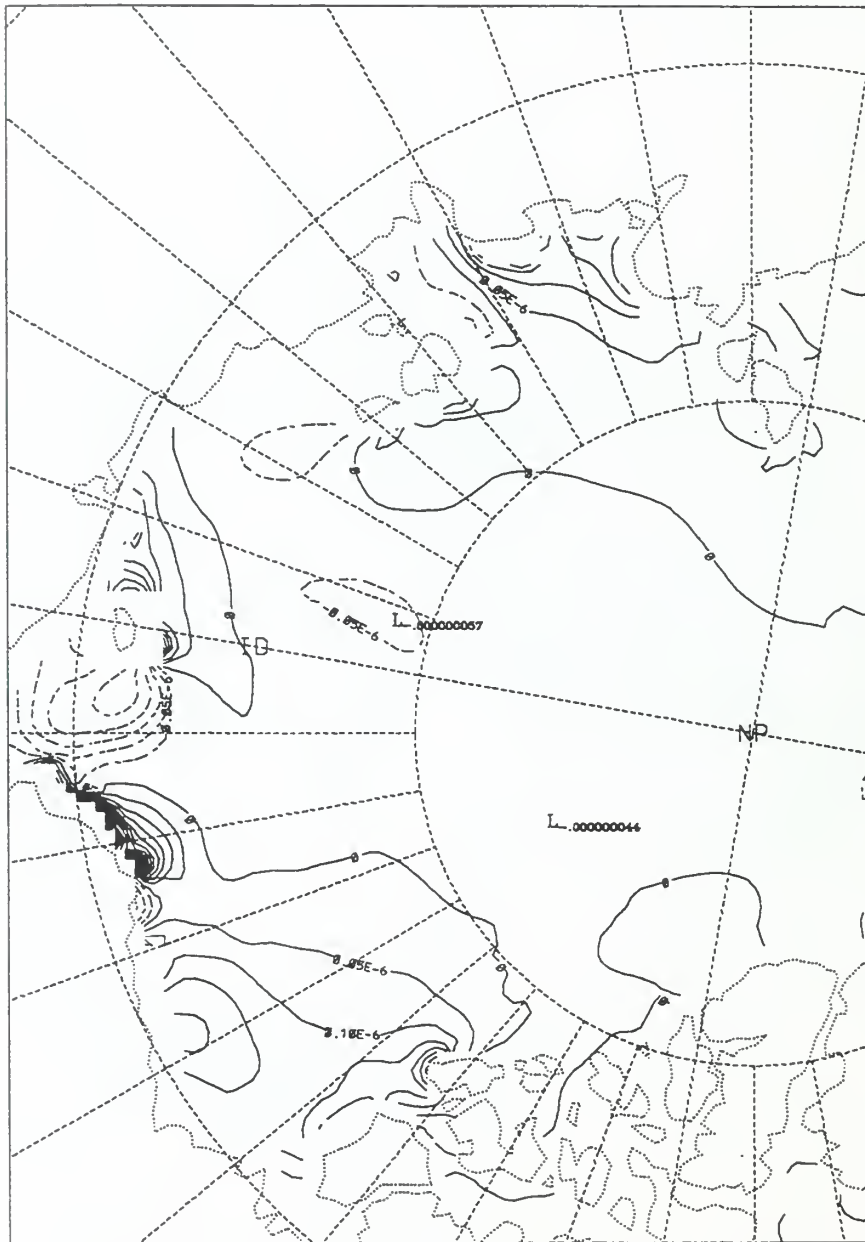
TAU = 24

ice_div

1/s

LEVEL =

0.0



CONTOUR FROM -.00000025 TO .00000145 BY .00000005

Figure 126. PIPS model ice divergence chart for 0000Z 19 Feb 98.

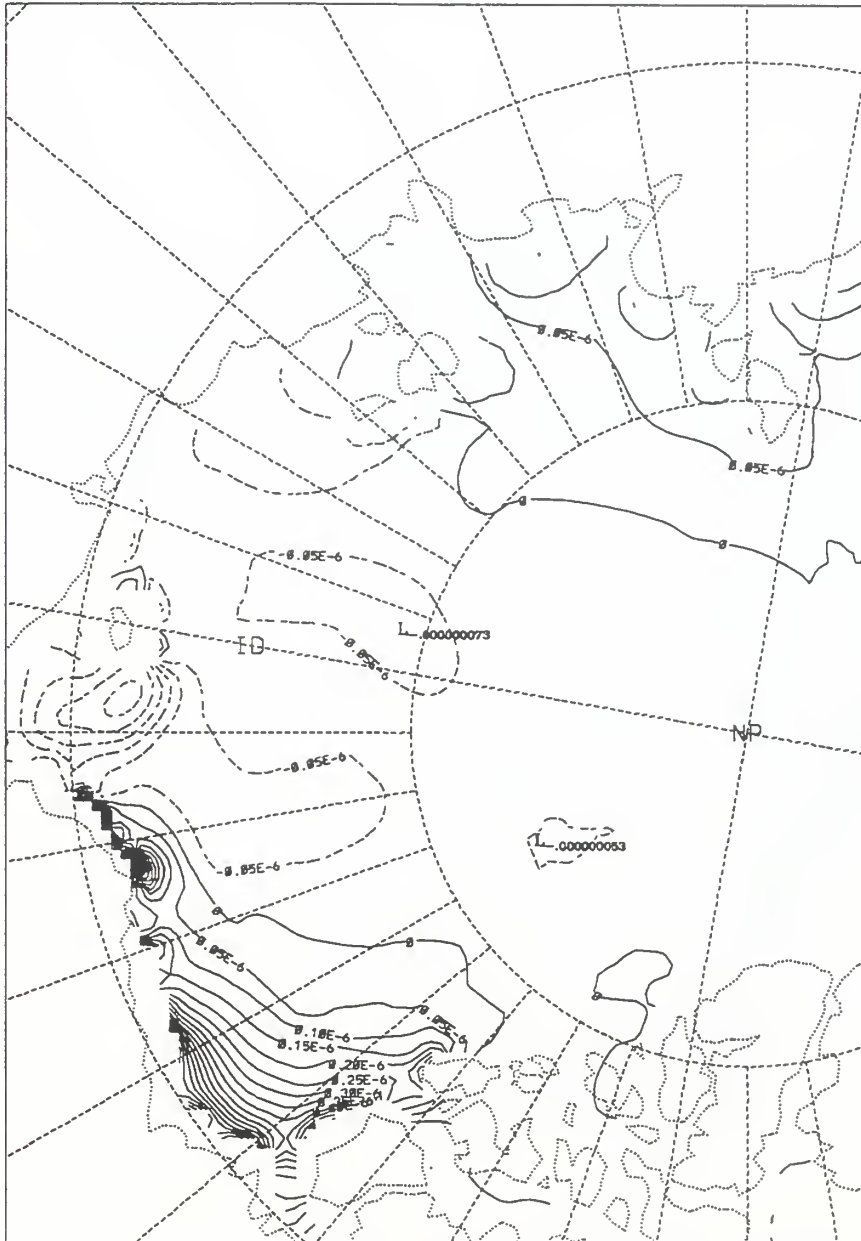
pips_zoom
1998021900

TAU = 24

ice_div

1/s

LEVEL= 0.0



CONTOUR FROM -.00000035 TO .00000325 BY .00000005

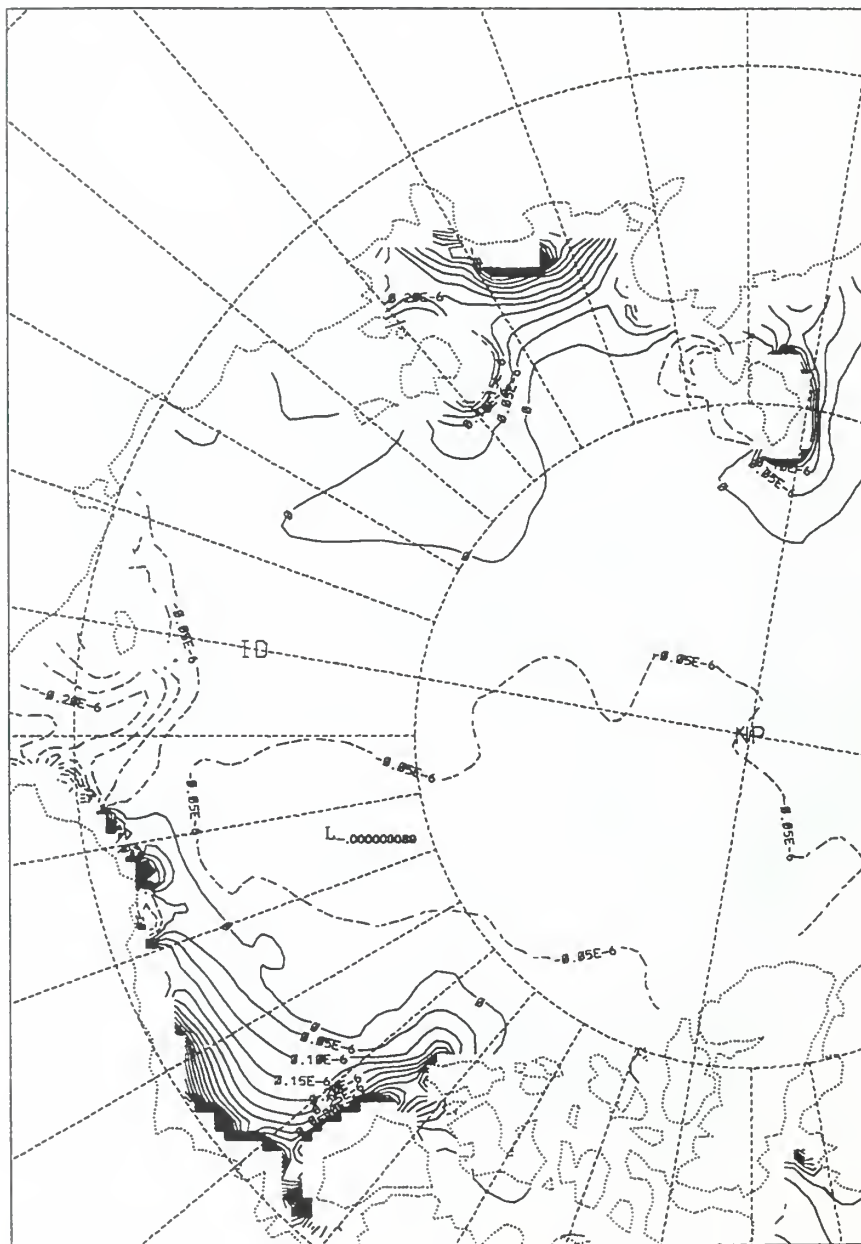
Figure 127. PIPS model ice divergence chart for 0000Z 20 Feb 98.

pips_zoom
1998022000 TAU = 24

ice_div

1/s

LEVEL= 0.0



CONTOUR FROM -0.000004 TO 0.000023 BY 0.0000005

Figure 128. PIPS model ice divergence chart for 0000Z 21 Feb 98.

pi ps_zoom
1998022200

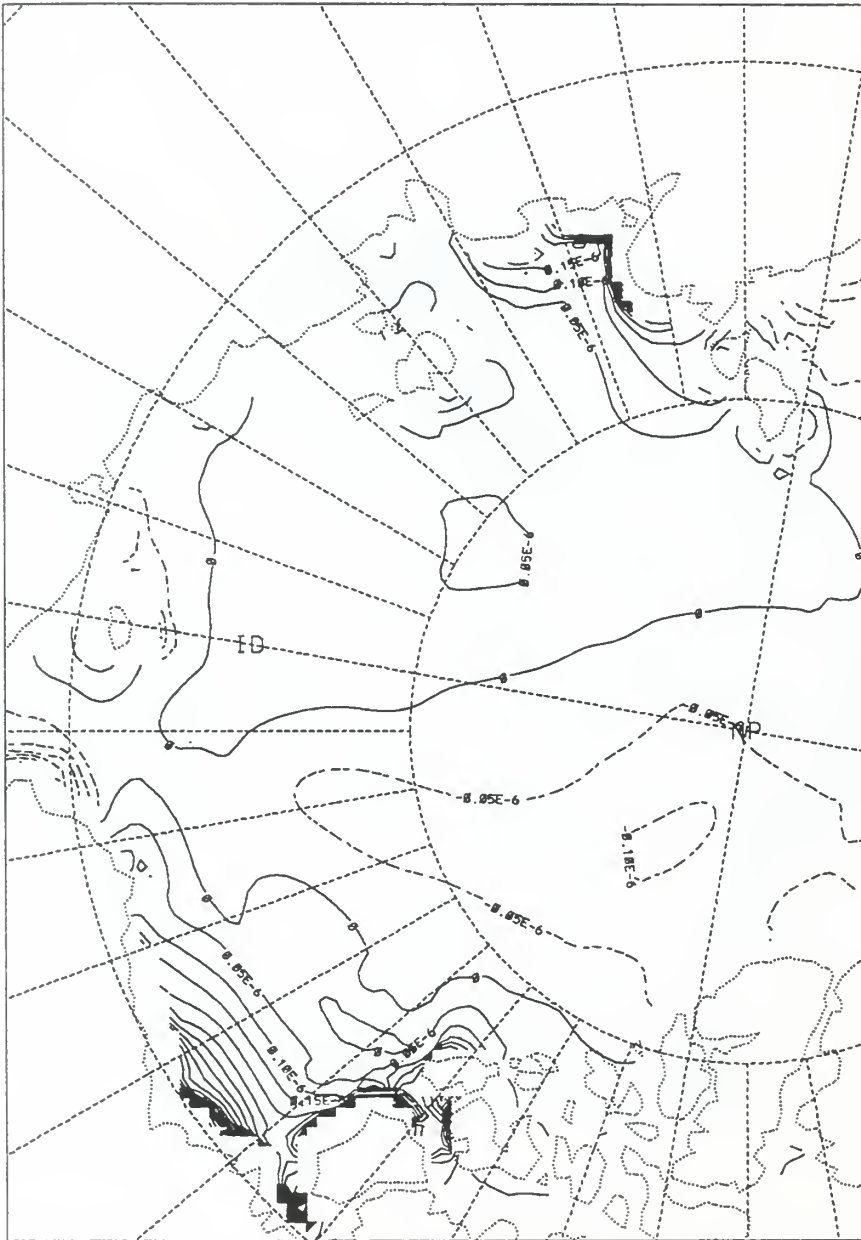
TAU = 24

ice_div

1/s

LEVEL =

0.0



CONTOUR FROM -0.000003 TO 0.000018 BY 0.0000005

Figure 130. PIPs model ice divergence chart for 0000Z 23 Feb 98.

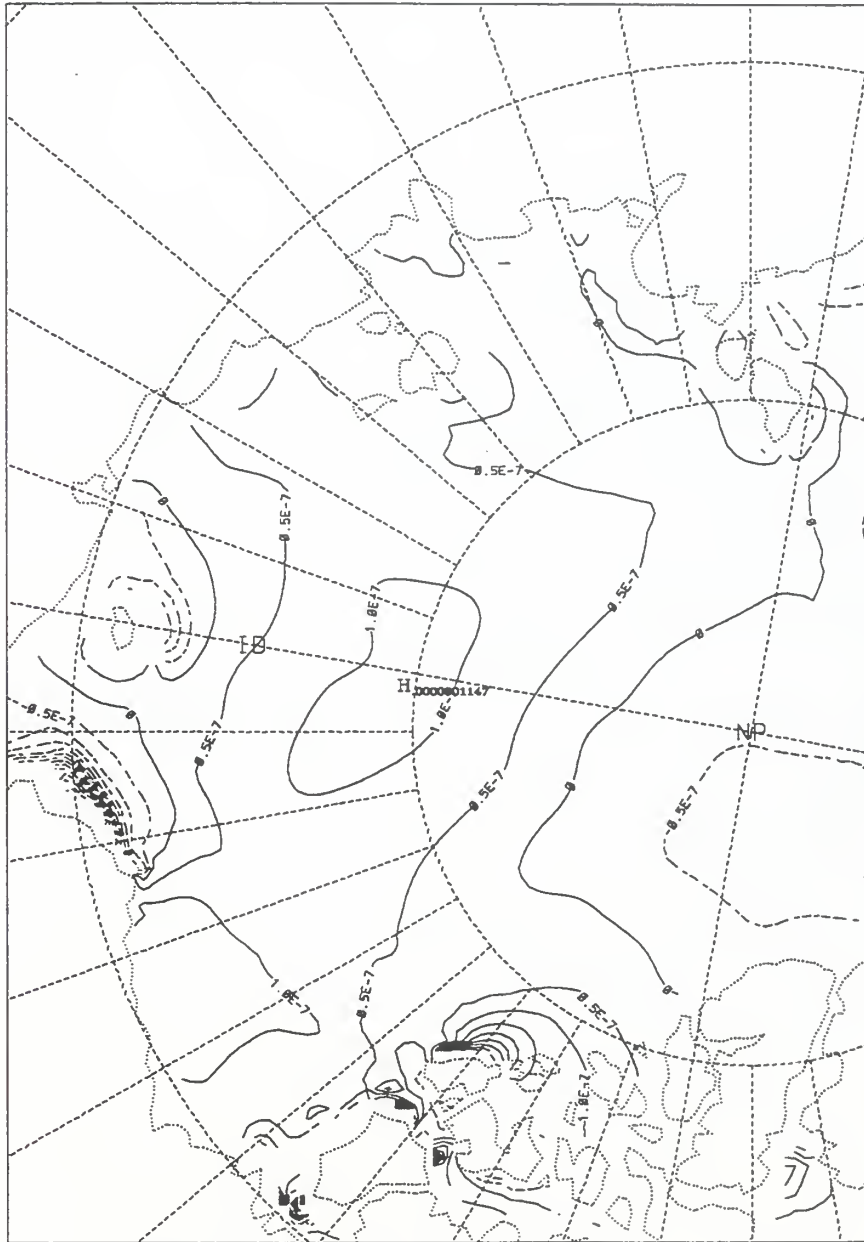
pips_zoom
1998022300

TAU = 24

ice_div

1/s

LEVEL= 0.0



CONTOUR FROM -0.00000085 TO 5×10^{-7} BY $.00000006$

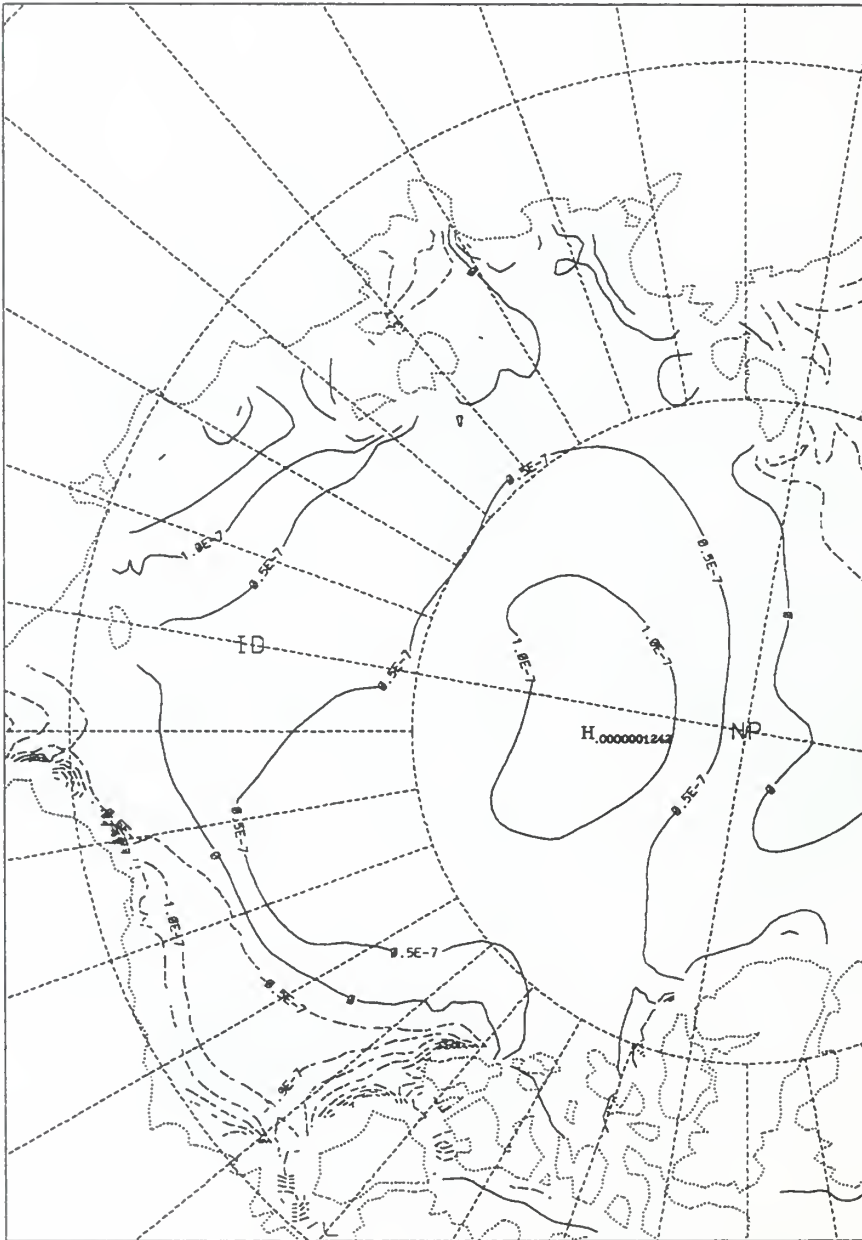
Figure 131. PIPS model ice divergence chart for 0000Z 24 Feb 98.

pips_zoom
1998022400 TAU = 24

ice_div

1/s

LEVEL= 0.0



CONTOUR FROM -.00000045 TO .00000025 BY .00000005

Figure 132. PIPS model ice divergence chart for 0000Z 25 Feb 98.

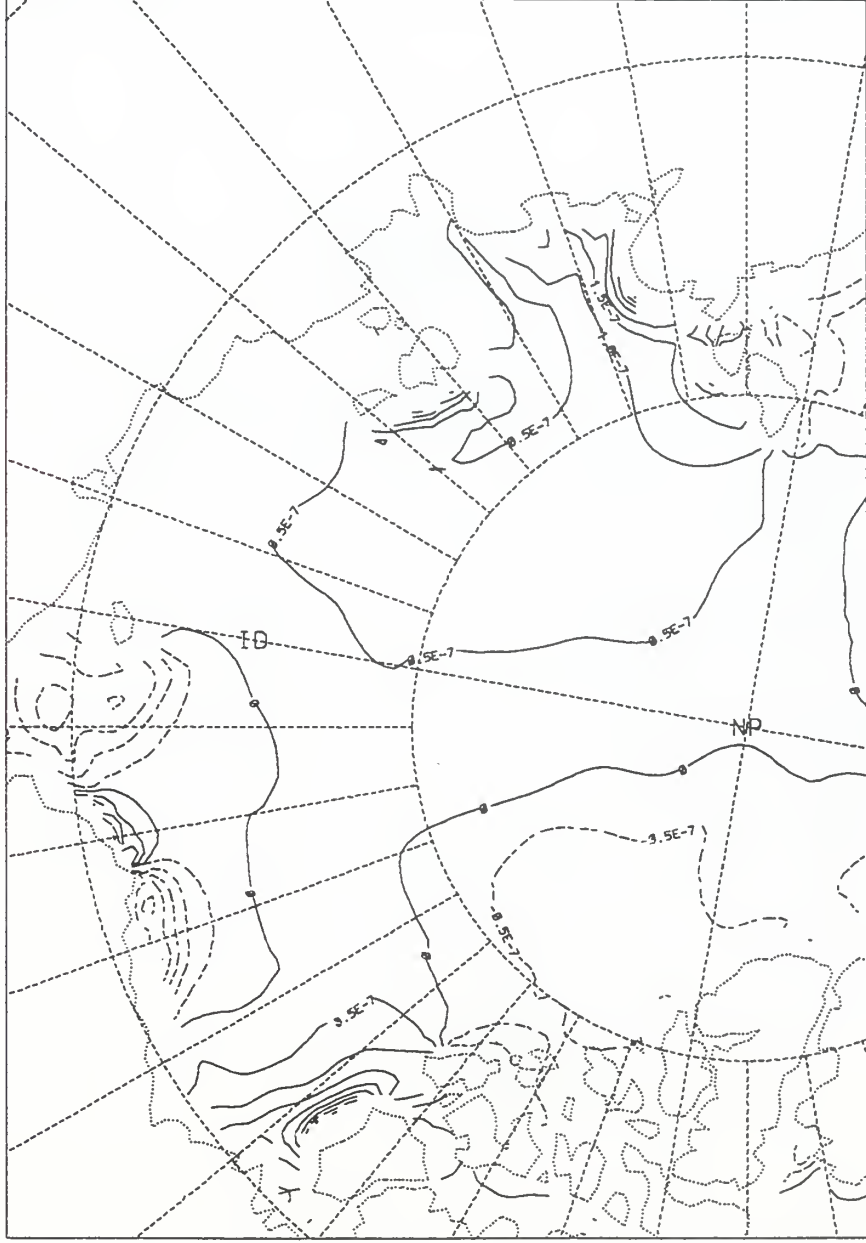
pips_zoom
1998022500

TAU = 24

ice_div

1/s

LEVEL= 0.0



CONTOUR FROM -0.0000025 TO 4×10^{-7} BY $.00000006$

Figure 133. PIPS model ice divergence chart for 0000Z 26 Feb 98.

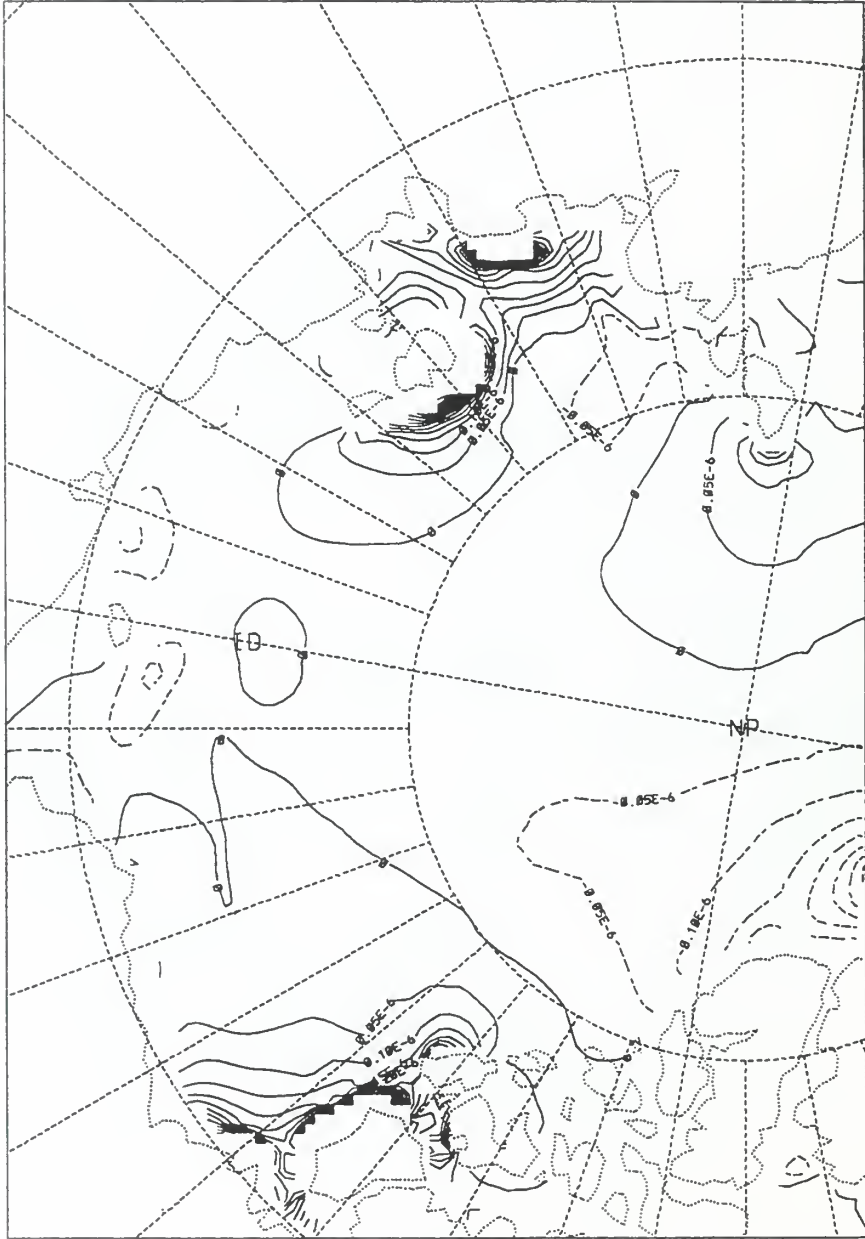
oips_zoom
1998022600

TAU = 24

ice_div

1/s

LEVEL= 0.0



CONTOUR FROM -0.0000035 TO 0.0000095 BY 0.0000005

Figure 134. PIPS model ice divergence chart for 0000Z 27 Feb 98.

piPs_zoom
1998022700

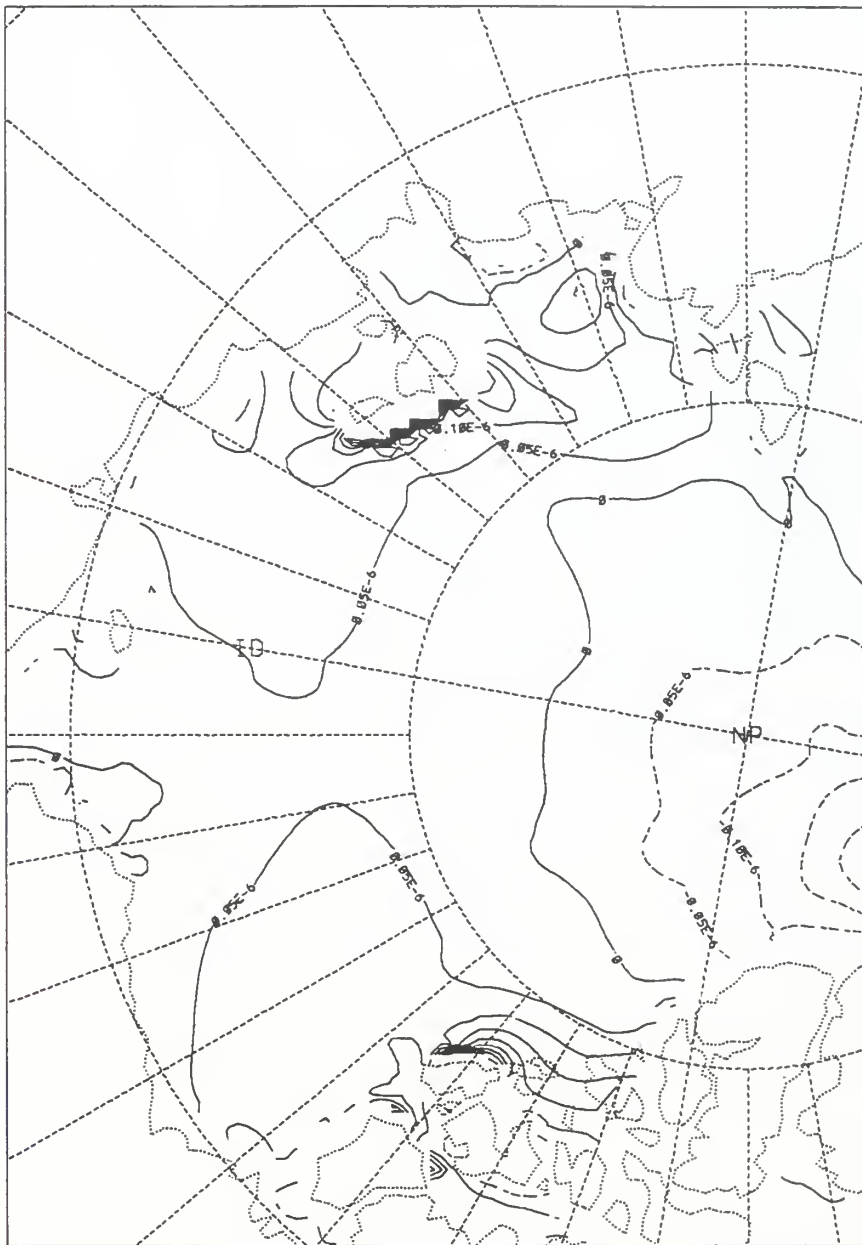
TAU = 24

ice_div

1/s

LEVEL =

0.0



CONTOUR FROM -.00000025 TO .00000105 BY .00000005

Figure 135. PIPS model ice divergence chart for 0000Z 28 Feb 98.

piPs_zoom
1998022800

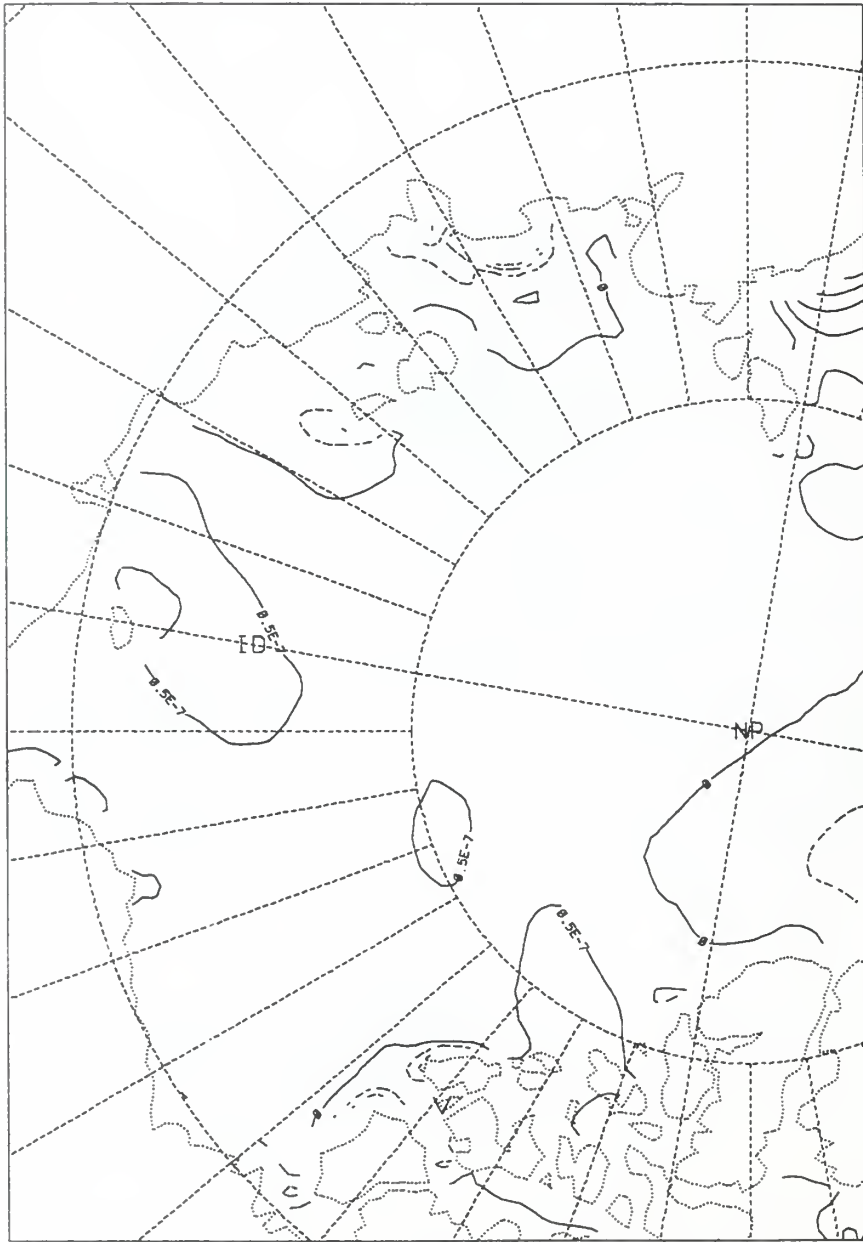
TAU = 24

ice_div

1/s

LEVEL =

0.0



CONTOUR FROM -.00000015 TO .00000025 BY .00000005

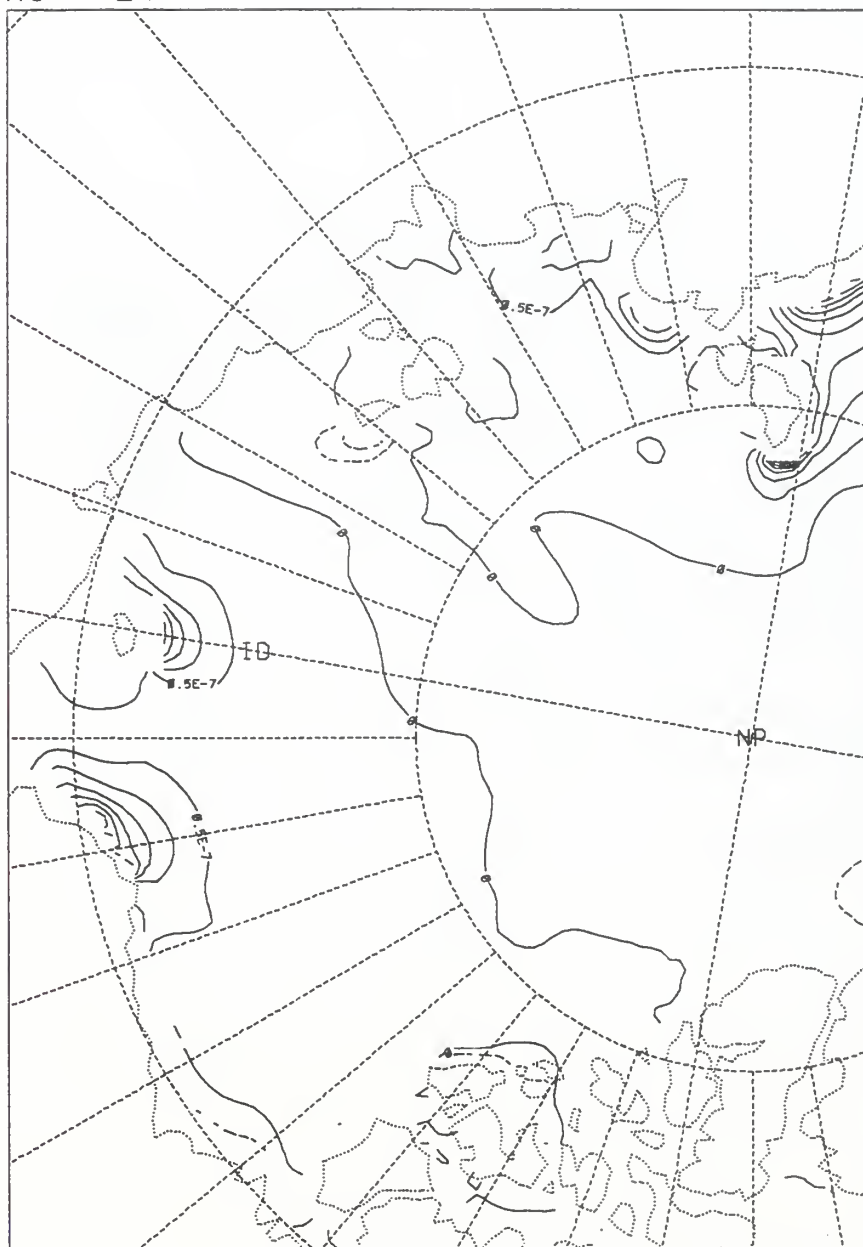
Figure 136. PIPS model ice divergence chart for 0000Z 01 Mar 98.

pips_zoom
1998030100 TAU = 24

ice_div

1/s

LEVEL = 0.0



CONTOUR FROM -.00000015 TO .00000045 BY .00000005

Figure 137. PIPS model ice divergence chart for 0000Z 02 Mar 98.

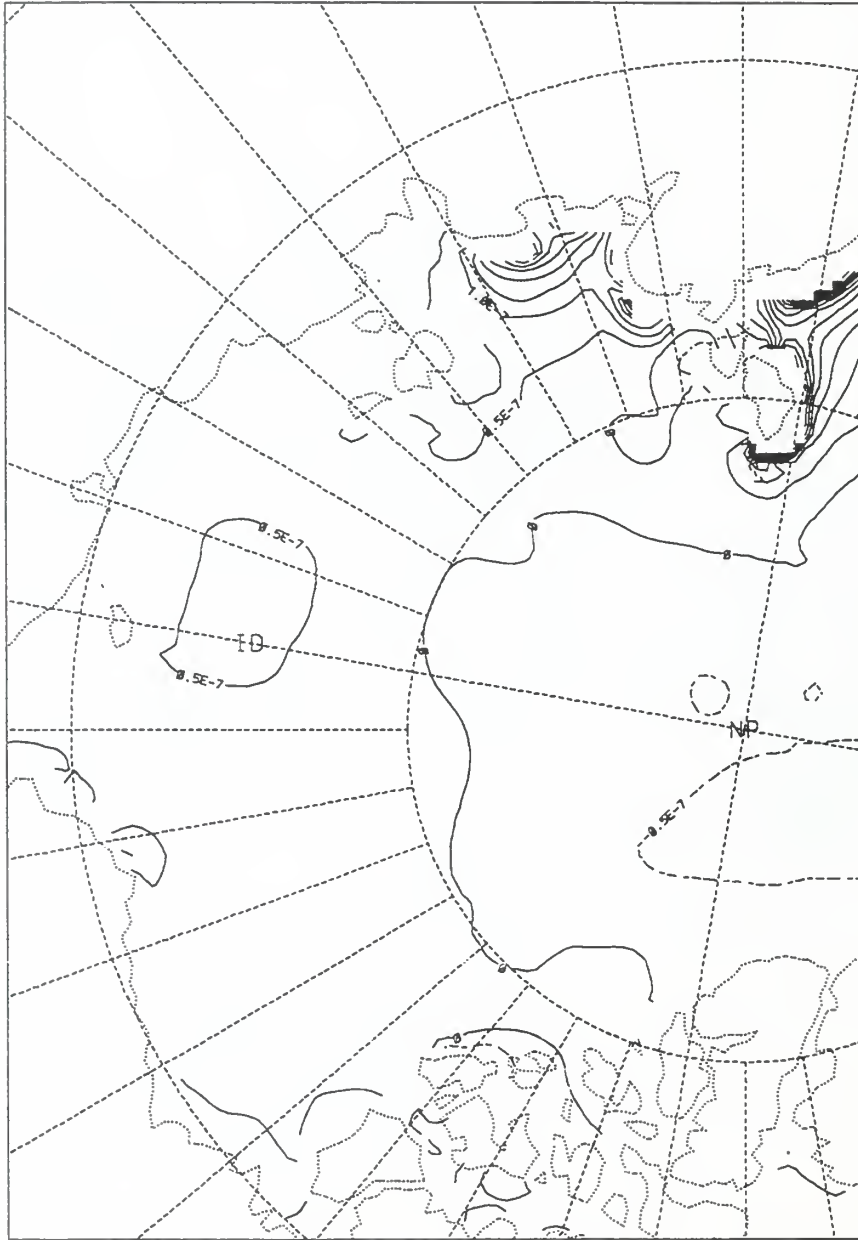
pips_zoom
1998030200

TAU = 24

ice_div

1/s

LEVEL= 0.0



CONTOUR FROM -0.0000005 TO 0.0000075 BY 0.0000005

Figure 138. PIPS model ice divergence chart for 0000Z 03 Mar 98.

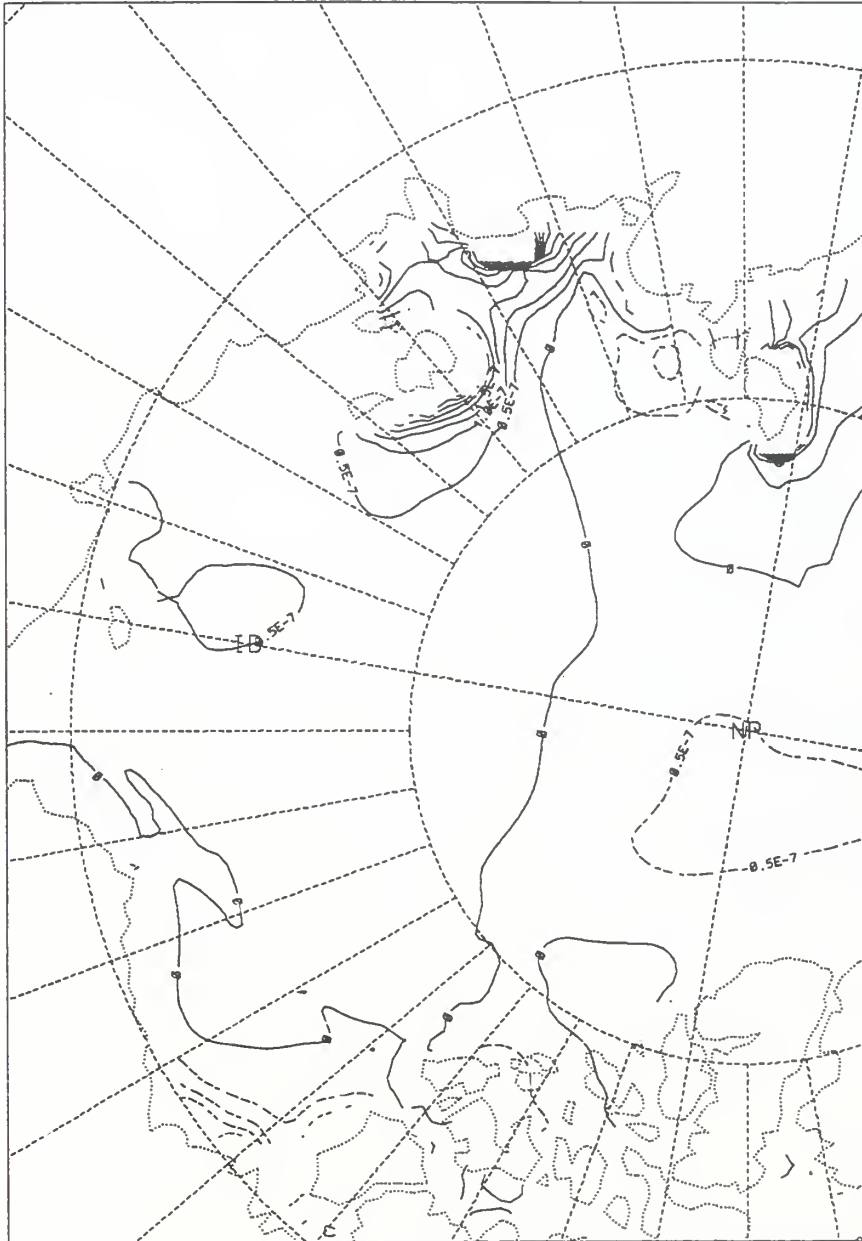
pips_zoom
1998030300

TAU = 24

ice_div

1/s

LEVEL= 0.0



CONTOUR FROM -2×10^{-7} TO .00000055 BY .00000006

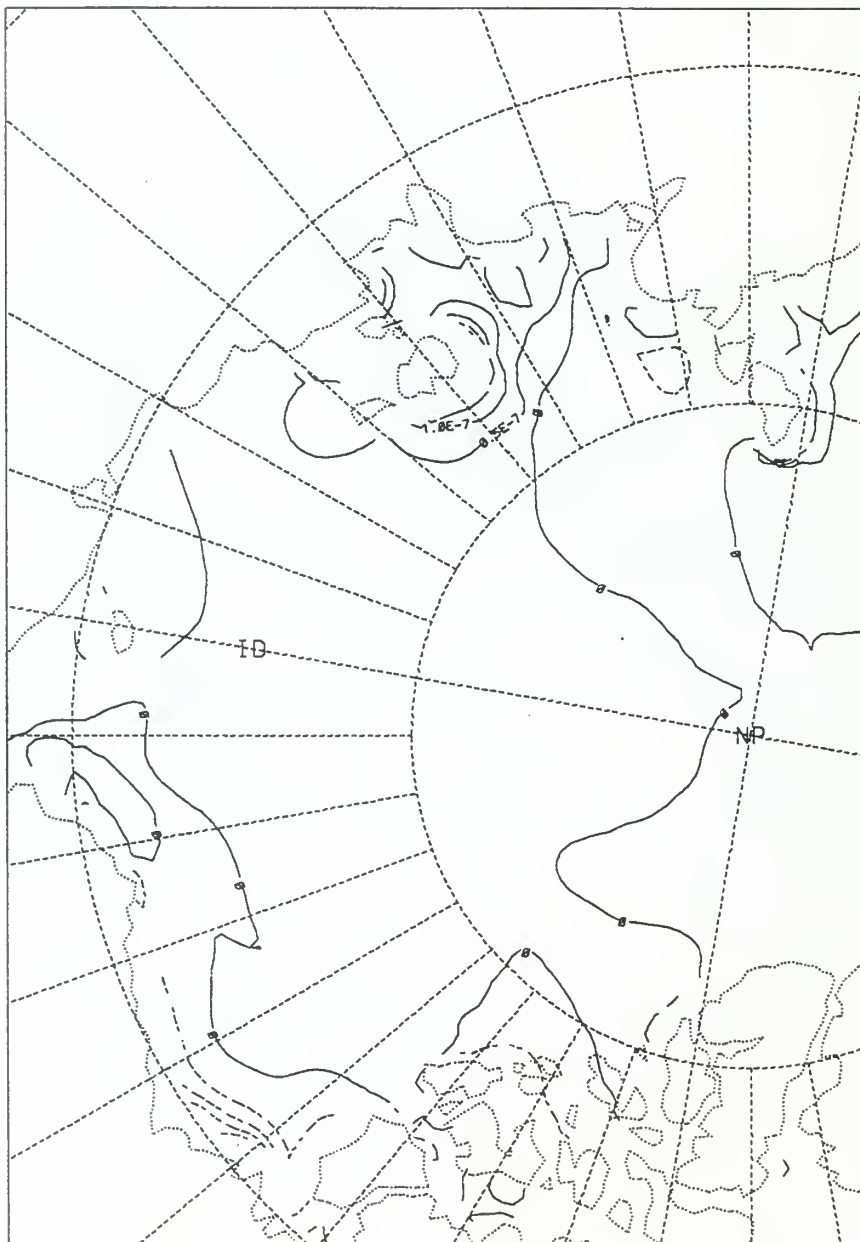
Figure 139. PIPS model ice divergence chart for 0000Z 04 Mar 98.

piPs_zoom
1998030400 TAU = 24

ice_div

1/s

LEVEL= 0.0



CONTOUR FROM -.00000025 TO .00000025 BY .00000005

Figure 140. PIPS model ice divergence chart for 0000Z 05 Mar 98.

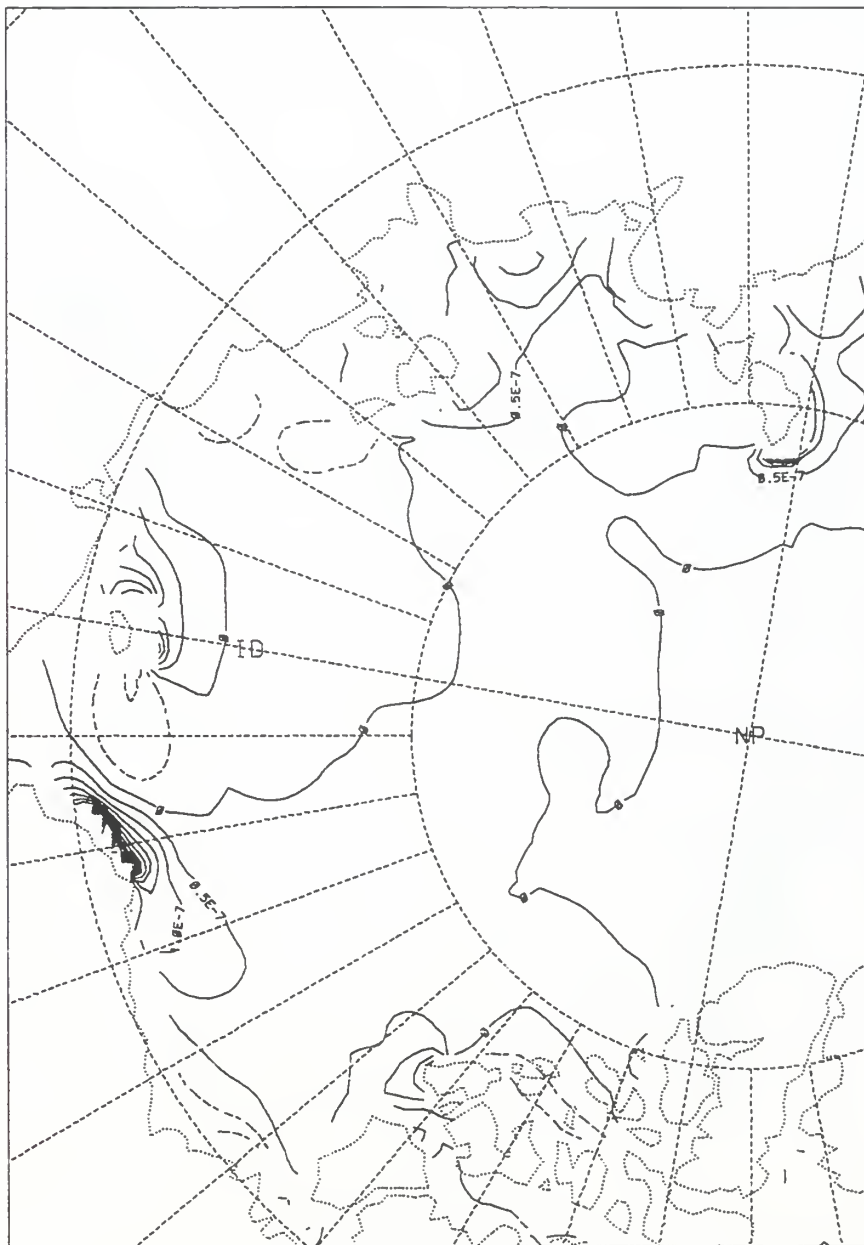
pips_zoom
1998030500

TAU = 24

ice_div

1/s

LEVEL = 0.0



CONTOUR FROM -10^{-7} TO 8×10^{-7} BY .00000006

Figure 141. PIPS model ice divergence chart for 0000Z 06 Mar 98.

piPs_zoom
1998030600

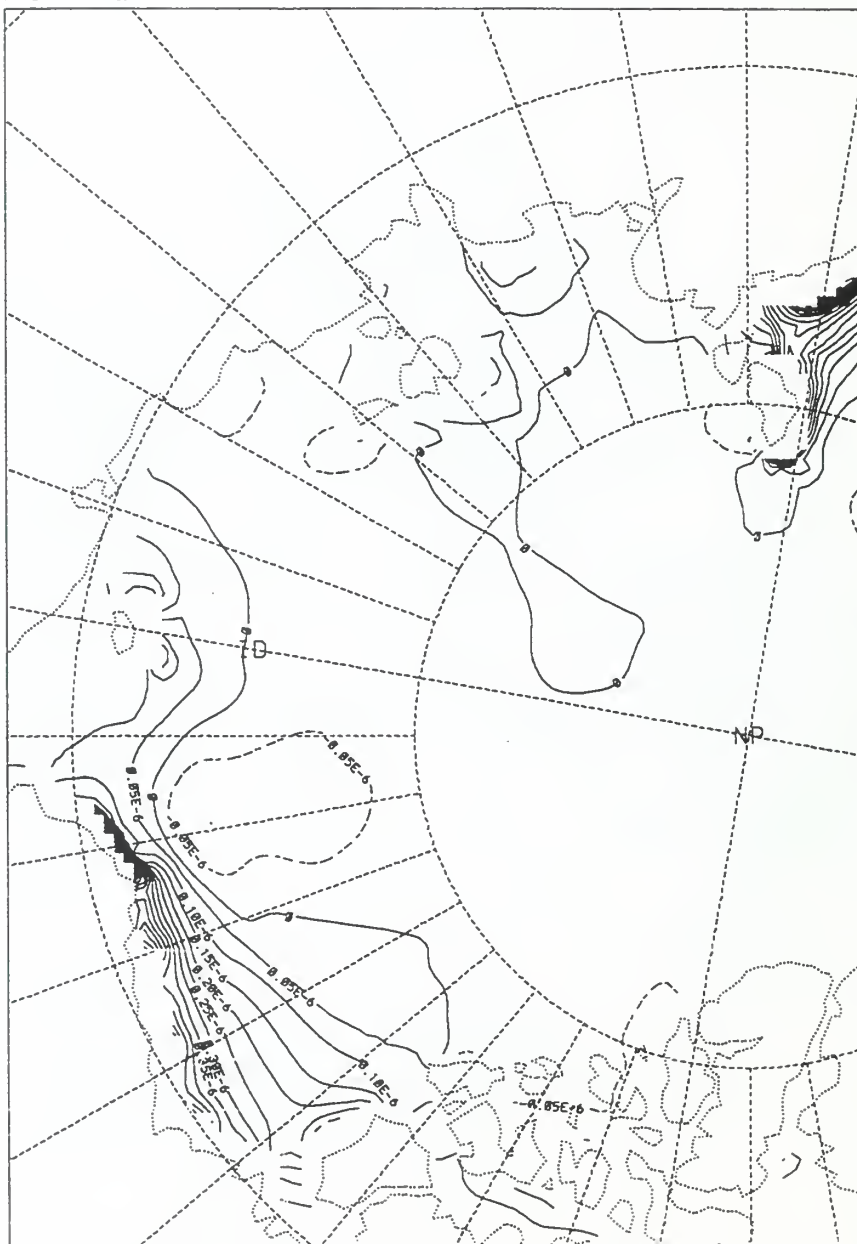
TAU = 24

ice_div

1/s

LEVEL=

0.0



CONTOUR FROM -.0000001 TO .00000145 BY .00000005

Figure 142. PIPs model ice divergence chart for 0000Z 07 Mar 98.

pips_zoom
1998030700

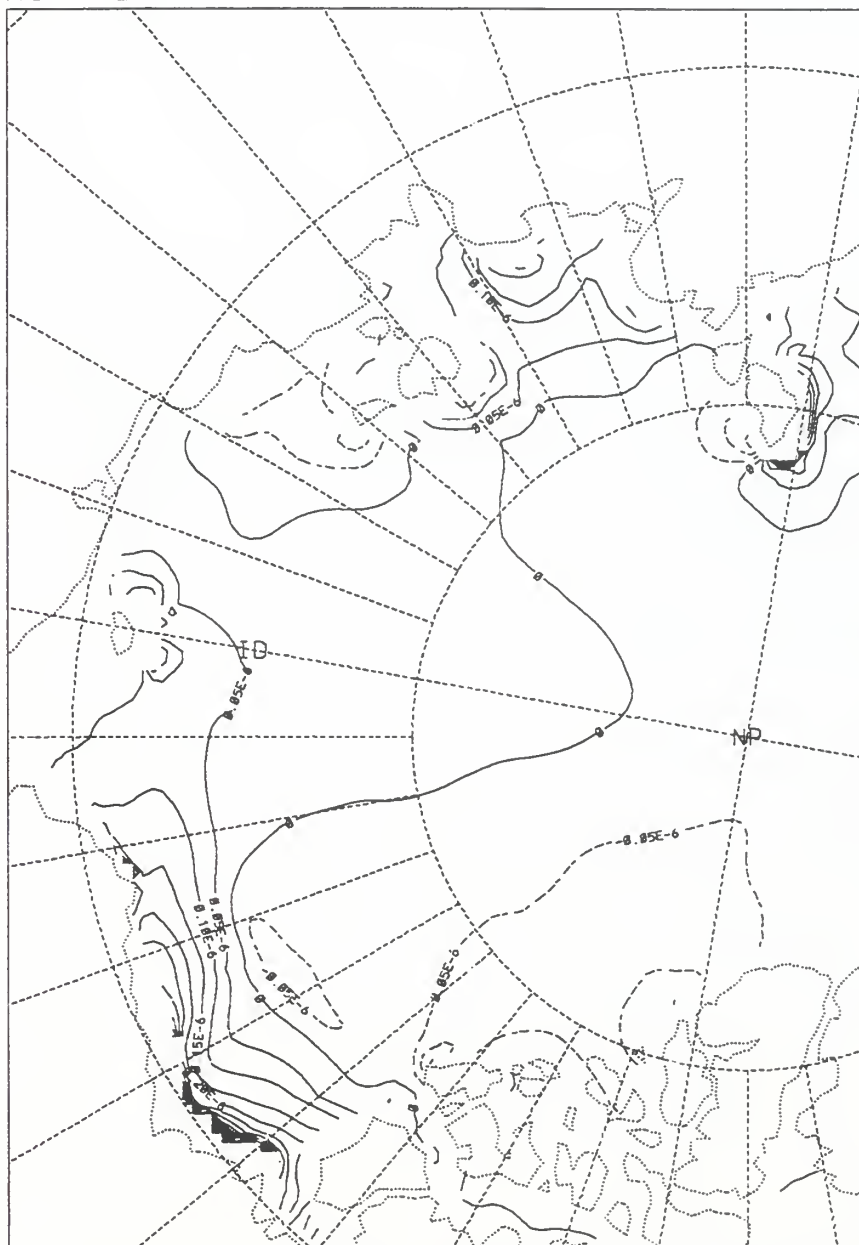
TAU = 24

ice_div

1/s

LEVEL =

0.0



CONTOUR FROM -.00000015 TO .00000125 BY .00000005

Figure 143. PIPS model ice divergence chart for 0000Z 08 Mar 98.

pips_zoom
1998030800

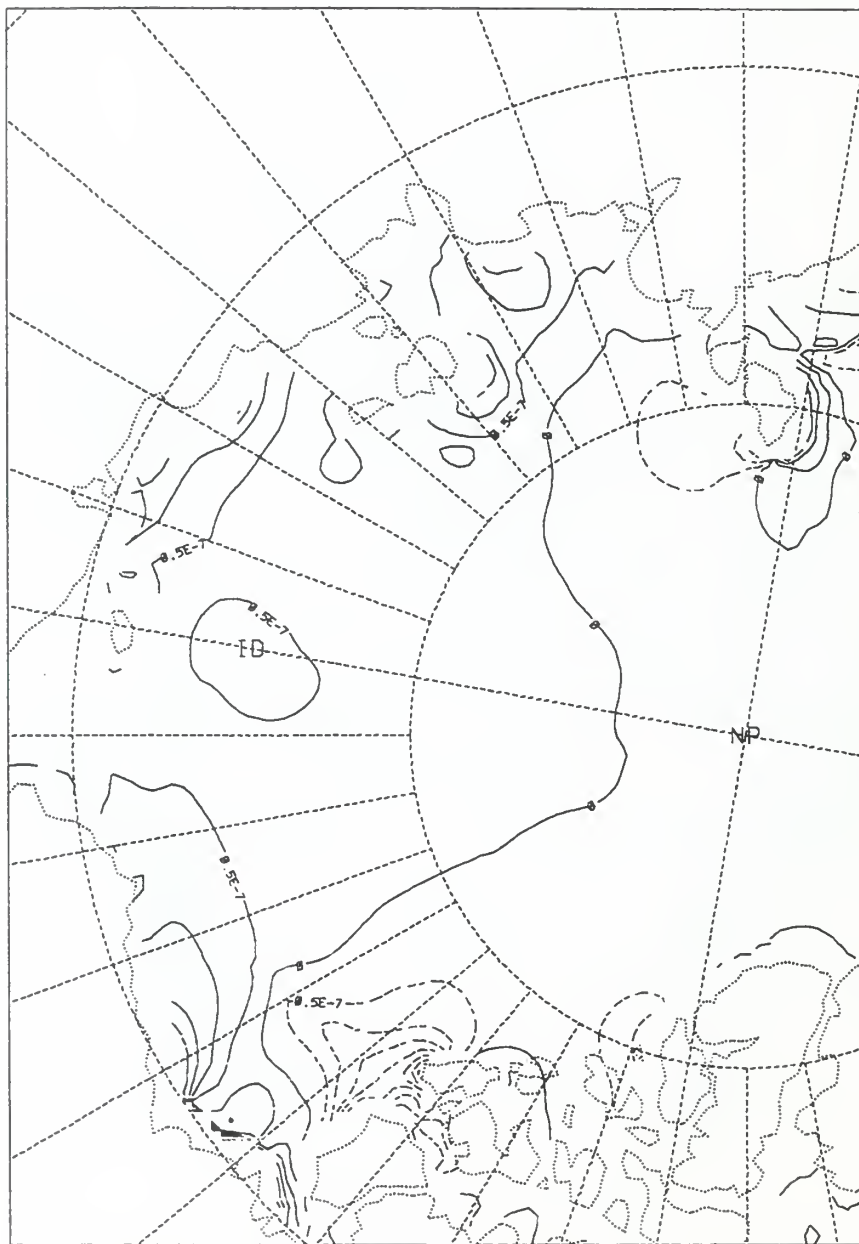
TAU = 24

ice_div

1/s

LEVEL =

0.0



CONTOUR FROM -.00000035 TO .00000035 BY .00000005

Figure 144. PIPs model ice divergence chart for 0000Z 09 Mar 98.

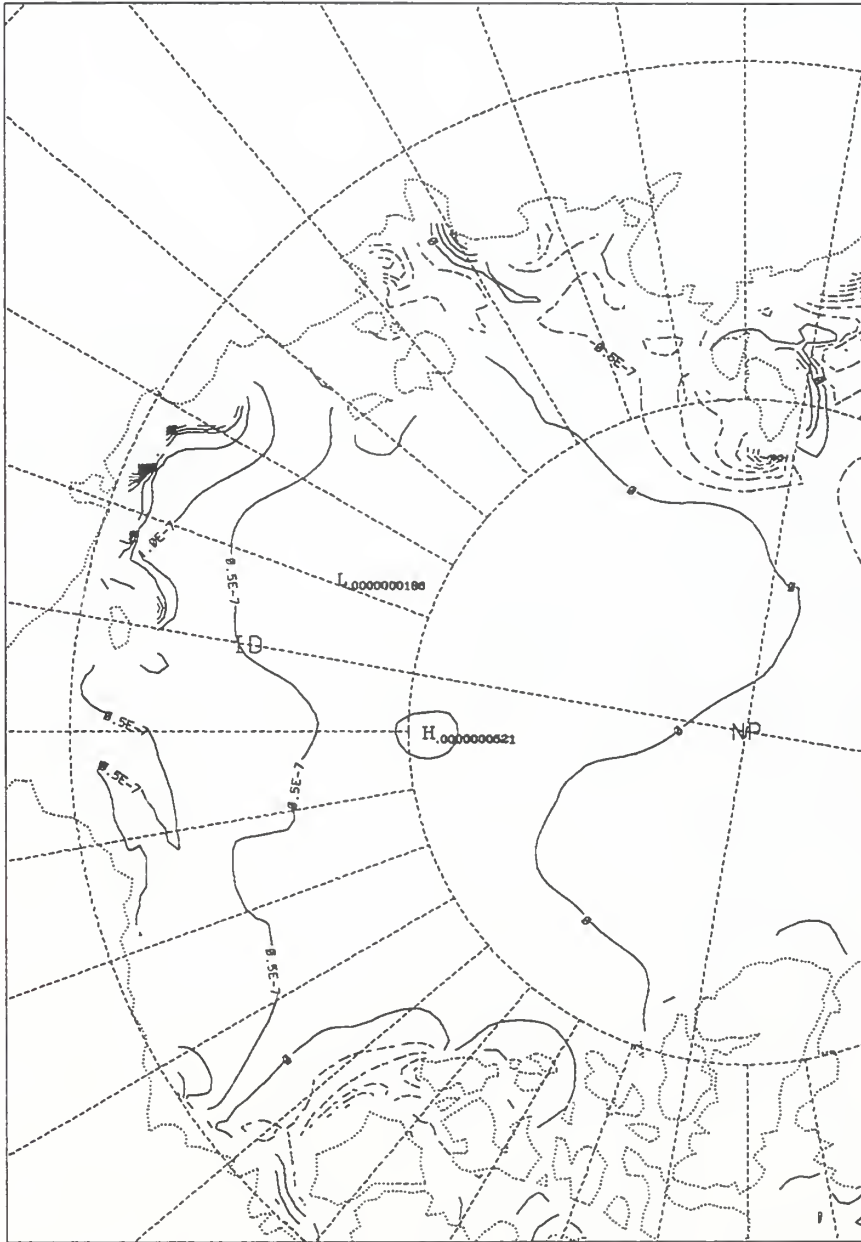
pips_zoom
1998030900

TAU = 24

ice_div

1/s

LEVEL= 0.0



CONTOUR FROM -4×10^{-7} TO 7×10^{-7} BY .00000005

Figure 145. PIPS model ice divergence chart for 0000Z 10 Mar 98.

pips_zoom
1998031000

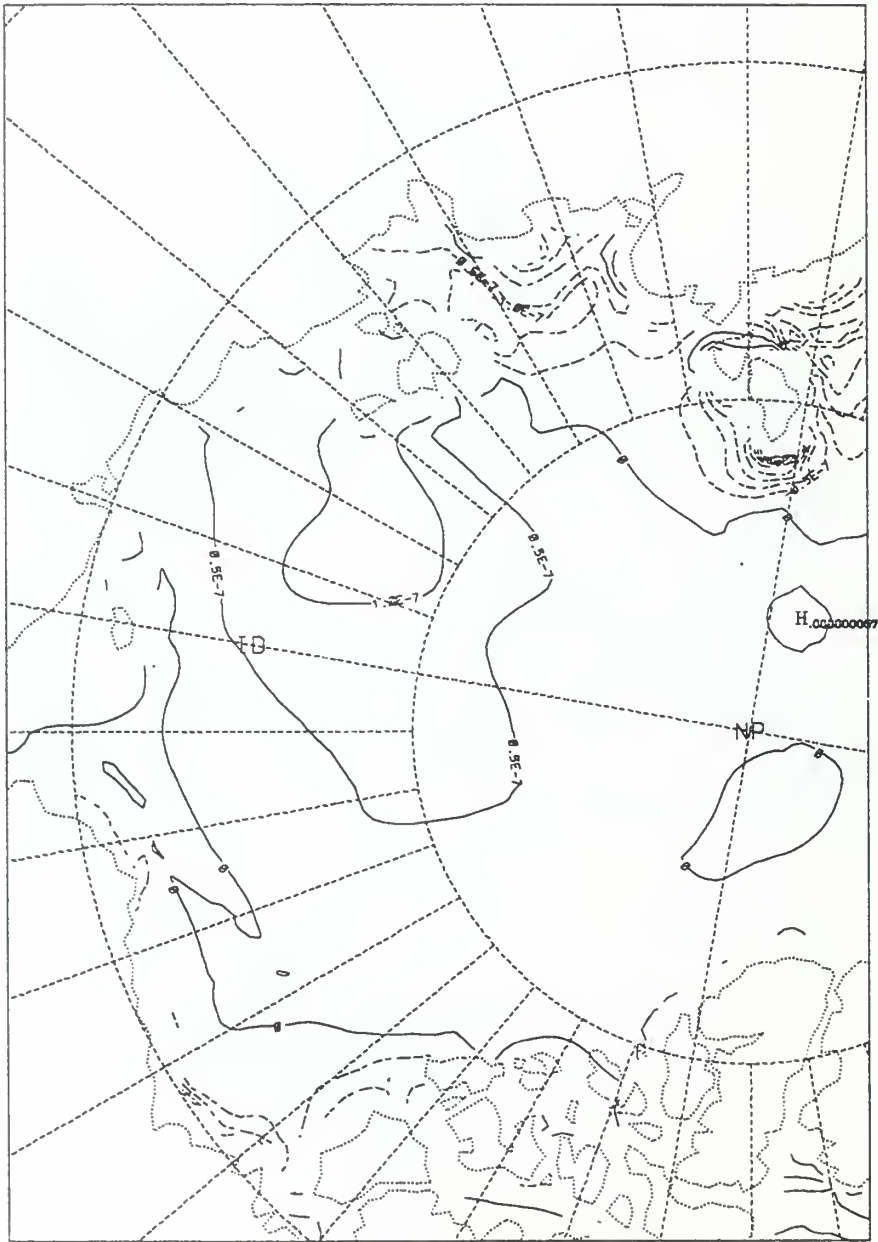
TAU = 24

ice_div

1/s

LEVEL=

0.0



CONTOUR FROM -.00000085 TO .00000025 BY .00000005

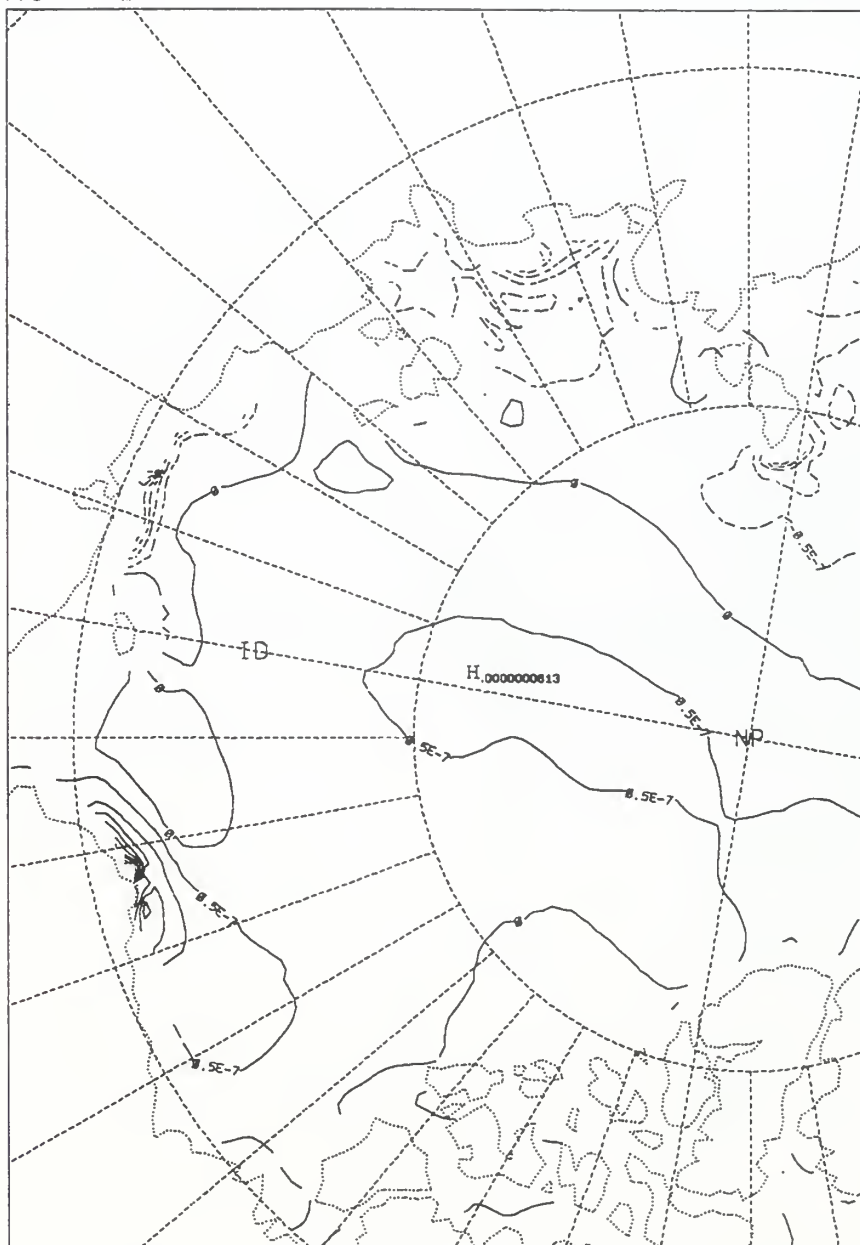
Figure 146. PIPS model ice divergence chart for 0000Z 11 Mar 98.

pips_zoom
1998031100 TAU = 24

ice_div

1/s

LEVEL= 0.0



CONTOUR FROM -.0000035 TO .0000045 BY .0000005

Figure 147. PIPS model ice divergence chart for 0000Z 12 Mar 98.

pips_zoom
1998031200

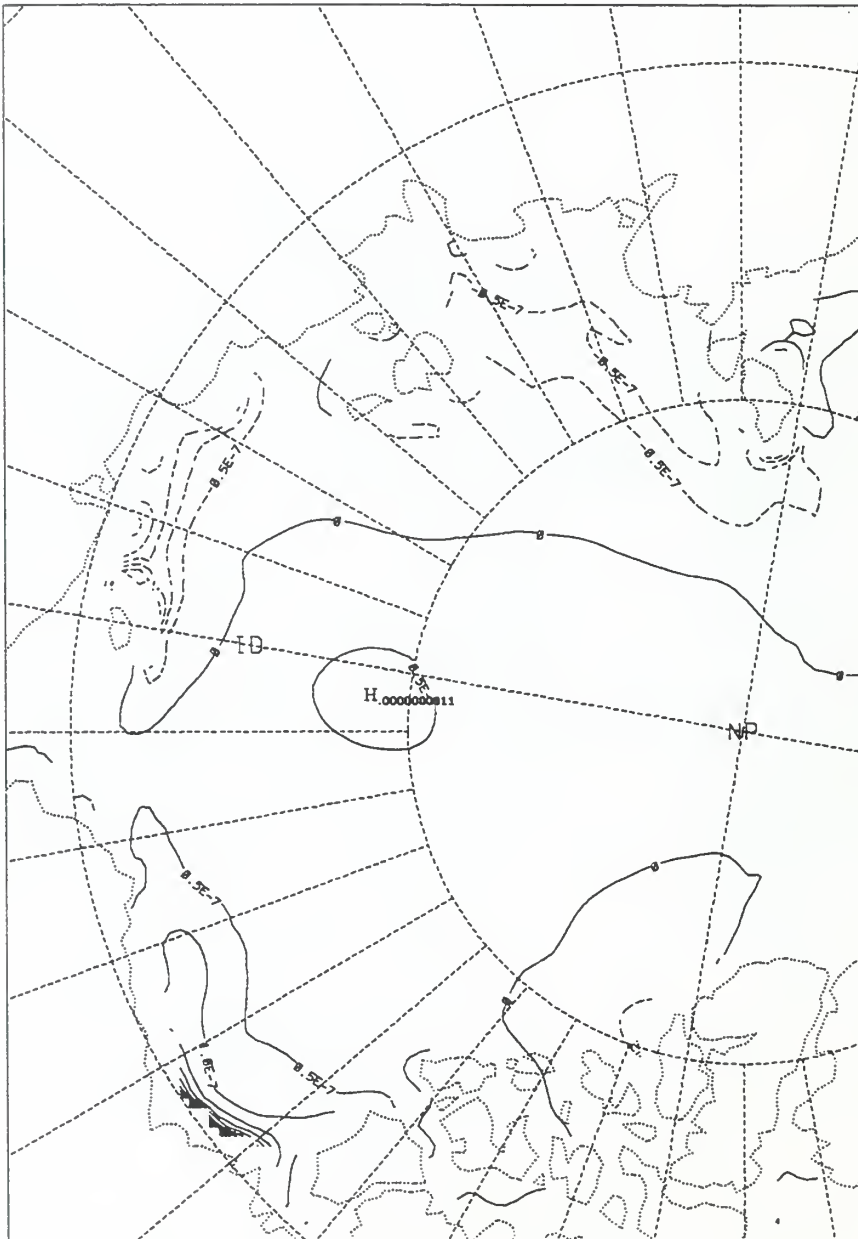
TAU = 24

ice_div

1/s

LEVEL=

0.0



CONTOUR FROM -0.00000025 TO 5×10^{-7} BY $.00000006$

Figure 148. PIPS model ice divergence chart for 0000Z 13 Mar 98.

Figure 149.
14 Mar 98
PIPS Ice Divergence Data Missing

pips_zoom
1998031400

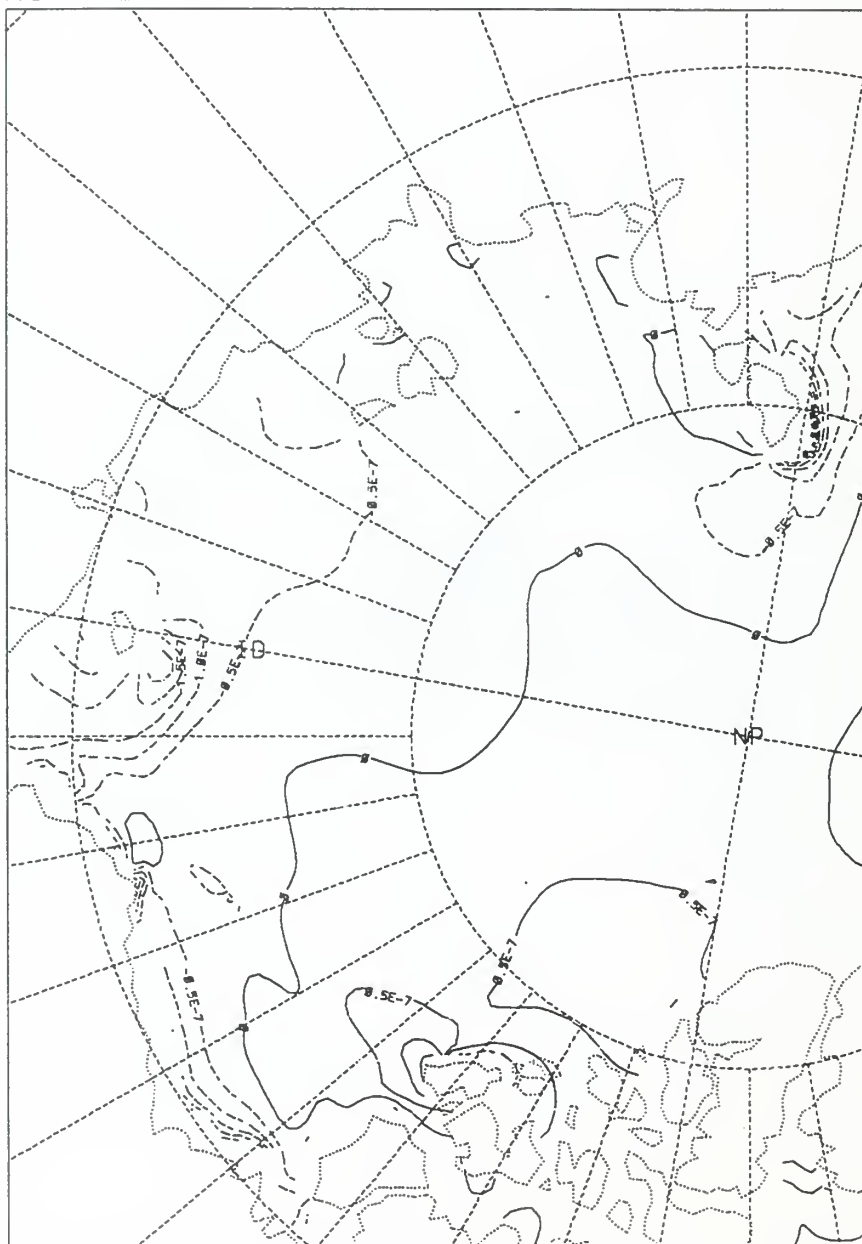
TAU = 24

ice_div

1/s

LEVEL=

0.0



CONTOUR FROM -5×10^{-7} TO .00000015 BY .00000006

Figure 150. PIPs model ice divergence chart for 0000Z 15 Mar 98.

pips_zoom
1998031500

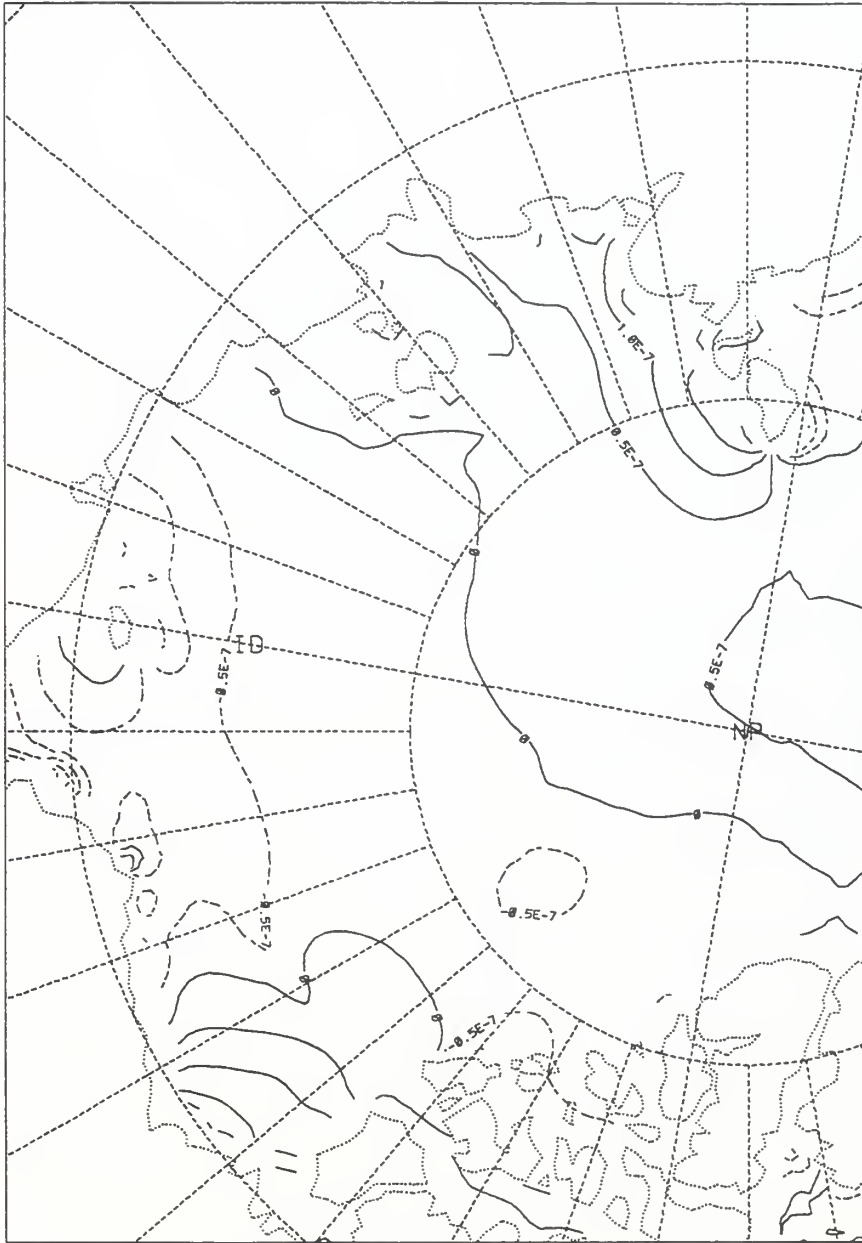
TAU = 24

ice_div

1/s

LEVEL =

0.0



CONTOUR FROM -0.0000025 TO 2×10^{-7} BY 0.0000005

Figure 151. PIPS model ice divergence chart for 0000Z 16 Mar 98.

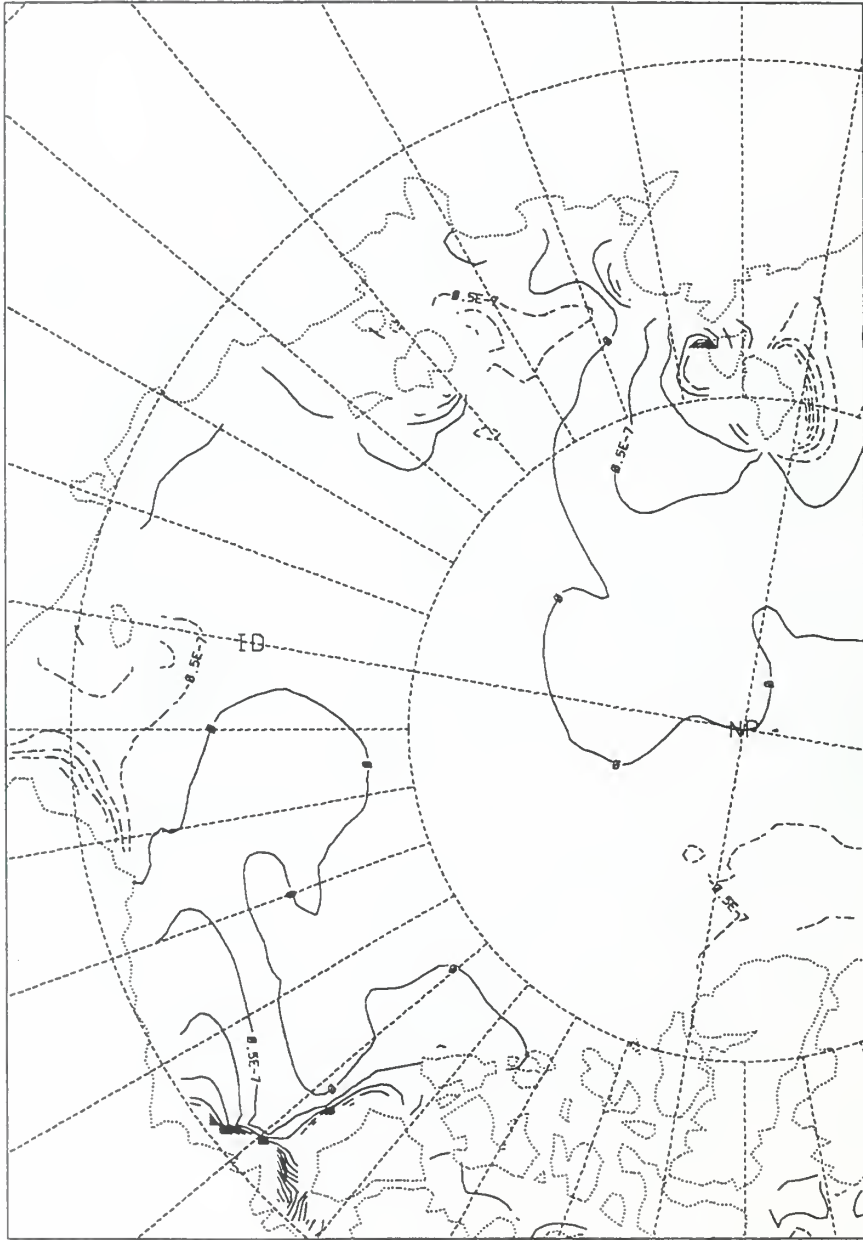
piPs_zoom
1998031600

TAU = 24

ice_div

1/s

LEVEL= 0.0



CONTOUR FROM -3×10^{-7} TO .00000055 BY .00000006

Figure 152. PIPs model ice divergence chart for 0000Z 17 Mar 98.

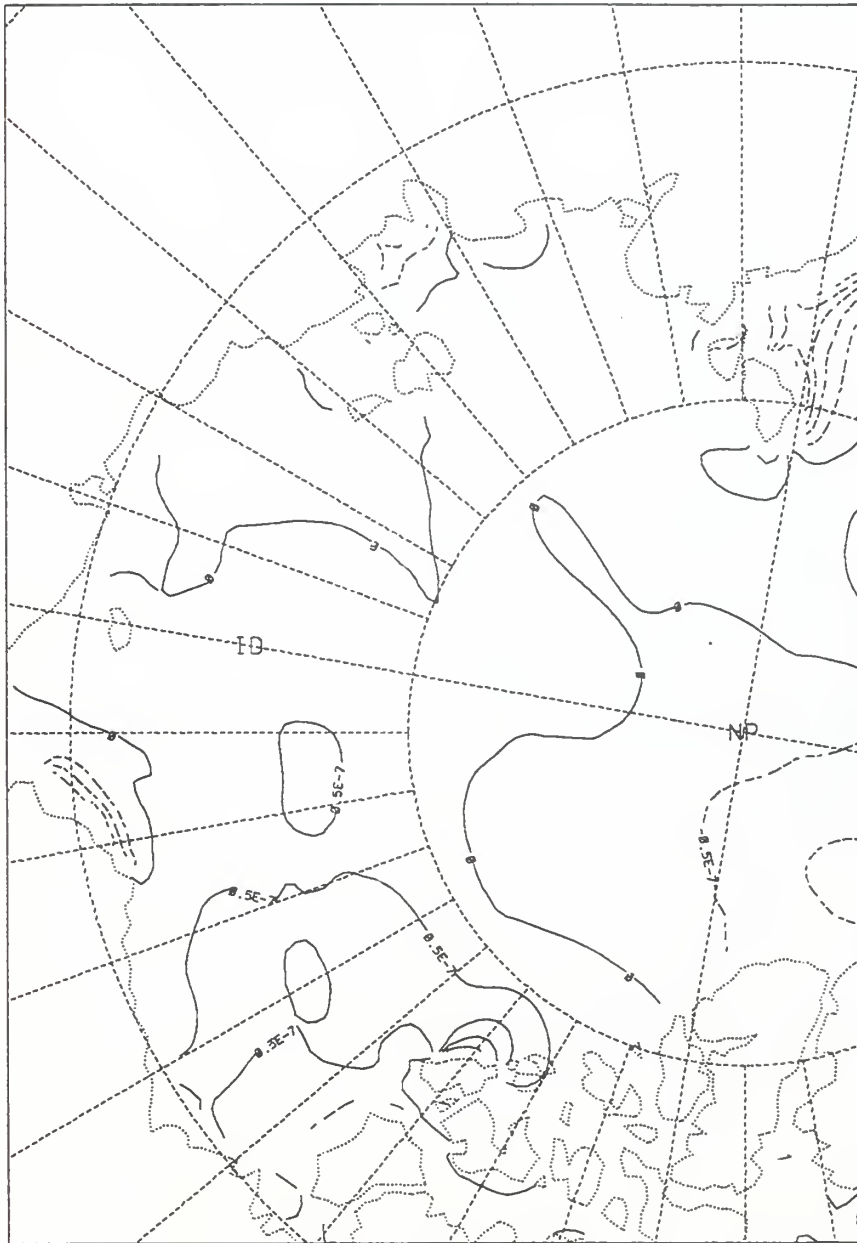
pips_zoom
1998031700

TAU = 24

ice_div

1/s

LEVEL= 0.0



CONTOUR FROM -0.00000025 TO 2×10^{-7} BY $.00000005$

Figure 153. PIPS model ice divergence chart for 0000Z 18 Mar 98.

pi ps_zoom
1998031800

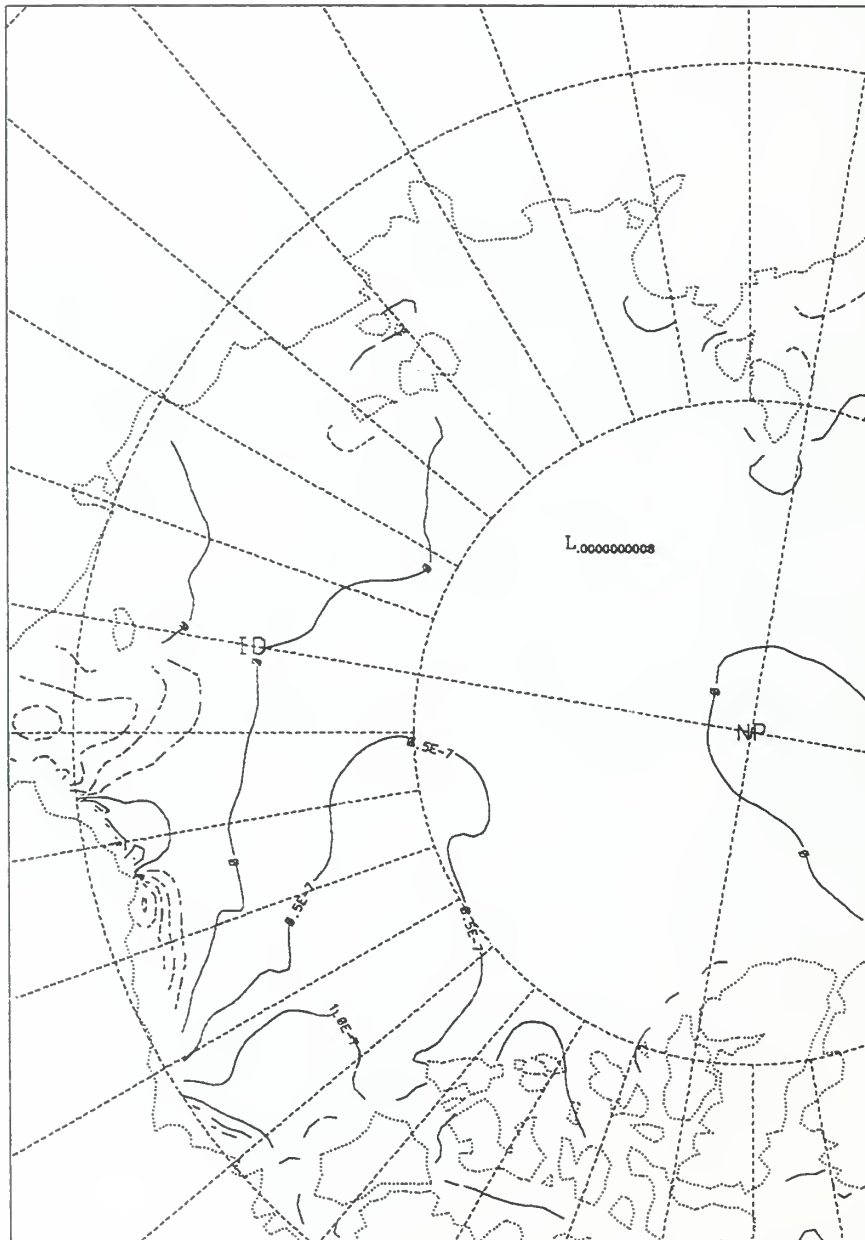
TAU = 24

ice_div

1/s

LEVEL =

0.0



CONTOUR FROM -3×10^{-7} TO .00000025 BY .00000005

Figure 154. PIPS model ice divergence chart for 0000Z 19 Mar 98.

pipe_zoom
1998031900

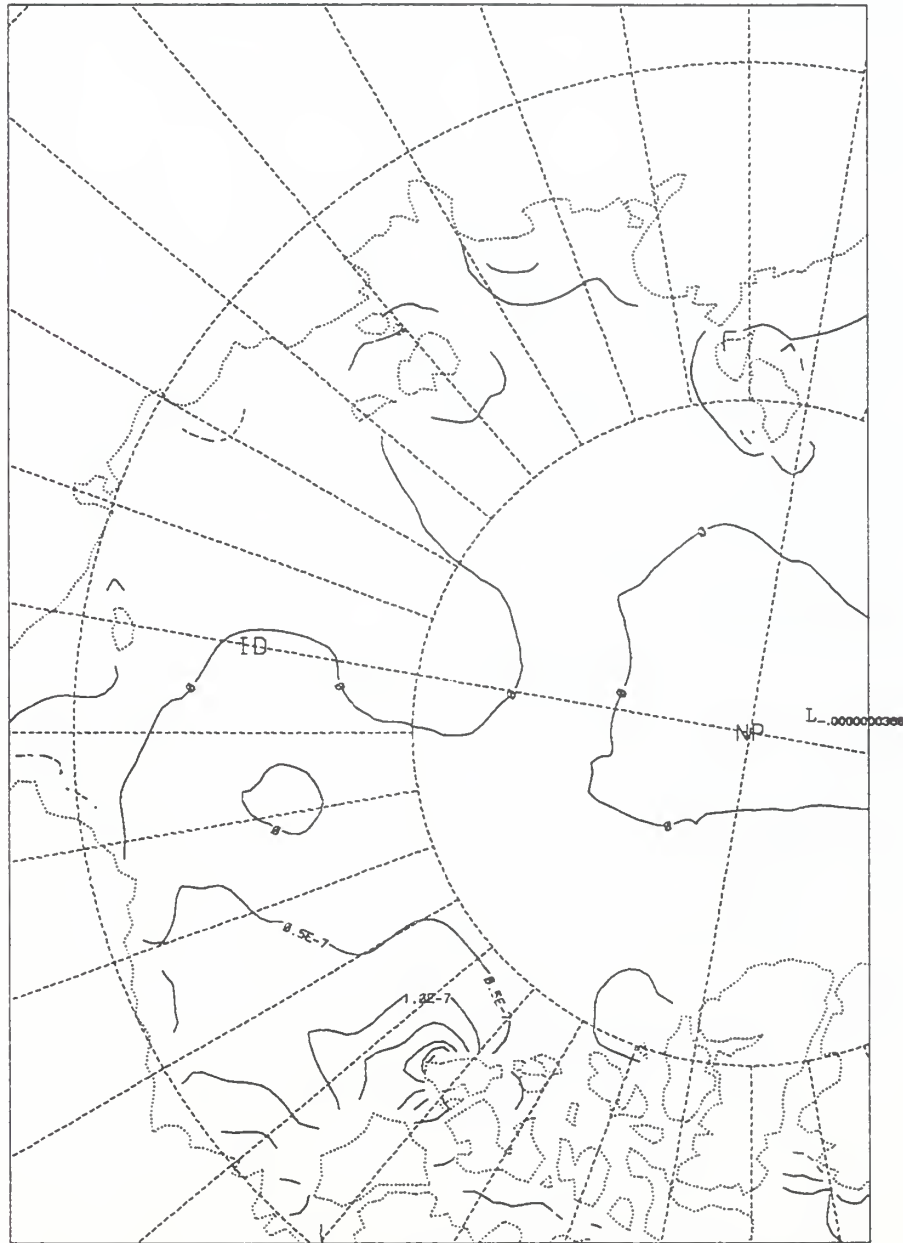
TAU = 24

ice_div

1/s

LEVEL=

0.0



CONTOUR FROM -10^{-7} TO 3×10^{-7} BY .00000005

Figure 155. PIPS model ice divergence chart for 0000Z 20 Mar 98.

pips_zoom
1998032000

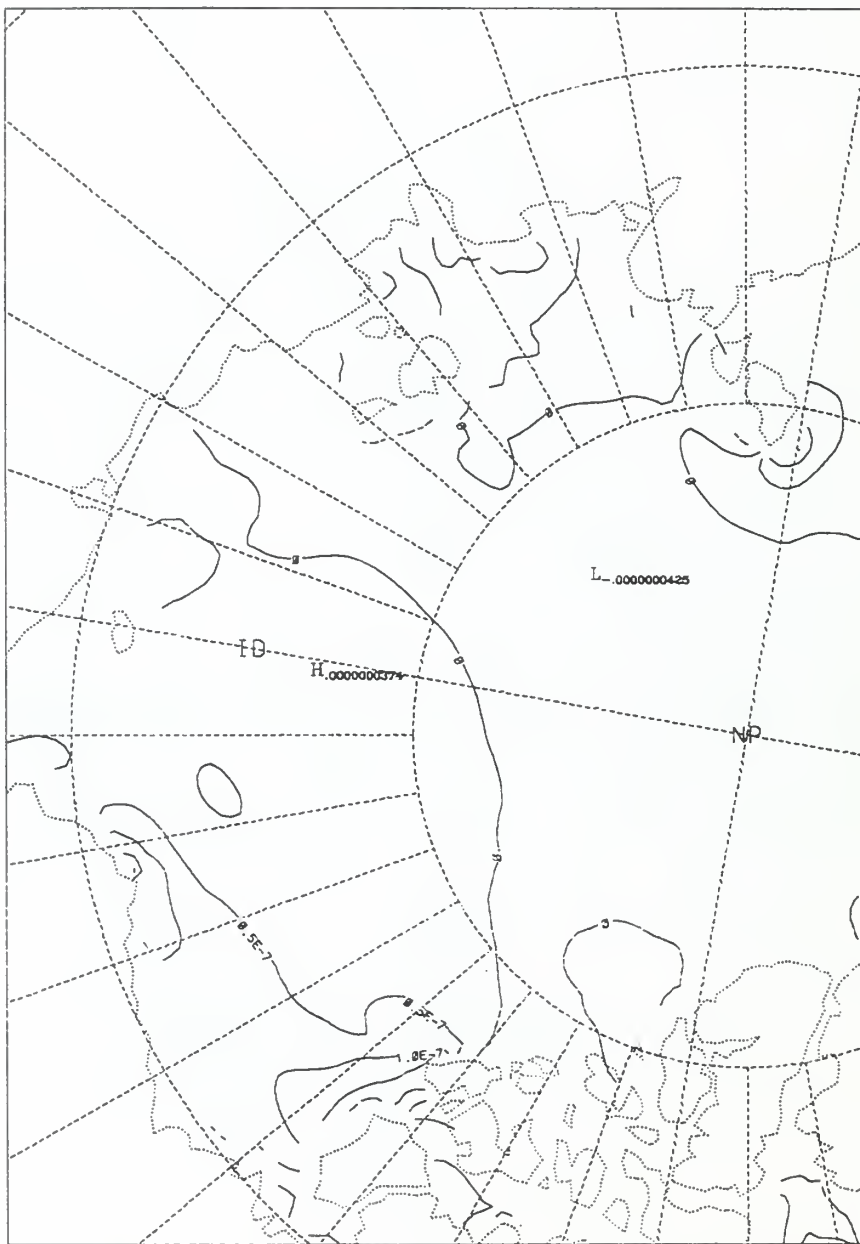
TAU = 24

ice_div

1/s

LEVEL=

0.0



CONCUR FROM -10^{-7} TO 2×10^{-7} BY .00000005

Figure 156. PIPs model ice divergence chart for 0000Z 21 Mar 98.

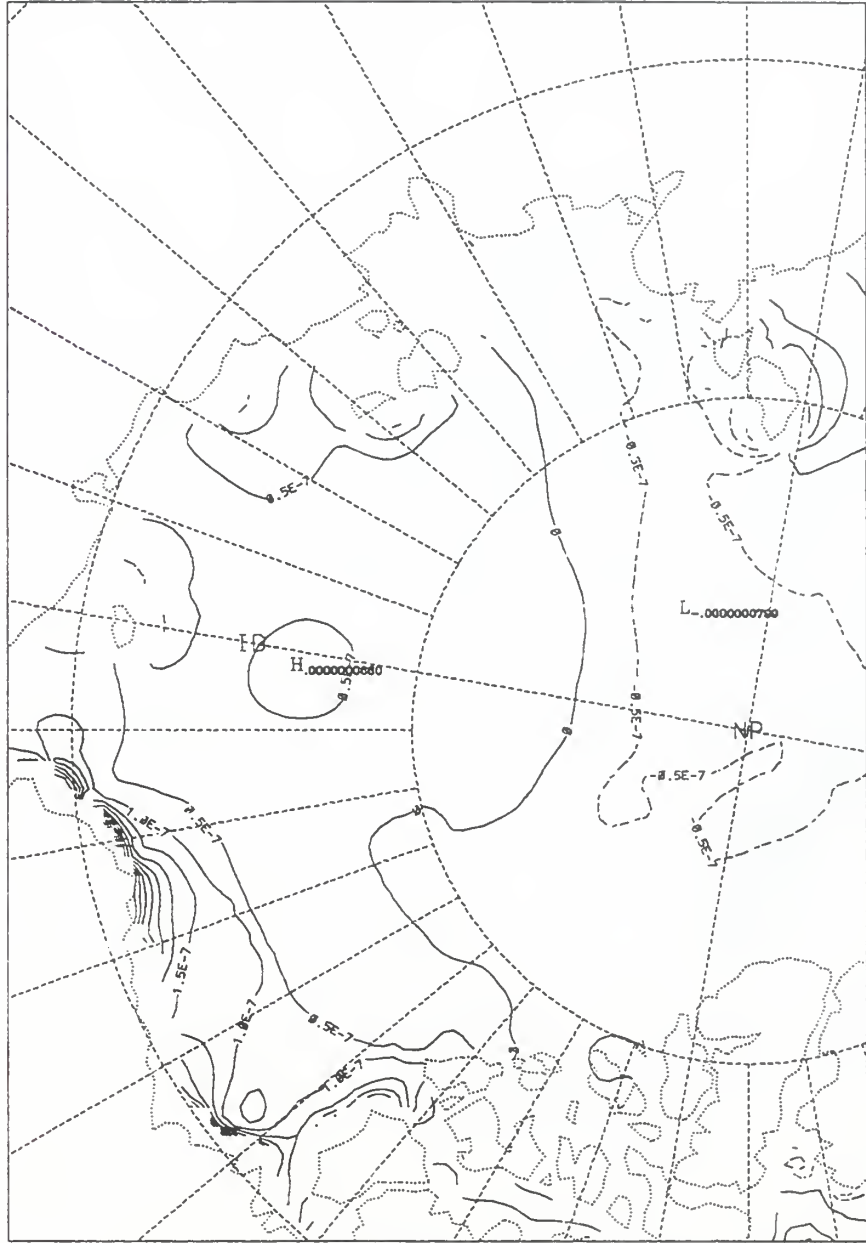
pips_zoom
1998032100

TAU = 24

ice_div

1/s

LEVEL = 0.0



CONTOUR FROM -2×10^{-7} TO .00000055 BY .00000006

Figure 157. PIPS model ice divergence chart for 0000Z 22 Mar 98.

pips_zoom
1998032300

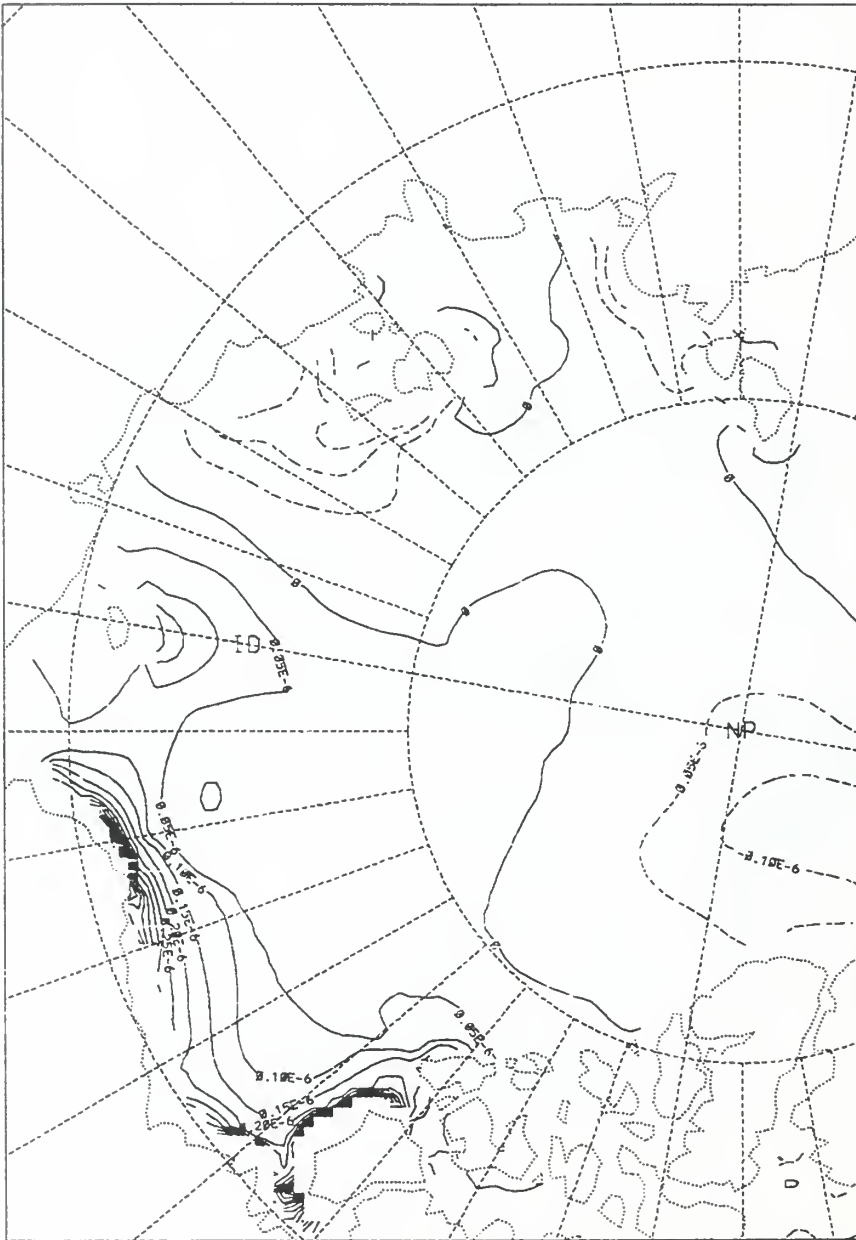
TAU = 24

ice_div

1/s

LEVEL =

0.0



CONTOUR FROM -.00000015 TO .00000095 BY .00000005

Figure 158. PIPS model ice divergence chart for 0000Z 23 Mar 98.

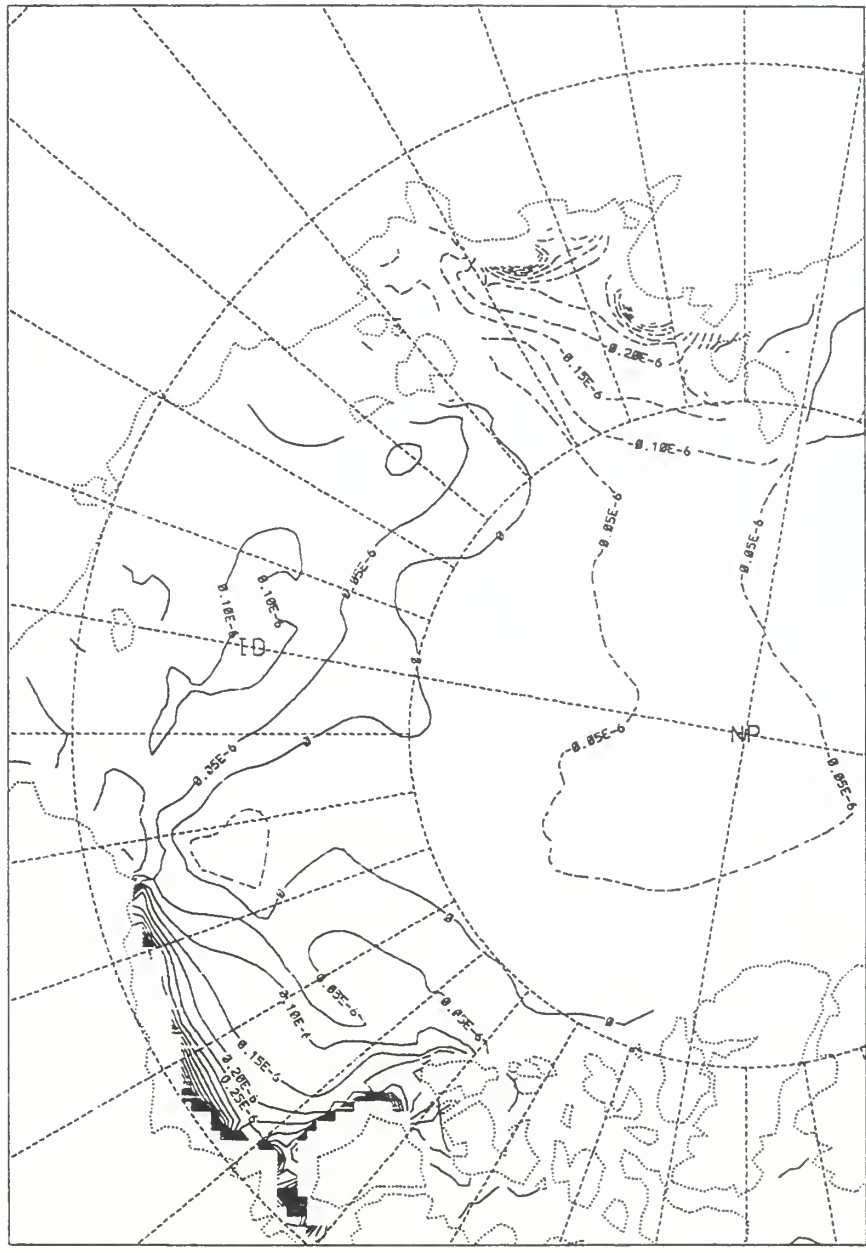
pips_zoom
1998032400

TAU = 24

ice_div

1/s

LEVEL= 0.0



CONTOUR FROM -.0000008 TO .0000019 BY .0000005

Figure 159. PIPS model ice divergence chart for 0000Z 24 Mar 98.

pips_zoom
1998032200

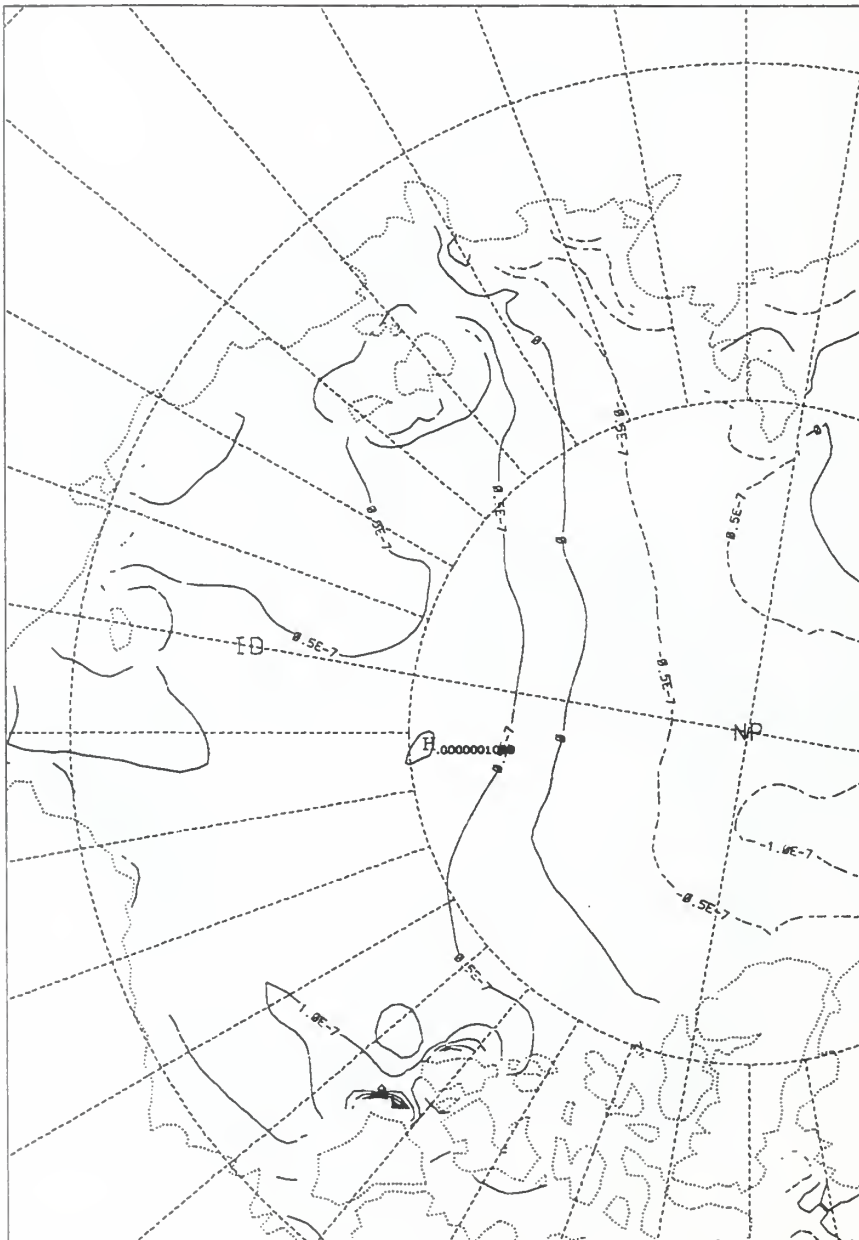
TAU = 24

ice_div

1/s

LEVEL=

0.0



CONTOUR FROM -2×10^{-7} TO .0000045 BY .0000006

Figure 160. PIPS model ice divergence chart for 0000Z 25 Mar 98.

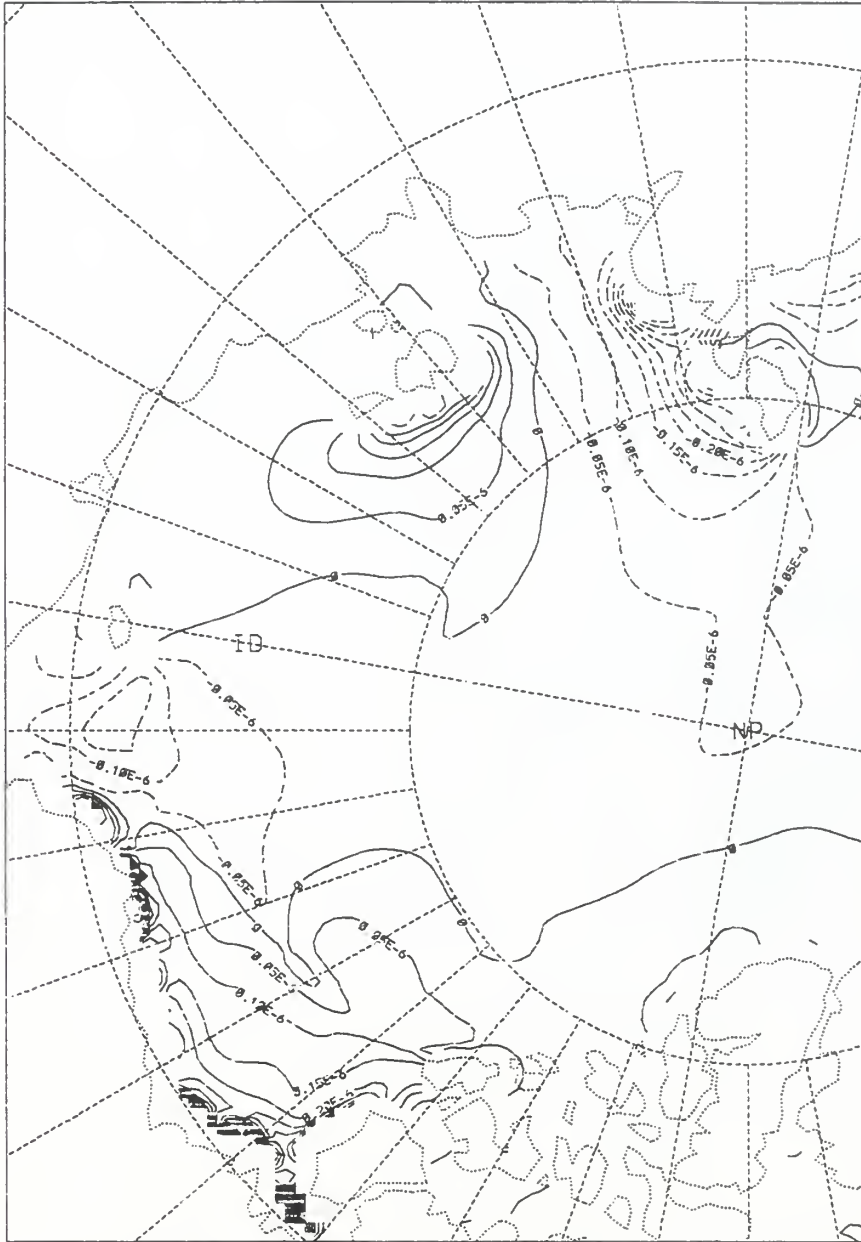
pi ps_zoom
1998032500

TAU = 24

ice_div

1/s

LEVEL = 0.0



CONTOUR FROM -.0000005 TO .0000014 BY .0000005

Figure 161. PIPS model ice divergence chart for 0000Z 26 Mar 98.

pi ps_zoom
1998032600

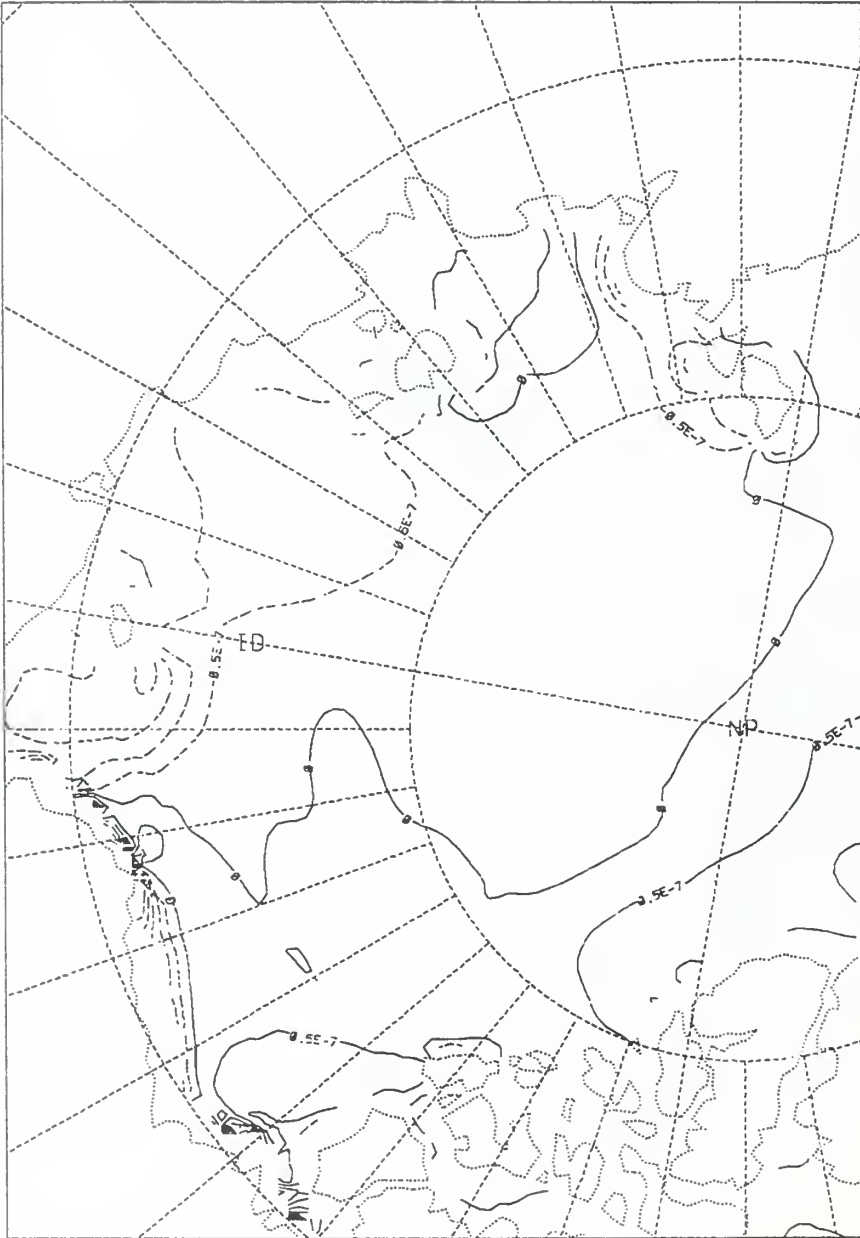
TAU = 24

ice_div

1/s

LEVEL =

0.0



CONTOUR FROM -3×10^{-7} TO 8×10^{-7} BY .00000005

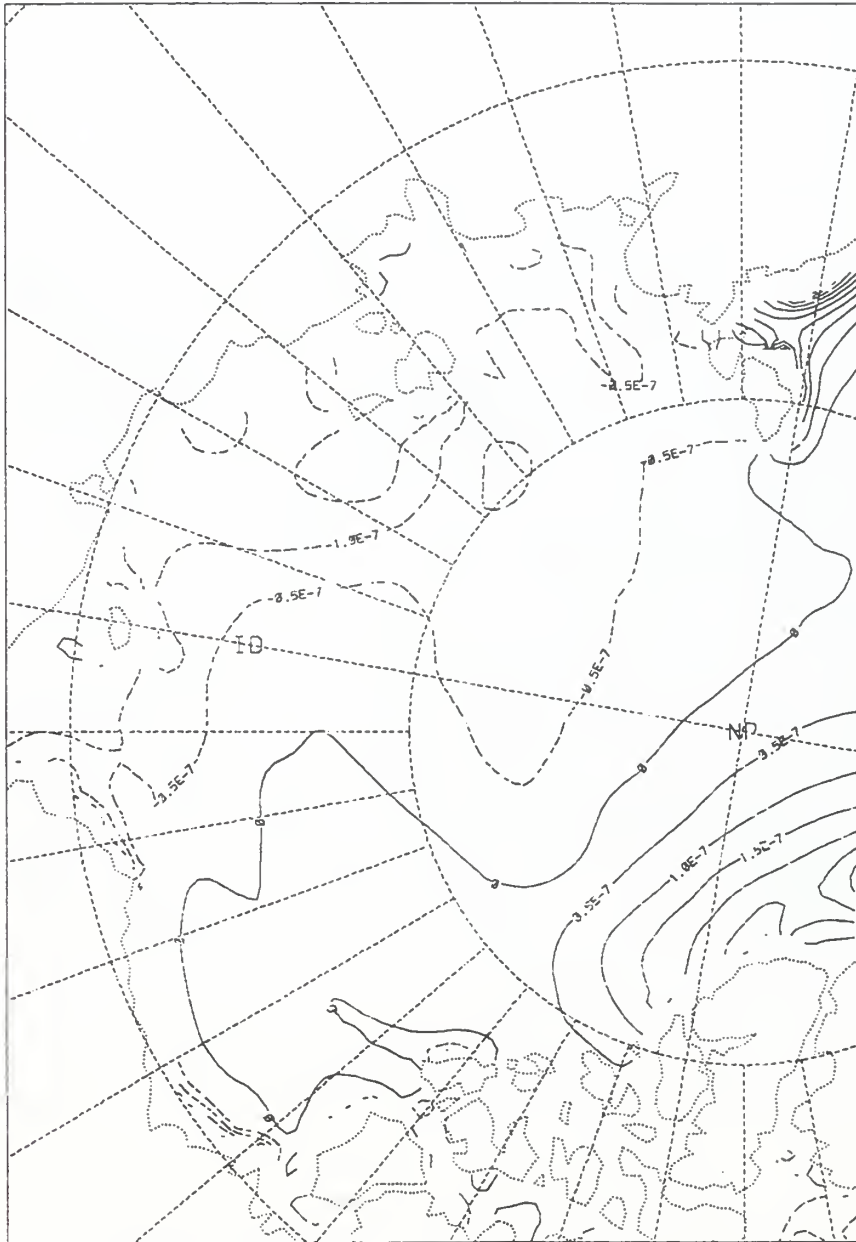
Figure 162. PIPS model ice divergence chart for 0000Z 27 Mar 98.

pijs_zoom
1998032700 TAU = 24

ice_div

1/s

LEVEL= 0.0



CONTOUR FROM -2×10^{-7} TO 5×10^{-7} BY .00000005

Figure 163. PIPS model ice divergence chart for 0000Z 28 Mar 98.

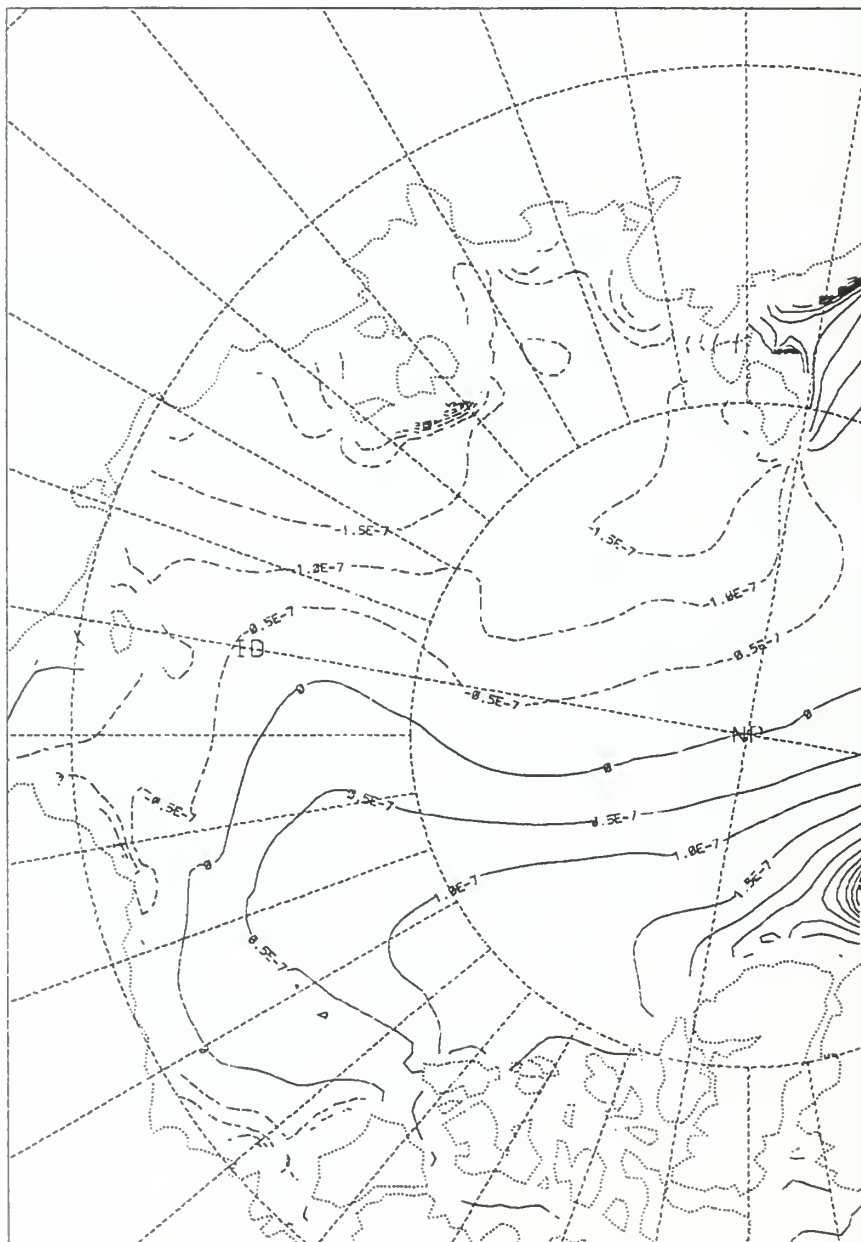
pips_zoom
1998032800

TAU = 24

ice_div

1/s

LEVEL= 0.0



CONTOUR FROM -5×10^{-7} TO .00000075 BY .00000006

Figure 164. PIPS model ice divergence chart for 0000Z 29 Mar 98.

pips_zoom
1998032900

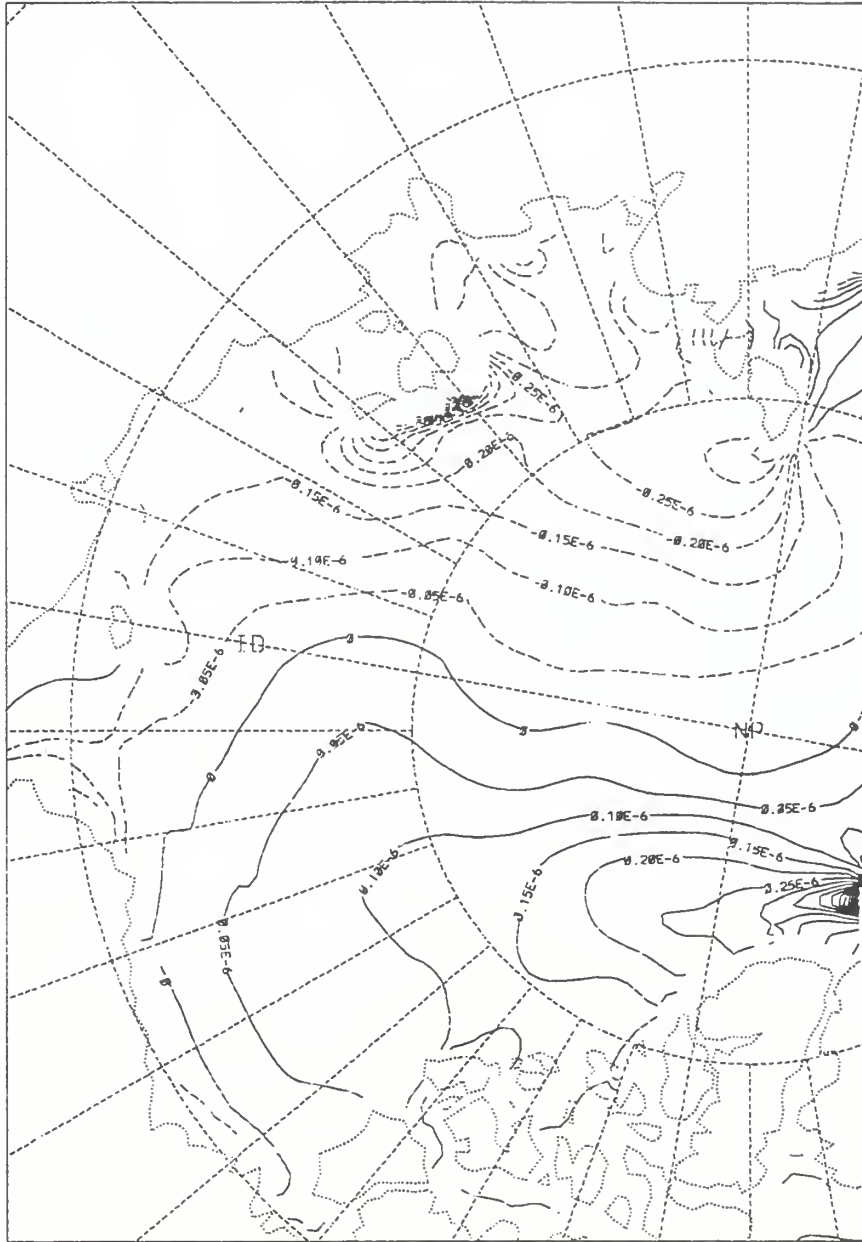
TAU = 24

ice_div

1/s

LEVEL =

0.0



CONTOUR FROM -.00000075 TO .0000013 BY .00000005

Figure 165. PIPS model ice divergence chart for 0000Z 30 Mar 98.

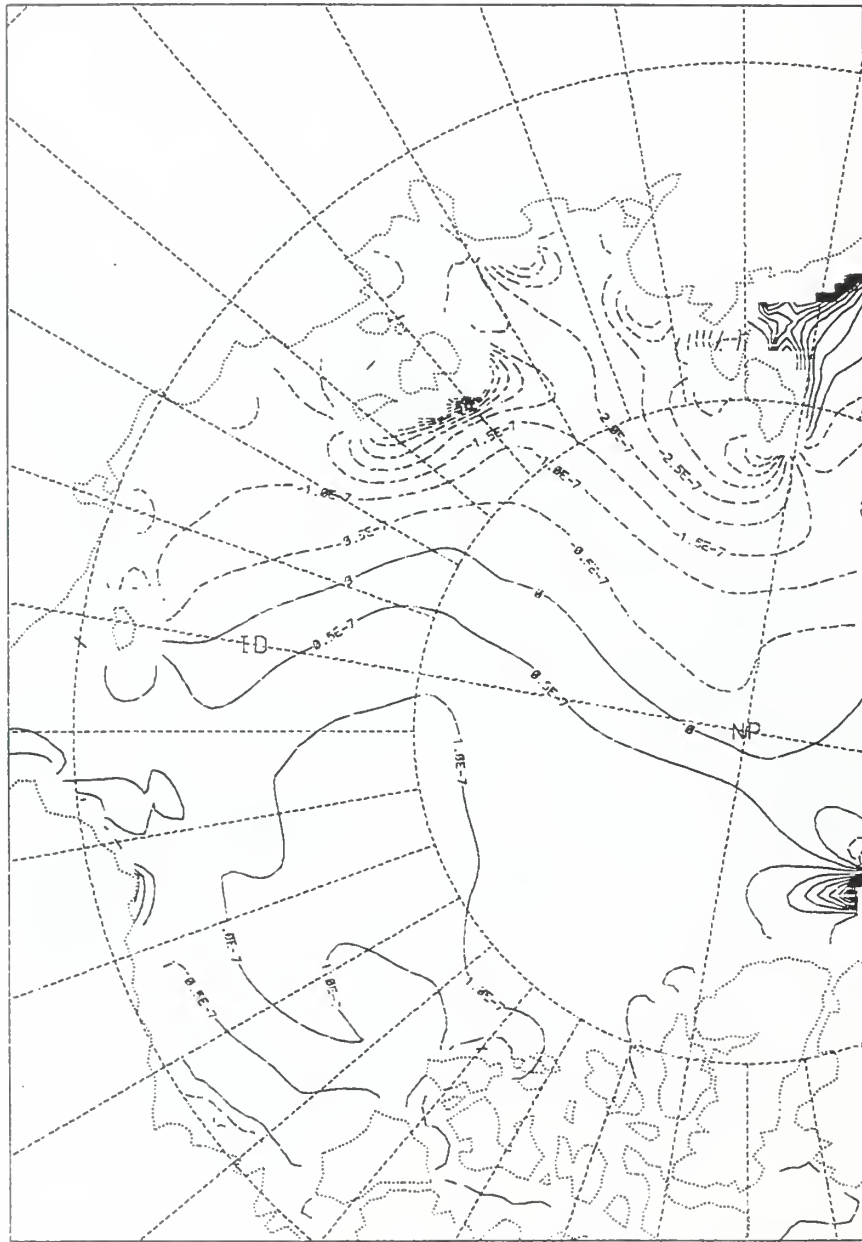
pips_zoom
1998033000

TAU = 24

ice_div

1/s

LEVEL = 0.0



CONTOUR FROM -7×10^{-7} TO 9×10^{-7} BY .0000005

Figure 166. PIPS model ice divergence chart for 0000Z 31 Mar 98.

APPENDIX H

**NOGAPS MODEL ICE DIVERGENCE DATA:
13 FEBRUARY TO 31 MARCH 1998**

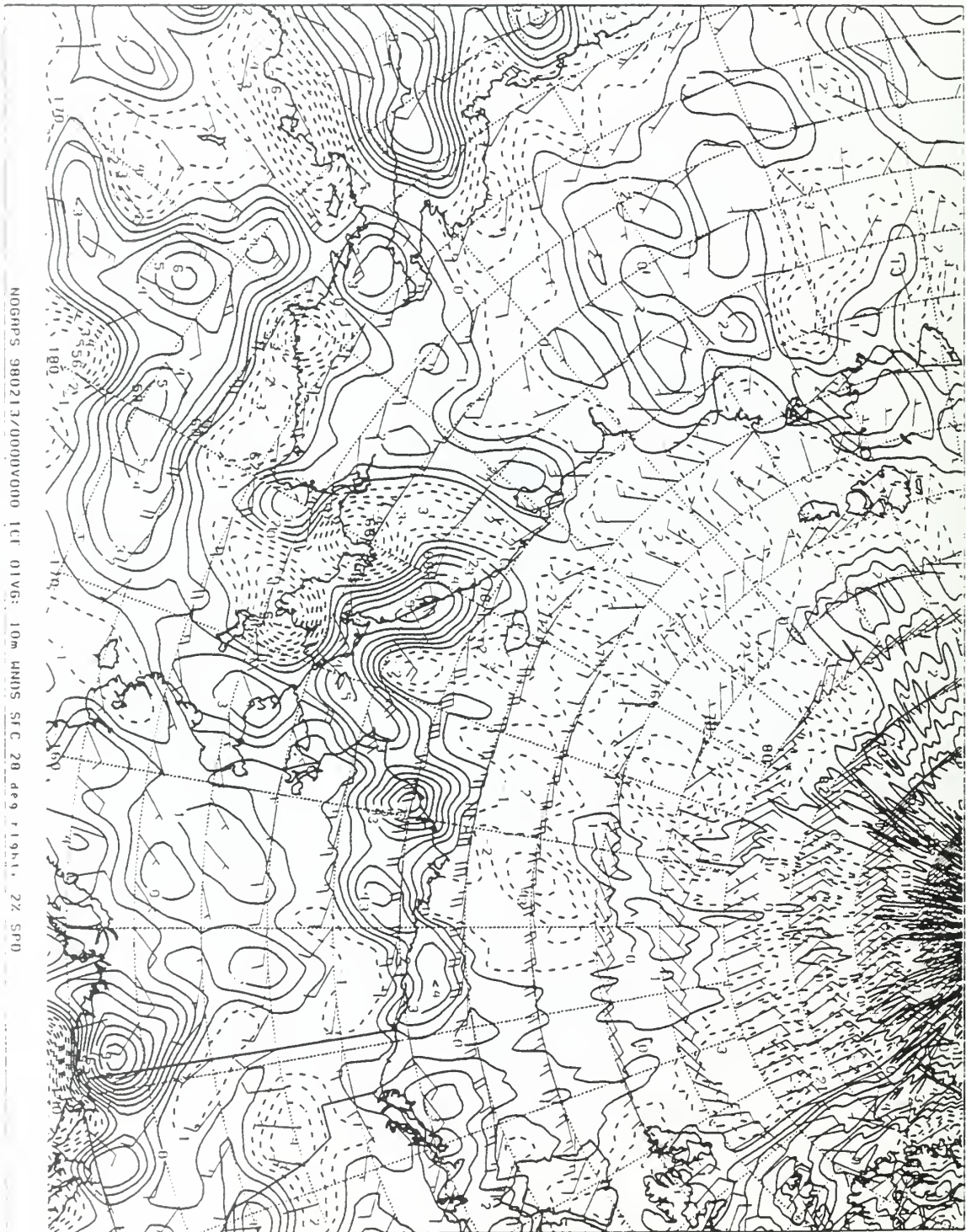


Figure 167. NOGAPS model ice divergence chart for 0000Z 13 Feb 98.

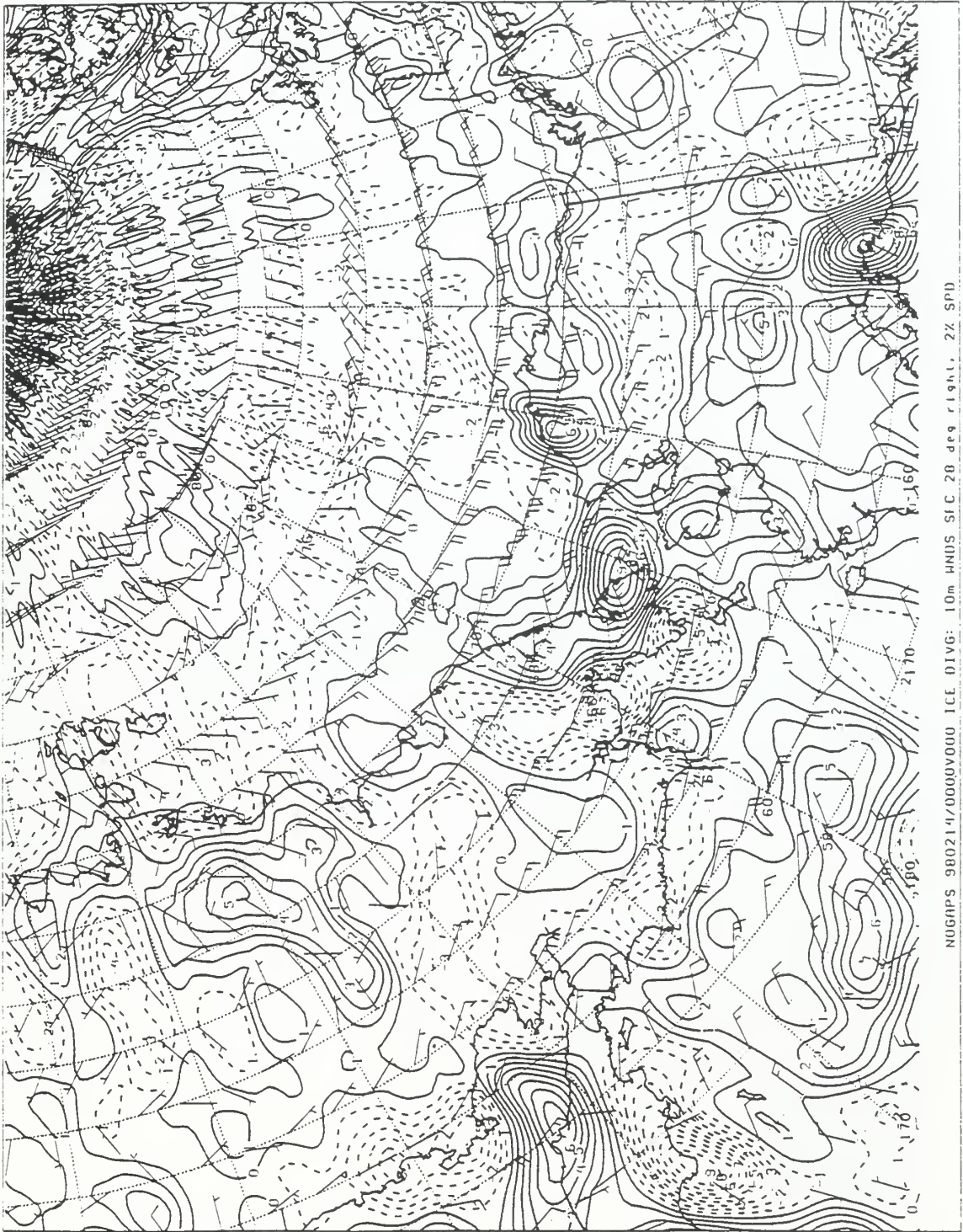


Figure 168. NOGAPS model ice divergence chart for 0000Z 14 Feb 98.

Figure 169.
15 Feb 98
NOGAPS Model Ice Divergence Data Missing

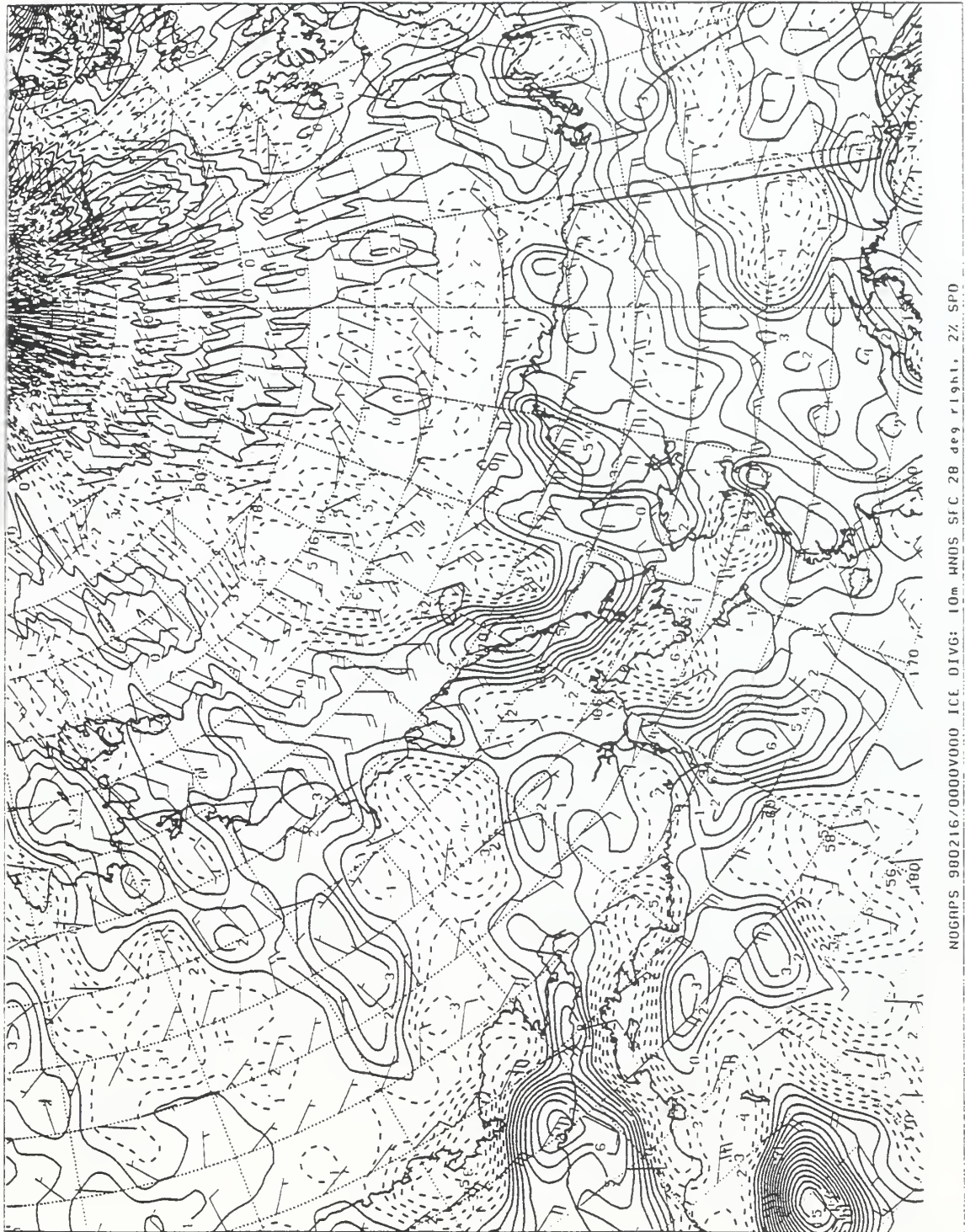


Figure 170. NOGAPS model ice divergence chart for 0000Z 16 Feb 98.

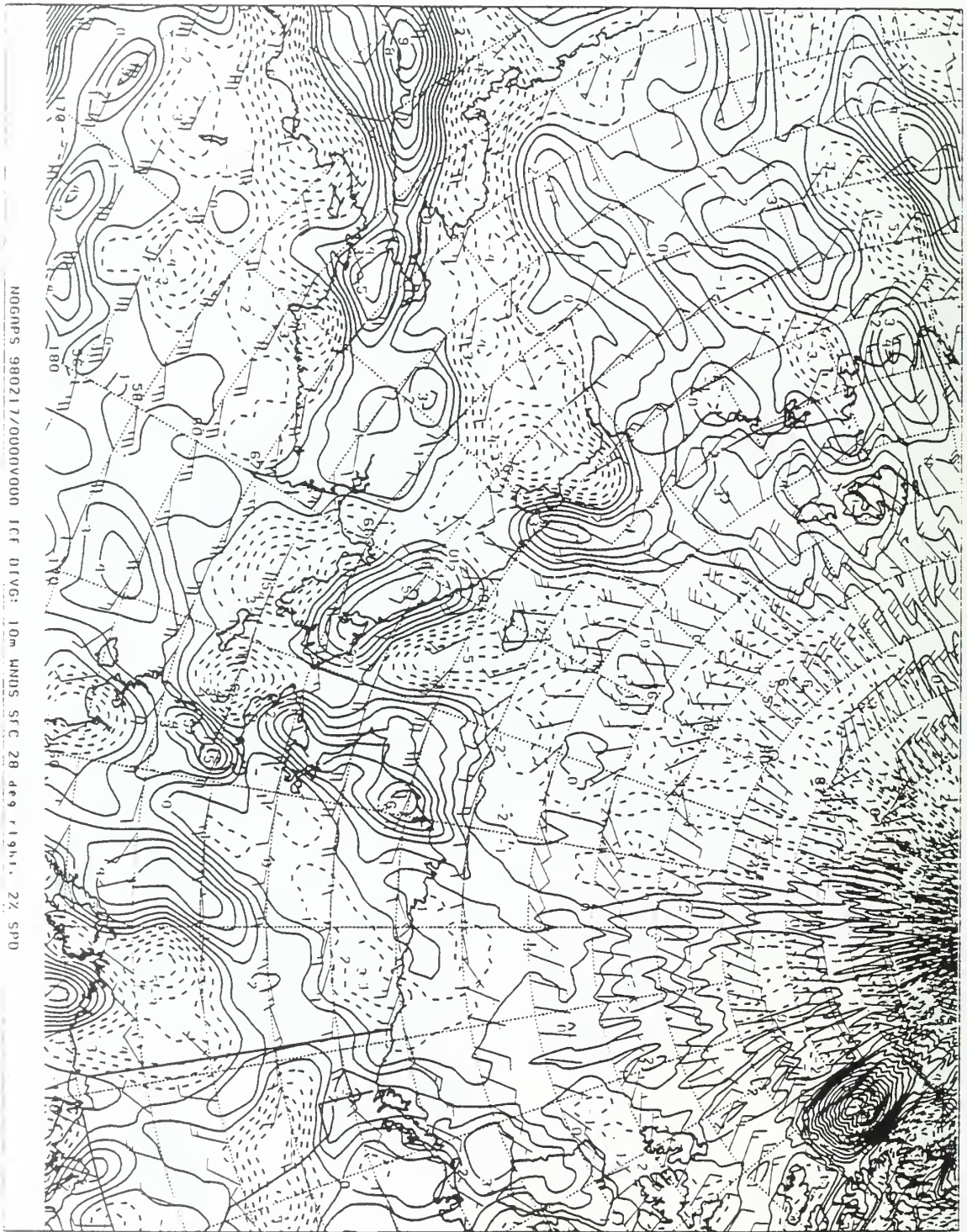


Figure 171. NOGAPS model ice divergence chart for 0000Z 17 Feb 98.

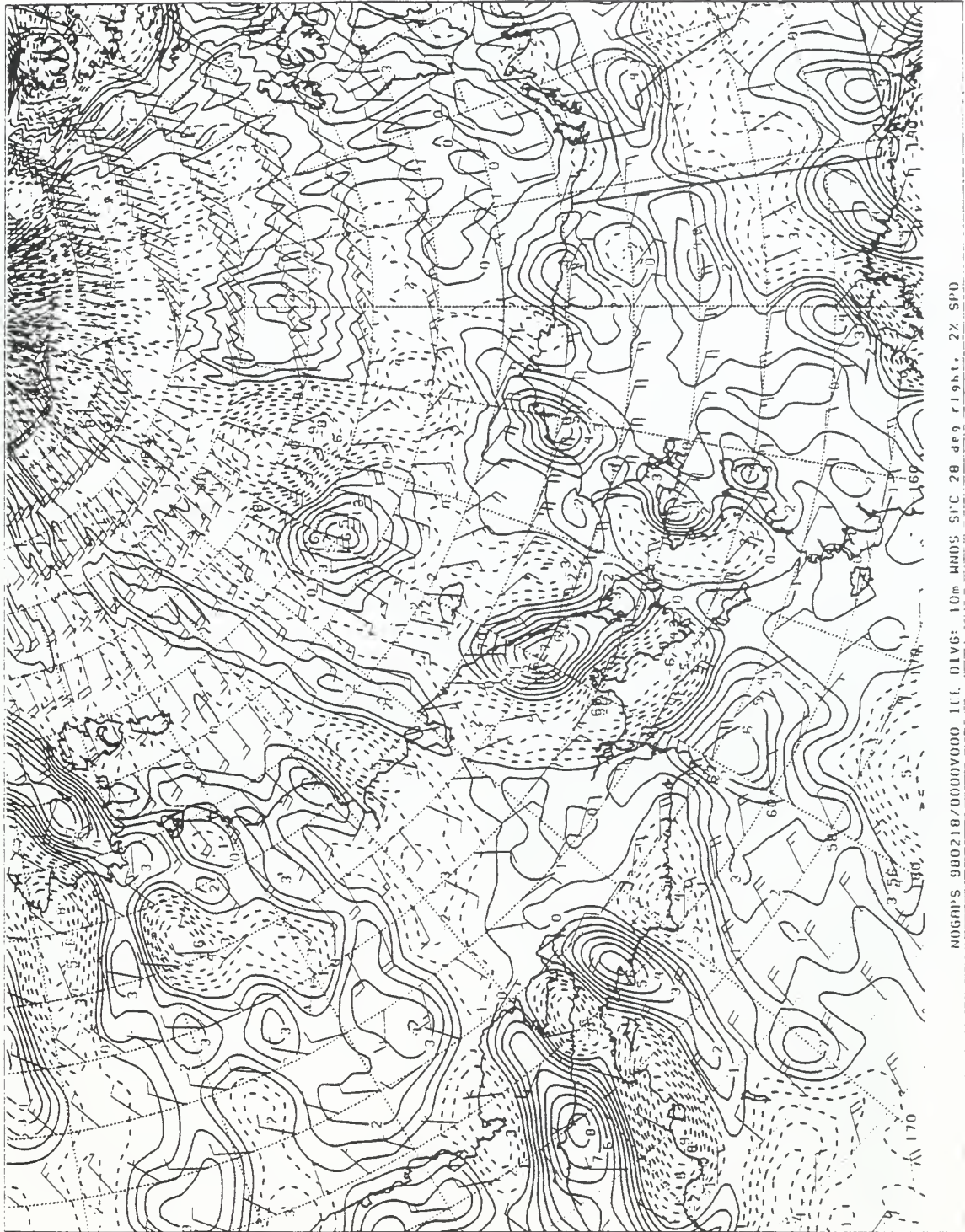


Figure 172. NOGAPS model ice divergence chart for 0000Z 18 Feb 98.

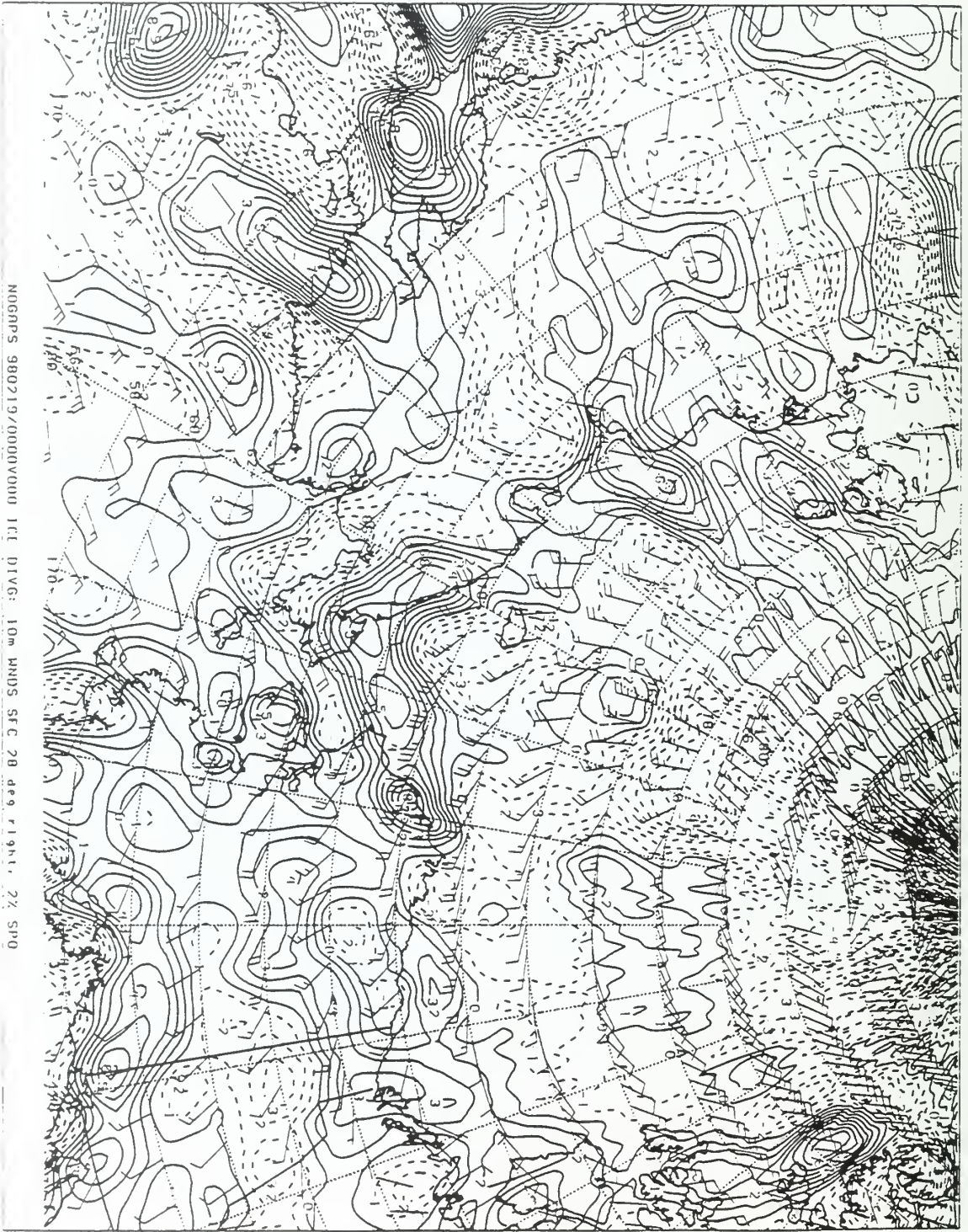


Figure 173. NOGAPS model ice divergence chart for 0000Z 19 Feb 98.

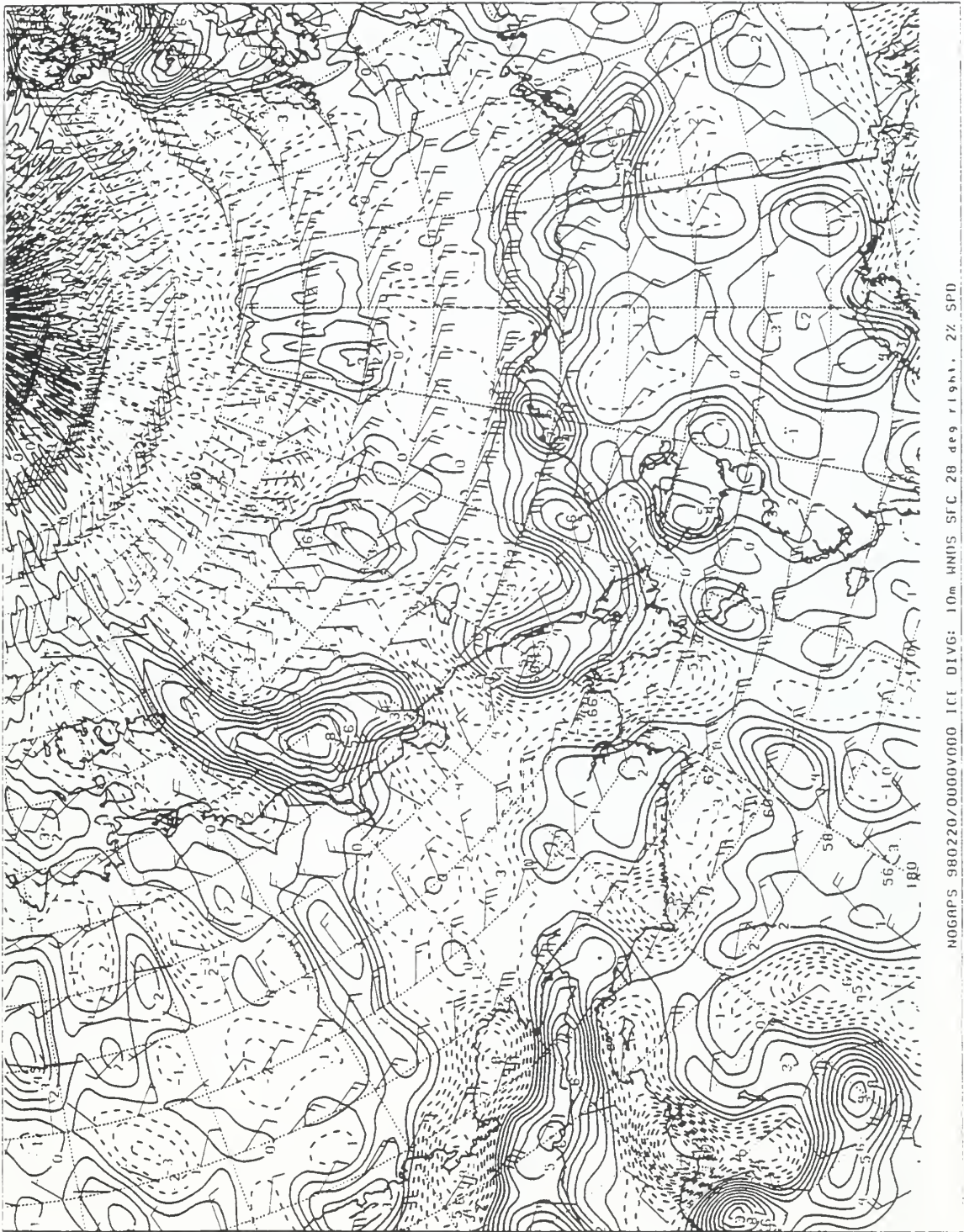


Figure 174. NOGAPS model ice divergence chart for 0000Z 20 Feb 98.

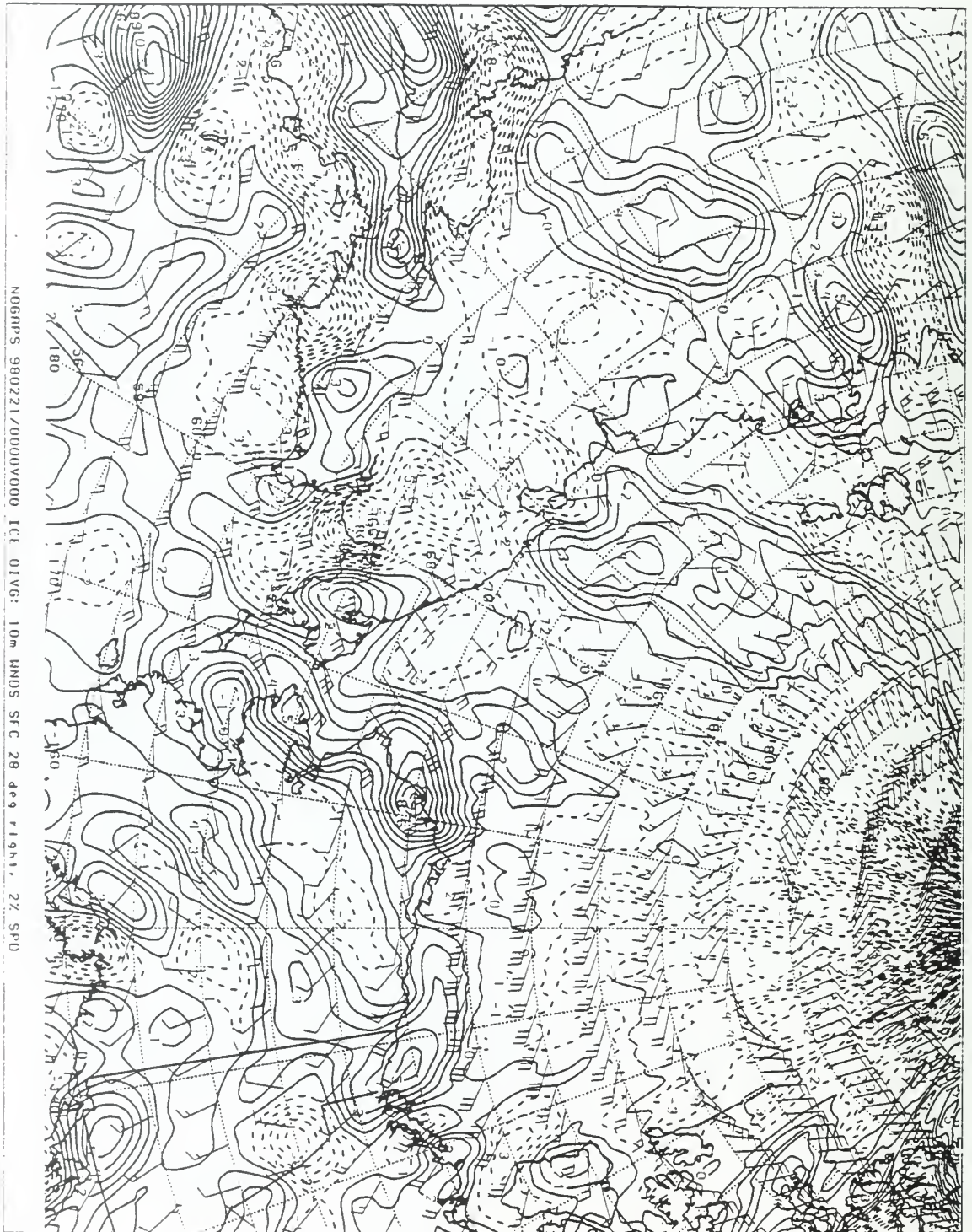


Figure 175. NOGAPS model ice divergence chart for 0000Z 21 Feb 98.

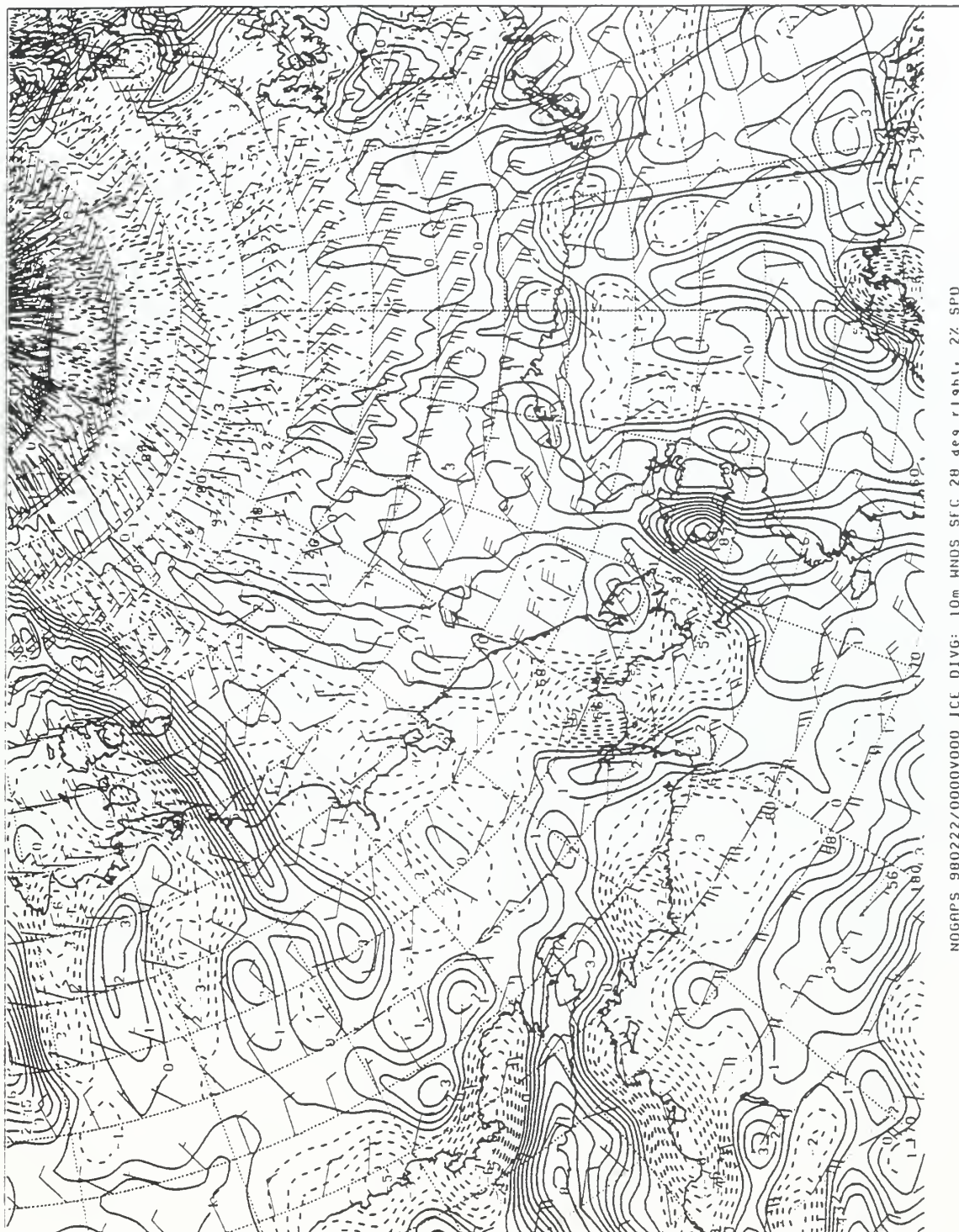


Figure 176. NOGAPS model ice divergence chart for 0000Z 22 Feb 98.

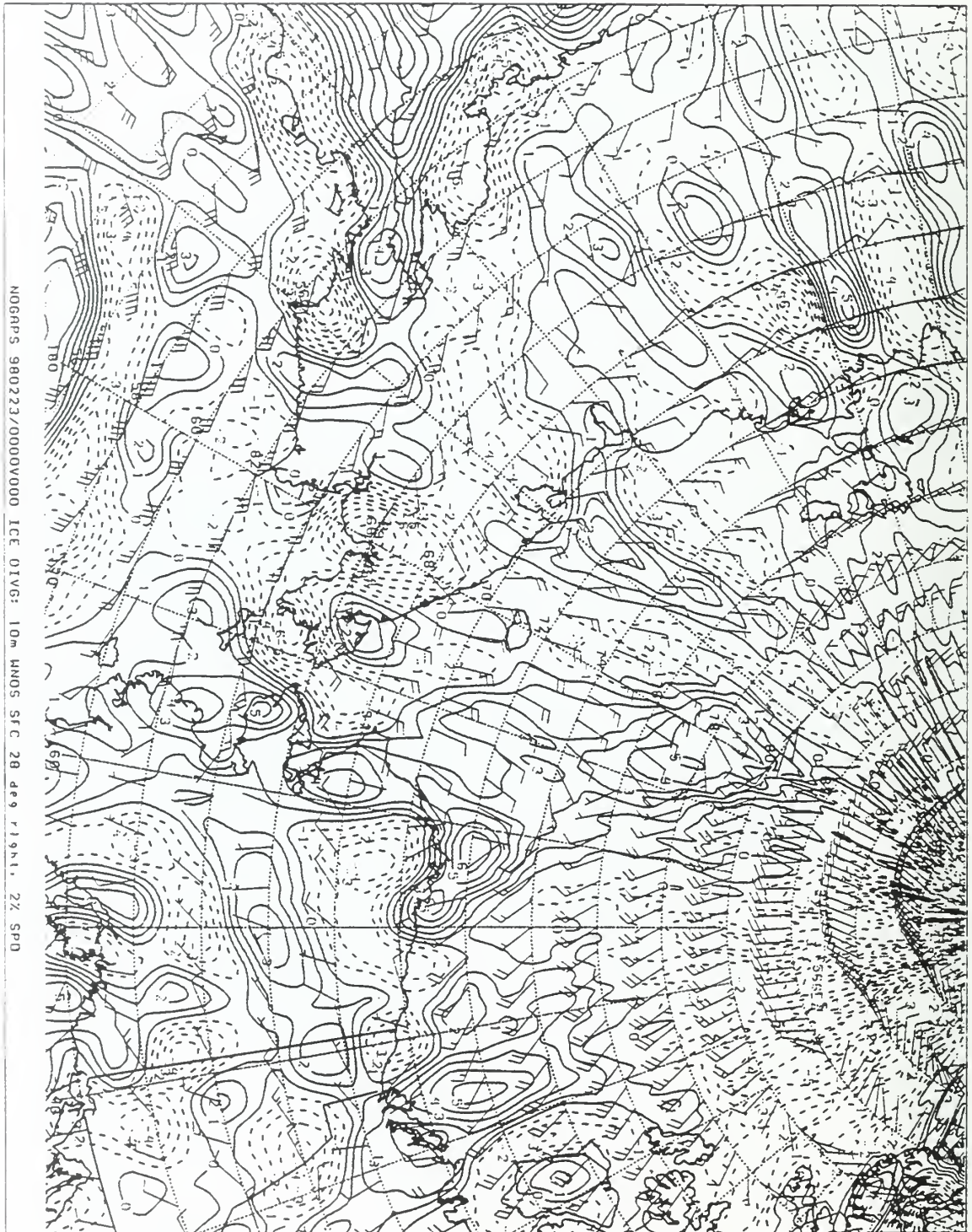


Figure 177. NOGAPS model ice divergence chart for 0000Z 23 Feb 98.



Figure 178. NOGAPS model ice divergence chart for 0000Z 24 Feb 98.

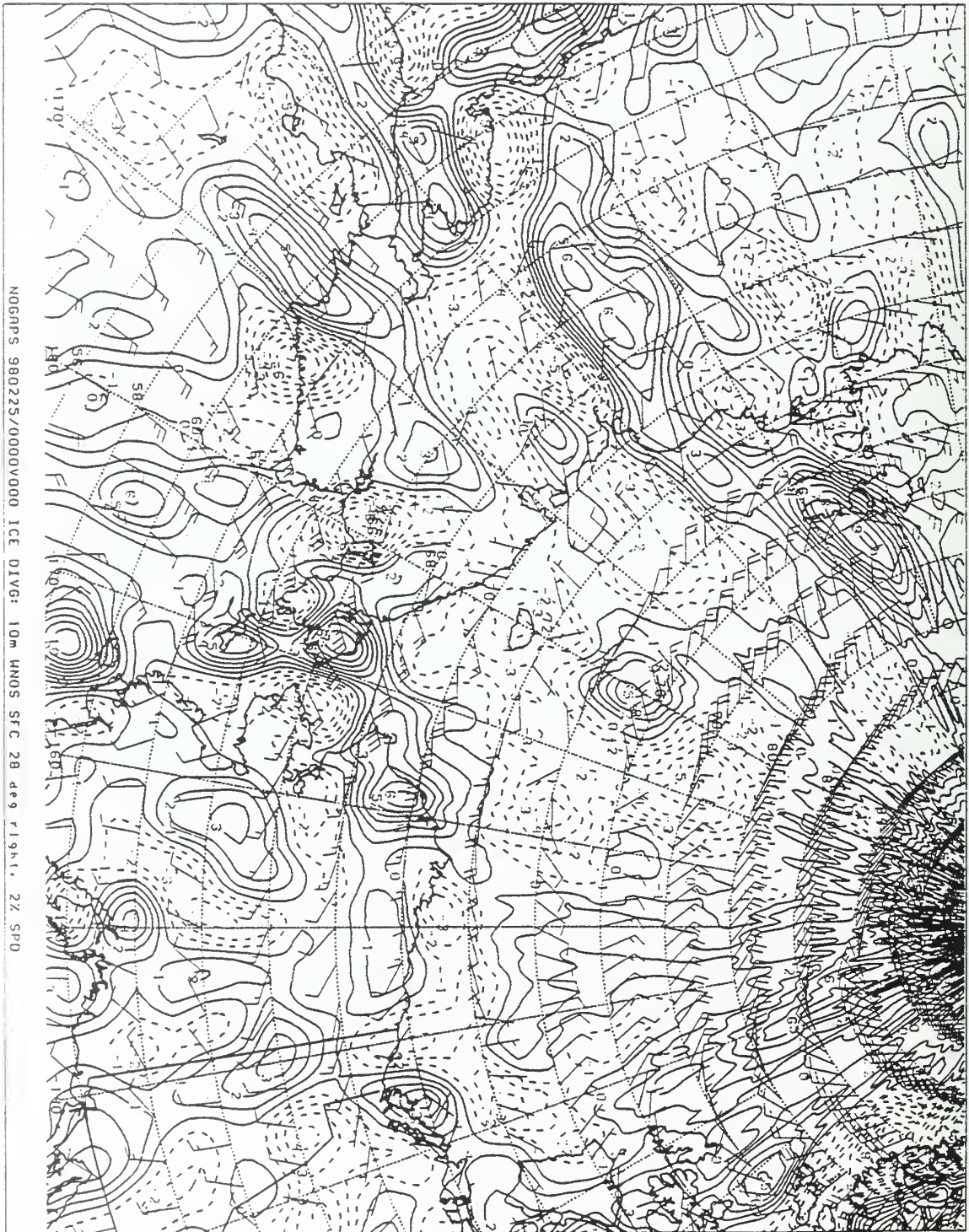


Figure 179. NOGAPS model ice divergence chart for 0000Z 25 Feb 98.

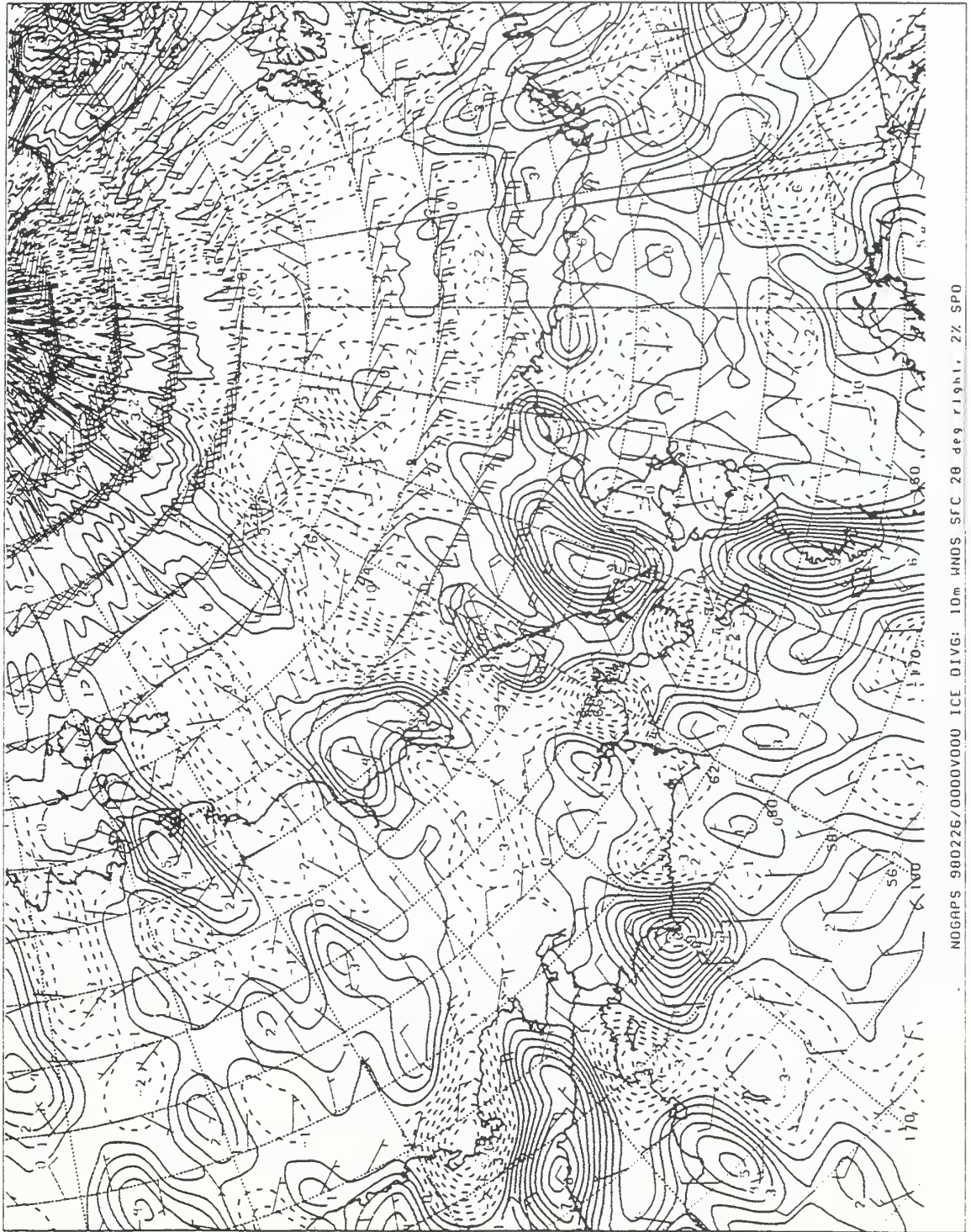


Figure 180. NOGAPS model ice divergence chart for 0000Z 26 Feb 98.



Figure 181. NOGAPS model ice divergence chart for 0000Z 27 Feb 98.



NOGAPS 980228/0000V000 ICE DIVG: 10m HNDS SFC 28 deg right, 2% SPD

Figure 182. NOGAPS model ice divergence chart for 0000Z 28 Feb 98.

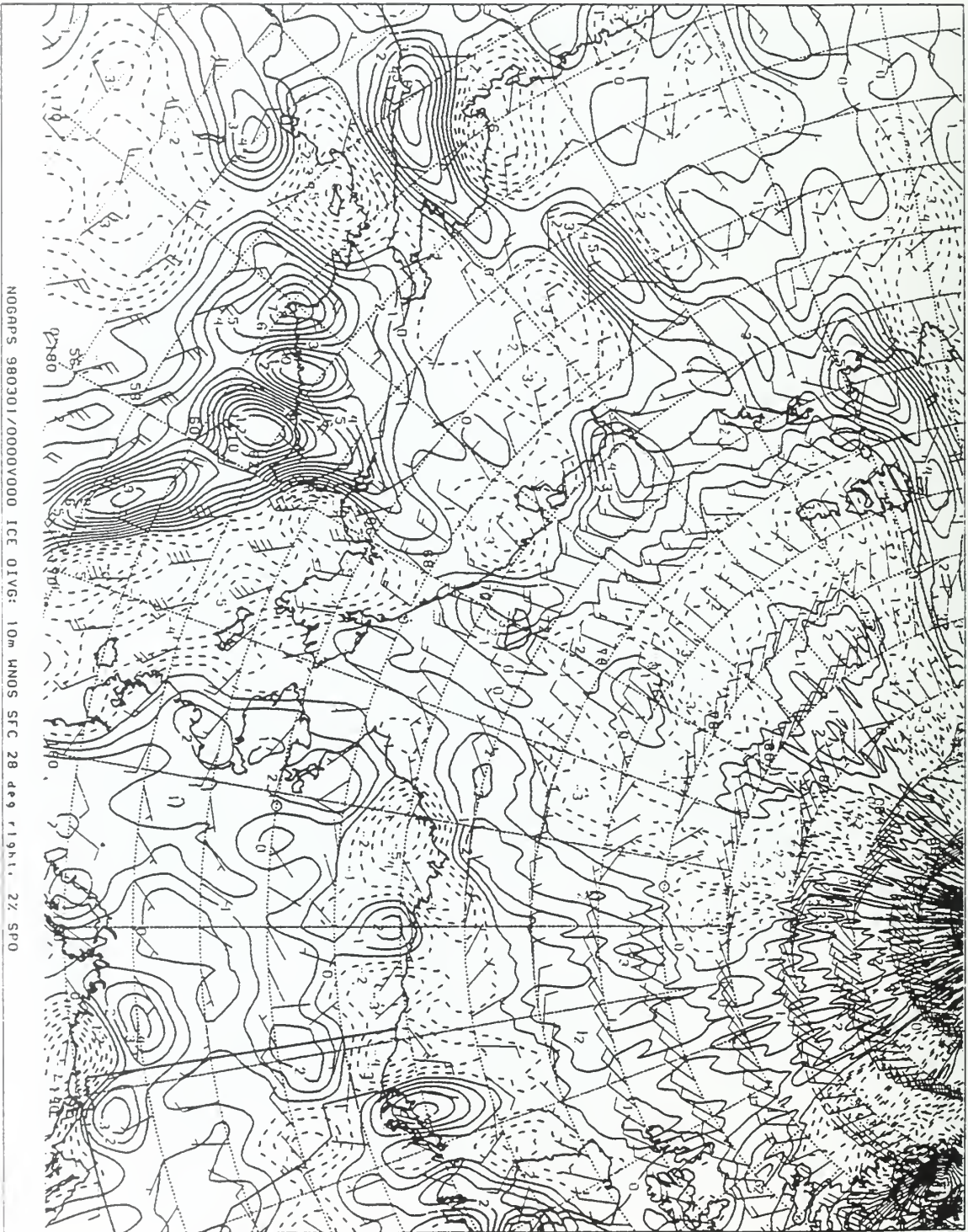


Figure 183. NOGAPS model ice divergence chart for 0000Z 01 Mar 98.

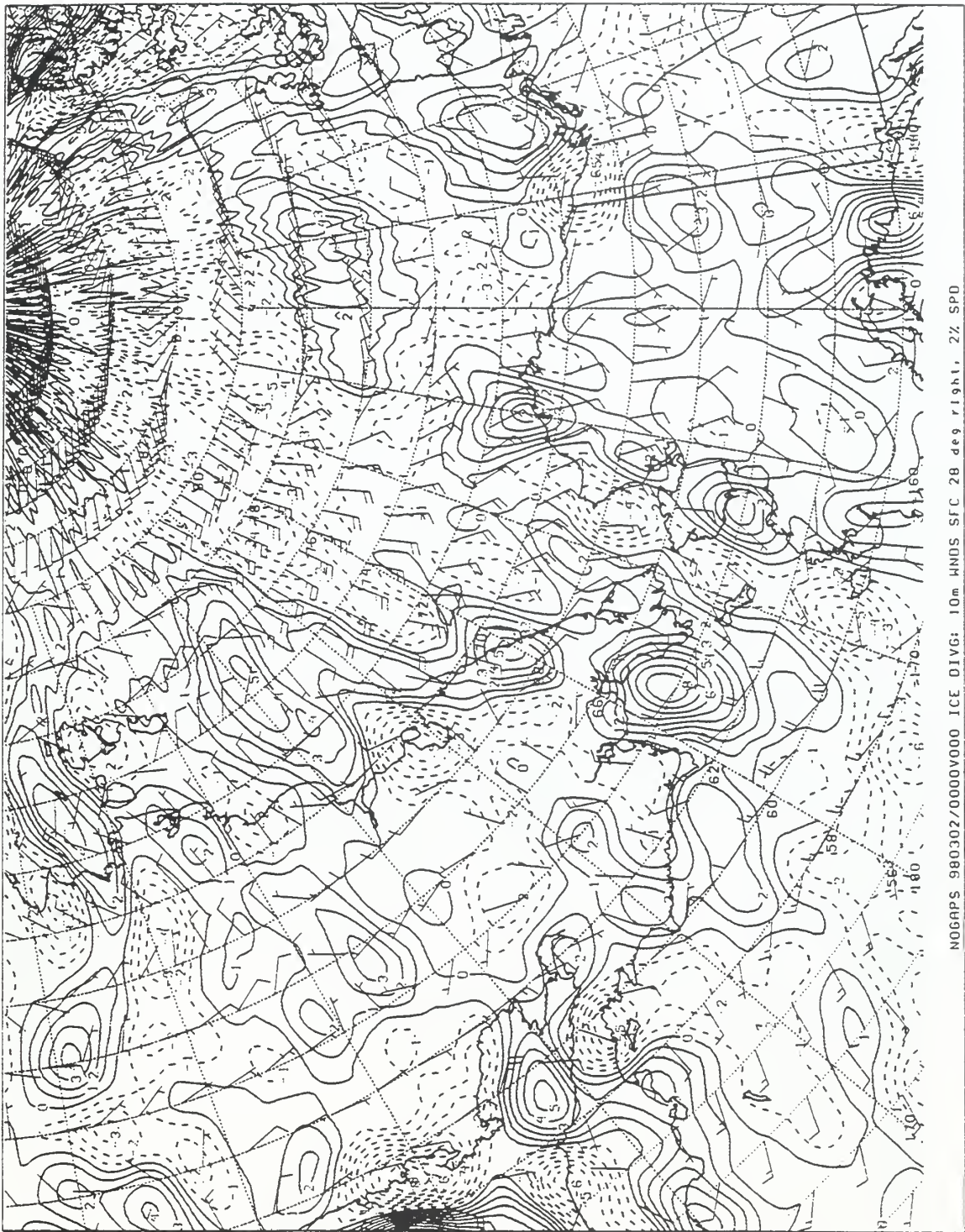


Figure 184. NOGAPS model ice divergence chart for 0000Z 02 Mar 98.

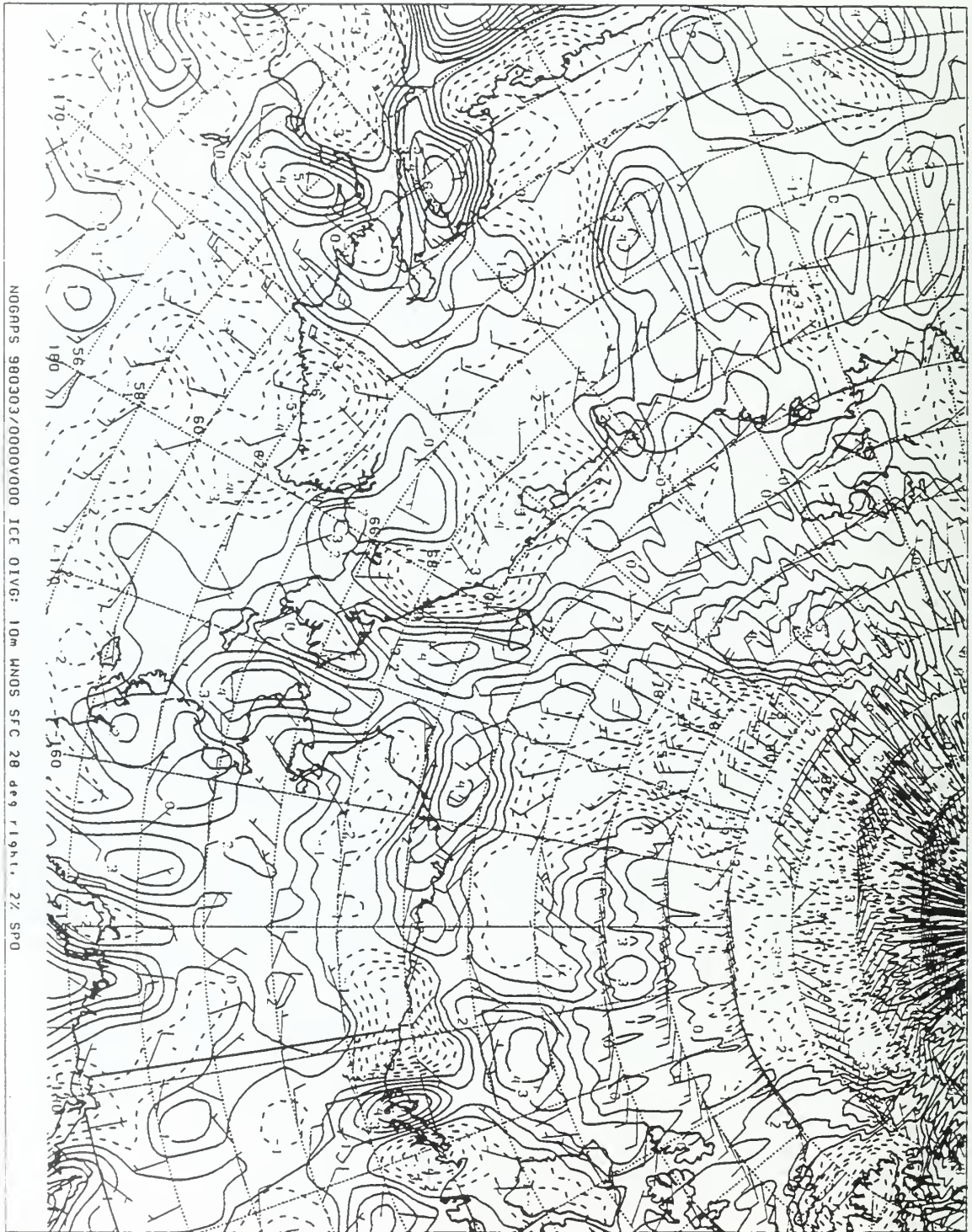


Figure 185. NOGAPS model ice divergence chart for 0000Z 03 Mar 98.

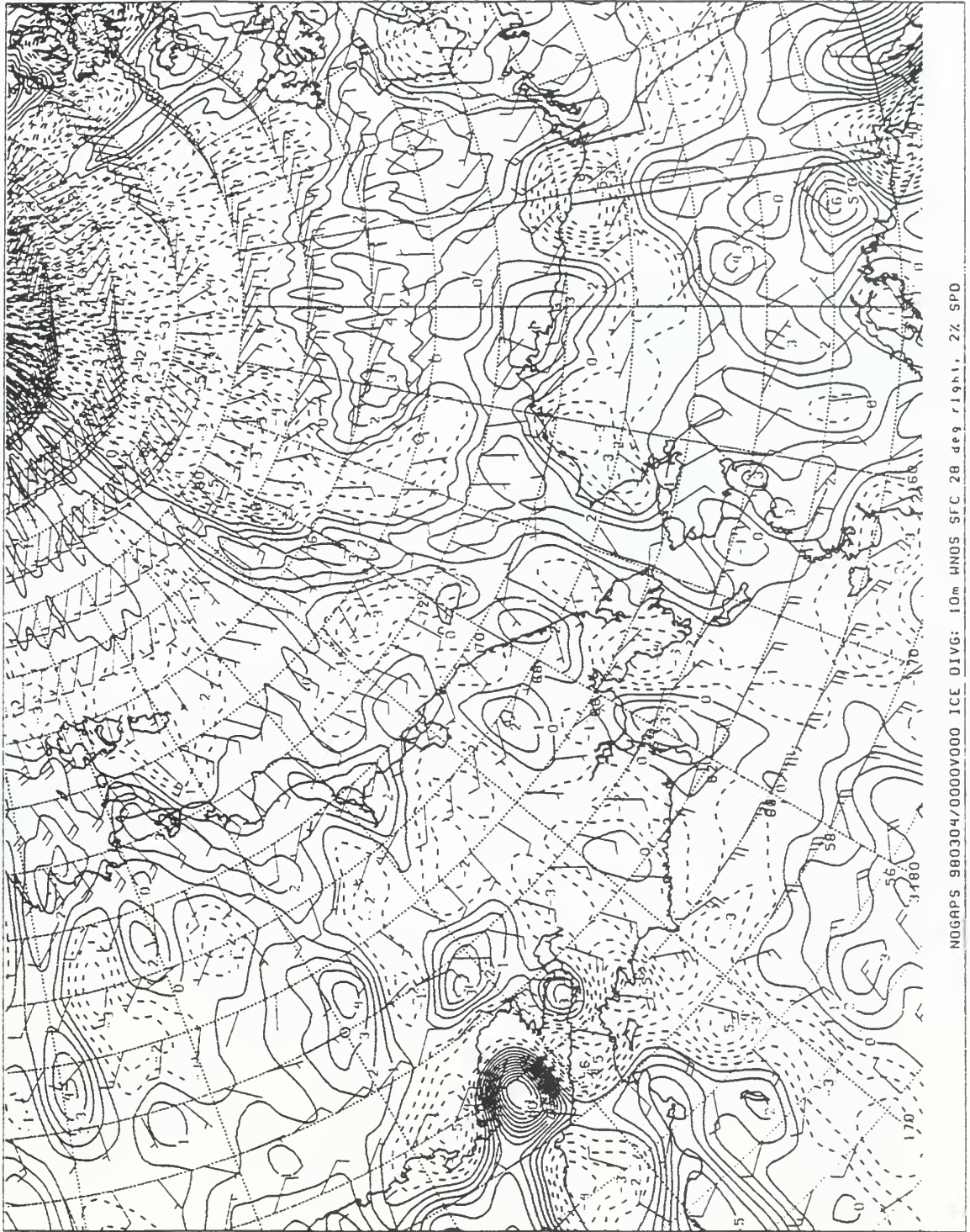


Figure 186. NOGAPS model ice divergence chart for 0000Z 04 Mar 98.

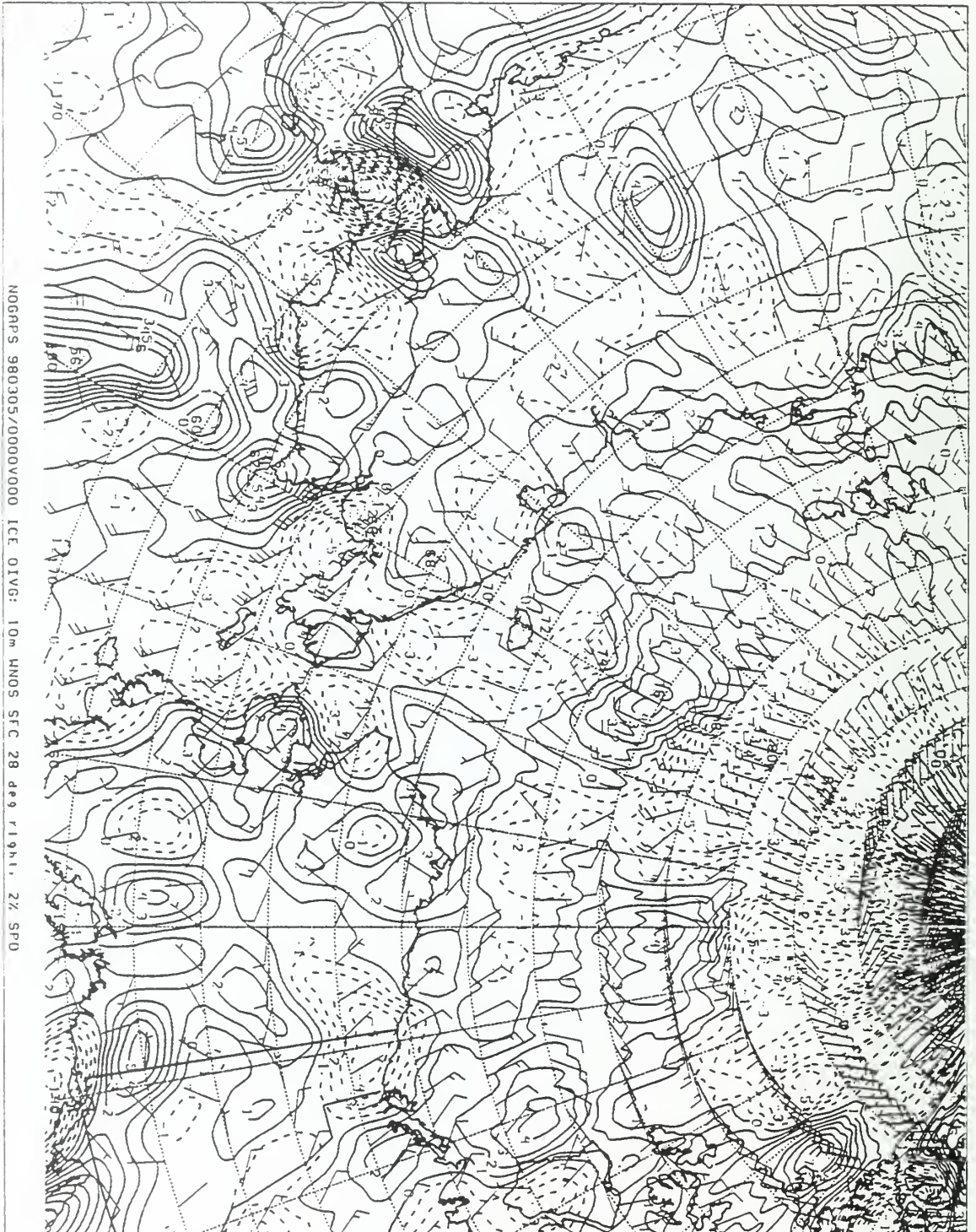


Figure 187. NOGAPS model ice divergence chart for 0000Z 05 Mar 98.

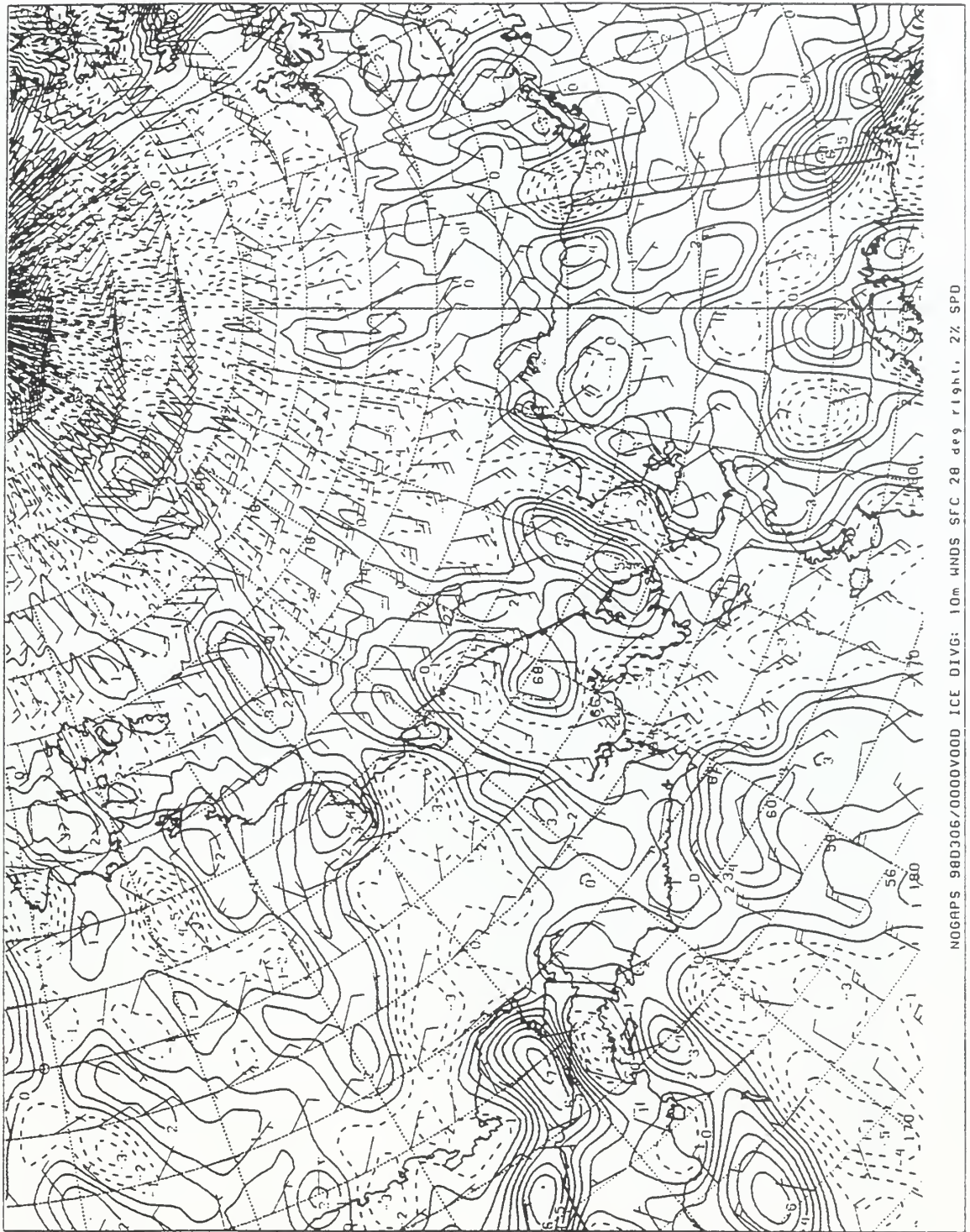


Figure 188. NOGAPS model ice divergence chart for 0000Z 06 Mar 98.

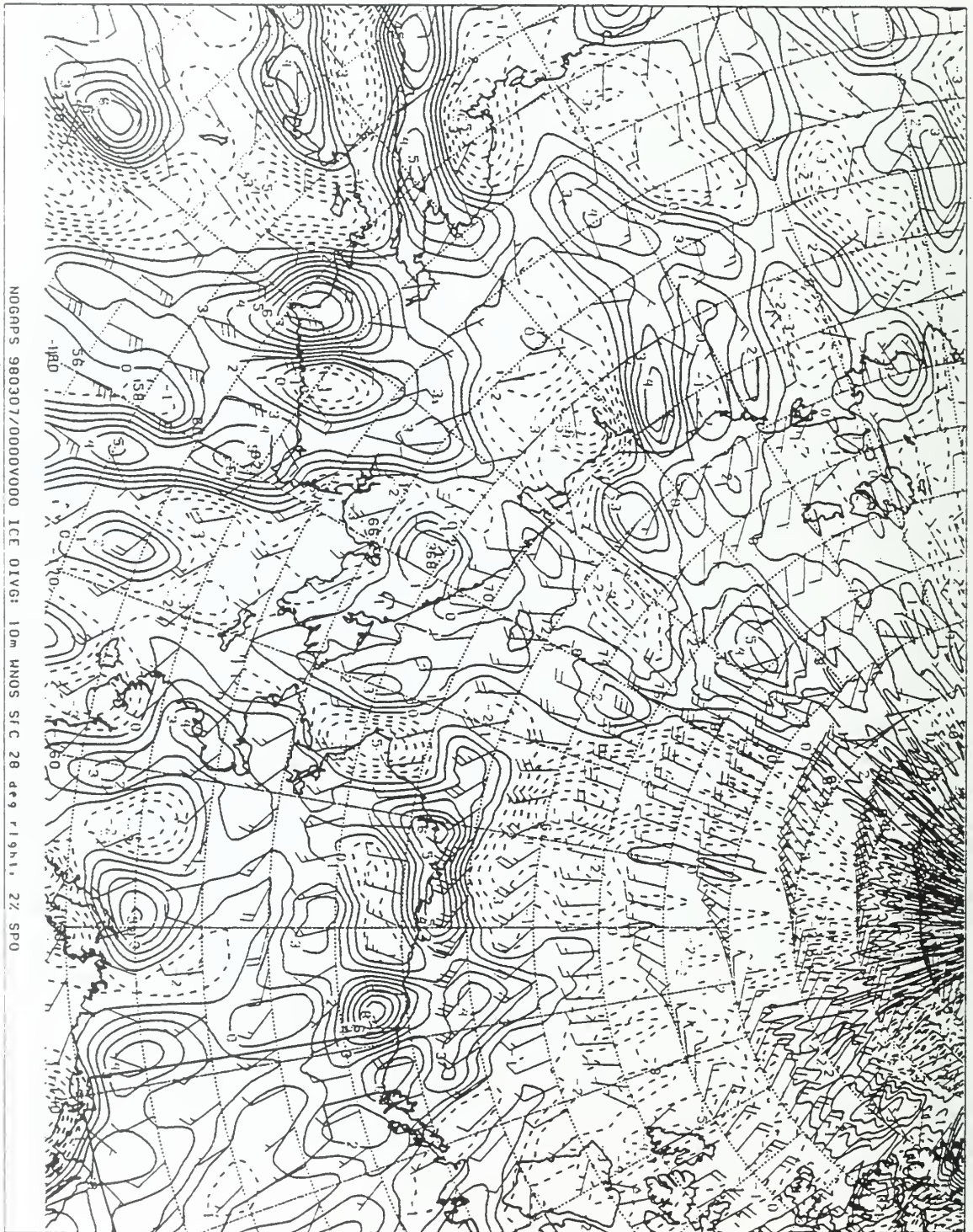


Figure 189. NOGAPS model ice divergence chart for 0000Z 07 Mar 98.

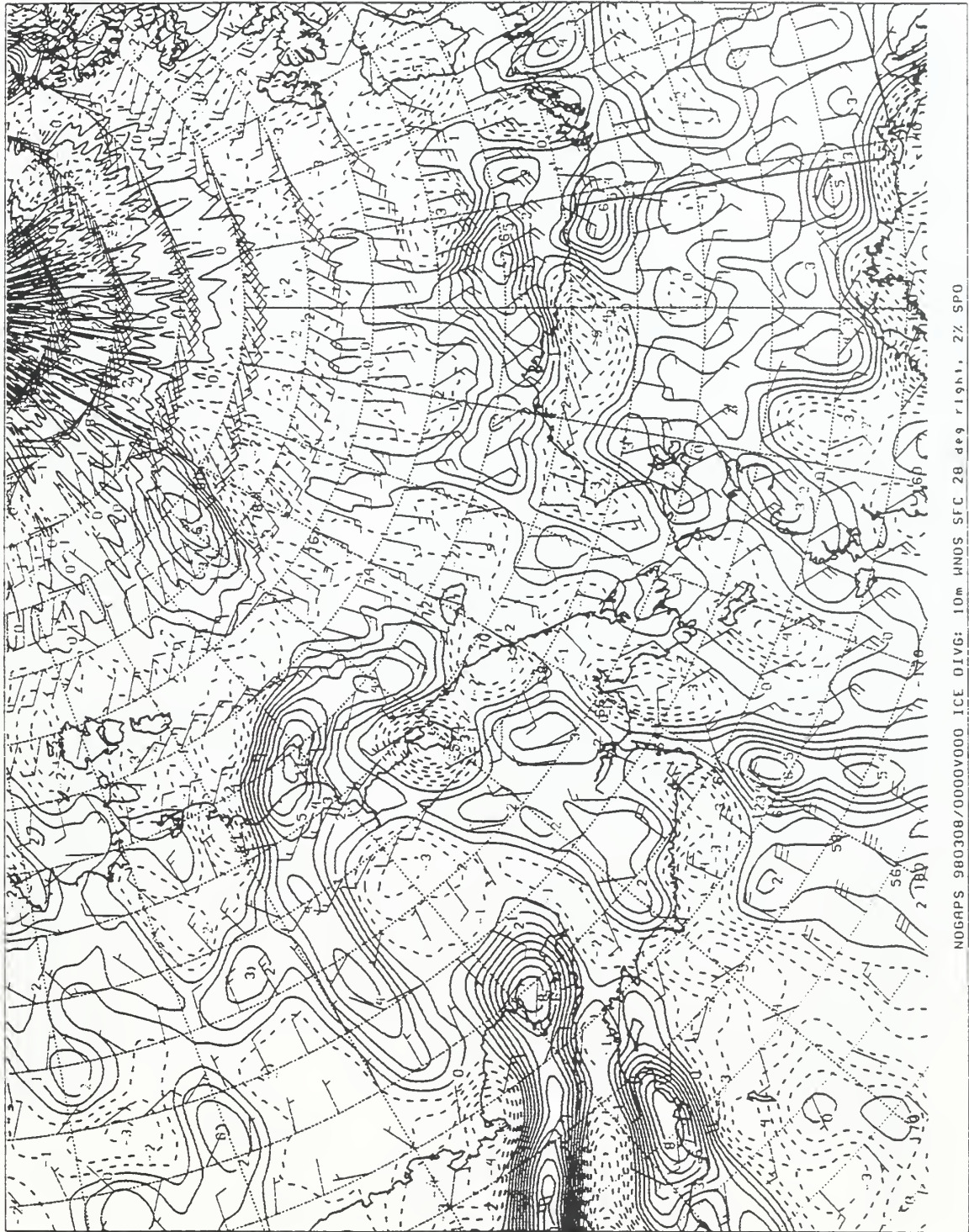


Figure 190. NOGAPS model ice divergence chart for 0000Z 08 Mar 98.

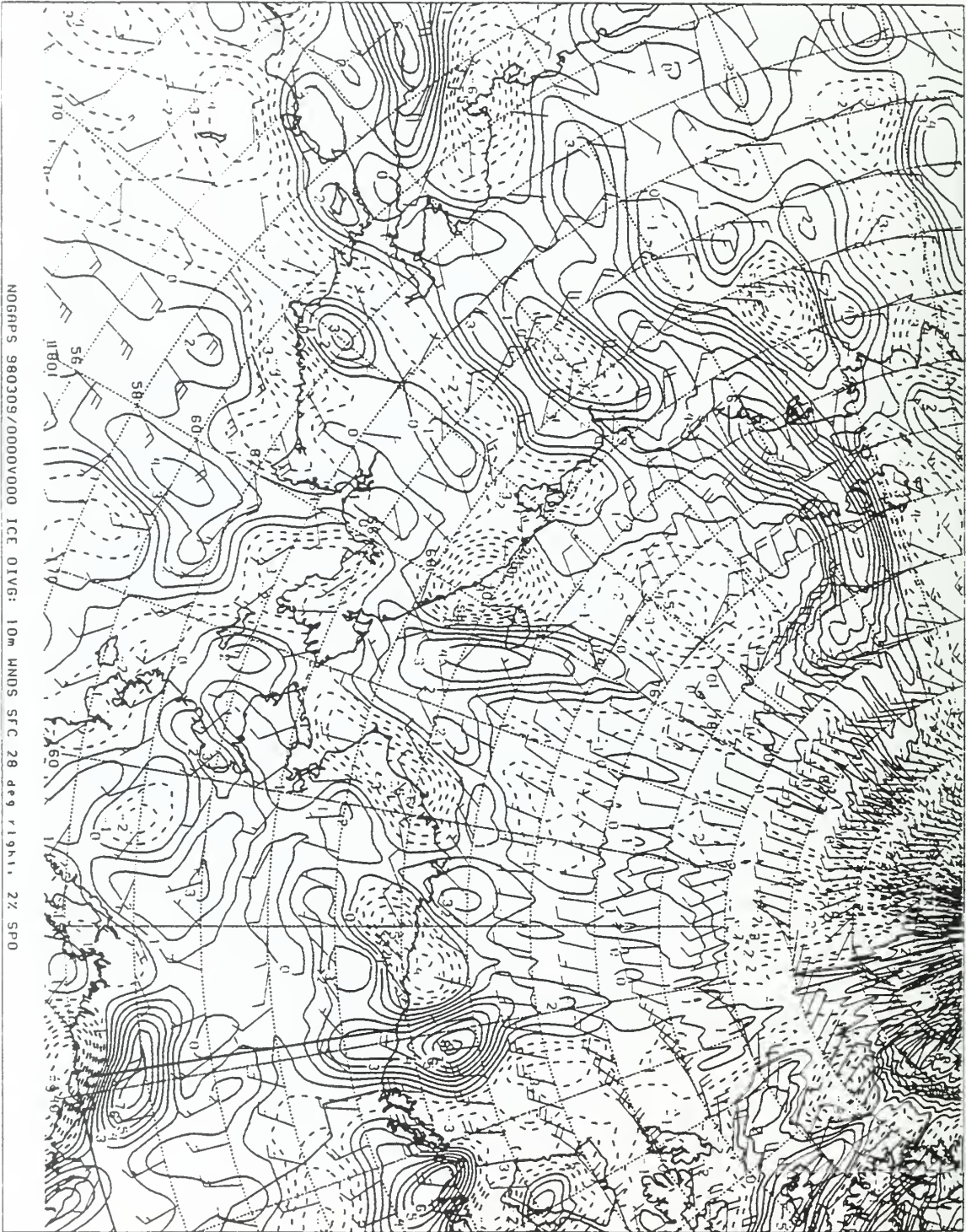


Figure 191. NOGAPS model ice divergence chart for 0000Z 09 Mar 98.



Figure 192. NOGAPS model ice divergence chart for 0000Z 10 Mar 98.

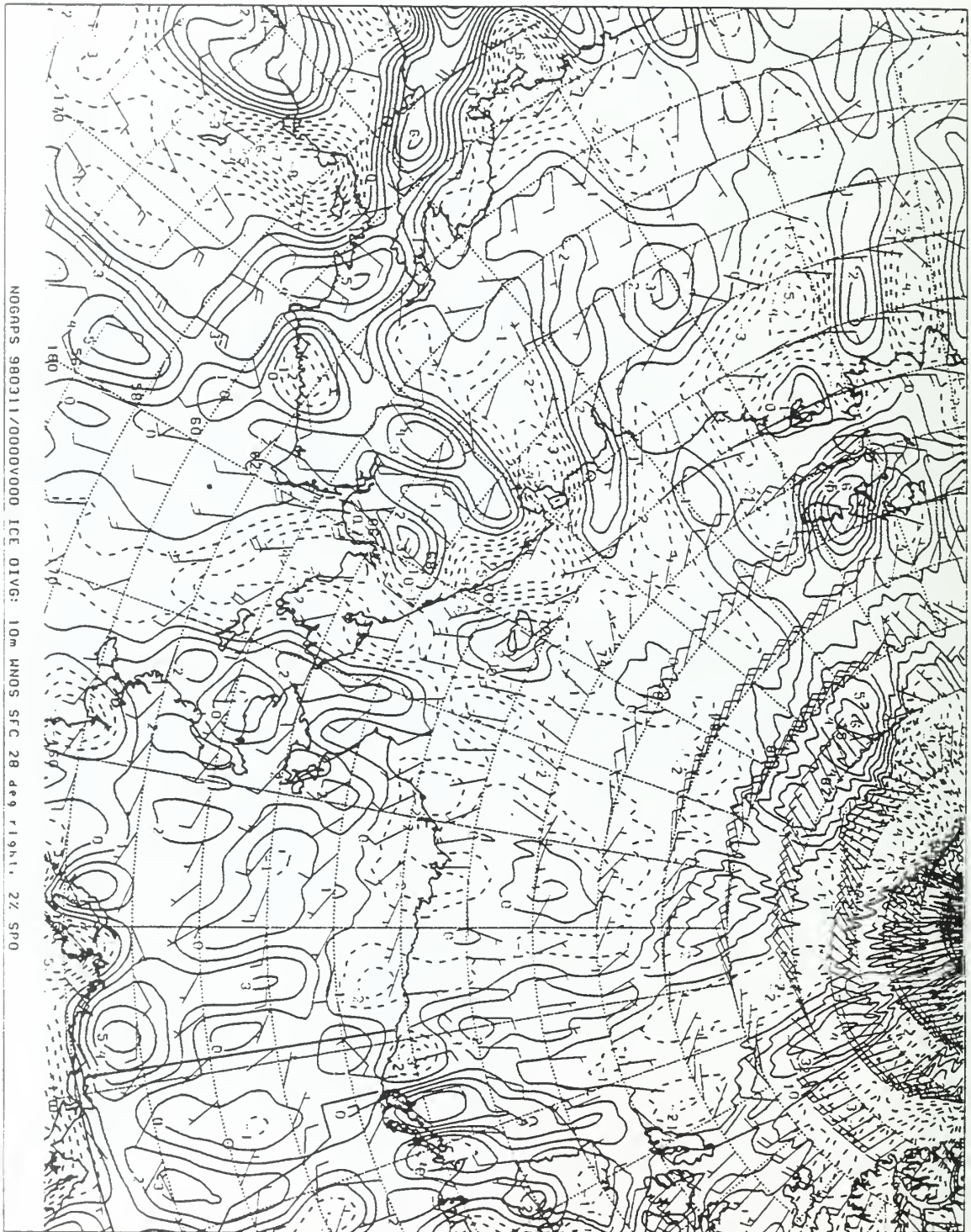


Figure 193. NOGAPS model ice divergence chart for 0000Z 11 Mar 98.

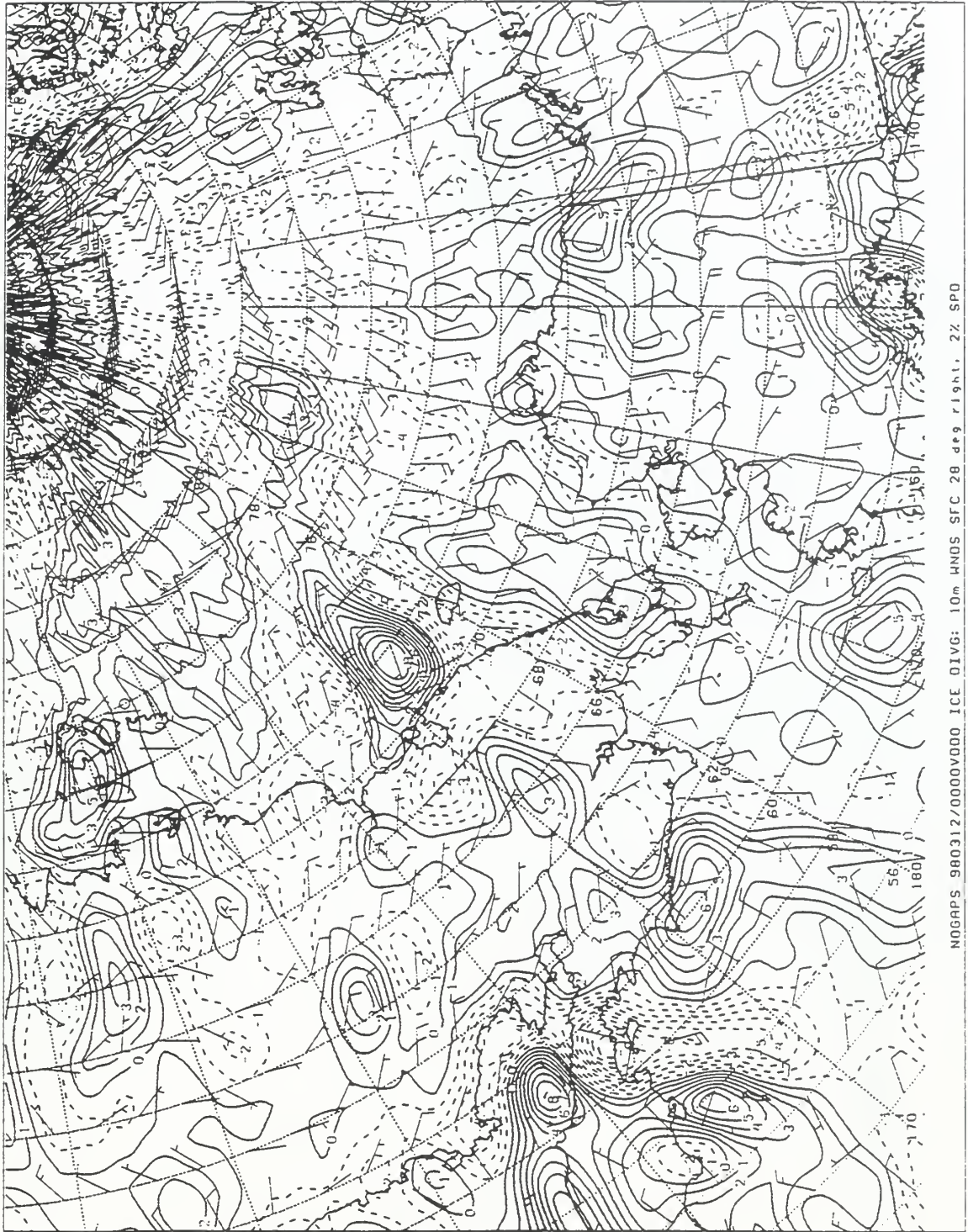


Figure 194. NOGAPS model ice divergence chart for 0000Z 12 Mar 98.

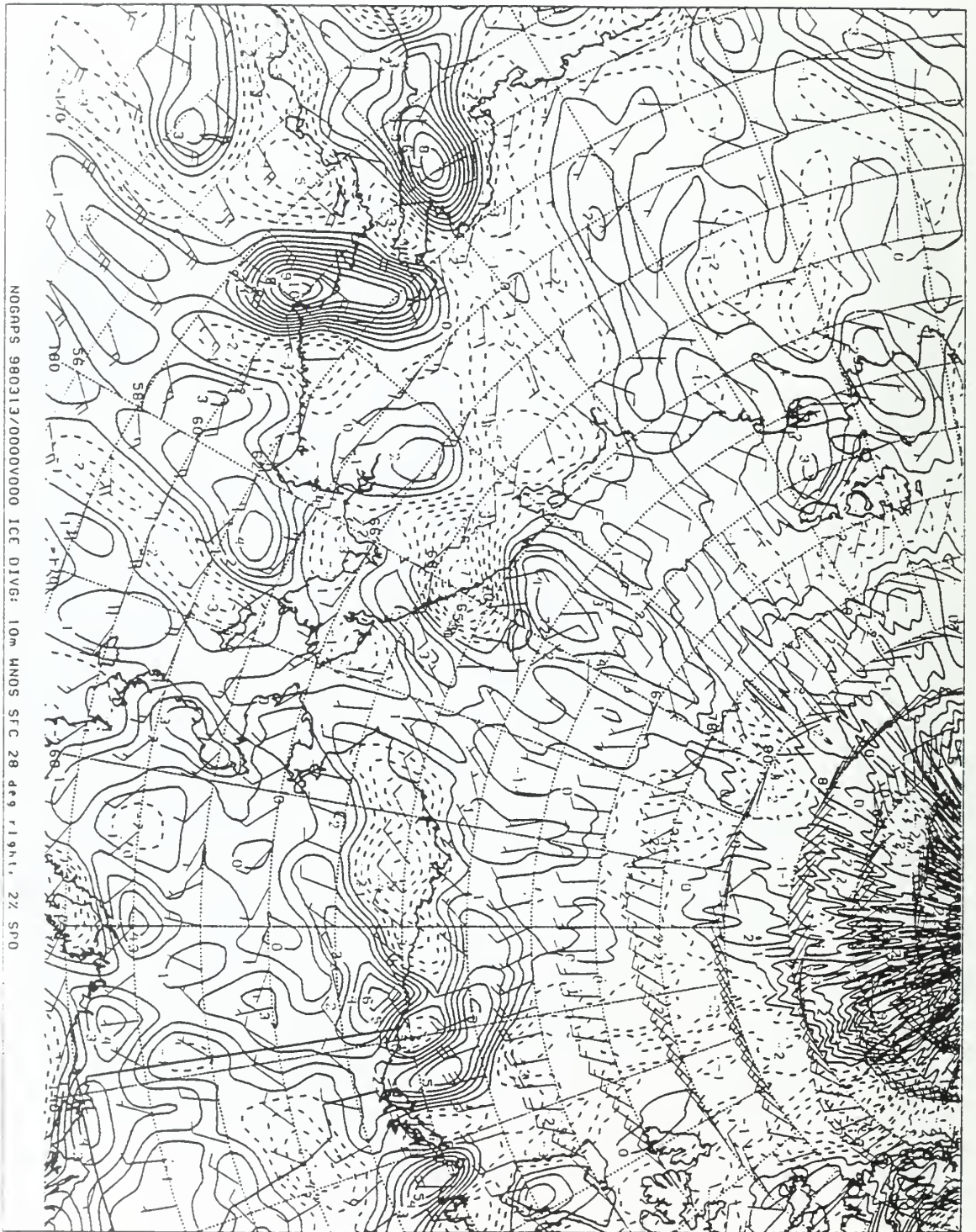


Figure 195. NOGAPS model ice divergence chart for 0000Z 13 Mar 98.

Figure 196.
14 Mar 98
NOGAPS Ice Divergence Data Missing

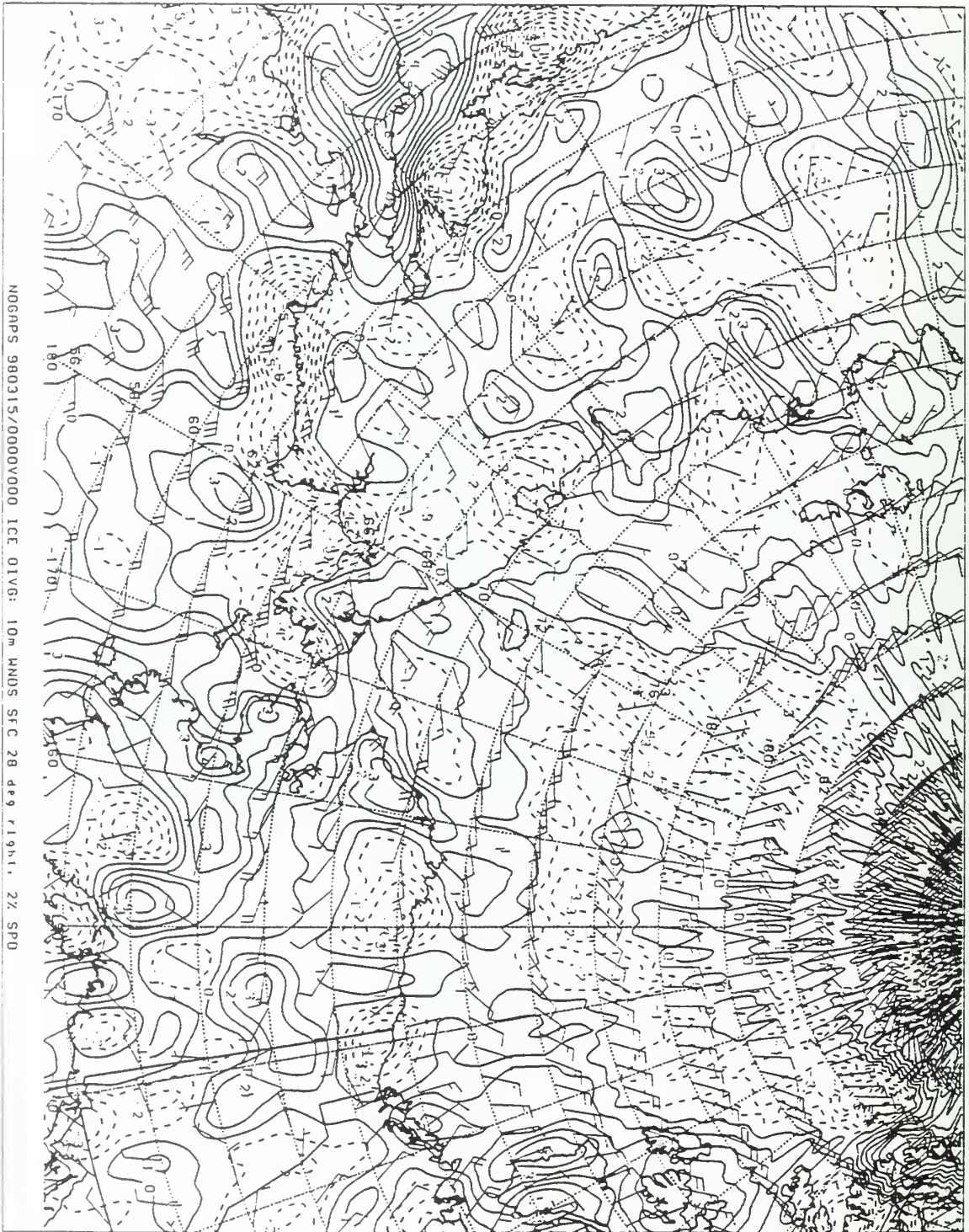


Figure 197. NOGAPS model ice divergence chart for 0000Z 15 Mar 98.

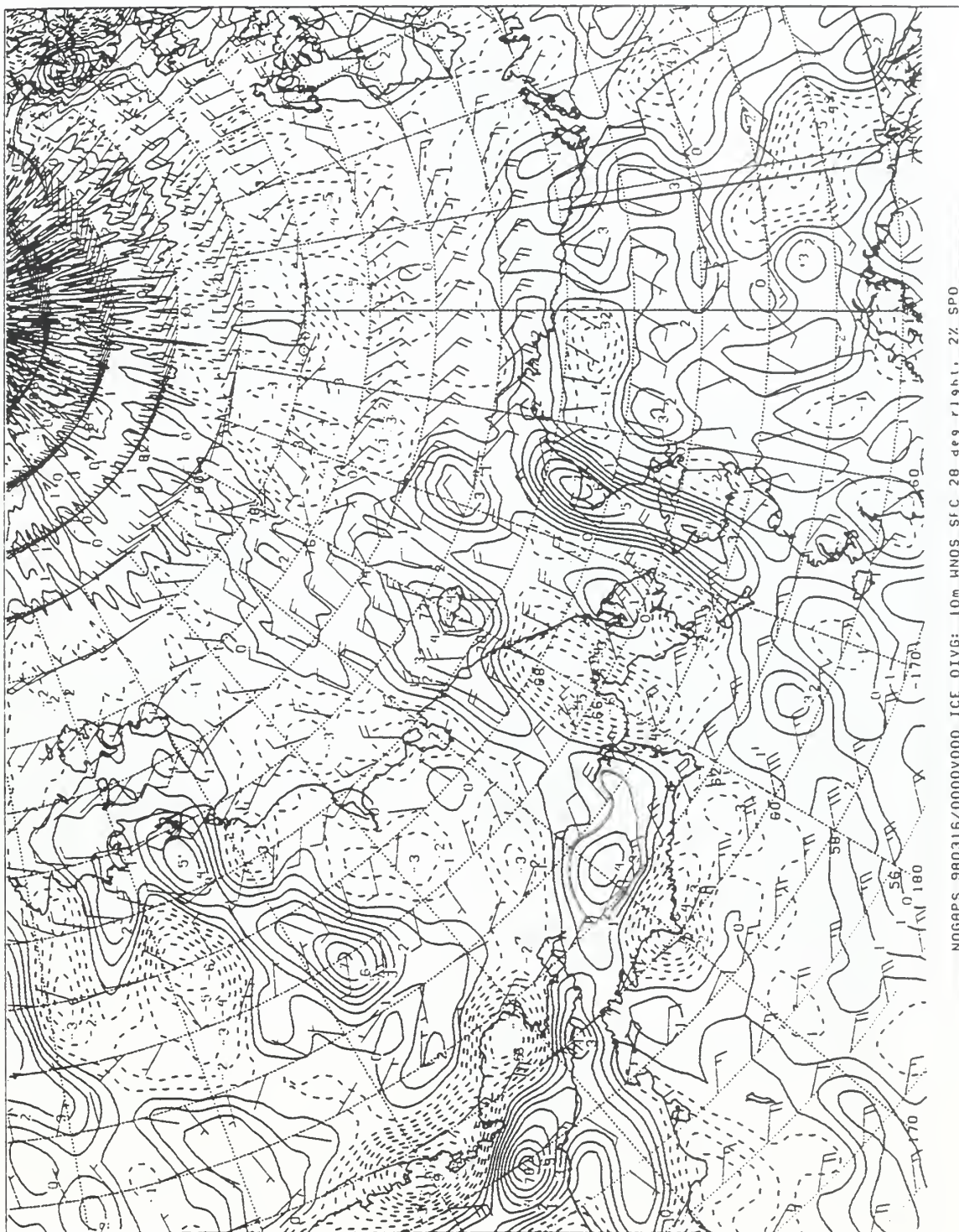


Figure 198. NOGAPS model ice divergence chart for 0000Z 16 Mar 98.

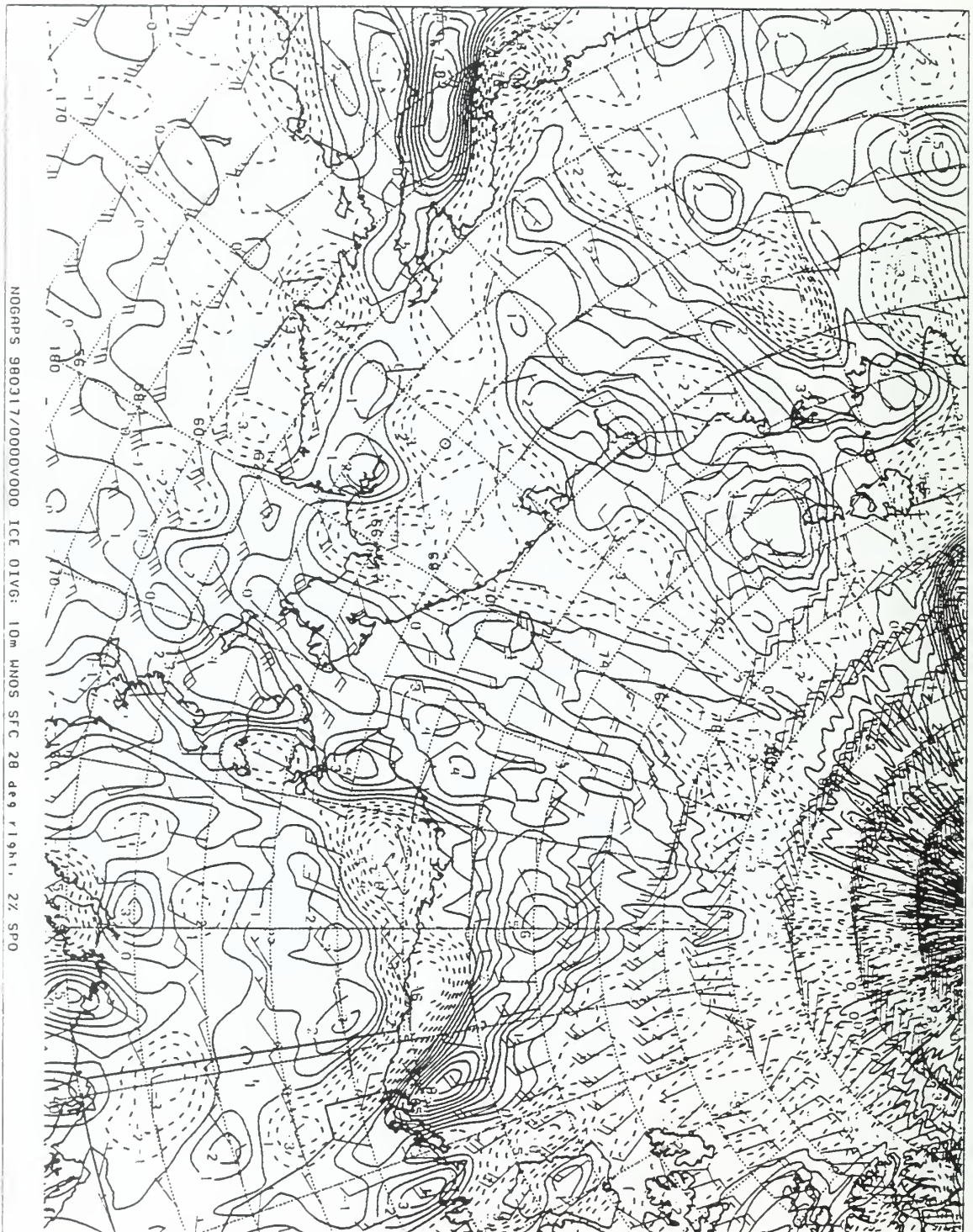


Figure 199. NOGAPS model ice divergence chart for 0000Z 17 Mar 98.

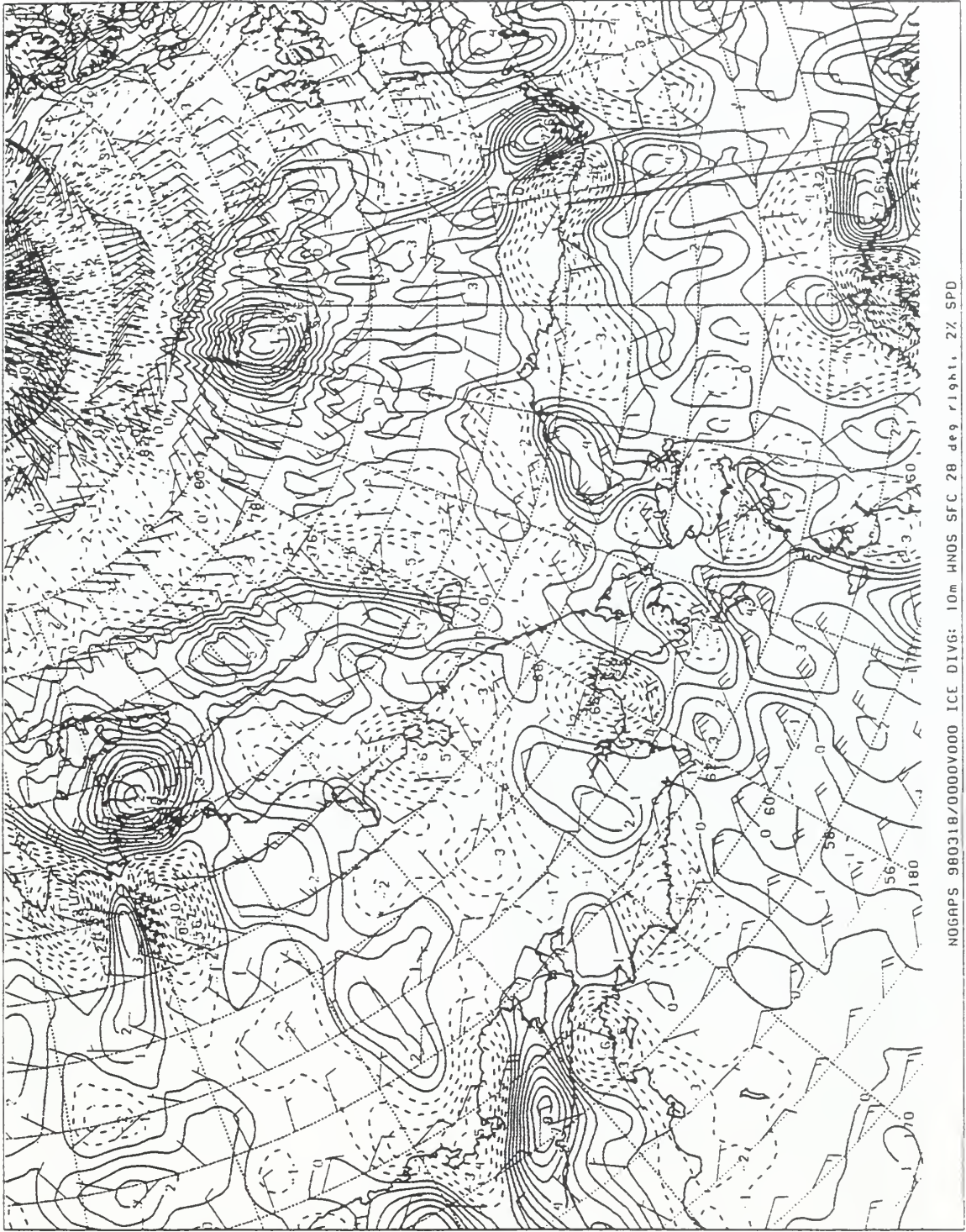


Figure 200. NOGAPS model ice divergence chart for 0000Z 18 Mar 98.

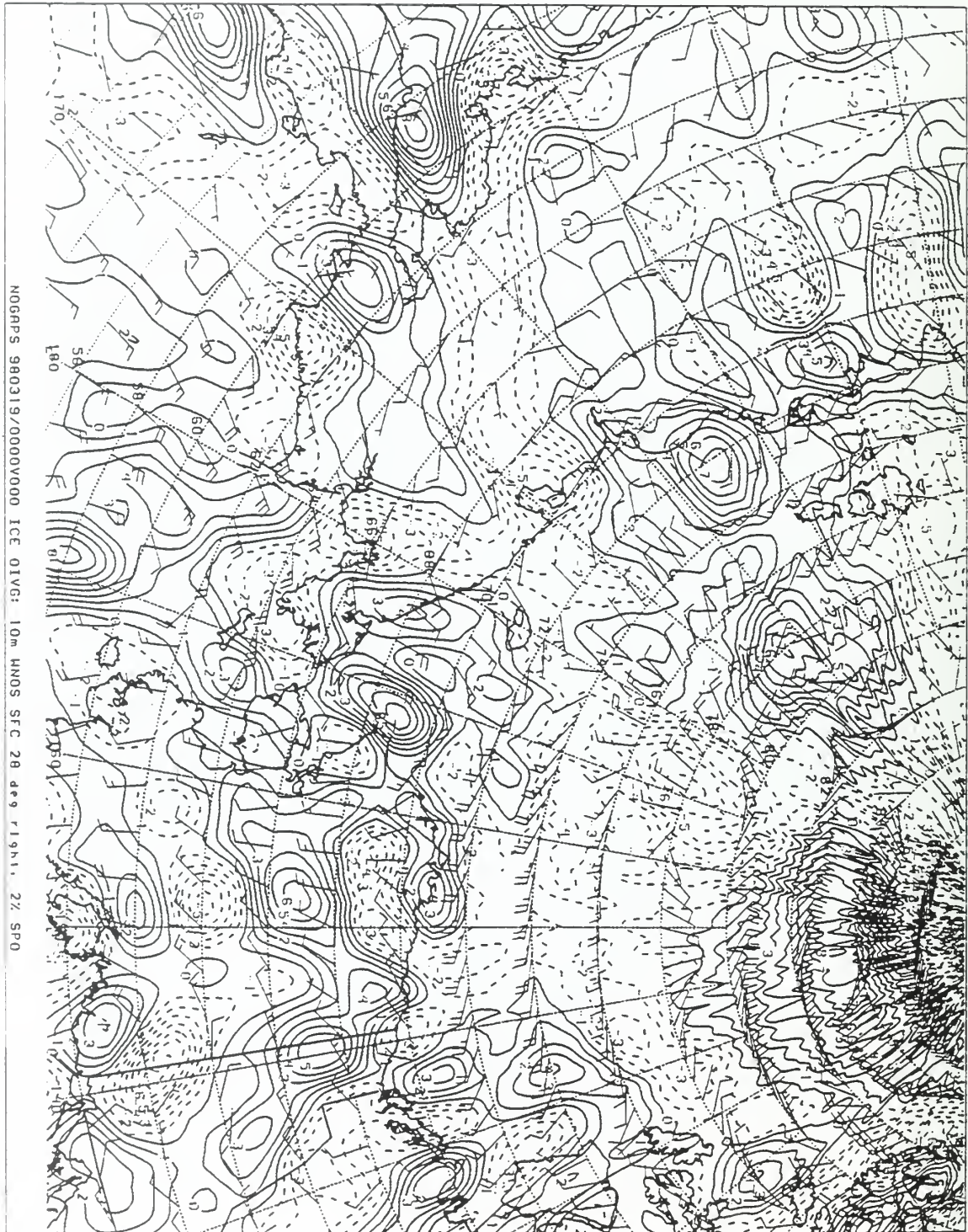


Figure 201. NOGAPS model ice divergence chart for 0000Z 19 Mar 98.



Figure 202. NOGAPS model ice divergence chart for 0000Z 20 Mar 98.

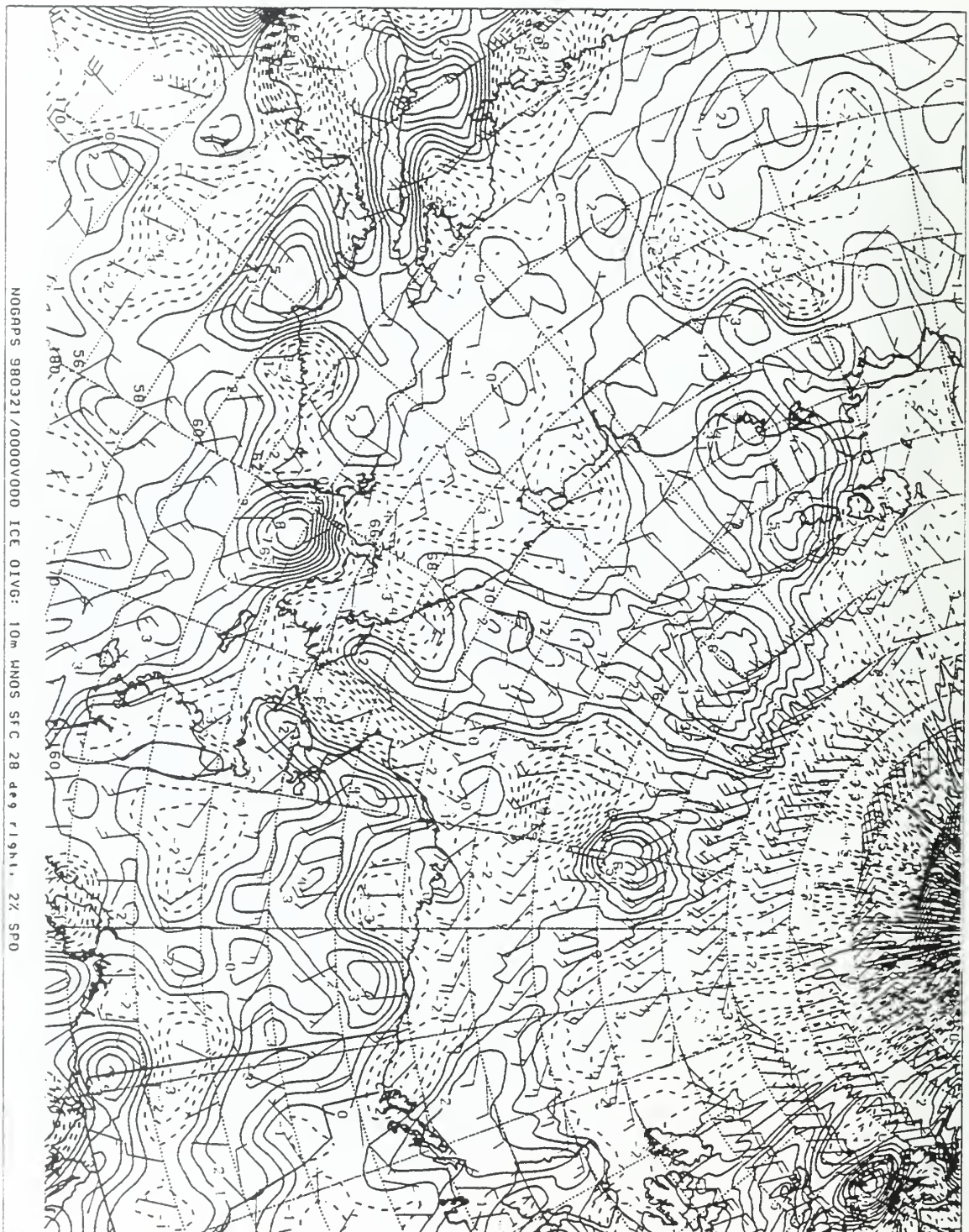


Figure 203. NOGAPS model ice divergence chart for 0000Z 21 Mar 98.

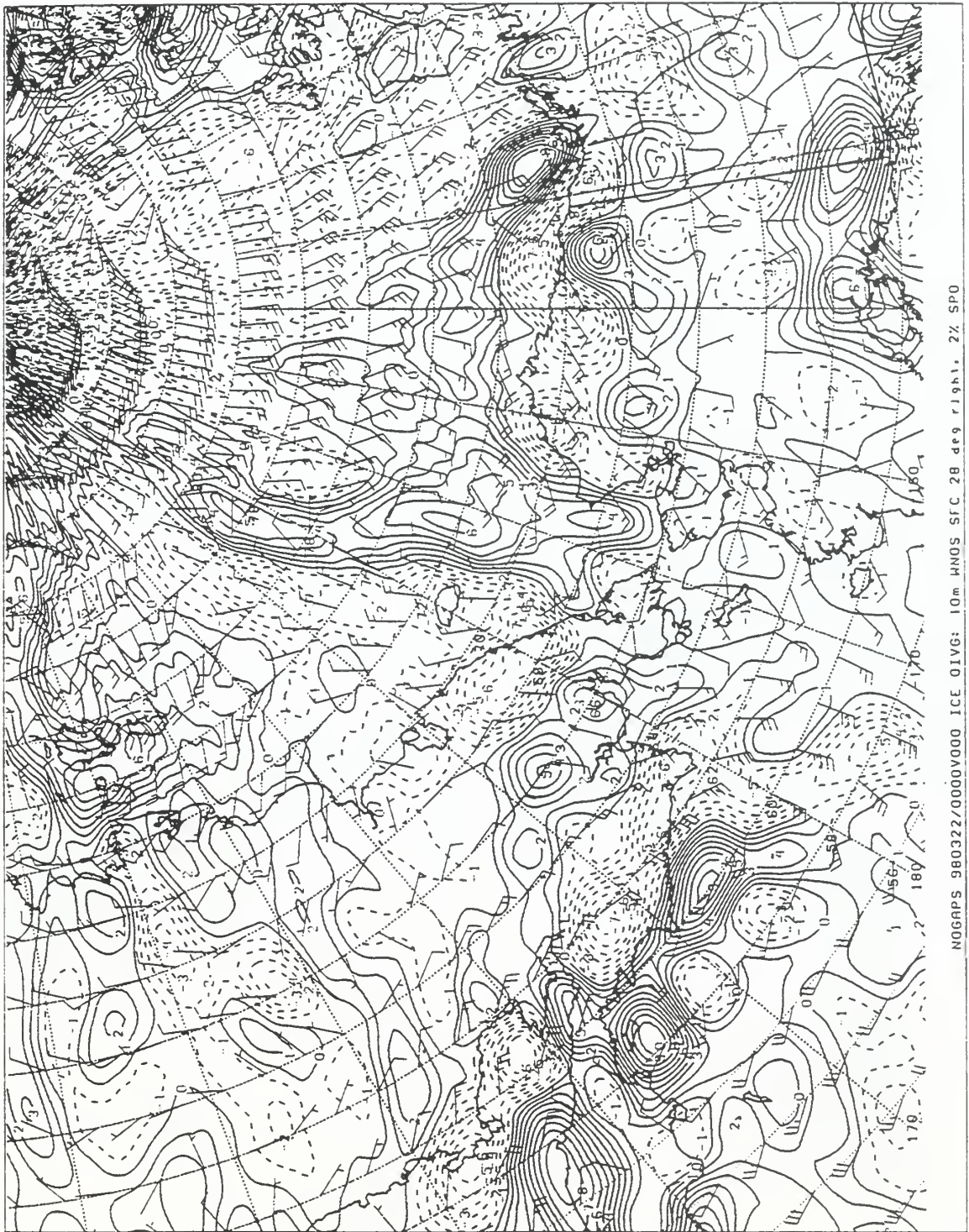


Figure 204. NOGAPS model ice divergence chart for 0000Z 22 Mar 98.

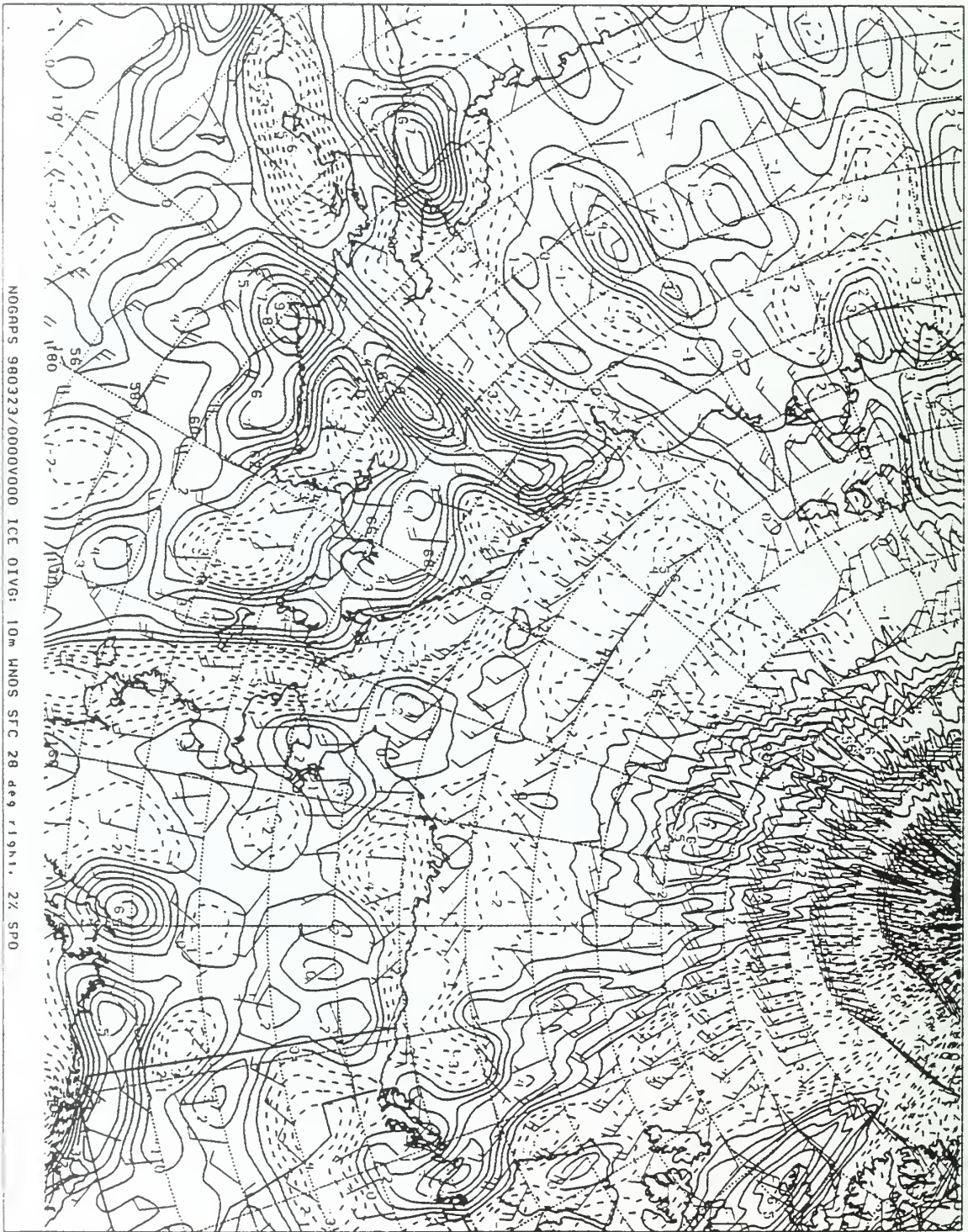


Figure 205. NOGAPS model ice divergence chart for 0000Z 23 Mar 98.

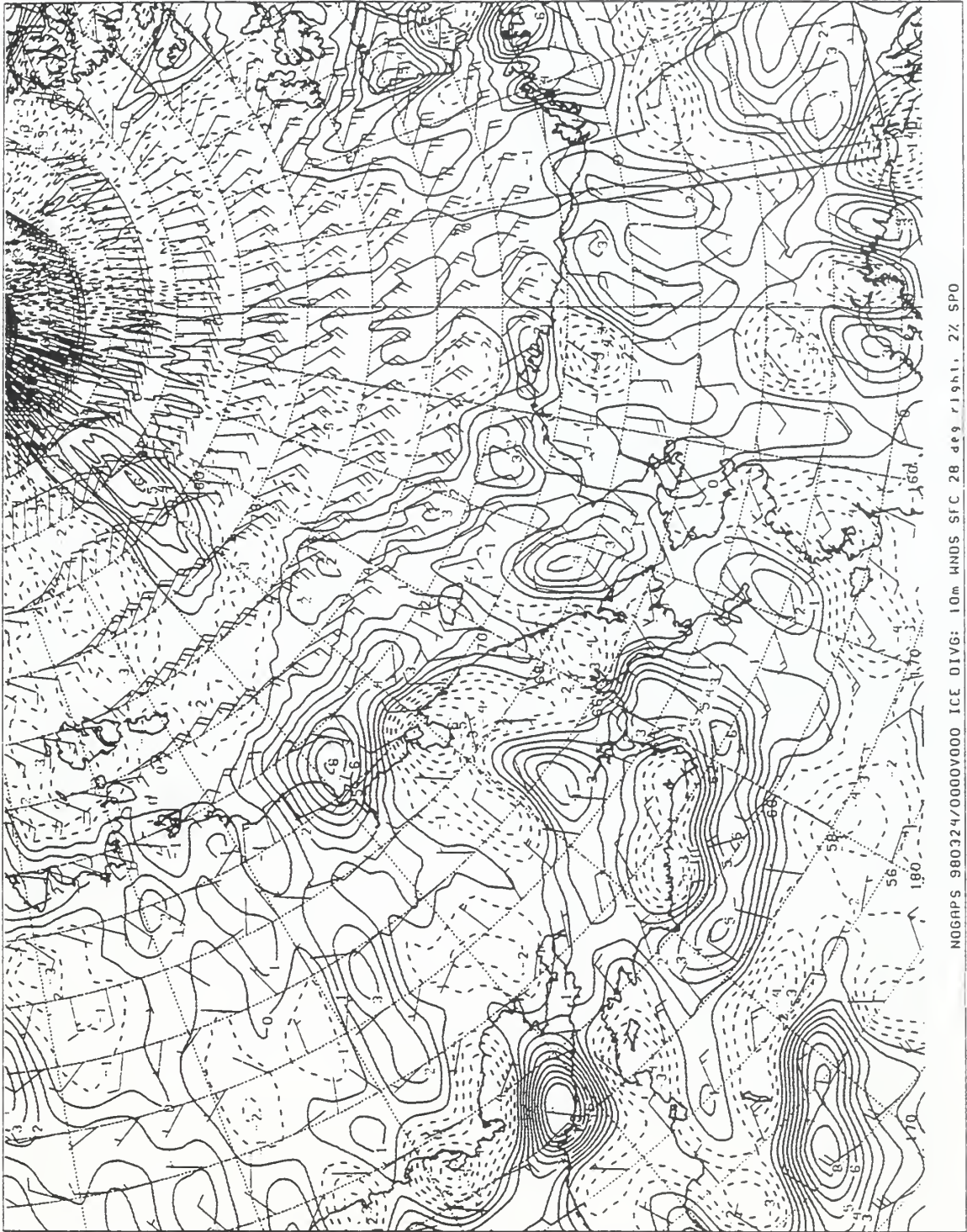


Figure 206. NOGAPS model ice divergence chart for 0000Z 24 Mar 98.

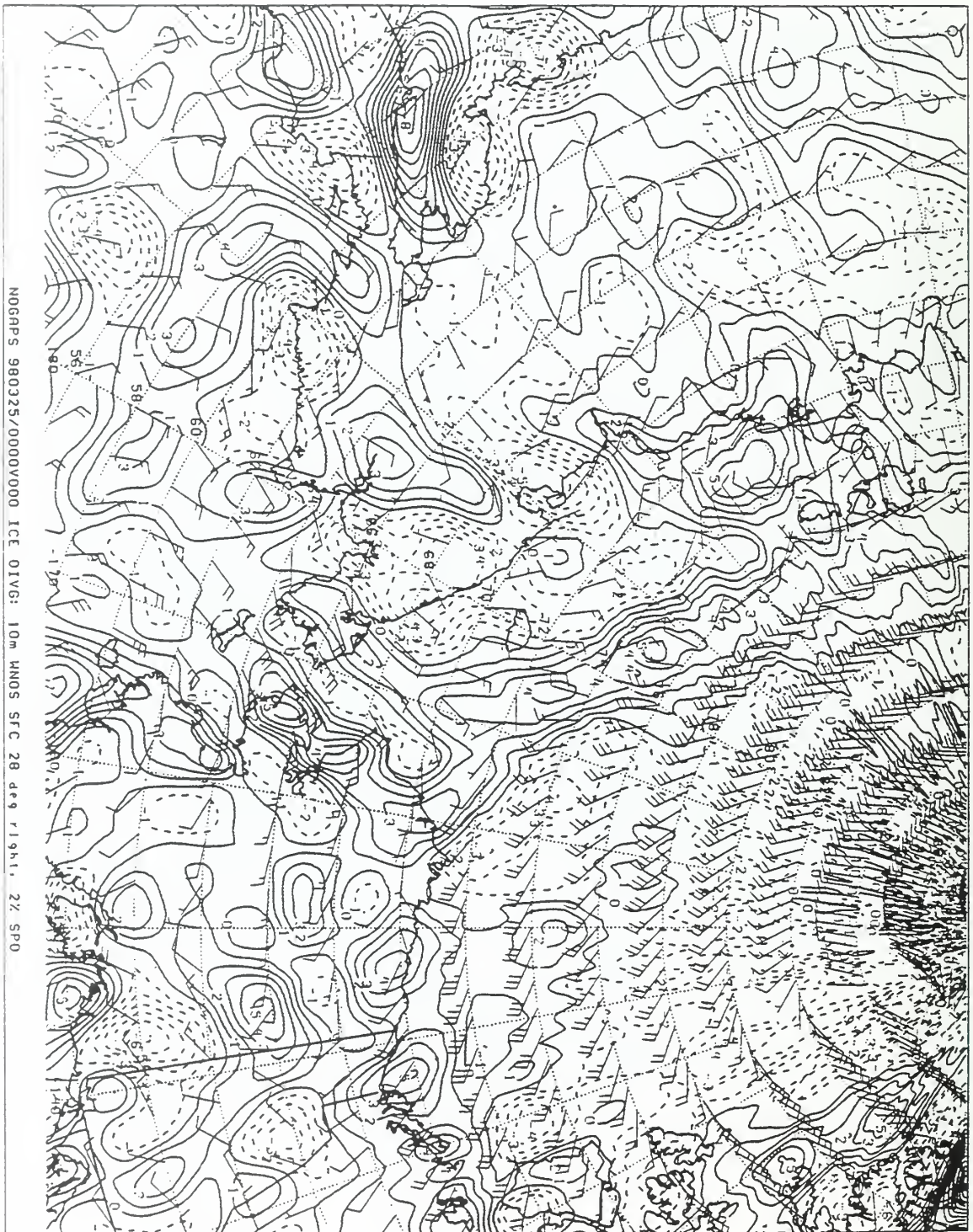


Figure 207. NOGAPS model ice divergence chart for 0000Z 25 Mar 98.

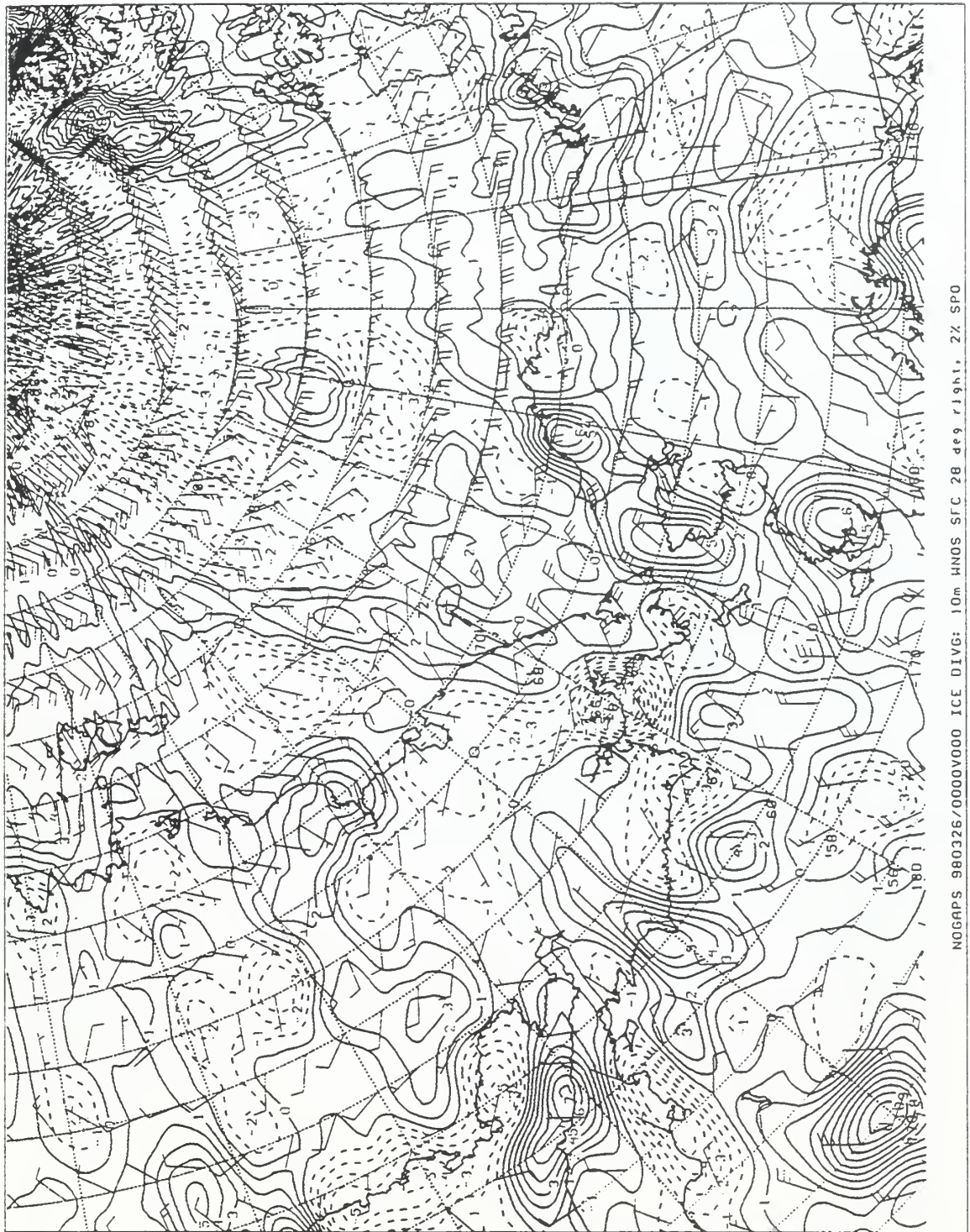


Figure 208. NOGAPS model ice divergence chart for 0000Z 26 Mar 98.

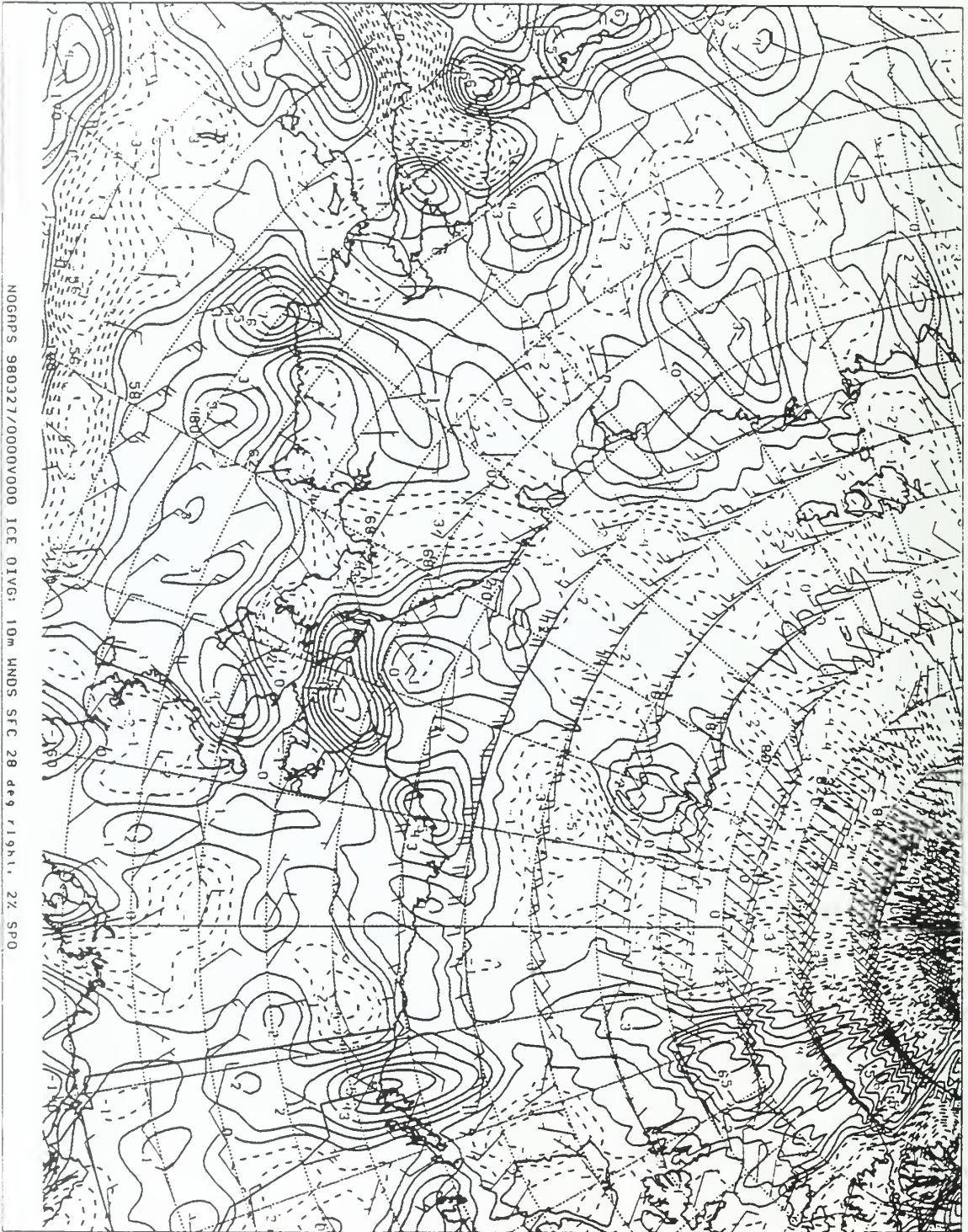


Figure 209. NOGAPS model ice divergence chart for 0000Z 27 Mar 98.



Figure 210. NOGAPS model ice divergence chart for 0000Z 28 Mar 98.

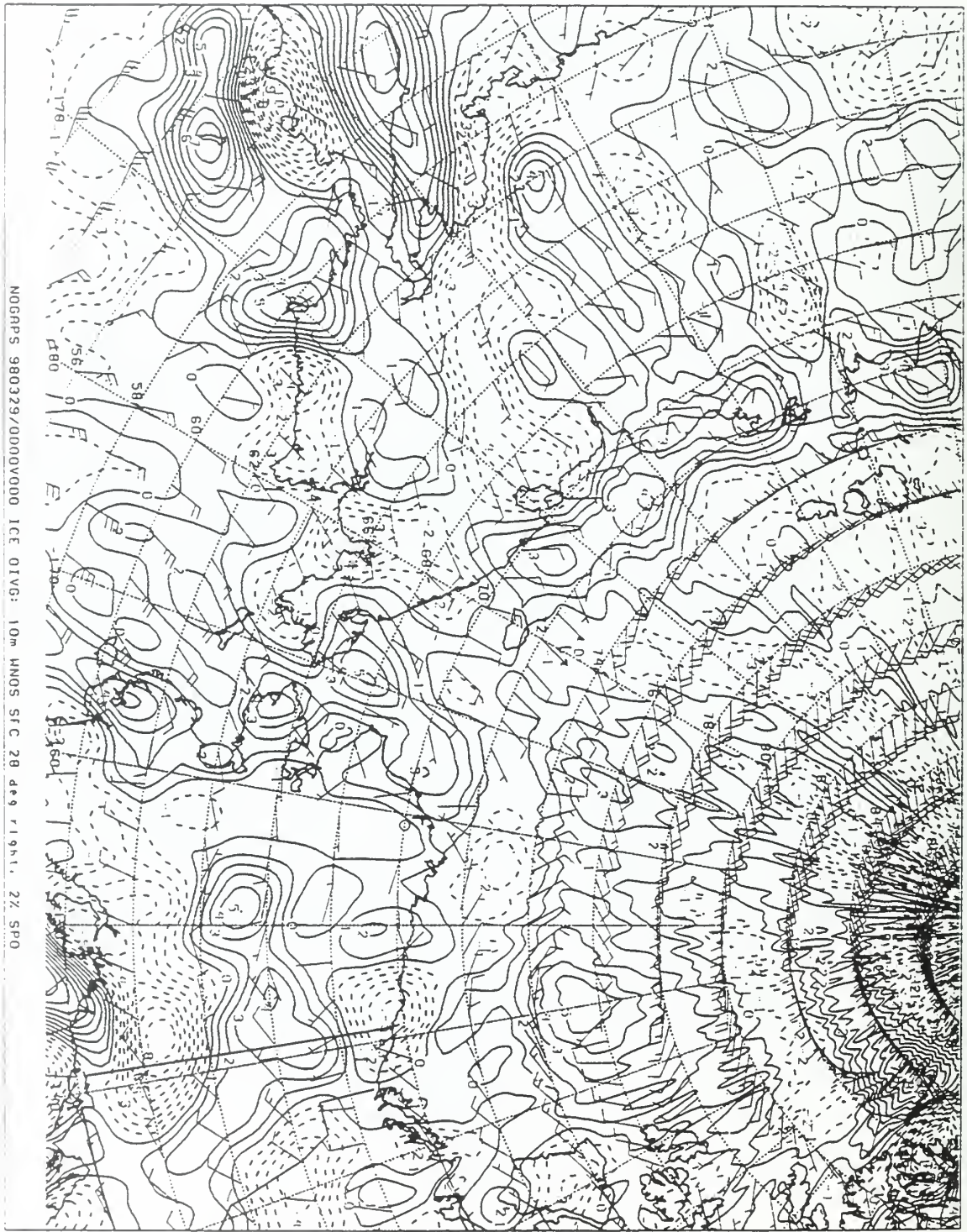


Figure 211. NOGAPS model ice divergence chart for 0000Z 29 Mar 98.

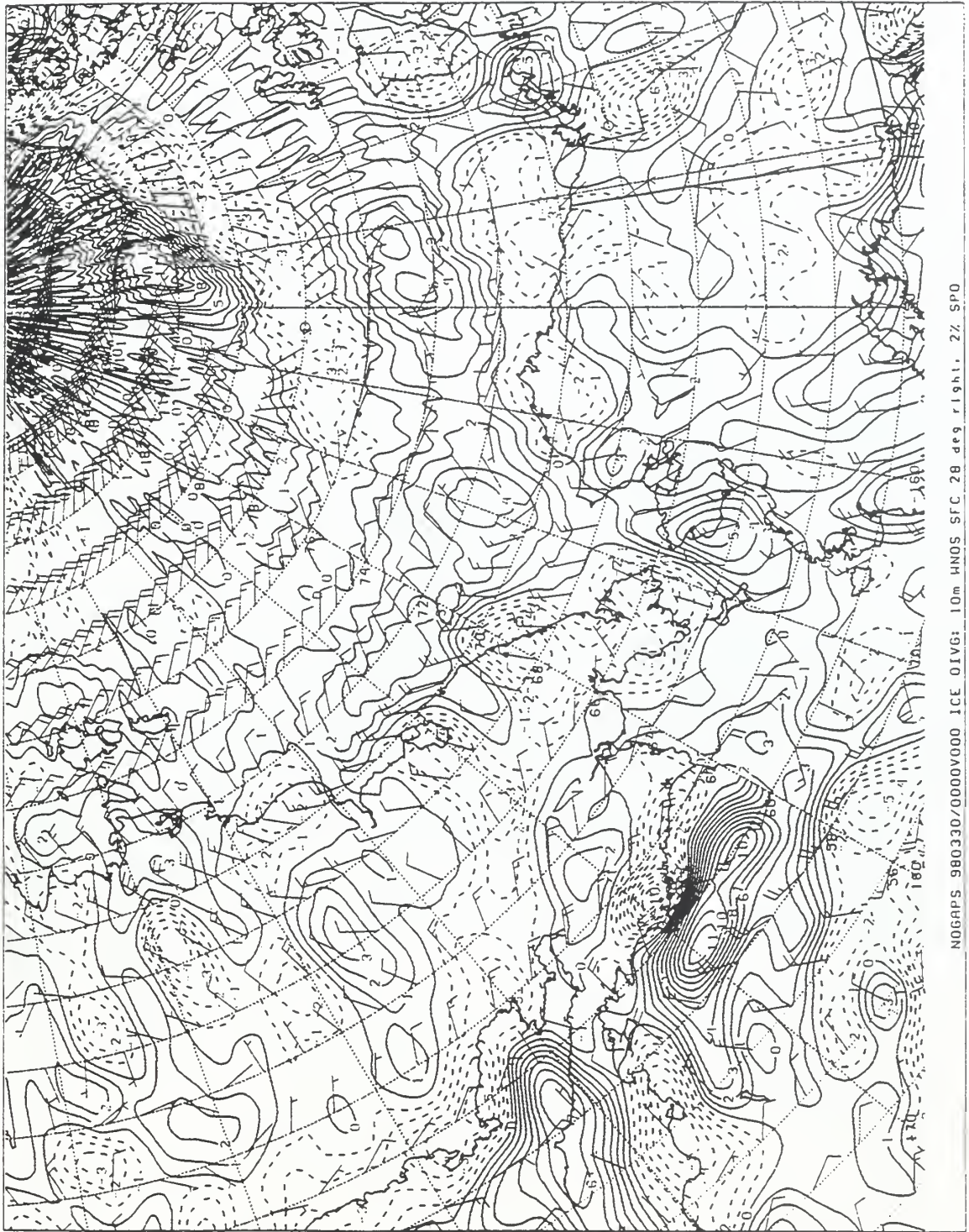


Figure 212. NOGAPS model ice divergence chart for 0000Z 30 Mar 98.

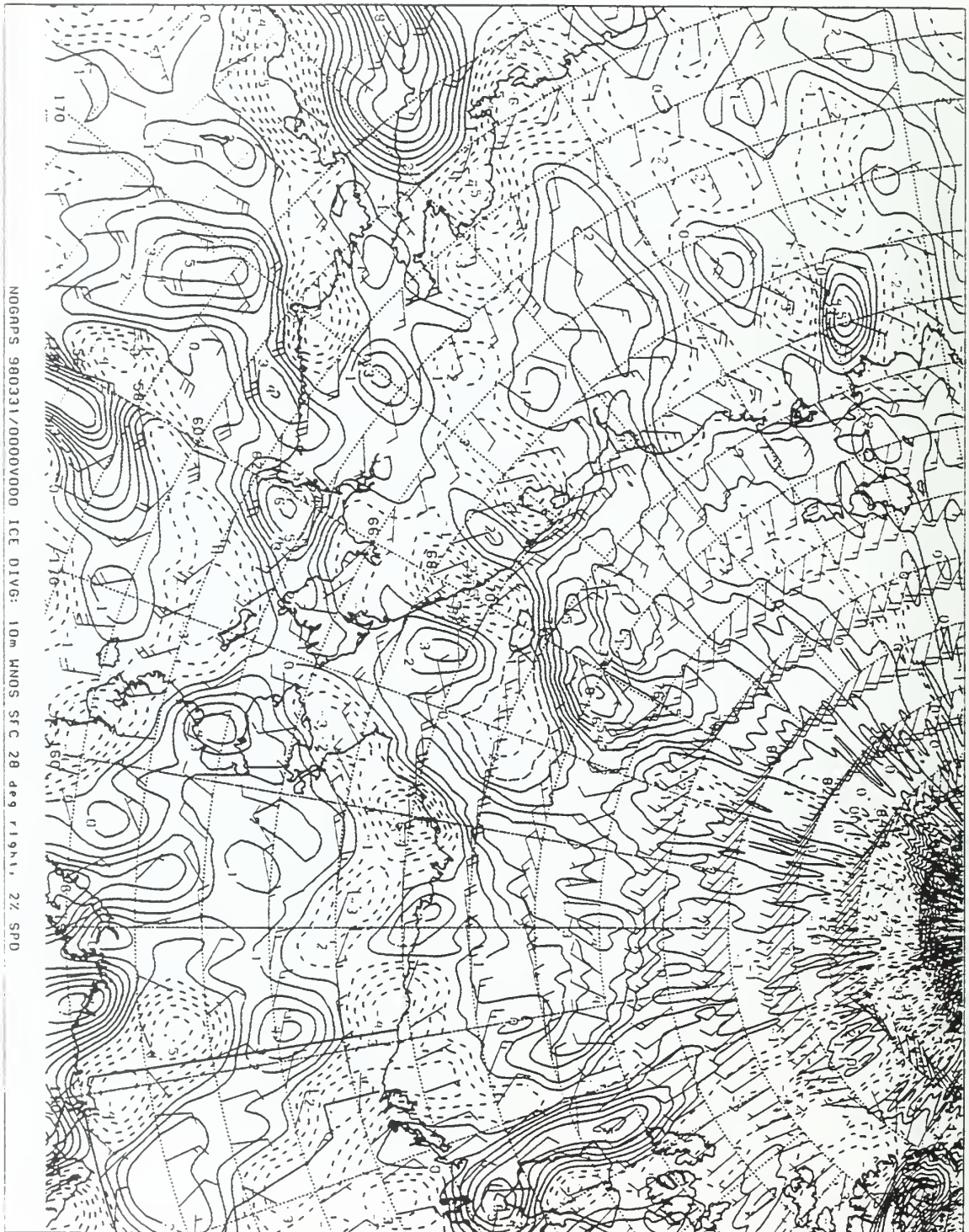


Figure 213. NOGAPS model ice divergence chart for 0000Z 31 Mar 98.

LIST OF REFERENCES

- Alaska SAR Facility Prelaunch Science Working Team, Science Plan for the Alaska SAR Facility Program, Phase 1: Data from the First European Remote Sensing Satellite, ERS-1, JPL Publication 89-14, September 1, 1989.
- Alaska SAR Facility, cited 1998: The Alaska SAR Facility. [Available on-line from <http://www.asf.alaska.edu>].
- Anderson, D. L., "Growth Rate of Sea Ice," *J. Glaciol.*, 3, 1170-1172, 1961.
- Bertoia, C., "FNMOC Uses Satellite Data in an Ice Forecast Model," *Naval Meteorology & Oceanography Command News*, 18(2), 18-19, 1998.
- Bourke, R. H. and A. R. Parsons, "Ambient Noise Characteristics of the Northwestern Barents Sea," *J. Acoust. Soc. Am.*, 94(5), 2799-2808, 1993.
- Bourke, R. H., (personal communication, 1998).
- Boyle, R and W. Lyon, "Arctic ASW: Have We Lost?" *Nav. Inst. Proceedings*, 124(6), 31-35, 1998.
- Bryan K., S. Manabe and R. Pacanowski, "A Global Ocean-Atmosphere Climate Model, Part II-The Oceanic Circulation," *J. Phys. Oceanogr.*, 5, 30-46, 1975.
- Buck, B. M. and J. H. Wilson, "Nearfield Noise Measurements from an Arctic Pressure Ridge," *J. Acoust. Soc. Am.*, 80(1), 256-264, 1986.
- Collins, D. A., "Development of a Low Frequency Ambient Noise Storm Model for the Arctic Ocean," Master's Thesis, Naval Postgraduate School, Monterey CA, December, 1996.
- Coon, M. D., S. Maykut, R. Pritchard, D. Rothrock and A. Thorndike, "Modeling the Pack Ice as an Elastic-Plastic Material," *AIDJEX Bulletin*, 24, 1-105, 1974.
- Coon, M. D., G. S. Knoke and D. C. Echert, "Compensating for Daily Lead Width Motion When Calculating Open Water Production from Weekly Data," *NWRA Report NWRA-CR-96-R158*, 1996.
- Cunningham, G. F., (personal communication, 1998).
- Curlander, J. C. and R. N. McDonough, *Synthetic Aperture Radar, Systems and Signal Processing*, John Wiley & Sons, Inc., New York, 28-44, 1991.
- Feller, D., "Environmental Forcing of Ambient Noise in the Nansen and Amundsen Basins of the Arctic Ocean," Master's Thesis, Naval Postgraduate School, Monterey CA, September, 1994.
- Fowler C., W. Emery and J. Maslanik, "The Consequences of 7-day Sampling for RADARSAT Ice Motions and Derived Fields," *NSIDC Report*, Boulder, Colorado, 1996.
- Freeman, A., NASA/JPL, cited 1998: What Is Imaging Radar? [Available on-line from <http://southport.jpl.nasa.gov/desc/imagingradarv3.html>].
- Fritsch, F., "Synoptic Atmospheric Forcing of Arctic Underice Ambient Noise," Master's Thesis, Naval Postgraduate School, Monterey CA, December, 1995.
- Greening, M. V., P. Zakarauskas and S. E. Dosso, "Matched-Field Localization for Multiple Sources in an Uncertain Environment, With Application to Arctic Ambient Noise," *J. Acoust. Soc. Am.*, 101(6), 3525-3538, 1997.

- Hibler III, W. D., "A Dynamic Thermodynamic Sea Ice Model," *J. Phys. Oceanogr.*, 9, 815-846, 1979.
- Hibler III, W. D., "Modeling a Variable Thickness Sea Ice Cover," *Monthly Weather Review*, 108, 1944-1973, 1980.
- Hibler III, W. D. and E. M. Schulson, "On Modeling Sea-Ice Fracture and Flow in Numerical Investigations of Climate," *Annals of Glaciology*, 25, 563-570, 1997.
- Hibler III, W. D., (personal communication, 1998).
- Hnatiuk J., A. Kovacs and M. Mellor, "Study of Several Pressure Ridges and Ice Islands in the Canadian Beaufort Sea," *Journal of Glaciology*, 20(84), 519-532, 1978.
- Kingsley, S. and S. Quegan, *Understanding Radar Systems*, McGraw-Hill Book Company, London, 15, 240-252, 1992.
- Kovacs A., "On Pressured Sea Ice," Paper presented at the International Sea Ice Conference, Nat. Res. Council of Iceland, Reykjavik, Iceland, 1971.
- Kwok R., J. C. Curlander, R. McConnell and S. Pang, "An Ice-motion Tracking System at the Alaska SAR Facility", *IEEE J. Oceanic Eng.*, OE-15(1), 44-54, 1990.
- Kwok R., E. Rignot, B. Holt and R. G. Onstott, "Identification of Sea Ice Type in Spaceborne SAR Data," *J. Geophys. Res.*, 97(C2), 2391-2402, 1992.
- Kwok R., D. A. Rothrock, G. F. Cunningham and H. Stern, "Determination of Ice Age: A Proposed Scheme for a RADARSAT Sea Ice Geophysical Processor System," *IEEE Trans. Geosci. Remote Sens.*, 32(2), 1750-1752, 1994.
- Kwok R., D. A. Rothrock, H. L. Stern and G. F. Cunningham, "Determination of the Age Distribution of Sea Ice from Lagrangian Observations of Ice Motion," *IEEE Trans. Geosci. Remote Sens.*, 33(2), 392-400, 1995.
- Kwok R. and T. Baltzer, "The Geophysical Processor System at the Alaska SAR Facility," *Photogrammetric Engineering & Remote Sensing*, 61(12), 1445-1453, 1995.
- Kwok R., "The RADARSAT Geophysical Processor System," Unpublished manuscript, 1997.
- Kwok, R., "RGPS Status and Overview," RADARSAT Geophysical Processor System Working Group Meeting, Pasadena, CA, NASA Jet Propulsion Laboratory, 1998.
- Kwok, R., (personal communication, 1997).
- La Belle-Hamer, N., "RGPS Data Coverage," RADARSAT Geophysical Processor System Working Group Meeting, Pasadena, CA, NASA Jet Propulsion Laboratory, 1998.
- Langley, A. J., "Acoustic Emission from the Arctic Ice Sheet," *J. Acoust. Soc. Am.*, 85(2), 692-701, 1989.
- Lebedev V. V., "Rost l'do v arkticheskikh rekakh i moriakh v zavisimosti ot otritsatel'nykh temperatur vozdukh," *Problemy Arktiki*, 5, 9-25, 1938, (no translation available).
- McLaren A. S., "The Under-Ice Thickness Distribution of the Arctic Basin as Recorded in 1958 and 1970," *J. Geophys. Res.*, 94(C4), 4971-4983, 1989.

- Makris, N. C. and I. Dyer, "Environmental Correlates of Pack Ice Noise," *J. Acoust. Soc. Am.*, 79(3), 1434-1440, 1986.
- Manabe, S., K. Bryan and M. Spelman, "A Global Ocean-Atmosphere Climate Model with Seasonal Variation for Future Studies of Climate Sensitivity," *Dynamics of Atmosphere and the Ocean*, 3, 393-426, 1979.
- Maslowski, W., (personal communication, 1998).
- Maykut, G. A., "The Surface Heat and Mass Balance," in *The Geophysics of Sea Ice*, Norbert Untersteiner, Ed., Plenum Press, New York, 395-463, 1986.
- Maykut, G. A. and N. Untersteiner, "Some Results from a Time-Dependent Thermodynamic Model of Sea Ice," *J. Geophys. Res.*, 76, 1550-1575, 1971.
- Newton, G. B. and J. F. Coles, "Thin Ice Feature Distribution Study, Final Report." Analysis & Technology, Inc. report prepared for Commander, Naval Sea Systems Command, 1991.
- Oard, V. T., "Characteristic Spectral Signatures of Arctic Noise Generating Mechanisms," Master's Thesis, Naval Postgraduate School, Monterey, CA, June, 1987.
- Onstott R. G., R. K. Moore and W. F. Weeks, "Surface-based Scatterometer Results of Arctic Sea Ice," *IEEE Trans. Geosci. Electron.*, GE-17(3), 78-85, 1979.
- Onstott R. G., R. K. Moore, S. P. Gogineni and C. V. Delker, "Four Years of Low Altitude Sea Ice Broadband Backscatter Measurements," *IEEE J. Oceanic Eng.*, OE-7(1), 44-50, 1982.
- Parkinson, C. L. and W. Washington, "A Large-Scale Numerical Model of Sea Ice," *J. Geophys. Res.*, 84, 311-337, 1979.
- Parmerter R. R. and M. Coon, "Model of Pressure Ridge Formation in Sea Ice," *J. Geophys. Res.*, 77, 6565-6575, 1972.
- Parsons, A. R., "Environmental Forcing of Ambient Noise in the Barents Sea," Master's Thesis, Naval Postgraduate School, Monterey CA, June, 1992.
- Pollak, K., (personal communication, 1998).
- Preller, R. H. and P. G. Posey, "The Polar Ice Prediction System – A Sea Ice Forecasting System," *NORDA Report 212*, April, 1989.
- Pritchard, R. S., "Arctic Ocean Background Noise Caused by Ridging of Sea Ice," *J. Acoust. Soc. Am.*, 75(2), 419-427, 1984.
- Pritchard, R. S., "Sea Ice Noise-Generating Mechanisms," *J. Acoust. Soc. Am.*, 88(6), 2830-2842, 1990.
- Reimnitz E., D. Dethleff and D. Nuernberg, "Contrasts in Arctic Ice Shelf Sea-Ice Regimes and Some Implications: Beaufort Sea versus Laptev Sea," *Marine Geology* 119, 215-225, 1994.
- Riedlinger S. H. and R. H. Preller, "The Development of a Coupled Ice-Ocean Model for Forecasting Ice Conditions in the Arctic," *J. Geophys. Res.*, 96(C9), 16955-16977, 1991.
- Rothrock, D. A., "The Energetics of the Plastic Deformation of Pack Ice by Ridging," *J. Geophys. Res.*, 80, 4514-4519.

Sandia National Laboratories, cited 1997: How SAR Works [Available on-line from http://www.sandia.gov/RADAR/sar_sub/sar_intro1.htm].

Science Applications International Corporation, "Arctic Ambient Noise Prediction System: Users and Operations Manual," SAIC Technical Report I-425-03-663, 1988

Semtner, A. J. Jr, "A Model for the Thermodynamic Growth of Sea Ice in Numerical Investigations of Climate," J. Phys. Oceano., 6, 379-389, 1976.

Stern, H. L., "RGPS Error Analysis," RADARSAT Geophysical Processor System Working Group Meeting, Pasadena, CA, NASA Jet Propulsion Laboratory, 1998.

Thorndike A. S. and R. Colony, "Sea-Ice Motion in Response to Geostrophic Winds", J. Geophys. Res., 87, 5845-5852, 1982.

Thorndike A. S., D. Rothrock, G. Maykut and R. Colony, "The Thickness Distribution of Sea Ice," J. Geophys. Res., 80, 4501-4513, 1975.

Tucker W. B. III, W. F. Weeks and M. Frank, "Sea Ice Ridging Over the Alaskan Continental Shelf," J. Geophys. Res., 84(C8), 4885-4897, 1979.

Urick, R. J., *Principles of Underwater Sound*, McGraw-Hill Book Company, New York, 209-210, 1983.

Wadhams P. and T. Davy, "On the Spacing and Draft Distribution for Pressure Ridge Keels," J. Geophys. Res., 91(C9), 10697-10708, 1986.

Washington, W. M., A. Semtner, C. Parkinson and L. Morrison, "On the Development of a Seasonal Change Sea Ice Model," J. Phys. Oceanogr., 6, 679-685, 1976.

Wiley, C. A., "Pulsed Doppler Radar Methods and Apparatus," United States Patent, No. 3,196,436, (filed August 1954), 1965.

Wilson, J. H. and R. S. Veenhuis, "Shallow Water Beamforming with Small Aperture, Horizontal Towed Arrays," J. Acoust. Soc. Am., 101(1), 384-394, 1997.

Wilson, J. H., (personal communication, 1998).

Zubov, N. N., "L'dy Arktiki," ("Arctic Ice"), Translation by the U.S. Navy Oceanographic Office, 1943.

INITIAL DISTRIBUTION LIST

		No. Copies
1.	Defense Technical Information Center..... 8725 John J. Kingman Rd, STE 0944 Ft. Belvoir, VA 22060-6218	2
2.	Dudley Knox Library..... Naval Postgraduate School 411 Dyer Rd Monterey, CA 93943-5101	2
3.	Chairman (Code OC/Bf)..... Department of Oceanography Naval Postgraduate School Monterey, CA 93943-5122	3
4.	Dr. James H. Wilson..... Neptune Sciences, Inc. 3834 Vista Azul San Clemente, CA 92674	3
5.	Dr. Peter S. Guest (Code MR/Gs)..... Department of Meteorology Naval Postgraduate School Monterey, CA 93943-5114	1
6.	Dr. William D. Hibler (Code OC/Hi)..... Department of Oceanography Naval Postgraduate School Monterey, CA 93943-5122	1
7.	Dr. Ronald Kwok JPL, California Institute of Technology M/S 300-235 4800 Oak Grove Drive Pasadena, CA 91109	1
8.	Dr. D. Andrew Rothrock..... Polar Science Center, Applied Physics Laboratory University of Washington 1013 N. E. 40 th Street Seattle, WA 98105	1

9. Dr. Harry Stern.....1
 Polar Science Center, Applied Physics Laboratory
 University of Washington
 1013 N. E. 40th Street
 Seattle, WA 98105

10. Dr. Robert S. Pritchard1
 Ice Casting, Inc.
 20 Wilson Court
 San Rafael, CA 94901-1230

11. Dr. Ruth Preller1
 Naval Research Laboratory (Code 7322)
 Stennis Space Center
 Bay St. Louis, MS 39579

12. Commanding Officer1
 Fleet Numerical Meteorology and Oceanography Center
 7 Grace Hopper Ave. Stop 1
 Monterey, CA 93943-5005
 Attn: Mr. Kenneth Pollak

13. Commanding Officer1
 Naval Ice Center, Suitland
 Washington, DC 20373

14. Office of Naval Research.....2
 800 N. Quincy St.
 Arlington, VA 22217-5660
 Attn: Dr. Dennis Conlon Code 322
 Dr. Thomas Curtin Code 322 HL

15. LCDR Marcus M. Speckhahn, USN2
 1133 Miramonte Glen
 Escondido, CA 92026

3 483NP6 2524
TH
10/99 22527-200

DUDLEY KNOX LIBRARY
NAVAL POSTGRADUATE SCHOOL
MONTEREY CA 93943-5101

DUDLEY KNOX LIBRARY



3 2768 00365910 3